RUSSIAN ACADEMY OF SCIENCES

INSTITUTE FOR PROBLEMS IN MECHANICAL ENGINEERING

Proceedings of the XXXIX Summer School – Conference

ADVANCED PROBLEMS IN MECHANICS

A P M 2 0 1 1

St. Petersburg (Repino)

July 1 – 5, 2011

`http://apm-conf.spb.ru`

St. Petersburg, 2011

GENERAL INFORMATION SCIENTIFIC COMMITTEE AND EDITORIAL BOARD

- **H. Altenbach** (Martin-Luter University Halle Wittenberg, Germany)
- **V. V. Beletsky** (Keldysh Institute of Applied Mathematics RAS, Moscow, Russia)
- **A. K. Belyaev** (IPME RAS, St. Petersburg, Russia)
- **E. K. Bezoyan** (Yerevan State University, Armenia)
- **I. I. Blekhman** (IPME RAS, Mekhanobr-tekhnika Corp., St. Petersburg, Russia)
- **M. Cartmell** (University of Glasgow, UK)
- **A. Castellanos** (University of Seville, Spain)
- **E. P. Chen** (Sandia National Laboratories, Livermore, USA)
- **V. A. Eremeyev** (Southern Scientific Center of RAS, Rostov State University, Rostov-on-Don, Russia)
- **A. B. Freidin** (IPME RAS, St. Petersburg, Russia)
- **S. N. Gavrilov** (IPME RAS, St. Petersburg, Russia)
- **J. Goddard** (University of California at San Diego, USA)
- **I. G. Goryacheva** (Institute for Problems in Mechanics RAS, Moscow, Russia)
- **E. F. Grekova** (IPME RAS, St. Petersburg, Russia)
- **D. Harris** (University of Manchester, UK)
- **D. A. Indeitsev** (IPME RAS, St. Petersburg, Russia) — *Co-Chairman*
- **H. Irschik** (Johannes Kepler University of Linz, Austria)
- **B. L. Karihaloo** (Institute of Theoretical, Applied and Computational Mechanics, UK)
- **A. M. Krivtsov** (St. Petersburg State Polytechnical University, IPME RAS, Russia) — *Co-Chairman*
- **O. S. Loboda** (St. Petersburg State Polytechnical University, IPME RAS, Russia) — *Scientific Secretary*
- **E. V. Lomakin** (Moscow State University, Russia)
- **A. Metrikine** (TU Delft, The Netherlands)
- **N. F. Morozov** (St. Petersburg State University, IPME RAS, Russia)
- **V. A. Palmov** (St. Petersburg State Polytechnical University, Russia)
- **E. Pavlovskaia** (University of Aberdeen, UK)
- **S. H. Sargsyan** (National Academy of Sciences, Armenia)
- **E. N. Vilchevskaya** (St. Petersburg State Polytechnical University, IPME RAS, Russia)
- **V. A. Vladimirov** (University of Hull, UK)
- **M. Wiercigroch** (University of Aberdeen, UK)
- **M. V. Zakrzhevsky** (Institute of Mechanics Riga Technical University, Latvia)

© IPME RAS, 2011

PREFACE

Dear Reader,

in this book you will find the Proceedings of the Summer School Conference "Advanced Problems in Mechanics (APM) 2011". The conference had been started in 1971. The first Summer School was organized by Prof. Ya.G. Panovko and his colleagues. In the early years the main focus of the School was on nonlinear oscillations of mechanical systems with a finite number of degrees of freedom. Since 1994 the Institute for Problems in Mechanical Engineering of the Russian Academy of Sciences organizes the Summer School. The traditional name of "Summer School" has been kept, but the topics covered by the School have been much widened, and the School has been transformed into an international conference. Now it is held under the patronage of the Russian Academy of Sciences. The topics of the conference cover now almost all fields of mechanics, being concentrated around the following main scientific directions:

— aerospace mechanics;
— computational mechanics;
— dynamics of rigid bodies and multibody dynamics;
— fluid and gas;
— mechanical and civil engineering applications;
— mechanics of media with microstructure;
— mechanics of granular media;
— nanomechanics;
— nonlinear dynamics, chaos and vibration;
— molecular and particle dynamics;
— phase transitions;
— solids and structures;
— wave motion.

The Summer School – Conference has two main purposes: to gather specialists from different branches of mechanics to provide a platform for cross-fertilization of ideas, and to give the young scientists a possibility to learn from their colleagues and to present their work. Thus the Scientific Committee encouraged the participation of young researchers, and did its best to gather at the conference leading scientists belonging to various scientific schools of the world.

We believe that the significance of Mechanics as of fundamental and applied science should much increase in the eyes of the world scientific community, and we hope that APM conference makes its contribution into this process.

We are happy to express our sincere gratitude for a partial financial support to Russian Foundation for Basic Research, Russian Academy of Sciences, and St. Petersburg Scientific Center. This support has helped substantially to organize the conference and to increase the participation of young researchers.

We hope that you will find the materials of the conference interesting, and we cordially invite you to participate in the coming APM conferences. You may find the information on the future "Advanced Problems in Mechanics" Schools Conferences at our websites:

`http://apm-conf.spb.ru`

With kind regards,

Co-Chairmens of APM 2011

Dmitri A. Indeitsev, Anton M. Krivtsov

Contents

E. L. Aero, A. N. Bulygin, Yu. V. Pavlov. Functionally invariant solutions of the double sine-Gordon equation 10

S. M. Aizikovich, A. S. Vasiliev, S. S. Volkov, L. N. Evich. Effective analytical solution method of contact problems for materials with functionally-graded coatings 21

A. A. Alabuzhev, A. A. Ogleznev. The non-linear oscillations of two bubbles in a volume of incompressible liquid 24

A. A. Alabuzhev. Instability of thin film on substrate in vibration filed 29

A. A. Alabuzhev, D. V. Lyubimov. Oscillations of an oblate drop 32

A. Al-Shyyab, A. F. Khadrawi. Transient hydrodynamics behavior of fluid flow in micro- converging plates 40

A. R. Arutyunyan, R. A. Arutyunyan, K. S. Yakimova. The energy approach to the solution of the high cycle fatigue problem 48

A. R. Arutyunyan, R. A. Arutyunyan. The strength of non linear elastic medium with a crack 53

M. B. Atmanskikh, A. Y. Botalov, P. T. Zubkov. Numerical investigation of shock waves damping in perfect viscous gas 58

J. M. Balthazar, J. L. P. Felix. On a Dynamic absorbers to Eletro-mechanical systems, including nonlinear phenomena in Macro, Mems and Nems scales 68

N. V. Banichuk, S. Yu. Ivanova, E. V. Makeev, A. V. Sinitsin. New approach for contact optimization problems with friction and wear 80

I. Blekhman. Oscillatory strobodynamics - an overview of advances and new results . 87

I. I. Blekhman, K. S. Ivanov. On a vibroimpact system in which chaos is caused by the rare attractor packing 95

S. A. Chivilikhin, I. Yu. Popov, V. V. Gusarov. Planar flows in nanoscale regions 101

A. I. Dmitriev, W. Österle, H. Kloß. About the influence of automotive brake pad composition on frictional performance. Results of nano-scale modeling 106

A. I. Dmitriev, A. Yu. Nikonov, V. P. Kuznetsov. The features of structure transformation caused by nano-burnishing process 114

A. Dobroskok, A. M. Linkov. Numerical approach to interpretation of acoustic emission occurring at different scales 121

M. Dosta, S. Antonyuk, S. Heinrich. Usage of a DEM approach for the modeling of fluidised bed agglomeration process 127

A. Ershova, S. Antonyuk, S. Heinrich, N. Menshutina. Population balance modeling of aerogel particles coating in fluidized bed 132

A. Ershova, S. Antonyuk, S. Heinrich, N. Menshutina. Influence of the particle properties on the fluidized bed dynamics during aerogel coating 138

A. N. Fedorova, M. G. Zeitlin. Dynamical aperture beyond perturbations: strong localization approach 145

M. Yu. Filimonov, N. A. Vaganova. Permafrost defrosting as a result of extractive wells operating 152

R. A. Filippov, A. B. Freidin, E. N. Vilchevskaya. On transition layers in nanocomposites as new phase areas 158

N. Förster, S. Palis, F. Palis. Load stabilisation of boom cranes on maritime vessels .. 168

L. Fries, S. Antonyuk, S. Heinrich, S. Palzer. Comparison of a spouted bed and a Wurster-coater using DEM-CFD simulations 175

O. K. Garishin, S. N. Lebedev. Simulation of elastic and plastic properties of polymeric composites with silicate lamellar nanofiller 185

L. A. Golotina. Simulation of failure processes of coarse grained elastomeric composites using a structural model 191

E. F. Grekova. Soils in terms of nonlinear elastic reduced Cosserat medium: small perturbations near a spherical prestressed state 195

E. F. Grekova. Elastic reduced Cosserat continuum by eyes of a "rotation blind" person 202

R. V. Guchinskiy, S. V. Petinov. Fatigue of fillet-welded joint assessment by the FEA simulation of damage accumulation 205

K. Ivanov. Modeling and optimization of vibrational screening process 213

A. A. Kireenkov. Generalized models of sliding and spinning friction 219

A. Karmazin, E. Kirillova, W. Seemann, P. Syromyatnikov. Identification of cracks in composite materials 227

V. A. Kocheryzhkin. Weakly-compressible SPH for viscous fluid flow 235

A. M. Kolesnikov. Radial deformation of cylindrical membrane 238

V. M. Kolykhalin. Dipole interaction of wagon wheels knock at the off-center railway 244

Ig. S. Konovalenko, A. Yu. Smolin, A. Yu. Nikonov, S. G. Psakhie. Multilevel approach to description of deformation and fracture of brittle materials with hierarchical porous structure on the basis of movable cellular automaton method 249

Iv. S. Konovalenko, K. P. Zolnikov, S. G. Psakhie. Molecular dynamics investigation of deformation response of thin-film metallic nanostructures under heating 256

A. S. Korlyakov. Modeling microstructural stresses in polymer-silicate nanocomposite with the influence of spherulitic structures 264

O. O. Kovalev, V. A. Kuzkin. Analytical expressions for bulk moduli and frequencies of volumetrical vibrations of fullerenes C_{20} and C_{60} 269

A. S. Kuleshov, M. Hubbard, D. L. Peterson, G. Gede. On the motion of the Oloid toy 275

G. M. Kuziomkina, O. I. Yakubovich, A. O. Shimanovsky, Yu. M. Pleskachevskii. The influence of cohesion between the materials on stress-strain condition of reinforced

composite 283

A. M. Linkov. On numerical simulation of hydraulic fracturing 291

T. A. Khantuleva, A. V. Litvinov. Evolution of nonstationary waves in the condensed medium 297

H. Mahbadi, M. R. Eslami. Ratchetting of spherical vessels 304

N. V. Makarova. Relation between structural parameters and abrasion in multiphase matrix–cement materials 314

M. A. Mazo, E. B. Gusarova, T. P. Tovstik, N. K. Balabaev. MD calculation mechanical properties of Fluorographene 318

J. Neuwirth, S. Antonyuk, S. Heinrich, M. Jacob. Process parameter study of a fluid bed rotor processor via CFD-DEM simulations 326

I. Neygebauer. MAC model for the linear elasticity theory 336

A. Yu. Nikonov, A. I. Dmitriev, S. G. Psakhie. Molecular-dynamic investigation of contact interaction of pure metals 343

E. A. Podolskaya, A. Yu. Panchenko, A. M. Krivtsov. Stability of 2D triangular lattice under finite biaxial strain 350

E. A. Podolskaya, A. Yu. Panchenko, K. S. Bukovskaya. Influence of shear strain on stability of 2D triangular lattice 358

A. G. Pelevin, A. L. Svistkov. Mechanical properties of polymer nanocomposites based on styrene butadiene rubber with different types of fillers 364

M. Perelmuter. Mechanical modelling of nanotube-polymer adhesion 371

A. V. Porubov, B. R. Andrievsky. Nonlinear dynamic variations in internal structure of a complex lattice 379

E. V. Prozorova. Influence of the dispersion in nonequilibrium models for continuous mechanics . . . 385

A. Linkov, L. Rybarska-Rusinek. Asymptotics of fields near common apex of functionally graded wedge(s) . . . 393

L. M. Margaryan, S. H. Sargsyan. Mathematical model of dynamics of micropolar anisotropic elastic thin bars with free rotation . . . 399

V. V. Smirnov, D. S. Shepelev, L. I. Manevitch. Localization of bending vibrations in the single-wall carbon nanotubes . . . 407

A. O. Shimanovsky, M. G. Kuznetsova, Yu. M. Pleskachevskii. Computer modeling of liquid sloshing in road tanker reservoirs . . . 412

I. V. Smirnov, Yu. V. Sudenkov. Quasi-static and dynamic studies of cracks dynamics in plates of PMMA . . . 418

M. N. Smirnova, A. V. Zvyaguin. Boundary effects on thin body motion in fluid or gas 423

N. N. Smirnov, V. F. Nikitin, V. R. Dushin, V. A. Nerchenko, N. V. Korolkova. Transition processes in non-uniform media combustion mathematical modeling and computer simulations . . . 434

A. Yu. Smolin, N. V. Roman, K. P. Zol'nokov, S. G. Psakhie, V. K. Kedrinskii. Simulation of structural transformations in copper nanoparticles under collision . . . 453

V. S. Sorokin. Compressibility as the main effect explaining why gas bubbles can sink in an oscillating fluid . . . 458

V. V. Struzhanov, N. V. Burmasheva. Newton-Kantorovich method of parametres' characterization of equilibrium of the system which realizes the triaxial strenght of the cube made from the nonlinear material with non-convex potencial . . . 468

M. A. Al-Nimr, S. E. Al-Lubani, A. F. Khadrawi. Effect of the Higher Order Terms on the Thermal Behaviour of Thin Layer Slab Under the Effect of Hyperbolic Heat Conduction Model . . . 477

V. D. Sulimov, P. M. Shkapov. Hybrid algorithms for multiobjective optimization of mechanical and hydromechanical systems . . . 483

V. A. Shekhovtsov, P. E. Tovstik, T. M. Tovstik. Dynamics of marine stationary platform under action of seismic loading 492

N. Uzhegova, A. Svistkov. Modeling the behavior of the cantilever of the atomic force microscope 502

E. M. Aryslanova, D. N. Vavulin, A. V. Alfimov, A. V. Panteleev, S. A. Chivilikhin, I. Yu. Popov, V. V. Gusarov. Numerical simulation of separation from the substrate double nanolayer 506

V. V. Vinnikov, D. L. Reviznikov, A. V. Sposobin. Performance optimization in direct numerical simulation of collisional particle dynamics in heterogeneous flows 508

I. Vulfson, M. Preobrazhenskaya. Investigation of vibrations in the multisection cyclic machines including branch and lattice structured systems with variable and nonlinear parameters 513

M. F. H. Wolff, V. Salikov, S. Antonyuk, S. Heinrich, V. A. Kuzkin, G. A. Schneider. Discrete Element Modelling of ceramic/polymer composites 522

A. V. Yakovenko, P. T. Zubkov, L. V. Abdubakova. Computation of vibrations in the area with perfect viscous gas 532

N. P. Yaroshevich, N. N. Tolstushko. Simulation of dynamic processes in vibration machine with unbalanced vibro-exites and asynchronous electric motor 542

V. Lalin, E. Zdanchuk. On the Cauchy problem for nonlinear reduced Cosserat continuum 549

A. N. Fedorova, M. G. Zeitlin. Multiscale representations for orbital beam motion in multipole fields 553

Functionally invariant solutions of the double sine-Gordon equation

E. L. Aero A. N. Bulygin Yu. V. Pavlov
bulygin_an@mail.ru

Abstract

Functionally invariant solutions $U(x, y, z, t)$ of double sine-Gordon equation with constant amplitudes are received. Solutions have the form of composition of two functions $U[W(x, y, z, t)]$. Function $W(x, y, z, t)$ simultaneously satisfies to two equations: the wave equation and the eikonal type equation. Functionally invariant solutions of these equations are found. Solutions contain an arbitrary function $F(\alpha)$. Ansatz $\alpha(x, y, z, t)$ may be found from the algebraic equation linear on independent variables (x, y, z, t). The coefficients of the algebraic equation are arbitrary functions of α. Ansatz is defined ambiguously. Simple expressions for the ansatz $\alpha(x, y, z, t)$ are found.

Dependence U from W is defined by the solution of the nonlinear ordinary differential equation of the second order. Its solutions are defined by two parameters: constant of integration and the ratio of amplitudes. The bifurcation lines and bifurcation points are marked on the plane of these parameters. Solutions are found for domains into which the plane of parameters is divided by the bifurcation lines, and also for bifurcation lines and points. For domains $U(x, y, z, t)$ is expressed by Jacobi functions, on the bifurcation lines — by elliptic integrals, and for bifurcation points — by elementary functions. Analytic properties of the obtained solutions are discussed.

1 Introduction

The double sine-Gordon (DSG) equation

$$\frac{\partial^2 U}{\partial x^2} + \frac{\partial^2 U}{\partial y^2} + \frac{\partial^2 U}{\partial z^2} - \frac{1}{V^2}\frac{\partial^2 U}{\partial t^2} = p_1 \sin U + p_2 \sin 2U \tag{1}$$

represents real physical interest. In nonlinear optics it describes propagation of ultrashort optical pulse in a resonant five-times degenerate medium [1, 2]. In condensed mediums the DSG equation models propagation of spin waves in anisotropic magnetic liquids [3, 4], domain walls in ferromagnets and ferroelectrics [5], waves of density of an electric charge in organic linear conductors [6], dislocations in solid states [7]. In the nonlinear theory of deformation of crystal lattice the DSG equation describes cardinal reorganization of the near order of atoms, fragmentation of a lattice at greater deformations, and formation defects [8]–[9]. In the dynamic theory of a crystal lattice two-dimensional equation (1) describes propagation of an optical mode and laws of transition of a periodic wave in a solitary wave [10]–[12]. DSG equation is non-integrable. It is non solvable by a method of a inverse problem of scattering. But the perturbations method is developed for it. The DSG equation is considered as a perturbed sine-Gordon equation [13, 14]. The analytical [15], [18] and effective numerical [19, 20] methods of solution of the DSG equation are developed. The method of construction functionally invariant solutions of the DSG equation is represented below. The basic ideas of this method are stated in [21]–[24].

2 New approach to solution of Double sine-Gordon equation

The solutions of Eq. (1) we shall search in the form of a composition of two functions

$$U(x,y,z,t) = U[\,W(x,y,z,t)]\,. \tag{2}$$

Let's accept, that function $W(x,y,z,t)$ simultaneously satisfies two equations: wave equation

$$\frac{\partial^2 W}{\partial x^2} + \frac{\partial^2 W}{\partial y^2} + \frac{\partial^2 W}{\partial z^2} - \frac{1}{V^2}\,\frac{\partial^2 W}{\partial t^2} = 0 \tag{3}$$

and the eikonal type equation

$$\left(\frac{\partial W}{\partial x}\right)^2 + \left(\frac{\partial W}{\partial y}\right)^2 + \left(\frac{\partial W}{\partial z}\right)^2 - \frac{1}{V^2}\left(\frac{\partial W}{\partial t}\right)^2 = \lambda\,, \qquad \lambda = \text{const.} \tag{4}$$

Then the solution of Eq. (1) is reduced to calculation of the integral

$$\int \frac{dU}{\sqrt{R(U)}} = \sqrt{\frac{4p_2 G}{\lambda}}\,(W + W_0). \tag{5}$$

Here (G, W_0) are the constant of integration, and

$$R(U) = \left(1 + a^2 \sin^2\frac{U}{2}\right)\left(1 - b^2 \sin^2\frac{U}{2}\right), \tag{6}$$

$$a^2 = \frac{1}{G}\left[\sqrt{\left(1 + \frac{p_1}{2p_2}\right)^2 + 2G} + \left(1 + \frac{p_1}{2p_2}\right)\right], \tag{7}$$

$$b^2 = \frac{1}{G}\left[\sqrt{\left(1 + \frac{p_1}{2p_2}\right)^2 + 2G} - \left(1 + \frac{p_1}{2p_2}\right)\right]. \tag{8}$$

The integral (5) is expressed through Jacobi functions, elliptic integrals or elementary functions depending on relationships between constants $(G, p_1/2p_2)$. Let's note, that if $U(x,y,z,t)$ satisfies to Eq. (1), then

$$U_\pm(x,y,z,t) = 2n\pi \pm U(x,y,z,t), \qquad n = 0, \pm 1, \ldots \tag{9}$$

is a solution of Eq. (1) also.

3 Functionally invariant solutions of the wave equation and the eikonal type equation

The solutions of Eqs. (3), (4) we search in the form of

$$W = a_1 x + a_2 y + a_3 z - \sigma V^2 t + \Psi(x,y,z,t)\,. \tag{10}$$

Here (a_1, a_2, a_3, σ) are arbitrary constants, $\Psi(x,y,z,t)$ is an arbitrary function. If

$$a_1^2 + a_2^2 + a_3^2 = \lambda + \sigma^2 V^2, \tag{11}$$

then (10) will be the solution of Eqs. (3), (4) provided that $\Psi(x,y,z,t)$ simultaneously satisfies to three equations:

$$\frac{\partial^2\Psi}{\partial x^2}+\frac{\partial^2\Psi}{\partial y^2}+\frac{\partial^2\Psi}{\partial z^2}-\frac{1}{V^2}\frac{\partial^2\Psi}{\partial t^2}=0, \tag{12}$$

$$\left(\frac{\partial\Psi}{\partial x}\right)^2+\left(\frac{\partial\Psi}{\partial y}\right)^2+\left(\frac{\partial\Psi}{\partial z}\right)^2-\frac{1}{V^2}\left(\frac{\partial\Psi}{\partial t}\right)^2=0, \tag{13}$$

$$a_1\frac{\partial\Psi}{\partial x}+a_2\frac{\partial\Psi}{\partial y}+a_3\frac{\partial\Psi}{\partial z}+\sigma\frac{\partial\Psi}{\partial t}=0. \tag{14}$$

The function $\Psi(x,y,z,t)$ we shall search in the form of an arbitrary function, depending from ansatz $\alpha(x,y,z,t)$:

$$\Psi(x,y,z,t)=F(\alpha). \tag{15}$$

Ansatz α we shall choose as a root of the algebraic equation

$$x\,l(\alpha)+y\,m(\alpha)+z\,n(\alpha)-tV^2p(\alpha)+q(\alpha)=0. \tag{16}$$

Here ($l(\alpha)$, $m(\alpha)$, $n(\alpha)$, $p(\alpha)$, $q(\alpha)$) are arbitrary functions of α. The equations (12), (13), (14) will be satisfied, if this functions are connected by the algebraic relationships

$$l^2+m^2+n^2=V^2p^2, \tag{17}$$

$$a_1l+a_2m+a_3n=\sigma V^2p. \tag{18}$$

The condition (11) is fulfilled, if

$$a_1=\sqrt{\lambda+\sigma^2V^2}\sin\theta\cos\varphi,\quad a_2=\sqrt{\lambda+\sigma^2V^2}\sin\theta\sin\varphi,\quad a_3=\sqrt{\lambda+\sigma^2V^2}\cos\theta, \tag{19}$$

where $(\theta,\varphi)=\text{const}$. The solution of the algebraic equations (17), (18) will be

$$l(\alpha)=\frac{Vp(\alpha)}{\sqrt{\lambda+\sigma^2V^2}}\left\{\sigma V\sin\theta\cos\varphi+\sqrt{\lambda}\left[\sin\varphi\cos f(\alpha)+\cos\varphi\cos\theta\sin f(\alpha)\right]\right\},$$

$$m(\alpha)=\frac{Vp(\alpha)}{\sqrt{\lambda+\sigma^2V^2}}\left\{\sigma V\sin\theta\sin\varphi-\sqrt{\lambda}\left[\cos\varphi\cos f(\alpha)-\sin\varphi\cos\theta\sin f(\alpha)\right]\right\},$$

$$n(\alpha)=\frac{Vp(\alpha)}{\sqrt{\lambda+\sigma^2V^2}}\left\{\sigma V\cos\theta-\sqrt{\lambda}\sin\theta\sin f(\alpha)\right\}, \tag{20}$$

In the present work we restrict the finding of solutions of the Double sine-Gordon equation by real solutions. In this case $\lambda>0$ and, not losing a generality, it is possible to accept, that

$$\lambda=1. \tag{21}$$

Then ($l(\alpha)$, $m(\alpha)$, $n(\alpha)$) take the form

$$l(\alpha)=Vp(\alpha)\,x_1,\quad m(\alpha)=Vp(\alpha)\,x_2,\quad n(\alpha)=Vp(\alpha)\,x_3, \tag{22}$$

$$x_1=\frac{1}{\sqrt{1+\sigma^2V^2}}\left\{\sigma V\sin\theta\cos\varphi+\sin\varphi\cos f(\alpha)+\cos\varphi\cos\theta\sin f(\alpha)\right\}, \tag{23}$$

$$x_2=\frac{1}{\sqrt{1+\sigma^2V^2}}\left\{\sigma V\sin\theta\sin\varphi-\cos\varphi\cos f(\alpha)+\sin\varphi\cos\theta\sin f(\alpha)\right\}, \tag{24}$$

$$x_3 = \frac{Vp(\alpha)}{\sqrt{1+\sigma^2V^2}}\left\{\sigma V\cos\theta - \sin\theta\sin f(\alpha)\right\}, \tag{25}$$

Ansatz $\alpha(x,y,z,t)$ can be found from Eq. (16). Taking into account (22)–(25), it contains two arbitrary functions $f(\alpha)$ and $q(\alpha)/p(\alpha)$. The concrete form of $\alpha(x,y,z,t)$ is defined by these functions. Let's consider the simplest case:

$$f(\alpha) = f_0 = \text{const}, \qquad \frac{q(\alpha)}{Vp(\alpha)} = -\alpha\,. \tag{26}$$

Then

$$\alpha = x\,x_1 + y\,x_2 + z\,x_3 - tV\,. \tag{27}$$

Here (x_1, x_2, x_3) are constants, which turn out if one puts in (25) $f(\alpha) = f_0 = \text{const}$.

4 Solutions of the double sine-Gordon equation

The analytical form of the solution $U(x,y,z,t)$ DSG equation is defined by two parameters G and $p_1/2p_2$. The set of values of these parameters can be presented in the form of a plane. If parameter G to choose for an axis of ordinates, and $p_1/2p_2$ for an axis of abscissas, then it is possible to lead lines of bifurcation of solutions $U(x,y,z,t)$ on the planes of parameters.

$$\textbf{1}.\ G=0; \quad \textbf{2}.\ G=-\frac{p_1}{p_2}; \quad \textbf{3}.\ G=2\left(2+\frac{p_1}{2p_2}\right); \quad \textbf{4}.\ G=-\frac{1}{2}\left(1+\frac{p_1}{2p_2}\right)^2. \tag{28}$$

These lines at numbers are represented on Fig. 1.

The plane is divided into domains by the bifurcation lines. In each domains the parameters (G, $p_1/2p_2$) and defined by them values (a^2, b^2) satisfy to the system of inequalities:

$$\textbf{I}.\quad G>0, \quad G>-\frac{p_1}{p_2}, \quad a^2+b^2>0, \quad 1+a^2>0, \quad 0<\frac{a^2+b^2}{1+a^2}<1. \tag{29}$$

$$\textbf{II}.\quad G>0, \quad G<-\frac{p_1}{p_2}, \quad a^2+b^2>0, \quad 1+a^2>0, \quad 0<\frac{1+a^2}{a^2+b^2}<1. \tag{30}$$

$$\textbf{III}.\quad G<0, \quad G<-\frac{p_1}{p_2}, \quad G>-\frac{1}{2}\left(1+\frac{p_1}{2p_2}\right)^2,$$
$$a^2+b^2<0, \quad 1+a^2<0, \quad 1-b^2<0, \quad 0<\frac{a^2+b^2}{1+a^2}<1. \tag{31}$$

$$\textbf{IV}.\quad G<0, \quad G>-\frac{1}{2}\left(1+\frac{p_1}{2p_2}\right)^2, \quad 1+\frac{p_1}{2p_2}<0. \tag{32}$$

$$\textbf{V}.\quad G<0, \quad G<-\frac{1}{2}\left(1+\frac{p_1}{2p_2}\right)^2, \quad (a^2,b^2)-\text{complex numbers}. \tag{33}$$

$$\textbf{VI}.\quad G<0, \quad G<-\frac{p_1}{p_2}, \quad G>-\frac{1}{2}\left(1+\frac{p_1}{2p_2}\right)^2,$$

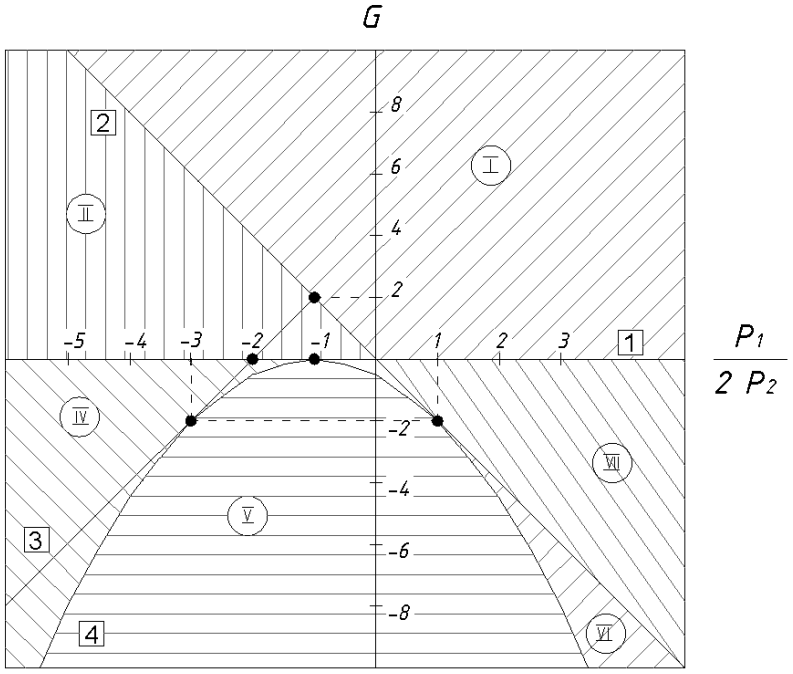

Figure 1: The lines of the solutions bifurcation.

$$a^2+b^2<0,\quad 1+a^2>0,\quad 1-b^2>0,\quad 0<-\frac{a^2+b^2}{1-b^2}<1. \tag{34}$$

VII. $G<0,\quad G>-\dfrac{p_1}{p_2}$,

$$a^2+b^2<0,\quad 1+a^2<0,\quad 1-b^2>0,\quad 0<\frac{1+a^2}{a^2+b^2}<1. \tag{35}$$

The domains $(I-VII)$ at corresponding numbers are represented on Fig. 1. The domain near the origin of coordinates without shading is III.

The system of inequalities of each domain defines the solution $U(x,y,z,t)$ in this domain. Special solutions exist on bifurcation lines The bifurcation lines are crossed (or are tangent) in some points. These are points of bifurcations of $U(x,y,z,t)$. Specific solutions exist in the bifurcation points also. The DSG equation solutions in the domains, on the bifurcation lines and in the bifurcation points are represented below.

4.1 Solutions in domains

In the domain **I** a solution of DSG equation has a form

$$\operatorname{tg}\frac{U}{2}=\frac{1}{\sqrt{1+a^2}}\frac{\operatorname{sn}(\zeta,\nu)}{\operatorname{cn}(\zeta,\nu)}. \tag{36}$$

Here and further we use the designation

$$\zeta=\frac{1}{L}(W+W_0), \tag{37}$$

$(\mathrm{sn}\,(\zeta,\nu),\ \mathrm{cn}\,(\zeta,\nu))$ are the Jacobi functions. In (36)

$$\frac{1}{L}=\sqrt{p_2G(1+a^2)},\qquad \nu^2=\frac{a^2+b^2}{1+a^2}. \tag{38}$$

From (36) one can receive for $U(\zeta)$ two analytic expressions:

$$U=2\,\mathrm{arctg}\,\left[\frac{1}{\sqrt{1+a^2}}\,\frac{\mathrm{sn}\,(\zeta,\nu)}{\mathrm{cn}\,(\zeta,\nu)}\right], \tag{39}$$

$$U=\pi-2\,\mathrm{am}\,[K(k)-F(\delta,k),k], \tag{40}$$

$(\mathrm{am}\,(\zeta,k),\ K(k),\ F(\delta,k))$ are Jacobi amplitude, complete and incomplete elliptic integrals of the first sort accordingly,

$$\delta=\mathrm{am}\,(\zeta,\nu),\qquad k=\sqrt{\frac{a^2}{1+a^2}}. \tag{41}$$

Dependence (40) follows from the formula

$$F(\varphi,k)+F(\psi,k)=K(k), \tag{42}$$

which establishes connection between incomplete elliptic integrals, if arguments (φ,ψ) satisfy to a condition

$$\mathrm{tg}\,\varphi\,\mathrm{tg}\,\psi=\frac{1}{k'},\qquad k'=\sqrt{1-k^2}\,. \tag{43}$$

Solutions (39), (40) coincide in an interval $-K(\nu)\le\zeta\le K(\nu)$ and differ outside of an interval. The solution (39) continues periodically, and (40) with growth of ζ grows. At transition from one period to another $U(x,y,z,t)$ increases on 2π. The plot of $U(x,y,z,t)$, which is defined by (40), has a form of a ladder. For a case $V=1$, $p_1=10$, $p_2=1$, $G=0.01$, $\sigma=1$, $\varphi=\pi/3$, $\theta=\pi/4$, $f_0=1$, $W_0=0$, $F(\alpha)=\alpha$ it is represented on Fig. 2. The plot of $U(x,y,z,t)$, which is defined by (39) under the same values of parameters, is

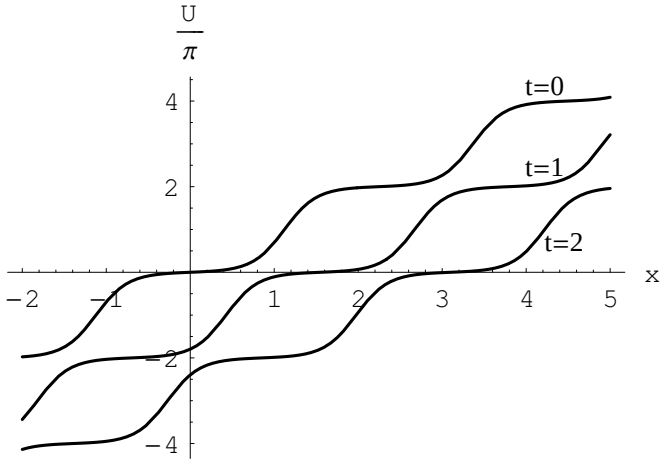

Figure 2: Solution (40) for $y=0$, $z=0$.

represented on Fig. 3. Let's note, that the solution in the domain **I** will be real, if $p_2>0$.

In the domain **II**

$$\mathrm{tg}\,\frac{U}{2}=\frac{1}{\sqrt{a^2+b^2}}\frac{\mathrm{sn}\,(\zeta,\nu)}{\mathrm{dn}\,(\zeta,\nu)},\qquad \frac{1}{L}=\sqrt{p_2G(a^2+b^2)},\qquad \nu^2=\frac{1+a^2}{a^2+b^2}\,, \tag{44}$$

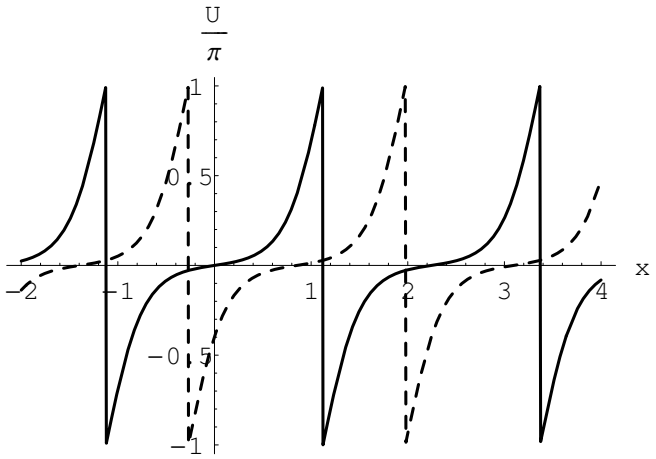

Figure 3: Solution (39) for $y = 0$, $z = 0$ (Continuous line at $t = 0$, dotted at $t = 2$).

where $\mathrm{dn}\,(\zeta, \nu)$ is the Jacobi delta amplitude. In the second domain $U(x, y, z, t)$ changes periodically with growth of ζ and accepts both positive, and negative values. This periodic function has singularity. Because $\mathrm{dn}\,(\zeta, \nu)$ does not equal to zero, $U(x, y, z, t)$ in one point does not reach value π. The solution in the second domain is real, if $p_2 > 0$.

In the domain **III**

$$\mathrm{tg}\,\frac{U}{2} = \frac{1}{\sqrt{-(1+a^2)}}\frac{1}{\mathrm{dn}\,(\zeta,\nu)}, \qquad \frac{1}{L} = \sqrt{p_2 G(1+a^2)}, \qquad \nu^2 = \frac{a^2+b^2}{1+a^2}\,. \tag{45}$$

Here $U(x, y, z, t)$ is periodic function of ζ also. Because $\mathrm{dn}\,(\zeta, \nu)$ accepts only positive values and does not equal to zero and infinity, $U(x, y, z, t)$ in the third domain is positive definite and does not accept values of zero and π. The solution $U(x, y, z, t)$ will be real, if $p_2 > 0$.

In the domain **IV**

$$\mathrm{tg}\,\frac{U}{2} = \frac{-1}{\sqrt{-(1+a^2)}}\frac{1}{\mathrm{sn}\,(\zeta,\nu)}, \qquad \frac{1}{L} = \sqrt{-p_2 G(1-b^2)}, \qquad \nu^2 = \frac{1+a^2}{1-b^2}\,. \tag{46}$$

Dependence $U(\zeta)$ in the domain **IV** can be considered as difference of kink and break $(-\pi, \pi)$. The solution $U(x, y, z, t)$ in domain **IV** will be real, if $p_2 < 0$.

In the domain **V**, according to (7), (8), values (a^2, b^2) are complex, hence, the DSG equation in domain **V** has no real solutions.

In the domain **VI**

$$\mathrm{tg}\,\frac{U}{2} = \frac{-1}{\sqrt{1+a^2}}\frac{\mathrm{cn}\,(\zeta,\nu)}{\mathrm{sn}\,(\zeta,\nu)}, \qquad \frac{1}{L} = \sqrt{p_2 G(1-b^2)}, \qquad \nu^2 = \frac{a^2+b^2}{b^2-1}\,. \tag{47}$$

The dependence $U(\zeta)$ in **VI** domain is similar to dependence $U(\zeta)$ in the domain **I**. Similarity of solutions in **I** and **IV** domains is caused by that analytical dependence (47) can be written down in the form of

$$U = \pi + 2\,\mathrm{am}\,[K(k) - F(\delta, k), k]\,, \quad \delta = \frac{\pi}{2} - \mathrm{am}\,(\zeta, \nu), \quad k = \sqrt{\frac{a^2}{1+a^2}}. \tag{48}$$

The solution in **VI** domain will be real, if $p_2 < 0$.

In the domain **VII**

$$\operatorname{tg}\frac{U}{2}=\frac{1}{\sqrt{-(1+a^2)}}\frac{1}{\operatorname{cn}(\zeta,\nu)},\qquad \frac{1}{L}=\sqrt{p_2G(a^2+b^2)},\qquad \nu^2=\frac{1+a^2}{a^2+b^2}\,. \tag{49}$$

In **VII** domain U is a periodic function with alternating sign, reaching values $(0,\pi)$. The solution will be real, if $p_2>0$.

4.2 Solutions on bifurcation lines

On bifurcation lines the genus g of algebraic function $R(U)$ is changed. In the domains $g=2$, and on the bifurcation lines $g=1$. For this reason solutions of DSG equation are expressed through the elementary functions on the bifurcation lines.

On the line $G=0$

$$\operatorname{tg}\frac{U}{2}=\frac{1}{\sqrt{1-\nu^2}}\frac{1}{\operatorname{sh}\zeta}\,,\qquad \frac{1}{L}=\sqrt{\frac{2p_2}{\nu^2}}\,,\qquad \nu^2=\frac{1}{1+\frac{p_1}{2p_2}}\,. \tag{50}$$

On the line $G=-p_1/p_2$

$$\operatorname{tg}\frac{U}{2}=\frac{1}{\sqrt{\nu^2-1}}\operatorname{ch}\zeta,\quad \frac{1}{L}=\sqrt{\frac{p_1}{\lambda}(\nu^2-1)},\quad \nu^2=\frac{2p_2}{p_1}>1 \tag{51}$$

On the line $G=4+p_1/p_2$

$$\operatorname{tg}\frac{U}{2}=\frac{1}{\sqrt{2}}\frac{\operatorname{sn}(\zeta,k)}{\operatorname{cn}(\zeta,k)},\quad \frac{1}{L}=\sqrt{\frac{p_2}{\nu^2}},\quad k^2=\frac{1+\nu^2}{2},\quad \nu^2=\frac{1}{2+\frac{p_1}{2p_2}} \tag{52}$$

On the line $G=-\dfrac{1}{2}\left(1+\dfrac{p_1}{2p_2}\right)^2$

a) $$\operatorname{tg}\frac{U}{2}=\frac{\operatorname{tg}\zeta}{\sqrt{1-\nu^2}},\quad \frac{1}{L}=\sqrt{\frac{-2p_2}{\lambda\nu^4}(1-\nu^2)},\quad \nu^2=\frac{2}{1+\frac{p_1}{2p_2}}<1 \tag{53}$$

b) $$\operatorname{tg}\frac{U}{2}=\frac{\operatorname{th}\zeta}{\sqrt{\nu^2-1}},\quad \frac{1}{L}=\sqrt{\frac{-2p_2}{\lambda\nu^4}(\nu^2-1)},\quad \nu^2=\frac{2}{1+\frac{p_1}{2p_2}}>1 \tag{54}$$

4.3 Solutions in bifurcation points

Solutions of the DSG equation in all bifurcation points are expressed through the elementary functions.

1. $$G=0,\quad \frac{p_1}{2p_2}=0,\quad \operatorname{tg}\frac{U}{2}=e^{\zeta},\quad \frac{1}{L}=\sqrt{2p_2},\quad p_2>0. \tag{55}$$

2. $$G=0,\quad \frac{p_1}{2p_2}=-1,\quad \operatorname{tg}\frac{U}{2}=-\frac{1}{\zeta},\quad \frac{1}{L}=\sqrt{-2p_2},\quad p_2<0. \tag{56}$$

3. $$G=0,\quad \frac{p_1}{2p_2}=-2,\quad \operatorname{tg}\frac{U}{2}=\frac{1}{\sqrt{2}\operatorname{sh}\zeta},\quad \frac{1}{L}=\sqrt{-2p_2},\quad p_2<0. \tag{57}$$

4. $$G=-2,\quad \frac{p_1}{2p_2}=-3,\quad \operatorname{tg}\frac{U}{2}=\frac{1}{\sqrt{2}}\operatorname{tg}\zeta,\quad \frac{1}{L}=\sqrt{-4p_2},\quad p_2<0. \tag{58}$$

5. $G=-2, \quad \dfrac{p_1}{2p_2}=1, \quad \operatorname{tg}\dfrac{U}{2}=\zeta, \quad \dfrac{1}{L}=\sqrt{-2p_2}, \quad p_2<0.$ (59)

6. $G=2, \quad \dfrac{p_1}{2p_2}=-1, \quad \operatorname{tg}\dfrac{U}{2}=\dfrac{1}{\sqrt{2}}\operatorname{sh}\zeta, \quad \dfrac{1}{L}=\sqrt{4p_2}, \quad p_2>0.$ (60)

There are also other elementary solutions of the DSG equation. It is possible to be convinced by direct calculation, that

7. $\operatorname{tg}\dfrac{U}{2}=\dfrac{A}{\operatorname{ch}\zeta}, \quad \dfrac{1}{L}=\sqrt{p_1\left(1+\dfrac{2p_2}{p_1}\right)}, \quad A^2=-\left(1+\dfrac{2p_2}{p_1}\right),$ (61)

8. $\operatorname{tg}\dfrac{U}{2}=A\operatorname{th}\zeta, \quad \dfrac{1}{L}=\sqrt{\dfrac{p_2}{2}\left(\dfrac{p_1^2}{4p_2^2}-1\right)}, \quad A^2=\dfrac{1+p_1/2p_2}{1-p_1/2p_2}$ (62)

satisfy Eq. (1). The solution (61) is soliton type, and (62) is kink type solution. The plots of (61), (62) are represented on Fig. 4 ($p_1=1,\ p_2=1$).

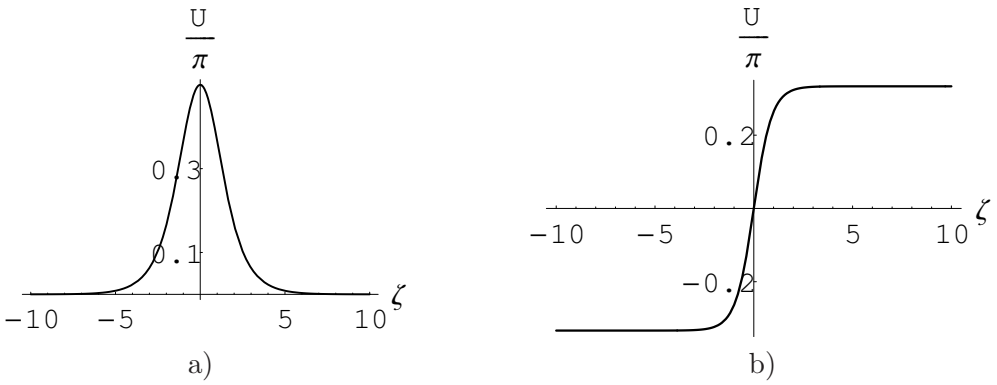

Figure 4: The solutions (61), (62).

5 Conclusion

New method of a finding of solutions of the nonlinear differential equations it is represented with reference to the DSG equation. The method supposes natural expansion of the domain of applications. It allows to construct the solution of the Klein-Gordon equation

$$\frac{\partial^2 U}{\partial x^2}+\frac{\partial^2 U}{\partial y^2}+\frac{\partial^2 U}{\partial z^2}-\frac{1}{V^2}\frac{\partial^2 U}{\partial t^2}=F(U), \tag{63}$$

which contains arbitrary function in the right part $F(U)$. Constructed solutions of the DSG equation have forms which are known in the literature: kink, anti-kink, periodic solutions, etc. It is correct, if ansatz $\alpha(x,y,z,t)$ is linear function of (x,y,z,t), and $F(\alpha)=\alpha$. Otherwise, depending on α and $F(\alpha)$, solutions will have other forms which are not known in the literature. In the present work the solutions of the $(3+1)$ DSG equations are received. The offered method can be easily generalized on the equations in the spaces of larger dimensions. As it was shown [25], that the quantity of algebraic functions, which can be chosen as ansatz at construction of function $W(x,y,z,t)$ increases with growth of dimension of the space. It is possible to hope, that the offered way of the solution of the nonlinear differential equations and found solutions of the DSG equation will be useful at the description of the physical phenomena and modeling of the modern technological processes.

Acknowledgements

This work was supported by RFBR, grants 09-08-00634-a and 10-01-00243-a.

References

[1] G. L. Lamb, Jr., Rev. Mod. Phys. **43**, (1971) 99–124.

[2] S. Duckworth, R. K. Bullough, P. J. Caudrey, J. D. Gibbon, Phys. Lett. A **57**, (1976) 19–22.

[3] P. W. Kitchenside, P. J. Caudrey, R. K. Bullough, Physica Scripta **20**, (1979) 673–680.

[4] K. Maki, P. Kumar, Phys. Rev. B **14**, (1976) 118–127.

[5] Yu. S. Kivshar, B. A. Malomed, Phys. Rev. B **42**, (1990) 8561–8570.

[6] M. R. Rice, *in* Solitons and Condensed Matter Physics, Eds. H. R. Bishop, T. Schneider, Springer, Berlin, 1978, pp. 246–253.

[7] M. El-Batanouny, S. Burdick, K. M. Martini, P. Stancioff, Phys. Rev. Lett. **58**, (1987) 2762–2765.

[8] E. L. Aero, A. N. Bulygin, Mechanics of Solids, **45**, No. 5, (2010) 670–688.

[9] E. L. Aero, A. N. Bulygin, *in* "Mechanics of Generalized Continua. One Hundred Years After the Cosserats", Eds. G.A. Maugin, A.V. Metrikine, Advances in Mechanics and Mathematics, Vol.21, Springer, 2010, pp.121–130.

[10] E. L. Aero, A. N. Bulygin, Comput. Continuum Mech. **2**, No. 4, (2009) 19–43.

[11] E. L. Aero, A. N. Bulygin, Acoustical Physics **56**, No. 6, (2010) 811–830.

[12] E. L. Aero, A. N. Bulygin, Continuum Mech. Thermodyn. **23**, (2011) 35–43.

[13] P. W. Kitchenside, A. L. Mason, R. K. Bullough, P. J. Caudrey, *in* Solitons and Condensed Matter Physics, Eds. H. R. Bishop, T. Schneider, Springer, Berlin, 1978, pp. 48–51.

[14] A. C. Newell, J. Math. Phys. **18**, (1977) 922–926.

[15] Q. Zheng, Z.-Z. Ren, Commun. Theor. Phys. **49**, (2008) 303-304.

[16] C. A. Condat, R. A. Guyer, M. D. Miller, Phys. Rev. B **27**, (1983) 474–494.

[17] P. B. Burt, Proc. R. Soc. London A, **359**, (1978) 479–495.

[18] M. M. Bogdan, A. M. Kosevich, G. A. Maugin, Condensed Matter Phys. **2**, (1999) 255–265.

[19] M. J. Ablowitz, M. D. Kruskal, J. F. Ladik, SIAM J. Appl. Math. **36** (1979) 428–437.

[20] A. A. Dolzhenkov, Vestnik Voronezh University: Physics, Mathematics, No. **1**, (2008) 195–204.

[21] E. L. Aero, A. N. Bulygin, Yu. V. Pavlov, Teor. Matem. Fiz. **158**, No. 3, (2009) 370–377 [English transl.: Theor. Math. Phys. **158**(3), (2009) 313–319].

[22] E. L. Aero, A. N. Bulygin, Yu. V. Pavlov, Nelineinii Mir **7**, N 7, (2009) 513–517.

[23] E. L. Aero, A. N. Bulygin, Yu. V. Pavlov, Proc. Int. Conf. "Days on Diffraction 2009", St.Petersburg, Russia, pp. 7–12.

[24] E. L. Aero, A. N. Bulygin, Yu. V. Pavlov, New approach to solution of sine-Gordon equation with variable amplitude, Proc. Int. Conf. "Days on Diffraction 2010", Saint Petersburg, Russia.

[25] N. P. Erugin, Uch. Zap. Leningrad Univ., **15**, N 96, (1948) 101–134.

E. L. Aero, A. N. Bulygin, Yu. V. Pavlov,
Institute of Problems in Mechanical Engineering, RAS,
61 Bol'shoy, V.O., Saint Petersburg, 199178, Russia

Effective analytical solution method of contact problems for materials with functionally-graded coatings

Sergey M. Aizikovich Andrey S. Vasiliev Sergey S. Volkov Ludmila N. Evich
saizikovich@gmail.com

Abstract

The work provides the statement of the effective solution method of the axisymmetric static contact problems of the theory of elasticity for the inhomogeneous layer, which allows receiving the approximated solution of a problem of an analytical kind. The layer can be both continuously inhomogeneous (functionally-graded) and layered (consisting of a package of homogeneous layers with various elastic properties). In case of a problem about layer's torsion by a non-deformable indenter, the layer is supposed to be linked to a substrate. For a problem about indentation of nondeformable indenter into a layer, a layer can be as linked, as lying without a friction on a rigid substrate.

The solution of contact problems for functional-gradient half-spaces with a random law of change of inhomogeneous on depth has been developed in works of Aizikovich S.M., Alexandrov V.M. etc., by a bilaterial asymptotic method [1]–[6].

Inhomogeneous coatings with elastic properties continuously changing on depth (functionally-graded coatings) give the opportunity to lower the concentration of stresses in an interface area of a coating with a substrate; and to redistribute contact stresses under an indenter [4], [5]. The earlier developed mathematical models of layered materials are insufficiently accurate in describing the functionally-graded coatings . One can observe both quantitative and qualitative differences in behavior of functionally-graded materials in comparison with homogeneous or layered ones [6].

This approach is close to one proposed in early pioneering works where solution of the contact problem for a layer of finite thickness in dependence on the characteristic geometric parameter of the problem has been obtained (Vorovich and Ustinov, 1959 [7]; Aleksandrov and Vorovich, 1960,1964 [8], [9]).

The recent work [10] gives the examination of the problem for a soft homogeneous layer on an elastic semiplane in case of flat statement of a problem.

Among variety of inhomogeneous coating with elastic properties smoothly changing on depth, we give the particular interest to the coatings, whose gradient of change of elastic properties changes a sign on one of coordinates. Thus, for example, these are the coatings, whose rigidity on a surface is maximum and is decreasing with depth to some value, and then, on the contrary, is increasing as approaching a substrate (coatings with nonmonotonic laws of change on depth of elastic properties).

The case of a torsion problem provides that the shear module changes on depth under the law:

$$G(z) = \begin{cases} G^0 f_i(z), & -H \leqslant z \leqslant 0 \\ G^S, & -\infty < z < -H \end{cases}$$

Here G_0 — some constant, nd $f_i(z)$ is changing under one of the laws.

It is supposed that on the boundary 'coating-substrate' the shear module has jump of properties in 10, 100, 1000 times, i.e. $G^S/G^0 = 10, 100\,1000$. The analogous change of Young's modulus is considered for a problem of indentation.

The problems are being solved by the method of integral transformations and are reduced to the solution of the integral equations. The method of numerical construction kernels' transforms of these integral equations is stated; their properties are investigated. On the basis of these properties' investigation we prove the possibility of approximation kernels' transforms by certain analytical expressions. The simple effective algorithm of construction of the fractional-rational function is offered, which approximates the transform of the kernels.

It is proved that the constructed solution is asymptotically exact both for big, and for small values of characteristic geometrical parameter of a problem.

The method allows from uniform positions the studying of the mixed problems of the elasticity theory both with fixed, and with unknown in advance contact area. The analytical kind of solutions provides the opportunities of their wide usage for an estimation both mechanical (rigidity functions) and protective properties of composite functionally-graded coatings of the rigid bases.

We obtained the simplest approximated engineering formulas for calculation of mechanical characteristics of the problem, which allows catching the qualitative differences of layered and functional-gradient layer. Characteristic examples of laws of inhomogeneity are considered, the accuracy of the received approximated solutions is analyzed. Results of calculations are given not only in an area of change of boundary conditions (on boundaries), but also inside the material, which is of great value for tribologists.

Acknowledgements

The work is performed with the financial support of RFBR (09-08-011410a, 10-08-01296-a, 10-08-90025-Bel-a, 11-08-91168-GFEN_a), GK No 02.740.11.0413, GK No P1107, GK No 02.740.11.5193, AVCP 2.1.2/10063.

References

[1] Aizikovich, S.M. Asymptotic solutions of contact problems in elasticity theory for media inhomogeneous with depth, J. Appl. Math. Mech., 1982. No. 46, 116-124.

[2] Aizikovich, S.M., Alexandrov, V.M. Axially symmetric problem about indentation circular indenter into elastic inhomogeneous with depth half-space. Mech Solids, 1984. No 19, 73-82

[3] Aizikovich, S.M., Alexandrov, V.M., Kalker, J.J., Krenev, L.I., Trubchik, I.S. Analytical solution of the spherical indentation problem for a half-space with gradients with the depth elastic properties, Int. J. Solids Structures, 2002. No 39, 2745-2772.

[4] Aizikovich, S.M., Alexandrov, V.M., Trubchik, I.S. Bilateral asymptotic solution of one class of dual integral equations of the static contact problems for the foundations inhomogeneous in depth In: Operator Theory: Advances and Applications, Birkhauser Verlag, Basel, 2009. P. 3-17.

[5] Aizikovich, S.M., Krenev, L.I., Trubchik, I.S. Asymptotic solutions of the problem of spherical indenter penetration into a half-space inhomogeneous with depth. Mech Solids, 2000. No 35, 107-117.

[6] Aizikovich S., Vasiliev A., Seleznev N. Inverse analysis for evaluation of the shear modulus of inhomogeneous media by torsion experiments / S. Aizikovich, A. Vasiliev, N. Seleznev // International Journal of Engineering Science. 2010. P. 936–942.

[7] Vorovich, I. I., Ustinov, Iu. A. Pressure of a die on an elastic layer of finite thickness. J. Appl. Math. Mech. 1959. No 23, 637–650.

[8] Aleksandrov, V. M. , Vorovich, I. I. The action of a die on an elastic layer of finite thickness . J. Appl. Math. Mech., 1960. No 24, 462–476.

[9] Aleksandrov, V. M. , Vorovich, I. I. Contact problems for the elastic layer of small thickness. J. Appl. Math. Mech., 1964. No 28, 425–427.

[10] Aleksandrov, V. M. Contact problems on soft and rigid coatings of an elastic half-plane. Mech Solids, 2010. No 45, 34-40.

Sergey M. Aizikovich, Andrey S. Vasiliev, Sergey S. Volkov, Ludmila N. Evich. Department of Scientific Research, Don State Technical University, Gagarin sqr., 1, Rostov-on-Don, 344000, Russia

The non-linear oscillations of two bubbles in a volume of incompressible liquid

Alekse A. Alabuzhev Andrey A. Ogleznev
alabuzhev@mail.ru

Abstract

The oscillations of two gas bubbles under the linearly - polarized vibrations are considered. Bubbles are surrounded by an incompressible fluid of final volume. Interaction of bubbles through a field of fluid pressure is considered. The distance between bubbles is much more than radiuses of bubbles. Both radial and translation oscillations and dynamics of the shape of bubbles are investigated. Eigen frequencies of oscillations are investigated. The translation motion and its interaction with radial oscillations has been studied. It is shown, that oscillations of bubbles always occurs in an antiphase. Each bubble radiates a spherical wave which creates a acoustic fields near other bubble. Interaction force of two oscillating bubbles is guided on a straight line, pairing their centres, and inversely proportional to a quadrate of distance between them. It is found, that with change of distance between bubbles and frequencies of exterior vibrations probably repulsion bubbles from each other. It is secondary Bjerknes's effect. The Attractive force between oscillating bodies is small and damps with distance more promptly, than Bjerknes's force, therefore in a viewed situation does not render essential influence in comparison with Bjerknes's force. Influence of an attractive force will be essential if distances between bubbles are congruent quantity with bubbles radiuses. In such situation it is possible both a repulsion, and an attraction of bubbles. It is a subject of the further investigations.

1 Problem formulation

In this paper we studied the eigen and forced oscillations of two gas bubbles in an incompressible fluid of finite volume. Distance L between the centers of the bubbles is much larger than the radii of the bubbles. In addition, the distance to the vessel walls is much larger than L. Let each spherical bubble with the gas density $\rho_k^*(k = 1, 2)$ is surrounded by an incompressible fluid density ρ_l^*. Gas is considered ideal (in the thermodynamic meaning). At the initial time, each bubble has a radius of R_{0i}^*. Heat exchange between the liquid and the bubble is neglected, the viscous dissipation and the phase transition liquid-vapor ignore.

For each bubble, we introduce our spherical coordinate system (r, α, ϑ). We will consider the axisymmetric problem, whose solution does not depend on the azimuthal angle α. We assume the amplitude of translational motion of the mass center of the bubble is small compared with the amplitude of oscillations of its surface. The motion of gas in the bubble do not consider, assuming that the gas and steam make only the radial motion. This assumption is valid in the case of small amplitude translational motion. The fluid motion is described by the Navier-Stokes equations and continuity equation:

$$\vec{v}_{kt} + (\vec{v}_k\nabla)\,\vec{v}_k = -\nabla p + \eta\Delta\vec{v}_l, \mathrm{div}\,\vec{v}_k = 0, \tag{1}$$

where $\vec{v}_k$ - the fluid velocity near the kth bubble, p - pressure, $k = 1, 2$ - code that is responsible for the number of the bubble. We agree that the indices of t, r, ϑ denote differentiation with respect to relevant variables.

Let the pressure of the gas component is changed by the adiabatic law:

$$p_k = p_{0k}(V_{0k}/Vk)^{\gamma} \tag{2}$$

Here V_k - the volume of a gas bubble. There are the following boundary conditions on the bubble surface:

$$\text{kinematic condition} F_t + \vec{v}\nabla F = 0, F = r - R\left(t\right) - \varepsilon\zeta\left(t, \vartheta\right), \tag{3}$$

$$\text{normal balance condition } [p] + \left[\overline{\overline{\eta}}\right]\vec{n}\cdot\vec{n} = \sigma \operatorname{div}\vec{n}, \tag{4}$$

$$\text{condition of the continuity normal component } [\vec{v}\vec{n}] = 0, \tag{5}$$

$$\text{condition of the continuity tangential component } \left[\overline{\overline{\eta}}\right]\vec{n}\cdot\vec{\tau} = 0, \tag{6}$$

where $\vec{n} = \nabla F/|\nabla F|$ is external normal vector to bubble surface, $\vec{\tau}$ is tangential vector.

Pressure is given in the liquid far from bubbles:

$$r \to \infty : p_\infty = p_0 + p_{int} + p_a \sin(\omega t), \tag{7}$$

where $p_a = p_a^{(0)} + \varepsilon p_a^{(1)} r\cos\vartheta$, $\varepsilon \ll 1$ - small parameter.

Since the fluid is incompressible, the total volume of bubbles must be constant:

$$V_1 + V_2 = V_{01} + V_{02} \tag{8}$$

All equations and boundary conditions are written in dimensionless form. As the unit of distance, time, velocity potential, the deviation of the free surface, the fluid pressure and density taken $R_0^* = (R_{01}^* + R_{02}^*)/2$, $\sqrt{\rho_l^* R_0^{*2}/(p_{01}^* + p_{02}^*)}$, $A^*\sqrt{(p_{01}^* + p_{02}^*)/\rho_l^*}$, A^*, $p_{0l}^*/(p_{01}^* + p_{02}^*)$, ρ_l^* respectively.

2 Radial oscillations

The radial oscillations of the two bubbles are considered. Liquid velocity in the local coordinate system for any of the bubble can be represented as:

$$\vec{v}_k = \vec{v}_k^{(0)}\vec{e}_r, \vec{v}_k^{(0)} = -U_k(t)/r^2. \tag{9}$$

Substituting solution (9) into (1)-(8), we get to find the amplitudes and radii in the first order of the equations system:

$$R_k R_{ktt} + \frac{3}{2}R_{kt}^2 = -\left(p_0 + p_a^{(0)}\sin\omega t + p_{\text{int}} - p_k - \frac{2\sigma}{R_{0k}}\left(\frac{R_{0k}}{R_k}\right)^{3\gamma} + \frac{2\sigma}{R_k} + \frac{4\eta R_{kt}}{R_k}\right) \tag{10}$$

$$R_1^3 + R_2^3 = R_{01}^3 + R_{02}^3 \tag{11}$$

The system of differential equations (10)-(11) contains three unknown quantities: the radii of the bubbles R_1 & R_2 and contribute to the liquid pressure p_{int}, which is arising from the interaction of bubbles. This contribution p_{int} stems from the fact that the fluid is non-compressible and has a finite volume. Therefore, increasing the volume of one bubble is possible only because of the decrease of another bubble. Amplitude U_k can be found, for example, from the kinematic condition, if you know the function R_k of solving the system (10)-(11). In fig.1 show the dependence of the oscillation radius of the bubble and the phase portraits at various para-meters of the problem.

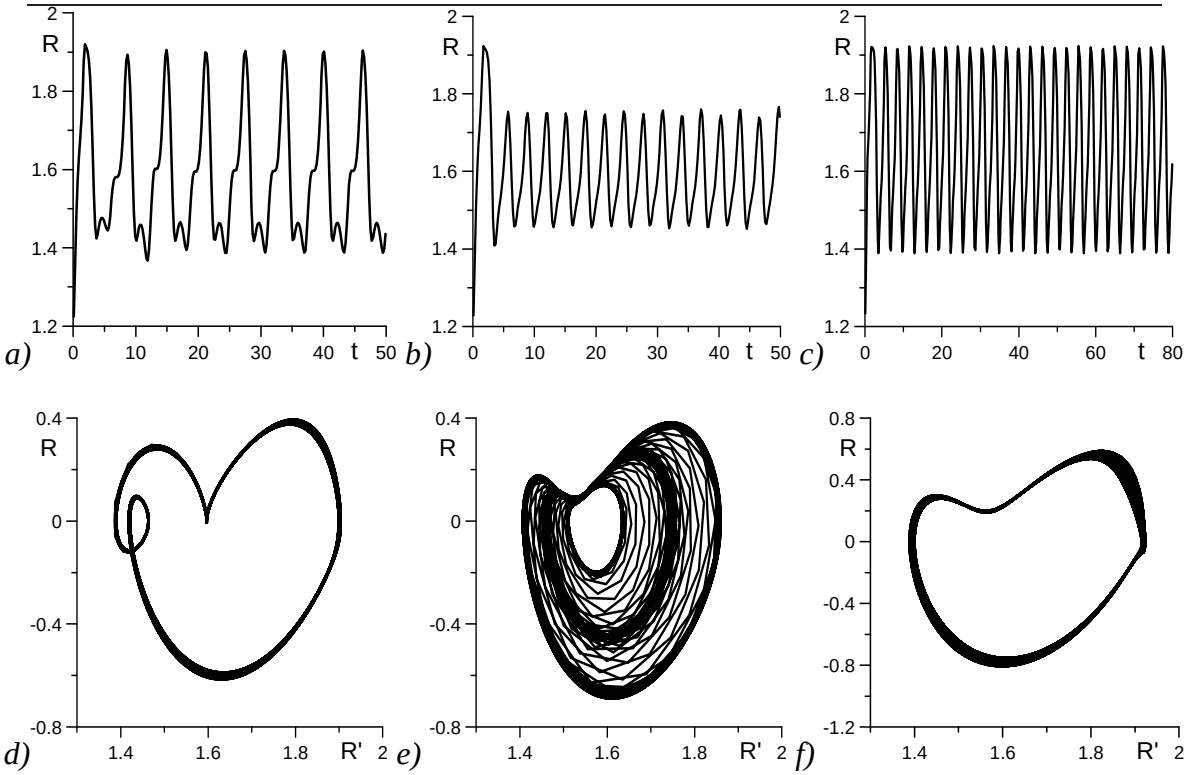

Figure 1: The dependence of the R_1 from time t (a-c) and phase portraits of (e-g).a), e) $A = 3.5$,$\omega = 2$,$\rho = 1$,$T = 300$,$V_0 = 30$,$\mu = 8 \cdot 10^3$,$\sigma = 2 \cdot 10^{-1}$,$\mu_0 = 1.2$ b), f) $A = 4.5$,$\omega = 2$,$\rho = 1$,$T = 300$,$V_0 = 30$,$\mu = 8 \cdot 10^3$,$\sigma = 2 \cdot 10^{-1}$,$\mu_0 = 1.2$ c), g) $A = 5.5$,$\omega = 2$,$\rho = 1$,$T = 300$,$V_0 = 30$,$\mu = 8 \cdot 10^3$,$\sigma = 2 \cdot 10^{-1}$,$\mu_0 = 1.2$

3 Translational oscillations

We assume that the amplitude of translational motion is small compared with the amplitude of radial oscillations. From the continuity equation (1) we find that the velocity of the fluid can be sought in the form of

$$\vec{v}_k = u_k^{(0)}(t,r)\vec{e}_r + \varepsilon u_k^{(1)}(t,r)\vec{e}_r. \tag{12}$$

Similarly to the case of radial oscillations in the principal order, we write the equation in terms of velocity potential $\varphi^{(1)}(r,t)$. The potential of liquid velocity is satisfying the Laplace equation near the k-th bubble has the form:

$$\varphi_k^{(1)} = U_k^{(1)}(t)\frac{1}{R_k} \tag{13}$$

where $U_k^{(1)}(t)$-time-dependent function. The equation of the liquid velocity is:

$$\varphi_t^{(1)} + \nabla\varphi^{(0)}\nabla\varphi^{(1)} = -\frac{1}{\rho}p_k^{(1)}, \tag{14}$$

where the pressure field in fluid is

$$p^{(1)} = p_b^{(1)} - p^{(1)}(t) + \rho\varphi_{it}^{(0)}. \tag{15}$$

When radial oscillation of a bubble, spherical wave is created, which creates additional pressure in the liquid:

$$p_{bk}^{(1)} \sim \frac{1}{V_k} \text{ or } p_k = \tfrac{1}{\rho R_k^2}. \tag{16}$$

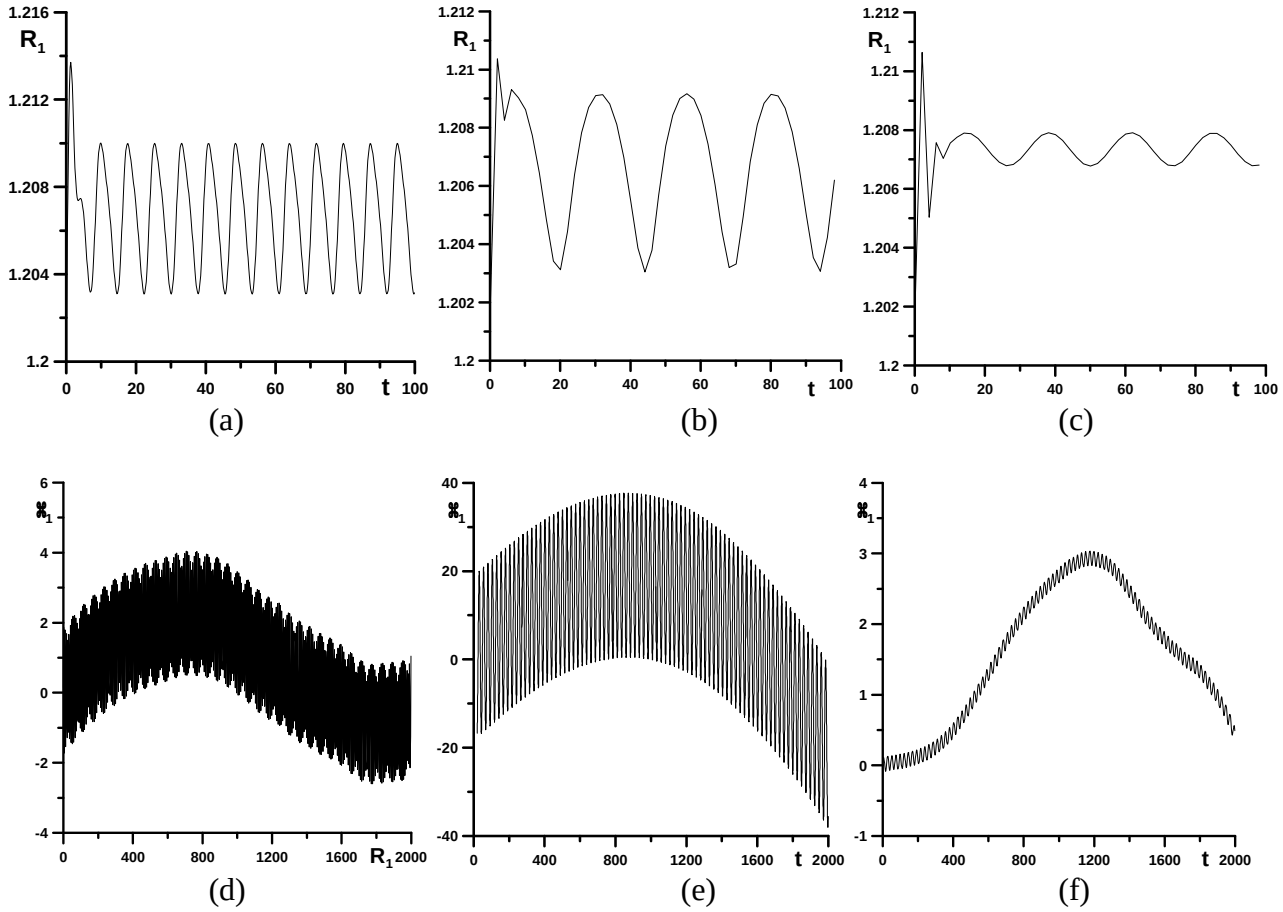

Figure 2: Dependence of the radius (a-c) and deviation of the surface (d-f) of the first bubble.a), d) $\rho = 1$, $V_0 = 15$, $R_1 = 1.2$, $R_{1t} = 0.02$, $L = 100$, $A = 1$, $\omega = 0.812$ b), e) $\rho = 1$, $V_0 = 15$, $R_1 = 1.2$, $R_{1t} = 0.02$, $L = 100$, $A = 1$, $\omega = 0.254$ c), f) $\rho = 1$, $V_0 = 15$, $R_1 = 1.2$, $R_{1t} = 0.02$, $L = 100$, $A = 1$, $\omega = 3.41$

External action contributes

$$p^{(1)}(t) = f_0 \frac{R_i}{\rho} \sin(\omega t) \tag{17}$$

Substituting (15) and (16) in (14), we obtain the equation $U_k^{(1)}(t)$:

$$\rho(U_{tk}^{(1)} \frac{1}{R_k} - U_k^{(0)} U_k^{(1)} \frac{1}{R_k^4}) = p_b^{(1)} - p^{(1)}(t) + \rho\varphi_{it}^{(0)} \tag{18}$$

Thus, we obtain differential equations for the amplitude of the potential k-th bubble:

$$U_{kt}^{(1)} = U_k^{(0)} U_k^{(1)} \frac{1}{R_k^4} \frac{R_k}{\rho} + \frac{R_k}{\rho R_k^3} - f_0 \sin(\omega t) \frac{R_k}{\rho} + \rho\varphi_{it}^{(0)} \tag{19}$$

Equation (2.8) together with equations for the radial vibrations were solved by Gear method. In fig.2 shows the radii and the surface deviations of first bubble dependent on time for different parameters and initial conditions.

Acknowledgements

The work was supported by FCP 2010-1.1-112-129-021.

Aleksey A. Alabuzhev, ICMM UB RAS, Perm, Russia
Andrey A. Ogleznev, PNPPK, Perm, Russia

Instability of thin film on substrate in vibration filed

Aleksey A. Alabuzhev
alabuzhev@mail.ru

Abstract

Non-linear dynamics of a thin dewetting liquid film on a vertically oscillating substrate is considered. We assume moderate vibration frequency and large (compared to the mean film thickness) vibration amplitude. Using the lubrication approximation and the averaging method, we formulate the coupled sets of equations governing the pulsatile and the averaged fluid flows in the film, and then derive the nonlinear amplitude equation for the averaged film thickness. We show that there exists a window in the frequency-amplitude domain where the parametric and shear-flow instabilities of the pulsatile flow do not emerge. As a consequence, in this window the averaged description is reasonable and the amplitude equation holds. The linear and nonlinear analysis of the amplitude equation and the numerical computations show that such vibration stabilizes the film against dewetting and rupture.

1 Problem formulation

We consider an unbounded fluid layer depth H_0^* on a planar horizontal substrate (see fig.1, [1]). Axis Ox and Oy of the Cartesian coordinate system are in the plane of the substrate and the axis Oz perpendicular to substrate. The system is in a gravitational field, the vertical axis Oz parallel to the direction of the vector of gravitational acceleration $\vec{g}_0$.

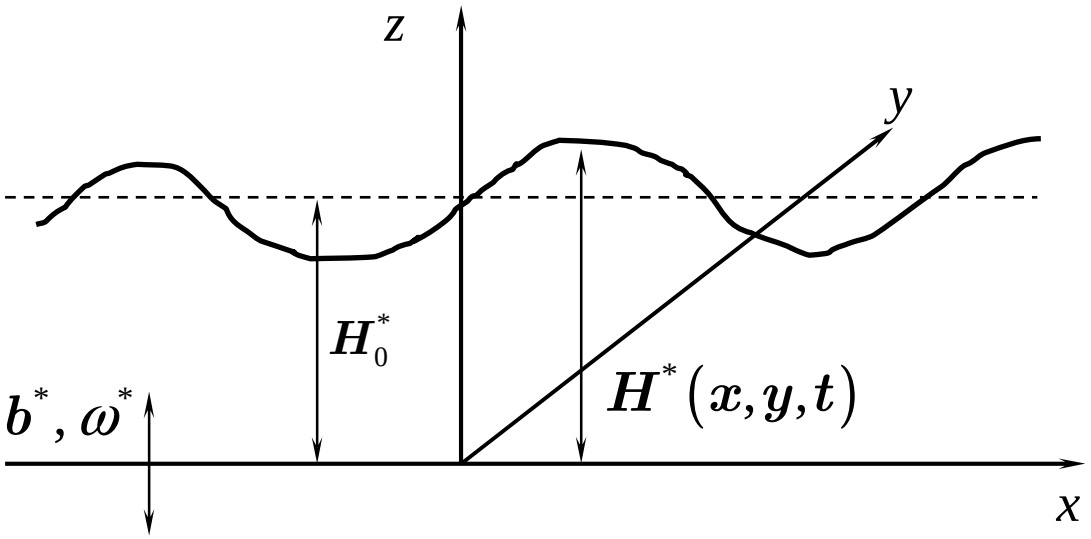

Figure 1: Geometry of a problem

The system is subjected to the vertical vibrations with the amplitude b^* and the

frequency ω^*. We introduce the modulated gravitational acceleration

$$g(t) = g_0 + b^*\omega^{*2}cos(\omega^* t) \tag{1}$$

The equilibrium film thickness H_0^* is so small that it takes into account the molecular interaction of the film to the substrate. We will denote $\phi(\hat{H})$ the potential energy of interaction per unit area of the surface layer. In this paper we consider only the attractive potential Van der Waals:

$$\phi(\hat{H}) = -\frac{A'}{6\pi H^{*3}}, \tag{2}$$

where $A' > 0$ is the Van der Waals parameter (the Hamaker constant).

We scale the time, the length, the velocity and the pressure by H_0^{*2}/ν, H_0^*, ν/H_0^*, $\rho(\nu/H_0^*)^2$, respectively (here, ν is the kinematic viscosity and ρ is the density of the liquid). Then, the liquid motion is governed by the following dimensionless problem:

$$\nabla \cdot \vec{v} = 0, \tag{3a}$$

$$\vec{v}_t + \vec{v} \cdot \nabla\vec{v} = -\nabla p + \Delta\vec{v} - (G_0 + B\Omega^2 \cos\Omega t)\vec{e}_z, \tag{3b}$$

$$\vec{v} = 0 \text{ at } z = 0, h_t + \vec{v} \cdot \nabla h = w,$$

$$(p + \phi - \mathrm{Ca}K)\,\vec{n} = \vec{n} \cdot \vec{T} \text{ at } z = h(x, y, t). \tag{4a}$$

Here, $\mathbf{v}$ is the fluid velocity, w is its z-component, p is the pressure in the liquid, $\mathbf{T}$ is the viscous stress tensor, $h = \hat{H}/\hat{H}_0$ is the dimensionless thickness of the layer, $\mathbf{e}_z$ is the unit vector directed along the $z-$ axis, $\mathbf{n} = (\mathbf{e}_z - \nabla h)/\sqrt{1 + (\nabla h)^2}$ is the normal unit vector to the free surface, $K = \nabla \cdot \mathbf{n}$ is the mean curvature of the free surface, $\phi = -A/h^3$. The subscripts denote partial derivatives with respect to the corresponding variables.

The boundary-value problem (3) and (4) is governed by the following dimensionless parameters: $A = A'/(6\pi\rho\nu^2\hat{H}_0)$ is the dimensionless Hamaker constant, $\mathrm{Ca} = \sigma\hat{H}_0/(\rho\nu^2)$ is the capillary number (where σ is the surface tension), $G_0 = g_0\hat{H}_0^3/\nu^2$ is the Galileo number, $B = \hat{b}/\hat{H}_0$ is the dimensionless amplitude, and $\Omega = \omega\hat{H}_0^2/\nu$ is the dimensionless frequency.

Next we introduce the conventional stretched coordinates and the time:

$$X = \epsilon x,\ Z = z,\ T = \epsilon^2 t,\ \tau = \Omega t, \tag{5}$$

such that $\partial/\partial t = \epsilon^2\partial/\partial T + \Omega\partial/\partial\tau$. Now we rescale the velocity components as follows:

$$u = \epsilon U,\ w = \epsilon^2 W. \tag{6}$$

At this point, the pressure p and the surface position h remain unscaled.

Throughout this paper the capillary number is assumed large:

$$\mathrm{Ca} = C\epsilon^{-2}. \tag{7}$$

You can see more detail in the article [1].

2 Nonlinear evolution of perturbations

The amplitude equation ([1])

$$h_T = \nabla \cdot \left[\frac{1}{3} h^3 \nabla \Pi - \frac{b^2 \Omega^2}{2} \vec{Q}(h) \right], \tag{8a}$$

$$\Pi \equiv p(Z=0) = -\phi(h) - C\nabla^2 h + G_0 h + \frac{b^2\Omega^2}{2} \mathrm{Re} H. \tag{8b}$$

$$\vec{Q} = Q_1(\gamma) h^2 (\nabla h)^2 \nabla h + Q_2(\gamma) h^3 \nabla^2 h \nabla h, \tag{8c}$$

$$f_r(\alpha h) = 1 - \frac{\varphi_+}{\gamma \psi_+}, \; f_i(\alpha h) = \frac{\varphi_-}{\gamma \psi_+}, \tag{8d}$$

$$Q_1 = 3 \frac{4 \sinh \gamma \sin \gamma - \gamma (\psi_+ \varphi_+ - \psi_- \varphi_-)}{2\gamma^2 \psi_+^2}, Q_2 = -\frac{1}{3} + \frac{11\varphi_- - 3\gamma\psi_-}{\gamma^3 \psi_+}, \tag{8e}$$

has the obvious solution $h_0 = 1$ corresponding to the equilibrium state. It follows from equations that

$$h_0 = 1, \; U_0 = W_0 = I_0 = K_0 = H_0 = 0, \tag{9a}$$

$$p_0 = G_0(1-Z) - \phi(1), \; q_0 = \Omega(1-Z). \tag{9b}$$

Thus in the reference frame of the substrate the fluid is motionless – vibration only adds the oscillatory component to the pressure field.

Let in Eq. (8) $h = 1 + \xi$, where ξ is small perturbation. Linearizing with respect to ξ. For its consideration of two-dimensional case the method of finite differences with the conservative scheme. Was created by a numerical algorithm using a parallel spatial computational domain using asynchronous communication between nodes on the boundary.

As a method of integration used a modification BDF-method (Backward Differentiation Formulas method) for solving stiff systems of differential equations - the approximation of polynomials with fixing the main factor of the polynomial (fixed-leading coefficient form).

Sampling was carried out of differential equations, finite difference method. We used the conservative scheme. For the time variable used two-point sampling, for three-point spatial variables. The resulting stack can be distributed by the number of computing nodes in multiples of four.

Communication between the calculated nodes were performed using the library Open-MPI, which implements messaging interface (MPI: The Message Passing Interface). Use asynchronous data transfer scheme between nodes. The coefficient of scalability of the program, because of the simplicity scheme used is not very large. The transition from one computing node to 4 yields increase computing speed by about a factor of 3 to 8 - 5. Some results are presented in fig.2 and fig.3

Acknowledgements

This work was supported by President grant MK-2368.2011.1.

References

[1] Shklyaev S., Khenner M., Alabuzhev A.A. Enhanced stability of a dewetting thin liquid in a single-frequency vibration field. PhysRevE77, 036320 (2008).

Aleksey A. Alabuzhev, IMCC UB RAS, Russia

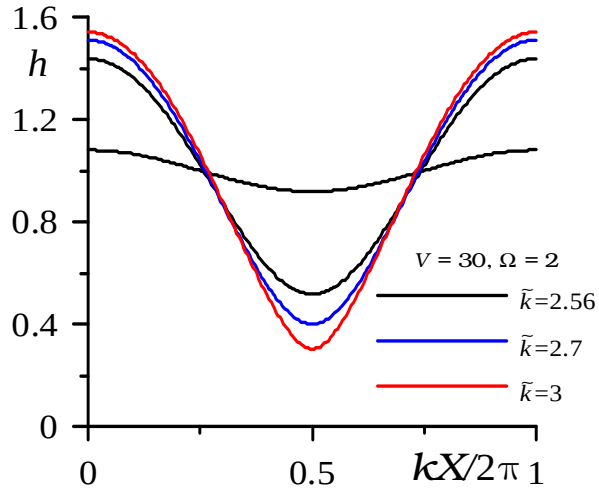

Figure 2: Unstable stationary solutions.

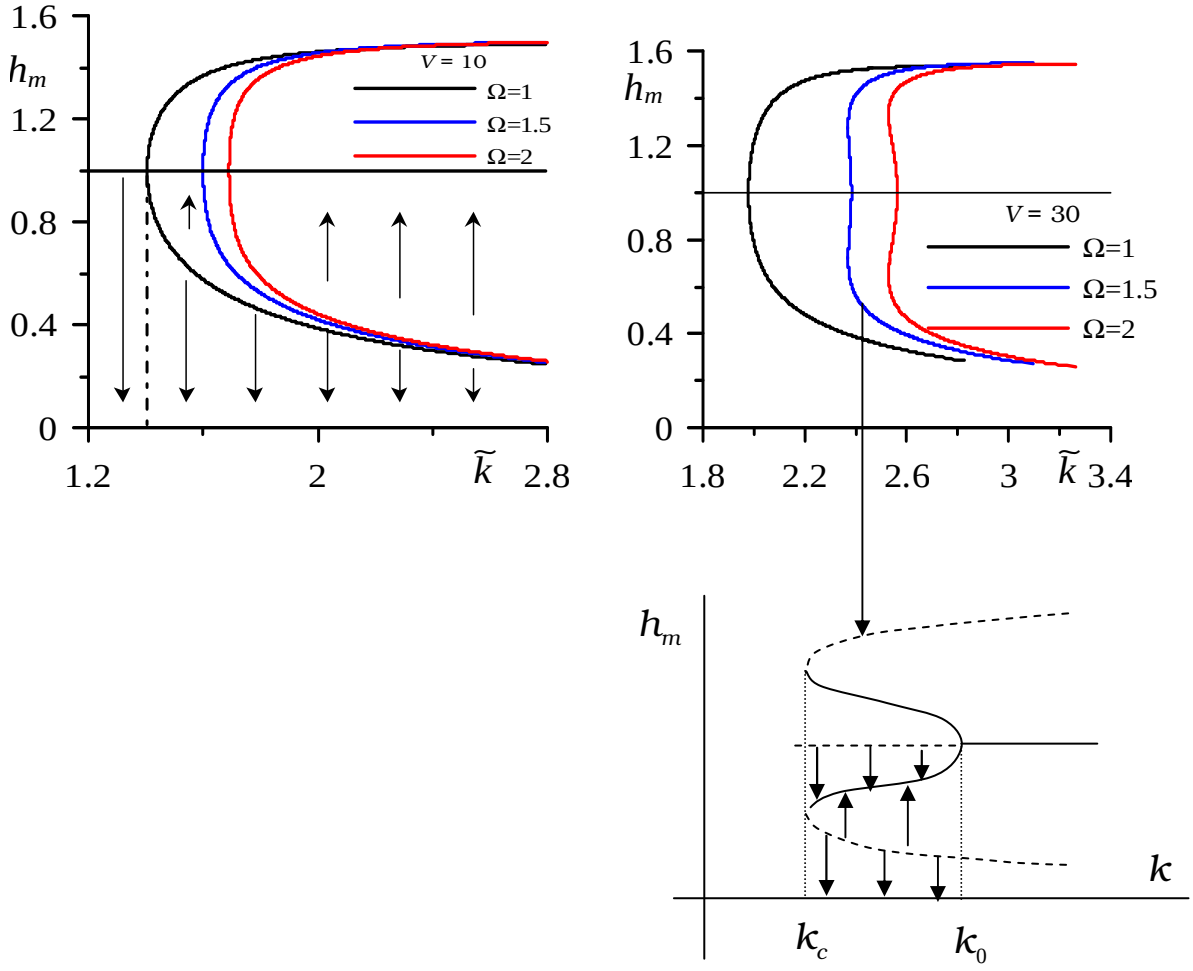

Figure 3: Minimal slower branch and maximal supper branch thickness of the film at the corresponding unstable stationary solution.

Oscillations of an oblate drop

A. A. Alabuzhev D. V. Lyubimov
alabuzhev@mail.ru

Abstract

The dynamics of an oblate fluid drop are considered in this report. The drop is suspended in the different fluid and confined by two parallel rigid plates. The external vibration force acts on the system. The vibration axis is perpendicular to the symmetry axis of the drop. The both vibration amplitude and drop's height are small in comparison with the drop's radius. Arbitrary values of equilibrium contact angle are considered. The specific boundary condition is applied to take the dynamics of contact line into account: the contact line's velocity is proportional to the deviation of contact angle.

1 Problem formulation

This investigation assumes that a drop with a density ρ_i^* is suspended in a fluid of different density ρ_e^*. In the absence of external forces the drop has cylindrical shape with radius R^*. The system is confined between two parallel rigid plates, subjected to vibrations perpendicular to the drop axis (fig.1). In the absence of vibrations a contact angle between a lateral surface of a drop and bounding plate equals $\pi/2$. The thickness of the layer is h. The equilibrium contact angle between the lateral surface of drop and the rigid plate is θ_0.

The vessel is closed at the infinity and undergoes high-frequency oscillations according to the law $\vec{r}=\vec{R}+\mathrm{A}\vec{j}\cos(\omega \mathrm{t})$ ($\vec{r}$, $\vec{R}$ are the radius - vectors of an arbitrary point of a drop surface in the plane parallel to the rigid plates (horizontal plane) in the presence and absence of vibrations, respectively, A is the amplitude of vibrations, $\vec{j}$ is the unit vector in a horizontal plane). The vibration amplitude A is small as compared to R. It is assumed, that the lateral surface of the drop is $r = R + \zeta(\alpha, z, t)$ where α is the polar angle.

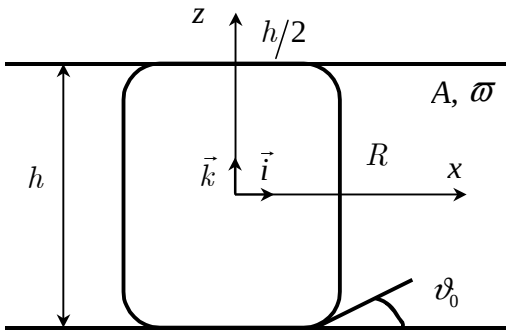

Figure 1: Geometry of a problem

Velocity of motion of a contact line is assumed to be proportional to a deviation of a contact angle from equilibrium value [1]:

$$\frac{\delta\zeta}{\delta t} = \Lambda\vec{k}\nabla\zeta \tag{1}$$

The following quantities are chosen as the scales: time - $\sqrt{\rho_e^* h^2 R_0/\sigma}$, length - $R_0 = R^*(0)$, height - h, potential of velocity - $\mathrm{A}\sqrt{\sigma R_0/(\rho_e^* h^2)}$, density -$\rho_e^*$, pressure - $A\sigma/h^2$, deviations of the drop surface - A.

$$\Delta\varphi = 0, \frac{\partial\varphi}{\partial t} + \frac{1}{2}(\nabla\varphi)^2 = -\frac{1}{\rho_k}p - \omega^2 r cos(\alpha)cos(\omega t), \tag{2}$$

$$\nabla = \frac{\partial}{\partial r}\vec{e}_r + \frac{1}{r}\frac{\partial}{\partial\alpha}\vec{e}_\alpha + b\frac{\partial}{\partial z}\vec{e}_z, \Delta = \frac{1}{r}\frac{\partial}{\partial r}(r\frac{\partial}{\partial r}) + \frac{1}{r^2}\frac{\partial^2}{\partial\alpha^2} + b^2\frac{\partial^2}{\partial z^2}, \tag{3}$$

$$r = R - \epsilon\zeta(\alpha, t) : [(\nabla\varphi)\,\vec{n}] = 0, \frac{\partial\zeta}{\partial t} = \nabla\varphi\nabla F, \epsilon\,[p] = -div(\vec{n}), \tag{4}$$

$$z = \mp 1/2 : \varphi_z = 0, \tag{5}$$

$$r = R - \epsilon\zeta(\alpha, t), z = \mp 1/2 : \zeta_t = \pm\lambda(\zeta_z - \zeta_{0z}), \zeta_{0z} = \tan(\theta_0). \tag{6}$$

where φ is the potential of velocity, $F = r - R - \epsilon\zeta(\alpha, t)$ - drop surface. The boundary problem contains the following dimensionless parameters: small vibration amplitude - $\epsilon = A/R_0$, the ratio of densities - $\rho{=}\rho_i^*/\rho_e^*$, $\rho_e = 1$, $\rho_i = \rho$, capillary parameter $\lambda{=}\Lambda\sqrt{h^2 R_0\rho_e/\sigma}$, vibrational frequency - $\omega = \omega^*\sqrt{\rho_e^* R_0 h^2/\sigma}$, the ratio of radius to height - $b = R_0/h$.

2 Equilibrium shape

The equilibrium shape of drop is determined by the condition of balance of normal stresses in the absence of movement ($\varphi = 0$):

$$div\vec{n} - c = 0, \tag{7}$$

where c is same constant, with boundary conditions:

$$z = \pm 1/2 : R_z = \mp b^{-1}\mathrm{ctg}\vartheta_0, \tag{8}$$

$$z = 02 : R = 1, \tag{9}$$

Given, that $\vec{n} = \nabla\,(r - R\,(z))/|\nabla\,(r - R\,(z))|$, we can written (100) as

$$RR_{zz} + \left(1 + b^2 R_z^2\right)\left(R\sqrt{1 + b^2 R_z^2} - 1\right) = c.$$

Consider the case of small layer thickness, assuming that $b \gg 1$, i.e. $\beta = b^{-1} \ll 1$. Expand the function $R(z)$ in the small parameter β:

$$R(z) = 1 + \beta R^{(1)}(z) + \beta^2 R^{(2)}(z) + ..., \tag{10}$$

i.e. we assume that the shape of the drop is little different from the cylindrical. In the first order we obtain the solution:

$$R^{(1)} = \frac{1}{2\cos\vartheta_0}\left(1 - \sqrt{1 - 4z^2\cos^2\vartheta_0}\right). \tag{11}$$

The equilibrium shape of drop for different values of contact angle shows on (fig.2).

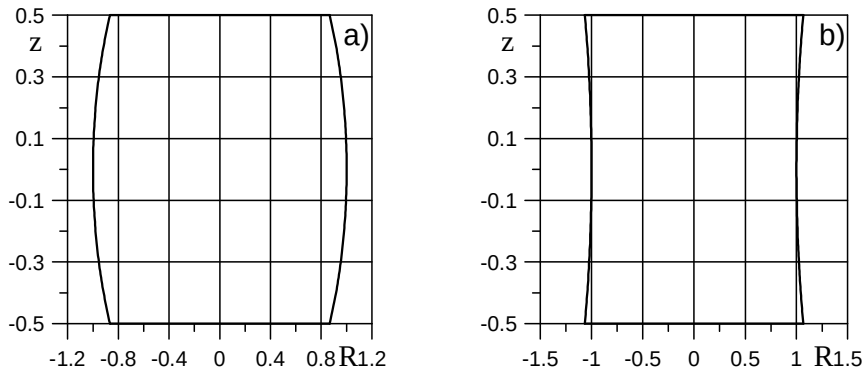

Figure 2: Equilibrium shape a) $\vartheta_0 = 60^o$, b) $\vartheta_0 = 105^o$

3 Eigen oscillations

We study the eigen oscillations of the considered drop in the case of small layer thickness $\beta \ll 1$. Flow region in the drop can be divided into regions having the shape of the cylinder of unit radius, and a thin transition region between the cylinder and the surrounding liquid. In the transition region, the velocity potential and pressure of fluids may undergo significant changes in the radial direction, which requires the introduction of "fast " radial coordinate $r_1 = (r - R(z))\,\beta^{-1}$.

For this problem, there are three typical range of natural frequencies. The highest frequencies have oscillations with a wavelength proportional to the height h. For such oscillations the contact line is fixed. The lowest frequencies are vibrations with a wavelength proportional to the radius R. In this case, the contact line moves freely along the solid surfaces. Average frequency oscillations have a wavelength which is proportional to the Hocking constant Λ. Such movement corresponds to the translational vibration mode, which describes the movement of the center of mass of the drop.

To find the eigen frequencies of the small parameter method is applicable and the method of matched expansions. We expand the velocity potential field, the surface deviation and the pressure in powers of small parameter β:

$$\varphi = \varphi^{(0)} + \beta\varphi^{(1)} + \ldots,\ \zeta = \zeta^{(0)} + \beta\zeta^{(1)} + \ldots,\ p = p^{(0)} + \beta p^{(1)} + \ldots. \tag{12}$$

As noted above, there are three typical range for the natural frequencies. Frequency scaling is used in dimensionless variables the system (2) - (6) corresponds to the scale of the fundamental frequency of the translational mode. Consider first the average range, corresponding to this mode. Substituting (12) into (2) - (6), without regard to external vibrations, the leading order system of equations and boundary conditions for the complex amplitudes of the potential, pressure and deflection of the surface in different regions of the flow we get:

$$\varphi^{(0)}_{rr} + r^{-1}\varphi^{(0)}_{r} + r^{-2}\varphi^{(0)}_{\alpha\alpha} = 0, p^{(0)} = -i\Omega\rho\varphi^{(0)}, \tag{13}$$

$$r = 1 : \left[\varphi^{(0)}_{r}\right] = 0, i\Omega\zeta^{(0)} = \varphi^{(0)}_{r}, \left[p^{(0)}\right] = 0, \tag{14}$$

where Ω - to be determined eigen frequency. The solution to this problem can be represented as:

$$\varphi^{(0)}_{ie} = c_i r e^{i\Omega t}\cos\alpha, \varphi^{(0)}_{ee} = c_e r^{-1} e^{i\Omega t}\cos\alpha, \zeta^{(0)}_{e} = g e^{i\Omega t}\cos\alpha. \tag{15}$$

In transitions region

$$\varphi^{(0)}_{r_1 r_1} + \varphi^{(0)}_{zz} = 0,\ p^{(0)} = -i\Omega\rho\varphi, \tag{16}$$

$$r_1 = R^{(1)} : \left[\varphi^{(0)}_{r_1}\right] - R^{(1)}_z \left[\varphi^{(0)}_z\right] = 0, i\Omega\zeta^{(0)} = \varphi^{(0)}_{r_1} - R^{(1)}_z \varphi^{(0)}_z, \left[p^{(0)}\right] = \frac{\zeta^{(0)}_{zz}}{\left(1 + R^{(1)2}_z\right)^{3/2}}, \tag{17}$$

$$z = \mp 1/2 : \varphi^{(0)}_z = 0 \tag{18}$$

$$z = \mp 1/2, r = 1, r_1 = R^{(1)} : i\Omega\zeta^{(0)} = \pm\lambda\zeta^{(0)}_z, \tag{19}$$

solution of task (16) - (18) has the form:

$$\varphi^{(0)}_{ii} = \left(c_{0i} + c_{1i} r_1 + \sum_{k=1}^{\infty} c_{1k} \exp\left(2\pi k r_1\right) \cos\left(2\pi k z\right)\right) e^{i\Omega t} \cos(\alpha), \tag{20}$$

$$\varphi^{(0)}_{ei} = \left(c_{0e} + c_{1e} r_1 + \sum_{k=1}^{\infty} c_{2k} \exp\left(-2\pi k r_1\right) \cos\left(2\pi k z\right)\right) e^{i\Omega t} \cos(\alpha), \tag{21}$$

$$\zeta^{(0)}_i = \left(c + dz^2 + \sum_{k=1}^{\infty} c_{3k} \cos\left(2\pi k z\right)\right) e^{i\Omega t} \cos(\alpha). \tag{22}$$

We use the method of matched expansions to combine the solutions (15), (20) - (22). Received frequency Ω for various cases of the equilibrium contact angle is shown in (fig.3(a, b)). It represented a real Ω_r and imaginary Ω_i (decrement) of the complex natural frequency Ω, depending on the capillary parameter λ. Damping due to dissipation at the contact line and is not related to viscosity. As in [2], [3], the fundamental frequency translational mode there is the characteristic value of the capillary parameter λ_c, such that $\Omega_r = 0$ for $\lambda = \lambda_c$ for the translational mode (fig.3(a)). This value corresponds to the appearance of two branches of damping rates (fig.3(b)).

In evaluating the characteristic values of eigen frequencies has been shown that high frequencies correspond to the capillary waves at the interface. These waves do not depend on the slow radial coordinate r.

We introduce a new unit of measurement for time $\sqrt{\rho^*_e h^3/\sigma}$, the velocity potential $A\sqrt{\sigma/(\rho^*_e h^3)}$ and the pressure $A\sigma R_0/h^3$. As a result, change the following dimensionless parameters of the problem: the vibration frequency $\omega = \omega^*\sqrt{\rho^*_e h^3/\sigma}$, the capillary parameter $\lambda = \Lambda\sqrt{\rho^*_e h^2/\sigma}$. Complex frequencies Ω for three different cases of the equilibrium contact angle shown in fig.3(c, d). In the case of a direct equilibrium contact angle, the solution for finding natural frequencies coincides with a similar solution in [3].

Low frequencies correspond to the motion of free moving drop. Such a movement depends only on the slow radial coordinate and does not depend on the fast radial and vertical coordinates. We introduce a new unit of measurement for time $\sqrt{\rho^*_e R^3_0/\sigma}$, the velocity potential $A\sqrt{\sigma/(\rho^*_e R^3_0)}$ and the pressure $A\sigma R_0/h^3$. Change the following dimensionless parameters: vibration frequency $\Omega = \omega^*\sqrt{\rho^*_e R^3_0/\sigma}$, the capillary parameter $\lambda = \Lambda\sqrt{\rho^*_e R^3_0/(\sigma h^2)}$. The frequencies for the azimuthal wave number $m = 2$ are shown in fig.3(e, f). In the case of a direct equilibrium contact angle, frequency, consistent with the results [3].

For the odd modes exist only high frequencies. Indeed, as noted above, the average frequencies correspond to the fundamental frequency translational modes, whose eigenfunctions are even, and the eigenfunctions corresponding to low frequencies do not depend on the coordinates, ie are also even. Fig.4 shows the frequencies and damping coefficients of the capillary parameter for different values of the equilibrium contact angle for the case of high-frequency oscillations.

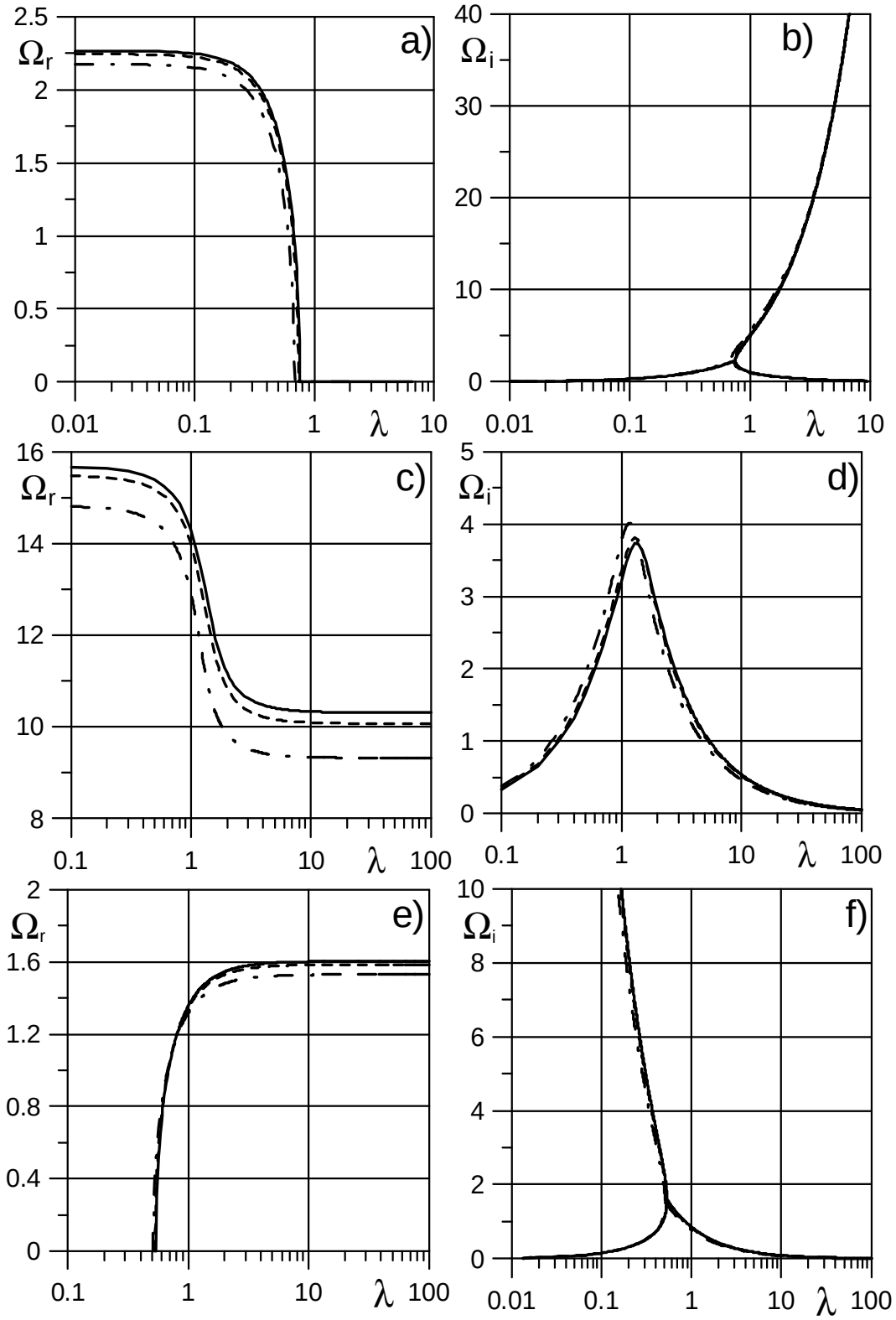

Figure 3: Dependence of the frequency (a, c, e) and damping coefficients (b, d, f) for complex frequencies Ω_{10} (a, b), Ω_{12} (c, D) and Ω_{20} (e, f) of natural oscillations of the capillary parameter for different values of the equilibrium contact angle ($\rho = 1.33$))

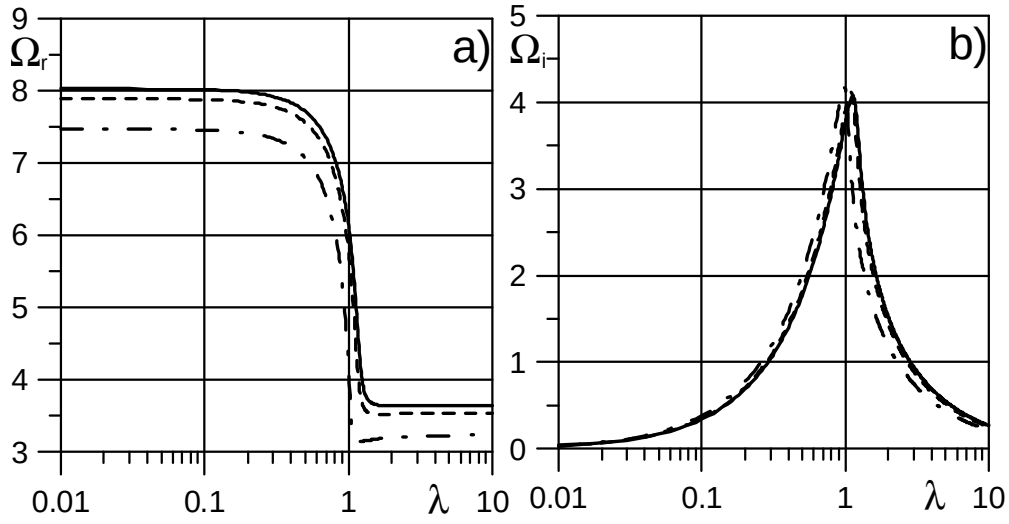

Figure 4: Dependence of the frequency (a) and damping coefficient (b) for Ω_{11} of the capillary parameter ($\rho = 1.33$) $\vartheta_0 = 60^o$ (dot-dash line), $\vartheta_0 = 75^o$ (dashed), $\vartheta_0 = 90^o$ (solid)

4 Conclusion

We are considered eigen oscillations of the highly compressed drop. It's shown that there are three characteristic scales of eigen frequencies. High frequencies are not depend on the azimuthal number and for the direct equilibrium contact angle correspond to the frequencies of capillary waves on liquid surface. Low frequencies are not depend on the wave number and large values of the capillary parameter coincide with the basic natural frequency of cylindrical drops. Intermediate characteristic scale of frequencies corresponds to the fundamental frequency of the translational mode.

Found that for finite values of capillary parameters of motion of the contact line leads to damping of free oscillations. Effect of dissipation leads to a limitation of maximum amplitude at resonance and to shift the resonant frequency. The largest amplitude of forced vibrations is achieved in the case of direct equilibrium contact angle.

Acknowledgements

The work was supported by the President RF grant MK-2368.2011

References

[1] Hocking L.M. The damping of capillary-gravity waves at a rigid boundary. J. Fluid Mech., 1987, v.179, pp.253-266.

[2] Lyubimov D.V., Lyubimova T.P., Shklyaev S.V. Behavior of a drop on an oscillating solid plate//Physics of Fluids. 2006. V.18(l). 012101.

[3] Alabuzhev A.A., Lyubimov D.V. Effect of the contact-line dynamics on the natural oscillations of a cylindrical droplet. J. Applied Mechanics and Technical Physics, V. 48, N. 5, pp.686-693

Aleksey A. Alabuzhev, ICMM UB RAS, Perm, Russia
Dmitriy V. Lyubimov, PSU, Perm, Russia

Transient hydrodynamics behavior of fluid flow in micro-converging plates

Ahmad Al-Shyyab A. F. Khadrawi
asalshyyab@just.edu.jo

Abstract

The hydrodynamics behavior of fluid flow in micro-converging plates is investigated analytically. Effects of Knudsen number and the location on the microchannel hydrodynamics behavior and the coefficient of friction are investigated. It is found that as Kn increases the slip in the hydrodynamic boundary condition increases. Also, the coefficient of friction decreases as Kn increases and the coefficient of friction decrease as the location proceeds. Keywords: converging plates, micro-plates, microchannel, hydrodynamic behavior, slip velocity

1 Introduction

Recently, a growing interest in microchannel fluid mechanics and heat transfer has emerged because of possible cooling applications in space systems, manufacturing and material processing operations, and in high-power-density chips in supercomputers and other electronics. As this area continues to grow, it becomes increasingly important to understand the mechanisms and fundamental differences involved in fluid mechanics and heat transfer in microchannels. It has been reported that the phenomena in microgeometry may differ from those in macroscopic counterparts. Several factors that are dominant in micro scale have been identified through a number of experimental, analytical and numerical works. Among them the noncontinuum effect, compressibility effect, and various surface effects have been under vigorous investigation. In micro geometries the flow is described as granular for liquids and rarefied for gases, and the walls "move" [1]. The approximations for continuum flow analysis fail for microscale flows as the characteristic length of the flow gradients (L) approaches the average distance traveled by molecules between collisions (mean free path,k). The ratio of these quantities is known as the Knudsen number($Kn = k = L$) and is used to indicate the degree of flow rarefaction or scale of the flow problem. Rarefaction or microscale effects are ignored by the Navier-Stokes equations and these equations are therefore strictly accurate only at vanishingly small$Kn, (Kn < 0.001)$. The appropriate flow and heat transfer models depend on the range of the Knudsen number, and a classification of the different gas flow regimes is as follows:$Kn < 10^{-3}$ for the continuum flow, $10^{-3} < Kn < 10^{-1}$ .for the slip flow, $10^{-1} < Kn < 10^{+1}$. for the transition flow, and $10^{+1} < Kn$ for the free molecular flow [2]. In the slip flow regime, the continuum flow model is still valid for the calculations of the flow properties away from solid boundaries. However, the boundary conditions have to be modified to account for the incomplete interaction between the gas molecules and the solid boundaries. The important features of gas flow in micro ducts are mainly due to rarefaction and compressibility effects. Two more effects due to acceleration and a non-parabolic velocity profile were found to be of second

order compared to the compressibility effect [3]. The rarefaction effect can be studied by solving the momentum and energy equations subjected to velocity slip and temperature jump boundary conditions. In spite of the large number of published research so far in the microflows literature (for more details, the reader may refer to the review papers [4] and [5]), many parts of the physical laws governing the fluid flow and heat transfer in micro-geometry remain unknown. Recently, discrepancies between microchannel flow behavior and macroscale Stokes flow theory have been summarized in a review by Ho and Tai [6]. It is widely accepted that the deviation observed in gas flows can be attributed to slip at the wall [7], and several researchers have reported results for gas flows([8]-[12]). Then, there has been an enormous interest in research works of micro-system over the last decade ([13]-[23]). The objective of this study is to investigate the gaseous flow characteristics, hydrodynamics and thermal behaviors, in micro Couette flow problem. In particular, this study will be focused on the effect of the velocity of the driving force on the slip velocity and temperature jump at the wall(s).

2 Mathematical Model

Consider an incompressible fluid flow between two converging plates toward a sink as shown in Fig. 1. The flow is assumed to be a Newtonian fluid. The governing equations of this flow are continuity and momentum. The continuity equation is ,

$$\frac{\partial u}{\partial x}+\frac{\partial v}{\partial y} \tag{1}$$

And the momentum equations are
a) x-momentum:

$$u\frac{\partial u}{\partial x}+v\frac{\partial v}{\partial y}=-\frac{1}{\rho}\frac{\partial p}{\partial x}+v\frac{\partial^2 v}{\partial y^2} \tag{2}$$

Applying this momentum component outside the boundary layer to get

$$U_e(x)=U\frac{L}{x} \tag{3}$$

Where the free stream velocity outside the boundary layer is

$$U_e(x)=U\frac{L}{x} \tag{4}$$

Here, U is the free stream velocity at some characteristic length L defined as distance from the fluid source.
b) y-momentum:

$$\frac{\partial p}{\partial x}=0 \tag{5}$$

By use of stream function $\psi(x,y)=-\sqrt{ULv}\ f(x,y)$, and the similarity variable is $\eta=(y/x)\sqrt{UL/v}$, the flow velocity components that satisfy the continuity equation would be defined as $u/U_e=\partial\psi\ /\partial y=-f'$, and $v/U_e=\sqrt{v/UL}\ \eta f$. With these definitions the fluid governing equations are reduced to third order nonlinear ordinary differential equation. Multiply this equation by f' and simplify to get,

$$(\frac{f''^2}{2})'-(\frac{f'^3}{3})'+(f')'=0 \tag{6}$$

Integrate the last equation (Eq. 6) and use the boundary conditions $f'(\eta \to \infty) \to 1$ and $f''(\eta \to \infty) \to 0$ to get,

$$(\frac{f''^2}{2})' - (\frac{f'^3}{3})' + (f')' = \frac{2}{3} \tag{7}$$

The no-slip boundary conditions represent a classical Newtonian fluid flow. Its solution is well established. However, for micro-fluid flow the velocity component along the boundary ($y = 0$) can be assumed to be proportional to its gradient along the boundary normal, where

$$u(x,y) = (\beta\lambda)\frac{\partial u(x,0)}{\partial y} \to f'(0) = \beta Kn\sqrt{\frac{UL}{v}}f''(0) \tag{8}$$

Where the Knudson number $Kn = \lambda/x$ and $\beta = (2-\sigma_v)/\sigma_v$. Substituting Eq.8 into Eq. 7 to get,

$$\frac{1}{2}(\frac{v}{UL}\frac{1}{\beta Kn^2})(f'(0))^2 - \frac{1}{3}(f'(0))^3 + f'(0) = \frac{2}{3} \tag{9}$$

The roots of the last equation satisfie the first order velocity slip boundary conditions. It has three roots; two of them are complex ones while the third one which is our interest here is real. Lets denote this real solution by F_0 . The Integration of Eq. 6 yields,

$$\eta = \sqrt{2}\, tanh^{-1}(\frac{\sqrt{2+f'(\eta)}}{3}) + C \tag{10}$$

Apply the slip boundary represented by the real root of Eq. 9, $f'(0) = F_0$, to get the value of the integration constant C as,

$$C = -\sqrt{2}\, tanh^{-1}(\frac{\sqrt{2+F_0}}{\sqrt{3}}) \tag{11}$$

And rewrite Eq. 10 as,

$$f'(\eta) = 3tanh^2(\frac{\eta + \sqrt{2}tanh^{-1}(\frac{\sqrt{2+F_0}}{\sqrt{3}})}{\sqrt{2}}) - 2 \tag{12}$$

Further integration of the last equation is not needed as both velocity components depend on the first derivative $f'(\eta)$.

The dimensionless coefficient of friction can be as,

$$C_f(x) = -\mu\frac{\partial u}{\partial y}/(\frac{1}{2}\rho(U_e(x))^2) = \mu U_e f''\frac{1}{x}\sqrt{\frac{UL}{v}}/(\frac{1}{2}\rho U_e^2) = 2\sqrt{\frac{1}{x}}f''(0) \tag{13}$$

3 Result and Discussions

Figure 2 shows the transient behavior of the axial velocity at different Knudson number. It is clear from this figure that the dimensionless velocity distribution increases as the Knudson number increases. Fig. 3 shows the dimensionless transient transverse velocity at different Knudson number. It is obvious that the dimensionless velocity increases as the time proceeds. The coefficient of friction as a function of Knudson number at different locations are shown in Figures (4-4). It is clear that the coefficient of friction decreases as Kn increases. Also, the C_f decrease with the location. The velocity slip at the boundaries increases as Kn increases as shown in Fig. 6.

4 Conclusion

Effects of Knudsen number and the location x on the microchannel hydrodynamics behavioras well as the coefficient of friction C_f are investigated. It is found that as Kn increases the slip in the hydrodynamic boundary condition increases. Also, the coefficient of friction C_f decreases as Kn increases and it decrease as the location proceeds.

5 Nomenclature

Kn	λ/L
L	characteristic length, m
u	axial velocity, m
v	transverse velocity
U_e	free stream velocity, [m/s]
x	x-coordinate, m
y	y-coordinate, m

Greek symbols

β	$= (2 - \sigma_v)/\sigma_v$
η	similarity variable $(y/x)\sqrt{UL/v}$
ψ	stream function $= -\sqrt{ULv}f(x, y)$
λ	mean free path, [m]
ρ	density, $[kg/m^3]$
ν	kinematic viscosity, $[m^2s^{-1}]$
σ_v	tangetial-momentum accommodation coefficient

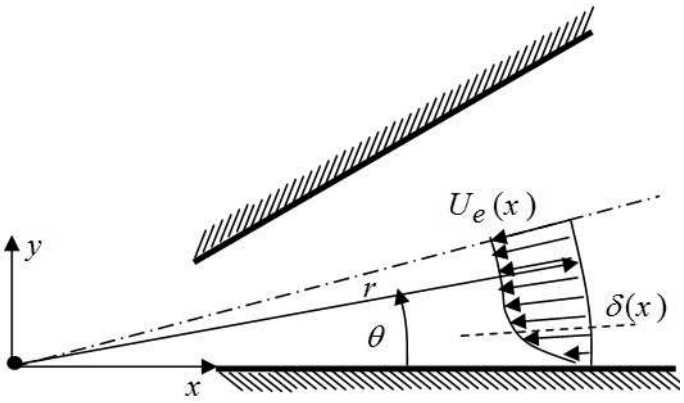

Figure 1: Convergent channel flow. Point Sink flow

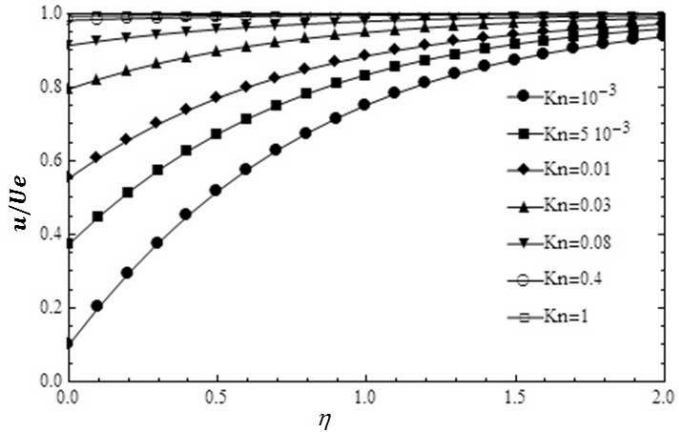

Figure 2: Dimensionless horizontal component of the velocity for different values of Knudson number Kn.

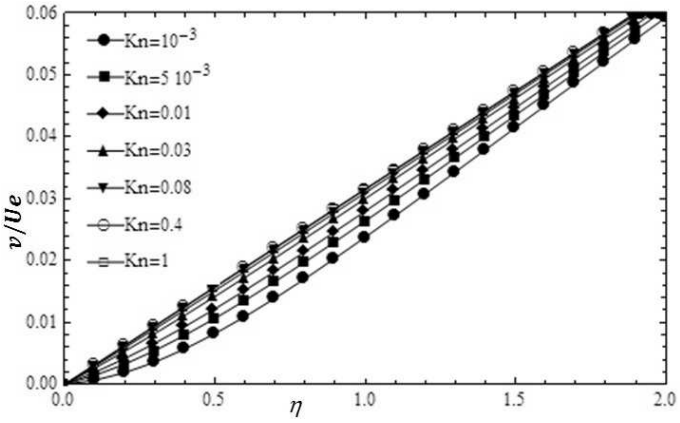

Figure 3: Dimensionless vertical component of the velocity for different values of Knudson number Kn.

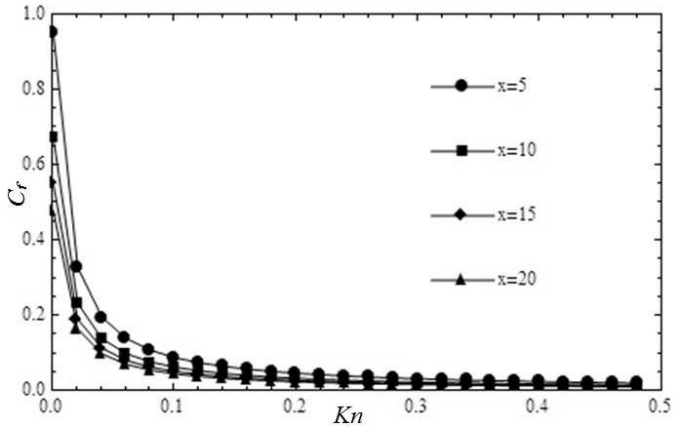

Figure 4: Coefficient of friction as a function of Knudson number Kn at different locations.

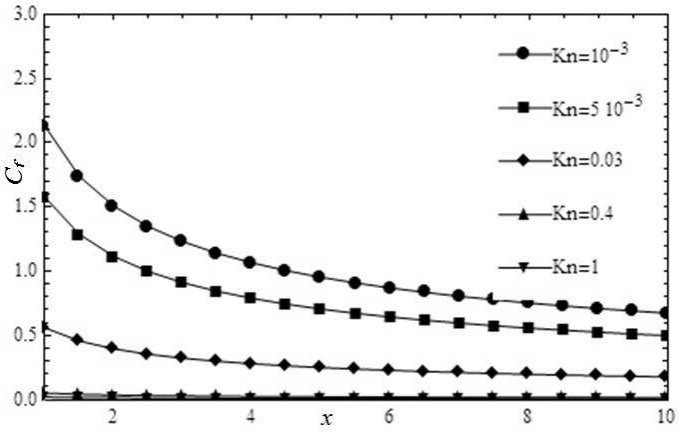

Figure 5: Coefficient of friction as a function of Knudson number Kn at different locations.

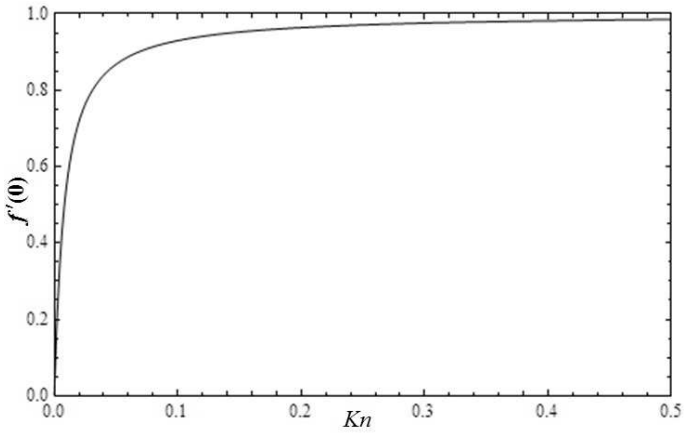

Figure 6: Velocity slip at the boundaries as a function of Knudson number Kn..

References

[1] Karniadakis, G., Beskok, A.: Micro flows fundamentals and simulation. New York: Springer 2002.

[2] Zohar, Y.: Heat convection in micro ducts. Kluwer 2003..

[3] Zohar, Y., Lee, W., Lee, S., Jiang, L., Tong, P.: Subsonic gas flow in a straight and uniform microchannel. J. Fluid Mech. 472, 125–151 (2002).

[4] Duncan, G. P., Peterson, G. P.: Review of microscale heat transfer. Appl. Mech. Rev. 47(9), 397–428 (1994).

[5] Obot, N. T.: Toward a better understanding of friction and heat transfer in microchannels – Literature review. Microscale Thermophys. Engng. 6, 155–173 (2002).

[6] Ho, C., Tai, Y.: Micro-electro-mechanical systems (MEMS) and fluid flows. Ann. Rev. Fluid Mech. 30, 579–612 (1998).

[7] Shih, J. C., Ho, C., Liu, J., Tai, Y.: Monatomic and polyatomic gas flow through uniform microchannels. Microelectromech. Sys. (MEMS) 59, 197–203 (1996).

[8] Wu, P., Little, W. A.: Measurement of friction factors for the flow of gases in very fine channels used for microminiature Joule–Thompson refrigerators. Cryogenics 23, 273–277 (1983).

[9] Choi, S. B., Barron, R. F., Warrington, R. O.: Fluid flow and heat transfer in microtubes.Micromech. Sensors Actuators Sys. 32, 123–134 (1991).

[10] Harley, J. C., Huang, Y., Bau, H., Zemel, J. N.: Gas flows in micro-channels. J. Fluid Mech. 284, 257–274 (1995).

[11] Choquette, S. F., Faghri, M., Kenyon, E. J., Sunden, B.: Compressible fluid flow in micron-sized channels. Nat. Heat Transfer Conf. 5, 25–32 (1996).

[12] Guo, Z. Y., Wu, X. B.: Compressibility effects on the gas flow and heat transfer in a microtube. Int. J. Heat Mass Transf. 40, 3251–3254 (1997).

[13] Al-Nimr, M. A. and Khadrawi, A. F.: Thermal behavior of a stagnant gas confined in a horizontal microchannel as described by the dual-phase-lag heat conduction model, Int. J. Thermophysics, Vol. (25), pp. 1953 (2004).

[14] Khadrawi, A. F., Othman A. and Al-Nimr, M.: Transient free convection fluid flow in a vertical microchannel as described by the hyperbolic heat conduction model, Int. J. Thermophysics, Vol. (26), pp.905 (2005).

[15] Haddad, O., Abuzaid, M. and Al-Nimr, M.: Entropy generation due to laminar incompressible forced convection flow through parallel-plates microchannel, Entropy, Vol. 6(5), pp. 413-426 (2004).

[16] Haddad, O. M., Al-Nimr, M. A. and Abuzaid, M. M.: The effect of frequency of fluctuating driving force on basic slip micro-flows, Acta Mechanica , Vol. 179, pp. 249-259 (2005).

[17] Haddad, O. M., Abuzaid, M. M. and Al-Nimr, M. A.: Developing free convection gas flow in a vertical open-ended micro-channel filled with porous media, Numerical Heat Transfer, Part A, Vol. 48 (2005).

[18] Haddad, O. M., Al-Nimr, M. A. and Taamneh, Y.: Hydrodynamic and thermal behavior of gas flow in micro channels filled with porous media, J. Porous Media, Vol. 9(5), pp. 403-414 (2006).

[19] Haddad, O. M., Al-Nimr, M. A. and Abuzaid, M. M.: Effect of periodically oscillating driving force on basic microflows in porous media, Journal Porous Media, Vol. 9(7), pp. 695-707 (2006).

[20] Haddad, O.M. , Al-Nimr, M. A. and Al-Omary, J. Sh.: Forced convection of gaseous slip-flow in porous micro-channels under local thermal non-equilibrium conditions, Transport in Porous Media, Vol. 67(3), pp. 453-471 (2007).

[21] Haddad, O.M. , Al-Nimr, M. A. and Sari, M.: Forced convection gaseous slip flow in circular porous micro-channels, Transport in Porous Media, Vol. 70(2), pp. 167-179 (2007).

[22] Al-Jarrah, J., Khadrawi, A. and Al-Nimr, M. A.: Film condensation on a vertical micro-channel, Int. Communication in Heat and Mass Transfer, Vol. 35(9), pp. 1172-1176 (2008).

[23] Haddad, O. M., Al-Nimr, M. A. and Shatnawi, G., Free convection gas flow in porous micro-channels, Accepted for presentation in the 6th IASME/WSEAS International Conference on Heat Transfer, Thermal Engineering and Environment (HTE'08), Rhodes Island, Greece, August 20-22, (2008).

[24] Kiwan, S. and Al-Nimr, M. A.: Flow and Heat Transfer over a Stretched Micro-Surface, Accepted for publication in ASME J. Heat Transfer (2008).

[25] Al-Nimr, M. A., Maqapleh, A. M., Khadrawi, A. F. and Ammourah S. A.: Fully developed thermal behaviors for parallel flow microchannel heat exchanger, Accepted for publication in International Communications in Heat and Mass Transfer (2009).

[26] Bataineh, K. and Al-Nimr, M. A.: 2-D NavierStokes Simulations of Microscale Viscous Pump with Slip Flow, Accepted for publication in ASME Journal of Fluids Engineering (2009).

Ahmad Al-Shyyab, Department of Aeronuatical Engineering, Jordan University of Science and Technology, Jordan
A. F. Khadrawi, Mechanical Engineering Department, Al-Balqa' Applied University, Al-Huson college P.O. Box 50, Irbid 21510, Jordan

The energy approach to the solution of the high cycle fatigue problem

Alexander R. Arutyunyan Robert A. Arutyunyan Kira S. Yakimova
Robert.Arutyunyan@paloma.spbu.ru

Abstract

From the extensive literature on the fatigue problem [1, 2], published for more than one hundred years, it follows that the fundamental amount of failures in engineering practice connect with the fatigue fractures of materials and structure elements. The fatigue problem is complicated one and it is not solved yet. So the theoretical and experimental investigations of this problem will be continued. In our paper the energy approach to formulate the fatigue strength criterion is proposed. The criterion is based on the latent energy investigations. This conception was not applied previously to the fatigue problem and can be found the most perspective for fatigue strength predictions of high-strength metallic alloys which work in gigacycle and teracycle fatigue regimes. On the base of experimental results the logistic function is used to describe the kinetics of latent energy accumulation as a function of irreversible deformation. Similar rule of latent energy kinetics is observed in experiments with different metals. When the high cycle fatigue criterion is formulated it is assumed that the cyclic strength of metals is defined by the latent energy, stored in specimen, when it is reached the critical value in accordance with the logistic curve in the saturation zone. Using the experimental results, the functions and parameters of logistic function and criterion are concretized and the predictions of fatigue strength in gigacycle regime were conduct.

Financial support of the Russian Foundation for Basic Research (Grant N 11-08-00763) is gratefully acknowledged.

1 Introduction

The energy methods are the most fundamental approach for receiving the deformation and fracture laws for materials and structures. It is well known that the fracture mechanics as a science was originated by the Griffith's energy concept. In this paper the results of recent experimental investigations on latent energy stored in metallic materials during the plastic deformation are used to formulate the fatigue fracture criterion for metallic materials.

In the process of plastic deformation the significant changes in metallic materials due to increasing the interior energy are occurred. During the plastic deformation heat is emitted so the deformation energy is transformed into the heat. But not the whole work is emitted to heat. A part of it, called the latent energy of deformation [3-7], is transformed to the potential energy of lattice distortion. The latent energy in average constitutes 10-15% of full deformation energy.

The methods of measuring the latent energy are reduced to measure, with a sufficient accuracy, the deformation energy and emitted heat. In this case the energy balance is defined by the first law of thermodynamics, which can be written as $U = E - Q$, where U is interior (latent) energy, E is the deformation energy and Q is the heat.

The results of experiments on latent energy carried out in recent years [8-10] show that the relation for the latent energy or the stored energy is expressed in the form of logistic function. Our experiments [11] conducted on cyclic bending of specimens made of construction materials show that the relations of different physical and mechanical characteristics from number of cycles has two precisely expressed regions. Similarly to the logistic function these relations have the precisely expressed point of inflection. These results are the additional confirmation for the introduction of the logistic function, when formulating the fatigue strength criterion. We assume that metals cyclic strength is defined by the value of latent energy, when it reaches the critical value.

2 Damage parameter, based on the latent energy

It is well known that the logistic function describes the different processes which lead to saturation [12-14], and in our consideration it is the solution of the following kinetic equation

$$\frac{dW}{d\varepsilon} = AW(W_* - W), \tag{1}$$

where W is latent energy, ε is deformation, A and W_* are constants.

Solving equation (1) with the initial conditions $\varepsilon = 0$, $W = W_0$, we will have the following relation, expressed in the form of logistic function

$$W = \frac{W_*}{1 + \left(\frac{W_*}{W_0} - 1\right) \cdot e^{-A\varepsilon W_*}}. \tag{2}$$

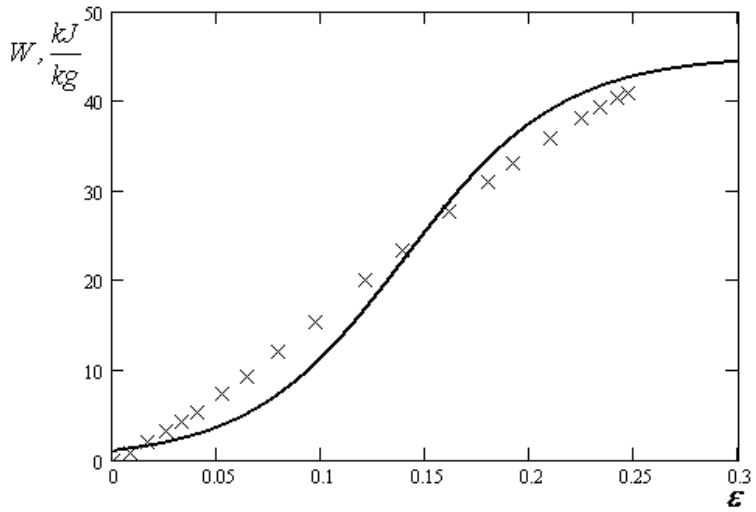

Figure 1: Logistic function: solid line - the theoretical curve (2), cross points - experimental results [10].

The theoretical curve (2) of latent energy accumulation is shown in Fig. 1. The results of experiments on specimens made of aluminum alloy 2024-T351 [10] are shown in this figure by cross points. In calculations the following values of constants were used: $A = 0,6kg/kJ$, $W_0 = 1kJ/kg$, $W_* = 45kJ/kg$. It is seen that the experimental points of latent energy accumulation are well described by the logistic function (2).

Introducing the fracture condition in the form $W = kW_*$, where k is constant, $0,5 \leq k < 1$, from (2) we can receive the following relation

$$\varepsilon_* = \frac{1}{AW_*} \ln\left(\frac{k}{1-k}\left(\frac{W_*}{W_0} - 1\right)\right). \tag{3}$$

3 The fatigue fracture criterion

Relation (3) is the fracture criterion for the case of static loading. It will be used to formulate the fracture criterion for cyclic loading. For this purpose we appeal to the experimental results on the deformation accumulation in cyclic loading process. According with these results, during the cyclic loading under the given value of stress amplitude the accumulation of irreversible deformation from cycle to cycle is occurred [15, 16]. The deformation accumulation curves as a function of number of cycles is a linear function on the steady state stage. At the some time the deformation accumulation law is non linear function of stress amplitude. With these assumptions the kinetic equation, expressed through the number of cycles N, can be written in the following form

$$\frac{d\varepsilon}{dN} = B\sigma^m e^{-\alpha\sigma}, \tag{4}$$

where σ is stress amplitude, B, α, m are constants.

We will assume that the stress in one cycle is constant and is equal to the amplitude of stress σ. Using the initial condition $N = 0$, $\varepsilon = 0$ the solution of equation (4) at fracture $\varepsilon = \varepsilon_*$ can be found as

$$\varepsilon_* = B\sigma^m e^{-\alpha\sigma} N. \tag{5}$$

From the relations (3) and (5) follows the fatigue fracture criterion

$$\sigma^m N = \frac{e^{\alpha\sigma}}{ABW_*} \ln\left(\frac{k}{1-k}\left(\frac{W_*}{W_0} - 1\right)\right). \tag{6}$$

As follows from experiments [9], in particular, the inflection point on the logistic curve corresponds to the value of yield deformation. In the general case the following condition is valid $W = \beta W_*$, where $0 < \beta \leq 0,5$ at $\varepsilon = \varepsilon_T = \sigma_T/E$, where σ_T is yield stress, E is elastic modulus. Using this relation the constant A is expressed as

$$A = \frac{E}{W_*\sigma_T} \ln\left[\frac{\beta}{1-\beta}\left(\frac{W_*}{W_0} - 1\right)\right]. \tag{7}$$

Introducing this relation into (6) we will receive the following fatigue fracture criterion

$$\sigma^m N = \frac{\sigma_T e^{\alpha\sigma}}{EB} \frac{\ln\left[\frac{k}{1-k}\left(\frac{W_*}{W_0} - 1\right)\right]}{\ln\left[\frac{\beta}{1-\beta}\left(\frac{W_*}{W_0} - 1\right)\right]}. \tag{8}$$

4 Comparison of the fatigue fracture criterion with the experimental results

The theoretical fatigue curve (8) were compared with the experimental results received in axial cyclic tensile tests on sheet specimens made of aluminum alloy 2024-T3 [15].

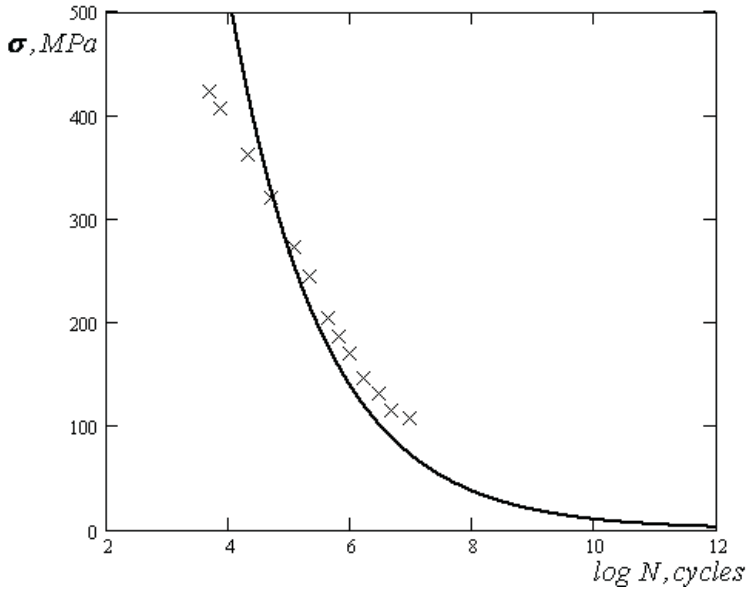

Figure 2: The theoretical fatigue curve (8) - solid line. Cross points - experimental results [15].

The mechanical properties of this alloy are more similar to the consequent properties of aluminum alloy used in paper [10].

The theoretical fatigue curve (8) is shown in Fig. 2 by solid line. The following values of constants were accepted: $W_0 = 1kJ/kg$, $W_* = 45kJ/kg$, $m = 3,5$, $k = 0,9$, $\beta = 0,3$, $B = 3 \cdot 10^{-16}[MPa]^{-3.5}[cycles]^{-1}$, $\alpha = 1 \cdot 10^{-5}[MPa]^{-1}$, $E = 7 \cdot 10^4[MPa]$, $\sigma_T = 350[MPa]$. The experimental results are marked by cross points. It is seen that the theoretical fatigue curve describes well the experimental points on the whole range of the investigated stress amplitude.

5 Conclusions

It is assumed that the cyclic strength is defined by the value of latent energy which is considered as the damage parameter. This parameter is governed by the differential equation with the solution in the form of the logistic function, capable to describe different processes leading to saturation.

The functions and parameters of the received criterion are concretized and comparisons with the experimental results for axial cyclic tension for sheet aluminum alloy specimens are given. A good agreement of theoretical and experimental results is received.

References

[1] S.S. Manson. Fatigue: A complex subject - Some simple approximations. The William M. Murray Lecture. Exp. Mechanics. 1965. N 7. P. 193-225.

[2] J. Schijve. Fatigue of structures and materials in the 20th century and the state of the art. Int. J. Fatigue. 2003. vol. 25. N 8. P. 679-702.

[3] Taylor G.I., Farren W.S. The heat developed during plastic extension of metals // Proc. Roy. Soc. (London). 1925. Ser. A. vol. 107. P. 422-451.

[4] Taylor G.I., Qunnney H. The latent energy remaining in a metal after cold working // Proc. Roy. Soc. (London). 1934. Ser. A. vol. 143. P. 307-326.

[5] Bolshanina M.A., Panin V.E. The latent energy of deformation // Issledovanie po fizike tverdogo tela. Moscow. Academy of Science of USSR. 1957. P. 193-234. (in Russian).

[6] Dillon O.W. The heat generated during torsional oscillations of copper tubes // Intern. J. solids and structures. 1966. vol. 2. P. 181-204.

[7] Bever M.B., Holt D.L., Titchener A.L. The stored energy of cold work // Progress in materials science. 1973. vol. 17. P. 5-177.

[8] Oliferuk W., Maj M., Raniecki B. Experimental analysis of energy storage rate components during tensile deformation of polycrystals // Materials science and engineering A. 2004. 374. P. 77-81.

[9] Plechov O., Saintier N., Naimark O. Experimental investigation of the processes of energy storage and dissipation in iron during the elastic plastic deformation // Journal of technical physics. 2007. vol. 77. N 9. 135-137. (in Russian).

[10] Rosakis P., Rosakis A.J., Ravichandran G., Hodowany J. A thermodynamic internal variable model for the partition of plastic work into heat and stored energy in metals // Journal of the Mechanics and Physics of Solids. 2000. vol. 48. P. 581-607.

[11] Arutyunyan A.R., Zimin B.A., Sud'enkov Yu.V. The application of optics-spectroscopy method to investigate fatigue of construction materials // Proceedings of International conference "Topical problems of Continuum Mechanics", 24-28 September 2007, Tsakhadzor, Armenia. Erevan. Institute of mechanics NAS of Armenia. 2007. P. 63-68. (in Russian).

[12] Arnold V.I. The ordinary differential equations. Moscow: Nauka. 1971. 240p. (in Russian).

[13] Arutyunyan R.A. The problem of deformation aging and prolonged fracture in material sciences. Sankt-Petersburg: S.-Petersburg university press. 2004. 252p. (in Russian).

[14] Orlov A.N. The long-time strength and physics of fracture // Trudy TsKTI. 1986. vol. 230. P. 42-46. (in Russian).

[15] Forrest P.G. Fatigue of metals. Moscow: Mashinostroenie. 1968. 352p. (in Russian).

Robert A. Arutyunyan, St.-Petersburg State University, Faculty of Mathematics and Mechanics, Sankt-Petersburg, Petrodvoretz, Universytetskii prospect, 28, 198504, Russia

The strength of non linear elastic medium with a crack

Alexander R. Arutyunyan Robert A. Arutyunyan
Robert.Arutyunyan@paloma.spbu.ru

Abstract

Taking into account the current value of the coefficient of lateral deformation the rheological relation describing the nonlinear elastic behavior of compressible medium is introduced. The energy consumption for the specimen with crack made of considered material is calculated and the fracture criterion is formulated. In particular, for the brittle material, when the coefficient of lateral deformation is equal to zero, the received criterion is identical with the Griffith's fracture law. In the general case, the criterion is dependent on the coefficient of lateral deformation. Similar to the Griffith's criterion, the critical value of crack length from the critical value of stress is governed by the hyperbolic law.

Financial support of the Russian Foundation for Basic Research (Grant N 09-01-00513) is gratefully acknowledged.

When formulating the rheological equations of theory plasticity and creep the assumption of material noncompressibility is accepted, which corresponds to the condition $\nu = 1/2$ (ν is the value of the current coefficient of lateral deformation). As for linear elastic material, it is compressible with the constant coefficient of lateral deformation (Poisson's ratio).

As shown in [1, 2] the nonlinear elastic equations may be formulated in terms of the current value of lateral deformation $\nu = -\varepsilon_y/\varepsilon_x = -\varepsilon_z/\varepsilon_x$ (ε_x, ε_y, ε_z are longitudinal and lateral deformations of a tension specimen) and the mass conservation law. These relations are represented as

$$\sigma = E\varepsilon e^{-2\nu\varepsilon}, \tag{1}$$

$$\sigma = E\varepsilon e^{-\varepsilon}\left(\frac{\rho_0}{\rho}\right), \tag{2}$$

where $\sigma = P/F_0$, P is tension force, F_0 - initial cross section area of the specimen, ρ_0, ρ - initial and current values of density, E - modulus of elasticity.

The relations (1)-(2) can be used to solve different deformation and fracture problems of nonlinear elastic materials, in particular, for the materials with the "week" nonlinearity. The nonlinear elastic stress-strain curves for the case of simple tension and for different values of coefficient ν are shown in Fig. 1.

Two limiting cases can be distinguished. When $\nu = 1/2$ we have noncompressible nonlinear elastic media. For the case $\nu = 0$ the elastic media is hard linear.

The laws (1)-(2) can be applied to describe the nonlinear elastic behavior of materials produced by the method of powder metallurgy, when the medium is compressible and its behavior is dependent on the initial and current porosity, determined by the values of ρ_0 and ρ. They also can be applied to describe the nonlinear effects in pure metals with the different crystal lattice and corresponding initial condition of porosity, defined by the atomic packing.

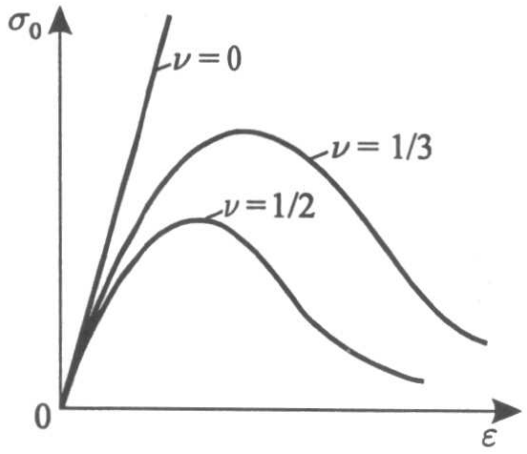

Figure 1: Elastic stress-strain curves according to the relation (1).

Further we will consider the relation (1) to formulate the strength criterion for the nonlinear elastic medium with a crack. As an example of this type of medium can be considered the behavior of ceramic composites. The experimental investigations [3, 4] show that in these materials the porous structures can be created using the corresponding technological treatments, provided up to 2-3% of nonlinear elastic deformation at room temperature. Taking into account these assumptions, the law (1) will be applied to formulate the strength criterion of a specimen with a crack using the Griffith's energy approach [5]. The material of the specimen is considered to be nonlinear elastic. The nonlinearity is governed by the current coefficient of lateral deformation. The relation $\nu = \nu(\varepsilon)$ my be defined experimentally. To specify this relation we will use the known in world literature experimental results [6]. Bauschinger was first to carry out such experiments in pure tension of specimens made of mild steel. It was shown that the relation $\nu = \nu(\varepsilon)$ is non-monotonic. At initial stage of deformation, when material passes from elastic to plastic state, the coefficient of lateral deformation increases monotonically to the maximal value $\nu = 1/2$. So the material becomes noncompressible. At the hardening stage the state of compressibility is observed. The coefficient of lateral deformation decreases monotonically and tends to zero at fracture stage. This effect is associated with developing in material many pores and cracks.

In experiments of other authors [7] the state of noncompressibility is observed, when material passes from elastic to plastic state.

In the case of brittle materials such as ceramic composites the experimental relation $\nu = \nu(\varepsilon)$ is observed to be monotonic, slow decreasing function at the initial stage of deformation. As one would expect the coefficient of lateral deformation will tent to zero at fracture stage. On this basis the coefficient of lateral deformation is expressed by the relation

$$\nu(\varepsilon) = \nu_0 \left(1 - \frac{\varepsilon}{\varepsilon_p}\right)^k, \tag{3}$$

where ν_0, ε_p, k are constants.

The theoretical curves according to (3) for different values of k (1 - $k = 1$, 2 - $k = 0,4$, 3 - $k = 0,15$) and $\nu_0 = 0,22$, $\varepsilon_p = 0,03$ are shown in Fig. 2.

Taking into account the mentioned feature of changing the value of the coefficient of lateral deformation, we will consider two cases of formulating the strength criterion of

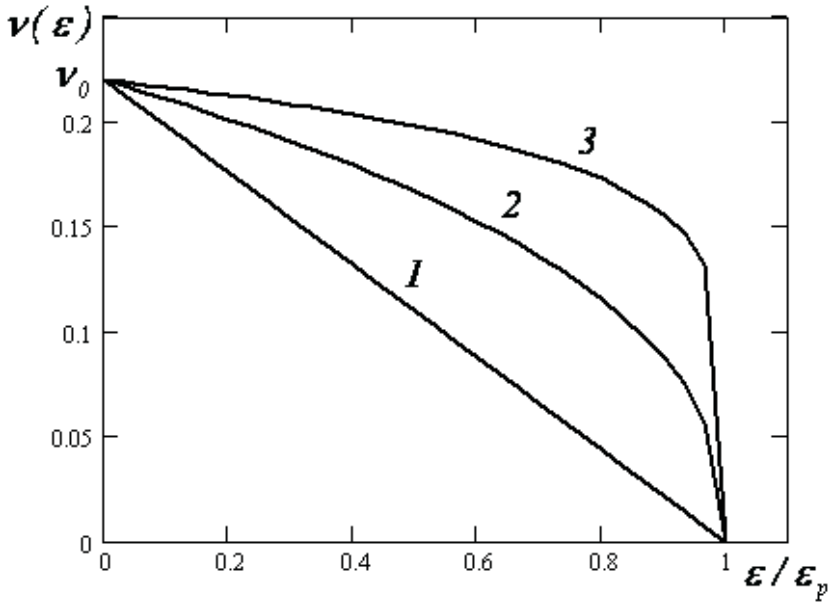

Figure 2: Theoretical curves $\nu = \nu(\varepsilon)$ for different values of k: 1 - $k = 1$, 2 - $k = 0,4$, 3 - $k = 0,15$.

a specimen with a crack using the Griffith's energy approach. In the first case we will assume $\nu_0 = const$. In this approximation the fracture problem of a thin plate with a crack, stretch by the given stress σ or strain ε, will be solved.

The elastic energy per unit area stored in the plate is equal

$$W(\varepsilon) = \int_0^{\varepsilon} \sigma d\varepsilon = \frac{1}{4}\frac{E}{\nu^2}\left[1 - (2\nu\varepsilon + 1)\cdot e^{-2\nu\varepsilon}\right]. \tag{4}$$

If in the plate a crack of small length $2l$ perpendicular to the tension direction appears the plate elastic energy will decrease at some value ΔW, which is equal to the product of mean area around the crack to the mean value of elastic energy. When taking into account that the considered area has an order of l^2 we will receive the relation for the released energy

$$W_1 = -c\Delta W l^2, \tag{5}$$

where constant c accounts for the shape and size of the detached area.

The released elastic energy (5) is consumed to produce the new surfaces. Let's denote by γ the fracture energy per unit area of the new surfaces, so the work done to create the crack of length $2l$ will be equal to

$$\Gamma = 4\gamma l. \tag{6}$$

As a result, the generation of a crack will change the plate energy to the value

$$W = -c\Delta W l^2 + 4\gamma l. \tag{7}$$

Considering the small variation of crack length, we will have

$$\frac{dW}{dl} = -2c\Delta W l + 4\gamma. \tag{8}$$

At the state of equilibrium the energy of the system has the extremal value ($dW/dl = 0$). Taking into account this condition and relation (4) we can calculate the critical value of crack length $l = l_*$ as a function of the critical value of deformation $\varepsilon = \varepsilon_*$

$$l_* = \frac{8\gamma\nu^2}{Ec}\left[1 - (2\nu\varepsilon_* + 1)\cdot e^{-2\nu\varepsilon_*}\right]^{-1}. \tag{9}$$

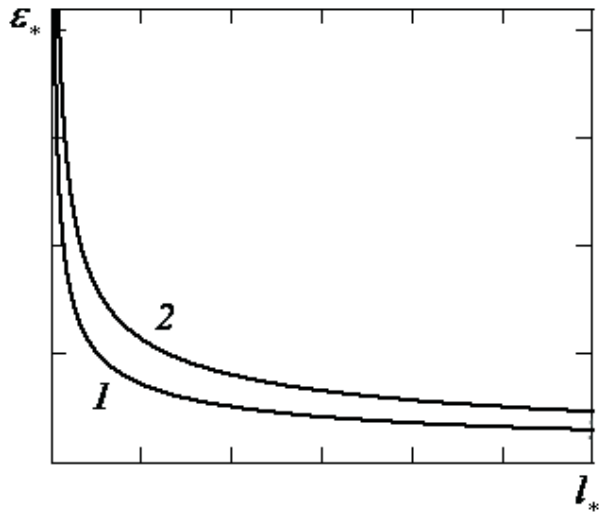

Figure 3: The theoretical strength curves: according to the Griffith's criterion ($\nu = 0$, curve 1) and to the formula (9) ($\nu = 0,3$, curve 2).

When material is brittle ($\nu = 0$, $\varepsilon_* = \sigma_*/E$) and $c = 2\pi$ from (9) follows the Griffith's fracture criterion

$$l_* = \frac{2\gamma}{\varepsilon_*^2 E\pi} = \frac{2\gamma E}{\pi\sigma_*^2}. \tag{10}$$

In Fig. 3 the theoretical curves $\varepsilon_* - l_*$ according to the Griffith's fracture criterion (curve 1) and to the formula (9) (curve 2) are presented.

When the coefficient of lateral deformation is a variable and is given by the relation (3), the solution of the fracture problem of a plate with the crack leads to formulation of the strength criterion different from the law (9). In this case, when $k = 1$, we will have the most simple relation for the strength criterion

$$l_* = \frac{12\gamma\varepsilon_p}{Ec\varepsilon_*^2}\left[3\nu_0\varepsilon_*^2 - 4\nu_0\varepsilon_p\varepsilon_* + 3\varepsilon_p\right]^{-1}. \tag{11}$$

When $\nu = 0$, $c = 2\pi$, $\varepsilon_* = \sigma_*/E$, from (11) follows the Griffith's strength criterion (10).

References

[1] R.A. Arutyunyan. The problem of deformation aging and prolonged fracture in material sciences. Sankt-Petersburg: S.-Petersburg university press. 2004. 252p. (in Russian).

[2] Robert A. Arutyunyan. Creep fracture of nonlinear viscoelastic media undergoing UV radiation // International Journal of Fracture. 2005. vol. 132. N 1. P. L3-L8.

[3] Kulkov S.N. Structure, phase constitution and mechanical properties of nanosystems based on ZrO_2 // Physical mesomechanica. 2007. vol. 10. N 3. P. 81-94. (in Russian).

[4] Kulkov S.N., Maslovski V.I., Buyakova S.P., Nikitin D.S. Nonhooks behavior of porous dioxide zirconium in active compressive loading // Journal of Technical Physics. 2002. vol. 72. N. 3. P. 38-42. (in Russian).

[5] Griffith A.A. The phenomena of rupture and flow in solids // Philosophical Transactions of the Royal Society of London. Series A. 1921. vol. 221. P. 163-198.

[6] Koster W., Franz H. Poisson's ratio for metals and alloys // Metal Rev. 1961. vol. 6. N 21. P. 1-55.

[7] Zhukov A.M. At the Poisson's ratio in plastic region // Izvestia of USSR Academy of Science. Otdel technicheskih nauk. 1954. N 12. P. 86-91. (in Russian).

Robert A. Arutyunyan, St.-Petersburg State University, Faculty of Mathematics and Mechanics, Sankt-Petersburg, Petrodvoretz, Universytetskii prospect, 28, 198504, Russia

Numerical investigation of shock waves damping in perfect viscous gas

Maria B. Atmanskikh Andrew Y. Botalov Pavel T. Zubkov
pzubkov@utmn.ru

Abstract

Motion of viscous gas with thermophysic characteristics of air in a plane layer without gravity force is considered. An impermeable membrane divides a rectangular area into two equal parts. Initial density distribution has a discontinuity. This problem simulates a shock tube. Density distribution is $\rho_0 + \Delta\rho_0$ behind the discontinuity and is $\rho_0 - \Delta\rho_0$ in front of the discontinuity in the first chamber where $\rho_0 = const$. The discontinuity is located in the center of the left part. Value of $\Delta\rho_0$ and thermal boundary conditions type are varied. Gas dynamics is described by the one-dimensional time-dependent system of equations in Cartesian coordinates, consisting of conservation laws for mass, momentum and energy in differential form. The Clapeyron perfect gas law is considered as the equation of state. Shock tubes are often used for research of physical-chemical kinetics including investigation of thermodynamic equilibrium time in gases. Numerical analysis of stationary mode time dependence on $\frac{\rho_0+\Delta\rho_0}{\rho_0-\Delta\rho_0}$ is presented in this work. The Control Volume Method and the modified SIMPLER algorithm for hydrodynamics of compressible medium were used for numerical solution of the present problem.

1 Introduction, problem formulation

One-dimensional problem of viscous gas motion in a double-chamber shock tube without gravity force is considered. A rectangular area of length L is divided by an impermeable fixed membrane at a distance $x = L/2$ from the edge. Initial distribution of density ρ in the left part has a discontinuity and in the right part is $\rho_0 = const$. The discontinuity is located at a distance $x = L/4$ from the left boundary. Density value is $\rho_0 + \Delta\rho_0$ behind the discontinuity and is $\rho_0 - \Delta\rho_0$ in front of the discontinuity. Initial distribution of temperature T is constant in the whole domain and is equal to T_0. Two cases are considered in relation to thermal boundary conditions: adiabatic (case A) and isothermal (case Is). The thermal conductivity coefficient k, the dynamic viscosity μ and the specific heat capacities c_v and c_p are assumed to be constant.

2 Mathematical model

The system of dimensionless equations describing one-dimensional unsteady-state motion of gas with Clapeyron law as the equation of state for gas has the form:

$$\frac{\partial\tilde{\rho}}{\partial\tau} + \frac{\partial\tilde{\rho}U}{\partial X} = 0,$$

$$\tilde{\rho}\frac{\partial U}{\partial \tau} + \tilde{\rho}U\frac{\partial U}{\partial X} = -\frac{\partial P}{\partial X} + \frac{4}{3}\frac{1}{Re}\frac{\partial^2 U}{\partial X^2},$$

$$\tilde{\rho}\frac{\partial \Theta}{\partial \tau} + \tilde{\rho}U\frac{\partial \Theta}{\partial X} = \frac{\gamma}{Pe}\frac{\partial^2 \Theta}{\partial X^2} - P\gamma(\gamma-1)\frac{\partial U}{\partial X} + \frac{4}{3}\frac{\gamma(\gamma-1)}{Re}(\frac{\partial U}{\partial X})^2,$$

$$P = \frac{\tilde{\rho}\Theta}{\gamma},$$

here

$$X = \frac{x}{L},\ \tau = \frac{tc}{L},\ U = \frac{u}{c},\ P = \frac{p}{\gamma p_0},\ \tilde{\rho} = \frac{\rho}{\rho_0},\ \Theta = \frac{T}{T_0},\ c = \sqrt{\gamma R T_0},$$

$$R = \frac{R_0}{m},\ Re = \frac{\rho_0 L c}{\mu},\ Pe = \frac{\rho_0 L c_p c}{k},\ \gamma = \frac{c_p}{c_v}.$$

Dimensionless parameters are calculated with thermophysic characteristics of standard air. Here R_0 is universal gas constant, m is gas molar mass. Introducing parameter $Delt = \frac{\Delta\rho_0}{\rho_0}$ initial conditions have the form:

$$0 \le X \le 0.25 : \tilde{\rho}|_{\tau=0} = 1 + Delt,\ P|_{\tau=0} = \frac{1+Delt}{\gamma};$$

$$0.25 < X \le 0.5 : \tilde{\rho}|_{\tau=0} = 1 - Delt,\ P|_{\tau=0} = \frac{1-Delt}{\gamma};$$

$$0.5 < X \le 1 : \tilde{\rho}|_{\tau=0} = 1,\ P|_{\tau=0} = \frac{1}{\gamma};$$

$$0 \le X \le 1 : \Theta|_{\tau=0} = 1,\ U|_{\tau=0} = 0.$$

Boundary conditions:

$$U|_{X=0} = U|_{X=1} = 0;$$

$$A.\ \frac{\partial \Theta}{\partial X}|_{X=0} = \frac{\partial \Theta}{\partial X}|_{X=1} = 0; Is.\ \Theta|_{X=0} = \Theta|_{X=1} = 1.$$

3 Parameters of calculation and numerical scheme

Present problem is solved by control volume approach and algorithm for numerical solution of problems in hydrodynamics of compressible medium which is developed on basis of SIMPLER [1] using power law scheme and the second order of boundary conditions approximation. The numerical scheme of solution is given in detail in [2]. Computations are carried out for fixed Peclet number (Pe=15645), Reynolds number (Re=22275) and adiabatic exponent $\gamma = 1.4$ on uniform grid which was consisted of 1000 nodes. Variation range of the parameter which defines amount of the initial discontinuity in the left chamber of shock tube is $0 \le Dens \le 19$.

The time step was taken to be $\Delta\tau = 0.1\Delta X$ (i.e., on condition that the wave will pass a distance of ΔX or less during the time $\Delta\tau$, where ΔX is the size of control volume).

Table 1: Computational values of parameters Delt and Dens

Case	I	II	III	IV	V
$Delt = \frac{\Delta\rho_0}{\rho_0}$	0.1	0.25	0.5	0.75	0.9
$Dens = \frac{\rho_0+\Delta\rho_0}{\rho_0-\Delta\rho_0}$	1.2	1.67	3	7	19

4 Analysis of the obtained results

The initial density and pressure distributions have arbitrary discontinuity in the left part of the domain. Such discontinuity is of the first kind that the values of characteristics are not linked by any relationship on the left and on the right sides of discontinuity [3].

At the initial time moment breakup of discontinuity is started. As a result complicated wave motion arises which consists of shock waves (SW), rarefaction waves (RW) and contact discontinuity (in case of density and temperature), propagating through the domain. In case when the domain is filled with gas, and is bounded, frequent reflection and interaction of waves takes place. At the initial time moment, disturbances propagate to both sides as two waves: shock wave and rarefaction wave. Wave motion arises because of the instantaneous substantial velocity changing, therefore at the initial moments rarefaction wave is a centered wave and compression wave is a shock wave.

Fig.1,2 illustrate that after initial time moment SW propagates to the right from discontinuity at a rate of more than adiabatic sound velocity c (Tab.2), RW propagates to the left at the adiabatic sound velocity. Therefore SW reaches central membrane faster than RW reaches left bound. (Fig.3) (Dimensionless adiabatic sound velocity is 1.)

Table 2: Cases A. Values of dimensionless average SW velocity in the left chamber at the time moment $\tau < 0.25$.

Case	I	II	III	IV	V
v_{wl}	1.15	1.22	1.35	1.56	1.85

We deal with weak shock waves in the cases AI, AII. These are the shock waves, where the jumps in the flow variables can be regarded as small quantities [3]. They were considered in the paper [4] in detail. Condition $\frac{P_1-P_0}{P_0} \ll 1$ is fulfilled for weak SW (Tab.3) where P_1 is pressure behind discontinuity, P_0 is pressure in front of discontinuity. This condition does not hold in the cases $AIII$, AIV, AV (Tab.3).

Table 3: Cases A. Value $\frac{P_1-P_0}{P_0}$ at the time moment $\tau = 0.125$.

Case	I	II	III	IV	V
$\frac{P_1-P_0}{P_0}$	$\frac{0.71-0.64}{0.64} = 0.1$	$\frac{0.7-0.54}{0.54} = 0.3$	$\frac{0.6-0.36}{0.36} = 0.7$	$\frac{0.43-0.18}{0.18} = 1.4$	$\frac{0.25-0.07}{0.07} = 2.6$

Upon reaching the central membrane the SW causes the release of energy. It leads to local temperature increasing, gas expansion behind the central wall and pressure rise near the membrane. As result, weak shock wave arise in the right chamber (Fig.3) Speed of the wave is 1.057 in the case AI and 1.125 in the case AV. (Tab.4) At the time $\tau = 0.375$

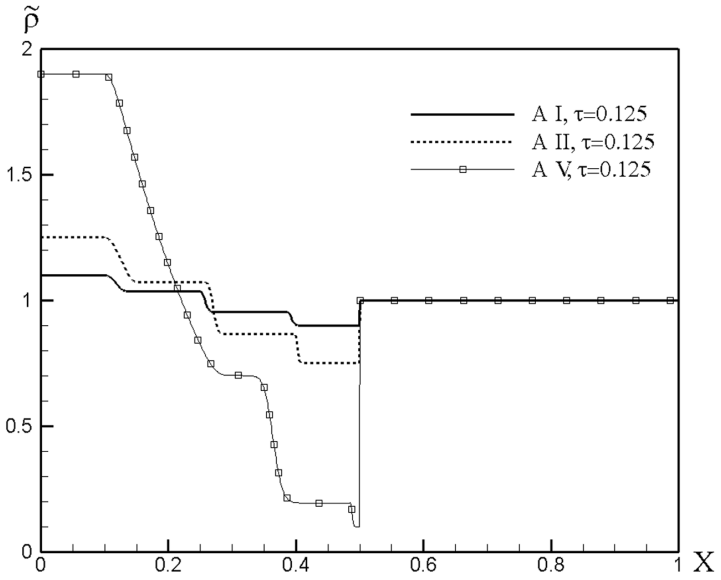

Figure 1: Cases AI, AII, AV. Dependence of density on space coordinate at the time moment $\tau = 0.125$.

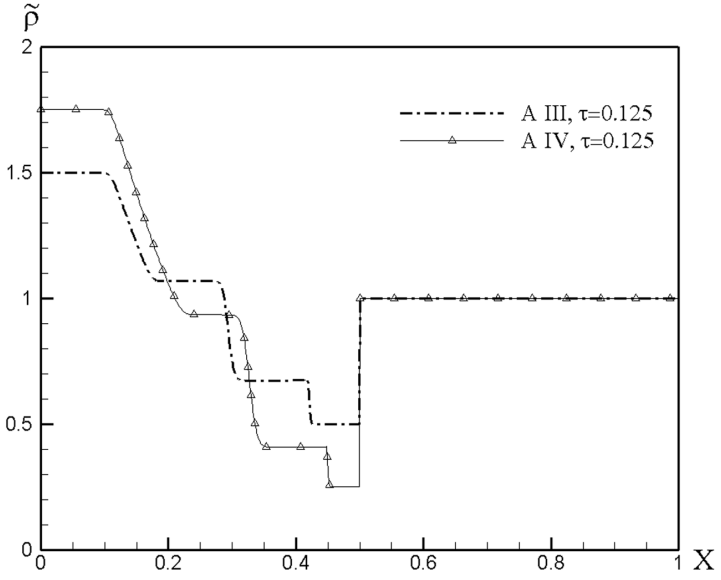

Figure 2: Cases $AIII$, AIV. Dependence of density on space coordinate at the time moment $\tau = 0.125$.

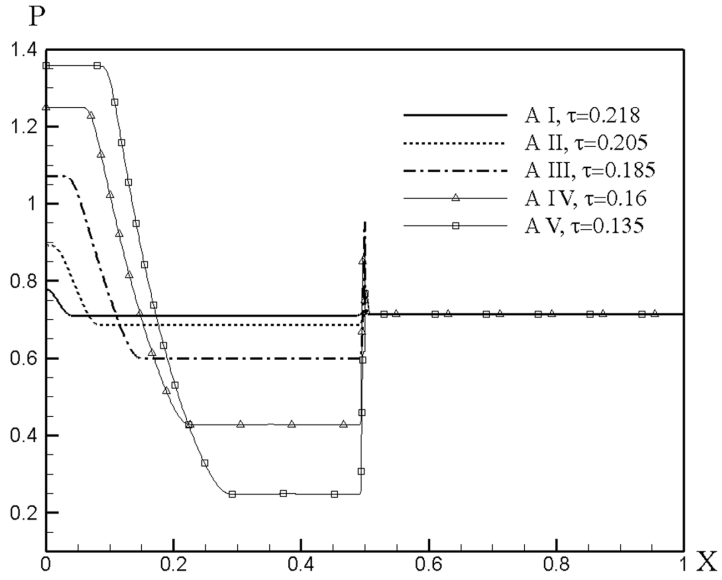

Figure 3: Cases AI, AII, $AIII$, AIV, AV. Dependence of pressure on space coordinate at the time moments $\tau < 0.25$.

amplitude of such wave ranges between 1.4% and 2.6% of the initial pressure drop in the shock tube in the cases A.

Table 4: Cases A. Values of dimensionless average SW velocity in the right chamber at the time moment $\tau = 0.375$.

Case	I	II	III	IV	V
v_{wr}	1.057	1.07	1.095	1.116	1.125

Propagation rates of the SW and the RW in the left chamber and the SW in the right chamber are approximately equal in cases AI, AII. Therefore characteristics oscillations (particularly pressure oscillations) are cophased in points located nearly on the left and on the right of the impermeable membrane.(Fig.4) Flow variable oscillations are shifted in phase on both sides of the central membrane in the cases $AIII$, AIV, AV. We will consider the case AV in detail. At the time moment $\tau = 1.03$ jump of pressure in the point $X = 0.501$ corresponds to the weak SW returning to the partition after the first period (Fig.5). However at the time moment $\tau = 1.03$ the SW of the left chamber has not reached the membrane yet because its speed sharply decreases after the partition's impact. At the time moment $\tau = 1.25$ the SW of the left chamber reaches the central wall and forms a new weak SW in the right part of the domain (Fig.5). Thus one new wave arises in the domain for each new period.

All above discussions are correct for the case Is because the solution at the initial time moments is determined by initial conditions, not by boundary conditions. For example, at the time moments $\tau < 10$ plots of flow variable distributions differ near bounds no more than on 11%, near contact discontinuity and SW front no more than on 5% of amplitude of function oscillation at the same time moments for different thermal boundary conditions.

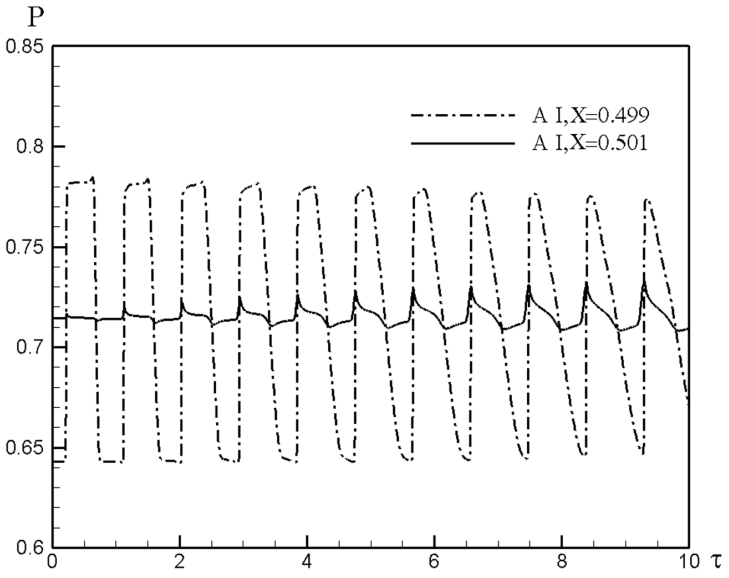

Figure 4: Case AI. Dependence of pressure on time in points $X = 0.499, 0.501$.

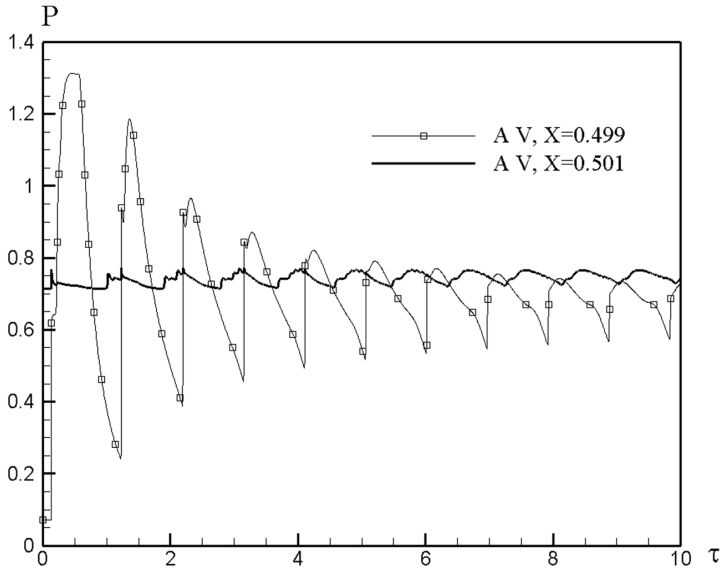

Figure 5: Case AV. Dependence of pressure on time in points $X = 0.499, 0.501$.

The wall's impact of compression wave the release of energy liberation near the bound. On the contrary, the RW results in the decrease of temperature near the wall when the wave reaches it. As a result, in the case Is temperature gradient appears on the bound which, in the case of compression wave, leads to heat outflow to surrounding environment and in a case of RW induces heat inflow. At the time moments $\tau < 1$ one wave reaches the right wall in the case IsV. It corresponds to one peak on the Fig.6. After that the RW reaches the right bound. Therefore at the time moments $1 < \tau < 1.5$ we observe positive heat flow density. Then two peaks correspond to two weak SW. The peaks number increases on one for each period.

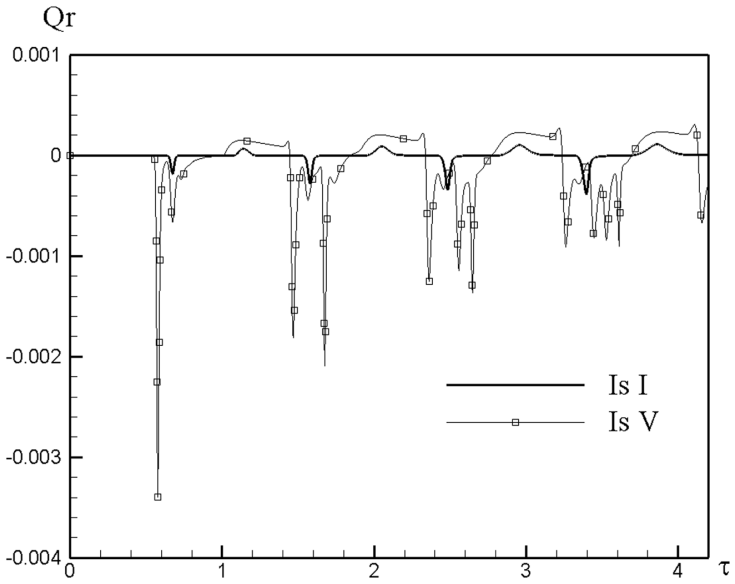

Figure 6: Cases IsI, IsV. Dependence of heat flow density on time in point $X = 1$.

Fig.7 illustrates that after initial time moment bulk temperature increases in the right part of the domain and decreases in the left part in the case Is. One-dimensional Riemann problem of arbitrary discontinuity in a cavity filled with perfect viscous gas is considered in the paper [5] where we obtained dependence of bulk temperature on time looking like left chamber bulk temperature in the present work. Thus bulk temperature decreasing till some time moment is explained with intensive heat exchange with environment due to the increasing convective heat transfer which associated with large gradients of flow variables after breakup of discontinuity. Greater fraction of energy outflows through bounds in [5] but part of it is spent on heating of the right chamber in the present problem. Therefore heat exchange of two chambers divided by partition causes the increase of whole domain bulk temperature for all cases till some time moment.(Fig.8,9) Dimensionless bulk temperature is calculated with formulas: $\Theta_b = \frac{T_b}{T_0}$, $T_b = \frac{\int_0^L T\rho dx}{\int_0^L \rho dx}$.

This wave motion is periodic but oscillations are decaying because of the existing RW, contact discontinuity in temperature and density distributions and dissipative processes. Evident that for $\tau \to \infty$ $\tilde{\rho} = 1$, $\Theta = 1$, $P = \frac{1}{\gamma}$, $\Theta_b = 1$.

At the time moments $\tau < 300$ shock wave motion decays in all cases and becomes fully motion of acoustic waves which also decays but later. Thermodynamic equilibrium time will be registered in numerical experiments if difference of dimensional maximal

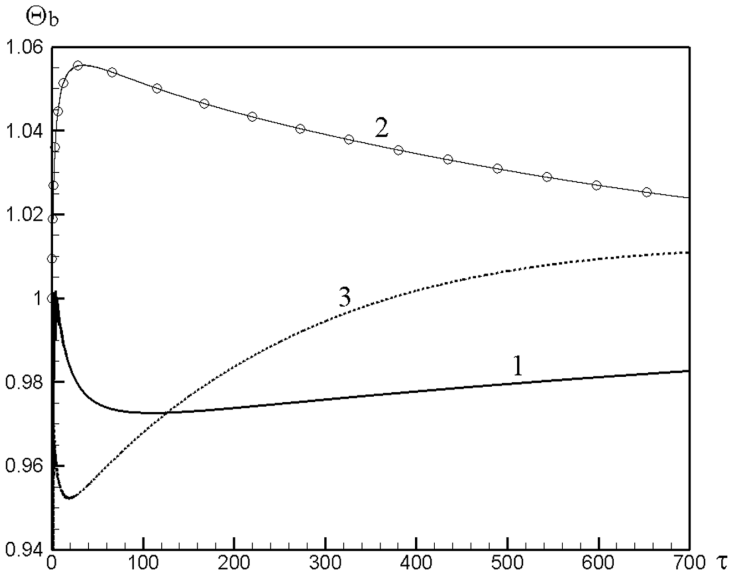

Figure 7: Cases IsV. Dependence of bulk temperature on time. 1 - result of paper [5], 2 - the right chamber, 3 - the left chamber.

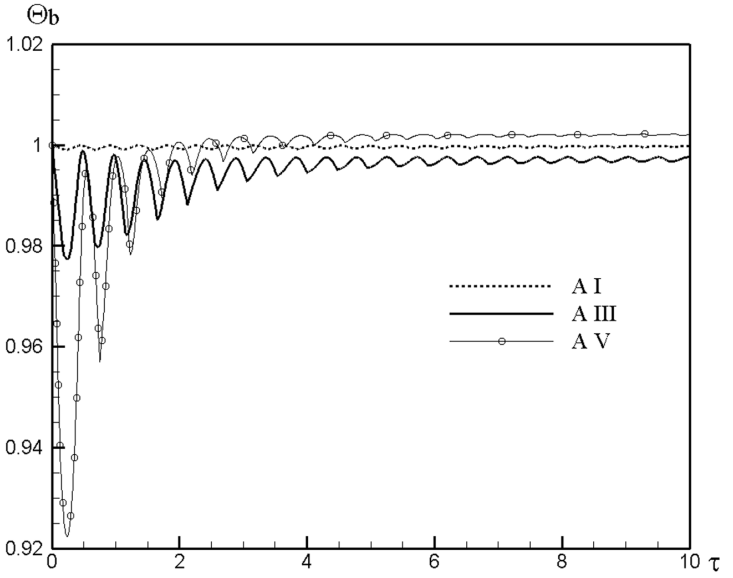

Figure 8: Cases AI, AII, AV. Dependence of bulk temperature on time.

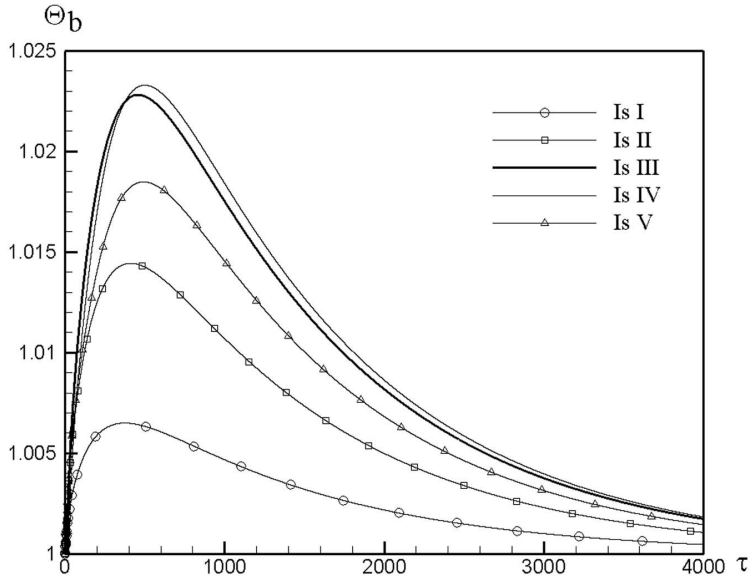

Figure 9: Cases IsI, $IsII$, $IsIII$, $IsIV$, IsV. Dependence of bulk temperature on time.

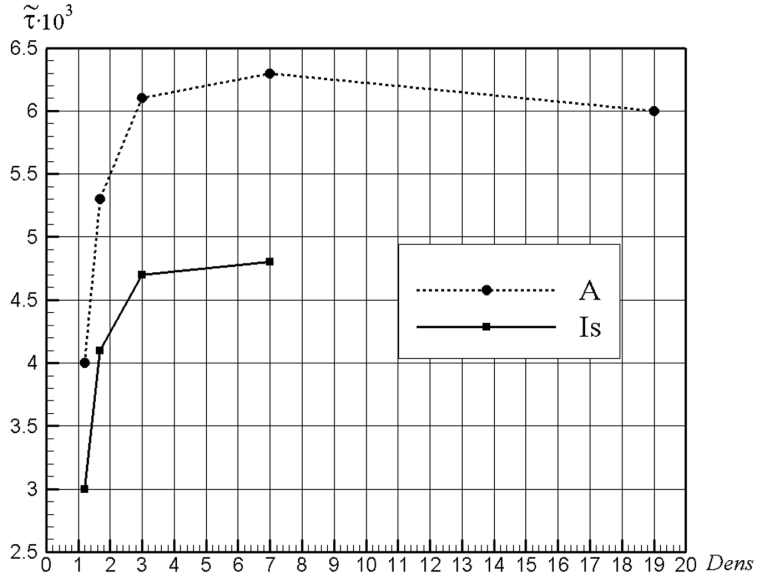

Figure 10: Cases A, Is. Dependence of thermodynamic equilibrium time on parameter Dens.

and minimal pressure is no more than 10 Pa and difference of dimensional maximal and minimal temperature is no more than 0.5 . Thus the relaxation time of the system to the stationary mode essentially depends on type of thermal boundary conditions.(Fig.10)

5 Conclusion

Numerical investigation of the propagation of shock waves effect on temperature, pressure, velocity and density distribution in a flat layer of perfect viscous gas with air thermophysic characteristics is presented in this article. In the course of the investigation it was obtained that:

a)Type A boundary conditions increase relaxation time of the system to the stationary mode. Acoustic oscillations decay faster in the case of type Is boundary conditions than in the case A because wave energy is used not only for gas motion within the domain but for heat exchange with surrounding environment.

b) Dependence of stationary mode time on parameter $Dens$ is nonmonotonic in the problems with type A boundary conditions.

References

[1] S. V. Patankar. Numerical heat transfer and fluid flow. Hemisphere, NY, 1980.

[2] L. V. Abdubakova, A. Y. Botalov, P. T. Zubkov, A. V. Yakovenko. Motion of the gas in the rotating cylinder. 2nd European Conference on Microfluidics, Toulouse, 2010. CD-ROM Proceedings, paper 000090.

[3] Ya. B. Zeldovich, Yu. P. Raizer. Physics of shock waves and high-temperature hydrodynamics phenomena. Academic Press, 1966.

[4] M. B. Atmanskikh, P. T. Zubkov. Propagation of wake shock waves in flat layer of perfect viscous gas. Proc. of 5th Russian national conference of heat exchange. MEI, Moscow, 2010. V. 2, P. 41-44. [in Russian]

[5] M. B. Atmanskikh, P. T. Zubkov. Breakup of arbitrary discontinuity in a perfect viscous gas layer. Materials of All-Russian conference "XXIX Siberian thermophysic seminar". IT of SB RAS, Novosibirsk, 2010. [in Russian]

Maria B. Atmanskikh, Perekopskaya str. 15 A, Tyumen, Russia
Andrew Y. Botalov, Perekopskaya str. 15 A, Tyumen, Russia
Pavel T. Zubkov, Perekopskaya str. 15 A, Tyumen, Russia

On a Dynamic absorbers to Eletro-mechanical systems, including nonlinear phenomena in Macro, Mems and Nems scales

José M. Balthazar Jorge L. P. Felix
jmbaltha@rc.unesp.br, jorge.felix@unipampa.edu.br

Abstract

The main purpose of this paper is to analyze the influence of the external force, generated by a non-ideal energy source to Macro structures and their applications to Engineering Sciences. Comparisons between numerical simulations, experimental and analytical methods were done near the fundamental resonance region, where the vibrating system presented some interesting nonlinear phenomena. They were concerning on recent results of an electro-mechanical vibration absorbers and Energy transference between oscillators, used for the vibration attenuations in a non-ideal structures, showing the existence of the Sommerfeld effect and the influence of the essentially nonlinearities on relevant problems. Lyapunov exponents were numerically calculated to prove the occurrence of chaotic vibrations in the non-ideal systems and in the quenching of chaotic vibrating systems, using the electro-mechanical vibration absorbers. Extensions to applications of new materials, from Micro and Nano structures were also addressed, as emergent areas in Engineering science and mechanics.

Keywords: Nonlinear and Chaotic Phenomena, Non-Ideal Vibrations, Electro-mechanical Absorbers, Energy Transference. Macro, Mems and Nens Vibrations

1 Introduction

Recently, there has been an increasing of attention to Electro-mechanical Systems (EMS) and the research work on their dynamics and control is developping, taking into account a full interaction between mechanical and electrical field quantities. First of all, this technology rests on multidisciplinary foundations and designing a commercially viable (EMS), with required dynamic performance demands an in-depth understanding and accurate prediction of its dynamic and control characteristics. Furthermore, the properties of materials, may change as the feature size of mechanical elements is scaled down, leading to difficulties in the modeling of their dynamic characteristics. (EMS) fall into three groups: The conventional electro-mechanical systems (MACRO), Micro-electromechanical systems (MEMS) and Nano-electromechanical systems (NEMS) and they can be modeled by coupled equations, understood in the context of simple lumped mechanical masses and electric and magnetic circuits. MEMS technology is still in its infancy, with global research and development actively under way. One of the challenges is to develop tools and methods for effective investigation of structural dynamics of MEMS. The advantages of MEMS devices include: Size; High sensitivity; Low noise; reduced cost and Batch Processing. Many of the NEMS device technologies use MEMS as a bridge to the nano-world. “MEMS” will

provide a bridge to enable the applications of nanotechnology as illustrated in the cantilever sensor. The atomic force microscope (AFM) used in this technique, has a tip made of silicon, using a typical MEMS device process and is of micron dimensions.

1.1 Goals of the Lecture (NIS)

The main goal of this text-lecture is to help students on the discussions of the progress in (EMS), which play important roles in the world development in the near future on Engineering Science and Mechanics. Here, we discussed some modern concepts and new methods of the qualitative and quantitative theory of Nonlinear Dynamics and Chaos and their Controls, according to the below topics: Non-ideal Systems(NIS) as an Energy transference phenomenon between an Energy source of Limited Power Supply and the oscillators. The absorption of the resonance vibrations of a non-ideal system (NIS); by means of a nonlinear sub-structure, with properties of nonlinear energy sink (NES).The investigation of the effectiveness of a nonlinear electro-mechanical vibration absorber (NEVA) in the vibration attenuation of non-ideal structures (NIS). Linear Optimal control Design, in order to stabilize some chaotic vibrations. We also include some emergent topics on Engineering Science and Mechanics, related to the fact that, In recent years a large amount of research has been dedicated to new materials and their use in new structural components; among new materials, functionally graded materials and other composites, shape memory alloys, magneto rheological materials, dielectric elastomers, polymers and thin-films have shown great potential for applications in all engineering fields. So, research has been conducted in applications of these materials from micro and nano structures to large space structures. These structures are usually rather slender leading to an eminently non-linear behavior, including new types of nonlinearities and forces.

2 Non-ideal Vibrating Problems(NIS)

The study of problems that involves the coupling of several systems,was explored widely in the last years, in function of the change of constructive characteristics of the machines and structures. In this way, some new phenomena are observed in a composed dynamic systems supporting structure and rotating machines, where are verified that the unbalancing of the rotating parts is the greatest causer of vibrations.

We also remarked that the study of the vibrating systems when the external excitation is influenced by the response of the system has been considered a major challenge in theoretical and practical engineering research.It is well known that structures supporting unbalanced machines capable of a limited power output are considered, as in the case of real motors. The motion of a vibrating structure under the action of such energy source is accompanied by interaction between these non-ideal motors and their support.In usual approaches, the excitation is considered as ideal; that is, the influence of the motion of the structure on the motor is disregarded. Here, the reciprocal influence of the system on the energy source is considered. As a consequence, in the region of resonance, unstable conditions of motion occur and the form of resonance curve depends on which direction the frequency of the excitation is being altered. We remarked that the problem of passage through resonance of unbalanced equipment with an operational speed higher than the lower frequencies of vibration of the supporting structure has been studied for a long time. However, the machine may not be able to supply the power necessary for this technique, as a large part of its energy is used in shaking the structure and not in accelerating the rotation of the shaft. This is well known Sommerfeld effect. Note that as long as

the rotation of the motor is assumed to be uncoupled from the vibrations excited upon the supporting structure, one has a known forcing function of time, corresponding to an unlimited or ideal power supply. If the structure has linear behavior, the problem will be a linear one. The introduction of real torque-speed curves for non-ideal motors renders the system nonlinear and capable of multiple steady-state periodic motions whose stability must be assessed. Further complexities may be introduced if the structure itself exhibits nonlinear behavior. We also found that the right branch of the amplitude frequency response curve may be unstable if the magnitude of its negative slope is larger than that of the torque-speed characteristic of the driving motor. Further comments on the subject are found in [1, 2, 3, 4, 5, 6, 7, 8, 9, 10], without undeserve others.We announced that a number of works have been done in order to investigate the resonant conditions of non-ideal vibrating systems, investigating how to drive a system through resonance and avoid Sommerfeld. In this paper we will illustrate this problem as a motivation before passing to several others related. Here, is present an overview of them in a systematic way and including new results on emerging area because, in recent years a large amount of research has been dedicated to new materials and their use in new structural components.

3 Governing Equations of Motion of (NIS)

The governing equations of motion of (NIS), are PDEs and result in coupled ordinary differential equations ODEs. Then (NIS) discretized mathematical model of a vibrating system, can be characterized by its governing equations of motion [10]:

$$\begin{aligned} m\ddot{x} + f(x,\dot{x}) + \frac{\partial U(x)}{\partial x} &= F(x,\dot{x},\varphi,\dot{\varphi}) \\ I\ddot{\varphi} + H(\dot{\varphi}) &= L(\dot{\varphi}) + R(x,\dot{x},\varphi,\dot{\varphi}) \end{aligned} \tag{1}$$

where m is the mass , x is displacement of the (NIS), φ is angular displacement of the rotor, $F(x,\dot{x},\varphi,\dot{\varphi})$ expresses the action of the source of energy on the oscillating system (angular velocity of motor, that is not constant), parameters r and m_0 are the eccentricity and mass of unbalanced shaft of the electric motor, I is the moment of inertia of the rotor, the function $R(x,\dot{x},\varphi,\dot{\varphi})$ expresses the action of the oscillating system on the source of energy, the function $H(\dot{\varphi})$ is the resistive torque applied to the motor, the function $L(\dot{\varphi})$ is the driving torque of the source of energy (motor). Note that, usually, the inductance is much smaller than the mechanical constant time of the system and, then in stationary regime, we can take $L(\dot{\varphi})$ as (linear) $L(\dot{\varphi}) = u_1 - u_2\dot{\varphi}$, where are u_1 related to voltage applied across to the armature of the DC motor, that is, a possible control parameter of the problem and u_2 is a constant for each model of DC motor considered. $\frac{\partial U(x)}{\partial x}$ is its conservative part (U is the potential, or strain energy), while $f(x,\dot{x})$ Is the nonlinear and non-conservative part of the restoring force.

The (NIS) model as a vibrating system, can be characterized by its nonlinear stiffness and damping as linear, cubic Duffing, cubic-quintic Duffing, Rayleigh and Van der Pol represented in the first, second, third, fourth and fifth term respectively of Eq. 1:

$$\begin{array}{lll} f(x,\dot{x}){=}c_1\dot{x} & f(x,\dot{x}){=}c_1\dot{x} & f(x,\dot{x}){=}c_1\dot{x} \\ U(x){=}\frac{1}{2}k_1x^2\ , & U(x){=}\frac{1}{2}k_1x^2+\frac{1}{4}k_2x^4\ , & U(x){=}\frac{1}{2}k_1x^2+\frac{1}{4}k_2x^4+\frac{1}{6}k_3x^6\ , \end{array}$$

$$\begin{array}{ll} f(x,\dot{x}){=}-c_1\dot{x}+c_2\dot{x}^3 & f(x,\dot{x}){=}-c_1\dot{x}+c_2x^2\dot{x} \\ U(x){=}\frac{1}{2}k_1x^2\ , & U(x){=}\frac{1}{2}k_1x^2\ . \end{array}$$

4 Control of (NIS)

The initial implementation of the vibration control to (NIS), using tuned liquid column dampers was done by [11, 12]. The saturation control was investigated on the non-ideal portal frame structure by [13, 14].They used 2:1 internal resonance and the saturation phenomenon to suppress steady-state vibrations of the system by connecting it to a second-order controller,using quadratic position coupling terms. The system composed for mono-rail system and modeled through the system: inverted pendulum, car and non-ideal motor was analyzed, for several motor torque constants through the analysis of the Floquet multipliers and the control was based on the Chebyshev polynomial expansion, in the Picard iterative method and in the Lyapunov-Floquet transformation, called Sinha's Theory by [15]. The linear feedback control problem for nonlinear systems has been formulated was developed by [16], under the viewpoint of optimal control theory. Asymptotic stability of the closed-loop nonlinear system is guaranteed by means of a Lyapunov function, which can clearly be seen to be the solution of the Hamiton-Jacobi-Bellman equation thus guaranteeing both stability and optimality. The formulated theorem expresses explicitly the form of minimized functional and gives the sufficient conditions that allow the use of linear feedback control for the nonlinear system.We mention that,it was applied by [17] to suppress the chaotic behavior, in a (NIS)-(SMA) oscillator.

5 Synchronization of (NIS)

We also announced that the nonlinear phenomena of shaft's self-synchronization has been studied extensively since the late 1940s, mostly with the aim of their application in designs of various shakers and exciters for purposeful vibration of objects [18]. The phenomenon had been studied extensively by asymptotic methods to predict possible (multiple) steady-state rotational motions and to evaluate their stability-mostly with application to the design of vibrators with a reduced number of driving motors. Certain cases of undesirable shaft self-synchronization in engineering had also been studied, but only steady-state motions were analyzed. Results of numerical simulation of transient self-synchronization of rotating shafts with one potential application being gas turbine engines with multiple shafts was studied by [19]. Finally,we mention that a practical problem of synchronization and self-synchronization of a non-ideal and nonlinear vibrating systems, were posed and investigated, by means of numerical simulations by [20, 21, 22, 23]. Fig. 1 illustrates a synchronization problem of a simple portal frame.

6 (NES)-Nonlinear Energy Sink Absorber to (NIS)

The realization of nonlinear energy pumping phenomenon,was first observed by [24], studying of the transient dynamics of a 2 DOFsystem,consisting of a damped vibrating system, weakly coupled to an essentially (strongly) nonlinear,damped attachment, i.e., an oscillator with zero linearized stiffness.As a result, an energy transfer occurs and a significant portion of the imparted energy to the oscillator gets passively absorbed and locally dissipated by the essentially nonlinear attachment,which acts, in essence, as nonlinear energy sink (NES). NES was then defined as the one-way (irreversible on average) channeling of vibrational energy from the directly excited primary structure to the attached NES. The underlying dynamical mechanism governing it was found to be a transient resonance capture of the dynamics of the nonlinear attachment on a 1:1 resonance manifold [25, 26]. A complete review of several approaches are given by [27]. We announced that, based in

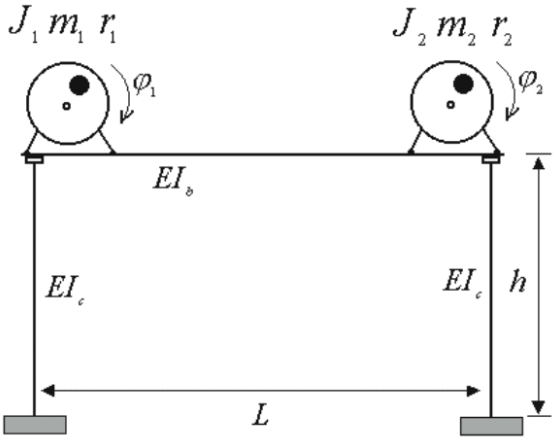

(a)

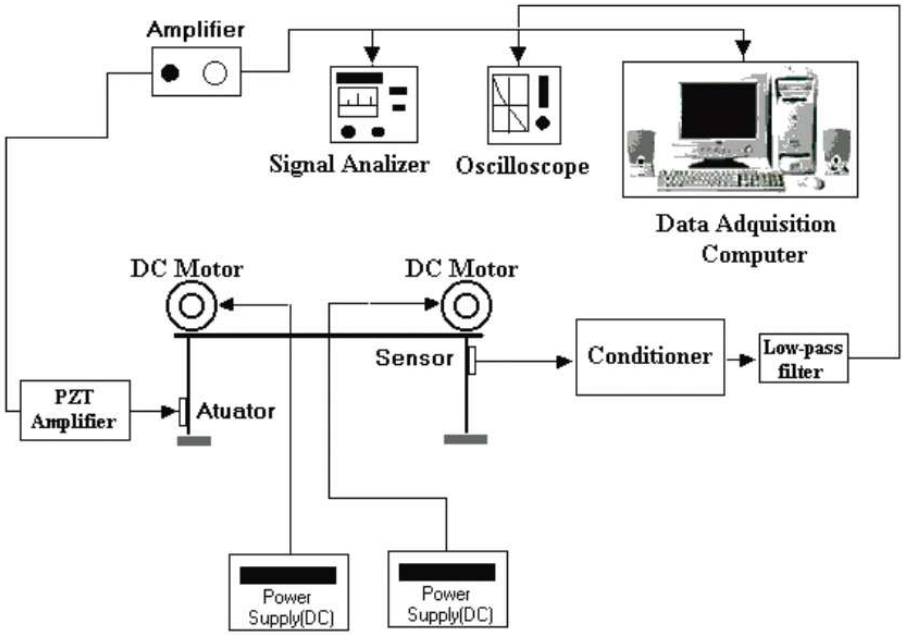

(b)

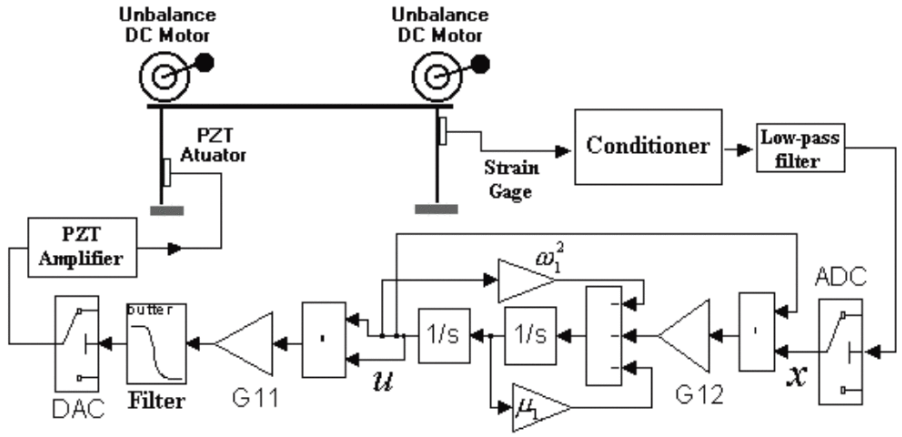

(c)

Figure 1: Indentification, Synchronization and saturation control problem of a simple portal frame.

an extension of the (IS) investigated by [28, 29] and taking into account that in a vibrating system, with small low viscous dissipation, the energy initially imparted to the primary sub-system, can be transferred to the nonlinear energy sink, named as (NES) [30],reduced the amplitudes of vibrations of the (NIS) and eliminated or reduced the occurrence of the Sommerfeld effect, inside and outside resonance region, respectively.In this case,we need to consider more one equation in Eq. 1

$$m_2\ddot{y} + c_2\dot{y} + g(y) + \frac{\partial V(x,y)}{\partial y} = 0 \tag{2}$$

where m_2 is the mass, c_2 is the coefficient of the viscous damping and y is the displacement of the (NES), $g(y)$ is the stiffness term not necessarily linear of the (NES), V is the potential energy not necessarily linear associated with the coupling spring. We also mention that, using a combination of the optimal active control for nonlinear systems [30] and the passive broadband boundary controller (nonlinear energy pumping), [31] reduced the amplitude of vibrations in a (NIS), coupled to an essentially nonlinearity, motived by the works done by [32, 33]. Figs. 2 and 3, illustrates the above mentioned problem.Taking into account,the (NIS) given by Fig. 2, according to [30]. Comparing the resulting oscillations of the NIS without NES (gray dotted line) and with NES (gray solid line) we have the amplitude reduction of 83 % inside the resonance region with elimination of the Sommerfeld effect and 63% outside the resonance region with the reduction of the Sommerfeld effect. On the other hand, the vibration amplitude of the NES is predominant on the NIS outside the resonance region so that the energy transfer between the NIS and the NES is verified.

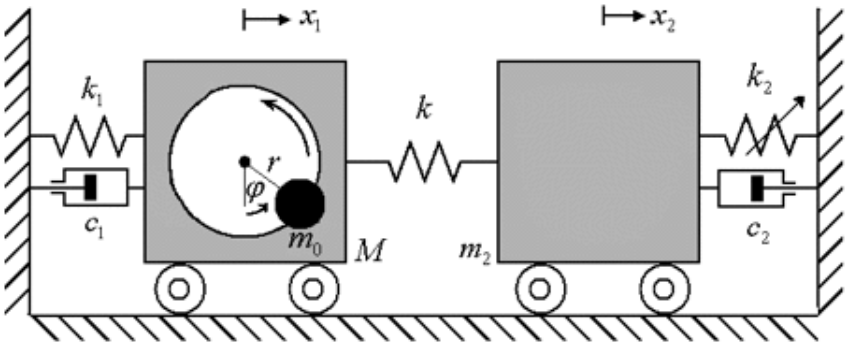

Figure 2: Schematic of a non-ideal oscillator attachment coupled to nonlinear essentially oscillator [30].

7 (NEVA) Electro-mechanical Absorber to (NIS)

We remarked that three approaches can be considered to control vibration levels. They are: (a) reducing the strength of the energy source, (b) modifying the dynamic characteristics of the receiver to reduce the ability of the structure to respond to the input energy, and (c) isolating the sensitive parts from the vibrating structures. In this paper, we consider the second alternative. A dynamic vibration absorber is a passive device, which is used to reduce excessive vibrations in a mechanical system. The absorber typically, consists of an inertial device, which changes the dynamic response of the original vibrating system over a certain frequency range. The absorbing device may be a linear mass-spring oscillator, a pendulum or rotary oscillator, a fluid or granular system, or a distributed

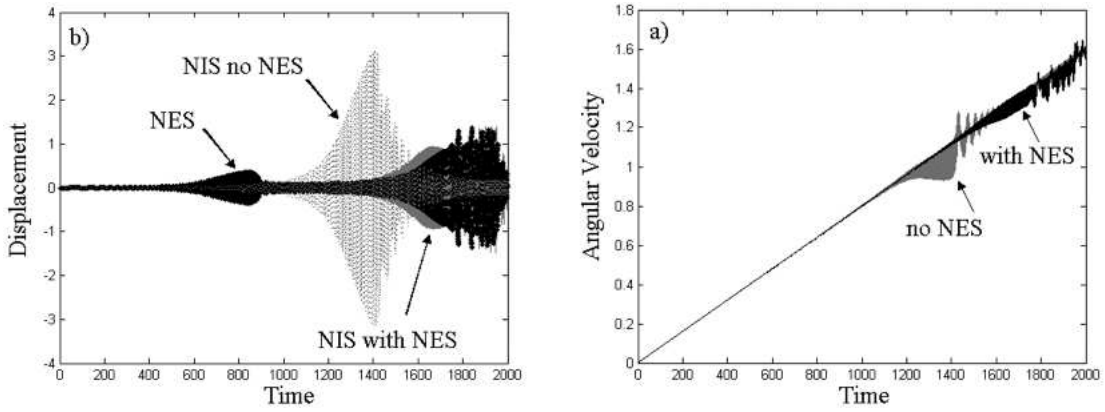

Figure 3: Responses of the a) angular velocity, b) displacement of NIS and NES relatively to Fig. 2 [30].

elastic structure. Although a vibration absorber can produce a reduction in the vibration amplitude of the original mechanical system, this improvement is obtained at the expense of large amplitude mechanical vibrations in the absorber. This large amplitude oscillation is one of the major problems in the design of practical absorber systems. Space and weight limitations or structural failures often limit the performance of the vibration absorber. The effectiveness of a (NEVA), in the vibration attenuation of a (NIS), was done by [34, 35]. They, have dealt with the study of a (NIS), coupled to a nonlinear electromechanical vibration absorber. They considered a nonlinear friction of type cubic-quantic Duffing oscillator and by considering the voltage of the resistor as being a nonlinear function of type Rayleigh oscillator. We observed that the passage of the resonance region, a dramatic decreasing of the vibration amplitude of the (NIS) and to with the possibility of the minimization of the Sommerfeld effect of (NIS). They taking into account that the electric part of the controller was consisted of a linear inductor , a nonlinear capacitor , and nonlinear resistor.

The expression of the voltage over the resistor and the condenser may be written respectively, as a nonlinear function of the instantaneous electrical charge q:

$$V_{NR} = -Ri_0 \left(\frac{\dot{q}}{i_0} - \frac{1}{3} \left(\frac{\dot{q}}{i_0} \right)^3 \right), \tag{3}$$

$$V_{NC} = \frac{q}{C_0} + \alpha_3 q^3 + \alpha_5 q^5, \tag{4}$$

where i_0 is an initial current, in the electrical part, C_0 is the linear value of the capacitive characteristic and the parameters α_3 and $alpha_5$, are a nonlinear coefficients, those depending on the type (or kind) of the capacitor, in use. Thus, we will obtain the following governing equations of motion:

$$m_1\ddot{x} + c_1\dot{x} + k_1 x + k_2 x^3 - T\dot{q} = m_0 r\ddot{\varphi}\cos(\varphi) - m_0 r\dot{\varphi}^2 \sin(\varphi), \tag{5}$$

$$I\ddot{\varphi} = \Gamma(\dot{\varphi}) + m_0 r\ddot{x}_1 \cos\varphi, \tag{6}$$

$$L\ddot{q} - R\left(1 - \frac{1}{i_0^2}\dot{q}^2\right)\dot{q} + \frac{1}{C_p}q + i_0^2\alpha_a q^3 + i_0^4\alpha_b q^5 + T\ddot{x} = 0 \tag{7}$$

The quantity $m_1 = m_0 + M$ is the total mass of the (NIS), c_1 is the linear damping coefficient, k_1 is the linear spring coefficient and k_2 is the cubic spring coefficient. The quantity T is the transducer (constant), which relates the current in the coil to the magnetic force on the considered coil. The simplest transducer constant model is given by $T = 2\pi nlB$, where n is the number of turns in the coil, l is the radius of the coil, and B is the uniform radial magnetic field strength in the annular gap. The transducer constant T also relates the electrical potential e, across to the terminals of the coil to the velocity of the coil, with respect to the permanent magnet. Figs. 4 and 5 illustrate the above mentioned problem.

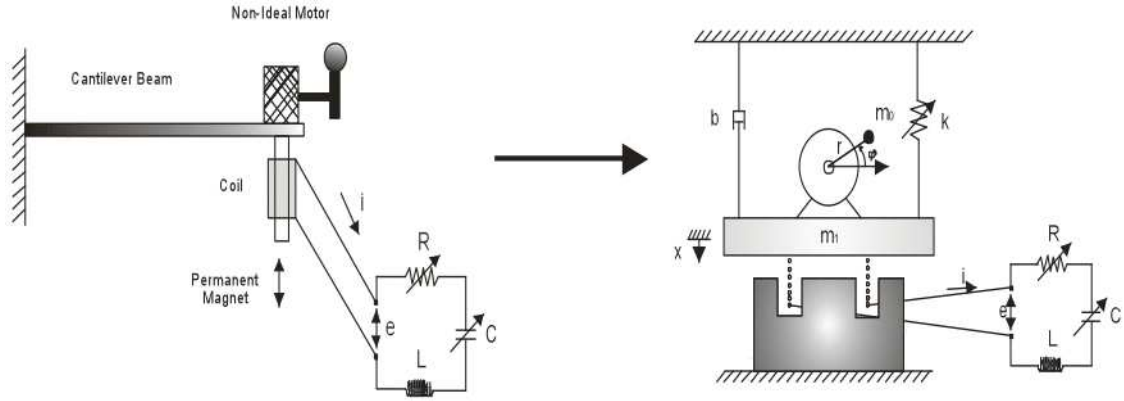

Figure 4: Schematic of a non-ideal structure coupled to nonlinear electromechanical vibration absorber device and its theoretical model [34, 35].

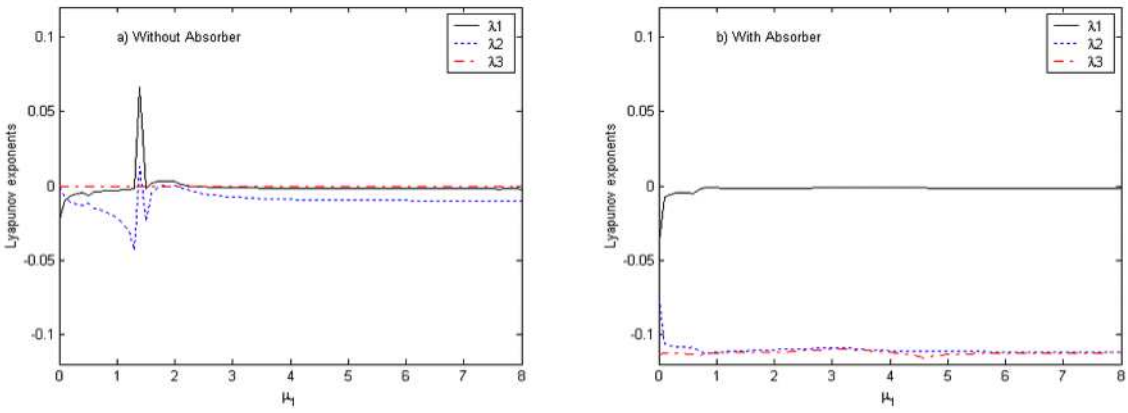

Figure 5: Lyapunov exponents of the system, a) without absorber, and b) with absorber [34, 35].

8 (NIS)-Emergent Areas

By one hand, in [36] it was considered the (NIS) Macro gyroscope tuning fork beam model (TFB), driven by a sinusoidal voltage. The (TFB) was represented by two inverted

pendulums, with suspension in both horizontal and vertical directions and it was excited by a nonlinear electro-magneto. By another hand in [37], an electrostatic transducer dynamics, composed by a non-ideal (MEMS) gyroscope, was analyzed taking into account the dynamic interaction, between the micro machined rate gyroscope and variable force actuators. We detected the presence of the energy transference, in both problems, due to the effects of the cubic nonlinearity and the suspension damping. We also observed in both mentioned problems that them presented mutual interations similar of those, in non-ideal vibrating problems (NIS). In these cases, we dealt with the known non-ideal phenomenon (the excitation force it is influenced by the response of the structure), until now restrict to MACRO vibrating systems.This is new topic to be explored in next future.

9 Conclusions

Recent studies, new phenomena and emergent areas, were addressed, concerning to (NIS) problems, covering the period from 2005 to 2010. It is known that, the non-ideal phenomenon, it is considered as the influence between the responses of two vibrations modes or of two coupled systems. In this case, for macro system, the excitation force it is influenced by the response of the structure. From the mathematical point of view, one must add a differential equation that describes how the energy source coupled with the differential equation of the structure. extended this study, by considering a conventional vibratory gyroscope and the full interaction between mechanical and electrical field quantities in "MEMS" by using numerical simulations.We proposed the use of an optimal linear feedback control strategy to reduce the movement of this system to a stable point, with success. The extension to any situation is easily done.

Acknowledgements

The authors acknowledge FAPESP and CNPq, both financial angencies.

References

[1] Kononenko, V. O.Vibrating systems with a limited power supply, English translation, IL life Books,(1969).

[2] Nayfeh A H and Mook D T., Nonlinear Oscillations, John Wiley and Sons, (1979).

[3] Evan-Iwanowsk, R. M.Resonance Oscillators in Mechanical Systems, Elsevier, (1976)

[4] Dimentberg, M.F., McGovern, L., Norton, R.L., Chapdelaine, J. and Harrison, R. Dynamic of an Unbalanced Shaft Interacting with a Limited Power Supply, Nonlinear Dynamics (13), (1997) 171-187.

[5] Balthazar, J.M., Mook, D.T., Weber, H.I., Brasil, R.M.L.R.F., Fenili, A., Belato and D., Felix, J.L.P. An overview on non-ideal vibrations, Meccanica, 38(6), (2003) 613-621.

[6] Balthazar, J., M, Felix, J.L.P Brasil and R.M.L.R.F. Nonlinear interactions in a piezoceramic Bar t transducer powered by a vacuum tube generated by a non-ideal source.Comput Nonliner Dynam 4, (2009) 011013

[7] Bolla, M., Balthazar, J.M., Felix, J.L.P., and Mook, D.T. On an approximate analytical solution to a nonlinear vibrating problem, excited by a non-ideal motor. Nonlinear Dynamics 50, (2007) 841-847.

[8] Dantas, M.J. H.and Balthazar J.M.On the existence and stability of periodic orbits in non-ideal problems: general results, Z.Angew. Mathematik and Physik ZAMP, (58), (2007) 940-958.

[9] Piccirillo, V., Balthazar, J.M., Felix, J.L.P and Pontes, Jr., B.R. On a nonlinear and chaotic Non-ideal vibrating system, with shape memory alloy (SMA).Journal of Theoretical and Ap plied Mechanics 46, (3), (2008) 597- 620.

[10] Felix, J.L.P, Balthazar, J., M, Brasil and R.M.L.R.F. Comments on nonlinear dynamics of a Non-ideal Duffing-Rayleigh oscillator: numerical and analytical approaches. Journal of Sound and Vibration, Vol.319, Issues 3-5, 23, (2009) 1136-1149

[11] Felix, J.L.P., Balthazar, J.M., Brasil and R.M.L.R.F.On tuned liquid column dampers mounted on a structural frame under a non-ideal excitation. Journal of Sound and Vibration 282, (2005) 1285-1292.

[12] De Souza, S.L.T., Caldas, I.L., R.L. Viana,Balthazar,J.M.and Brasil, R.M.L.R.F.:Dynamics of vibrating systems with tuned liquid column dampers and limited power supply.Journal of Sound and Vibration,Vol. 289, Issues 4-5, (2006) 987-998

[13] Balthazar JM, Felix JLP, and Brasil MLRF.Nonlinear dynamics of a particular portal frame foundation model, excited by a non-ideal motor. Material Science Forum.Vol.440-4, (2003) 371-378

[14] Felix, J.L.P., Balthazar, J.M., Brasil, R.M.L.R.F.On saturation control of a non-ideal vibrating portal frame foundation type shear-building. Journal of Vibration and Control, 11, (2005)121-136

[15] Peruzi, N.J., Balthazar, J, M, Pontes, B.JR and Brasil, R.M.L.R F. Nonlinear dynamics and control of an ideal/nonlideal load transportation system with periodic coefficients.J.Comput. Nonlinear Dynam. 2, (2007),32

[16] Rafikov, M. and Balthazar, J.M.On control and synchronization in chaotic and hyper Chaotic system via linear control feedback.Comm.in Nonl Sci.Num.Sim 13, (2008)1246-1255.

[17] Piccirillo, V., Balthazar, J.M., Pontes Jr., B.R. and Felix, J.L.P. Control of a Nonlinear Oscillator with shape memory alloy, using an optimal linear control: Part II: Non-ideal energy Source Nonlinear Dynamics, Vol. 56(3), (2009) 243-253

[18] Blekhman, I.I., Self-Synchronization in Science and Technology, ASME Press,New York, 1998.

[19] Dimentberg, M Cobb,E. and Mensching, J., Self-Synchronization of Transient Rotation in Multiple Shaft Systems, Journal of Vibration and Control, (7),(2001) 221-232.

[20] Balthazar JM, Felix JLP and Brasil R.M.L.R.D.Some Comments on the numerical simulation of self-synchronization of for non-ideal exciters. Applied Mathematics and Computation, V.164, N 2, (2005) 615-625

[21] Balthazar JM, Felix JLP and Brasil MLRD. Short comments on self-synchronization of Two non-ideal sources supported by a flexible portal frame, Journal of Vibration and Control. 10, N 2, (2004) 1739-1748

[22] Felix JLP., Balthazar, J.M and Brasil MLRD.A short note on a nonlinear system vibrations under two non-ideal excitations. J. Braz. Soc. Mech. Sci. & Eng., vol.25, no.4, (2003) 391-395.

[23] Felix, J.L.P, Balthazar, J., M and Brasil, R.M.L.R.F.: A short note on transverse vibrations of a shaft carrying two (or one) disk, excited by a non-ideal motor.J.Comput.Nonlinear Dynam.4, (2009) 014501

[24] Gendelman,O.V.Transition of energy to a nonlinear localized mode in a highly asymmetric system of two oscillators, Nonlinear dynamics, vol. 25,(2001) 237-253.

[25] Gendelman,O.C.,. Manevitch, L.I.,Vakakis,A.F. and McCloskey,E.Energy pumping in nonlinear mechanical oscillators : part I - dynamics of the underlying hamiltonian systems, Journal of Applied Mechanics, vol. 68,(2001) 34-41.

[26] Vakakis A. F and. Gendelman,O.V. Energy pumping in nonlinear mechanical oscillators : Part II - resonance capture, Journal of Sound and Vibration, vol. 68, (2001) 42-48.

[27] Vakakis, A. F., Gendelman, O. V., Bergman, L. A., MacFarland, D. M., Kerscher G., Lee Y. S. nonlinear target energy transfer in mechanical and structural systems. Springer Verlag Holland (2008)

[28] Dantas, M.J.H. and Balthazar, J.M.On energy transfer between linear and non-linear oscillator.Journal of Sound and Vibration,Vol,315, (2008) Issues 4-5.

[29] Costa, S.N.J., Hassmann, C.H.G., Balthazar, J.M and Dantas, M.H.J.Energy transfer between vibrating systems under linear and nonlinear interactions.Nonlinear Dynamics, ,Vol. 57, Numbers 1-2, (2009) 57-67

[30] Felix, J.L.P, Balthazar,J., M. and Dantas, M.H.G.On energy pumping, synchronization and beat phenomenon in a non-ideal structure coupled to an essentially nonlinear osillator.Nonlinear Dynamics, Vol. 56, Numbers 1-2, (2009) 1-11

[31] Chavarette, FR; Balthazar, JM and Felix, J.L.P.: Remarks on non-ideal structure coupled to an essentially nonlinear oscillator non-ideal and ideal structure coupled to an essentially nonlinear oscillator.J.Comput.Nonlinear Dynam, Vol.4, Issue, 3, (2009)031005

[32] Costa, S.N.J and Balthazar, J.M.On an Active control for a structurally nonlinear mechanical System, taking into Account an Energy Pumping.J.Comput.Nonlinear DyN, Vol.4, Issue 3, (2009)031005.

[33] Costa, S.N.J and Balthazar. Suppression of vibrations in strongly nonhomogeneous 2DOF systems. Nonlinear Dyn.58. (2009) 623-632

[34] Felix, J.L.and Balthazar, J., M. Comments on a nonlinear and non-ideal electromechanical damping vibration absorber, Sommerfeld effect and energy TransFer.Nonlinear Dynamics, Volume 55, Numbers 1-2, (2009)1-11

[35] Felix, J.L.P, Balthazar, J., M, Dantas, MJH.On a non-ideal (MRD) damped-electro-mechanical absorber dynamics. International Journal of Bifurcation and Chaos World Scientific Publishing Company,(2011), in press.

[36] Balthazar, J.M, Felix, J.L.P, Brasil, R.M.L.R.F.Chaotic dynamics of a macro tuning fork beam (TFB), under an eletro-dynamical shaker excitation. Proceedings of 11th Pan-American Congress of Applied Mechanics (PACAM XI), CD ROM, January 04-08,010, (2008)Foz do Iguacu, Pr, Brazil, (2008)

[37] Balthazar, J.M., Chavarette, F.R Felix, J.L.P., On Nonlinear Interactions in a Non-ideal MEMS Gyroscope. In: IUTAM Symposium on Nonlinear Dynamics for Advanced Technologies and Engineering Design. Aberdeen, 2010, in press(2011)

José M. Balthazar, UNESP - Universidade Estadual Paulista, Rio Claro, SP, Brazil
Jorge L. P. Felix, UNIPAMPA - Universidade Federal do PAMPA, Campus Bagé

New approach for contact optimization problems with friction and wear

Nickolay V. Banichuk Svetlana Yu. Ivanova Evgeniy V. Makeev
Alexander V. Sinitsin
banichuk@ipmnet.ru

Abstract

The problem of optimization of contact interaction of a moving rigid punch and elastic half-space is investigated taking into account friction of contacted surfaces, wear of materials and arising pressure distributions. The relative movement is considered in frame of quasi-static formulation. The punch shape is accepted as a desirable design variable. The wear volume rate, the friction dissipation power and the discrepancy functional (between optimized contact pressure and some given distribution) are taken as components of the minimized vector-functional. Such an optimization problem for multiple objectives is called multi-objective or multi-criteria optimization or Pareto-optimization. Necessary conditions for the optimality of the vector-functional are derived and studied taking into account quasi-steady state of wear process. The solution of the optimization problem results from transformation into scalar substitute problems by means of preference functions. Formulated optimization problem is investigated analytically using the developed decomposition approach and exact solutions are obtained for the punch which has a rectangular contact region and moves translationally with a constant velocity.

1 Basic relations and problem formulation

Let us consider the interaction of a rigid punch with the elastic half-space ($z \geq 0$) taking into account friction and wear. The system of coordinates $Oxyz$ is fixed with the punch, which moves in x-direction with the constant relative velocity V. The relative movement is considered in frame of quasi-static formulation. It is supposed that the rectangular contact region Ω_f is symmetric with respect to the axes Ox, Oy: $\Omega_f = [-a \leq x \leq a,\ -b \leq y \leq b]$, where a, b are the given constants. The normal stresses σ_{zz} and the tangential stresses σ_{xz}

$$\begin{aligned} &\sigma_{zz}(x,y,0) = -p(x,y), \quad p(x,y) \geq 0 \\ &\sigma_{xz} = \tau_0 + \mu p(x,y) \end{aligned} \tag{1}$$

are acting in the contact region Ω_f, where $p \geq 0$ is the contact pressure and τ_0, μ are the friction constants [1]. The boundary conditions for the theory of elasticity problem in the half-space $z \geq 0$ are written in the form

$$\begin{aligned} &w = f(x,y), \quad \sigma_{xz} = \tau_0 - \mu\sigma_{zz}, \quad \sigma_{yz} = 0 \quad (x,y) \in \Omega_f \\ &\sigma_{zz} = 0, \quad \sigma_{xz} = 0, \quad \sigma_{yz} = 0, \quad (x,y) \in \Omega_0 \end{aligned} \tag{2}$$

Here $w = w(x,y)$ iz the z-component of the vector of elastic displacements, $f(x,y)$ denotes the punch shape contacting with the elastic medium and Ω_0 - the region of elastic half-space surface free from loads.

For the known distribution $p(x,y)$, $(x,y) \in \Omega_f$ the resulting force P and the total moment M with respect to the y-axis which acted on the punch are defined as

$$P = J_P = \int_{\Omega_f} p d\Omega_f, \quad M = J_M = \int_{\Omega_f} xp d\Omega_f \tag{3}$$

The punch shape $f = f(x,y)$ is accepted as a desirable design variable. The friction dissipation power

$$J_F(f) = \int_{\Omega_f} (\tau_0 + \mu p(f)) V d\Omega_f \tag{4}$$

the wear volume rate

$$J_W(f) = \int_{\Omega_f} K_W p^n(f) V^m d\Omega_f \tag{5}$$

and the discrepancy functional

$$J_D(f) = \int_{\Omega_f} (p(f) - p_g)^2 d\Omega_f \tag{6}$$

are taken into account as the components of the minimized vector-functional J

$$J(f) = \{J_F(f),\ J_W(f),\ J_F(f)\}^T \to \min_f \tag{7}$$

Here K_W is the wear constant, $n > 1$, $m > 0$ - given parameters of contacting materials [1] and $p_g = p_g(x,y)$ - given objective function.

The optimization problem is to find the optimal punch shape $f(x,y)$ that minimizes the vector-functional (7) under the constraints

$$J_P = P^*, \quad J_M = M^* \tag{8}$$

where $P^* \geq 0$ and $M^* \geq 0$ are the given values. We suppose that the value of the total force P^* is sufficiently large in comparison with the value of the moment M^*, i.e. the condition $p(x,y) \geq 0$, $(x,y) \in \Omega_f$ is satisfied [2].

2 Solving of optimization problem

Formulated optimization problem can be decomposed to two separately solved problems [2]. The first problem consists in finding of the optimal pressure distribution $p_* \in \Omega_f$ that minimizes the vector-functional

$$J(p) = \{J_F(p),\ J_W(p),\ J_F(p)\}^T \to \min_{p \in \Lambda_f} \tag{9}$$

$$\Lambda_p = \{p \geq 0,\ J_P(p) = P^*,\ J_M(p) = M^*\} \tag{10}$$

The second problem is to find the normal displacements $w_*(x,y)$ for the optimal pressure distribution $p_*(x,y)$ and corresponding friction forces, i.e. to define the optimal punch shape $f_*(x,y) = w_*(x,y)$.

For solving of the multi-criteria problem (9)-(10) (Pareto-optimization) the scalar linear weight-functional J_C is constructed and minimized (see, for example, [3], [4]):

$$\begin{array}{l} J_C(p) = C_F J_F(p) + C_W J_W(p) + C_D J_D(p) \to \min_{p \in \Lambda_p} \\ C_F \geq 0,\ C_W \geq 0,\ C_D \geq 0, \quad C_F + C_W + C_D = 1 \end{array} \tag{11}$$

As a result the optimal pressure distribution $p_*(x,y)$ depending on the weight coefficients C_F, C_W, C_D can be defined with application of well known technique of Lagrange multipliers. The necessary condition of optimality of the functional (11) under the constraints (8) can be written as

$$\begin{array}{l}\delta J_C^L(p) = \delta\{J_C(p) - \lambda_P J_P(p) - \lambda_M J_M(p)\} = \\ = \int_{\Omega_f}\{C_F\mu V + nC_W K_W p^{n-1}V^m + 2C_D(p-p_g) - \lambda_P - \lambda_M x\}\delta p d\Omega_f = 0\end{array} \tag{12}$$

where λ_P and λ_M - Lagrange multipliers defined from the conditions (8). We assume for simplicity $n=2$, $m=1$, $p_g = P^*/S$, where S is the area of contact region Ω_f. If μ is the constant value and the region Ω_f is symmetric with respect to the axes Ox, Oy, the optimal pressure distribution p_* can be defined as

$$p_* = \frac{P^\star}{S} + \frac{M^*}{I_y}x \tag{13}$$

where I_y - the moment of inertia of Ω_f. Note that in this special case p_* don't depend on the weight coefficients C_F, C_W, C_D. If $\mu = \mu(x,y)$ we have more general dependence

$$p_* = \frac{P^\star}{S} + \Delta_1 + \left(\frac{M^*}{I_y} + \Delta_2\right)x \tag{14}$$

$$\Delta_1 = \frac{C_F V}{2\left(C_W K_W V + C_D\right)}\left(\frac{1}{S}\int_{\Omega_f}\mu d\Omega_f - \mu\right),\ \Delta_2 = \frac{C_F V}{2\left(C_W K_W V + C_D\right)I_y}\int_{\Omega_f}\mu x d\Omega_f$$

In accordance with considered decomposition approach the second problem must be solved to define the optimal shape distribution $f_*(x,y)$ corresponding to the defined optimal pressure $p_*(x,y)$ and acting friction forces. For this purpose we use the exact solution [5]

$$w(x,y) = \kappa_0\frac{Q_z^0}{\rho} + \kappa_f\frac{(x-x')Q_x^0}{\rho^2},\quad \rho^2 = (x-x')^2 + (y-y')^2 \tag{15}$$

$$\kappa_0 = \frac{1-\nu^2}{\pi E},\ \kappa_f = \frac{(1+\nu)(1-2\nu)}{2\pi E}$$

of the problem for the pointed force

$$q = \{Q_x,\ Q_y = 0,\ Q_z\} = \left\{Q_x^0\delta(x-x', y-y'),\ 0,\ Q_z^0\delta(x-x', y-y')\right\} \tag{16}$$

loaded at the point (x,y). Here $Q_x^0 = \left(\tau_0 + \mu p_*\left(x', y'\right)\right)dx', dy'$, $Q_z^0 = p_*(x',y')dx'dy'$, ν - Poisson coefficient, E - Young modulus, δ - Dirac function. By integration of the right side of the expression (15) on the region Ω_f we obtain

$$f_*(x,y) = \kappa_0\int_{\Omega_f}\frac{p_*(x',y')dx'dy'}{\sqrt{(x-x')^2+(y-y')^2}} + \kappa_f\int_{\Omega_f}\frac{(x-x')(\tau_0+\mu p_*(x',y'))dx'dy'}{(x-x')^2+(y-y')^2} \tag{17}$$

Let us introduce the new variables ρ, θ. We have

$$\begin{array}{l}x' - x = \rho\cos\theta,\quad y' - y = \rho\sin\theta \\ \rho(x,y,x',y') = \sqrt{(x-x')^2+(y-y')^2},\quad d\Omega = \rho d\rho d\theta\end{array} \tag{18}$$

and

$$f_*(x,y) = \kappa_0\int_0^{2\pi}d\theta\int_0^{R(\theta)}p_*(x+\rho\cos\theta,\ y+\rho\sin\theta)d\rho - \tag{19}$$

$$-\mu\kappa_f \int_0^{2\pi} \cos\theta d\theta \int_0^{R(\theta)} p_*(x+\rho\cos\theta,\ y+\rho\sin\theta)d\rho - \tau_0\kappa_f \int_0^{2\pi} R(\theta)\cos\theta d\theta$$

The expression (13) can be rewritten as

$$\begin{array}{l} p_* = p_*(x) = C + Ax' = C + A(x+\rho\cos\theta) \\ C = P^*/S, \quad A = M^*/I_y \end{array} \tag{20}$$

Then we obtain the following relation for the optimal punch shape

$$\begin{array}{l} f_*(x,y) = \kappa_0(C+Ax)D_0(x,y) + \kappa_0 A D_C(x,y)/2 - \\ -\mu\kappa_f[(C+Ax)D_{0C}(x,y) + AD_{CC}(x,y)/2] - \tau_0\kappa_f D_{0C}(x,y) \end{array} \tag{21}$$

where

$$D_0 = \int_0^{2\pi} R d\theta,\ \ D_C = \int_0^{2\pi} R^2\cos\theta d\theta,\ \ D_{0C} = \int_0^{2\pi} R\cos\theta d\theta,\ \ D_{CC} = \int_0^{2\pi} R^2\cos^2\theta d\theta$$

For considered rectangular region Ω_f function D_0 can be written in the form

$$D_0 = \frac{1}{2}[(a-x)\varphi_1(x,y) + (b-y)\varphi_2(x,y) + (a+x)\varphi_3(x,y) + (b+y)\varphi_4(x,y)]$$

$$\varphi_1 = \ln\left(\frac{\rho_1+b+y}{\rho_1-b-y}\,\frac{\rho_2+b-y}{\rho_2-b+y}\right),\quad \varphi_2 = \ln\left(\frac{\rho_2+a-x}{\rho_2-a+x}\,\frac{\rho_3+a+x}{\rho_3-a-x}\right)$$

$$\varphi_3 = \ln\left(\frac{\rho_3+b-y}{\rho_3-b+y}\,\frac{\rho_4+b+y}{\rho_4-b-y}\right),\quad \varphi_4 = \ln\left(\frac{\rho_4+a+x}{\rho_4-a-x}\,\frac{\rho_1+a-x}{\rho_1-a+x}\right)$$

$$\rho_1^2 = (a-x)^2 + (b+y)^2,\quad \rho_2^2 = (a-x)^2 + (b-y)^2$$

$$\rho_3^2 = (a+x)^2 + (b-y)^2,\quad \rho_4^2 = (a+x)^2 + (b+y)^2$$

Performing the analogues transformations we obtain the following expressions for the functions D_C, D_{0C}, D_{CC}:

$$\begin{array}{l} D_C = (a-x)^2\varphi_1/2 - (a+x)^2\varphi_3/2 + (b-y)^2(1/\cos\gamma_3 - 1/\cos\gamma_4) + \\ +(b+y)^2(1/\cos\gamma_8 - 1/\cos\gamma_7) \end{array}$$

$$D_{0C} = (a-x)(\gamma_1+\gamma_2) + (a+x)(\gamma_5+\gamma_6) + (b-y)\ln\frac{\cos\gamma_4}{\cos\gamma_3} - (b+y)\ln\frac{\cos\gamma_8}{\cos\gamma_7}$$

$$\begin{array}{l} D_{CC} = (a-x)^2(\gamma_1+\gamma_2) + (a+x)^2(\gamma_5+\gamma_6) - (b-y)^2(\gamma_3+\gamma_4) - \\ -(b+y)^2(\gamma_7+\gamma_8) + (b-y)^2(\cot\gamma_2 + \cot\gamma_5) + (b+y)^2(\cot\gamma_6 + \cot\gamma_1) \end{array}$$

where

$$\gamma_1 = \arcsin\frac{b+y}{\rho_1},\ \ \gamma_2 = \arcsin\frac{b-y}{\rho_2},\ \ \gamma_3 = \arcsin\frac{a-x}{\rho_2},\ \ \gamma_4 = \arcsin\frac{a+x}{\rho_3}$$

$$\gamma_5 = \arcsin\frac{b-y}{\rho_3},\ \ \gamma_6 = \arcsin\frac{b+y}{\rho_4},\ \ \gamma_7 = \arcsin\frac{a+x}{\rho_4},\ \ \gamma_8 = \arcsin\frac{a-x}{\rho_1}$$

Function D_0, D_C, D_{0C}, D_{CC} are shown in fig.1-4 for $a = b = 1$. In fig.5 the quantity $z = f_*/\kappa_0$ characterizing the optimal punch shape for $C = 1$, $A = 0.1$, $a = b = 1$, $\nu = 0.25$, $\mu = \tau_0 = 0.3$ is presented.

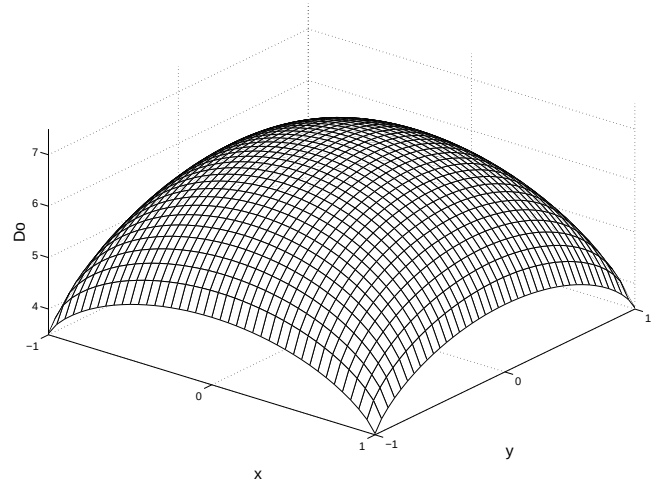

Figure 1: Shape function D_0

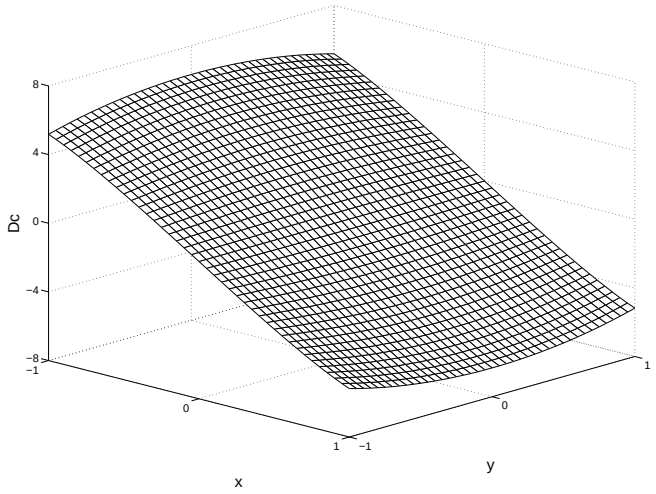

Figure 2: Shape function D_C

Acknowledgements

The work is performed under support of RFBR (grant 11-08-00030-a), RAS Program 13, Program of Support of Leading Scientific Schools (grant 169.2008.1).

References

[1] Goryacheva I.G. The Mechanics of Frictional Interaction. Moscow: Nauka, 2001.

[2] Banichuk N.V. Optimization of the contact pressure in the problem of the interaction of a punch and an elastic medium. J. of Appl. Math. and Mech., 74(2010), p. 334-340.

[3] Stadler W. Multicriteria optimization in mechanics (A survey), Appl. Mech. Review, Vol. 37, 3, 1984, p. 227-286.

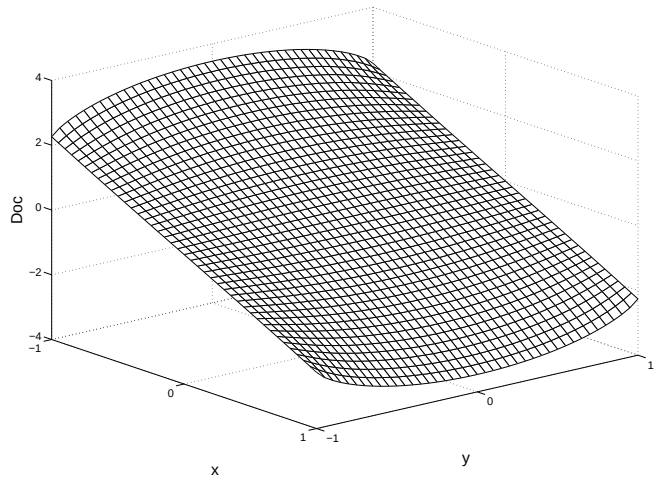

Figure 3: Shape function D_{0C}

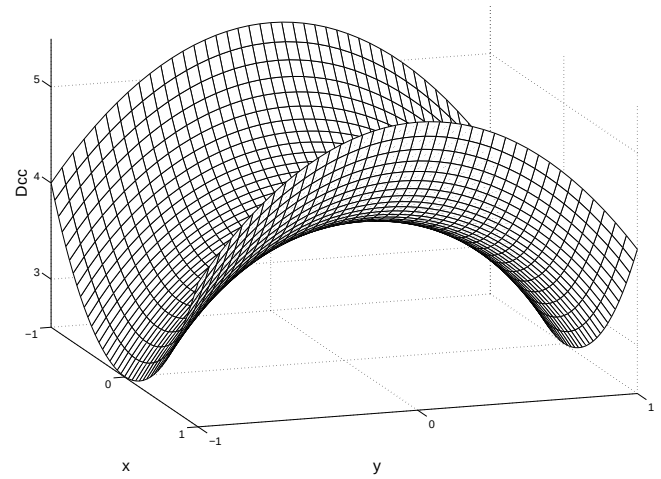

Figure 4: Shape function D_{CC}

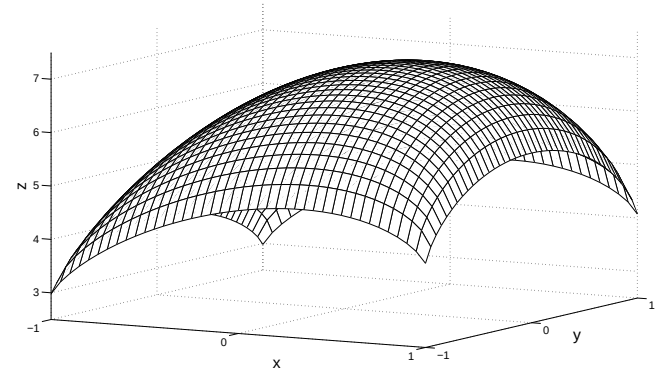

Figure 5: Optimal punch shape $z = f_*/\kappa_0$

[4] Banichuk N.V. Introduction to Optimization of Structures, New York: Springer, 1990.

[5] A.E.H. Love. A Treatise on the Mathematical Theory of Elasticity. Dover Publications. Inc., New York, 1944.

Nickolay V. Banichuk, Prospekt Vernadskogo, 101, bld.1, Moscow, Russia
Svetlana Yu. Ivanova, Prospekt Vernadskogo, 101, bld.1, Moscow, Russia
Evgeniy V. Makeev, Prospekt Vernadskogo, 101, bld.1, Moscow, Russia
Alexander V. Sinitsin, Prospekt Vernadskogo, 101, bld.1, Moscow, Russia

Oscillatory strobodynamics - an overview of advances and new results

Iliya Blekhman
iliya.i.blekhman@gmail.com

Abstract

The definition of the "oscillatory strobodynamics" is given as an interdisciplinary field of knowledge, which explores the slow component of dynamics of a system in the presence of a high-frequency in engineering, natural science and sociology. The general approach to the solution of corresponding problems is formulated. Its application to generic and specific models employed in different sciences, particularly to oscillators' models, are considered.

1 Introduction

A number of experimental and theoretical results have been accumulated by now with respect to the problem of relatively high frequency action on dynamic at systems in physics, chemistry, biology, physiology, economics and even sociology. Some of those investigations revealed a number of unusual and seemingly paradoxical phenomena, appearing to be of significant fundamental and applied value. Unfortunately, the theoretical studies were carried out by different methods and their results were treated differently. Many of the fundamental and applied problems considered there remain to be solved later on. It is hard to indicate a dynamical problem in any of the above listed sciences for that the investigation of oscillatory influence is meaningless.

In this paper the author attempts to formulate a general approach both to the solution of the above mentioned problems and to the analysis of the results obtained. The approach in question consists in transition from the description of a common ("true") dynamics of certain processes to the description of a dynamics, which takes into account only one component of the processes, the slow one, which is of the utmost interest for the applications. Such dynamics is much different from the conventional one, it is simpler but rather paradoxical; in particular, the laws of conservation break down there, the non-conservative system might be transformed into potential one and, conversely , additional summands may appear in the equations or parameter values may be changed. All aforesaid makes it expedient to single out the class of studies under review into a separate interdisciplinary field of knowledge called oscillatory strobodynamics (OS). This field may be regarded as a section in the theory of non-linear oscillations or in the non-linear dynamics. One part of OS, namely the vibrational control of physical processes, can be regarded as a section in cybernetical physics [1]. Now we introduce the definition and the description of the OS approach and give a brief review of results obtained earlier and a number of new results.

2 OS approach and definition

The essence of OS approach can be described in the following way. Let the process dynamics be described by the following relation:

$$\tilde{\mathrm{Z}}(\tilde{\mathrm{x}}, \tilde{\mathrm{a}}, t) = 0, \tag{1}$$

where $\vec{x}$ is vector of the system state, $\vec{a}$ - vector of parameters, t - time, $\vec{Z}$ -operator that may represent finite, differential, integral and other equations. In condition of fast oscillating influences the same correlation will take the form:

$$\tilde{\mathrm{Z}}\left[\tilde{\mathrm{x}} + \vec{\psi_{\mathrm{x}}}(t, \omega t), \vec{\mathrm{a}} + \vec{\psi_{\mathrm{a}}}(t, \omega t), t\right] = \vec{\mathrm{F}}(t, \omega t), \tag{2}$$

where $\vec{\psi_{\mathrm{x}}}$, $\vec{\psi_{\mathrm{a}}}$ and F - are some functions periodic in relation to "fast time" $\tau = \omega t$ and $\omega >> 1$ (Notions such as "fast", "slow", "high frequency" can be formalized [2, 3]).

Practically in all cases the change of the vector $x(t)$ at high frequency influences can be represented as

$$\vec{\mathrm{x}}(t) = \vec{\mathrm{X}}(t) + \vec{\psi}(t, \omega t), \tag{3}$$

where $\vec{X}$ is slow component, $\vec{\psi}$ is fast 2π - periodic in time τ component, with average zero. The component $\vec{X}$ is of utmost interest here. By a certain mathematical procedure and with some assumptions in relation to operator $\vec{Z}$ characteristics it is possible to obtain a relation including only a slow component $\vec{X}$:

$$\vec{\mathrm{Z}}^*(\vec{\mathrm{X}}, \vec{\mathrm{a}}^*, t) = 0. \tag{4}$$

The method of direct separation of motions appears to be the most appropriate one to be used in this procedure. Such method is widely used in solution of mechanics problems [2, 3] and can be easily extends to more general case considered here. Schematically the procedure is as follows. Since, according to (3), a single initial variable $\vec{x}$ is replaced by two variables - $\vec{X}$ and $\vec{\psi}$, hence, the equation (2) in general case can be replaced by the following two integro-differential equations:

$$\left\langle \vec{\mathrm{Z}}\left[\vec{\mathrm{X}} + \vec{\psi} + \vec{\psi_{\mathrm{x}}}, \vec{\mathrm{a}} + \vec{\psi_{\mathrm{a}}}, t\right] \right\rangle = \langle \mathrm{F} \rangle \tag{5}$$

$$\vec{\mathrm{Z}}\left[\vec{\mathrm{X}} + \vec{\psi} + \vec{\psi_{\mathrm{x}}}, \vec{\mathrm{a}} + \vec{\psi_{\mathrm{a}}}, t\right] - \left\langle \vec{\mathrm{Z}}\left[\vec{\mathrm{X}} + \vec{\psi} + \vec{\psi_{\mathrm{x}}}, \vec{\mathrm{a}} + \vec{\psi_{\mathrm{a}}}, t\right] \right\rangle = \vec{\mathrm{F}} - \left\langle \vec{\mathrm{F}} \right\rangle, \tag{6}$$

where the angular brackets denote averaging at $\tau = \omega t$ in period 2π. Further, the equation of fast motions (6) is solved in approximation with regard to the fast variable $\vec{\psi}$; the main approximation consists in assumption that slow variables can be considered in this case as "frozen" i.e. constant parameters. Substitution of $\vec{\psi}$ into the equation (5) of slow motions yields equation (4) (for details refer to [2, 3]). It is worth mentioning that approximation applied in solution of equation (6) will slightly affect the accuracy of equation (4) because function $\vec{\psi}$ is included in this equation under the sing of averaging. Meanwhile, it is to be taken into account that the approximations assumed will hold true only with certain limitations in the system parameters.

In general, both operator $\vec{Z}^*$ and parameter $\vec{a^*}$ values in equation (4) may be largely different from operator $\vec{Z}$ and parameter $\vec{a}$, which describe change of the initial variable $\vec{x}$. Usually relation (4) is much simpler then (2), whereas vectors $\vec{X}^*$ and operator $\vec{Z}^*$ may have much less dimensionality. *Let us call relation (4) the equation of oscillatory strobodynamics and define the oscillatory strobodynamics as dynamics describing evolution*

of the slow motion component under the action of high frequency upon a system or a process.

One can say that the slow component $\vec{X}$ is the result of observations made over $\vec{x}$ under stroboscopic light with the frequency of flashes equal to the frequency of oscillations ω. Hence the OS is the dynamics perceived by an observer watching a system subjected to high frequency influence under stroboscopic light or through special spectacles preventing him from seeing quick motions. It seems natural to suppose that the view of such observer is much simpler than the view of the observer watching the process $\vec{x}$ directly. It is to be emphasized that conservation laws in their usual form are not valid there.

3 General fundamental equation of natural sciences

3.1 Mechanics

The equation of dynamics

$$m\ddot{\vec{\mathrm{x}}} = \vec{F}(\dot{\vec{\mathrm{x}}}, \vec{\mathrm{x}}, t) + \vec{\Phi}(\dot{\vec{\mathrm{x}}}, \vec{\mathrm{x}}, t, \omega t), \tag{7}$$

where $\vec{F}$ is a slow force, and $\vec{\Phi}$ is a fast force 2π periodic in relation to ωt, corresponds to the equation of OS (vibrational mechanics).

$$m\ddot{\vec{\mathrm{X}}} = \vec{\mathrm{F}}(\dot{\vec{X}}, \vec{\mathrm{X}}, \mathrm{t}) + \vec{\mathrm{V}}(\dot{\vec{X}}, \vec{\mathrm{X}}, t), \tag{8}$$

where $\vec{V}$ is additional slow force called vibrational force (the term introduced by P.L. Kapitsa). The approach of the vibrational mechanics along with the solution of some applied problems was given in books [2, 3]. This paper can be considered as a generalization of that approach. Principal results are cited below. The following equations are in correlation to *the Navier-Stokes equation* and the equation of continuity:

$$\rho\frac{\partial\vec{\mathrm{U}}}{\partial t} + \rho(\vec{\mathrm{U}}\cdot\vec{\nabla})\vec{\mathrm{U}} = -\vec{\nabla}\mathrm{P} + \mu\vec{\nabla}^2\vec{\mathrm{U}} + \vec{\mathrm{v}}, \quad \vec{\nabla}\cdot\vec{\mathrm{U}} = 0, \tag{9}$$

where

$$\vec{\mathrm{v}} = -\left\langle \vec{\mathrm{u}'}\cdot\vec{\nabla})\vec{\mathrm{u}'}\right\rangle$$

while $\vec{U}$ and P are slow components of flow velocity and pressure , u' is a fast component of flow velocity, ρ - density, μ - viscosity coefficient, $\vec{\nabla}$ - Hamilton operator.

Note that the first equation (9) corresponds to well known *equation of Reynolds* describing turbulent motion of the viscous incompressible liquid while vector represents so called turbulent stresses, and averaging is accomplished in relation to corresponding "large" period. It is to be noted that expressions for $\vec{V}$ and $\vec{v}$ in equations (8) and (9) depend both on right parts of the initial dynamics equations and on approximations taken in solution of fast motions equations. A wide scope of problems is associated with the influence of vibration on liquids, bulk solids and multiphase media in vibrating vessels. Of high interest appear to be the effects of sinking gas bubbles and floating denser particles , stability of heavy liquid layer floating over lighter liquid, generation of slow flowing streams (see books [2-5],paper [6] and collection [7]. Almost in all cases those effects can be sufficiently described by OS equations.

For one dimensional case the equation of vibrational hydraulics [3] will correspond to *Bernoulli equation* [3]

$$\frac{1}{2}\rho(U_1^2 - U_2^2) + \Delta P + \Delta P_v = 0, \tag{10}$$

where ΔP is a "usual" pressure difference, and is an additional, vibrational pressure difference.

Vibrational rheology, vibrational dynamic materials and composites.

Suppose $\varepsilon = E(t)+\psi_\varepsilon(\omega t, \sigma = \sum(t) + \psi_\sigma(\omega t)$, then the governing rheological equation $\sigma = f(\dot{\varepsilon}, \varepsilon)$ will be transformed in OS as $\sum = F(\dot{E}, E)$, where function F may be largely different from that of f[7]. Quite another dynamic effect involving transformation of solid body elasticity under the action of vibration we see in parametric mechanism of dynamic materials generation [8] (the effect of Indian Magic Rope, transformation of a string into a bar, increase in pipe rigidity under pulsed liquid flow and others (see below and [3, 7, 8]).

In celestial mechanics problems the results of pulsating spacing between the masses interacting by the law of gravitation can be interpreted with respect to slow motion in the relation either as increase of gravity constant or as emergence of additional force. This phenomenon was put into the basis of the invention of Gravilet by V.V.Beletsky and M.E.Giverts [2], where dragging force in a space ship is generated by cyclic variation of distance between the weights of dump-bells placed in the space ship.

3.2 Heat conduction and diffusion

As for the linear equations describing *heat conduction and* ***diffusion*** neither the pulsation of the coefficient nor the pulsation of the source will entail any change in the oscillatory strobodynamics equation at first approximation though such change is certain to be substantial when a non-linear summand is present. Significant changes will be also caused by introducing summand $\partial^2 T/\partial t^2$, when the equation becomes hyperbolic one.

3.3 Maxwell's electrodynamics equations

In their simplest case (flat wave) these equations can be reduced to a wave equation

$$\frac{\partial^2 u}{\partial t^2} = c^2 \frac{\partial^2 u}{\partial x^2} \tag{11}$$

for potential $u(x,t)$:

$$\frac{\partial u}{\partial t} = E, \quad \frac{\partial u}{\partial x} = B,$$

where $c = \sqrt{1/\mu\varepsilon}$ is velocity of light in a medium with dielectric permittivity ϵ and magnetic permeability, μ (in corresponding units), E is electric field intensity and B is magnetic induction. If c^2 varies in accordance with the law $c^2 = c_0^2(1 + \alpha \sin \omega t)$ the OS equation in comparison with (3) acquires an additional summand $\frac{1}{2}(n_0^2\alpha/\omega)^2 \partial^4 U/\partial x^4$ like it was observed in the string-bar case (see below).

3.4 Electromechanical systems

Speaking of such systems in particular electric machines one should say that mechanical processes to run much slower than electromagnetic ones. This circumstance permits to pass from the classical *Gorev-Park system* of equations to simpler equations of slow motions i.e. OS equations [9]. The same can be said about the theory describing *the effects of bodies steady levitation* observed in a quickly oscillating field. In addition as it follows from the earn show theorem, such effect is unlikely to occur in static condition [1, 3].

4 Some interdisciplinary problems

4.1 Vibrational displacement

By the effect of vibrational displacement we mean the emergence of the "directional on the average", as a rule - slow, change (particularly of motion) at the expense of the

undirected on the average (as a rule - fast, oscillatory) effects. Since much attention is attracted to the velocity of slow change of state (i.e. the velocity of vibrational displacement) it appears to be reasonable in finding this component to pass from the initial equations to those of OS. The problems associated with the theory of vibratory displacement are likely to appear apart from mechanics in other sciences such as chemistry, biology, biomechanics etc. A number of new problems in this field have been considered lately [2, 3, articles in 7, 12].

4.2 Synchronization of vibrations and rotations

In solution of these problems relating to various fields in science and technology a transition from initial rather complicated non-linear differential equations to OS equations, comprising only slowly variable motion phases of objects, is believed to simplify the task to a great extent [2, 3].

5 Some fundamental equations

By taking into account oscillatory action in differential equations, which describe some fundamental phenomena, we can detect considerable change of the system behavior - this is reflected in corresponding OS equations. Take for example the well-known *Lorenz's equation system* (see [13])

$$\begin{aligned} &\ddot{\xi} + (\eta - 1)\xi + \xi^3 = -\mu\dot{\xi}, \\ &\dot{\eta} = -\frac{\mu}{\sigma + 1}\left[b\eta - (2\sigma - b)\xi^2\right] + A\cos\omega t \end{aligned} \tag{12}$$

where μ, σ and b are positive parameters, A and ω are correspondingly the amplitude and the frequency of action. In this case we obtain the following OS equation for the slow component B of the variable ξ:

$$\ddot{B} + (\frac{1}{2}\frac{A^2}{\omega^4} - 1)B + B^3(1 + \frac{3}{2}\frac{A^2}{\omega^6}) = -\mu\dot{B} \tag{13}$$

hence, one can see that as $A > \sqrt{2}\omega^2$ the equilibrium position $B = 0$ becomes stable and no self-oscillations including chaotic ones will arise. The equation (13) is obtained after the simplest introduction of oscillating action according to (10) and only on condition of approximate solution of the fast motion equations, when $\psi_1 = AB\sin\omega t/\omega^5$, $\psi_2 = A\sin\omega t/\omega$ (Supposing $\xi = B(t) + \psi_1(\omega t)$, $\eta = \psi_2(\omega t)$). Other ways of introducing the disturbance and more accurate solution of the equations are certain to yield more complete results.

The other example is the classic *Lotka - Volterra system "prey-predator"* [13]. With periodic action this system takes the form:

$$\begin{aligned} &\dot{n}_1 = n_1(\varepsilon_1 - \gamma_1 n_2) + A\sin\omega t \\ &\dot{n}_2 = -n_2(\varepsilon_2 - \gamma_2 n_1) + B\sin(\omega t + \delta), \end{aligned} \tag{14}$$

where n_1 and n_2 denote animals population, substances concentration and so on and $\varepsilon_1, \varepsilon_2, \gamma_1, \gamma_2, A, B, \delta$ are positive constants. In the simplest approximation the solution of the fast motion equations $\dot{\psi}_1 = -A\sin\omega t$, $\dot{\psi}_2 = B\sin(\omega t + \delta)$ will yield the following OS equations:

$$\begin{aligned} &\dot{N}_1 = N_1(\varepsilon_1 - \gamma_1 N_2) - \gamma_1 a, \\ &\dot{N}_2 = -N_2(\varepsilon_2 - \gamma_2 N_1) + \gamma_2 a \end{aligned}$$

$$(a = AB\cos\delta/\omega^2) \tag{15}$$

These equations are distinguished from the classic ones by the presence of constant summands in their right hand parts. This tends to change the behavior of the phase trajectories of the system which becomes not conservative any more. Quantities N_1 and N_2, depending on parameter a values, either approach some constant values or depart from those; the latter case corresponds to the "extinction" of populations. There exists a remarkable variance of OS equations to initial ones in models of self-oscillatory chemical reactions (see [13]) as well as in Lancaster's war model. The behavior of corresponding systems is to be changed under the influence oscillatory action.

Wave equations are also subjected to such changes, the alterations being not only quantitative but qualitative too. If in the equation of string oscillation

$$m\frac{\partial^2 u}{\partial t^2} = T\frac{\partial^2 u}{\partial x^2} \tag{16}$$

The string tension changes according to the rule $T = T_0(1 + \alpha\sin\omega t)$ we obtain the following OS equation:

$$m\frac{\partial^2 U}{\partial t^2} = T_0\frac{\partial^2 U}{\partial x^2} + (EY)_v\frac{\partial^4 U}{\partial x^4} \tag{17}$$

where

$$(EY)_v = \frac{1}{2}(T_0\alpha/\omega)^2$$

is bending rigidity acquired by the string in its slow motion $U = \langle u\rangle$. To put it otherwise, the string appears to be transformed into a bar. Identical results can be obtained in solution of other problems such as the problem of Indian Magic Rope and the problem of pipe stability with some pulsating liquid flowing through it [2, 8] as well as the problems described by *Sinus - Gordon non-linear wave equations*. Specification of above mentioned results with accompanying reference list is given in [14].

6 Oscillators

Non-linear and parametrically excited oscillators possessing a single degree of freedom are widely used as models of many oscillatory processes. A great number of studies accomplished mainly by digital simulation technique have been devoted to investigation of "controlling" influence on oscillators.[1,13]. In this paper this task is treated by OS approach. *Mathieu's oscillator* is described by the equation:

$$m\ddot{x} + (c_0 + c_{\approx}\sin\omega t)x = 0 \tag{18}$$

where m, c_0 and $c_{\approx}$ are constants. When $\omega >> \lambda = \sqrt{c_0/m}$, OS equation has the form:

$$\ddot{x} + (c_0 + c_v)x = 0, \tag{19}$$

where $c_v = c_0^2/2\omega^2$. Hence, equilibrium position $x = 0$ unstable if $c_0 < 0$, $c_{\approx} = 0$ becomes stable for $X = 0$, if $c_v > -c_0$. This explains in particular the effect of stabilization a reversed pendulum with a vibrating suspension axis [2, 31, 5].

Fidlin's oscillator [6] is described by the following equation:

$$\ddot{x} + (\beta - a\omega\cos\omega t)\dot{x} + x = 0 \tag{20}$$

where $a \sim 0(1)$, $\beta \sim 0(1)$, $\omega >> 1$ Corresponding OS equation takes the form:

$$\ddot{X} + \beta\dot{X} + I_0^2(a)X = 0 \tag{21}$$

where $I_0(a)$ is modified Bessel's function. It is worthwhile to note that the strong oscillation of the damping coefficient in equation (20) leads to the essential change of the rigidity coefficient in equation (21). Double-frequency exitation in *Duffing oscillator* leads to the effect of conjugate resonances and bifurcations [3]. For the oscillator with a positional - *viscous resistance* $(a_0 + a_1x + ...)\dot{x}$ the OS equation describes the phenomena of *asynchronous excitation and asynchronous depression of self-excited oscillations* as results of resistance characteristics transformation. This case includes *Van-der-Pol's oscillator* as well [2].

At first sight *oscillation of an independent variable* t seems to be exotic one. Such oscillation implies transition from time t to a variable $\tau = t + \alpha \sin \omega t$, where $\alpha << t$. For a linear oscillator $\ddot{x} + \lambda^2 x = 0$ the OS equation in corresponding approximation looks like:

$$\frac{d^2X}{d\tau^2} + \frac{1}{2}(\alpha\omega)^2\frac{dX}{d\tau} + \lambda^2(1 + 2\alpha^2\lambda^2)X = 0 \tag{22}$$

i.e. time pulsation entails the appearance of dissipation!

It is to be noted that the employment of the pulsating independent variable - called as "true anomaly" is characteristic for a number of problems in celestial mechanics. As it was shown by V.S. Sorokin, the reverse transition to time t in the known Beletsky's equation, describing the travel of a satellite in relation to the mass center [16], transforms this equation into one devoid of the summand depending on $\dot{x}$. The corresponding OS equation will be also in line with the conservative system.

7 Conclusion

The above - cited examples taken from various sciences are believed to prove the expedience of defining dynamic systems as a separate interdisciplinary field of knowledge. This science may be called *oscillatory strobodynamics*. The problems of the OS allow to make use of a general mathematical approach and an identical interpretation of results which at first appear to be paradoxical.

Acknowledgements

The work is carried out with financial support of Russian Foundation of Basic Research, Grant 10-08-00201-a

References

[1] Fradkov A.L.Cybernetical physics. Principles and examples. St.Petersburg: Nauka, (In Russian), 2003.

[2] Blekhman I.I.Vibrational mechanics. Moskow: Physmatlit, 1994 (In Russian, English transl.: Vibrational Mechanics. World Scientific. Singapore at al. 2000, 509 p.)

[3] Edited by I. Blekhman Selected Topics in Vibrational Mechanics. Singapore at al.: World Scientific, 2004

[4] Lubimov D.V.,Lubimova T.P.,Cherepanov A.A. Dynamics of 2004 interfaces in vibrational fields. Moscow: Physmatgiz,. (In Russian), 2003

[5] Ganiev R.F.,Ukrainsky Ya.E. Non-linear wave mechanics and technology. Moskow: Regular and chaotic dynamics. (In Russian), 2008

[6] Fedotovsky V.S. Generalized conductance and oscillatory wave processes in heterogenous media. Transactions of the 4-th Russian International Conference on heat exchange. October 23-27, 2006

[7] Non-linear problems in the theory of oscillations and the theory of control. Vibrational mechanics.Collection. St.Petersburg: Nauka,(In Russian and English), 2009

[8] Blekhman I.I.On vibrational dynamic materials and composites. Doklady RAS, v. 414, No 5, (In Russian, English transl.: Doklady Physics, , v. 52, No 6, pp. 335–338), 2007

[9] Lurie K.A.An introduction to the Mathematical Theory of Dynamic Materials. Springer, 2007

[10] Skubov D. Yu.Khodjaev K.Sh. Non-linear electromechanics.. Moskow: Physmatlit. (In Russian), 2003

[11] Martynenko Yu.G.Motion of a solid body in electric and magnetic fields. Moskow: Nauka. (In Russian), 1988

[12] XI Internat.Conf. Stability and oscillations of non-linear control systems. Paper summaries. Moskow: Inst. of control problems. RAS, 2010

[13] Neymark Yu.I.,Landa P.S.Stohastic and chaotic oscillations. Moskow: Librocom. (In Russia), 2009

[14] Shishkina E.V., Blekhman I.I., Cartmell M.P., Gavrilov S.N.Application of the method of direct separation of motions to the parametric stabilization of an elastic wire. Nonlinear Dynamics, No 54, 2008

[15] Kapitsa P.L.A pendulum with a vibrating suspension. Achievements in physical sciences, , v. 44, issue 1. (In Russia), 1951

[16] Beletsky V.V.In: Current problems in theoretical and applied mechanics. Kiev: “Naukova dumka”, 1978

Iliya I. Blekhman, V.O., Bolshoy av., 61, Saint-Petersburg, 199178, Russia

On a vibroimpact system in which chaos is caused by the rare attractor packing

Ilyia I. Blekhman Kirill S. Ivanov
ivanoff.k.s@gmail.com

Abstract

A particle motion on the horizontal plane being transversal harmonic oscillated is considered. This problem is a constituent part of a more general problem which deals with a vibrational displacement of a particle on a harmonic vibrating rough surface. Analytical investigation shows that when the restitution coefficient is close to one there exist an enumerable set of stable in the small modes with the period multiple to the period of the plane oscillations. It is enough to make a numerical solution behavior look as chaotic because of error of calculations. Despite the state of chaos, a number of the process important technical characteristics has the certain value, practically not dependent on initial conditions.

1 Introduction

An important part of the problem dealing with vibrational displacement of a material particle along a vibrating surface is the problem of particle motion over a horizontal surface performing vertical harmonic vibrations. As shown by analytical investigations when coefficient of restitution approximates a unit there exists a great number of motions that are stable in the small and have a period that is a multiple in relation to that of the surface vibrations, the motions termed as “rare Attractors”. This is sufficient for the system behavior to be regarded in numerical simulation as chaotic one owing to calculation error.

In spite of previously mentioned chaotic state, a number of significant process engineering characteristics were found to possess certain values that were practically independent of initial conditions. One of such characteristics inherent in condition of longitudinal vibration component existence is the transportation velocity. An approximate expression for such velocity can be obtained analytically.

This paper deals with some peculiarities of such chaos type and contains the author’s view on propagation of this phenomenon in various non-linear systems.

2 Particle motion over a harmonically vertical vibrating horizontal plane. Periodic and chaotic regimes.

Let us considerthe motion of a particle bouncing over a horizontal plane that is vibrating vertically with amplitude A and frequency according to the law (Fig. 1):

$$\eta = A \sin \omega t \tag{1}$$

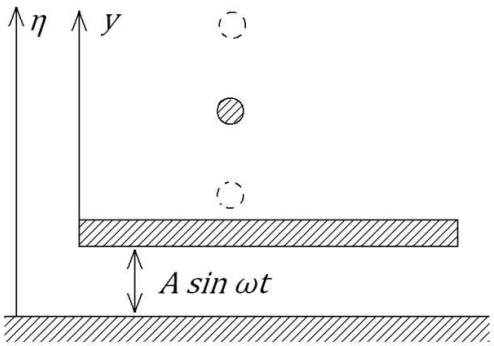

Figure 1: Principial model diagram

The problem of behavior of such a particle represents a partial case and is a component of a more common problem of particle motion along an inclined rough plane performing harmonic vibrations at some angle β (Fig.2).

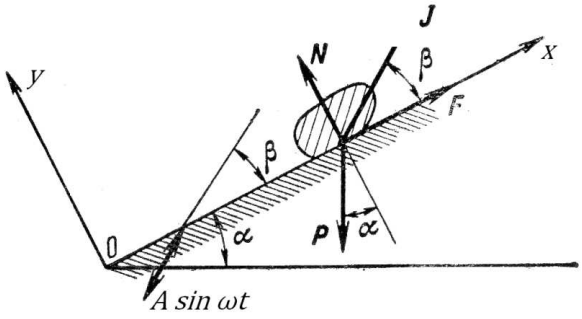

Figure 2: General model diagram

The latter problem is one of the basic ones in the theory of vibrational displacement processes having a multiplicity of practical applications [1,2].

In the problem under consideration the particle motion is defined by two non-dimensional parameters, namely the coefficient of overload w and the coefficient of restitution R. It was shown by analytical investigation that on condition of:

$$\pi p \frac{1-R}{1+r} < w_0 < \frac{\sqrt{\pi p^2 \left(1-R^2\right)\left(1+R^2\right)+4\left(1+R^2\right)^2}}{\left(1+R^2\right)}$$

$$(p = 1, 2, ...) \tag{2}$$

there exist some stable in the small (in Lyapunovs sense) periodic motions of a particle when the latter keeps to be positioned over a vibrating plane and is colliding with the same at a period $T = pT_0 = p\ 2\pi/\omega$, that is a multiple in relation to the plane vibration period. The domains of existence and stability for such modes are shown in Fig.3.

At $\omega < 1$ there always exists such a state stable in the small when the particle keeps being disposed on the vibrating plane. In Fig.3 such domains are shown as shaded. As it

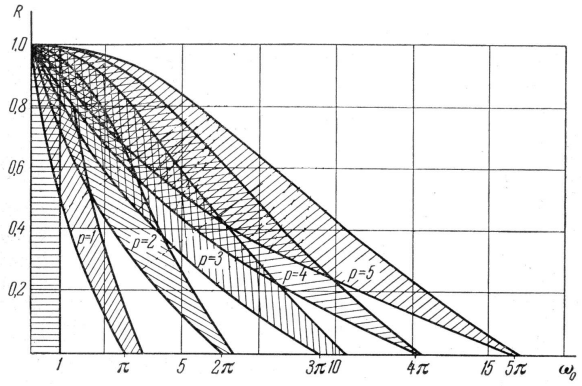

Figure 3: Existence and stability domains

is seen, with values relatively close to a one there exists a great (rather infinitely great) number of regimes to be considered while the domains of their existence and stability in the parameter space are either superimposed or critically adjacent. Such regimes stable in the small are believed to correspond to the notion of *rare attractors*. This notion was introduced by M.V. Zakrzevsky : a number of works accomplished by him and his collaborators [3] was devoted to the study of the rare attractor systems. It is natural that each of those regimes corresponds to a certain sufficiently small domain of attraction within the system phase space. It is easy to conclude that with computer simulation the situation described above is likely to be perceived as some chaotic behavior of a particle.

This can be explained in terms of several reasons. Firstly, the attraction domains in the phase space of mentioned above stable regimes are less extent than the integration step so that the particle can jump over from one attraction domain to the other one. Secondly, and this feature appears to be noticed for the first time, the degree of overlapping of stability domains in different regimes tends to intensify because of the finite precision of computing in numerical simulation . In this condition the system behaves in such a way as if its parameters were changing with every integration step. Such a seemingly negligible change happens to be sufficient when the simulation takes place in the domain of rare Attractors accumulation. It is to be noted that the same behavior was observed in the physical experiment.

In Figs. 4 to 6 phase diagrams of a particle behavior on a plane $\eta, \dot{\eta}$ corresponding to different values of parameters w and R are represented. The portions of the diagrams adjacent to the axes $\dot{\eta}$ represent a spasmodic variation in the particle velocity while it is falling on the plane $y = 0$.

Fig. 4 ($w = \pi, R = 0$) corresponds to a regime with period $T = T_0 = 2\pi/\omega$ that is $p = 1$. The initial point corresponds to the values $y_0 = 0.01, \dot{y}_0 = 0$.

One can observe that a stable regime is established rather quickly. With $w = 2, R = 0.95$ a chaotic behavior of the particle is revealed, the maximum height of bounce varying from one cycle to another within a sufficiently wide range (Fig. 5) reaching about 1.7 m. The chaotic state of bouncing gets intensified when $w = 3$ (Fig.6) with the maximum bounce height increasing almost to 10 m.

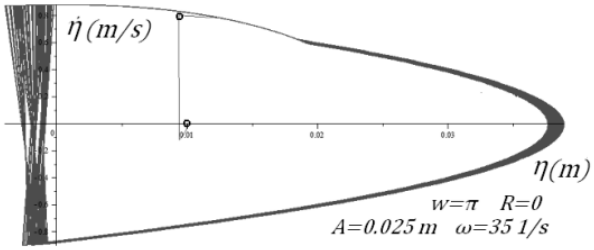

Figure 4: Phase-plane portrait

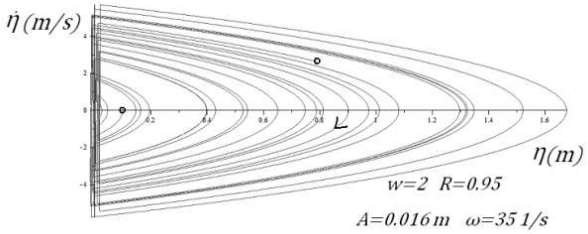

Figure 5: Phase-plane portrait

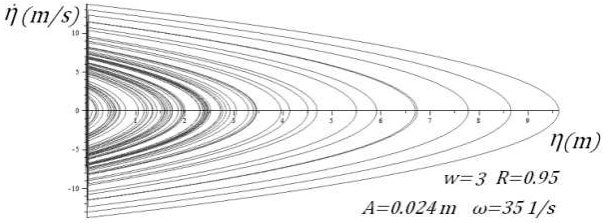

Figure 6: Phase-plane portrait

3 The character of the particle bounce over a plane. Comparison with liquid behavior.

The authors of this paper are aware of V.I. Arnolds study (though no pertinent reference have been found) where it was shown that with $R = 1$ there exists an enumerable set of phase space points corresponding to an infinitely great height of the particle bounce. In view of this finding great heights of particle bounce do not appear to be incredible. The same inference may be drawn after the following physical reasoning. If some particle drops on a plane during the time instant when the plane velocity is positive then the particle at $R \sim 1$ at each collision instant is imparted some velocity increment. Since during chaotic motion the conditions may arise when all or sufficiently often occurring collisions take place at above mentioned time instants, the velocity of the particle tends to be increased after the collision along with the increase in the bounce height. Of course, if one takes into account the resistance to motion such increase in velocity and bounce height is certain to be limited.

It is to be noted that similar phenomena, that is paradoxically high splashes, can

be observed on a free surface of liquid contained in a vertical vibrating vessel [5]. Such phenomenon was observed in our experiments too. At vibration frequency $\omega = 190\ \ 1/c$ and amplitude $A = 0.1\ \ cm$ ($w = 3.81$) the height of splashes exceeded 30 cm.

Both of the effects described took place with close vibration parameters ($w \approx 3 \div 4$).

4 3. Some other systems distinguished by the chaos under consideration.

However different the systems under study are from that of a liquid contained in a vibrating vessel , the latter also has a multiplicity of periodic oscillations of the surface that are stable in the small. Such modes are caused by usual and parametric resonances.

The same type of chaos origination can be found in the systems studied by M.V.Zakrzevsky and his collaborators [3] as well as in others.

One may infer that such type of chaos formation is spread much wider than it was thought.

5 On Lyapunov exponents

There is a striking peculiarity in the numerical definition of Lyapunov exponents applied to the systems in question. As the behavior of system was studied at values of the parameters lying within the steady in the small modes area, Lyapunov exponents should be negative on condition that deviations of initial conditions are enough small. However owing to errors of calculations in computer modeling the representing point in phase space will leave area of an attraction of one mode in any case that will lead to positive values of Lyapunov exponents as a result.

6 On a determinability of the vibrational displacement velocity

It is to be emphasized that in spite of chaotic in corresponding conditions behavior of a particle the practically useful integral characteristics of the motion possess quite definite values independent on the initial conditions. Average velocity of the particle (the velocity of vibrational displacement) is one of such characteristics.

In the problem corresponding to Fig.2 the following expression found by analytical approach may be used for assessment of such velocity:

$$V = \frac{\pi p'(w,R)\, g}{\omega}\left[\frac{1-R}{1+R}\cot\beta\cos\alpha - \frac{2-\lambda}{\lambda}\sin\alpha\right] \tag{3}$$

where

$$p'(w,R) = \begin{cases} \frac{1}{\pi}\sqrt{w^2-1}, & R = 0 \\ \frac{1}{\pi} w^{\frac{1+R}{1-R}}, & 0 < R < 1l \end{cases}$$

And λ is the coefficient of instantaneous impact friction.

A numerical solution confirmed applicability of this formula both for the periodic and a part of the chaotic modes.

7 Conclusion

By taking investigation of a relatively simple non-linear system as an example there was examined the emergence of its chaotic behavior caused by an appearance of a great number of stable in the small periodic regimes at the certain values of parameters (rare Attractors) that are stable in the small. Specific features of such kind of chaos have been described and a supposition on its comparatively wide existence in dynamic systems has been proposed.

Acknowledgements

The work is carried out with financial support of Russian Foundation of Basic Research, Grants 10-08-00201, 09-08-00620.

References

[1] Vibrational Displacement. - Moscow, Nauka, 1964. 410 p. (in Russian).

[2] Vibrational Mechanics. World Scientific Publishing Co. Pte. Ltd. Singapore, New Jersey, Hong Kong, 2000. - 509 p.

[3] Rare Attractors, Paradoxes of Dissipation and Asymmetry in the Problems of Vibrational Mechanics and Nonlinear Dynamics. In collection: Nonlinear Problems of the Oscillation Theory and Control Theory. Vibrational Mechanics// Edited by V.V. Beletsky, D.A. Indeitsev and A.L. Fradko. St. Petersburg: Nauka, 2009, pp. 304-323

[4] Nonlinear Oscillations and Waves in Dynamical Systems. Dordrecht-Boston-London: Kluwer Acad. 1996, 551 p. (Russian second issue: Moscow, "Librocom", 2010, 552 p.)

[5] On a Drops Formation Effect on a Surface of Liquid in a Vertically Vibrated Vessel// Acoustical Journal. 1957. Vol. 3, N. 3, pp. 262-273 (in Russian)

Iliya I. Blekhman and Ivanov K.S., V.O., Bolshoy av., 61, Saint-Petersburg, 199178, Russia

Planar flows in nanoscale regions

S. A. Chivilikhin I. Yu. Popov V. V. Gusarov
sergey.chivilikhin@gmail.com

Abstract

Last years, fluid flows in nano-sized domains are intensively studied [1] - [4] due to nontriviality of observed effects and practical importance of this part of hydrodynamics. At present, there are no general equations of nano-hydrodynamics. Usually, the molecular dynamics is used for computations. As for analytical approaches, the simplest one involves introducing the slip condition at the boundary [5] together with classical hydrodynamics equations. The small scale of nanochannels gives us the possibility to use, in some cases, the Stokes approximation for motion equations [6].

In this work we apply the planar Stokes model [7] with slip boundary conditions for describing nano-flows. We have developed a method of flow calculation, which is based on the expansion of pressure in a complete system of harmonic functions. Using the pressure distribution, we calculate the velocity field and stress on the boundary. This method can be used for description of various problems of nanofluidics: hydrodynamics of nanochannels, flows along superhydrophobic surfaces, etc.

1 Introduction

The equations of motion in the quasi-stationary Stokes approximation and the continuity equation in the region g have the form:

$$\partial_\beta P_{\alpha\beta} = 0, \quad \mathbf{x} \in g, \tag{1}$$

$$\partial_\beta V_\beta = 0, \quad \mathbf{x} \in g, \tag{2}$$

where $P_{\alpha\beta} = -P\delta_{\alpha\beta} + \mu(\partial_\alpha V_\beta + \partial_\beta V_\alpha)$ is the Newtonian stress tensor; V_α are the components of the velocity; P is the pressure; μ is the coefficient of the dynamic viscosity, wich is assumed to be constant, $\delta_{\alpha\beta}$ is the delta symbol of Kronecker. Summation over repeated indices is assumed.

We take in account four types of boundary parts: inlet, outlet, solid wall and free boundary. The total boundary γ is the union of these parts.

On the inlet we specify the velocity field

$$V_\alpha = V_\alpha^{in}, \quad \mathbf{x} \in \gamma^{in}. \tag{3}$$

On the outlet we use soft boundary conditions

$$\partial_n V_\alpha = 0, \quad \mathbf{x} \in \gamma^{out}, \tag{4}$$

where ∂_n is the derivative along the normal to the boundary.

On the solid wall we specify slip boundary conditions

$$L\partial_n V_\tau = V_\tau, V_n = 0, \quad \mathbf{x} \in \gamma^{wall}, \tag{5}$$

where V_τ and V_n are the tangent and normal components of liquid velocity on the wall, L is the slip length.

On the free boundary we assume the action of the capillary force

$$P_{\alpha\beta}n_\beta = -\sigma n_\alpha \partial_\beta n_\beta, \quad \mathbf{x} \in \gamma^{free}, \tag{6}$$

where σ is the coefficient of surface tension.

The law of free boundary evolution is determined from the condition of equality of normal velocity U of boundary and the normal component of liquid velocity at the boundary:

$$U = V_\beta n_\beta, \qquad \mathbf{x} \in \gamma^{free}, \tag{7}$$

The absence of the time derivative in the quasi-stationary motion equation (1) lets us specify the initial conditions only for the shape of the free boundary:

$$\gamma^{free}|_{t=0} = \gamma_0^{free}. \tag{8}$$

In this work we take in account two-dimensional problems only ($g \subset R^2$).

2 Calculation of the pressure and velocity with given force on the boundary

Let f_α be the force applied to the total boundary γ. Then we can write one boundary condition

$$P_{\alpha\beta}n_\beta = f_\alpha, \quad \mathbf{x} \in \gamma, \tag{9}$$

instead of boundary conditions (3-6). We need to remark that we really know the force f_α on the free boundary only. On other parts of the boundary we will calculate the force during the solution. Let χ_α and ψ be smooth fields in the region g related by

$$\partial_\alpha \chi_\beta + \partial_\beta \chi_\alpha = 2\psi\delta_{\alpha\beta}, \tag{10}$$

Multiplying the motion equation (1) by χ_α , integrating over g , and using (2), (9), (10), we obtain

$$\int P\psi dg = -0.5 \int f_\alpha \chi_\alpha d\gamma. \tag{11}$$

According to (10), ψ and χ_α are harmonic functions and

$$d(\chi_1 + i\chi_2) = (\psi + i\omega)dz. \tag{12}$$

where ω is a harmonic function conjugate to ψ. Let ψ_k be a complete set of harmonic functions in the region g. Using (12) we obtain the correspondent functions $\chi_{\alpha k}$.

The complete set of analytical functions w_k in the finite region g with simple connected boundary consists of functions $z^k, k = 0, 1, \ldots$. We obtain the complete set of harmonic functions ψ_k in the form $Re(w_k), Im(w_k)$. According to (1),(2) the pressure P is a harmonic function. We present it in the form

$$P = \sum_k p_k \psi_k. \tag{13}$$

Using the expressions (11), (13) we obtain the algebraic system for coefficients p_k:

$$\sum_k \left(\int \psi_k \psi_n dg \right) p_k = -0.5 \int f_\alpha \chi_{\alpha n} d\gamma, \quad n = 0, 1, ... \tag{14}$$

The stress tensor, expressed in terms of the Airy function φ,

$$P_{\alpha\beta} = \partial^2_{\alpha\beta}\varphi - \delta_{\alpha\beta}\partial^2_{\gamma\gamma}\varphi \tag{15}$$

satisfies the equation of motion (1) identically. The Airy function satisfies the biharmonical equation

$$\Delta^2 \varphi = 0, \quad \mathbf{x} \in g. \tag{16}$$

The boundary conditions (9) take the form

$$\partial_\tau \partial_\alpha \varphi = e_{\alpha\beta} f_\beta, \quad \mathbf{x} \in \gamma, \tag{17}$$

where ∂_τ is the derivative along the tangent to the boundary. Integrating (17) from a fixed point of the boundary to current one, we obtain

$$\partial_\alpha \varphi = e_{\alpha\beta} \int\limits_{\mathbf{x}_0}^{\mathbf{x}} f_\beta d\gamma, \quad \mathbf{x} \in \gamma. \tag{18}$$

Using (15) and the expression for the Newtonian stress tensor, we obtain

$$d(\partial_\alpha \varphi) = 2\mu dV_\alpha + d\Phi_\alpha, \quad d(\Phi_1 + i\Phi_2) = P + i\Omega, \tag{19}$$

where

$$\partial_\alpha \Phi_\beta + \partial_\beta \Phi_\alpha = 2P\delta_{\alpha\beta}, \tag{20}$$

$\Omega = \mu(\partial_2 V_1 - \partial_1 V_2)$ is the harmonic function conjugate to P. Comparing (20) with (10) and using (13), we get the expression for Φ_α:

$$\Phi_\alpha = \sum_k p_k \chi_{\alpha k}. \tag{21}$$

Therefore, we obtain the expression for velocity:

$$V_\alpha = \frac{1}{2\mu}(\partial_\alpha \varphi - \Phi_\alpha), \quad \mathbf{x} \in g. \tag{22}$$

On the boundary $\partial_\alpha \varphi$ was calculated above (18). To find φ (and, correspondently, the velocity V_α) in the region g, we solve the equation (16) with boundary conditions (18).

3 Calculation of the pressure and velocity with various boundary conditions

If the free boundary conditions are specified on the total boundary, then (22) gives us the solution of our problem. In a general case (22) is true too, but on the inlet, outlet and the wall the force f_α is unknown.

On the inlet we can calculate the force with the help of (3) and differentiating (22) along of boundary:

$$f_\alpha = -e_{\alpha\beta}(2\mu\partial_\tau V_\beta^{in} + \partial_\tau \Phi_\beta), \quad \mathbf{x} \in \gamma^{in}. \tag{23}$$

On the outlet we obtain the force using (4) by differentiating (22) along of boundary:

$$f_\alpha = -n_\alpha P - \tau_\alpha n_\beta \partial_\tau \Phi_\beta, \quad \mathbf{x} \in \gamma^{out}. \tag{24}$$

The slip boundary conditions (5) on the wall and (22) give us the force distribution

$$f_\alpha = -n_\alpha f_n + \tau_\alpha f_\tau, \quad \mathbf{x} \in \gamma^{wall}, \tag{25}$$

where $f_\tau = \frac{1+KL}{1+2KL} n_\beta \partial_\tau \Phi_\beta$, $f_n = \tau\partial_\tau(\Phi_\beta + \frac{L\tau_\beta f_\tau}{1+KL})$, K is the scalar curvature of the boundary.

Expressios (23 - 25) contain $P = \sum_k p_k \psi_k$ and $\Phi_\alpha = \sum_k p_k \chi_{\alpha k}$. By substituting these expression into (14) we obtain the system of algebraic equations conserning coefficients p_k. After solving this system we obtain the pressure (13) and velocity distributions (22).

Acknowledgements

The work is supported by state contract 16.740.11.0030 of the program "Scientific and Pedagogical staff of innovation Russia 2009 - 2013" and Russian Foundation for Basic Research (project N 11-08-00267-)

References

[1] Abramyan A.K., Bessonov N.M., Indeitsev D. A., Mirantsev L.V. Influence of the confining wall structure on the fluid flow in nanochannels //Mechanics of Solids, 2010, V. 45, No.3, pp. 379389

[2] Rivera J.L., Starr F.W. Rapid transport of water via carbon nanotube syringe// J. Phys. Chem. C, 2010, V.114, pp.37373742

[3] Murad S., Puri I.K. Anomalous flow behavior in closed and open thin walled nanochannels// Phys. Lett. A, 2010, V.374, pp. 4242-4246

[4] Song X., Chen J.K. A comparative study on poiseuille flow of simple fluids through cylindrical and slit- like nanochannels// Phys. Lett. A, 2010, V.374, pp. 4242-4246

[5] Ershova A.A., Popov I.Yu., Chivilikhin S.A., Gusarov V.V.Waveguide modes and adhesion conditions for flow in a nanochannel //2010, Doklady Physics, V.55, No.6, pp. 271 - 273

[6] Chivilikhin S.A., Popov I.Yu., Gusarov V.V. Dynamics of Nanotube Twisting in a Viscous Fluid // 2007, Doklady Physics, V.52, No.1, pp. 60 - 62

[7] Chivilikhin S.A. Plane capillary flow of a viscous fluid with multiply connected boundary in the Stokes approximation // 1992, Fluid Dynamics, V.27, No.1, pp. 88 - 92

[8] I.N.Vekua. New methods of solution of elliptic equations [in Russian]. Gostekhizdat. Moscow. 1948.

S.A.Chivilikhin and I.Yu.Popov St. - Petersburg State University of Information Technologies, Mechanics and Optics, Kronverkskiy, 49, Saint-Petersburg, 197101, Russia; V.V.Gusarov - Saint-Petersburg State Institute of Technology (Technical University), Moskovsky, 26, 190013, Saint-Petersburg, Russia

About the influence of automotive brake pad composition on frictional performance. Results of nano-scale modeling

A. I. Dmitriev W. Österle H. Kloß
dmitr@ispms.tsc.ru

Abstract

The main problem in manufacturing friction materials is still a lack of sufficient information about the processes occurring in the surface layers of contacting bodies. This is due to the complexity of the processes which are taking place during friction and wear and by interdependency of mechanisms at various scale levels. This also may partly explain the complexity of structure of the composite materials which are used as brake pads, because a wide range of requirements have to be satisfied for modern braking systems. How variations of material composition affect the frictional characteristics of the friction pair is still an area of intense research. The present study used a computational method of the discrete approach a method of movable cellular automata - to investigate the interaction of nano-scale features which are typical for the pad-disc-interface during automotive braking. The results can be useful for understanding the features of interaction of materials and control their performance properties.

1 Introduction

Since commercial brake pads usually are distinguished by very complicated formulations and the third body is formed by compaction of wear debris, its chemical composition usually is more complicated than the ones observed for the former applications [1, 2]. In fact, third bodies produced during braking contain chemical elements from all ingredients of the pad formulation in addition to iron oxide from the cast iron brake disc mixed on a nanoscopic scale with grain sizes between 10 and approximately 100 nm depending on the type of ingredient. This can be seen most clearly by sampling wear particles emitted during a braking simulation in a test rig into size classes <1000 nm and subsequent investigation in an analytical transmission electron microscope (TEM) [3]. The same nanostructure was observed at the surfaces of pads and discs, proving that tribofilms are formed on both sides by compaction of wear debris. The films are discontinuous and usually about 100 nm thick. This finding inspired us to simulate the sliding behaviour of single asperity contacts covered by such friction layers with a granular computer model choosing a cell size of 10 nm, according to the smallest detected grain size of the experimentally observed nanostructure. In a recent review paper [4] we described friction and wear mechanisms taking place at different length scales during dry friction in automotive braking. The present paper will recapitulate the essentials for the simulation of smooth sliding conditions at a constant friction level with the method of movable cellular automata. Furthermore, an extension of the model will be presented by regarding more complicated material combinations in respect to type and size of automata, thus resembling more the real nanostructures observed experimentally.

Table 5: Parameters of model materials

	Young modulus E, GPa	Poisson ratio ν	Elastic limit σ_{y1}, MPa	Yield strength σ_{y2}, MPa	Ultimate tensile strength σ_s, MPa	Strain at σ_{y2} ϵ_{y2}	Breaking strain ϵ_s
Ferritic steel	206	0.28	450	500	550	0.04	0.106
Pearlitic steel	206	0.28	520	800	920	0.04	0.106
Iron oxide	380	0.3	290	305	340	0.008	0.009
Graphite	20	0.3	15	35	45	0.05	0.15
Copper	125	0.35	350	390	430	0.03	0.11
Soft copper	120	0.35	175	185	215	0.03	0.11
SiC	150	0.35	3000	4325	5000	0.06	0.18

2 MCA setup description

Theoretical investigation was carried out on the basis of modeling by the method of movable cellular automata (MCA). This choice was determined by the features of the MCA method to simulate such complicated processes as: mass mixing, damage generation and accumulation and so on. The formalism of the MCA method has already been described in [5]. The scheme of chosen two-dimensional setup is depicted in Fig. 1. It simulates a primary contact site according to Eriksson et al. [6], which is realized on the scale of the order of 1 micron. From pad site is a steel fibre as supporting substrate material. The supporting material on the disc side is pearlitic steel which is the matrix of cast iron. The free surfaces of both contacting bodies (first bodies) were covered with an oxide film consisting of nanoparticles of iron oxide and inclusions of solid lubricant. All previous simulations were based on the assumption that the solid lubricant had properties similar to graphite. Than we check the impact of substitution of graphite inclusions by soft nanoparticles of copper. All parameters of model materials are summarized in Table 5.

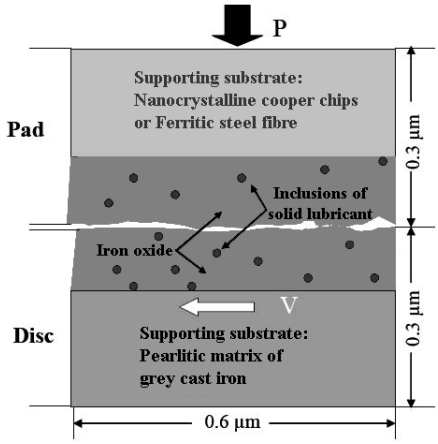

Figure 1: Schematic presentation of the modelled pad-disc interface.

The following boundary conditions for modelling were used. A constant sliding velocity (V) equal to 10 m/s was applied on all particles of the bottom layer of the disc. At the same time their position in vertical direction was fixed. A constant normal force corresponding to the contact pressures in the range between P= 15 MPa and P= 50 MPa for different calculations was acted upon all the elements of the upper layer of pad. For both types of loading a linear procedure of value increasing was used with the following scheme. Initially the surfaces of pad and disc were separated. Then the loading with increasing velocity was applied on the particles of the bottom layer of the disc. Normal pressure was applied on the

pad after all particles of the disc (not only layer under loading) reach the maximum value of sliding velocity. Periodic boundary conditions were applied along the sliding direction. So, the number of particles was constant in the simulation, only redistribution of particles in the contact zone was studied. A surface profile with roughness on the nanometer scale was set deliberately prior to simulation. As shown previously, this setting exerts no major impact on the results of simulation [4, 5]. The model calculates position and binding state of each automaton (particle) as well as resulting tangential forces or Coefficients of Friction (CoF) at the micro-contact for each time step.

3 Pressure dependency of a basic model structure

The main results of previous studies can be summarized as follows [4]: Neither metal-on-metal contacts nor oxide-on-oxide contacts provide stable friction conditions and a coefficient of friction (COF) around 0.4 which is desired for braking. A certain amount of soft inclusions within a rather soft but brittle oxide, like magnetite, is essential for achieving the desired properties. A prerequisite for smooth sliding behaviour is that a mechanically mixed granular layer (MML) is formed at the interface between the two first bodies. It has been shown that a volume fraction of at least 10 vol. % of soft nanoparticles (graphite in this case) is needed to form a MML irrespective of the applied pressure. Increasing the volume fraction of soft inclusions leads to a decrease of the COF. Since for braking we need smooth sliding, but a COF as high as possible, the fraction of soft particles should not be increased much beyond 10 vol %. A value of 13 vol % has proved to provide an optimum for both, smooth sliding and acceptable friction level. Although it would be most desirable for braking to have smooth sliding conditions and a COF irrespective of the applied pressure, a certain impact of pressure on structure formation and COF is unavoidable. This is demonstrated by Fig. 2 which shows the structures formed during simulation while applying different amounts of normal pressure. It can be seen clearly in Fig. 2 that, irrespective of applied pressure, there is always a zone of unlinked particles at the interface between the two third body layers (orange and green). This zone of unlinked particles originating from both third body films is the MML already mentioned at the beginning of this section. It is quite clear that the thickness of the MML depends on the applied pressure. This dependency is shown quantitatively in Fig. 3. The lowest pressure applicable in the model is 17.5 MPa for the structure with 13 % graphite and 7.5 MPa for a structure with 17.5 % graphite [4]. This is a quite large value compared to the nominal pressure in the range of 1-4 MPa which usually is applied during braking. We must keep in mind that we are considering micron-sized asperity contacts in the model. Therefore a factor of 10 compared to nominal pressure, which is related to the whole pad area, is reasonable. Furthermore, it should be mentioned that a constant sliding velocity of 10 m/s was maintained during modelling and that the time step of modelling of such nanostructures is of the order of 10^{-13} s, whereas the total time of one simulation was approximately 5×10^{-7} s.

The impact of pressure on MML-thickness does also affect COF-values which are calculated during modelling for each time step. This is shown in Fig. 4. The decrease of the COF-value with increasing pressure can be attributed to the increasing thickness of a quasi-fluid granular layer [7], which provides velocity accommodation between the fixed pad and rotating disc.

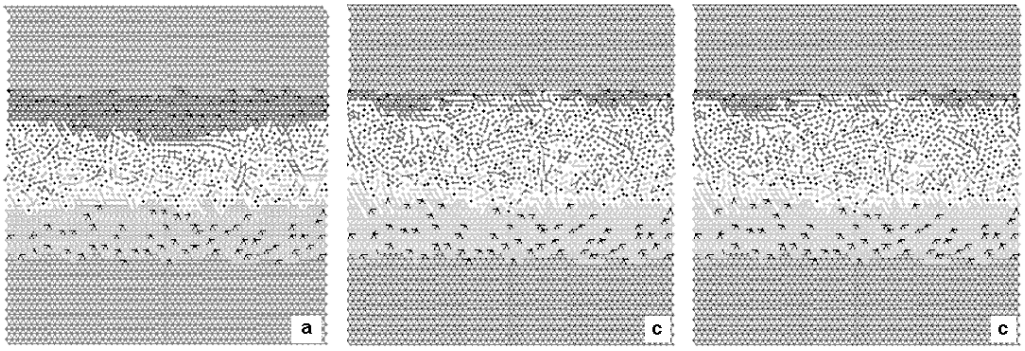

Figure 2: Pressure dependency of the basic model structure after sliding simulations. The value of normal pressure: a) 17.5MPa; b) 26.3MPa; c) 30.0MPa.

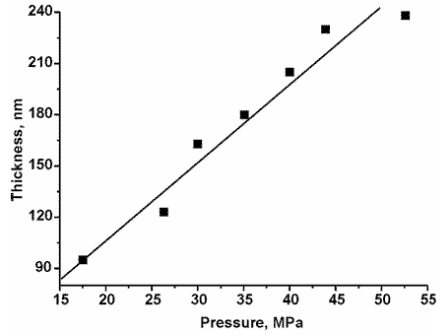

Figure 3: MML-thickness of basic model structure as function of pressure

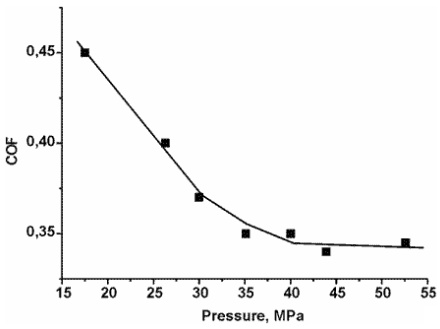

Figure 4: COF of basic model structure as function of pressure

4 Effect of additional soft particles of larger size

Larger particles were defined as clusters of the basic nanoparticles with linked states to their neighbours. Soft copper as defined in [5] was selected as soft ingredient, because such species was observed experimentally in the third body of automotive brakes. Complete substitution of graphite nanoparticles with the copper clusters did not yield stable sliding conditions, although breaking of links within the clusters and the release of single copper nanoparticles at the interface occurred during the simulation. But, since the soft particles were not distributed homogeneously in the third body, the formation of a mixed layer together with unlinked oxide particles did not take place.

On the other hand, if only half of the graphite particles of the basic structure were substituded by the copper clusters, a MML was formed and stable sliding conditions were achieved. This is shown in Fig. 5a and 5b, respectively. The copper clusters, still visible within the lower unaffected third body layer, are shown in magenta, and it is obvious that a MML has formed in which oxide, graphite and copper nanoparticles are distributed homogeneously. The corresponding COF-evolution during the simulation is shown by the black band and green curve in Fig. 5b, displaying momentary and averaged COF-values, respectively. A completely different behaviour was obtained with third body layers containing only 5 % graphite nanoinclusions without additional copper clusters. In this case no MML was formed (Fig. 6a) and COF-fluctuations between successive time steps remained high (Fig. 6b).

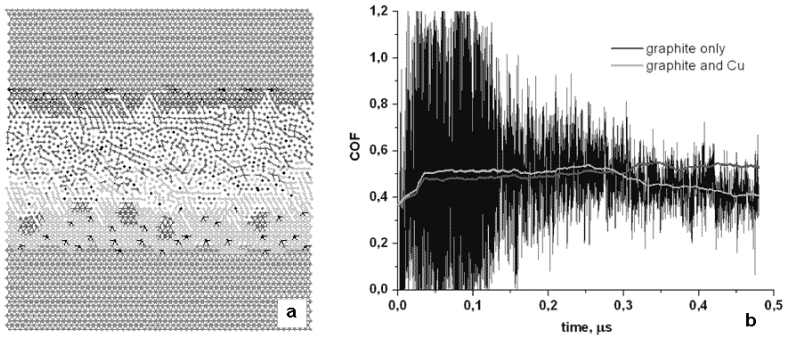

Figure 5: a) Structure formation during sliding simulation for third body layers with 5.5 % graphite and 7.5 % coarse copper particles (P=30 MPa); b – Corresponding COF-evolution.

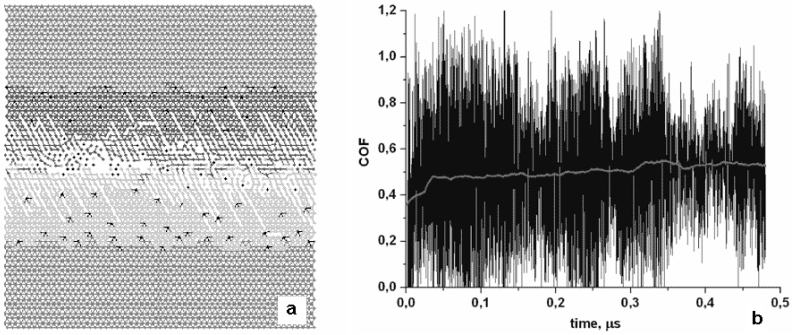

Figure 6: a) Structure formation during sliding simulation for third body layers with 5.5 % graphite only (P=30 MPa); b – Corresponding COF-evolution.

5 Effect of additional hard particles of larger size

The next step towards a more complicated nanostructure, albeit quite realistic with respect to experimentally observations, is to introduce a certain amount of hard particles into the basic model structure. We selected SiC as hard particles because the stress-strain behaviour of this material is well known from nanoindentation measurements not only at ambient but also at elevated temperatures [8]. Although SiC clusters were built in the same way as the copper clusters of the previous section, they behaved completely different during sliding simulation, as shown in Fig. 7. Because of the high mechanical strength of SiC, the bonds between adjacent nanoparticles within a SiC cluster (magenta colour) are not broken, while the oxide matrix, weakend by the graphite nanoparticles, forms the same granular layer as without SiC addition. Since a well developed MML with embedded SiC clusters was formed, smooth sliding with reduced COF fluctuations between adjacent time steps can be expected. This is shown in Fig. 8, where the scatter band of instantaneous COF-values corresponds to the structure with 4.8 % SiC. Similar results were obtained with 10 % SiC clusters. The coloured curves show average COF-values for the different model structures. A slight increase of the stationary COF-level while adding SiC clusters to the basic structure is revealed, but no significant difference between 4.8 and 10 % SiC is observed. Further simulations based on mechanical properties of SiC at elevated temperatures also did not change the results significantly (not shown here). This is because SiC is a hard material compared to magnetite even at 800°C. Fig. 9 provides an overview on the impacts of pressure and nanostructure on steady-state COF-values as

determined by our model. Obviously, the pressure dependency of COF is not changed by adding hard particles, provided that these particles are small enough to be incorporated in the MML which forms during sliding simulation. Nevertheless the COF-level is increased over the whole range of applied pressures.

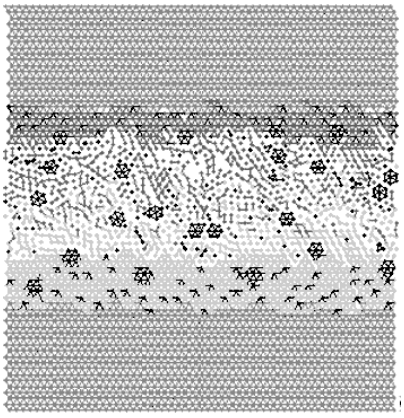

Figure 7: Structure formation during sliding simulation for third body layers with 13 % graphite and additional coarse SiC particles (p = 35 MPa)

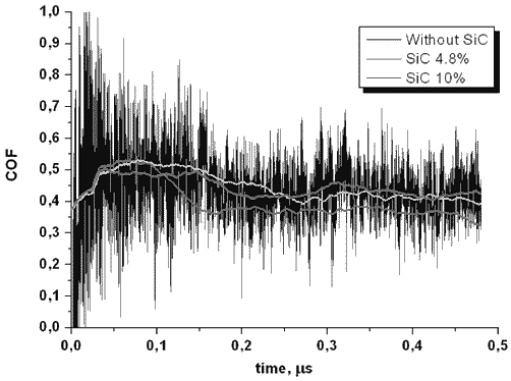

Figure 8: COF-evolution of third body layers with 13 % graphite and additional coarse SiC particles (p = 35 MPa)

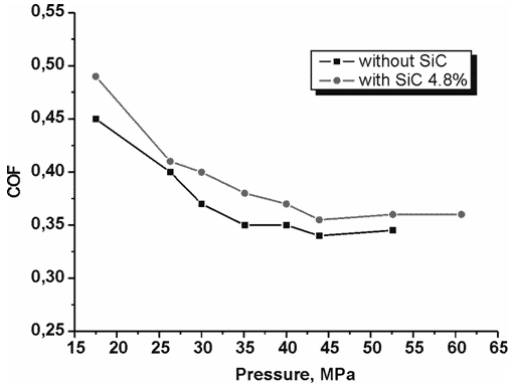

Figure 9: Impact of SiC addition to pressure dependency of COF for friction layers with 13 % graphite

6 Conclusion

Owing to modelling, the role of solid lubricant inclusions in metal oxide based surface films can be assessed much better now. In particular, it has been shown that a homogeneous distribution of at least 10 vol % of soft nanoparticles is sufficient to provide smooth sliding conditions. Inhomogeneous distribution of the same amount of particles in the form of clusters would not be sufficient to initiate smooth sliding, but since the clusters are broken into their constituents easily, the number of effective nanoparticles will increase during tribological stressing, and, if the volume fraction is high enough, a solid lubricant film may form at the surface. Anyway, in the case of low volume fractions of the order of 10 %, a combination of single nanoparticles and clusters shows the same smoothing effect

as a homogeneous distribution of the same volume fraction of single nanoinclusions. Thus we can conclude that as long as a certain amount of about 5 % of soft nanoinclusions is available, the size of additional solid lubricant additions is not relevant, but only its volume fraction. The additional solid lubricant constituent will be crushed down to nanometric size and mixed with released oxide particles within the MML forming at the interface of the tribological couple. Thus one of the features which determine the COF of a micro-contact is the volume fraction of the soft ingredient in its third body layer. In respect to braking this finding is quite important because both types of solid lubricant inclusions i.e. graphite nanoparticles of 10 nm size and copper nanoparticles of 100 nm size were observed experimentally. Whereas soft constituents from first bodies will be transformed to nanoparticles easily, the same can not be expected for hard particles. In fact, this was revealed by the model as well. Although bonds between automata of the hard material forming clusters of hard particles are not broken, the bonds between elements at the cluster surface and adjacent third body matrix as well as within the third body itself are broken during sliding simulation, at least within a narrow zone at the interface. Thus a granular layer providing velocity accommodation can form, provided that the diameter of hard particle clusters is not larger as the MML-thickness. This scenario, revealed by modelling, correlates with experimental observations at third body layers of brakes which showed hard particles of various sizes.

Acknowledgements

Financial support for this work was obtained by German Research Foundation contract No.: OS 77/18-1 and Russian Science Support Foundation, program of the specialized branches of RAS, project No. 13.13.3 and program No. 127 of SB RAS with exterior organization.

References

[1] Rigney, D.A., Hammerberg, F.E.: Unlubricated sliding behaviour of metals. MRS Bull. 32-36 (1998)

[2] Singer, I.L.: How third body processes affect friction and wear. MRS Bull. 37-40 (June 1998)

[3] Österle, W., Bresch, H., Dörfel, I., Fink, C., Giese, A., Prietzel, C., Seeger, S., Walter, J.: Examination of airborne brake dust. In: Proc. 6th European Conf. on Braking, JEF 2010, Lille, France, 24.-25.11. 2010, GRRT 20 rue Elisée Reclus P.P.317 59666 Villeneuve dAscq CEDEX-France (ed.), pp. 55-60

[4] Dmitriev, A.I., Österle, W.: Modeling of Brake Pad-Disc Interface with Emphasis to Dynamics and Deformation of Structures. Tribol.Int. 43 719-727 (2010)

[5] Österle, W., Prietzel, C., Kloß, H., Dmitriev, A.I.: On the role of copper in brake friction materials. Tribol.Int. 43, 2317-2326 (2010)

[6] Eriksson, M., Bergmann, F., Jacobson, S.: On the nature of tribological contact in automotive brakes. Wear 252, 26-36 (2002)

[7] Popov, V.L., Psakhie, S.G., Dmitriev, A.I., Shilko, E.: Quasi-fluid nano-layers at the interface between rubbing bodies: Simulations by MCA. Wear 254, 901-906 (2003)

[8] Milman, Y.V., Gridneva, I.V., Golubenko, A.A.: Construction of stress-strain curves for brittle materials by indentation in a wide temperature range. Science of Sintering 39, 67-75 (2007)

Andrey I. Dmitriev, Akademichesky 2/4, 634021, Tomsk, Russia
Werner Österle, Unter den Eichen 87, Berlin D-12200, Germany
Heinz Kloß, Unter den Eichen 87, Berlin D-12200, Germany

The features of structure transformation caused by nano-burnishing process

A. I. Dmitriev A. Yu. Nikonov V. P. Kuznetsov
dmitr@ispms.tsc.ru

Abstract

In the paper the method of molecular dynamics is used to investigate the features of structure transformation, which are taking place during the process of surface treatment. The force field of a cylindrical shape was used to imitate the motion with constant velocity of hard indenter. The following parameters of tasks were varied: the radius of indenter, initial immersion depths, surface roughness, number of passes and the initial position of the indenter. Calculations were performed for the pure crystallites of copper and iron. According to the modeling the treatment of the surface layer can leads to formation of numerous structural defects, which can provide effect of nano-fragmentation of material near the surface. A comparison of surface topography before and after treatment was analyzed also. Results of our study are in good agreement with experimental data.

1 Introduction

Performance properties of various assemblies and machine components are determined by the qualitative characteristics of the surface layer, obtained during the finishing processing. One of the modern efficient techniques of finishing processing surface of parts in mechanical engineering is a method of surface plastic deformation, which is called burnishing. Established that processing of surfaces by the burnishing can improve the wear resistance of parts by 20-40%, fatigue resistance by 30-70%, resistance to contact fatigue by 20-40% [1]. Changing the properties burnished surfaces is connected with the change in the structure of a thin surface layer owing to plastic deformation. Under the influence of the indenter of burnishing tool a change of orientation and shape of grains, which are crushed, flattened and stretched, forming the texture of the surface layer is occur [2].

Investigation of the structural changes occurring in the surface layer of material directly in the process of burnishing, it is extremely difficult. In this regard, methods for the numerical simulation can be an important complement to experimental studies. However, models based on the methods of continuum mechanics do not allow us to completely reveal the mechanisms of structural rearrangements in the surface layer of the material. Therefore, the purpose of this research was to study the origin and development of structural defects in the modeling of nano-burnishing process by molecular dynamics method [3, 4].

2 The object under simulation

As a model material for studying features of the process nano-burnishing was chosen a copper crystal. Selecting an object of investigation is caused by available expertise of

simulation of such material and using previously verified the interatomic potential constructed within the embedded-atom method [4, 5]. This potential describes with a high degree of accuracy the elastic and surface properties, and energy parameters of the defects of the modeled system. The equations of motion were integrated with time step $\Delta t = 0,001$ ps. The calculations were performed on a multiprocessor cluster Skif Cyberia using a software package LAMMPS [6]. The total number of atoms exceeds 1.5 million. The simulated crystal was oriented in such a way that the crystallographic directions [100] [010] and [001] fcc lattice match the X, Y and Z. Dimensions of the model sample in the direction of the coordinate axes were equal to $40.13 \times 24.95 \times 16.63$ nm, respectively.

Schematic representation of the model sample is shown in Figure 1. At the initial stage in the simulated crystallite the roughness of the surface layer with a maximum depth of 2.5 nm is explicitly specified. The initial roughness was created by the removal of surface-layer atoms that situated within the sphere of radius, which ranged from 0 to 2.5 nm. Center of the sphere was located at the level of initial surface layer, and its position in the plane XoZ determined using random numbers. In the Z direction were simulated periodic boundary conditions, repetitive simulated fragment and, thus, allowing to simulate the length of the sample in a given direction. The rest of the surfaces (along the X and Y) were simulated as free. The lower layer of atoms (dark bottom layer in Figure 1) was fixed, simulating the substrate. Thickness of the substrate was 0.73 nm. Over a layer of substrate was set a special "damping" layer of atoms, where the procedure to reduce the kinetic energy accumulated due to dynamic loading was used. Using the layer with the properties removing of heat simulates the length of the model sample in depth of the material in the direction of the axis Y. The thickness of the "damping" layer was 1.45 nm. His kinetic temperature - the temperature obtained from the equality of thermal and kinetic energy, was maintained in the range from 125K to 135K.

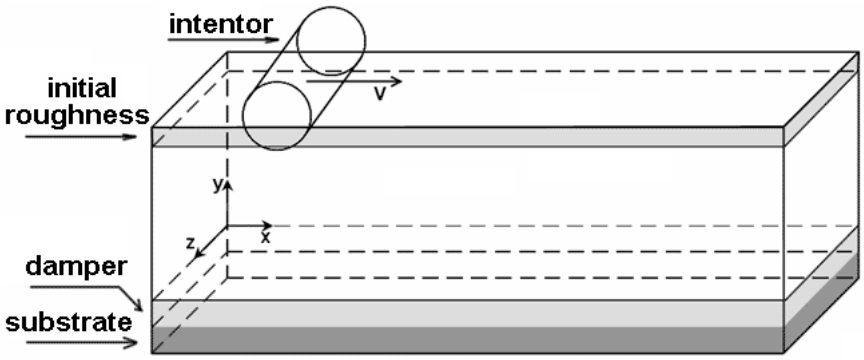

Figure 1: Schematic presentation of the simulated sample.

Process of burnishing was performed using an indenter, whose action has been realized through the force field in the shape of the cylinder with certain radius and the axis along the axis Z. Forces acted on the atoms that situated into this area in the direction of the axis of the cylinder. The direction and magnitude of the force is described by $F(r) = -K(r-R)^2$ where K – constant, r – distance from the center of the cylinder to the atom, and R – radius of the cylinder, while at r > R $F(r) = 0$. The process of burnishing the model material was carried out using two indenters with radii differ by 4 times: 4 nm and 16 nm.

3 Burnishing by the indenter with a radius of 4 nm

The simulation results showed that the process nano-burnishing with a radius of cylindrical indenter 4 nm on a small spatial interval resembles the process of cutting or scratching. When the horizontal movement of the indenter in front of it the bulge of the atoms of the upper layer formed. As it moves, the height of the bulge is growing. This is clearly seen in Fig. 2 and Fig. 3, which show the topography at different times of a single central layer of atoms arranged in parallel planes XoY and the structure of the simulated crystallite with at time t = 2 ns. Arrows indicate the position of the axis of the cylindrical indenter at a given time. If we compare the surface profile before and after the passage of the indenter (for example, in Fig. 2 profiles at t = 0 and t = 2 ns), we can see that the characteristic size of the roughness of the surface layer decrease markedly. The difference in the scale reaches the same order as that for data sizes of the simulated pattern may be interpreted as an imitation of burnishing. Indeed, after the passage of the indenter the surface roughness does not disappear completely, but it is burnished. Features of the indenter (its small size or large radius of curvature) will lead to what generated in the course of the movement bulge of the atoms of the surface layer should further increase the resistance force to the movement of indenter. We should expect that at a certain magnitude of the force of resistance to tangential movement the indenter starts to move in the Y direction over the surface of the crystallite, thereby creating an induced periodic roughness due to the features of the process. Such behavior can be compared with the results nano-burnishing within framework of the dynamic instability of the process.

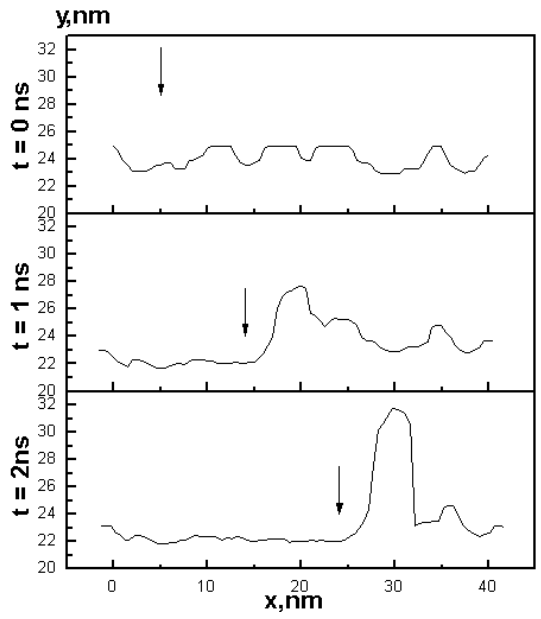

Figure 2: The surface profile of model crystal at different times. The arrow shows the position of the indenter. At time t = 0 the indenter is over the surface of the crystallite.

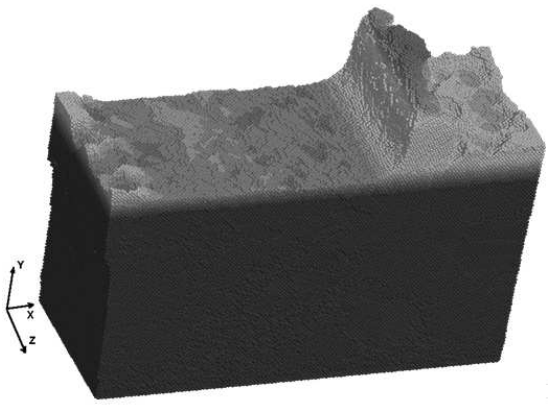

Figure 3: The structure of the model crystal at time t = 2 ns. Indenter radius r = 4 nm.

To analyze the features of structural transformations in the process nano-burnishing algorithm of the search of the local structural changes was used, which allows you to identify the occurrence of defects such as dislocations and stacking faults in the fcc lattice. Description of the algorithm is given in [7]. The results of research showed that in the bulk

of the sample at modeling process of burnishing numerous structural defects are appearing. There are dislocation, walls of dislocations and stacking faults. During the movement of the indenter their numbers are growing, and they extend from the surface into the bulk material. Thus, as a result of plastic deformation formed a modified surface layer with properties different from properties of the material in bulk. Formation of numerous defects in the surface layer also means the possibility of surface nanofragmentation and forming nanograin structure.

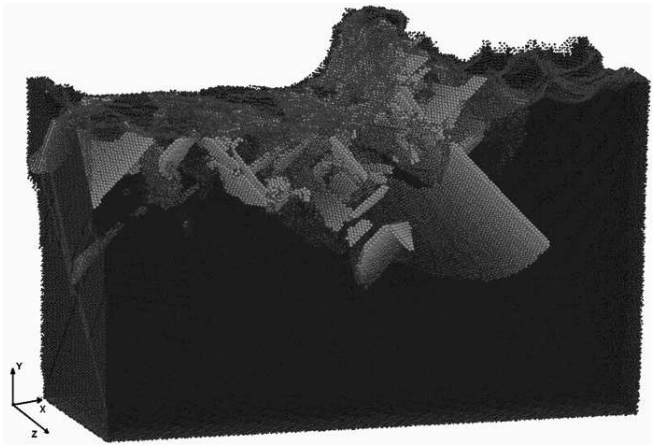

Figure 4: 3D image of the local structural changes in the simulated crystallite at time t = 1.8 ps.

Fig. 4 shows the simulated fragment at the time when the structure of surface defects was formed. Centers of the atoms with a local topology of the structural bonds of the fcc lattice, marked with small spheres (defect-free areas). Centers of the atoms with a local topology of the structural links is different from the fcc lattice are marked by large spheres. For better visualization centers of surface atoms are marked by small dots.

4 Burnishing by the indenter with a radius of 16nm

Since the size of the indenter with a radius of 16 nm was comparable to the size of the modeled fragment, the loading procedure to simulate the nano-burnishing process was differed from the previous task. Thus, the initial position of the center of the indenter was set outside of the modeled fragment. Then, as in the first case, the loading was divided in two stages: indentation phase and horizontal motion of the indenter. Initially indenter was pressed into a depth of 3 nm, comparable to the maximum surface roughness. As a result of interaction with force field of indenter atoms start pressed out from the surface. After reaching a given depth the procedure of so-called relaxation of the sample began. At this stage during the time interval of 5 ps no additional external loading was applied on the modeled specimen, indenter was unmovable and the system reaches the equilibrium state. In the second stage of loading the motion of indenter alone the direction of X-axis (Fig. 5) with a constant velocity 10 m/s was simulated. During the complete calculation the indenter moves along the X axis on the distance of 56 nm.

According to the results of calculations in case of the indenter with radius of 16nm behavior of the system are more close to the technological process of nano-burnishing. It is because of smaller indenter curvature does not promote the formation of the bulge from surface atoms in front of the indenter (Fig. 7). There are deformation and indentation of

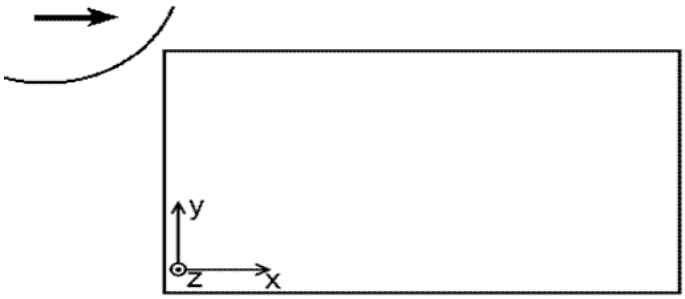

Figure 5: Schematic presentation of nano-burnishing. Indenter radius is 16 nm.

individual roughs of the surface into bulk of the material. That gives rise to both plastic and a large part of the elastic components of deformation of the surface layer. In the central part of the modeled fragment burnishing of the initial roughness of the surface within the same order of magnitude (from 2 nm to 0.5 nm) is taking place. However, a significant part of stored elastic strain due to the influence of the indenter with small curvature, leads to the fact that after the loading (since the passage of the indenter), the level of the surface increased by an average of 0.5 nm up to a value of y = 22.5 nm (Fig. 6).

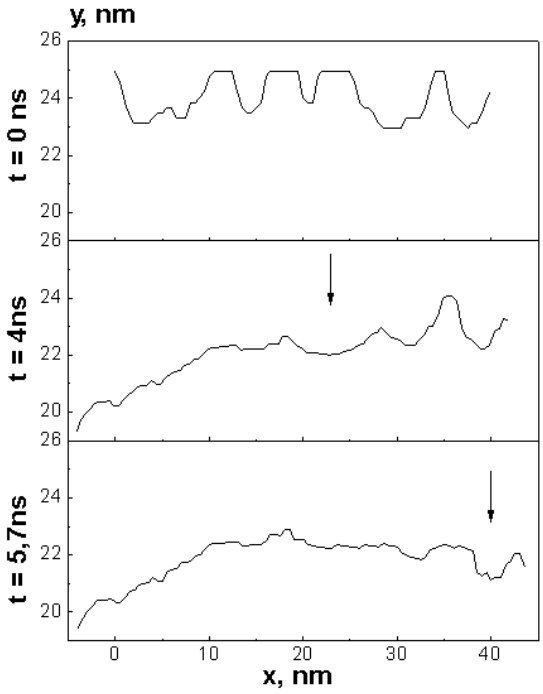

Figure 6: The surface profile of model crystal at different times. The arrow shows the position of the indenter. At time t = 0 indentor is left and above the surface of the crystallite

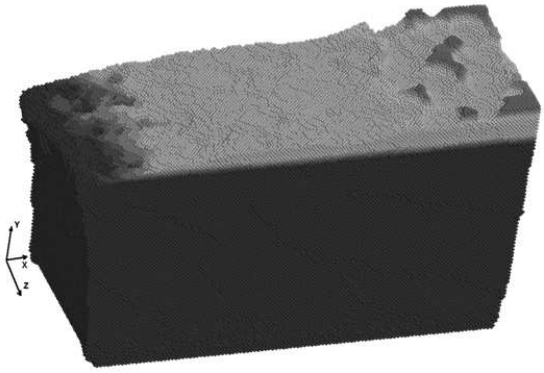

Figure 7: The structure of the model crystal at time t = 4 ns. Indenter radius r = 16 nm

Structure analysis of the modeled fragment showed that much larger number of different structural defects appears in the bulk of the sample in case of the indenter with a radius of 16 nm. This difference is the result of greater contact area and greater deformation. During the movement of the indenter number of structural defects is also growing,

and they extend from the surface into the bulk of the material. Thus the result of plastic deformation is the formation of a modified surface layer, which properties are differ from properties of the material in bulk. Analyzing the cellular structure formed by many intersecting planes of stacking faults can also talk about possible nano-fragmentation and grain structure formation in the surface layer of the modeled fragment. Fig. 8. depicts the simulated fragment at a time, which corresponds to a moment of structural defects formation near to surface area. Centers of the atoms with a local topology of the structural links of the fcc lattice, marked with small spheres (defect-free areas). Centers of the atoms with a local topology of the structural links is different from the fcc lattice are marked by large spheres. For better visualization centers of surface atoms are marked by small dots.

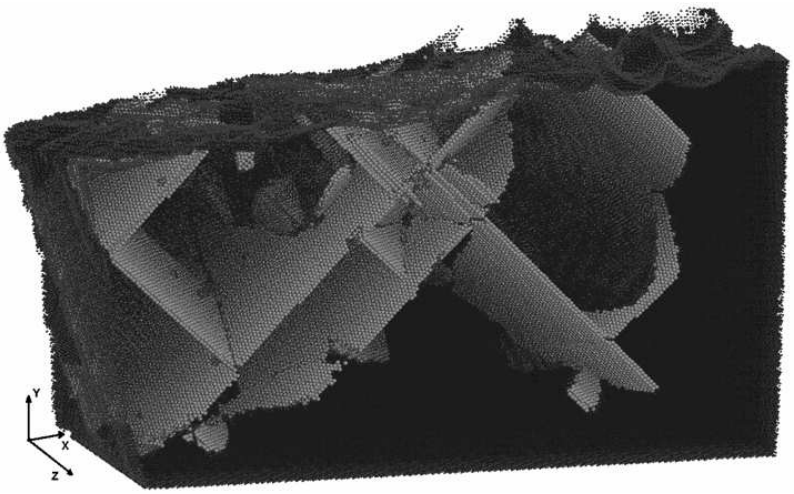

Figure 8: 3D image of the local structural changes in the simulated crystallite at time t = 3.5 ps.

In conclusion, we note that the results of simulations agree well with experimental studies, obtained using scanning electron microscope Tescan Mira 3 LMU [8]. Fig. 9 shows the structure of the surface layer of steel 20×13 in the initial state and subjected to burnishing procedure by diamond spherical indenter with a radius of sharpening R = 4 mm with a force smoothing P = 230 N, feed S = 0,08 mm/rev, speed burnishing V = 100 m/min. It was established that the nano-burnishing treatment changes the structure of a thin surface layer, namely, as a result of plastic deformation the formation of fine-grained structure, which increases the microhardness, elastic limit and yield strength of the surface layer [1] was observed.

Acknowledgements

Financial support for this work was obtained by the program of the specialized branches of RAS, project No. 13.13.3 and program No. 127 of SB RAS with exterior organization.

References

[1] Odintsov V.G. Final processing of details and diamond by burnishing vibroburnishing. – M: Mashinostroenie, 1981. 160 p.

[2] Pshibylsky V. Technology of surface plastic processing. – M.: Metallurgy, 1991. 478 p.

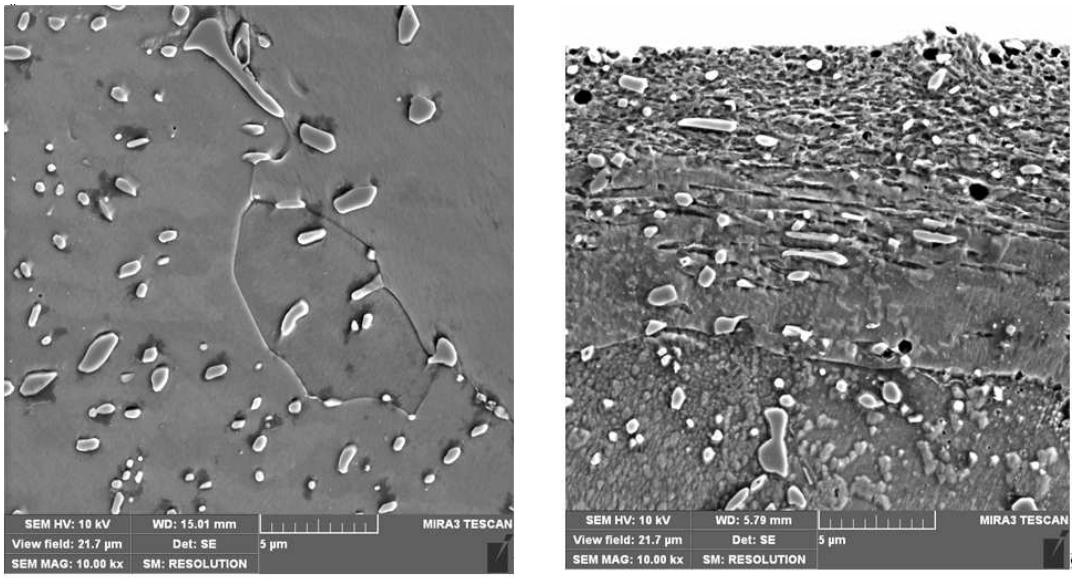

a) ×10000 b) ×10000

Figure 9: Structure of the surface layer of steel 20X13: a) in the initial state and b) were subjected to the burnishing of diamond processing.

[3] Guld H. Tobochnik Ja. Computer Simulation in Physics. – M.: Mir, 1990. V.1. 350 p.

[4] 1.A.Suzuki, Y.Mishin Atomistic modeling of point defects and diffusion in copper grain boundaries // Interface Sci, 2003. V. 11, 1. P. 131148

[5] S.M. Foiles Embedded-atom and related methods for modeling metallic systems // MRS Bull, 1996. V. 21, 2, P. 24–28.

[6] S.J. Plimpton, Fast Parallel Algorithms for Short-Range Molecular Dynamics // J. Comp. Phys. 1995. V. 117. No. 1, P. 1–19.

[7] J. Dana Honeycutt, Hans C. Andemen Molecular Dynamics Study of Melting and Freezing of Small Lennard- Jones Clusters // J. Phys. Chem. 1987, V. 91,P. 4950–4963

[8] Kuznetsov V.P., Makarov A.V., Kiryakov A.E. Experimental studies of the formation of the surface layer of parts at finishing smoothing by turn/mill machine // Sovremennie problemi mashinostroeniya. Proceedings of V international scientific and technical conference. – Tomsk, 2010. – P. 571–576. (in russian)

Andrey I. Dmitriev, Akademichesky 2/4, 634021, Tomsk, Russia
Anton Yu. Nikonov, Akademichesky 2/4, 634021, Tomsk, Russia
Viktor P. Kuznetsov, Gogol str. 25, 640000, Kurgan, Russia

Numerical approach to interpretation of acoustic emission occurring at different scales

Anastasia Dobroskok Alexander M. Linkov
anastasiadobroskok@hotmail.com

Abstract

The paper presents a computer-aided technique based on the unification of passive seismic monitoring with numerical simulations. The paper also discusses the technique application to the interpretation of acoustic emission data at different scales. The technique is based on the joint analysis of two types of data i) geophysical (passive seismic) data recorded in a laboratory experiment or in field and ii) synthetic data simulated using geomechanical approaches. This allows one to match the numerical results with the data of observations. Illustrative examples demonstrate the effectiveness of the approach. Simulated seismicity also serves to compare two methods of seismic data interpretation: the principal component analysis (PCA) currently employed in the industry, and the strip ray scanning (SRS), recently suggested by the authors. Examples indicate that the SRS technique is superior over the PCA on the time steps.

1 Introduction

Acoustic or microseismic emission in materials and structures, being induced by a time-dependent internal process (e.g., damage accumulation, heat transfer, stress redistribution, etc.), can provide useful information characterizing the process. Thus, interpretation of emission can contribute to the solution of such engineering problems as structural health monitoring and characterization of the internal structure of a material or engineering system. In practice emission occurs at various connections: i) in laboratory specimens, ii) in engineering systems (e.g., bridges and subsurface reservoirs), iii) seismicity and rock bursts in mines, and iv) earthquakes in the earth crust.

Interpretation of acoustic emission and seismicity is driven majorally by the growing demand to use non-destructive techniques to characterize engineering systems and their development in time. The idea is not new: data of microseismic monitoring is routinely used for maintaining bridges and safety monitoring in mines. However, in the majority of applications, interpretation of acoustic (seismic) data is limited to statistical analysis. Such analysis does not allow one to make use of deterministic description of the considered system. As a result some features of the considered systems and processes remain unnoticed or misinterpreted.

This paper presents a novel computer-aided technique, based on the unification of seismic (acoustic emission) monitoring with numerical simulations. The paper also discusses the technique application to the interpretation of acoustic emission data at different scales.

2 Background and numerical realization

Analysis of microseismicity in mines often yields the conclusion that microseismisity cannot serve to reliably predict dynamic events (e.g., roof falls, rock bursts). For instance, the study conducted by [1] has shown that there is no direct correlation between elevated microseismic activity and roof falls. This result is in agreement with the study conducted by the authors and is discussed in section 3.1.

Problems with interpreting seismicity in reservoir engineering applications are of different nature. The problem of stability rarely arises in reservoir engineering. Instead, the problems of poor characterization of the subsurface system and of assessing the efficiency of stimulation present significant challenges. Statistical analysis of microseismic data [2] leads to too general conclusions which can be obtained using less sophisticated monitoring techniques.

Similar problems are encountered in other applications. For instance, recording acoustic emission during mechanical testing has become almost a golden standard at least for scientific experiments. Meanwhile, analysis of the recorded data is rarely conducted. In civil engineering microseismic monitoring serves only for warning on severe damage taking place in constructions. However, the most impressive example of underutilization of seismic data is given by earthquake applications: despite continuous monitoring with distributed arrays of accelerometers these data usually serve only for geophysical studies of wave forms.

This paper discusses the approach allowing for more meaningful interpretation of acoustic emission (microseismic) data. The approach makes use of joint analysis of two types of data i) acoustic emission or seismic data recorded in a laboratory experiment or in field and ii) synthetic data simulated using geomechanical approaches.

Numerical simulations utilize approach introduced by Salamon [3] and developed over a few decades. The approach suggests that a single seismic event occurs on a discontinuity (crack, flaw, fault, etc.) instantaneously when the strength of the contact is reached. In this case stability is lost and the discontinuity reaches a new stable state by a jump. The accumulated elastic energy is then released in the form of acoustic (seismic) waves. However, if the imbedding medium is stiff enough, while a fracture surface has sifficient capacity to absorb the elastic energy, the loss of stability does not take place. Instead a different type of event, aseismic slip, occurs [4]. An event runs smoothly without elastic energy excess. Still its characteristic time may be very small if it occurs under a combination of parameters close to a critical value, corresponding to the point of dynamic instability. On the level of the earth crust, such a smooth movement with small characterisitic time appears as a 'silent earthquiake' (see, e.g. the paper [5] and references in it). The elasticity-softening-creep (ESC) model [4] is the simplest model, developed for numerical simulation of the both types of the events, seismic and aseismic; the latter may have arbitrary characteristic times, including those, which are whatever small. The model allows one to distinguish the type of a simulated event and to obtain quantitative data on its features.

The ESC-model may be used in frames of any computational method serving to find stresses. To the date, the hypersingular boundary element method (H-BEM) [6] has served as a basis for evaluation of stresses at time steps. Realization of the approach consists of two major components: i) solution of the problem of elasticity by the H-BEM, and ii) statistical procedures to simulate seismicity. The H-BEM serves for tracing changes in stresses occurring due to a time dependent process (e.g., mining steps, pressure or temperature changes following hydraulic or thermal shock, hydraulic fracture propagation,

etc.). Subroutines for simulating seismicity allow for a) random seeding of rectangular cracks (flaws), b) detecting the flaws which have reached a critical state and are to produce a seismic or aseismic event, c) distinguishing between seismic and aseismic events, d) accounting for mutual influences of the flaws and tracing chains of seismic and aseismic events on multiple flaws, and e) statistical analysis of simulated seismic and aseismic data. Simulations use Poisson's distribution of sizes and uniform distribution of location and orientation. Specific choice of mechanical parameters of interfaces conforms to the recommendations given in [4].

The workflow employed is as follows. We conduct simulations of seismicity for a numerical model of a considered system. The results of simulations are formulated in terms of seismic quantities. This allows us to match the numerical results with the data of seismic monitoring. History matching requires that the limited number of the parameters of the model be adjusted in iterative steps. After history matching is completed, simulations with the adjusted model may provide the following information: stress and permeability tensors, geometry of the system, pore pressure, etc.

In practice numerical simulations remain unaffected by the technical limitations imposed by the resolution of monitoring instrumentation. Consequently, simulations yield more statistical data and provide more details on the development of the studied system. Synthetic seismic data also serve to compare two methods of seismic data interpretation: the principal component analysis (PCA) currently employed in the industry, and the strip-ray scanning (SRS), recently suggested by the authors. Application of the both techniques to simulated seismicity indicates that the SRS is superior over the PCA on the time steps. The advantage is due to the SRS capability to highlight the features of the considered processes, which are missed when using standard statistical interpretation.

3 Numerical examples

To illustrate the enhancement provided by the joint acoustic emission (seismic) monitoring and numerical modelling, we revisit example considered in [7]. We also discuss some preliminary results of the analysis of acoustic emission recorded in a laboratory experiment.

3.1 Analysis of seismicity in mines

The field data were recorded in the the longwall opening 712-c in the coal seam No. 4 of the Komsomolskaya mine in February 2008. The details of the geological settings are presented in [7]. The total number of seismic events recorded was small (295 events) what prevented substantial statistical analysis. The locations and the energies of the events are the only parameters recorded. Due to the mentioned limitations, the conclusions directly available from the analysis of the field data are not extensive. Analysis of the locations of the events indicated that the majority of the events occurred at a distance of about 20m from the seam plane and were similarly distributed in the mine roof and floor. This clearly indicates that the events are triggered by stress changes in the vicinity of the advancing mining front.

Deeper insight becomes possible when following the workflow outlined in the preceding section. To this end we used the available data on in-situ settings to create an H-BEM numerical model of the considered system. Further adjustment of the model allowed for reasonable agreement between recorded and simulated seismic data. Specifically, the flaws are seeded in a rectangular parallelepiped block with height of 100m in the vertical direction, length of 300m in the direction of strike, and width of 150m in the direction

of dip. Number of flaws is N = 20 000 what provides the density of the flaws within the interval recommended in [4]. The average size of flaws is taken 2.2m to agree the average energy of the simulated events with that recorded in mine (1800J); the average cohesion of flaw surfaces is 2.5MPa; the average friction angle is 15 deg.

The adjusted model serves us to delineate zones of increased rock pressure (IRP). These zones are most susceptible to hazardous dynamic events. Calculations indicate that the IRP zone follows the mining front, extending approximately 70 - 80m ahead of the front. The boundary of the IRP zone rounds the area where the majority of seismic events occurred. The numerical model also indicates the existence of the zone of high compressive stresses in the middle plane of the seam ahead of the mining front. Stress state in the zone is almost hydrostatic yielding small shear stresses what results in low microseismic activity in this zone. Nevertheless, due to high magnitude of normal stresses this zone clearly can produce dangerous events. This would not be possible to predict if not conducting geomechanical calculations in addition to the analysis of seismic data. Note that similar effects can underlie the observation of [1] that microseismic activity does not necessarily increase in the areas producing dynamic events. More detailed discussion of the results of joint seismic monitoring and geomechanical modelling for the considered problem can be found in [7]. The results are briefly summarized as follows:

Numerical simulation of seismicity in the considered problem provides more data than seismic monitoring. The number of simulated events is higher than that of the recorded events because numerical simulations are not limited by the resolution of monitoring instrumentation. This allows for more meaningful statistical analysis of the synthetic data. Numerical simulations also provide more geophysical information regarding a single event. As opposed to the field data where only locations and magnitudes were recorded, numerical simulations allow distinguishing between events occurring in tension and in shear, define shear displacements and seismic moments of the events. Other seismic attributes of interest also can be obtained when necessary.

In the considered problem statistical analysis of the orientations of the activated flaws did not reveal any preferential directions. However, further investigations involving a variety of problems are required to provide solid conclusions regarding potential use of the analysis of the orientations.

3.2 Analysis of acoustic emission data recorded in a laboratory experiment

Acoustic emission data were recorded during experiments described in [9]. However, following the request by the authors, Professor Labuz provided the data without the description of the experimental settings. The motivation for the request is that the authors wanted to check which system parameters are readily available from the data of acoustic emission without any a priory knowledge of the settings. While detailed joint geophysical and numerical analysis is a subject of on-going research, this section summarizes the results obtained from statistical analysis of acoustic data. Statistical treatment also outlines a problem which cannot be solved without numerical modeling.

Statistical analysis was conducted using standard principal component analysis (PCA) and strip-ray scanning (SRS) technique recently suggested by the authors. The important feature of the SRS analysis is that the totality of the events is divided into groups. The events are grouped in accordance to their locations so that each group of the events is located within a strip of a fixed width. Initially the orientation of the strip is arbitrary. Further different orientations of the strip within a hemisphere are checked to determine which orientation corresponds to the maximum number of events within the strip. Previous

investigations [8], [10] have shown that this orientation of the strip can be associated with the plane containing the source which triggers the events (e.g., hydrofracture plane or mining front). The analysis yielded the following conclusions:

Distribution of the totality of microseismic events allowed for reconstructing geometrical parameters of the tested specimen: it was determined that the region was a rectangle; its width and height were determined with the accuracy of 2% and 0.1% respectively. The length was uncertain, but was estimated to exceed 72.9mm (note that actual length of the specimen was 100mm);

Analysis of the density of the events yielded an estimate of the approximate size of a typical flaw (microcrack). This estimate agrees with a grain size of the specimen;

Distribution of the events within strips of a fixed width indicated that the geometry of the problem did not change during the experiment (i.e. no fracturing has occurred) and that the events were triggered by the changes in the external load. This conclusion coincides with the description presented in [9];

The results obtained by PCA and SRS methods roughly agree. However, the analysis indicates that PCA may serve to estimate the reasonable width W of the strip used in the SRS method. In the meantime SRS seems to provide more accurate interpretation of acoustic data.

The specific grouping of the events cannot be explained in details using only statistical analysis of the events. Thus, joint statistical analysis and numerical modelling may be required for better understanding of the underlying physical process and for more meaningful interpretation of the acoustic data.

4 Conclusion

Unification of statistical analysis of acoustic emission and numerical simulations enhances the understanding of the underlying physical processes. It improves the interpretation of acoustic data and allows for more rigorous inversion of observed microseismicity in well-established terms of solid mechanics.

5 Acknowledgment

The first of the authors appreciates the support of the European Research Agency (FP7-PEOPLE-2009-IAPP Marie Curie IAPP transfer of knowledge programme, Project Reference # 251475). The second author gartefully acknowledges the support of the Russian Fund for Fundamental Researches (Grant # 09-05-00104). The authors also express their gratitude to Professor Joseph F. Labuz and Mr. Chu-Shu Kao for provided laboratory data.

References

[1] Ellenberger J., Bajpayee T. An evaluation of microseismic activity associated with major roof falls in a limestone mines: a case study. Proc. SME Annual Meeting & Exhibit. Publisher: Soc. For Mining, Metallurgy & Exploration, 2007.

[2] Du J., Warpinski N. R., Davis E. J., Griffin L. G., Malone S. Joint inversion of downhole tiltmeter and microseismic data and its application to hydraulic fracture mapping

in tight gas sand formation. In Proceeding 42nd U.S. Rock Mechanics Symposium, 2008, San Francisco, CA.

[3] Salamon M. D. G. Keynote address: some applications of geomechanical modeling in rockburst and related research. In Proceedings 3rd Int. Symposium "Rockbursts and Seismicity in Mines", R.P. Young (ed.), 1993, Rotterdam, Balkema, 297-309.

[4] Linkov A. M. Numerical modeling of seismic and aseismic events in three-dimensional problems of rock mechanics. J. Mining Sci. 2006, 42(1), 1-14.

[5] Kawasaki I. Silent earthquakes occuring in a stable-unstable transition zone and implications for earthquake prediciton. Earth Planete Space, 2004, 56, 813-821.

[6] Linkov A. Boundary integral equations in elasticity theory. Dordrecht, the Netherlands, Kluwer Acad. Publ., 2002.

[7] Dobroskok A. A., Linkov A. M., Zoubkov V. V. On joint geomechanical and geophysical monitoring in mines. J. Min. Sci., 2010, 46(1), 13-20.

[8] Dobroskok A. A., Linkov A. M. Numerical simulation of seismicity accompanying hydraulic fracture propagation. In Proceedings 42nd U.S. Rock Mechanics Symposium, 2008, San Francisco, CA.

[9] Riedel J. J., Labuz J. F. Propagation of a shear band in sandstone. Int. J. Num. and Anal. Meth. Geomech. 2007, 31(11), 1281-1299.

[10] Dobroskok A. A., Linkov A. M . Joint numerical simulation of stress changes, acoustic emission and/or microseismicity. Proceedings 23-rd International Conference "Mathematical Modeling of Solids and Constructions. Methods of Boundary and Finite Elements", 2009, 72-74.

Anastasia A. Dobroskok: New Mexico State University; Alexander M. Linkov: IPME, Saint-Petersburg, Russia; Rzeszow University of Technology, Rzeszow, Poland

Usage of a DEM approach for the modeling of fluidised bed agglomeration process

Maksym Dosta Sergiy Antonyuk Stefan Heinrich
dosta@tuhh.de

Abstract

Due to a good mixing behaviour, intensive heat and mass transfer between the phases, the fluidized bed is applied for many processes, e.g. drying, cooling, calcination, combustion, gasification as well as for complex multiphase processes like spray granulation, agglomeration, particle layering and coating and also for chemical reactions.

The kinetics of the agglomeration process is governed on the microscale. While the global process time is in the order of hours, the underlying micro-mechanisms have much smaller time constants in the order of seconds. This is a challenging situation in the field of process modelling, as a detailed simulation cannot cover the entire process time, while on the other hand a macroscopic model cannot take into account material micro-properties.

For this reason a multiscale simulation system was developed. On the micro scale, the fluid and particle dynamics as well as wetting and drying of the individual particles is modeled. From this simulation, rate constants such as the collision frequency and relative collision velocity are extracted. Agglomeration and breakage criteria are defined based on the kinetic energy of an impact and the moisture content of the colliding particles. Using this data, a simulation at full process scale is performed using the flowsheet simulation system SolidSim.

1 Introduction

Solids processes play an important role in chemical, pharmaceutical and food industries. More than 60% of all products, which companies such as DuPont, BASF or ICI sell to customers, are amorphous, crystalline or polymeric solids [7]. In order to satisfy the quality standards, these products should consists not just from a specified chemical compounds, but they should have specific clearly defined size, shape and physical microproperties. To transform the raw material into a product, industrial process can consist from a complex interconnection of different process steps (unit operations), such as screening, crushing, solids transportation, etc. [6]. To minimize the production costs and create effective plant structures the material and energy streams are often re-used in the process. It leads to increased structure complexity due to the existence of additional recycled streams. That is why, in mostly cases, even coarse analytical prediction of process steady-state and transient behaviour is impossible. To solve this problem, the numerical calculations in form of flowsheet simulation can be used. In recent years, especially for the steady-state flowsheet simulation of solids the SolidSim system has been developed [5]. This system is applicable for general solids processes. However, due to the using of empirical and semi-empirical models of different apparatuses the material microproperties are weakly considered in it. To solve this problem the multiscale modeling methodology can be used.

One of the main idea of multiscale modeling - is a process description by submodels on the different time and length scales (as it is shown in Figure 1) with a combination of submodels in one multiscale model.

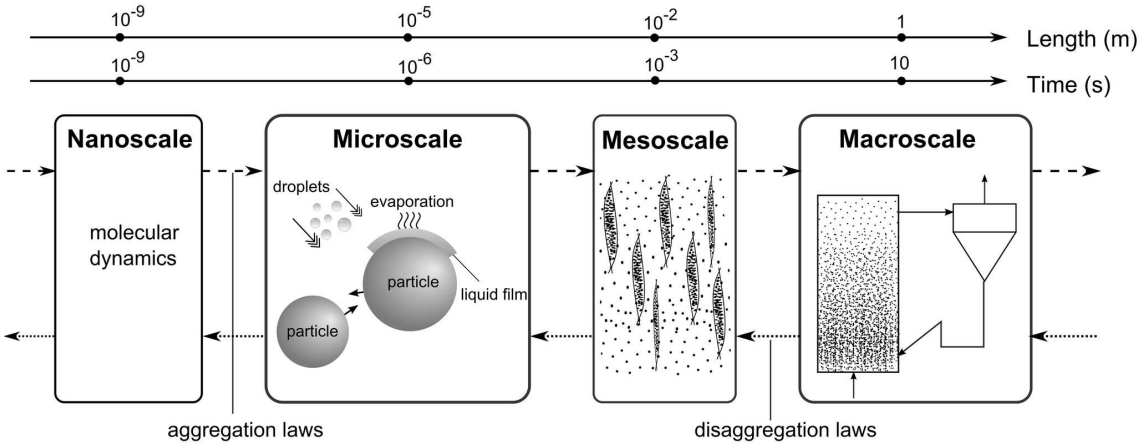

Figure 1: Mutliscale modeling of a circulating fluidized bed.

2 Microscale process description by DEM

The Discrete Element Method (DEM) is used as a basis for the microscale calculations. In the DEM each particle is considered as a separate entity [2]. Afterwards Newton's equations of motion are solved for each individual particle. By this approach the physic-chemical material properties and geometry of the apparatus can be considered.

To take into account the gas phase in the fluidized bed apparatus, the DEM method has been coupled with a Computational Fluid Dynamics (CFD) model, with help of which the fluid profile has been calculated. For the numerical approximation of fluid, apparatus is discretized into the mesh cells for which the volume-averaged Navier Stokes equations of motion are solved. In Figure 2 the coupling scheme between CFD and DEM systems is shown. The particle positions are considered in the CFD system via the cell porosities. The gas velocity profile received from the CFD simulation is then used in the DEM code for the calculation of the drag force, which acts on each particle.

The interactions between particles in the DEM are described by a contact model, where the restitution coefficient plays one of the major roles. With help of the restitution coefficient (e) the amount of dissipated energy is described. The experimental results have shown that a liquid film presented on the contacting surfaces has a significant influence on the restitution coefficient [1]. To consider the fact that during fluidized bed granulation, the surface of the particles is wetted with a suspension, three different types of the collisions have been distinguished. For each of the collision, the probability has been defined, as it is shown in Figure 3.

To consider the different amount of the liquid on the particle surfaces, the wetted surface fraction φ parameter has been used. It is calculated as $\phi = \frac{A_{cov}}{A_{tot}}$, where A_{cov} is the particle surface covered with a liquid film and A_{tot} the total particle surface. The global restitution coefficient has been defined as:

$e^* = e_1(1-\varphi)^2 + 2e_2\varphi(1-\varphi) + e_3\varphi^3$

The time-consuming microscale simulation has been performed for the short time interval in order of seconds. The received particle trajectories and air properties have been

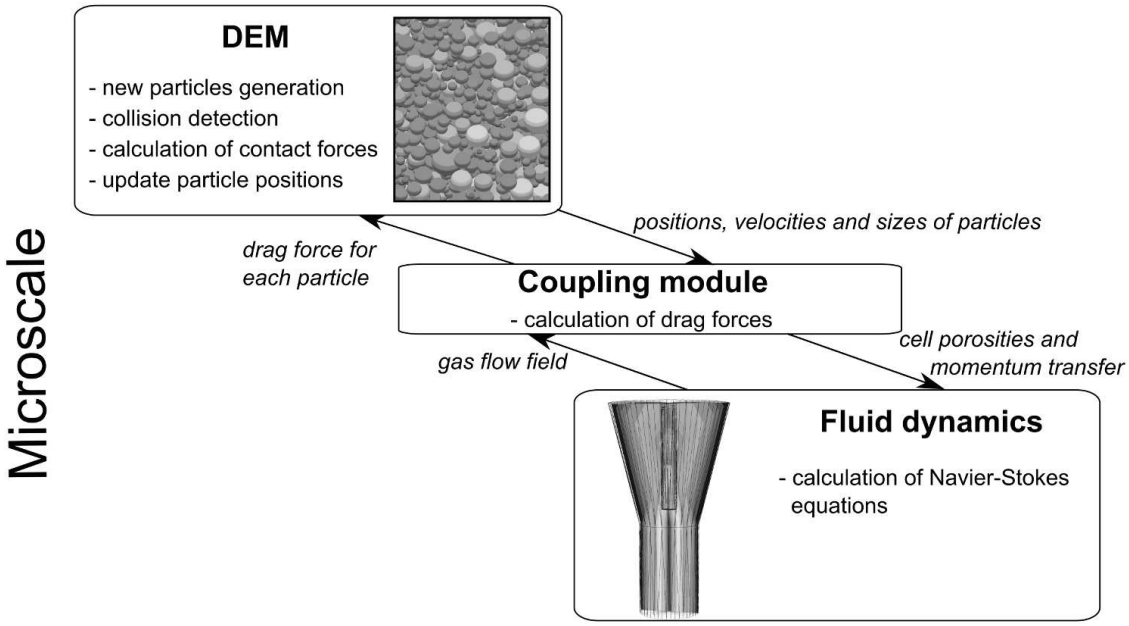

Figure 2: Coupling between DEM and CFD systems.

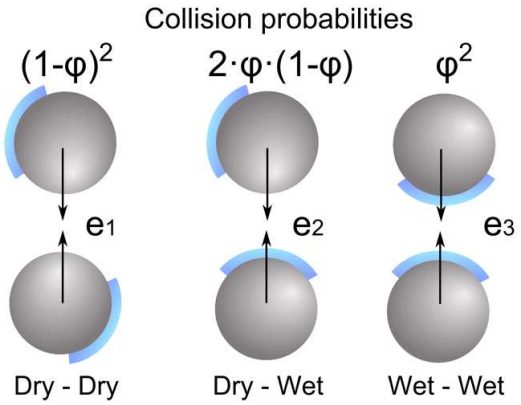

Figure 3: Collision types.

saved and extrapolated for the mesoscale simulations. Afterwards the process calculation on the mesoscale has been done for the time interval in order of minutes.

3 Mesoscale modeling

On the mesoscale the wetting of the particles by a liquid film with its further drying has been approximated. The geometry of the apparatus from the microscale has been extended by a simplified nozzle model [4]. This model in each time step predicts the amount of the liquid which reaches the particle. The amount of the solution covered the particle depends on the distance between particle and nozzle, the porosity in the nozzle zone, the liquid mass flow via the nozzle and the particle surface. The spray zone is represented by a cone-shaped region, which is discretized through the height by a set of layers.

Simultaneously to particle wetting the drying process is calculated. For this purpose the heat- and mass transfer equations are solved for each particle. The following heat

streams are considered: heat transfer between air and particles $\dot{Q}_{ap}$, between particle and liquid film $\dot{Q}_{pf}$ and between air and liquid film $\dot{Q}_{af}$, as it is shown in Figure 4.

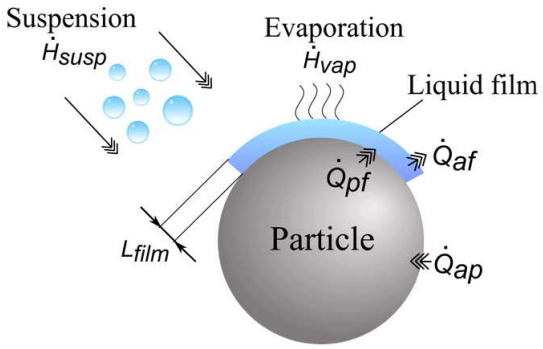

Figure 4: Heat and mass transfers on the particle surface.

4 Flowsheet simulation on the macroscale

A continuous agglomeration process circuit, which consists of a fluidized bed (FB) was simulated on the macroscale. The general scheme of this process is shown in Figure 5. The production process consists of a fluidized bed agglomerator, a separator, two screens and a mill (size reduction unit).

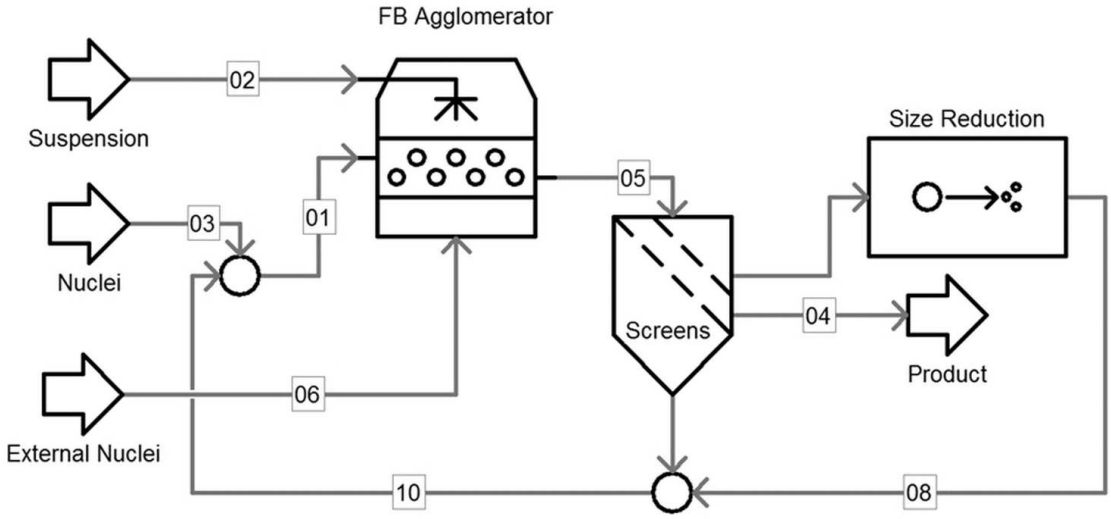

Figure 5: Flowsheet of the fluidised bed agglomeration process.

The agglomeration process has been described by one dimensional population balance model. One of the main parameters in the PBM model is a coalescence kernel, with help of which the agglomeration velocity of the particles from different size classes is described. In order to obtain this parameter, the micro- and mesoscale calculations has been iteratively performed. The total calculation has been performed in following order:

1. Design of the scaled geometry on the microscale;

2. DEM simulation of the process with an calculation of particles trajectories;
3. Obtaining of the time-progression of the wetness-degree by mesoscale model;
4. DEM-based calculation of the coalescence kernel, which is depends on the collision velocities between individual particles, wetted surface fraction of the particle and viscosity of the liquid bridge. In order to predict the sticking of particles together the Stokes criterion has been used.
5. Dynamic flowsheet simulation of the total production process in the modified SolidSim system was done [3].

5 Conclusion

The using of the discrete element method on the lower scale allows to consider material microproperties and apparatus geometry. However the calculation of the whole production process by the time-consuming microscale calculations is impossible. That is why in this contribution an approach for the multiscale simulation of a continuous fluidised bed agglomeration process is presented. The proposed framework can be applied to different solids processes. However, the inclusion of the lower scales into the model causes a large computational effort. That is why the proposed simulation system can only be applied for a limited number of applications.

References

[1] Antonyuk, S., Heinrich, S., Deen, N.G. and J.A.M. Kuipers. Influence of liquid layers on energy absorption during particle impact, Particuology, 7, 245-259, 2009.

[2] Cundall P.A., Strack O.D.L. A discrete numerical model for granular assemblies. Geotechnique, 29, 47-65, 1979.

[3] Dosta M., Heinrich S., Werther J. Fluidized bed spray granulation: Analysis of the system behaviour by means of dynamic flowsheet simulation, Powder Technology, 204, pp. 71-82, 2010.

[4] Dosta M., Antonyuk S., Fries L., Heinrich S. Discrete element modelling of the fluidised bed granulation by coupling of different simulation systems, International Drying Symposium, 2010.

[5] Hartge E.-U., Pogodda M., Reimers C., Schwier D., Gruhn G., Werther J. Flowsheet simulation of solids processes, KONA, 24, 147-158, 2006.

[6] Werther J., Heinrich S., Dosta M., Hartge E.-U., The ultimate goal of modeling - simulation of system and plant performance, Particuology, In press.

[7] Wintermantel K. Process and product engineering - achievements, present and future challenges, Chemical Engineering Science, 54, 1601-1620,1999

Maksym Dosta, Denickestr. 15, 21073 Hamburg, Germany

Population balance modeling of aerogel particles coating in fluidized bed

A. Ershova S. Antonyuk S. Heinrich N. Menshutina
stasenk@yandex.ru antonyuk@tu-harburg.de

Abstract

The modeling of the particle growth during a coating process was carried out by the population balance. In the fluidized beds the rotation of particles could be very high allowing a nearly uniform distribution of the droplets on particle surface. In this case the linear growth of particles due to layering process can be assumed. The growth of each particle is proportional to the amount of substance supplied to the coating, solids content in the coating solution and it is inversely proportional to the total surface area of all particles in the fluidized bed.

The coating of aerogel particles by an aqueous dispersion of anionic polymers (Eudragit L) was modeled in this work. To provide a good prediction of this process, the loss of droplets as an overspray was taken into account, i.e. some part of suspension in the fluidized bed is transformed to the dried droplets and so not all suspension flow is consumed to the coating particles. The polymer substance loss some quantity to the droplet and other part of substance goes to cover aerogel particles and dried droplets.

The results of performed simulations are in a good agreement with the experimental observations. To achieve a coating thickness of 18 μm the process of coating aerogels particles should be continued 20 minutes. The obtained results can be used for the optimization of process parameters (time of process, flow rate of suspension and air, water content in the solution of the coating substance etc.).

1 Introduction

Aerogel is a porous substance, the gel, in which the liquid phase was completely replaced by air without alteration and destruction of internal structure. Due to high surface area and open pore structure, aerogels can be useful for the pharmaceutical industry for delivering a medicinal substance in an amorphous form to the human body. In order to protect the medicinal substance and aerogels from destruction before it is transported to the target place in the human body, a special protection layer can be used (in this work for protection used an aqueous dispersion of anionic polymers (Eudragit L)). This layer can be realized in the fluidized bed apparatus.

The present work concerns processes where a spouted bed coater is used. In modeling mass transfer in the coating process in systems with intensive motion of particles, such as fluidized and spouted beds, the leaner particle growth is considered. In a spouted bed coater, a liquid is sprayed onto an already existing bed of aerogels that is fluidized by air. The liquid partially evaporates, leaving a dry material and particles that have grown. Such particle growth can be the result of so-called onion growth, where the material is deposited onto the particles layer by layer (e.g. Heinrich et al., 2002). A graphical representation of growth process (layer by layer) is provided in the Fig. 1. It is obvious that these processes influence on the particle size distribution.

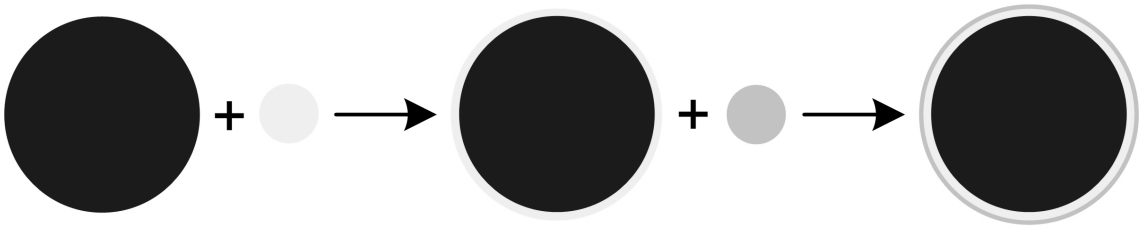

Fig. 1. The growth of particles during the coating process

To model the particle size distribution, the so-called population balance approach can be quite helpful (Randolph and Larson, 1988; Hounslow et al., 1988; Ramkrishna, 2000; Heinrich et al., 2002; Peglow et al., 2007). The present paper considers a basic population balance model, which was developed to describe the coating of aerogels in the spouted bed coater. Macroscopic models like Population Balance Models are widely used to evolve the particle size distribution in granulation and coating processes.

2 Experimental work

To perform the coating of the aerogels an experimental spouted bed apparatus was built (Fig. 2). The pilot plant has a fluidization chamber with conic and prismatic parts, with two horizontal gas inlets for adjustable gas supply. The velocity of the inlet air can be varied changing the height of these slots h.

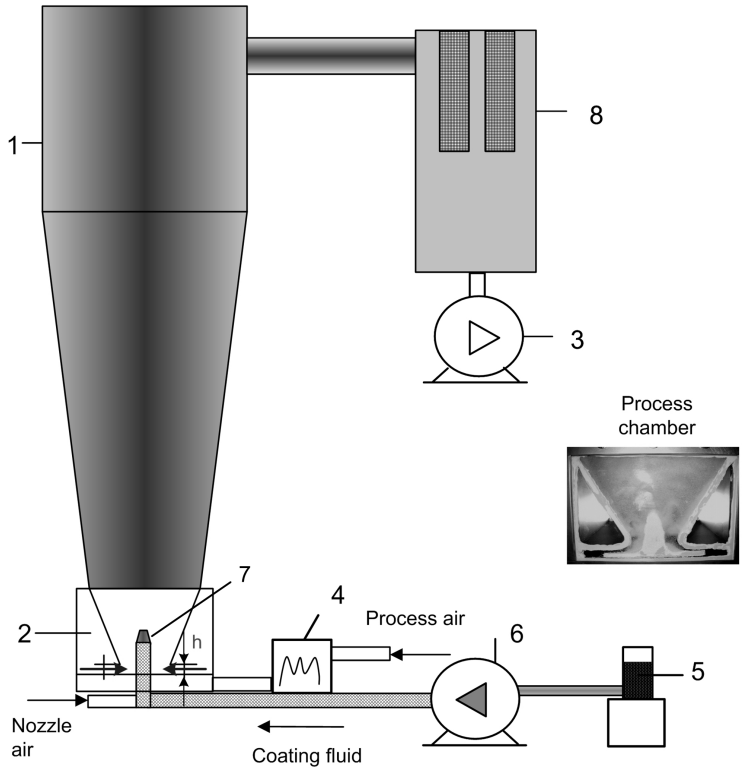

Fig. 2. Experimental spouted bed apparatus for coating: 1 - cylindrical chamber; 2 - prismatic fluidization chamber, with two horizontal gas inlets (slots) for adjustable gas supply; 3 - blower; 4 - 500 W heater; 5 - vessel; 6 - peristaltic pump; 7 - two-component nozzle; 8 - fabric filter.

Liquid is sprayed on to solid particles by the nozzle. The liquid drops are deposited onto the solid particles and are distributed through spreading. In the coating process the particle grows as a result of spreading of the liquid binder on the surface of the particles.

3 The Population Balance Model. Simulation Parameters and Results

The population balance modeling with the linear growth of particles was performed. Population balance equations are used to determine the particle number density distribution on a macroscopic level. Let us denote the population density by $n(d_p, t)$, based on the total number of particles in the bed. The population density is a function of particle diameter (d_p) and time (t). We assume spatial homogoneity of the population in the bed. The amount $n(d_p,t)dd_p$ denotes the number of particles within the size class $[d_p, d_p + dd_p]$. Some spray droplets dry entirely before they hit any other particle in the bed. These dried droplets are considered as new nucleus. With nucleation we mean the process of formation of the smallest particles present in the bed. The growth of the particles is primarily due to the spraying of solution upon existing particles. Because of the high bed temperature, fast drying of the spray is assumed, such that temperature, saturation state and humidity do not appear in the system of equations.

Consider the process of film formation on the surface of the particle for definition the rate of growth of particles. Drops of suspension collisions with particles and spreads to the surface, forming a coating film. In the case of linear growth of particles, the particle size is proportional to the amount of the solution supplied to the coating, content of the solid phase in the coating substance and is inversely proportional to the total surface area of all particles in the fluidized bed. Assumed, that the coating polymer with equal probability connect with particles of aerogels and with dried droplets. As result not all quantity of coating polymer spent to the growth of particles.

The linear growth model assumes:

1. The fluidized bed is ideal mixed. Thus, all particles are uniformly wetted with the liquid.

2. The aerogels particles are spherical.

3. The particles of aerogels in the initial time have normal distribution.

4. There is no internal nuclei formation by attrition, overspray or breakage and no agglomeration of particles.

5. There are no diffusion phenomena in the particles.

6. The amount and the concentration of the injected liquid is constant.

7. The drops of the suspension from the nozzle have a log-normal distribution, whose parameters are not dependent on the time.

8. Collisions of the drop of suspension with the particles of aerogel are successful, resulting in a layer thickness increases.

9. The number of empty droplets formed in unit time depends only on the properties of the suspension and temperature in the apparatus, and does not change during the process.

10. Only dried droplets removed from the zone of apparatus. The distribution of these droplets is similar to the distribution of droplets at the exit of nozzle.

11. The flow of the suspension covers the dried droplets and particles of aerogels.

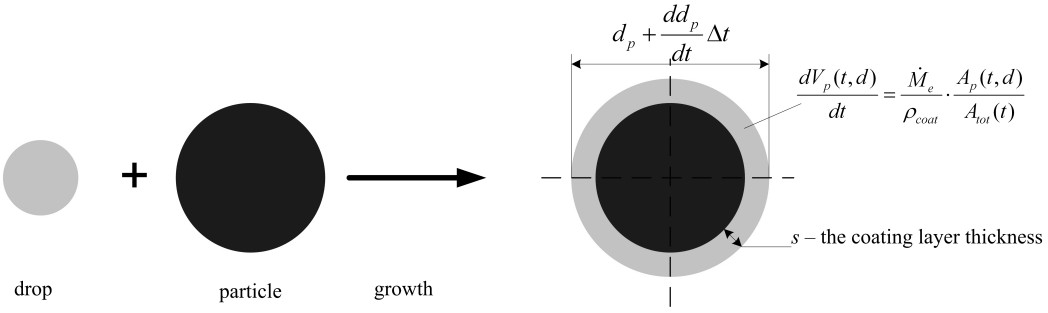

Fig. 3. The growth of thickness

The growth of particles in time:

$$\frac{\partial[n(t,d)]}{\partial t} = \dot{n}_{n_{in}}(t,d) + \dot{n}_{n_{out}}(t,d) - \frac{\partial[G_e(t,d)n(t,d)]}{\partial d} \quad (1)$$

$\dot{n}_{n_{in}}(t,d)$ - the particles flux input (the number of drops of a size formed from the suspension per time);

$\dot{n}_{n_{out}}(t,d)$ - the particles flux outlet (the number of drops of a size which remove from the apparatus per time);

n(t, d) - the number of particles with a size d at some time point t;

G_e(t, d) - the effective growth rate of the particles:

$$G_e = \frac{dd_p}{dt} = 2\frac{ds}{dt} = \frac{2\dot{M}_e}{\rho_{coat}A_{tot}(t)} \quad (2)$$

$$\dot{M}_e = \dot{M}_{susp}(1 - x_w)(1 - y) \quad (3)$$

$$A_{tot}(t) = \sum A_p(t) + \sum A_{nucl}(t) \quad (4)$$

ρ_{coat} - the density of dry coating material, g/mm^3; $\dot{M}_{susp}$- the suspension flux, g/s; $\dot{M}_e$- the efficient suspension flux, flow of suspension without water and part of matter, which don't cover the particles, g/s; x_w- the content of the liquid phase in the coating substance, mass fraction; y - amount of substance to the drops formed, fraction; t - time, s; d - diameter of spherical particles, m; $N_{tot}(t)$ - the total number of particles; $A_p(t,d)$ - the surface area of one particle, m^2; $A_{tot}(t)$ - the total surface area of the particles in the fluidized bed to this point of the time, m^2; $\sum A_{nucl}(t)$ - the total surface area of the new formed nucleus, which doesn't carried away from apparatus, m^2; $\sum A_p(t)$ - the total surface area of the particles aerogels, m^2.

With the assumption: only dried droplets removed from the zone of apparatus, η - the part of the dried droplets, which removed from the apparatus:

$$\dot{N}_{nucl_{out}} = \eta\dot{N}_{nucl_{in}} \quad (5)$$

Numerical approximation of the growth of particles in time:

$$\frac{dN_{tot}q_0[i](t)}{dt} = -G_eN_{tot}\frac{q_0[i]-q_0[i-1]}{\Delta d} + (1-\eta)\dot{N}_{nucl_{in}}q_{0_{nucl}}[i] \quad (6)$$

The parameters for the modeling process of coating are given in Table 1.

Table 6: Parameters of process

Parameter	Value
Weight of aerogels , g	50
Density of aerogels particles (ρ_a),g/mm^3	19*10^{-5}
Density of coating material (ρ_{coat}),g/mm^3	77*10^{-5}
Suspension flux,($\dot{M}_{susp}$) g/s	0.25
Content of the liquid phase (x_w), mass fraction	0.7864
Amount of substance to the drops formed (y), fraction	0.3
Part of the dried droplets, which removed from the apparatus (η), fraction	0.65
Parameters of particles distribution:	
Mean, mm	0.5
Variance, mm	0.09
Parameters of drops distribution:	
Mean, mm	0.067
Variance, mm	0.52

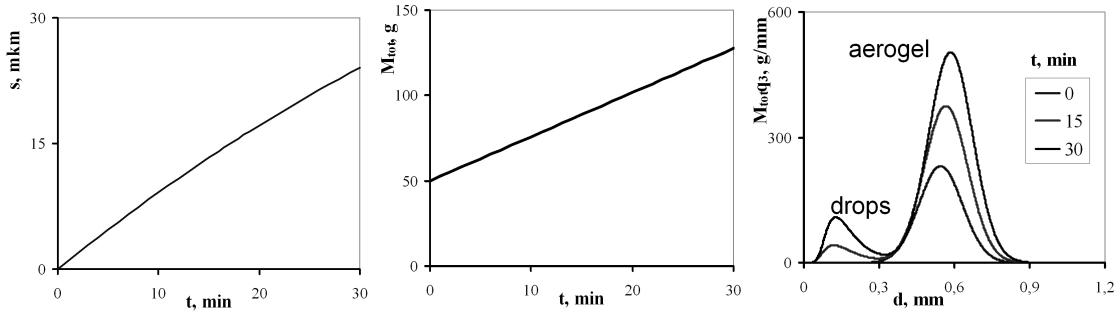

Fig. 4. Results of modeling

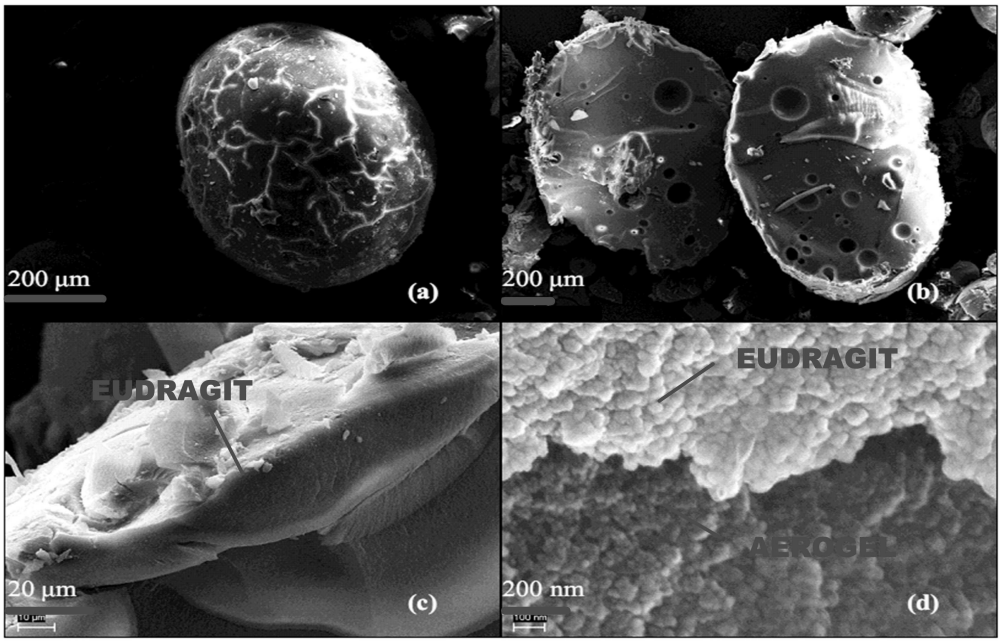

Fig. 5. a-d The particles of aerogels, results of coating

In the process fine drops formed (you can see on the Fig. 4 two fractions: drops and aerogels, which grow up together) and as result - growth of thickness coating is not linear.

The Eudragit layer showed many cracks (Fig. 5). Hence, to avert the breaking of the particles the coating with two materials was carried out. Firstly the PEG 2000 was sprayed in the apparatus forming a protection layer on the aerogel.

Conclusions

The present population balance model describe the coating of aerogels in the spouted bed coater. The obtained results can be used for the optimization of process parameters (time of process, flow rate of suspension and air, water content in the solution of the coating substance etc.) and apparatus geometry.

The results of these simulations are in a good agreement with the experimental observations. To achieve a coating thickness of 18 μm the process of coating aerogels particles should be continued 20 minutes.

References

[1] Randolph, A.D., Larson, M.A., 1988. Theory of particulate processes. Academic Press, New York.

[2] Hounslow, M.J., Ryall, R.L., Marshall, V.R., 1988. A discretized population balance model for nucleation, growth and aggregation. A.I.Ch.E. Journal 34, 1821-1832.

[3] Ramkrishna, D., 2000. Population balances: theory and applications to particulate systems in engineering. Academic Press, San Diego.

[4] Heinrich, S., Peglow, M., Ihlow, M., Henneberg, M., Moerl, L., 2002. Analysis of the start-up process in continuous fluidized bed spray granulation by population balance modelling. Chemical Engineering Science 57, 4369-4390.

[5] Peglow, M., Kumar, J., Heinrich, S., Warnecke, G., Tsotsas, E., Moerl, L., Wolf, B., 2007. A generic population balance model for simultaneous agglomeration and drying in fluidized beds. Chemical Engineering Science 62, 513-532.

A. Ershova, CAPE Faculty, MUCTR, Geroev Panphilovtcev str. 20/1, 125480 Moscow, Russia
S. Antonyuk, SPE Institute, TUHH, Denickestrasse 15, 21073 Hamburg, Germany
S. Heinrich, SPE Institute, TUHH, Denickestrasse 15, 21073 Hamburg, Germany
N. Menshutina, CAPE Faculty, MUCTR, Geroev Panphilovtcev str. 20/1, 125480 Moscow, Russia

Influence of the particle properties on the fluidized bed dynamics during aerogel coating

A. Ershova S. Antonyuk S. Heinrich N. Menshutina
stasenk@yandex.ru antonyuk@tu-harburg.de

Abstract

The spouted fluidized bed can be applied for coating of the light and small aerogel particles (particle density of about 180 kg/m^3 and size from 30 μm to few mm). In the fluidized beds the particle dynamics is influenced by fluidizing air and contact interactions of particles at impacts. These effects show a significant influence on the homogeneity of the solid film on the particle surface forming during a coating process. In this work the dynamics of the coated and uncoated particles in a spouted bed apparatus were studied.

The coupled CFD and Discrete Element Method (DEM) have been applied for the simulation. Using DEM, the mechanical behaviour of solid particles in the spouted bed apparatus was described, where the contact forces for each impact of particles were calculated. The actual particle positions obtained from DEM were transmitted after each synchronization step to a CFD simulation system. This tool describes the complex gas dynamics in the fluidized bed, where the drag forces on the particles and the fluid pressure field are calculated. The particle properties were experimentally obtained and implemented in a DEM contact model.

It was found that the properties of fluidized bed are influenced by geometry of the apparatus, properties of the gas phase and particles. During the coating process the particle density increases, the bed height decreases and the inlet gas flow and velocity must be increased to keep constant particle dynamics and to exceed the sticking and agglomeration in the bed. The obtained results from simulation can directly be used for the optimization of process parameters and apparatus geometry.

1 Introduction

Aerogel is the lightest solid, with the lowest-density of all the porous materials known in the world. Silica aerogels have an open cell structure composed of primary particles (usually less than 10 nm in size) connected to each other and forming a three-dimensional network with a porosity in the mesoporous range (20-50 nm) [1]. They are used in multiple applications such as thermal insulation, as drug delivery systems, or as catalysts. The application of aerogels as a host matrix for biomaterials and drug carriers has an intensified interest in the last decade [2-4].

Their structure might be destroyed by contact with water because of capillary forces which are higher than the strength (Antonyuk et al. [4]). This drawback could be overcome by coating of aerogels with a polymeric protection material. In this work the aerogel particles were coated in a spouted bed apparatus. This technology offers the fluidization of small and light or very large particles, which can be non-spherical or sticky with a broad size distribution (Moerl et al. [5]).

The objectives of this work were to investigate and optimize the coating process parameters of the particle and fluid dynamics of spouted bed apparatus through modelling by DEM coupled with CFD.

2 Modeling of particle and fluid dynamics

The coupled CFD (which calculates the gas phase) and Discrete Element Method (DEM, which describes the motion of every individual element) have been applied to study the particle and fluid dynamics of spout bed apparatus used for the coating of aerogel. The particle properties from experiment were implemented in a DEM contact model. The description of multiphase flows as fully interpenetrating continua includes the concept of phasic volume fractions [6]. The sum of the volume fractions of all contributing phases i (i equals g for the gas phase and p for the solid phase (for particles)) is (1):

$$\sum_{i=1}^{n} \alpha_i = 1 \quad (1)$$

The motion of each phase i can completely be described using volume-averaged Navier-Stokes equations. The mass conservation equation for phase i (2) and the moment balance equation for phase i (3) are:

$$\frac{\partial}{\partial t}(\alpha_i \rho_i) + \nabla(\alpha_i \rho_i \vec{v}_i) = \sum_{j=1}^{n} \dot{m}_{ji} \quad (2)$$

$$\frac{\partial}{\partial t}(\alpha_i \rho_i \vec{v}_i) + \nabla(\alpha_i \rho_i \vec{v}_i \vec{v}_i) = -\alpha_i \nabla p + \nabla \bar{\bar{\tau}}_i + \sum_{j=1}^{n} (\vec{R}_{ji} + \dot{m}_{ji} \vec{v}_{ji}) + \frac{(\sum F_{ext} + \sum F_{i-i})}{V_c} \quad (3)$$

Where α_i is the phasic volume fraction, ρ_i the density and $\vec{v}_i$ the velocity of phase i, whereas $\dot{m}_{ji}$ denotes the inter phase masstransfer from the j-th phase to the i-th. $\vec{R}_{ji}$ denotes an interacting force between the phases, **p** is the pressure shared by all phases and $\bar{\bar{\tau}}_i$ the i-th phase stress-strain tensor.

The motion of each particle k of solid phase p can completely be described using Newton's (4) and Euler's (5) laws:

$$m_k \frac{d\vec{v}_k}{dt} = -V_k \nabla p + \frac{V_k \beta_{g-p}}{(1-\alpha_p)} (\vec{v_g} - \vec{v_k}) + m_k \vec{g} + \sum_{j=1}^{J} \vec{F}_{c,j,k} \quad (4)$$

The force balance on the right side of this equation consists of the force due to pressure gradient, drag, gravity and contact forces by a particle-particle and particle-wall collision.

$$I_k \frac{d\vec{\omega}_k}{dt} = \sum_{j=1}^{J} \vec{M}_{k,j} \quad (5)$$

I_k and ω_k are the moment of inertia and angular velocity for particle k. $M_{k,j}$ are the moments generated from tangential contact forces acting on the particle k. The interphase momentum transfer coefficient β_{g-p} is modelled by combining the Ergun equation (1952) for dense regimes ($\alpha \leq 0.8$) and the correlation proposed by Wen and Yu (1966) for more dilute regimes ($\alpha > 0.8$).

Contact forces between particles are calculated according to a viscoelastic contact model based on the Kelvin-Voigt law with a constant restitution coefficient (Cundall and Strack [7]).

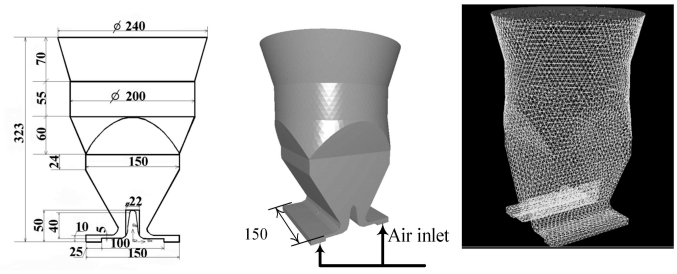

Fig.1: Model of spouted apparatus for simulation

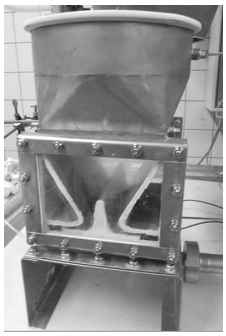

Fig.2: Process chamber

3 Simulation Parameters and Results

The scheme, model and mesh (Fig.1) of the fluidization chamber (Fig.2) are descriebed bellow.

The mesh for modeling consists of 76.725 tet/hybrid cells with an interval size of 0.008 and minimum volume of 4 mm^3. The air with the temperature of 25°C, density of 1.18 kg/m^3 and kinematic viscosity of $15.7 \cdot 10^{-6}$ m^2/s was used for the calculation. To describe the effects of turbulent fluctuations of velocities on the pressure drop in the apparatus a k-ϵ model (with the turbulence intensity of 5%, which showed good results for the spout beds in CFD simulations of Gryczka et al. [8]) was applied for the calculation.

The first simulations were performed for the empty apparatus without the solid particles, the inlet velocity of the gas was varied in the range of 1-2 m/s. The calculated pressure drop increases with increasing inlet velocity. This fact and magnitude of pressure drop from simulation are predicted with the experimental measurements that were carried out for the full spout bed apparatus included its cylindrical chamber, therefore pressure drop from experiments a little more than from simulations (Fig.3). The gas velocity reaches its maximum at the bottom, in inlet slots and in the vertical central part of apparatus and becomes wider and slower with the height (Fig.4). Due to turbulence, two vortices are arisen. That generate the secondary flow moving from the top to down in the near-wall region.

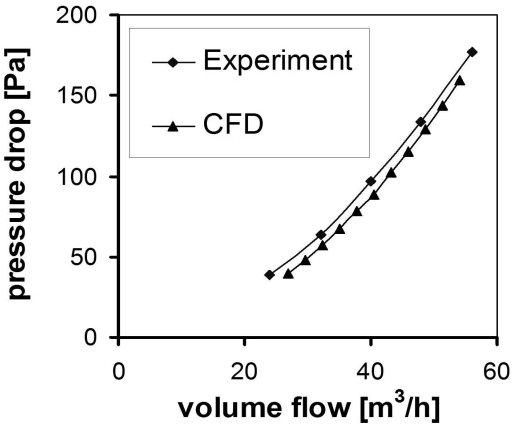

Fig.3: Pressure drop depending on the volume flow of the inlet gas

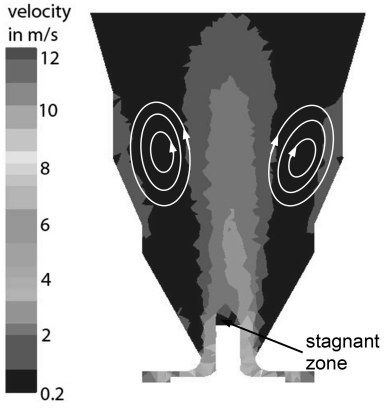

Fig.4: The plot of time-averaged fluid velocities in the empty apparatus at the inlet velocity of 2 m/s.

The coupled CFD and DEM simulations were performed for simulation of the particle and fluid dynamics of spouted bed apparatus for two types of particles: the dry uncoated aerogel particles and the coated particles. These simulations were compared. For the modelling fluid and particles dynamic the inlet gas velocity was given 1.3 m/s (air inlet showed on Fig.1). The coated particles are significantly heavier than dry uncoated aerogel. The parameters of the DEM model are given in Table 1.

Table 7: Properties of the particles in DEM model

Parameter	Uncoated	Coated
diameter in μm	800	820
density in kg/m^3	190	300
stiffness in N/mm	10	10
shear modulus in MPa	6.25	6.25
restitution coefficient	0.6	0.4
friction coefficient	0.8	0.8
rolling friction coefficient	0.01	0.01
number of the particles	150.000	150.000

Influence of particle density on the velocity and bed high (Fig.5-6 and Table 2) are presented bellow. The Fig.5 shows that the wet coated aerogel particles showed a lower translation and rotation velocities in comparison with dry and light aerogels. The Fig.6 compares the calculated bed heights. The maximum bed height depends on the gas velocity, particle mass and restitution coefficient. With increasing of the particle mass during the coating process the bed heigh decreases.

The Fig.7 shows the instantaneous particle positions in the apparatus. The maximum velocity of particles is in the spout region. Here the inlet gas accelerates the particles and picks up nearly vertically according to primary flow. The gas velocity is decreased gradual over the apparatus height and leads to decreasing the particle velocity. The particles deviate from vertical air flow and moves downward along the walls in the spout region, the particles are circulating.

Table 8: Time-averaged motion parameters

Parameter	Uncoated particles	Coated particles
maximum bed height in mm	165	130
mean/maximum particle velocity in m/s	0.36/1.62	0.28/1.20
average particle rotation in 1/s	275	226

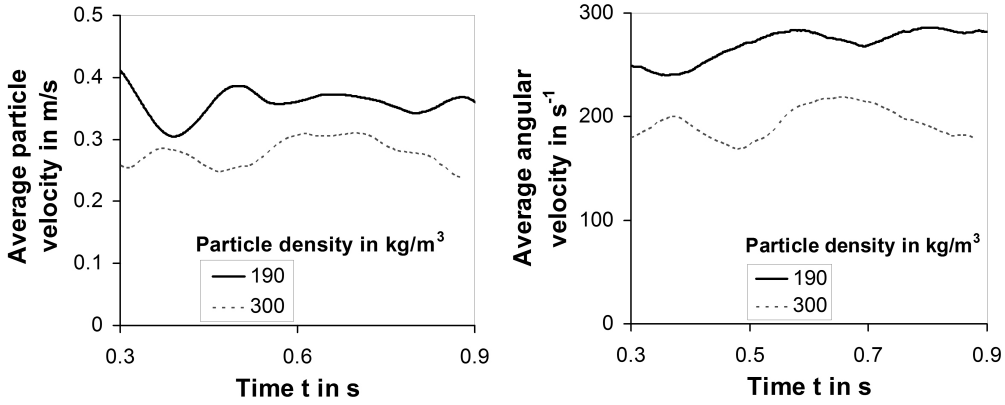

Fig.5: Influence of the particle density on the particles velocity in the spout bed apparatus (inlet gas velocity 1.3 m/s, flow 35 m^3/h)

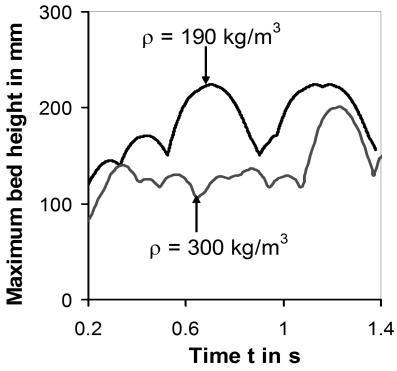

Fig.6: Influence of the particle density on the maximum bed height in the apparatus (inlet gas velocity 1.3 m/s)

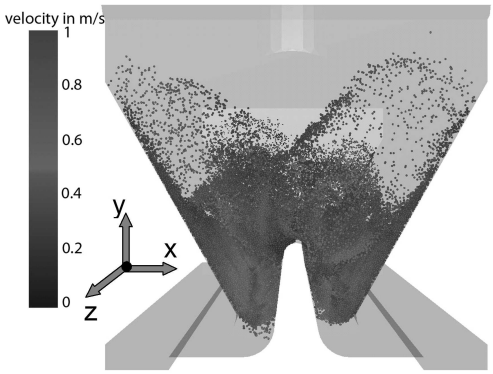

Fig.7: Instantaneous particle positions and velocity distributions inside the spout bed apparatus (particle density 190 kg/m^3, inlet gas velocity 1.3 m/s)

Therefore, during the coating process, the inlet gas flow and the velocity must be increased in order to keep constant particle dynamics and to avoid sticking and agglomeration. The obtained distributions of the average particle velocity and impact velocity in spouted bed can be described with a lognormal distribution function, as it shown in Fig.8. The average particle-particle impact velocity (Fig.8 right) is about 7 times smaller than the absolute particle velocity at the same simulation time. The mean impact velocity by particle-wall impact is at the average 15% higher than that by impact of particles.

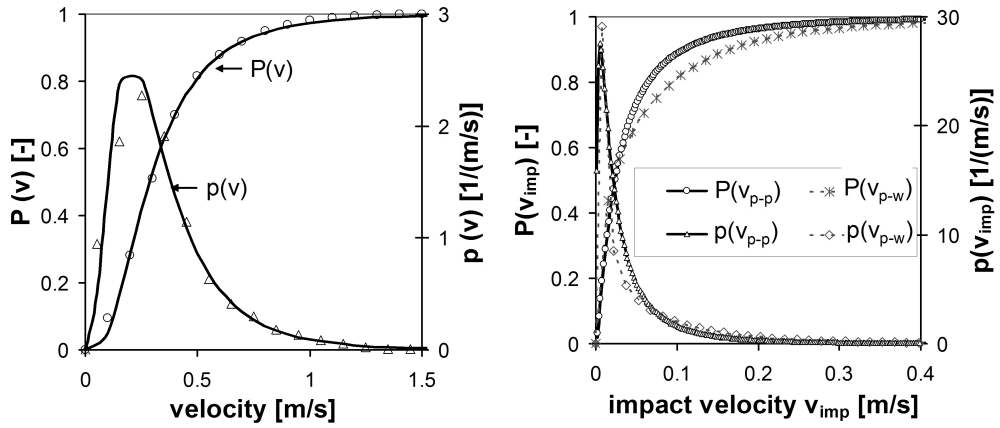

Fig.8: Distribution function P and its density p for: (left) average absolute particle velocity and (right) relative impact velocity in the spout bed apparatus. (particle density 300 kg/m^3 ; p-p - particle-particle impacts, p-w - particle-wall impacts)

Table 9: Mechanical characteristics of aerogels

Diameter in mm	Breakage force in N	Strength in kPa	Stiffness in N/mm
0.70 ± 0.14	0.37 ± 0.2	970 ± 0.50	10.3 ± 2.0
0.80 ± 0.12	0.33 ± 0.1	650 ± 460	10.0 ± 3.0
3.71 ± 0.40	0.61 ± 0.2	60 ± 30	3.0 ± 0.6

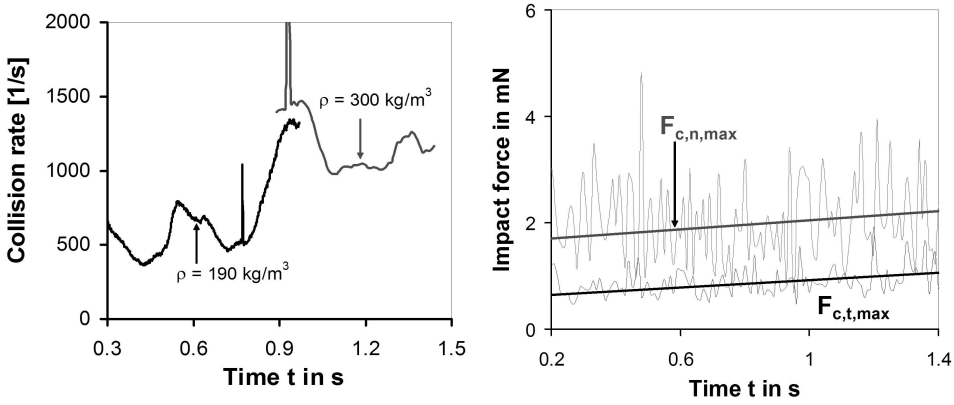

Fig.9:(left) Collision rate of the particles during the fluidization time;
(right) Maximal values of the normal and tangential impact forces during the fluidization time (particle density 300 kg/m^3)

Fig.9 shows the calculated particle-particle collision rates. The fluidized bed of wetted particles shows smaller height and so higher collision rates than for dry aerogels. The particle collides with another particle almost ten times more frequently than with a wall. The calculated forces acting on the particles during collisions in the bed (Fig.9 right) are significantly smaller than breakage range of the aerogels (Table 3). This confirms the experimental fact that no breakage occurs during fluidization of aerogels. The small magnitude of the force can be explained by relative small particle impact velocities in the presented spouted bed apparatus (Fig.8).

Conclusions

The combination of CFD and DEM allows to describe and to optimize the complex process of coating ultralight particles of aerogels. These simulations showed a high gas velocity in the bottom part of the apparatus and its gradual decrease over the apparatus.

The modelling confirmed that mass, energy dissipation at the contact and collisions rate during the coating are increases, herewith the bed height and particle velocities are decreases. It was found that the impact forces acting on the particles in the fluidized bed are significantly smaller than the measured breakage force for aerogel particles, as result the breakage of aerogels does not happening.

References

[1] L. W. Hrubesh, J. Non-Crystalline Solids 225 (1998), p. 335.

[2] I. Smirnova et al., J. Non-Crystalline Solids 350(2004), p. 54.

[3] I. Smirnova et al., Pharm. Dev. Techno. 9 (2004), p. 443.

[4] Antonyuk, S., Heinrich,S., Alnaief, M. and I. Smirnova: Application of a novel spouted bed process for the drying and coating of silica aerogel microspheres for advanced drug delivery, 17th International Drying Symposium, Magdeburg, 2010.

[5] Moerl, L., Heinrich, S., Peglow, M., The Macro Scale I: Processing for Granulation,in Handbook of Powder Technology, Vol. 11, Elsevier Science, (2005), 21-188.

[6] Fries L., Antonyuk, S., Heinrich, S., Palzer, S.: DEM-CFD modelling of a fluidized bed spray granulator, Chemical Engineering Science (2011), in Press.

[7] Cundall, P.A., Strack, O.D.L., A discrete numerical model for granular assemblies. Geotechnique 29 (1979), 47-65.

[8] Gryczka, O., Heinrich, S., Deen, N. van Sint Annaland, M., Kuipers, J.A.M. and L. Moerl: CFD-modeling of a prismatic spouted bed with two adjustable gas inlets, Can. J. Chem. Eng. 87 (2009), 318-328.

A. Ershova, CAPE Faculty, MUCTR, Geroev Panphilovtcev str. 20/1, 125480 Moscow, Russia
S. Antonyuk, SPE Institute, TUHH, Denickestrasse 15, 21073 Hamburg, Germany
S. Heinrich, SPE Institute, TUHH, Denickestrasse 15, 21073 Hamburg, Germany
N. Menshutina, CAPE Faculty, MUCTR, Geroev Panphilovtcev str. 20/1, 125480 Moscow, Russia

Dynamical aperture beyond perturbations: strong localization approach

Antonina N. Fedorova Michael G. Zeitlin
anton@math.ipme.ru, zeitlin@math.ipme.ru

Abstract

We present the applications of the multiresolution analysis approach in the constrained variational framework for calculation of dynamical aperture for particle/beam motion in accelerators. We construct an exact multiscale representation by decomposition via nonlinear high-localized eigenmodes, which allows to control contributions to motion from the whole underlying hidden multiscale structure. We consider a qualitative approach to the aperture problem based on the detailed analysis of smoothness classes in the underlying functional space.

1 Introduction

The estimation of the dynamic aperture of accelerators is an important, complicated and long standing problem. From the formal point of view the aperture is some border between two types of dynamics: relative regular and predictable motion along of acceptable orbits or fluxes of orbits corresponding to KAM tori and stochastic motion with particle losses blown away by the Arnold diffusion and/or chaotic motions.

According to the standard point of view this transition is being done by some analogues with map technique [1]. Consideration for aperture of n-pole Hamiltonians with kicks

$$H = \frac{p_x^2}{2} + \frac{K_x(s)}{2}x^2 + \frac{p_y^2}{2} + \frac{K_y(s)}{2}y^2 + \frac{1}{3!B\rho}\frac{\partial^2 B_z}{\partial x^2}(x^3 - 3xy^2)L\sum_{k=-\infty}^{\infty}\delta(s-kL) + \dots \tag{1}$$

is done by linearisation and discretization of canonical transformation and the result resembles (pure formally) standard mapping. This leads, by using the Chirikov criterion of resonance overlapping, to evaluation of aperture via amplitude of the following global harmonic representation ([1] for designations and description):

$$x^{(n)}(s) = \sqrt{2J_{(n)}\beta_x(s)}\cdot \cos\Big(\psi_1 - \frac{2\pi\nu}{L}s + \int_0^s \frac{\mathrm{d}s'}{\beta_x(s')}\Big). \tag{2}$$

The goal of this paper is is two-fold. In part 2, we consider some qualitative criterion which is based on the attempts of more realistic understanding of the observable existing difference between motion in KAM regions and stochastic regions: motion in KAM

regions may be described by regular functions only (without the influence of complicated internal structures leading to nonuniform hyperbolicity generating chaos) while motion in stochastic regions/layers may be described by functions with internal self-similar structures (definitely, created by actions of symmetry generated groups, like discrete groups, or by actions of hidden symmetries of background functional space, like affine group in the most simple case) i.e. fractal type functions as realizations of proper orbits.

So, the difference is fundamental because it is related to different functional spaces in background and different hidden structures inside them. The wavelet analysis (multiresolution technique) approach [2], [3] provides the possibilities for relative analytical description based on calculations of wavelet coefficients/wavelet transform asymptotics.

In part 3, we consider an attempt to the same problem on the more quantitative level. In the constrained variational framework we construct an explicit representation for all dynamical variables as expansions in the base of (nonlinear) periodic high-localized eigenmodes. Such the approach provides, in principle, the possibility for the control of aperture behaviour in the space of machine parameters.

2 Qualitative analysis

The fractal or chaotic image is a function (distribution) which has structure at all underlying scales. Such objects have additional nontrivial details on any level of resolution. But they cannot be represented by smooth functions, because they resemble constants at small scales [2], [3]. We need to find self-similarity behaviour during movement to small scales for the functions describing non-regular motion. So, if we look on a "fractal" function f (e.g. the Weierstrass function) near an arbitrary point at different scales, we find the same function up to the scaling factor. Consider the fluctuations of such function f near some point x_0

$$f_{loc}(x) = f(x_0 + x) - f(x_0), \tag{3}$$

then we have the renormalization (group)–like behaviour/transformation

$$f_{x_0}(\lambda x) \sim \lambda^{\alpha(x_0)} f_{x_0}(x), \tag{4}$$

where $\alpha(x_0)$ is the so-called local scaling exponent or Hölder exponent of the function f at x_0.

According to [3] general functional spaces and scales of spaces can be characterized through wavelet coefficients or wavelet transforms. Let us consider continuous wavelet transform

$$W_g f(b, a) = \int_{R^n} \mathrm{d}x \frac{1}{a^n} \bar{g}\left(\frac{x-b}{a}\right) f(x),$$

$b \in R^n, \quad a > 0$, w.r.t. analyzing wavelet g, which is strictly admissible, i.e.

$$C_{g,g} = \int_0^\infty \frac{\mathrm{d}a}{a} |\hat{g}(\bar{a}\ k)|^2 < \infty.$$

Wavelet transform has the following covariance property under action of the underlying affine group:

$$W_g(\lambda a, x_0 + \lambda b) \sim \lambda^{\alpha(x_0)} W_g(a, x_0 + b). \tag{5}$$

So, if the Hölder exponent of (distribution) $f(x)$ around the point $x = x_0$ is $h(x_0) \in (n, n+1)$, then we have the following behaviour of $f(x)$ around $x = x_0$:

$$f(x) = c_0 + c_1(x - x_0) + \cdots + c_n(x - x_0)^n + c|x - x_0|^{h(x_0)}.$$

Let the analyzing wavelet has n_1 ($> n$) vanishing moments, then

$$W_g(f)(x_0, a) = Ca^{h(x_0)} W_g(f)(x_0, a) \tag{6}$$

and

$$W_g(f)(x_0, a) \sim a^{h(x_0)},$$

when $a \to 0$. But if $f \in C^\infty$ at least in the point x_0, then

$$W_g(f)(x_0, a) \sim a^{n_1},$$

when $a \to 0$. This shows that the localization of wavelet coefficients at small scale is linked to local regularity. As a rule, the faster the wavelet coefficients decay, the more the analyzed function is regular. So, transition from regular motion to chaotic one may be characterised as the changing of the Hölder/scaling exponent of the function which describes motion. This gives a criterion of the appearance of fractal behaviour and may determine, at least in principle, the dynamic aperture.

3 Constrained problem for quasi-periodic orbits

We consider the extension of our approach [4]–[15] to the case of constrained quasi-periodic trajectories. The equations of motion corresponding to (polynomial) Hamiltonian families like (1) may be formulated as a particular case of the general system of ordinary differential equations

$$dx_i/ds = f_i(x_j, s), \quad (i, j = 1, ..., 2n),$$

where f_i are not more than rational functions of dynamical variables x_j and have arbitrary dependence on time but with periodic boundary conditions. Let us consider our set-up as an operator equation for the operator S which satisfies the equation

$$S(H, x, \partial/\partial s, \partial/\partial x, s) = 0, \tag{7}$$

which is polynomial/rational in $x = (x_1, \ \dots \ , x_n, p_1, \ \dots \ , p_n)$ and have arbitrary dependence on s together with the additional operator $C(H, x, \partial/\partial t, \partial/\partial x, s)$, which is an operator describing some constraints, as differential as integral, on the set of dynamical variables. E.g., we may fix a part of non-destroying integrals of motion (e.g., energy) or areas in phase space (fluxes of orbits). So, we may consider our problem as the problem of constructing orbits described by Hamiltonian families like (1), but with needful geometrical-like properties. In this way we may fix a given acceptable aperture or vice versa by feedback via parametrisation of orbits by coefficients of the initial dynamical problem we may control different levels of aperture as a function of the parameters of the system (7) under consideration. As a result, our variational problem is formulated for pair of operators (C, S) on the extended set of dynamical variables, which includes Lagrangian multipliers λ. Then we use the (weak) variation formulation

$$\int < (S + \lambda C)x, y > \mathrm{d}t = 0. \tag{8}$$

We start with a hierarchical sequence of approximations spaces:

$$\dots V_{-2} \subset V_{-1} \subset V_0 \subset V_1 \subset V_2 \dots, \tag{9}$$

and the corresponding expansions:

$$x^N(s) = \sum_{r=1}^{N} a_r \psi_r(s), \qquad y^N(s) = \sum_{k=1}^{N} b_k \psi_k(s). \tag{10}$$

As a result of our approach [4]–[15], we obtain, from (7), the following reduced system of algebraical equations (RSAE) on a set of unknown coefficients a_i of expansions (10), the so-called Generalized Dispersion Relations:

$$L(S_{ij}, C_{kl}, a, \Lambda) = 0, \tag{11}$$

where operator L is algebraization of the initial problem (7) after variational procedure. In addition, in the general situation, we need to find also objects Λ

$$\Lambda^{d_1 d_2 \ldots d_n}_{\ell_1 \ell_2 \ldots \ell_n} = \int_{-\infty}^{\infty} \prod \psi^{d_i}_{\ell_i}(x) \mathrm{d}x. \tag{12}$$

We consider the procedure of their calculations in the case of quasi/periodic boundary conditions in the bases of periodic wavelet functions with periods T_i on the interval [0, T] for the corresponding expansions (10) inside our variational-wavelet approach [4]–[15]. Periodization procedure gives

$$\begin{aligned} \hat{\varphi}_{j,k}(x) &\equiv \sum_{\ell \in Z} \varphi_{j,k}(x - \ell), \\ \hat{\psi}_{j,k}(x) &\equiv \sum_{\ell \in Z} \psi_{j,k}(x - \ell). \end{aligned} \tag{13}$$

So, $\hat{\varphi}, \hat{\psi}$ are periodic functions on the interval [0, T]. Because $\varphi_{j,k} = \varphi_{j,k'}$ if $k = k' \mathrm{mod}(2^j)$, we may consider only $0 \le k \le 2^j$ and as consequence, our generic multiresolution decomposition for the background functional space has the form [16]:

$$\bigcup_{j \ge 0} \hat{V}_j = L^2[0, T]$$

with

$$\hat{V}_j = \mathrm{span}\{\hat{\varphi}_{j,k}\}_{k=0}^{2j-1}.$$

Integration by parts and periodicity give useful relations between the objects (12) in the particular quadratic case ($d = d_1 + d_2$):

$$\begin{aligned} \Lambda^{d_1,d_2}_{k_1,k_2} &= (-1)^{d_1} \Lambda^{0,d_2+d_1}_{k_1,k_2}, \\ \Lambda^{0,d}_{k_1,k_2} &= \Lambda^{0,d}_{0,k_2-k_1} \equiv \Lambda^{d}_{k_2-k_1}. \end{aligned} \tag{14}$$

So, any 2-tuple can be represented by Λ^d_k. Then our second (after (11)) additional algebraic (linear) problem is reduced according to [16] to the eigenvalue problem for $\{\Lambda^d_k\}_{0 \le k \le 2^j}$ by creating a system of 2^j homogeneous relations in Λ^d_k and additional inhomogeneous equations. If we consider generic dilation equation in the form

$$\varphi(x) = \sqrt{2} \sum_{k \in Z} h_k \varphi(2x - k),$$

then we have the following homogeneous relations

$$\Lambda^d_k = 2^d \sum_{m=0}^{N-1} \sum_{\ell=0}^{N-1} h_m h_\ell \Lambda^d_{\ell+2k-m}, \tag{15}$$

or in such a clear form

$$A\lambda^d = 2^d\lambda^d, \qquad \text{where} \qquad \lambda^d = \{\Lambda^d_k\}_{0\le k\le 2^j}.$$

Inhomogeneous equations are:

$$\sum_\ell M^d_\ell \Lambda^d_\ell = d!2^{-j/2}, \tag{16}$$

where objects $M^d_\ell(|\ell| \le N-2)$ can be computed by recursive procedure

$$M^d_\ell = 2^{-j(2d+1)/2}\tilde{M}^d_\ell, \tag{17}$$
$$\tilde{M}^k_\ell =< x^k, \varphi_{0,\ell} >= \sum_{j=0}^{k} \binom{k}{j} n^{k-j} M^j_0, \quad \tilde{M}^\ell_0 = 1.$$

Anyway, all these problems are the standard linear algebraical problems solvable by means of standard routines and it is not a big deal to solve explicitly all that to provide the base for numerical modeling and simulation. Then, we may solve generic Generalized Dispersion Relations, RSAE (11) (what is much more complicated procedure), and determine unknown coefficients of the formal expansion (10) corresponding to multiresolution decomposition of the background functional space. Therefore, in such a manner, we obtain the solution of our initial problem. It should be noted that if we consider only truncated expansion with N terms then we have, from (11), a system of $N \times 2n$ algebraical equations and the degree of this algebraical system coincides with the degree of the initial differential system. As a result, we obtained the following explicit representation for (quasi)periodic orbits/trajectories in the base of periodized (period T_i) localized wavelets (10) (properly chosen accordingly to the background functional space):

$$x_i(s) = x_i(0) + \sum_k a^k_i \psi^i_k(s), \quad x_i(0) = x_i(T_i). \tag{18}$$

Because the affine group of translation and dilations is inside the approach, this method resembles the action of a microscope. We have contributions to the final result from each scale of resolution from the whole infinite scale of spaces. More exactly, the closed subspace $V_j(j \in \mathbf{Z})$ corresponds to the level j of resolution, or to the scale j. The final multiscale/multiresolution representation for solution has the following form

$$x(s) = x^{slow}_N(s) + \sum_{j\ge N} x_j(\omega_j s), \quad \omega_j \sim 2^j, \tag{19}$$

which corresponds to the full multiresolution expansion in all time scales. Formula (19) gives us expansion into the slow part x^{slow}_N and fast oscillating parts (generating out-of-KAM behaviour) for an arbitrary N. So, we may move from coarser scales of resolution to a finer scale for obtaining more detailed information about our dynamical process. The first term in the RHS of the equation (19) corresponds on the global level of the function space decomposition to resolution space and the second one to detail space. In this way we give contributions to our full solution from each scale of resolution or each time scale. On Fig. 1 we present (quasi) periodic regime on the section $x - p_x$ corresponding to the model (1).

So, in such a way, by means of multiresolution decomposition for the explicit solution of the properly/geometrically constrained Hamiltonian set-up we provide analytical background for the dynamical aperture evaluation. Definitely, above we used nothing related to the orthodox perturbation technique.

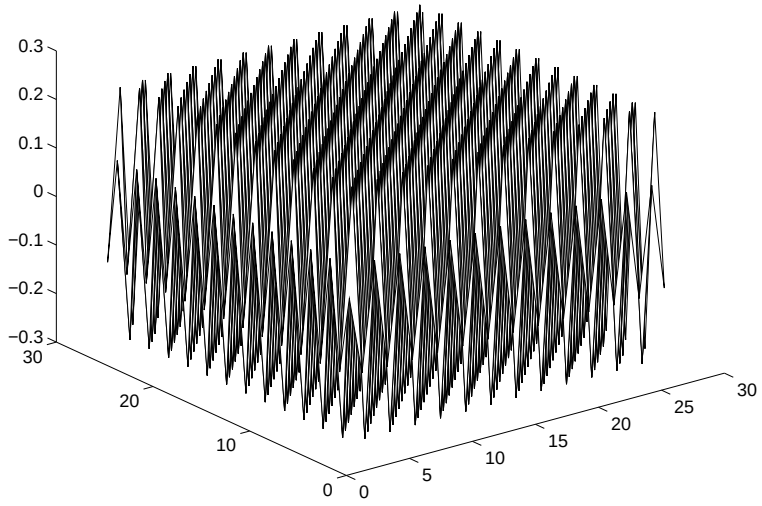

Figure 1: Periodic structure on level 6 of multiresolution.

Acknowledgements

We would like to thank The U.S. Civilian Research & Development Foundation (CRDF) for support (Grants TGP-454, 455), which gave us the possibility to present and discuss this and related results for the first time during PAC Conference, Chicago, IL. We are also grateful to Dr. A.G. Sergeyev for his permanent encouragement.

References

[1] W. Scandale, in CERN-95-06, p. 109, 1995; J. Gao, Los Alamos preprint, physics/0005023; A. Chao, Handbook of Accelerator Physics and Engineering, World Scientific, 1999.

[2] A. Arneodo, in Wavelets, p. 349, Oxford, 1996.

[3] M. Holschneider, Wavelets, Clarendon, 1998.

[4] A.N. Fedorova and M.G. Zeitlin, Wavelets in Optimization and Approximations, *Math. and Comp. in Simulation*, **46**, p. 527, 1998.

[5] A.N. Fedorova and M.G. Zeitlin, Wavelet Approach to Mechanical Problems. Symplectic Group, Symplectic Topology and Symplectic Scales p.31; Wavelet Approach to Polynomial Mechanical Problems, p. 101, in *New Applications of Nonlinear and Chaotic Dynamics in Mechanics*, Ed. F. Moon, Kluwer, 1998.

[6] A.N. Fedorova and M.G. Zeitlin, Nonlinear Dynamics of Accelerator via Wavelet Approach, in **CP405**, p. 87, American Institute of Physics, 1997.
Los Alamos preprint, physics/9710035.

[7] A.N. Fedorova, M.G. Zeitlin and Z. Parsa, Wavelet Approach to Accelerator Problems, parts I, II, III, in Proc. PAC97 **2**, pp. 1502, 1505, 1508, American Physical Society/IEEE, 1998.

[8] A.N. Fedorova, M.G. Zeitlin and Z. Parsa, Nonlinear Effects in Accelerator Physics: from Scale to Scale via Wavelets, p. 930; Wavelet Approach to Hamiltonian, Chaotic and Quantum Calculations in Accelerator Physics, p. 933, in Proc. EPAC98, Institute of Physics, 1998.

[9] A.N. Fedorova, M.G. Zeitlin and Z. Parsa, Variational Approach in Wavelet Framework to Polynomial Approximations of Nonlinear Accelerator Problems, p. 48, in **CP468**, American Institute of Physics, 1999. Los Alamos preprint, physics/990262.

[10] A.N. Fedorova, M.G. Zeitlin and Z. Parsa, Symmetry, Hamiltonian Problems and Wavelets in Accelerator Physics, p. 69, in **CP468**, American Institute of Physics, 1999. Los Alamos preprint, physics/990263.

[11] A.N. Fedorova, M.G. Zeitlin, Nonlinear Accelerator Problems via Wavelets, Parts 1-9, in Proc. PAC99, pp. 1614, 1617, 1620, 2900, 2903, 2906, 2909, 2912, American Institute of Physics/IEEE, New York, 1999. Los Alamos preprints: physics/9904039,physics/9904040, physics/9904041, physics/9904042, physics/9904043, physics/9904045, physics/9904046, physics/9904047.

[12] A.N. Fedorova, M.G. Zeitlin, Variational-Wavelet Approach to RMS Envelope Equations, p. 235, in The Physics of High Brightness Beams, World Scientific, 2000. Los Alamos preprint: physics/0003095.

[13] A.N. Fedorova, M.G. Zeitlin, Spin-Orbital Motion: Symmetry and Dynamics, p. 415; Local Analysis of Nonlinear RMS Envelope Dynamics, p. 872; Multiresolution Representation for Orbital Dynamics in Multipolar Fields, p. 1101; Quasiclassical Calculations in Beam Dynamics, p. 1190; Multiscale Representations for Solutions of Vlasov-Maxwell Equations for Intense Beam Propagation, p. 1339; Nonlinear Beam Dynamics and Effects of Wigglers, p. 2325, in Proc. EPAC00, Austrian Acad. Sci., 2000. Los Alamos preprints: physics/0008045, physics/0008046, physics/0008047, physics/0008048, physics/0008049, physics/0008050.

[14] A.N. Fedorova, M.G. Zeitlin, Multiscale Analysis of RMS Envelope Dynamics, p. 300; Multiresolution Representations for Solutions of Vlasov - Maxwell - Poisson Equations,p. 303, in Proc. 20 International Linac Conf., SLAC, Stanford, 2000. Los Alamos preprints: physics/0008043, physics/0008200.

[15] A.N. Fedorova, M.G. Zeitlin, Localized Coherent Structures and Patterns Formation in Collective Models of Beam Motion, p. 527; Quasiclassical Calculations for Wigner Functions via Multiresolution, p. 539, in Quantum Aspects of Beam Physics, ed. P. Chen, World Scientific, 2002. Los Alamos preprints:physics/0101006, physics/0101007.

[16] G. Schlossnagle,e.a. Technical Report ANL-93/34; Y. Meyer, Wavelets and Operators, CUP, 1990.

Antonina N. Fedorova, Michael G. Zeitlin,
IPME, RAS, V.O. Bolshoj pr., 61, 199178, St. Petersburg, Russia,
http://www.ipme.ru/zeitlin.html, http:/mp.ipme.ru/zeitlin.html

Permafrost defrosting as a result of extractive wells operating

Mikhail Yu. Filimonov Natalia A. Vaganova
fmy@imm.uran.ru

Abstract

On the base of a 3D mathematical model of thermal interaction in a zone of extractive well in permafrost a numbers of effects of wells operating are simulated and investigated. Relative location of multiple wells is considered. Taking into account intensity of sunlight and temperature changing defrosting of the upper layers of the soil is simulated. Effects of heat accumulation under the various versions of platform insulation of the wells zone are investigated.

1 Introduction

In developing the oil and gas fields in a permafrost zone an important objective is to reduce the influence of different heat sources (construction and production wells) on permafrost. The problem of reducing the intensity of the thermal interaction on permafrost is of particular importance for solving problems energy saving, environmental protection, safety, cost savings and improve operational reliability of wells. In the design one should provide both insulation of production wells, and construction of platforms on which these wells located.

On the base of a mathematical model of thermal interaction in the "well–permafrost" [1] we consider processes of freezing (thawing) of permafrost and frozen soils. The effects of permafrost defrosting are particularly relevant for the countries bordering the Arctic.

2 Mathematical model of heat distribution in a well–permafrost system

Let $T = T(t, x, y, z)$ — distribution of temperature for the time moment t, (x, y, z) — a point of a considered domain. The considered domain is a three-dimensional parallelepiped from which a vertical cylindrical well (or wells) is removed. Axes x and y are parallel to the ground surface, and an axis z is inside of the parallelepiped. The materials and soils inside of the parallelepiped may be different in dependence of engineering constructions around the well. Process of heat distribution taking into account phase transition is described by the following heat equation [2]:

$$\rho\big(c_\nu(T) + k\delta(T - T^*)\big)\frac{\partial T}{\partial t} = \operatorname{div}\left(\lambda(T)\operatorname{grad} T\right), \tag{1}$$

where ρ is density $[kg/m^3]$, T^* is temperature of phase transition $[K]$,

$$c_\nu(T) = \begin{cases} c_1, & T < T^*, \\ c_2, & T > T^*, \end{cases} \text{ is specific heat [J/kg K]},$$

$\lambda(T) = \begin{cases} \lambda_1, & T < T^*, \\ \lambda_2, & T > T^*, \end{cases}$ is thermal conductivity coefficient [Wt/m K],

k is a heat of phase transition, δ is the Dirac delta function. Possibility of using this equation to describe the permafrost defrosting in a soil without the explicit separation of the phase boundary is given in [3].

Let in the initial time moment the temperature in the soil is

$$T(0, x, y, z) = T_0(x, y, z). \tag{2}$$

We assume that the coefficients in equation (1) may vary at different points in the computational domain (heterogeneity of soil by layers and possible thermal insulation of the well).

On the surface $z = 0$ the following condition is given:

$$\alpha q + b(T_{air} - T_{z=0}) = \varepsilon\sigma T^4 + \lambda\frac{\partial T}{\partial z}. \tag{3}$$

Thus, the simulation of heat transfer in three-dimensional domain with the phase transition is reduced to solving the initial-boundary value problem (1)–(3). In contrast to the known results on the calculations of permafrost defrosting, in this mathematical model includes not only geometric and thermal insulation characteristics of engineering structures around the well but also various options for thermal insulating the outer surface of the well.

To compute heat distribution by equations (1)–(3) in a three-dimensional domain a finite-difference method with splitting by spatial variables is used. Computations are carried out on orthogonal grid, uniform or adapted by layers and to the well. The basic heat equation is approximated by an economical implicit finite-difference pattern in each of spatial dimensions. System of linear difference equations has a three-diagonal form and may be solved by a sweep method.

3 Defrosting of upper layers of soil

Let consider seasonal thawing (freezing) of the upper layer of the soil. The mathematical model takes into account two basic factors: monthly dependent changes of solar energy reaching surface of the soil and changes of air temperature. Figure 1 shows the averages month of intensity of sunlight and air temperature for the considered region.

The computational domain is a cube with edge of 10 m. Radius of the well is 0.084 m. Oil temperature in the well is 45°C. It is assumed that the well has no insulation. Initial temperature of the soil is $-3°C$ and the soil parameters are shown in Table 1. Let consider the effects of platform insulation of ground surface on the process of thawing.

In Figure 2a the front of thawing from the well is shown for the ground without platform insulation. In Figure 2b a concrete slab (0.3 m.) is on the ground surface. Dynamics of freezing and thawing of soil in compare with the soil without platform insulation almost does not change, although the presence of the concrete slab allows to freez soil deeper in winter.

In Figure 3a platform insulation consists of two layers: a concrete slab and sand layer (1.7 m.). In Figure 3b there are three layers of platform insulation: a concrete slab, a layer of Penoplex (0.06 m) and a layer of sand (1.7 m). Inspite of the fact that Penoplex has good insulation properties and it is designed to prevent expantion of heat into the ground, in August the value of radius of thawing under platform insulation is not reduced (Figure 3b)

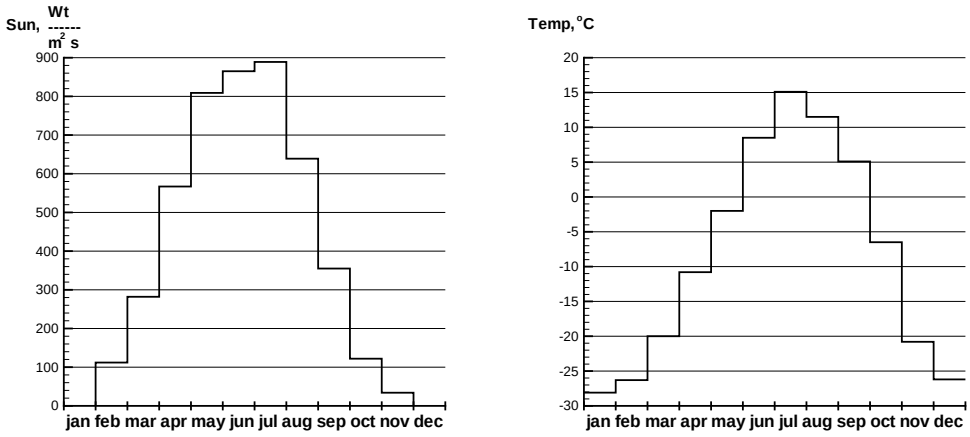

(a) (b)

Figure 1: Intensity of sunlight (a) and average month temperature (b) during the year.

Table 1.

soil humidity 20 %		frozen	melted
Heat conductivity	Wt/m K	2.4	2.2
Volumetric heat	$J/(m^3K)$	$2.2 * 10^6$	$2.7 * 10^6$
Volumetric heat of phase transition	J/m^3	$10.0 * 10^7$	

Table 2.

Parameter	**Units**	**Value**
Concrete (slab thickness of 0.3 m)		
Density	kg/m^3	2500
Heat conductivity	Wt/(m K)	1.69
Specific heat	J/(kg K)	$0.84 * 10^3$
sand (layer thickness 1.7 m)		
Density	kg/m^3	1600
Heat conductivity	Wt/(m K)	0.47
Specific heat	J/(kg K)	$0.84 * 10^3$
penoplex (layer thickness 0.06 m)		
Density	kg/m^3	80
Heat conductivity	Wt/(m K)	0.031
Specific heat	J/(kg K)	$1.53 * 10^3$

in compare with platform insulation with no Penoplex (Figure 3a), but increased by 6% due to the effect of accumulation of heat from the well. Thus, using Penoplex for platform insulation is inefficiently.

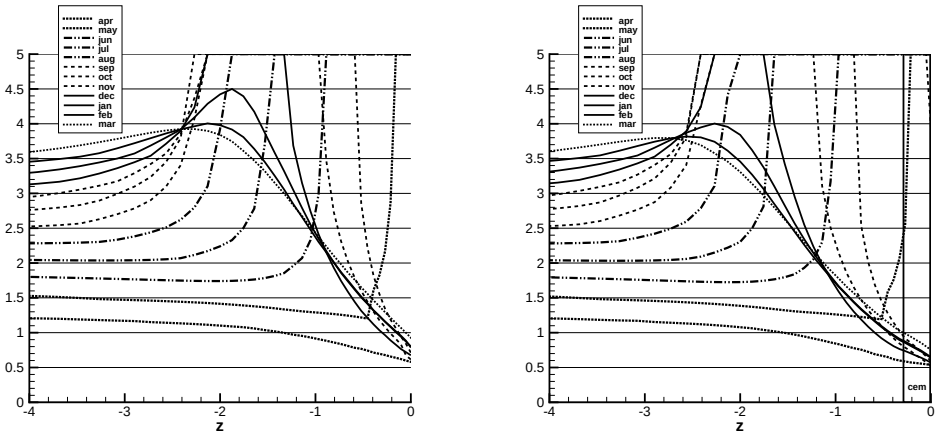

(a) (b)

Figure 2: 0°C isotherm movement during the year: (a) — no insulation of the ground surface; (b) — insulation by a concrete slab (cem).

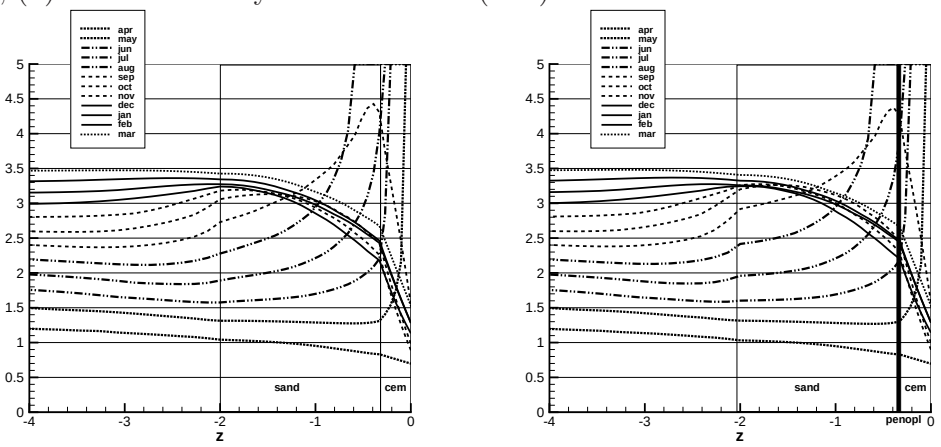

(a) (b)

Figure 3: 0°C isotherm movement during the year: (a) — insulation by a concrete slab (cem) and sand layer (1.7 m); (b) — insulation by a concrete slab (cem), penoplex (0.06 m) and sand layer (1.7 m).

For insulation of the ground surface materials presented in Table 2 will be used.
Figures 2 and 3 show the dynamics of soil thawing front (isotherm of 0°C) from wells for different variants of platform insulation. It is assumed that the snow cover is absent. The abscissa is the depth by z-axis, it is shown a surface layer up to 4 m. The movement of the thawing front is presented during the year by month. Beginning in March, the soil thawing front moves from the surface and reaches its maximum depth by August or September, then there is freezing, which reaches a maximum by February. In addition, the heated well, the center of which coincides with the horizontal axis, generates another front of thawing, which interacts with the front of thawing from the ground surface.

4 Thermal interaction of 3 wells

Let consider the thermal effect of multiple wells on each other. In the calculation 3 wells are located at a distance of 10 m. and 20 m. The radius of each well is 0.084 m., temperature is 40°C, there are no thermal insulation. Parameters of the computational domain are presented in Table 3.

Table 3.

Parameter	**x**	**y**	**z**
Size of area, m	50	50	40
Number of points	101	101	101
soil (top layer to 10 m.)		**frozen**	**melted**
Heat conductivity	Wt/m K	2.4	2.2
Volumetric heat	$J/(m^3K)$	$2.2 * 10^6$	$2.7 * 10^6$
Volumetric heat of phase transition	J/m^3	$10.0 * 10^7$	
soil (bottom layer after 10 m)			
Heat conductivity	Wt/m K	2.5	2.3
Volumetric heat	$J/(m^3K)$	$2.25 * 10^6$	$2.6 * 10^6$
Volumetric heat of phase transition	J/m^3	$10.4 * 10^7$	

Figures 4 and 5 show the temperature distribution in the plane (z, x) from three wells in 10 years after the start of their operation. The basic areas: the temperature is below than -0.5°C (white), from -0.5 to 0°C, from 0 to 0.5°C and above than 0.5°C(gray).

In Figure 4a effect of two closely spaced wells are shown: thermal boundaries are more diffuse. In Figure 4b, these boundaries are merged. In Figure 5a zone of defrosted soil between of two close wells is completely fused except for layer of seasonal freezing of soil near the surface. In Figure 5b zone of freezing near the surface becomes smaller. Furthermore, in Figure 5b the influence of conditions at the lateral boundaries is present, and to calculate for a longer period of time it is necessary to choose large computational domain.

Thus, the developed program complex allows to carry out a series of computational experiments which allow to make the long-term forecasts of permafrost defrosting in the presence of a heat source (well and engineering constructions) taking into account the annual cycle of thawing/freezing upper layers of soil under the influence of seasonal changes in air temperature and intensity of sunlight. The results of numerical simulation allow experts to examine and make recommendations for thermal insulation and placement of wells on working platform.

Acknowledgements

This work is partially supported by Russian Foundation for Basic Research – URAL 10–08–96014.

References

[1] M. Yu. Filimonov, A. G. Kravets, N. A. Vaganova. Simulation of thermal interaction in a zone of extractive well in permafrost. Proc. of APM-2010. Pp 220–224.

[2] A. A. Samarsky, B .D. Moiseenko. ZhVMiMF, **5**, 5 1965.

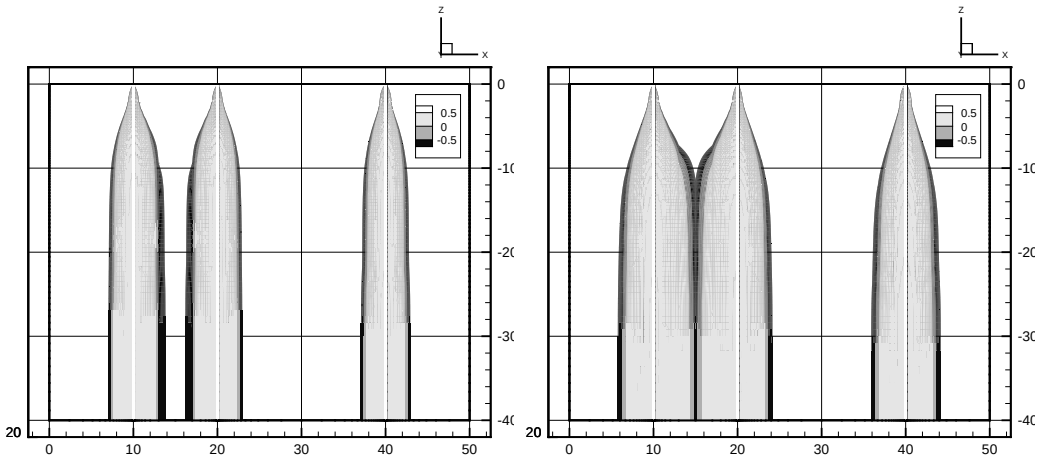

(a) (b)

Figure 4: Temperature (°C) arount the wells: (a) — 1 year; (b) — 2 years.

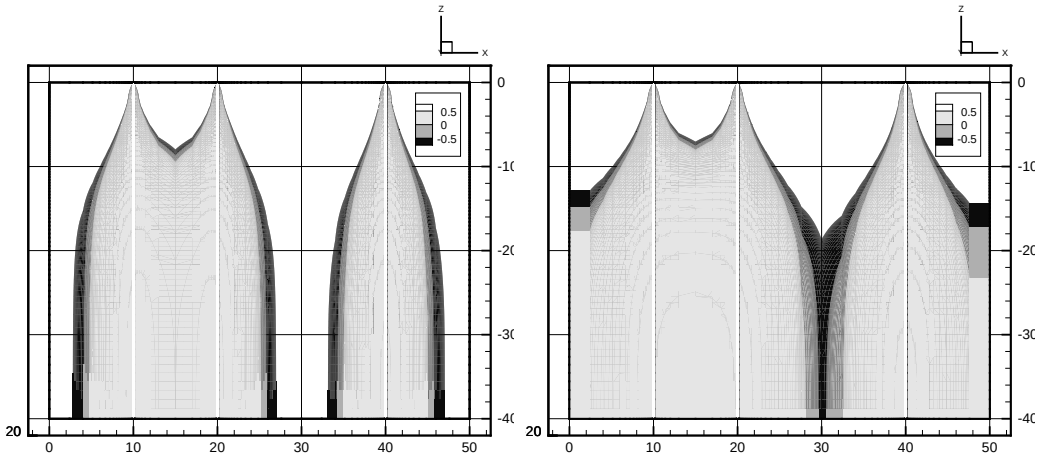

(a) (b)

Figure 5: Temperature (°C) arount the wells: (a) — 5 years; (b) — 10 years.

[3] A. A. Samarsky, P .N. Vabishchevich. Computational Heat Transfer. M.: Editorial URSS, 2003.

Mikhail Yu. Filimonov
Institute of Mathematics and Mechanics UrB RAS, S. Kovalevskaya str. 16, Ekaterinburg, 620990, Russia

On transition layers in nanocomposites as new phase areas

Roman A. Filippov Alexander B. Freidin Elena N. Vilchevskaya
rmnfilippov@gmail.com, alexander.freidin@gmail.com, vilchevska@gmail.com

Abstract

We study an opportunity to change elastic moduli of a nanocomposite due to stress induced phase transformations which lead to the formation of intermediate new phase layers around nanoparticles. These layers enlarges the effective size of the particles which from now become kernels (the initial nanoparticles) enclosed by transition layers shells. As a result the effective volume fraction of particles increases. This in turn can change the effective elastic moduli of the composite much more than one could expect in a case of the composite with a small volume fraction of initial nanoparticles. As an example we consider a case of spherical particles. First, we study the new phase formation around an isolated inclusion including the stability analysis. We are interested in a case of the elastic moduli growth and show that the stable two-phase states are possible if the bulk modulus increases due to the phase transformation. Then, basing on a self-consistent (the effective field) approach, we describe the new phase formation around spatially distributed particles and study how the external strain effects the new phase areas growth. Finally we demonstrate that the new phase layers formation can lead to increasing the effective bulk modulus of the composite.

1 Introduction

Carbon nanotube and fulleren reinforced nanocomposites have received increased attention in recent years because of their mechanical, electrical, optical and magnetoelectrical properties [4, 12, 11]. One of the surprising fact is that a small volume fraction of nanoinclusions may lead to significant effects, which cannot be predicted by usual mathematical model of composite materials. In a number of papers (see, e.g., [4, 1]) it was suggested that these effects may be related to the quality of the boundaries, which separate the inclusions and matrix. Note that classical theories of composite material consider ideal contacts at the boundaries and even in this case do not give the effects declared.

To explain how a small volume fraction of inclusions may lead to disproportionately significant changes of mechanical properties of nanocomposites we suppose that this may be a result of the formation of intermediate layers surrounding the particles. This increases the "effective" size of the particles and, thus, effective volume concentration of inclusions.

To simplify the consideration and obtain result, which can be more or less easily verified, we consider a composite with isotropic spherical inclusions in isotropic matrix. This gives us a foreseeable script of general consideration and analytical basement for further verifications of numerical simulations.

In the case of spherical inclusions stress-induced phase transformations can be induced by thermal stresses, because of difference between thermal expansion coefficients of the matrix and inclusions or/and by external all-round compression/tension. In fact, new phase areas can be formed around inclusions under combined thermo-mechanical actions at the stage of the composite production.

Since from the mathematical point of view thermal stresses can be reduced to stresses produced by mechanical loading, we consider further only all-round tension/compression.

The following questions are being discussed within the elementary problem:

1. Is it possible to form the stable transition layers of a new phase if the elastic moduli increase?

2. How much can we control the growth of effective elastic moduli as a result of the formation of two-phase equilibrium states?

3. Is it possible to reduce stress concentration in the matrix due to the formation of new phase transition layers?

2 Constitutive equations

We consider stress-induced phase transformations of martensite type accompanied by the transformation strain and changes of elastic moduli. Let new phase areas V_+ be bounded by interfaces Γ. A problem on the equilibrium two-phase configurations of an elastic body is reduced to the determination of Γ and displacement $\mathbf{u}(\mathbf{x})$ sufficiently smooth at material points $\mathbf{x} \notin \Gamma$, continuous across Γ, and satisfying equilibrium and boundary conditions, including conditions on the interface:

$$\mathbf{x} \notin \Gamma \quad : \qquad \nabla \cdot \boldsymbol{\sigma} = 0, \quad \theta = \text{const}, \tag{1}$$

$$\mathbf{x} \in \Gamma \quad : \qquad [\mathbf{u}] = 0, \quad [\boldsymbol{\sigma}] \cdot \mathbf{n} = 0, \tag{2}$$

$$[f] - \langle \boldsymbol{\sigma} \rangle : [\boldsymbol{\varepsilon}] = 0, \quad \langle \boldsymbol{\sigma} \rangle = \frac{1}{2}(\boldsymbol{\sigma}_+ + \boldsymbol{\sigma}_-) \tag{3}$$

where $\boldsymbol{\varepsilon}$ and $\boldsymbol{\sigma}$ are strain and stress tensors, θ is the temperature, $f = f(\boldsymbol{\varepsilon}, \theta)$ is the Helmholtz free energy density, $\mathbf{n}$ is the unit normal to the interface Γ, super- or subscripts "$-$" and "$+$" identify the values being taken for a material in the "$-$" and "$+$" phase states, respectively, the brackets $[\cdot] = (\cdot)_+ - (\cdot)_-$ denote the jump across Γ, $\langle \boldsymbol{\sigma} \rangle : [\boldsymbol{\varepsilon}] = \boldsymbol{\sigma}_\pm : [\boldsymbol{\varepsilon}]$. Body forces, thermoelastic effects and surface energy are not taken into account.

The thermodynamic equilibrium condition (3) imposes the restrictions on the possibility of the existence of new phase areas and their geometry.

We consider a two-well strain-energy function:

$$f(\boldsymbol{\varepsilon}, \theta) = \min_{-,+} \left\{ f^-(\boldsymbol{\varepsilon}, \theta), f^+(\boldsymbol{\varepsilon}, \theta) \right\}, \tag{4}$$

$$f^\pm(\boldsymbol{\varepsilon}, \theta) = f_0^\pm(\theta) + \frac{1}{2}(\boldsymbol{\varepsilon} - \boldsymbol{\varepsilon}_\pm^p) : \mathbf{C}_\pm : (\boldsymbol{\varepsilon} - \boldsymbol{\varepsilon}_\pm^p).$$

Upper and lower scripts "$+$" and "$-$" in relationships correspond to each other. 1D-sketch of free energy dependence is shown in Fig. 1.

The constitutive relations take the form:

$$\boldsymbol{\sigma}_\pm(\boldsymbol{\varepsilon}) = \mathbf{C}_\pm : (\boldsymbol{\varepsilon} - \boldsymbol{\varepsilon}_\pm^p), \quad \boldsymbol{\varepsilon} \in \mathcal{E}_\pm \tag{5}$$

where $\mathcal{E}_\mp$

$$\mathcal{E}_- = \{\boldsymbol{\varepsilon} : \ \varphi(\boldsymbol{\varepsilon}) > 0\}, \quad \mathcal{E}_+ = \{\boldsymbol{\varepsilon} : \ \varphi(\boldsymbol{\varepsilon}) < 0\}, \quad \varphi(\boldsymbol{\varepsilon}) = f^+(\boldsymbol{\varepsilon}) - f^-(\boldsymbol{\varepsilon})$$

are the domains of definition of the phases "$-$" and "$+$" in strain space.

The parameters $\mathbf{C}_\pm$, $f_0^\pm$ and $\boldsymbol{\varepsilon}_\pm^p$ are the elasticity tensors, free energy densities and strain tensors in unstressed phases "$\pm$", respectively. If $\boldsymbol{\varepsilon}_+^p = 0$ or $\boldsymbol{\varepsilon}_-^p = 0$, then $[\boldsymbol{\varepsilon}^p] \equiv \boldsymbol{\varepsilon}^p$ is the transformation eigenstrain.

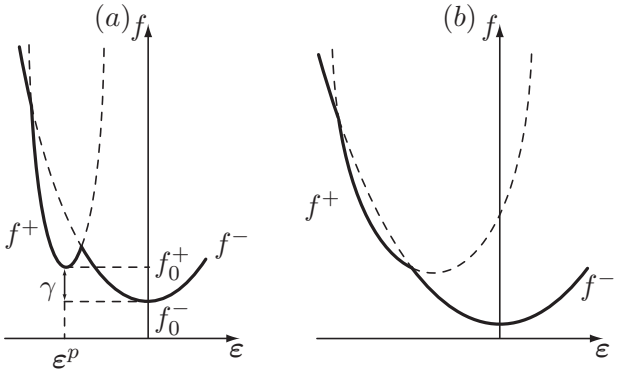

Figure 1: Free energy (a) –case I, (b) –case II

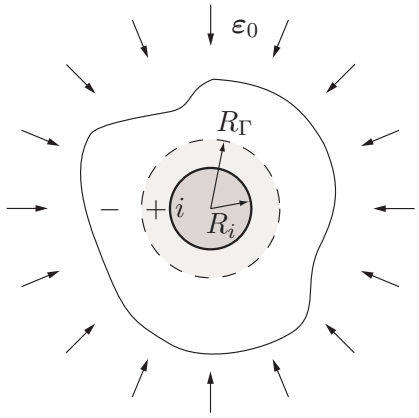

Figure 2: Two-phase matrix with the inclusion

We emphasize that one of the unstressed states can be only hypothetical – deformation $\boldsymbol{\varepsilon} = \boldsymbol{\varepsilon}^p_+$ belongs to the domain of the phase "−", not "+"-phase if $f^+(\boldsymbol{\varepsilon}^p_+) > f^-(\boldsymbol{\varepsilon}^p_+)$. Further, we say that we are dealing with the case I if $f^+(\boldsymbol{\varepsilon}^p_+) < f^-(\boldsymbol{\varepsilon}^p_+)$ (Fig. 1 (a)) and with the case II, if $f^+(\boldsymbol{\varepsilon}^p_+) > f^-(\boldsymbol{\varepsilon}^p_+)$ (Fig. 1 (b)).

If $\mathbf{C}_1^{-1}$ is nonsingular, (3) can be rewritten in terms of $\mathbf{q}$ taken on one side of the interface [10]:

$$\chi(\mathbf{q}_\pm, \gamma_*, \mathbf{n}) \triangleq \gamma_* + \frac{1}{2}\,\mathbf{q}_\pm : \left(\mathbf{C}_1^{-1} \pm \mathbf{K}_\mp(\mathbf{n})\right) : \mathbf{q}_\pm = 0 \tag{6}$$

where

$$\mathbf{q}_\pm = -\mathbf{C}_1 : \boldsymbol{\varepsilon}_\pm + [\mathbf{C} : \boldsymbol{\varepsilon}^p], \quad \gamma_* \triangleq \gamma + \frac{1}{2}\,[\boldsymbol{\varepsilon}^p] : \mathbf{B}_1^{-1} : [\boldsymbol{\varepsilon}^p], \quad \mathbf{B}_1 = \mathbf{C}_+^{-1} - \mathbf{C}_-^{-1} \tag{7}$$
$$\mathbf{K}_\mp(\mathbf{n}) = \{\mathbf{n} \otimes \mathbf{G}_\mp(\mathbf{n}) \otimes \mathbf{n}\}^s, \quad \mathbf{G}_\mp(\mathbf{n}) = (\mathbf{n} \cdot \mathbf{C}_\mp \cdot \mathbf{n})^{-1}, \mathbf{C}_1 = \mathbf{C}_+ - \mathbf{C}_-$$

Thermodynamic condition (6) cannot be satisfied for all strains. This leads to the concept of phase transitions zones (PTZs) [9] – areas formed in the space of deformations by all strains that may exist in the body at the equilibrium phase boundaries; in other words, strains, for which the equation (6) can be solved with respect to the unit normal $\mathbf{n}$. PTZs presents all possible local orientations of the equilibrium phase boundaries and strain jumps at the boundaries for given parameters of material and parameter γ. PTZ is the passport of material undergoes a phase transition (see, e.g.[9, 3]). In this paper, the construction of PTZs is used to reject the equilibrium, but unstable solutions.

Further we consider a matrix that can undergo phase transformations and inclusions, which act as stress concentrators and induce phase transformation. The material of the matrix is piece-wise linear elastic described by the constitutive equations (4), (5). Material of the inclusion is also linear-elastic, its free energy density is given by the dependence

$$f_i\,(\boldsymbol{\varepsilon}) = \frac{1}{2}\boldsymbol{\varepsilon} : \mathbf{C}_i : \boldsymbol{\varepsilon} \tag{8}$$

3 Spherically-symmetric two-phase deformations induced by a spherical inclusion

We consider an unbounded matrix with a spherical inclusion V_i of the radius R_i under allround tension/compression. Let $\boldsymbol{\varepsilon}^p_- = 0$, $\boldsymbol{\varepsilon}^p_+ = \boldsymbol{\varepsilon}^p = (\theta^p/3)\mathbf{E}$, $\boldsymbol{\varepsilon}_0 = (\theta_0/3)\mathbf{E}$ be external

strain. Suppose that there exist a two-phase deformation with one spherical interface (Fig. 2), and find the equilibrium interface radius R_Γ in dependence of external strain and material parameters.

Radial displacement u in areas V_i, V_+, V_- is given by Lame formula,

$$u = Ar + \frac{D}{r^2} \tag{9}$$

where dependencies of $A = \{A_i, A_+, A_-\}$ and $D = \{D_i, D_+, D_-\}$ on $\boldsymbol{\varepsilon}_0$ and the inverse relative interface radius

$$\rho = \frac{R_i}{R_\Gamma}, \quad \rho \in [0,1]$$

can be found from the conditions

$$r = R_i,\ r = R_\Gamma : \quad [u] = 0, \quad [\sigma_r] = 0$$

$$\varepsilon_r \mid_{r\to\infty} = \theta_0/3 \equiv \varepsilon_0, \quad u \mid_{r=0} < \infty,$$

σ_r, ε_r, ε_φ are stress and strains in spherical coordinates.

It can be shown that

$$\begin{aligned}
&A_i = A_i^\varepsilon \varepsilon_0 + A_i^\vartheta, \quad D_i = 0, \quad A_i^\varepsilon = \frac{d_+^+ d_-^-}{Z}, \quad A_i^\vartheta = \frac{4\mu_1(1-z)t}{Z} \\
&A_- = \varepsilon_0, \quad \frac{D_-}{R_\Gamma^3} \equiv \widehat{D}_- = D_-^\varepsilon \varepsilon_0 + D_-^\vartheta \\
&D_-^\varepsilon = \frac{3(d_-^+ k_{1i}^+ z - d_i^+ k_1)}{Z}, \quad D_-^\vartheta = \frac{d_i^+(1-z)t}{Z} \\
&A_+ = A_+^\varepsilon \varepsilon_0 + A_+^\vartheta, \quad A_+^\varepsilon = \frac{d_i^+ d_-^-}{Z}, \quad A_+^\vartheta = \frac{(d_i^+ - 4\mu_1 z)t}{Z} \\
&\frac{D_+}{R_i^3} \equiv \widehat{D}_+ = D_+^\varepsilon \varepsilon_0 + D_+^\vartheta, \quad D_+^\varepsilon = \frac{3d_-^- k_{1i}^+}{Z}, \quad D_+^\vartheta = -\frac{d_i^- t}{Z} \\
&Z = d_i^+ d_+^- - 12\mu_1 k_{1i}^+ z \\
&z = \rho^3,\ k_1 = k_+ - k_-,\ k_{1i}^+ = k_+ - k_i,\ \mu_1 = \mu_+ - \mu_-,\ t = k_+ \vartheta^p \\
&d_\pm^+ = 3k_\pm + 4\mu_+,\ d_\pm^- = 3k_\pm + 4\mu_-,\ d_i^\pm = 3k_i + 4\mu_\pm
\end{aligned} \tag{10}$$

Given material parameters, the dependence of the interface radius on external strain ε_0 is determined by the thermodynamic condition (6) that takes the form

$$\begin{aligned}
&2\gamma_* + \frac{3\Big(t - 3k_1 A_+ + 4\mu_1 z \widehat{D}_+\Big)^2}{d_-^-} + \frac{(t - 3k_1 A_+)^2}{k_1} + 12\mu_1 z^2 \widehat{D}_+^2 = 0 \\
&\gamma_* = \gamma - \frac{k_- k_+ (\vartheta^p)^2}{2k_1}
\end{aligned} \tag{11}$$

The equation (11) gives dependence of the inverse relative equilibrium interface radius ρ^* on ε_0.

New phase nucleation starts at the initial inclusion boundary at $\varepsilon_0 = \varepsilon_{0S}$, the value ε_{0S} can be found from (11) if substitute $\rho = 1$ into formulae for D_+ and A_+. The whole matrix transforms to the phase state "+" at $\varepsilon_0 = \varepsilon_{0F}$, the value ε_{0F} corresponds to $\rho = 0$.

4 Energy changes due to new phase areas growth and stability with respect to interface radius perturbations

The interaction energy is determined as

$$E_\rho = \Pi_\rho - \Pi_- \tag{12}$$

where Π_ρ and Π_- are Gibbs free energy of a body with an inclusion embedded into two-phase matrix with the interface radius ρ, and Gibbs free energy of a body with an inclusion embedded into one-phase matrix in a "$-$" phase state, correspondingly, at the same boundary conditions.

In the case under consideration

$$E_\rho = \int_{V_i} (f_i(\boldsymbol{\varepsilon}_\rho) - f_i(\boldsymbol{\varepsilon}_i^0))\, dV + \int_{V_+} (f_+(\boldsymbol{\varepsilon}_\rho) - f_-(\boldsymbol{\varepsilon}_-^0))\, dV + \int_{V_-} (f_-(\boldsymbol{\varepsilon}_\rho) - f_-(\boldsymbol{\varepsilon}_-^0))\, dV$$

where $\boldsymbol{\varepsilon}_\rho$ is a strain field in a body with a two-phase matrix. $\boldsymbol{\varepsilon}_i^0$ is a strain inside the inclusion when the matrix is in a "$-$" phase state, $\boldsymbol{\varepsilon}_-^0$ is a strain in one-phase matrix in a "$-$" phase state.

Following [2] we note that from (4) (8) it follows that

$$\frac{E}{4\pi R_i^3} = \left(\gamma + \frac{1}{2}t(\vartheta^p - 3\boldsymbol{\varepsilon}_0) + \frac{3}{2}(3k_1\boldsymbol{\varepsilon}_0 - t)A_+\right)\frac{1-z}{3z} + 2\mu_1\widehat{D}_+\widehat{D}_-^0(1-z),$$

$$\widehat{D}_-^0 = \frac{D_-^0}{R_i^3}, D_-^0 = \frac{3\varepsilon_0(k_- - k_i)R_i^3}{3k_i + 4\mu_-}$$

Examples of the dependencies of the interaction energy on the interface radius are given in Fig. 3b1 (case I) and Fig. 3b2 (case II) ($\mu_- > \mu_+$). Minimum points in Fig. 3b1,b2 demonstrate that the equilibrium solutions are stable with respect to interface radius perturbations if $\mu_- > \mu_+$. If $\mu_- < \mu_+$ then similar calculations show that the dependence of the interaction energy has a maximum at the equilibrium radius of a spherical layer of a new phase, which means instability of the interface. Therefore, we discuss in detail phase transformation, resulting in the shear modulus decreases, but the bulk modulus increases.

Thus, we can talk about origin of a new phase stable region around the inhomogeneity only if the shear modulus of the new phase is less than the shear modulus of the initial phase ($\mu_+ < \mu_-$). At the same time stable homogeneous spherical region of a new phase with the full extension – compression of a homogeneous material is possible only if $\mu_+ > \mu_-$ [5]. Therefore, depending on the ratio of shear moduli of the phases, two types of new phase growth are available: if $\mu_+ < \mu_-$ – new phase can only grow around inhomogeneities, if $\mu_+ > \mu_-$ – new phase grows in the areas of homogeneous material.

5 Free energy density spatial re-distribution and release due to phase transformations

Two-phase deformations are always accompanied with some stress concentration at the interface. To clarify why two-phase deformation can be preferential from the energy point of view we study free energy distribution and redistribution in a body.

Fig. 3 (c1) and (c2) shows the spatial distributions of the difference $\psi(r)$ between free energy density in an equilibrium two-phase state of a matrix with embedded inclusion and

free energy density in one-phase matrix with embedded inclusion for the cases I and II,

$$\psi(r) = \begin{cases} f_i(\boldsymbol{\varepsilon}_\rho) - f_i(\boldsymbol{\varepsilon}_i^0), & 0 < r < R_i \\ f_-(\boldsymbol{\varepsilon}_\rho) - f_-(\boldsymbol{\varepsilon}_-^0), & R_i < r < R_\Gamma \\ f_+(\boldsymbol{\varepsilon}_\rho) - f_-(\boldsymbol{\varepsilon}_-^0), & r > R_\Gamma \end{cases}$$

Negative values of $\psi(r)$ means local energy release due to equilibrium new phase zone formation around the inclusion. We emphasize that the energy release in the vicinity of the inclusion means the reduction of the stress concentration and, thus, may be considered as a reinforcing factor.

If the bulk modulus increases, while the shear modulus decreases, the phase boundaries remains stable with respect to perturbations of radius, as seen from Fig. 3($b1$), ($b2$). But when reaching some radius become unstable with respect to axisymmetric perturbations. It shows additional analysis of the stability of equilibrium centrally symmetric solutions with respect to axisymmetric perturbations. A comparison of stability with respect to axisymmetric perturbations with PTZ shows, that for save stability, it is necessary that the strain at the interface belongs to the outer boundaries of the PTZs. In the case of spherical symmetry under hydrostatic loading, this means that it is necessary that

$$(\varepsilon_\theta^- - \varepsilon_r^-)\,|_\Gamma > 0$$

Range of external deformations is determined in which two-phase structure remain stable. The effective elastic moduli of the composite are calculated for this range.

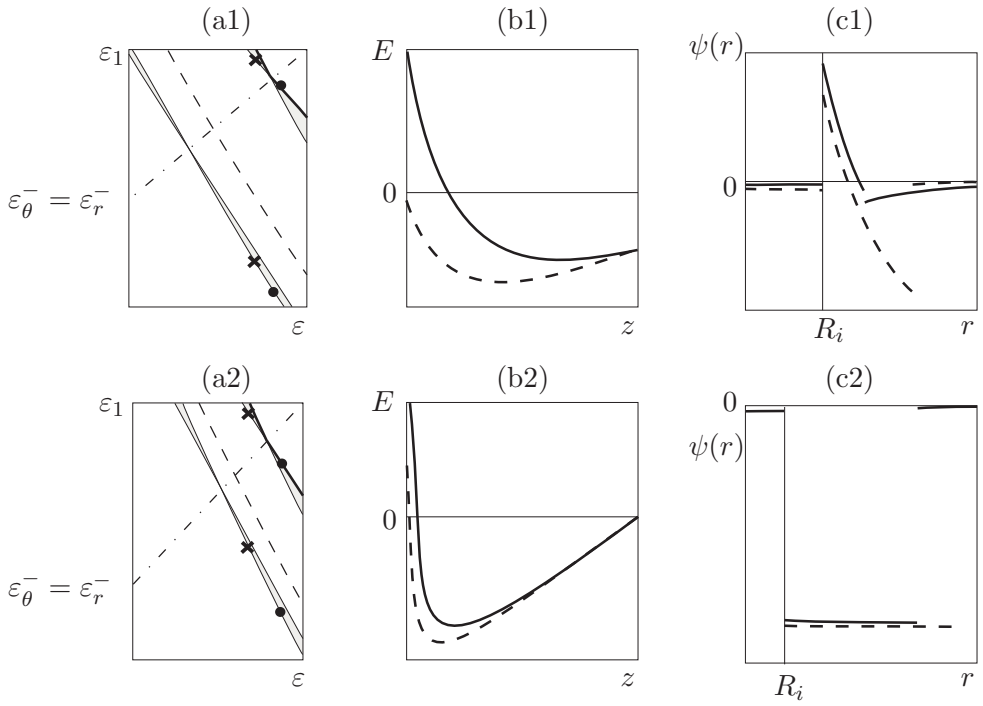

Figure 3: (a1) – PTZ for case I, (b1) – interaction energy $E(z)$ for case I, (c1) – free energy density $\psi(r)$ for case I;
(a2) – PTZ for case II, (b2) – interaction energy $E(z)$ for case II, (c2) – free energy density $\psi(r)$ for case II.

The results of analysis carried out below the equilibrium two-phase configurations for the cases I and II on Fig. 3. The results for two values of the external deformation

$\varepsilon_0 = \varepsilon_{01}$ and $\varepsilon_0 = \varepsilon_{02}$ shows, $\varepsilon_{02} < \varepsilon_{01} < 0$. Values ε_{01} and ε_{02} are chosen so that the deformations at the interface corresponding ε_{01} (point on Fig. 3 $(a1)$, $(a2)$; solid lines on the curves of interaction energy E from the radius of the interface Fig. 3 $(b1)$, $(b2)$ and the spatial distributions of the free energy density $\psi(r)$ Fig. 3 $(c1)$, $(c2)$) are located at the external borders of PTZs. In case $\varepsilon_0 = \varepsilon_{02}$ (crosses on Fig. 3 $(a1)$, $(a2)$; dotted lines on the curves of interaction energy E from the radius of the interface Fig. 3 $(b1)$, $(b2)$ and the spatial distributions of the free energy density $\psi(r)$ Fig. 3 $(c1)$, $(c2)$), one of the deformations is located on internal borders of PTZs.

Straightforward calculations show that the transformation range $|\varepsilon^f - \varepsilon^s|$ is larger in case II, that is, if the value $\gamma(\theta)$ chosen that $f^+(\boldsymbol{\varepsilon}^p) > f^-(\boldsymbol{\varepsilon}^p)$. Comparison case I and II shows that case II is more preferable for reset the energy of deformations.

6 Composites with a matrix undergoing phase transformations induced by interacting inclusions

Our goal is to design a composite with variable structure. We consider a composite material with spherical inclusions. As in previous sections, the material of matrix can undergo phase transformations. The constitutive relationships of the material of the matrix and inclusions are the same as in a case of isolated inclusion, (4) and (8), correspondingly.

We consider a composite material under allround tension/compression. Following self-consistent method [6], every inclusion in the composite is considered as an isolated one embedded into the homogeneous medium with elastic properties $\mathbf{C}_-$ of the matrix. Existence of other inhomogeneities is taken into account by the effective exciting field acting on this inclusion. The effective exciting field of strain $\boldsymbol{\varepsilon}^*$ is the sum of the external field $\boldsymbol{\varepsilon}^0$ applied to the medium and the fields induced by surrounding inclusions. We use the simplest version of the method, the effective field is taken as constant and the same for all the inclusions.

The details of the method are given in [6]. Following [6], we start with the integral equilibrium equation in a form

$$\begin{aligned}
&\boldsymbol{\varepsilon}(\mathbf{x}) = \boldsymbol{\varepsilon}_0 + \int \mathbf{K}_-(\mathbf{x}-\mathbf{x}') : \mathbf{q}(\mathbf{x}')V(\mathbf{x}')\,dV', \qquad (13)\\
&\boldsymbol{\sigma}(\mathbf{x}) = \boldsymbol{\sigma}_0 + \int \mathbf{S}_-(\mathbf{x}-\mathbf{x}') : \mathbf{m}(\mathbf{x}')V(\mathbf{x}')\,dV',\\
&\mathbf{K}_-(\mathbf{x}) = -\left(\nabla \otimes \mathbf{G}_-(\mathbf{x}) \otimes \nabla\right)^s, \qquad \mathbf{S}_-(\mathbf{x}) = \mathbf{C}_- : \mathbf{K}_-(\mathbf{x}) : \mathbf{C}_- - \mathbf{C}_-\delta(\mathbf{x})
\end{aligned}$$

where x is a point of a body, V is a areas occupied by all complex inclusions $V = V_i \cup V_+$, $\mathbf{K}(x)$ is the Green tensor for strains, $\mathbf{G}_-(\mathbf{x})$ – is the Green tensor for displacement, $\delta(\mathbf{x})$ – delta-function, $\boldsymbol{\sigma}_0 = \mathbf{C}_- : \boldsymbol{\varepsilon}^0$ – external stress.

$$\mathbf{q}(\mathbf{x}) = \begin{cases} -\mathbf{C}_1 : \boldsymbol{\varepsilon}(\mathbf{x}) + \mathbf{C}_+ : \boldsymbol{\varepsilon}^p & \mathbf{x} \in V_+, \\ -\left(\mathbf{C}_i - \mathbf{C}_-\right) : \boldsymbol{\varepsilon}(\mathbf{x}) & \mathbf{x} \in V_i, \end{cases},$$

$$\mathbf{m}(\mathbf{x}) = \mathbf{B}_- : \mathbf{q}(\mathbf{x}) = \begin{cases} \mathbf{B}_1 : \boldsymbol{\sigma}(\mathbf{x}) + \boldsymbol{\varepsilon}^p & \mathbf{x} \in V_+, \\ \left(\mathbf{B}_i - \mathbf{B}_-\right) : \boldsymbol{\sigma}(\mathbf{x}) & \mathbf{x} \in V_i, \end{cases}$$

Let $V_x(\mathbf{x}')$ – characteristic function of inclusion V_x, contains $\mathbf{x}$. Then characteristic function

$$V(\mathbf{x}, \mathbf{x}') = V(\mathbf{x}') - V_x(\mathbf{x}')$$

exclude inclusion V_x from set of inclusions. Equation (13) transforms to

$$\boldsymbol{\varepsilon}(\mathbf{x}) = \boldsymbol{\varepsilon}_{ex}(\mathbf{x}) + \int \mathbf{K}_-(\mathbf{x}-\mathbf{x}') : \mathbf{q}(\mathbf{x}')V_x(\mathbf{x}')\,dV', \tag{14}$$

where

$$\boldsymbol{\varepsilon}_{ex}(\mathbf{x}) = \boldsymbol{\varepsilon}_0 + \int \mathbf{K}_-(\mathbf{x}-\mathbf{x}') : \mathbf{q}(\mathbf{x}')V(\mathbf{x},\mathbf{x}')\,dV' \tag{15}$$

may consider as local external field act at inclusion V_x.

For the constant $\boldsymbol{\varepsilon}^*$, the solution of equation (14) for the field inside inclusion is presented in the form $\boldsymbol{\varepsilon}(\mathbf{x}) = \boldsymbol{\Lambda}_*(\mathbf{x}) : \boldsymbol{\varepsilon}_*(\mathbf{x}) + \hat{\boldsymbol{\varepsilon}}^p$, where $\boldsymbol{\Lambda}_*(\mathbf{x})$ – fourth-rank tensor depends on the elastic properties and the form of the inclusion. $\hat{\boldsymbol{\varepsilon}}^p$ is the tensor of disturbance deformation associated with eigestrain of phase transition. $\boldsymbol{\Lambda}_*(\mathbf{x})$ and $\hat{\boldsymbol{\varepsilon}}^p$ may be found from solution of isolated complex inclusion in matrix with $\mathbf{C}_-$ in the effective field.

If we average equation (15) under the condition that $\mathbf{x} \in V$ and identify the mean $\langle \boldsymbol{\varepsilon}_{ex}(\mathbf{x}) | \mathbf{x} \in V \rangle$ with the effective exciting field $\boldsymbol{\varepsilon}^*$, we obtain a equation for the effective field $\boldsymbol{\varepsilon}^*$.

We assume statistical independence of the inclusion properties on their spatial locations and use ergodic properties of the considering functions. After averaging (15) once more over the ensemble realizations of the random set of inclusions we derive the following equation for the effective field

$$\boldsymbol{\varepsilon}_* = \boldsymbol{\varepsilon}_0 + p\mathbf{A} : (\mathbf{P}_0 : \boldsymbol{\varepsilon}_* - \mathbf{P}_0^p) \tag{16}$$

where p is a volume concentration of layered inclusions, $p = p^0 + p^+$, p^0 is a volume concentration of initial inclusions, p^+ is a new phase volume fraction, the tensor $\mathbf{A}$ take the form [6]

$$\mathbf{A} = \frac{1-æ_-}{9\mu_-}\mathbf{EE} + \frac{5-2æ_-}{15\mu_-}(\mathbf{I} - \frac{1}{3}\mathbf{EE}), \quad æ_- = \frac{3k_- + \mu_-}{3k_- + 4\mu_-}$$

$\mathbf{I}$ – isotropic unity fourth-range tensor, $I_{ijkl} = 1/2(\delta_{ik}\delta_{jl} + \delta_{jk}\delta_{il})$. The effective field must be spherical for hydrostatic loads $\boldsymbol{\varepsilon}_* = \varepsilon_*\mathbf{E}$. We have

$$\varepsilon_* = \frac{\varepsilon_0 d_-^- - P_0^p}{d_-^- - 3P_0}, \qquad P_0 = (k_1 A_+^\varepsilon p_+ - k_{1i}^- A_i^\varepsilon p_0), P_0^p = (\frac{tp_+}{3} + k_{1i}^- A_i^\vartheta p_0 - k_1 A_+^\vartheta p_+)\vartheta^p \tag{17}$$

A_i^ε, A_+^ε,A_i^ϑ, A_+^ϑ are determined by (10) at $z = p_0/p_+$.

If $p \to 0$ then the solution of a composite problem becomes the solution for the isolated inclusion given in previous sections.

Averaging the expression for the stress and deformations (13) by the ensemble of realizations for finding the effective elastic moduli of the composite.

$$\bar{\boldsymbol{\varepsilon}} = \langle \boldsymbol{\varepsilon}(x) \rangle = \boldsymbol{\varepsilon}_0 + \int \mathbf{K}_-(\mathbf{x}-\mathbf{x}')\,d\mathbf{x}' : \langle \mathbf{q}(\mathbf{x})V(\mathbf{x}) \rangle, \tag{18}$$

$$\bar{\boldsymbol{\sigma}} = \langle \boldsymbol{\sigma}(x) \rangle = \boldsymbol{\sigma}_0 + \int \mathbf{S}_-(\mathbf{x}-\mathbf{x}')\,d\mathbf{x}' : \mathbf{B}_- : \langle \mathbf{q}(\mathbf{x})V(\mathbf{x}) \rangle$$

As action of the operators $\mathbf{K}$ and $\mathbf{S}$ on constant are determined by the relations at a fixed average strain [6]:

$$\int \mathbf{K}(\mathbf{x}-\mathbf{x}') : \mathbf{m}\,d\mathbf{x}' = 0, \qquad \int \mathbf{S}(\mathbf{x}-\mathbf{x}') : \mathbf{m}\,d\mathbf{x}' = -\mathbf{C}_- : \mathbf{m}, \tag{19}$$

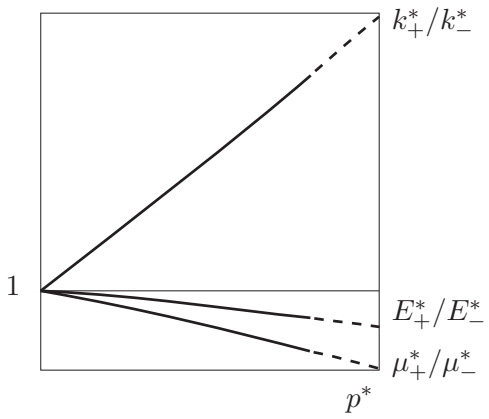

Figure 4: The relative effective bulk modulus k_+^*/k_-^*, The relative effective share modulus μ_+^*/μ_-^*, The relative effective Young's modulus E_+^*/E_-^* (case II).

then

$$\bar{\varepsilon} = \boldsymbol{\varepsilon}_0, \qquad \bar{\boldsymbol{\sigma}} = \mathbf{C}_- : \bar{\varepsilon} + p(\mathbf{P}_0 : \boldsymbol{\varepsilon}_* - \mathbf{P}_0^p) \tag{20}$$

The tensor of effective elastic moduli of the composite has the form in case of hydrostatic loading:

$$\mathbf{C}_* = k_* \mathbf{E}\mathbf{E} + 2\mu_* \left(\mathbf{I} - \frac{1}{3}\mathbf{E}\mathbf{E} \right)$$

$$k^* = k_- - \frac{d_-^- P_0}{d_-^- - 3P_0}, \qquad \mu^* = \mu_- - \frac{3d_-^- P_0}{2(d_-^- - 3P_0)}$$

The dependencies of relative effective bulk modulus k_+^*/k_-^*, relative effective share modulus μ_+^*/μ_-^* and relative effective Young's modulus E_+^*/E_-^* from the concentration of layered inclusions are shown at Fig. 4. The dotted line corresponds to the outer part of the strains under which the local deformation of the interface of effective inclusion from phase "− are on inner boundary of the PTZ.

7 Conclusion

We developed a model to describe intermediate layers in composite materials as new phase areas. Phase transformation around spherical isolated inclusion were analyzed in detail. Then the growth of new phase areas around the particles in composite materials was described by a self-consistent approach. Impossibility of simultaneous increase of both bulk and shear moduli due to the phase transition was shown. The possibility of increasing the effective bulk modulus due to phase transitions was demonstrated.

8 Acknowledgement

This work was supported by RFBR (grant No 10-01-00670-a).

References

[1] M. Cadek, J. N. Coleman, V. Barron, K. Hedicke, W. J. Blau. Morphological and mechanical properties of carbon-nanotube-reinforced semicrystalline and amorphous polymer composites. Applied Physics Letters, Vol.81 (2002), 27, pp. 5123-5125.

[2] A. B. Freidin. On new phase inclusions in elastic solids. ZAMM, V.87 (2007), 2, pp. 102-116.

[3] A.B. Freidin, Y.B. Fu, L.L. Sharipova, E.N. Vilchevskaya. Spherically symmetric two-phase deformations ans phase transition zones. Int. J. Solids and Struct, Vol. 43 (2006), pp. 4484-4508.

[4] R. George, K.T. Kashyap, R. Rahul, S. Yamdagni. Strengthening in carbon nanotube/aluminum (CNT/Al) composites. Scripta Materialia 53 (2005), pp. 1159-1163.

[5] A.B. Freidin, E.N. Vilchevskaya. Multiple development of new phase inclusions in elastic solids. International Journal of Engineering Science, Vol. 47 (2009), pp. 240-260.

[6] S.K. Kanaun, V.M. Levin. Self-consistent methods for composites, Vol. 1: Static Problems, Springer, 2007.

[7] L.B. Kublanov, A.B. Freidin. Solid phase seeds in a deformable material. Journal of Applied Mathematics and Mechanics (PMM), 52 (1988), pp. 382-389.

[8] L. A. Kunin. Elastic media with Microstructure. II. Three Dimensional Models. Springer Series in Solid State Sciences. Berlin, New York, etc. Springer-Verlag (1983), 272 p.

[9] N.F. Morozov, A.B. Freidin. Phase transition zones and phase transformations of elastic solids under different stress states. Proc. Steklov Math. Inst. 223 (1998), pp. 220-232.

[10] N.F. Morozov, I.R. Nazyrov, A.B. Freidin. One-dimensional problem on phase transformation of an elastic ball. Dokl. Akad. Nauk, 346 (1996), pp. 188-191.

[11] E.T. Thostenson, Zhifeng Ren, Tsu-Wei Chou. Advance in the science and technology of carbon nanotubes and their composites: A review. Composites Sciece and Technology 61 (2001), pp. 1899-1912.

[12] Xiao-Lin Xie, Yiu-Wing Mai, Xing-Ping Zhou. Dispersion and alignment of carbon nanotubes in polymer matrix: A review. Materials Science and Engineering 49 (2005), pp. 89-112.

Roman A. Filippov, Alexander B. Freidin, Elena N. Vilchevskaya, IPME RAS, V.O. Bolshoj pr., 61, 199178, St. Petersburg, Russia

Load stabilisation of boom cranes on maritime vessels

Niklas Förster Stefan Palis Frank Palis
Niklas.Foerster@st.ovgu.de

Abstract

For loading processes on ships load positioning is a huge problem. Depending on sea conditions load motions induced by waves can be significant and result in severe positioning degradation or even in operation suspension. In order to counteract load motion and guarantee high positioning accuracy in a wide range of sea conditions a load stabilizing control is proposed. As the controller should stabilize the system irrespective of variations in rope length, jib luffing etc. a robust H_∞ -loopshaping design procedure is used. The proposed control strategy has been validated by various simulations.

1 Introduction

Due to further development in the sector of renewable energy building offshore wind farms is becoming more and more important. For their construction the use of large ship mounted cranes 1 is necessary in order to lift up and install the wind turbines and wings of the wind mill. For economic and safety reasons it is necessary to keep the load position stabilized even in severe sea states. Although there are several results on anti-sway control for various types of cranes in land operation [3, 2, 5, 6, 7], so far only little has been done for offshore operation [4, 1]. Before deriving a load stabilizing control law in the first two sections models for the sea state ship interaction and crane motion are proposed. As can be seen from open loop simulations load motions can be critical for certain sea states. After further simplifications and linearization a robust control law has been derived and tested.

Figure 1: Installation ship [11]

2 Modelling of sea state and ship movement

In order to model the wave induced ship motions the model procedure presented in [8] has been used. For wave modelling the standard assumptions are: incompressible, irrotational

fluid without viscosity. Considering these there exists a potential for the fluid velocity field being described by the Laplace equation. Applying the kinematic and dynamic boundary conditions on the surface gives the following equation for the wave elevation 1.

$$\zeta(z,y,t) = \sum_{i=1}^{n} \zeta_a(i) cos\left[\omega(i)t + \phi(i) - W(i)(xcos(\psi(i) + ysin(\phi(i))))\right] \tag{1}$$

Here the parameters of the wave equation are ζ_a - vector of harmonic wave amplitudes in [m], ω - vector of harmonic wave frequencies in [rad/s], ϕ - vector of harmonic wave phases in [rad], W - vector of harmonic wave numbers in [1/m] and ψ - vector of harmonic wave directions in [rad]. To calculate the movement of the ship for a given sea state a transfer function, reflecting the fluid structure interaction, is generated using the WAMIT Tool.

It is well known that wave movement is a complex stochastic process therefore the use of spectra is appropriate. Here the use of the Bretschneider spectra 2 is a very common approach in order to describe waves. In our case the parameters A and B of the Bretschneider spectra are given by the Pierson-Moskowitz equation 3 which connect the wave spectra to a given sea state. In consequence we can calculate the wave height in respect to the given sea state.

$$S_{\zeta\zeta}(\omega) = \frac{A}{\omega^5} exp\left(\frac{-B}{\omega^4}\right) \tag{2}$$

$$A = \frac{487 H_{1/4}^2}{T^4} \tag{3}$$

Sea state code	Seaway description	Wind speed in [kn]	Significant wave height $H_{1/3}$ in [m]	Period T in [s]
1	Calm (glassy)	0 - 1	0 - 0	0,5
1	Calm (rippled)	1 - 3	0 - 0,1	0,5 - 2,7
2	Smooth (wavelets)	3 - 10	0,1 - 0,5	2,7 - 3,8
3	Slight	10 - 15	0,5 - 1,25	3,8 - 4,8
4	Moderate	15 - 21	1,25 - 2,5	4,8 - 5,4
5	Rough	21 - 27	2,5 - 4	5,4 - 6,6
6	Very rough	27 - 33	4 - 6	6,6 - 8
7	High	33 - 47	6 - 9	8 - 11,3
8	Very High	47 - 54	9 - 14	11,3 - 16
9	Phenomenal	> 54	> 14	16 - 17,2

Table 10: World meterological sea state definitions

3 Crane Model

In order to describe motion of rotary crane, the equivalent kinematic scheme with concentrated masses represented in fig. 2 is used.

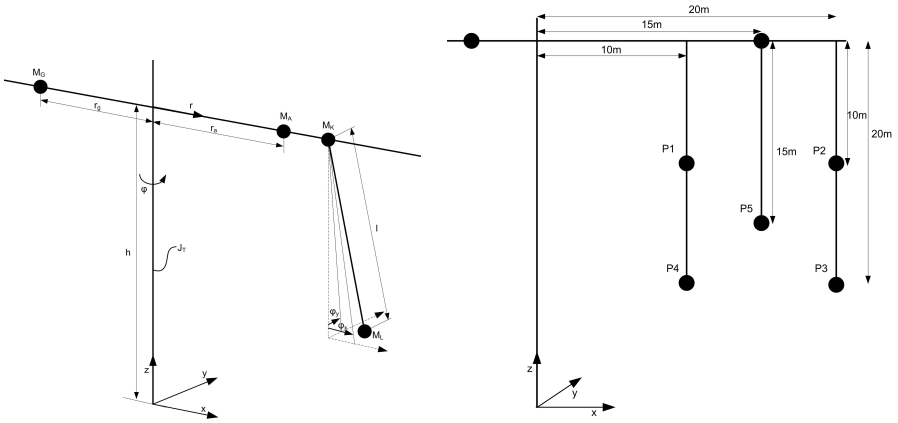

Figure 2: Kinematic equivalent scheme of a boom crane (left) and operating points (right)

$$T_L = \frac{1}{2} m_L \left[\begin{array}{l} \left(\begin{array}{l} -\dot{\varphi} \sin\varphi \left(-\sin\varphi_x + r\right) + \cos\varphi \left(\dot{l} \sin\varphi_x + \dot{\varphi}_x l \cos\varphi_x + \dot{r} \right) \\ -\dot{l} \sin\varphi \sin\varphi_y - l\dot{\varphi} \cos\varphi \sin\varphi_y - l\dot{\varphi}_y \sin\varphi_y \cos\varphi_y \end{array} \right)^2 \\ + \left(\begin{array}{l} \dot{\varphi} \cos\varphi \left(l \sin\varphi_x + r\right) + \sin\varphi \left(\dot{l} \sin\varphi_x + l\dot{\varphi}_x \cos\varphi_x + \dot{r} \right) \\ +\dot{l} \cos\varphi \sin\varphi_y - l\dot{\varphi} \sin\varphi \sin\varphi_y + l\dot{\varphi}_y \cos\varphi \end{array} \right)^2 \\ + \left(\dot{l} \cos\varphi_x \cos\varphi_y - l\dot{\varphi}_x \sin\varphi_x \cos\varphi_y - l\dot{\varphi}_y \cos\varphi_x \sin\varphi_y \right)^2 \end{array} \right]. \quad (8)$$

Hence, dynamics of the generalized rotating crane represents a multibody system with 5 independent degrees of freedom $(\varphi, r, l, \varphi_x, \varphi_y)$. Referring to the equivalent kinematic scheme in fig. 2 the following energies can be established:

- potential energy of the load:

$$V = m_L g \left(h - l\, cos\varphi_x cos\varphi_y\right) \quad (4)$$

- kinetic energies of the tower T_T, the boom T_B, the trolley T_R and the load T_L:

$$T_T = \frac{1}{2} J_T \dot{\varphi}^2 \quad (5)$$

$$T_B = \frac{1}{2} m_B r_B^2 \dot{\varphi}^2 \quad (6)$$

$$T_R = \frac{1}{2} m_R \left(r^2 \dot{\varphi}^2 + \dot{r}^2\right) \quad (7)$$

Defining the system Lagrangian L as the difference between all kinetic energies and the potential energies gives:

$$L = T_T + T_B + T_R + T_L - V. \quad (9)$$

Using Lagrange's equation for all 5 degrees of freedom $(i = 1, \ldots, 5)$:

$$\frac{d}{dt}\left(\frac{\partial L}{\partial \dot{q}_i}\right) - \frac{\partial L}{\partial q_i} = Q_i \tag{10}$$

results in the following equation of motion:

$$Q = D(q)\ddot{q} + C(q,\dot{q}) + G(q) \tag{11}$$

where C is the coupling matrix containing the matrices for centrifugal and coriolis forces and G is the gravitation matrix.
$C = C_{centr} + C_{cor}$

In the further calculations we assume that the movement of the boom, hoisting gear and trolley are realized by position controlled drives and therefore feedback of load swinging on the drives can be neglected. In order to avoid interfering with the subordinate speed and position controllers of the drives the actuated variables for our controller design aren't forces nor momentums but angels and positions.
As the vessel moves due to the waves we assume that sway, roll and heave have got a much bigger influence on load swinging and that therefore yaw, surge and sway can be neglected. In consequence for the coupling between ship and crane motion sway, roll and heave enter as constraints for the crane base.

4 Open loop simulation

At wind speeds of 30 knots, which correspond to sea state 6 see table 2, the ship and load motions have been computed. As can be seen in fig. 4 at this sea state load motions become critical and would prohibit crane operation. The very high amplitudes of load oscillations are due to the fact that the rope is modelled as a pure rigid body and no load damping, i.e. viscous friction in the joint or air resistance, is present. Nevertheless, this motivates the design of an appropriate control structure for anti-sway control.

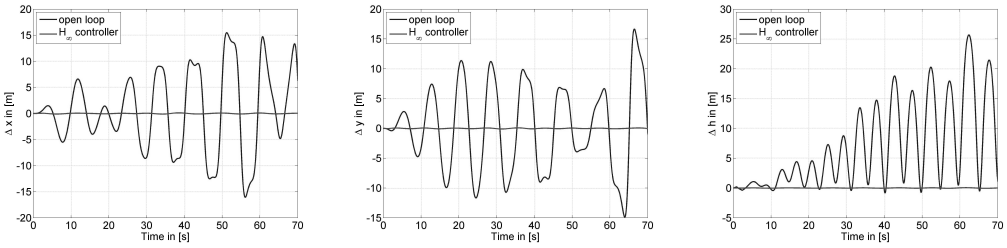

Figure 3: Load movement in x and y direction and load heave

5 Control design

For the design of the controller we use the setup shown in fig. 4. Here the measured load positions x, y and h are the controled variables. The positions of the three gears are the control inputs and the wave motions act as a external disturbance on the load motion. In

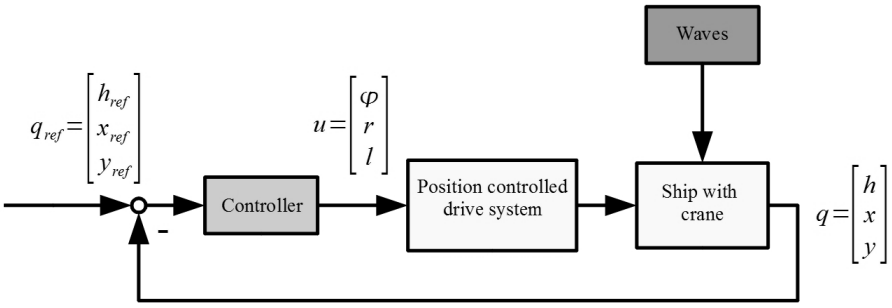

Figure 4: Controller model

order to design a controller, which is capable to stabilize the load for different rope lengths and trolley positions, the model equations are linearized around five different set points 2.

$$\begin{pmatrix} y \\ x \\ h \end{pmatrix} = \begin{pmatrix} G_{11}(s) & G_{12}(s) & G_{13}(s) \\ G_{21}(s) & G_{22}(s) & G_{23}(s) \\ G_{31}(s) & G_{32}(s) & G_{33}(s) \end{pmatrix} \begin{pmatrix} \phi \\ r \\ l \end{pmatrix} \tag{12}$$

Taking a look at the Bode diagrams it can be stated that the system is diagonal dominant, i.e. it has strong coupling between φ and y, r and x and between l and h. Therefore the three transfer functions G_{11}, G_{22} and G_{33} are most important for control design. As can be seen in the amplitude response 5 for the linear models from the set points P1 to P5 these transfer functions differ mainly in their load related Eigen frequencies, due to rope length variations. This difference can be incorporated into the robust control design procedure as an additional model uncertainty. Here the most appropriate uncertainty model is the coprime factor uncertainty [9], [10], i.e. the plant is represented by its normalized left coprime factorization with additive uncertainties $\Delta M(s), \Delta N(s)$ in each factor.

$$G_\Delta(s) = (M(s) + \Delta_M(s))^{-1} (N(s) + \Delta_N(s)) \tag{13}$$

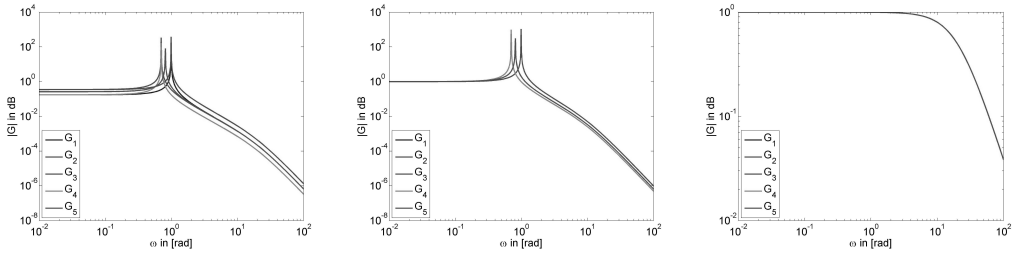

Figure 5: Amplitude response $\varphi \to y$, $r \to x$ and $l \to h$

A controller K_∞ robustly stabilizes the perturbated feedback system with respect to coprime model uncertainties $\left\| \begin{bmatrix} \Delta_N & \Delta_M \end{bmatrix} \right\|_\infty < \epsilon$, if and only if it stabilizes the nominal system

$$G(s) = M(s)^{-1} N(s) \tag{14}$$

and

$$\left\| \begin{bmatrix} K_\infty \\ I \end{bmatrix} (I + GK_\infty)^{-1} M^{-1} \right\|_\infty \leq \frac{1}{\epsilon}. \tag{15}$$

As the controller K_∞ gives only robust stability usually pre- and postcompensator $W_1(s)$ and $W_2(s)$ are used in order to shape the open loop singular values of the plant before calculating a robustly stabilizing controller K_∞. The overall controller K is then calculated using the pre- and postcompensator $W_1(s)$ and $W_2(s)$.

$$K = W_1 K_\infty W_2 \tag{16}$$

6 Closed Loop simulation

In order to verify the designed controller, the proposed control scheme is tested for the same sea state as in the open loop simulation at the different set points. As can be seen in 6 the load swing can be reduced from the range of more than 10m to about 10cm. Where the actuator forces and the required motion drive dynamics are in acceptable levels. The maximum trolley acceleration is for example $a_t = 8\frac{m}{s^2}$. In addition the proposed control law achieves good performance irrespective of the set point.

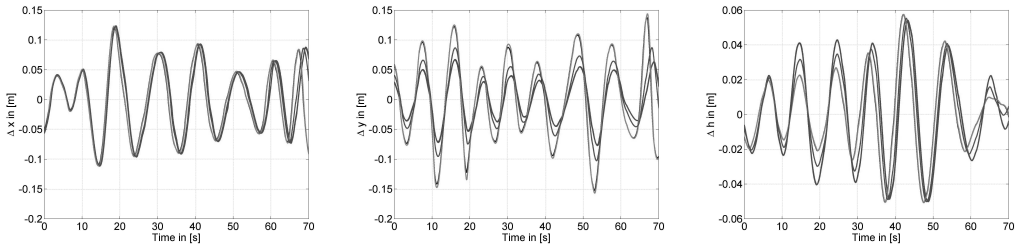

Figure 6: Load movement in closed loop operation

7 Conclusion

In this contribution an anti-sway control scheme for ship cranes has been proposed, which is capable to compensate for wave induced load motions. Due to the robust control approach a good performance with reasonable control effort could be achieved irrespective of the chosen load position. Future works will investigate the influence of additional limitations in the drive system and safety related limits in the working area.

References

[1] Palis,S; Förster,N; Palis,F; Lehnert,M Lastpendelwinkeldämpfung für Offshore Drehkrane 19. Kranfachtagung ,2011

[2] Palis, S;Palis, F;Lehnert, Anti-Sway System for Slewing Cranes. 22nd ISARC Italy, Ferrara, Sept 2005

[3] Palis,F Prozessangepasste Steuerung von elektrischen Kranantrieben mit Mikrorechnern, Habilitationsschrift 1989

[4] Lonnie J. Love; John F. Jansen; Francois G. Pin Report: Compensation of Wave-Induced Motion and Force Phenomena for Ship-Based High Performance Robotic and Human Amplifying Systems, 2003

[5] Arnold, E.; Neupert, J.; Sawodny, O. Trajectory Tracking for Boom Cranes Based on Nonlinear Control and Optimal Trajectory Generation, Proceedings of Control Applications, pp.1444-1449, ISBN: 1085-1992, Singapore, Oct. 2007

[6] Sawodny, O.; Aschemann, H.; Kumpel, J.; Tarin, C.; Schneider, K. (2002). Anti-sway control for boom cranes, Proceedings of American Control Conference, pp. 244-249 vol. 1, ISBN: 0-7803-7298-0, Alaska, May 2002, Anchorage

[7] Kim, Y. S.; Hong, K. S.; Sul, S.K., R. (2001). Anti-Sway Control of Container Cranes: Inclinometer, Observer and State Feedback. International Journal of Control, Automation and Systems, Vol. 2., No. 4, (December 2004) pp. 435-449

[8] Perez Tristan Ship Motion Control Course Keeping and Roll Stabilisation using Rudder and Fins, 2005, Springer Verlag ISBN: 1852339594

[9] D. C. McFarlane & K. Glover, Robust Controller Design using Normalised Coprime Factor Plant Descriptions, Springer Verlag, Lecture Notes in Control and Information Sciences, vol. 138, 1989

[10] D.C. McFarlane & K. Glover, A Loop Shaping Design Procedure using H_∞ Synthesis, IEEE Transactions on Automatic Control, vol. 37, no. 6, June 1992, pp. 759- 769

[11] http://www.maritimeandenergy.com/sider/tekst.asp?side=5536,02.05.2011

Niklas Förster, IESY, University of Magdeburg, Germany
Stefan Palis, IFAT, University of Magdeburg, Germany
Frank Palis, IESY, University of Magdeburg, Germany

Comparison of a spouted bed and a Wurster-coater using DEM-CFD simulations

Lennart Fries Sergiy Antonyuk Stefan Heinrich Stefan Palzer
lennart.fries@tu-harburg.de

Abstract

Two fluidised bed spray granulator configurations with internal particle circulation, a Wurster-coater and a prismatic shaped spouted bed, were compared through numerical simulations. Coupled DEM-CFD simulations were used to characterise the particle and collision dynamics for both granulator configurations. While the spouted bed shows a higher particle collision frequency and faster overall particle motion, the draft tube inserted in the Wurster-coater reduces the frequency of collisions involving surface-wet particles.

1 Introduction

Fluidised bed spray granulation and agglomeration both play an important role in the manufacturing of powder granules in the food, fine chemicals snd pharmaceutical industries as dust-free and free-flowing particles can be produced in a process with favourable heat and mass transfer conditions and good solids mixing [1]. Liquid binder is sprayed into a bed of solids to achieve granule growth by adhesion of surface-wet particles. The Wurster-coater (Fig. 1 a) is a common device in the pharmaceutical industry used to coat tablets [2, 3]. It is described by Teunou and Poncelet [4] as the most efficient batch fluid bed coating equipment. A cylindrical draft tube is inserted vertically into the granulator. The segmented air distributor plate has larger orifices below the Wurster tube and therefore the fluidization gas enters at higher velocity at the centre than in the annulus. Due to the central gas/liquid injection which is concurrent to the particle motion, a circulating movement of the particles is induced and the geometry can be divided into a wetting and a drying zone. Spouted beds (Fig. 1 b) are frequently used for the production of detergent, pharmaceutical, food and fertilizer granules or agglomerates [5]. The powder is entrained by a spout at the centre of the bed and slides back downwards along the wall of the prismatic process chamber. Spouted beds have a number of advantages, such as homogeneous wetting due to the internal particle circulation and the excellent heat transfer. They allow handling of both cohesive material and particles with a wide particle size distribution. A homogeneous distribution of the spray liquid is a prerequisite for uniform particle growth, whereas local overwetting leads to the formation of oversize particle clusters. The moisture distribution in the apparatus is a key parameter affecting both particle size and structure of the product [6]. The fluid bed granulation process is controlled by many parameters which can influence size and structure of the product. Since so far operating conditions and the equipment geometry have been developed empirically, the actual influence of fundamental mechanisms in the process (e.g. wetting of the particle surface, collisions, adhesion mechanisms) is not well understood. For instance the wetting

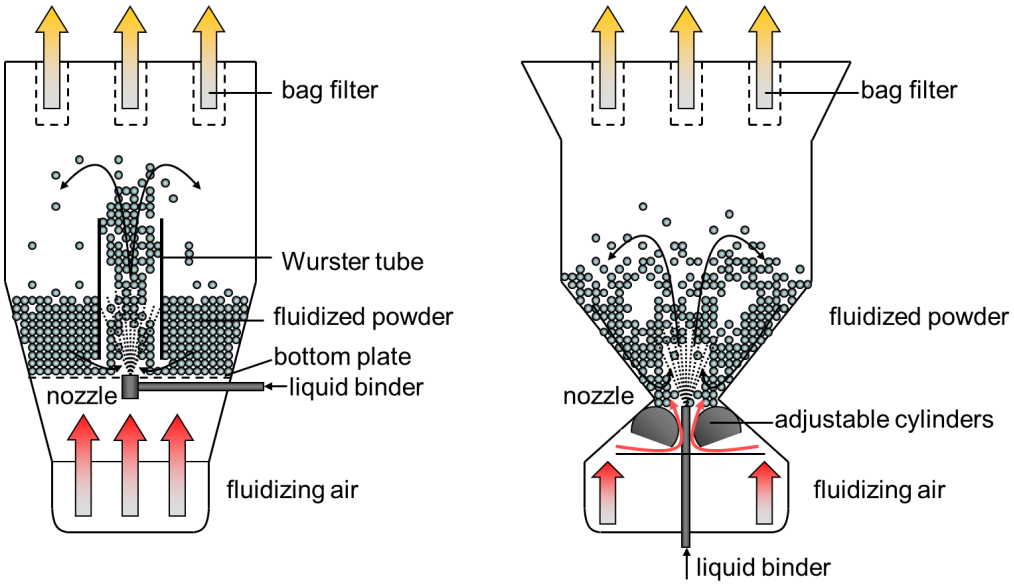

Figure 1: Schematic illustration of the investigated fluidised bed granulator configurations: a) Wurster-coater, b) Prismatic shaped spouted bed.

and drying rates are highly dependent on the flow field of the gas and particle phases in the equipment [3].

To describe the process in detail on the scale of individual particles, the Discrete-Element-Method (DEM) offers large potential. As each particle is tracked individually, the method allows a complete representation of the particle-particle and particle-wall interactions and their influence on the process dynamics. In this contribution, a DEM model is coupled with a CFD simulation to consider the interactions between fluid and particle phase using the Euler-Lagrange approach. The performance of two fluidised bed granulator configurations with internal circulation of the material is compared numerically and experimentally.

Mathematical model

The translational motion of each particle i in the system is calculated using Newton's second law:

$$m_i \frac{\partial \mathbf{u}_i}{\partial t} = -V_i \nabla \mathrm{p} + \frac{V_i \beta_{g-p}}{1-\varepsilon_g} (\mathbf{u}_g - \mathbf{u}_i) + m_i \mathbf{g} + \sum_{j=1}^{n} \mathbf{F}_{c,i,j} \tag{1}$$

The forces on the right hand side of Eq. 1 are representing the pressure gradient, fluid drag, gravity and contact forces (i.e. due to collisions), respectively. The interphase momentum transfer coefficient β_{g-p} is modelled by combining the Ergun equation [7] for dense regimes (porosity $\epsilon < 0.8$) and the correlation proposed by Wen & Yu [8] for more dilute regimes (porosity $\epsilon > 0.8$). Particle rotation is accounted for by introducing Eq. 2, where I_i, i and T_i denote the moment of inertia, the angular velocity and the torque of particle i, respectively.

$$I_i \frac{\partial \omega_i}{\partial t} = \sum_{j=1}^{k} \mathbf{M}_{\mathrm{i,j}} = T_i, \tag{2}$$

The gas phase is treated as continuum. The geometry of the apparatus is discretized in mesh cells and the motion of the gas phase is calculated using volume-averaged Navier-Stokes equations:

$$\frac{\partial}{\partial t}\left(\varepsilon_g \rho_g\right) + \nabla \cdot \left(\varepsilon_g \rho_g \mathbf{u}_g\right) = 0 \tag{3}$$

and the equation of momentum:

$$\frac{\partial}{\partial t}\left(\varepsilon_g \rho_g \mathbf{u}_g\right) + \nabla \cdot \left(\varepsilon_g \rho_g \mathbf{u}_g \mathbf{u}_g\right) = -\varepsilon_g \nabla p_g - \nabla \cdot \left(\varepsilon_g \bar{\bar{\tau}}_g\right) + \varepsilon_g \rho_g \mathrm{g} - \mathbf{S}_p, \tag{4}$$

Here, τ_g denotes the gas phase stress tensor [9]. The gas flow field influences the motion of the particles via the drag force, but also the particles influence the velocity profile of the gas phase due to their required volume fraction. This effect is accounted for by adding a sink term S_p to the momentum balance [9], which contains the interphase momentum transfer coefficient β_{g-p} and closes the two-way-coupling. Forces between the gas and particle phase are of opposite direction and of equal magnitude. The flow around particles is not fully resolved, as the size of the fluid mesh cells is 2-10 times larger than the particle diameter.

Contact model

Contact forces between the particles a and b (Fig. 2) are calculated according to a contact model based on the theory by Hertz [4] for the normal impact and a no-slip approximation of the model by Mindlin and Deresiewicz [5] for the tangential component, as proposed by Tsuji [6].

$$\mathbf{F}_{ab,n} = -k_n \cdot \delta^{\frac{3}{2}} \cdot \mathbf{n}_{ab} - \eta_n \cdot \mathbf{u}_{ab,n} \tag{5}$$

For the tangential component of the contact force $\mathbf{F}_{ab,t}$ an equation analogous to Eq. 5 is used, where $\mathbf{t}_{ab}$ is the tangential unit vector. The elastic part of the contact force is represented by a non-linear spring, where the force is proportional to the spring stiffness $k_{d,n}$ and the displacement $\delta_n^{3/2}$. Additionally, to account for visco-elastic material properties that cause energy dissipation, a damping factor η_n [12] is included in the model.

$$\eta_n = 2\alpha\sqrt{m^* k_n} \cdot {\delta_n}^{\frac{1}{4}} \tag{6}$$

Here, α is a function of the normal coefficient of restitution e_n:

$$\alpha = \begin{cases} \frac{ln e_n}{\sqrt{ln^2 e_n + \pi^2}} & \text{if } 0 < e_n \leq 1 \\ 1 & \text{if } e_n = 0 \end{cases} \tag{7}$$

The normal coefficient of restitution is defined as the ratio of the rebound velocity v_R to the impact velocity v:

$$e_n = \sqrt{\frac{E_{kin,R}}{E_{kin}}} = \left|\frac{v_R}{v}\right| \tag{8}$$

2 Simulation conditions

Simulations were performed using the commercial simulation software EDEM 2.3 coupled with the software Ansys Fluent 12 to describe the particle and fluid dynamics in a fluid bed granulator. For two different granulator configurations the gas and particle dynamics as well as the collision velocity and collision frequency inside a conical spray zone starting at the nozzle tip were analyzed. Simulations were performed using 150,000 monodisperse spherical particles of 2 mm diameter, which corresponds to a batch size of 0.94 kg at a particle density of 1500 kg/m^3. A constant coefficient of restitution of 0.8 was set in this study, according to experimental results obtained by Antonyuk et al. for γ-Al_2O_3 [13]. All used simulation parameters are listed in Table 1. The geometry of the GF3-Wurster-insert (Fig. 2 a) and the ProCell 5 insert (Fig. 2 b) were supplied by Glatt Ingenieurtechnik GmbH, Weimar, Germany and slightly simplified for the DEM-CFD simulations (Fig. 2 c and d).

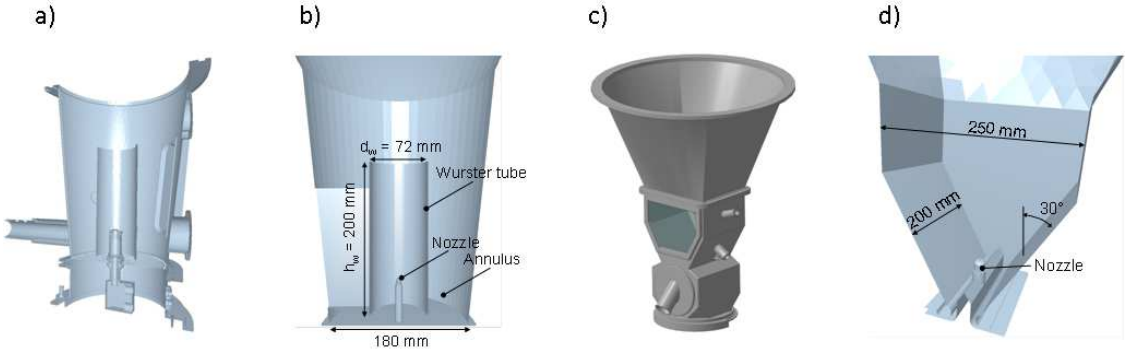

Figure 2: Cross-cut through a fluidised bed granulator: (a) Wurster-coater (Glatt GF3), (b) Spouted bed (Glatt ProCell5), (c) and (d): Simplified geometries for DEM-CFD.

Table 11: Overview on simulation parameters.

Parameter	Symbol	Unit	Value
Fluidisation air flow rate	$\dot{m}_F$	kg/h	360
Atomizer flow rate	$\dot{m}_{spout}$	kg/h	5.7
Gap distance below Wurster	h_{gap}	mm	30 (= 15·d_p)
Normal coefficient of restitution	e_n	-	0.8
Friction coefficient of particles	μ	-	0.1
Poisson's ratio of particles	n	-	0.25
Shear modulus of particles	G	Pa	$1{\cdot}10^8$
DEM simulation time step	Δt_{DEM}	s	$1{\cdot}10^{-6}$
CFD simulation time step	Δt_{CFD}	s	$1{\cdot}10^{-4}$
Total simulation time	t	s	4
Number of particles	N_p	-	150,000
Number of grid cells (CFD)	N_{cell}	-	12,000

Particle wetting is a key mechanism in granulation and agglomeration. Therefore, in this contribution we analyse the particle and collision dynamics specifically for particles positioned inside the spray zone, which are generally surface-wet. The biconical spray zone was defined in the simulations as shown in Fig. 3. A constant length L of 45 mm was used, based on the jet injection depth found in previous DEM simulations of the Wurster-

coater performed by the authors [14]. The biconical shape of the spray zone is related to DEM simulations of droplet deposition according to Link et al. [15]. Throughout the simulations the spraying angle φ was kept constant at 40°, which is a realistic value for the nozzle type used in the experiments (Schlick model 970).

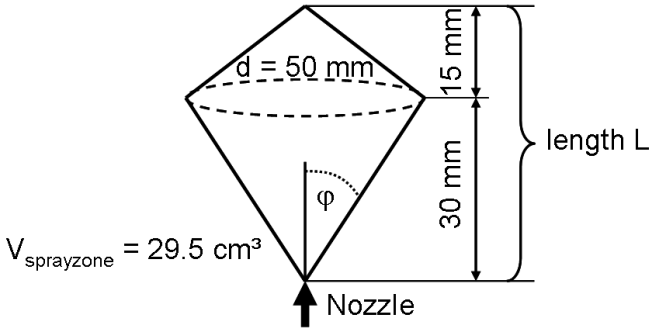

Figure 3: Geometry of the spray zone.

The collision frequency and the distribution of the relative collision velocity obtained from DEM simulations gives useful information for the definition of a sticking criterion. According to such a criterion it is decided whether a collision leads to aggregation or rebound of the involved particles. For amorphous water-soluble particles like dextrose syrup the surface moisture content determines the stickiness of the particles. Palzer [6] showed that below a surface viscosity of 10^8 Pa particle collisions lead to adhesion. The model presented in this contribution is an important step towards a physically based description of agglomeration in a fluidized bed, although it is assumed that wetting does not affect the collision properties of the particles in the current state of the model.

3 Simulation results

To describe specific properties of both granulator configurations, the time-averaged gas and particle velocities, the collision velocity and frequency of the particles with each other and with the walls of the equipment were analysed. These kinetic values are characteristic for the applied process conditions and the geometry of the apparatus. Specificities of both granulator configurations, which affect the granulation process dynamics and thus the structure and strength of the product are elaborated in this chapter based on the results of the coupled DEM-CFD-simulations.

Particle velocity distribution

The average velocity magnitude of all particles in the Wurster-coater and in the spouted bed is presented in Fig. 4 a. While the average particle velocity in the Wurster-coater is almost constant, small fluctuations of 0.1 m/s are found in the spouted bed. Taking the average over the total simulation time, the particle velocity in the spouted bed is 40x higher than in the Wurster-coater at equal gas throughput. This is mainly linked to the smaller area of the air inlet zone in the spouted bed and the low particle motion in the dense bed in the annulus of the Wurster-coater. The small gap distance between the bottom plate and the draft tube limits the number of particles entering the Wurster tube, where they are accelerated. A comparison of the time-averaged particle velocities and collision dynamics is given in Table 2.

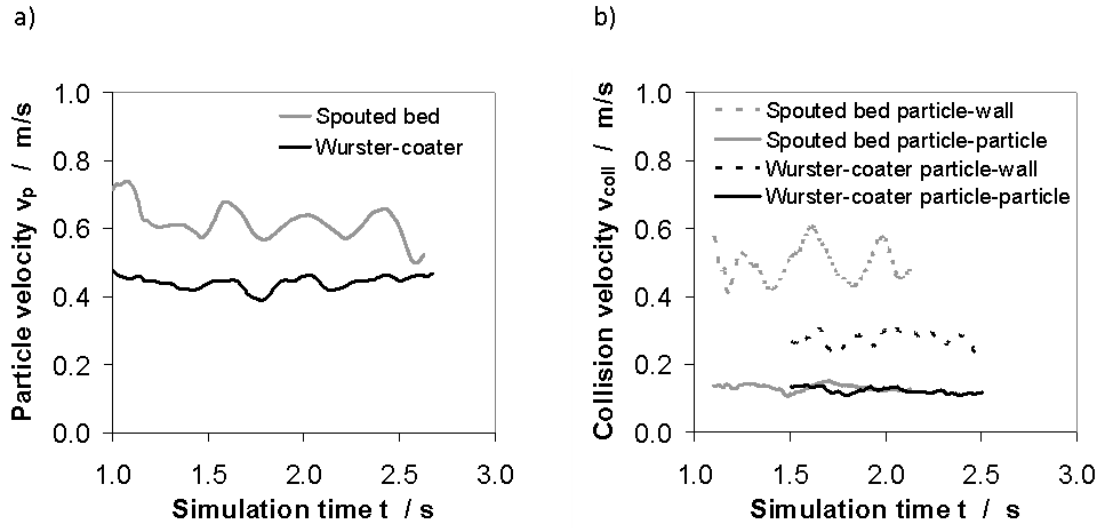

Figure 4: (a) Average particle velocity in the Wurster-coater and in the spouted bed, (b) average particle-particle and particle-wall collision velocity in the Wurster-coater (WC) and in the spouted bed (SB).

In Fig. 4 b. the average collision velocity is shown as a function of time for the two granulator configurations. The solid lines correspond to particle-particle collisions, where a nearly constant average collision velocity is found for both configurations. In the spouted bed the average particle-particle collision velocity is 8x higher than in the Wurster-coater for the given simulation conditions. The dashed lines correspond to particle-wall collisions. Here, the average collision velocity in the spouted bed is nearly twice as high as in the Wurster-coater. While the process chamber of the Wurster-coater is only slightly conical, showing an inclination of 7° against the vertical axis, the side walls of the spouted bed granulator are inclined by 30° against the vertical axis. Therefore, the impact velocity of particles falling downwards against the wall is higher in the spouted bed than in the Wurster-coater. Furthermore, many particles collide at high velocity with the central T-profile in the spouted bed, whereas only few collisions of particles with the Wurster tube are observed. Due to the elevated particle-wall collision velocity, granules produced in the spouted bed are expected to show a higher strength than those produced in the Wurster-coater, based on the simulation results.

In Fig. 5 a. the average angular velocity of the particles is plotted as a function of the simulation time. In the DEM simulation particle rotation arises from particle collisions, wall friction and gas velocity gradients. While the average particle rotation in the Wurster-coater is nearly stationary, some fluctuations between 65 and 85 rad/s are seen in the spouted bed. At the chosen simulation conditions the Wurster-coater shows a stable particle circulation, whereas in the spouted bed periodic pulsations occur. Averaged over the total simulation time, the angular velocity of all particles in the granulator is more than twice as high in the spouted bed as in the Wurster-coater. The spout fluidization via the two slots at the bottom promotes particle rotation au well as the inclined side walls of the spouted bed granulator, where the particles are rolling downwards. Along with the higher angular velocity of the particles, the inter-particle friction should be much higher in the spouted bed, which should limit the growth rate and favour the formation of compact agglomerates. Especially for coating purposes, fast particle rotation inside the spray zone is desirable, since it assures a homogeneous distribution of the spray liquid over

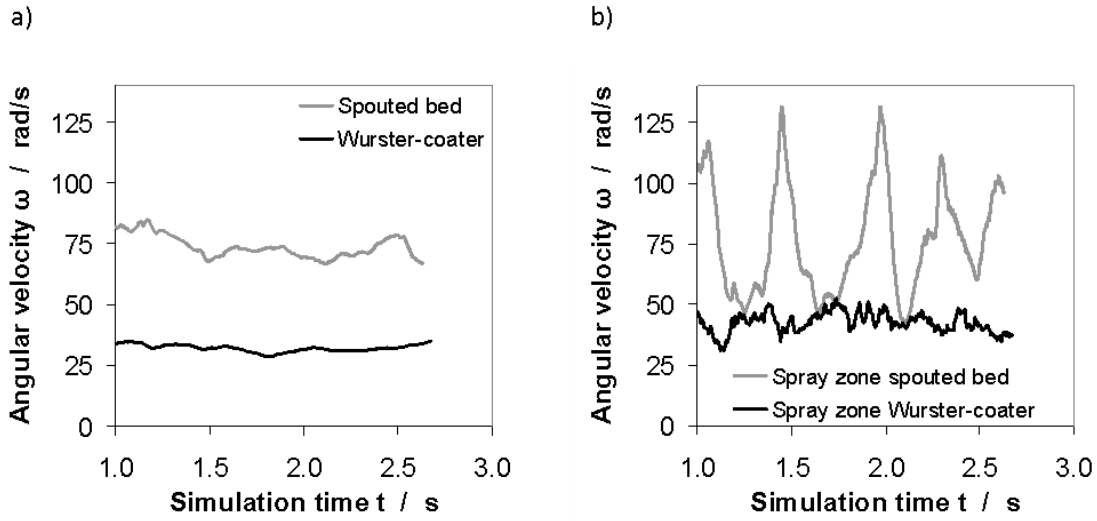

Figure 5: (a) Average angular velocity of all particles in the Wurster-coater and in the spouted bed, (b) average angular velocity of the particles positioned inside the spray zone in the Wurster-coater and in the spouted bed.

the particle surface and thus less oversize particles. The angular velocity specifically for particles positioned inside the spray zone is shown in Fig. 5 b. It can be seen that in the spouted bed the angular velocity of the particles in the spray zone is always higher than in the Wurster-coater and shows very strong oscillations. Averaged over the total simulation time, the angular velocity in the spouted bed is 83 % higher in the spouted bed than in the Wurster-coater. In contrast to the spouted bed the Wurster-coater shows uniform particle rotation for the given simulation conditions. Based on these results particle wetting in the Wurster-coater is expected to be more homogeneous than in the spouted bed.

Table 12: Time-averaged particle velocities and collision dynamics in the Wurster-coater and the spouted bed.

Parameter	Unit	Wurster-coater	Spouted bed
Particle velocity	m/s	0.441	0.616
Angular velocity	rad/s	32.02	72.91
Relative collision velocity P-P	m/s	0.121	0.131
Relative collision velocity P-W	m/s	0.274	0.498
Particle fraction inside spray zone	%	0.53	0.95
Angular velocity (spray zone)	rad/s	42.58	78.11
Rel. collision velocity P-P (spray zone)	m/s	0.390	0.249

Opposite to the result obtained for the whole granulator, the average collision velocity of particles positioned inside the spray zone is 57 % higher in the Wurster-coater than in the spouted bed (see Table 2). This effect can be related to the directed flow profile in the Wurster-coater, where the particles are accelerated inside the draft tube. In the Wurster-coater the wetting zone above the bottom spray nozzle is protected by the draft tube from lateral particle motion into the spray zone. Since this is not the case in the spouted bed, the particle trajectories are less regular, which causes a lower average collision velocity. Since particles inside the spray zone are generally surface-wet, the relative collision velocity in this zone is an indicator for the agglomeration rate. Based on the simulation results,

a lower agglomeration rate is expected for the Wurster-coater than for the spouted bed. Agglomerates formed in the spouted bed should be stiffer and more compact in shape.

At the beginning of the rotational disk movement, the particles move by centrifugal force horizontally in the direction of the camber wall. They are lifted up axially by the gas stream in the area of the gap. Hence, a spiralic material motion occurs. Also the motion is amplified by the centrifugal force on the particles on the rotor disc. After a short time the bed porosity decreases and an uniform material movement at steady-state occurs.

Collision frequency

One of the most interesting possibilities of a detailed DEM simulation is the analysis of the particle collision dynamics. In a fluidized bed granulator the agglomeration rate is strongly dependent on the particle collision velocity and the collision frequency. Colliding particles will rebound, if the kinetic energy of the contact partners cannot be dissipated by viscous or capillary forces.

Table 13: Time-averaged collision frequency in the Wurster-coater and in the spouted bed.

Parameter	Unit	Wurster-coater	Spouted bed
Collision frequency P-P	s^{-1}	385	833
Collision frequency P-W	s^{-1}	20	52
Collision frequency P-P (spray zone)	m/s	88	864

Below a certain critical impact velocity, the particles will stick to each other and form an agglomerate. In Table 3 the collision frequency for particle-particle and particle-wall collisions is given for both granulator configurations. For both granulator configurations particle-particle collisions occur 16-20 times more often than particle-wall collisions. While each particle will encounter on average 385 collisions with other particles per second in the Wurster-coater, the collision frequency in the spouted bed is more than twice as high. Similarly, particle-wall collisions occur 2.7 times more often in the spouted bed than in the Wurster-coater. In the Wurster-coater the particle circulation around the Wurster tube includes a long free-flight phase in the expansion chamber, where only very few particle collisions take place. Most likely the higher collision frequency in the spouted bed can be related to the fact that the dense bed in the bottom region is much more agitated compared to the Wurster-coater. Looking at the spray zone alone, the difference between the two granulator configurations becomes even more pronounced. 10 times less particle-particle collisions inside the spray zone are observed in the simulation of the Wurster-coater in comparison to the spouted bed.

4 Conclusion

Two advanced fluidized bed spray granulator configurations with internal particle circulation (a GF3 Wurster-coater and a ProCell5 spouted bed, both supplied by Glatt) are compared numerically. The numerical analysis consists of coupled DEM-CFD simulations to study particle motion and collision dynamics as well as the collision frequency. The simulation results show that for the given parameters the spouted bed provides a higher average particle collision velocity and higher collision frequency than the Wurster-coater. Due to compaction and breakage of weaker particles it can be expected that the strength of agglomerates produced in the spouted bed is higher compared to the agglomerates from the Wurster-coater. More frequent and more energetic collisions in the spouted

bed should lower the growth rate compared to the Wurster-coater. Regarding the particle dynamics only inside the spray zone a regular particle flow pattern was observed in the Wurster-coater, which indicates more homogeneous particle wetting. In the Wurster-coater collisions between wet and sticky particles inside the spray zone occur at lower frequency and at higher relative velocity. Since adhesion of two particles is only possible if the kinetic energy of the collision can be dissipated by viscous forces, the flow conditions in the Wurster-coater should avoid particle agglomeration, except for very sticky particles.

Acknowledgements

We would like to thank Nestec Ltd. for the financial support and Dr.-Ing. Michael Jacob from Glatt Ingenieurtechnik GmbH, Weimar for the supply of geometry data.

References

[1] Heinrich, S., Peglow, M., Ihlow, M., Mörl, L., 2003. Particle population modelling in fluidized bed-spray granulation - analysis of the steady state and unsteady behaviour. Powder Technology, 130, 154-161.

[2] Wurster, D. E., 1966. Particle Coating Process. U.S. Pat. No. 3,253,944 (Wisconsin Alumni Research aoundation).

[3] Karlsson, S., Rasmuson, A., van Wachem, B, Niklasson Björn, I., 2009. CFD Modelling of the Wurster Bed Coater. AIChE Journal 55, 10, 2578-2590.

[4] Teunou, E., Poncelet, D., 2002. Batch and continuous fluid bed coating - review and state of the art. Journal of food engineering, 53, 325-340.

[5] Mörl, L., Heinrich, S., Peglow, M., 2007. Fluidized bed spray granulation. In: Salman, A.D., Hounslow, M.J., Seville, J.P.K. (Eds.), Handbook of powder technology, Volume 11: Granulation, Elsevier, Amsterdam, pp. 21-188.

[6] Palzer, S., 2009. Influence of material properties on the agglomeration of water-soluble amorphous particles. Powder Technology, 189, 318-326.

[7] Ergun, S., 1952. Fluid flow through packed columns. Chemical Engineering Progress, 48, 89-94.

[8] Wen, Y.C., Yu, Y.H., 1966. Mechanics of Fluidization. Chemical Engineering Progress Symposium Series 62, 100-111.

[9] Hoomans, B.P.B., Kuipers, J.A.M., Mohd Salleh, M.A., Stein, M., Seville, J.P.K., 2001. Experimental validation of granular dynamics simulations of gas-fluidised beds with homogeneous in-flow conditions using Positron Emission Particle Tracking. Powder Technology, 116, 166-177.

[10] Hertz, H., 1882. Über die Berührung fester elastischer Körper. Journal für die Reine und Angewandte Mathematik 92, 156-171.

[11] Mindlin, R.D., 1949. Compliance of elastic bodies in contact. Journal of Applied Mechanics 16, 259-268.

[12] Tsuji, Y., Tanaka, T., Ishida, T.,1992. Lagrangian numerical simulation of plug flow of cohesionless particles in a horizontal pipe. Powder Technology 71, 239-250.

[13] Antonyuk, S., Heinrich, S., Tomas, J., Denn, N.G., van Buijtenen, M.S., Kuipers, J.A.M., 2010. Energy absorption during compression and impact of dry elastic-plastic spherical granules, Granular Matter, 12, 15-47.

[14] Fries, L., Dosta, M., Antonyuk, S., Heinrich S., Palzer, S., 2010. Proceedings os the 17th Int. Drying Symposium. (Eds. Tsotsas, E. Metzger, T., Peglow, M.), Docupoint, Magdeburg, 1093-1100.

[15] Link, J.M., Godlieb, W., Deen, N.G., Kuipers, J.A.M., 2007. Discrete element study of granulation in a spout fluidized bed. Chemical Engineering Science, 62, 195-207.

Lennart Fries, Sergiy Antonyuk, Stefan Heinrich, Institute of Solids Process Engineering and Particle Technology, Hamburg University of Technology, Denickestr. 15, 21073 Hamburg, Germany
Stefan Palzer, Nestlé Product Technology Centre York, Haxby Road, York YO91 1XY, United Kingdom

Simulation of elastic and plastic properties of polymeric composites with silicate lamellar nanofiller

Oleg K. Garishin Sergey N. Lebedev
gar@icmm.ru

Abstract

Polymer/silicate nanocomposites mechanical behaviour under finite deformation is investigated at structural level. Outcomes of computer simulation are presented. Nano-filler particles are modeled represented as sheaves from the several parallel ultrathin silicate plates parted by beds of polymer (tactoids), a matrix - as a nonlinear-elastic or elastoplastic material.

The stress-strain state round separate inclusion in dependence on its orientation to a exterior load direc-tion and properties of a matrix is researched. The problem of the macro-homogeneous elongation of a periodic cell in the form of the rectangular field with a tactoid at centre has been solved for this purpose. Conditions at which a filler particle losses of a bending stability happens in the course of macroelongation of material are defined.

The estimate of nanocomposite macro mechanical behaviour depending on properties of a matrix, filler concentration and orientation of corpuscles is spent on the basis of the gained solutions. Appropriate dependencies between macro and microstructural parameters associations are built.

The object of this study are polymer / silicate nanocomposites based on a polyolefin binder and filler of layered clay minerals — smectites [1, 2, 3]. The idea of creating such materials is not new. Still in 1974 [4] was proposed to use as a filler layered silicate nanoparticles with a thickness commensurate with the length of the polymer molecule. But only now, these materials began to be widely used in industry. For such systems, managed to achieve a substantial increase of elastic modulus, strength, fire resistance, resistance to thermal warpage, improved barrier properties with respect to the diffusing substance [3, 4, 5, 6].

In its structure, the systems are essentially mechanically heterogeneous medium consisting of a polyolefin matrix and implanted in her ultra-thin silicate flakes. Characteristic sizes the inclusions are a few nanometers in thickness and from 30 to 1000 nm in diameter. These particles can be randomly distributed over the volume of a material or to form separate sheaves — tactoids — from several (order of tens) collaterally allocated plates between which are a thin layer of polymer. In the first case of exfoliated nanocomposites are called (Fig. 1*b*), the second -intercalated (Fig. 1*a*).

Experimental studies have shown that the properties of these materials depend strongly on whether any of the particles is filler (intercalated tactoids or separate lamellae [5, 6, 7]. This circumstance was the reason for in-depth theoretical study of the formation of the mechanical properties of nanocomposites on the scale of “the matrix — the separate inclusion”.

Computational scheme of the problem was as follows. In a rectangular area (cell periodicity), consisting of polymer material (matrix) was placed the inclusion in the bundle

Figure 1: Schematic representation of different types of structure of polymer nanocomposites with a layered silicate filling: a — intercalated nanocomposite; b — exfoliated nanocomposite.

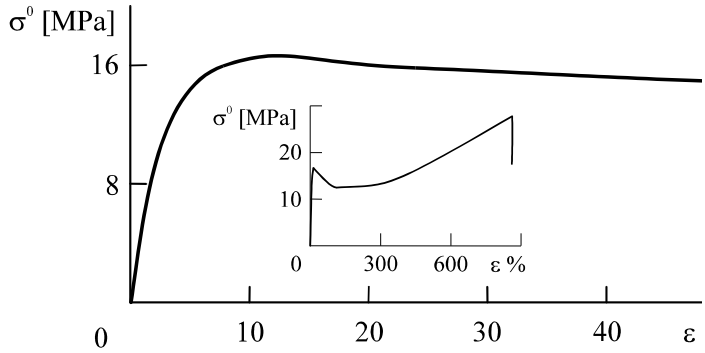

Figure 2: Experimental basic loading curves for the matrix material (σ^0 — the nominal stress, ε — tensile strain

of several parallel plates. Uniaxial macro-stretching of the cell with preservation its volume is simulated by expansion of lower and upper boundaries vertically with the simultaneous pulling up the lateral sides horizontally. The problem of cell loading containing such an inclusion is solved in two-dimensional formulation (plane deformation) using the finite element method.

For each specific geometry of the cell boundary value problem was solved several times using grids with different nodes as the number and type of finite elements. The result is considered valid if the difference in the stresses at the control points does not exceed 5%.

Elastoplastic properties of the matrix were determined from the real stress-strain curve of pure polyethylene [8]. The properties of high density polyethylene (HDPE) brand "RA" produced by "Orgsynthes"(Kazan) were taken as the basis. Initial experimental loading curve is shown in Fig. 2. The initial modulus $E_m = 480$ MPa, yield strength is equal to 9 MPa. Associated flow rule used in solving the elastoplastic problem.

The mechanical properties of the matrix in solving the nonlinear elastic problem described by Treloar potential (neo-Hookean) [9]. Initial modulus of elasticity of the polymer matrix $E_m = 480$ MPa (the same as for the elastoplastic case).

In accordance with the experimental data obtained in the Institute of Petrochemical

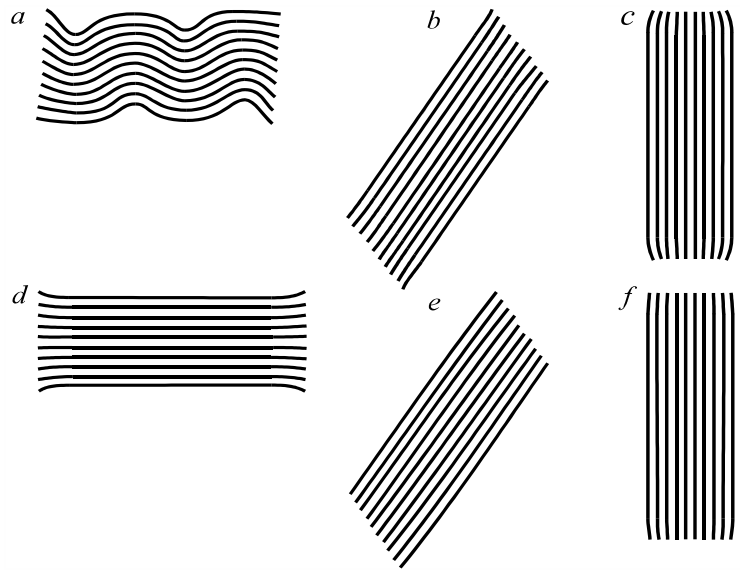

Figure 3: Tactoid form distortion at 25% of the material macro-deformation. $\varphi = 10\%$

Synthesis (IPS RAS) the length of individual silica plate was assumed to be 80 nm, the thickness of – 1 nm. Intercalated tactoid modeled as a stack of 10 parallel plates located (in the unloaded state) at a distance $\delta = 2$ nm. In the gaps was the polymer with the same properties as the matrix. Young's modulus of single silicate nano flake was $E_p = 72000$ MPa.

Inclusion of this type are essentially thin plates (even in a pack) and the difference by two orders in stiffness between the polymer and the silica they should behave as a rather flexible constructions, that is, we can expect that in the process of deformation nanocomposite will experience a noticeable distortion of the particles – the loss of elastic stability.

Changes the shapes of plates in the intercalated tactoid, when cells are vertically stretched (macro deformation $\varepsilon = 25\%$) is shown in Fig. 3. The filler concentration $\varphi = 10\%$, β — the angle between the normal to the flat surface of silica nanoplate and the direction of the external load.

Variants when tactoid is initially perpendicular to the direction of stretch ($\beta = 0°$), tilted at an angle of 45 degrees and parallel ($\beta = 90°$) are presented. Figures 3a, 3b and 3c correspond to elastic matrix, 3d, 3e and 3f — to elastic-plastic.

The greatest distortion of the inclusions observed in its position perpendicular to the direction of extraction, the lowest in parallel. For the case ($\beta = 45°$ there is a shift of plates with respect to each other.

The maximum local stretching of the matrix was observed near the edges of the outer plates — in areas where the matrix material becomes into gaps between tactoid silicate flakes. In this case, they are more than an order of magnitude higher than the macroscopic. In the elastic-plastic matrix (due to the plastic flow of material), the maximum principal strains were about one and a half to two times more than in purely elastic.

The above numerical solutions have allowed not only to investigate the stress-strain state around the nanofiller particles, but also to evaluate from structural positions the

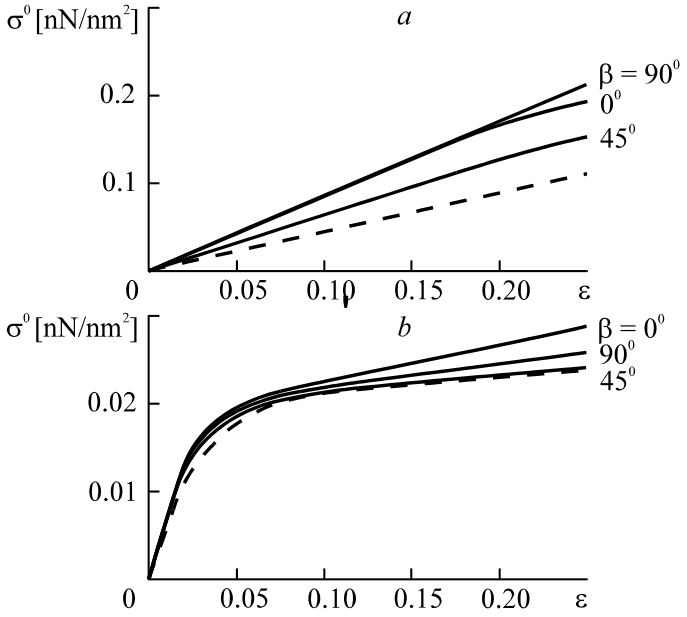

Figure 4: Strain dependence of nominal macro stresses on the angle of inclusion orientation (β ($\varphi = 10\%$). a — a cell with the elastic matrix, b — elastic-plastic. Dashed line — no particle in the cell

effective mechanical properties of polymer / silicate nanocomposite materials. Composite was regarded as a mechanically inhomogeneous medium with a regular ordered structure. This assumption allowed applying the classical method of regularization, widely known in the mechanics of composite materials.

Calculated dependences of nominal stress σ^0 on the strain ε, constructed for the elastic and elastoplastic cells with orientation angle ($\beta = 0°$, $45°$ and $90°$ (concentration of $\varphi = 10\%$) are shown in Fig. 4. Dashed lines show the loading curves for cells without inclusion.

Fig. 5 shows concentration dependences of the effective secant modulus calculated for the extended to $\varepsilon = 25\%$ of the periodicity cell, — E_{25}. Evaluation of the mechanical stiffness of elastomeric material on its secant modulus at a given standard strain is commonly used in practice by specialists in polymers [10]. Such an approach allows us to quantify (in first approximation) the difference between the nonlinear loading curves, typical for finite deformable polymeric materials.

Calculations showed that at 25 per cent of nanocomposite macro-elongation secant modules in elastic cells were an order of magnitude higher than in the elastic-plastic (with the same initial geometry and the same initial modulus). As for the influence of orientation of inclusions, in both cases, the most "soft" were composite cells with particles located at $45° \pm 10°$ in the direction of elongation (due to the shear of plates in tactoid — see also Fig. 3*b*, and 3*d*), and the relative change of secant modulus for the elastic problem was much larger.

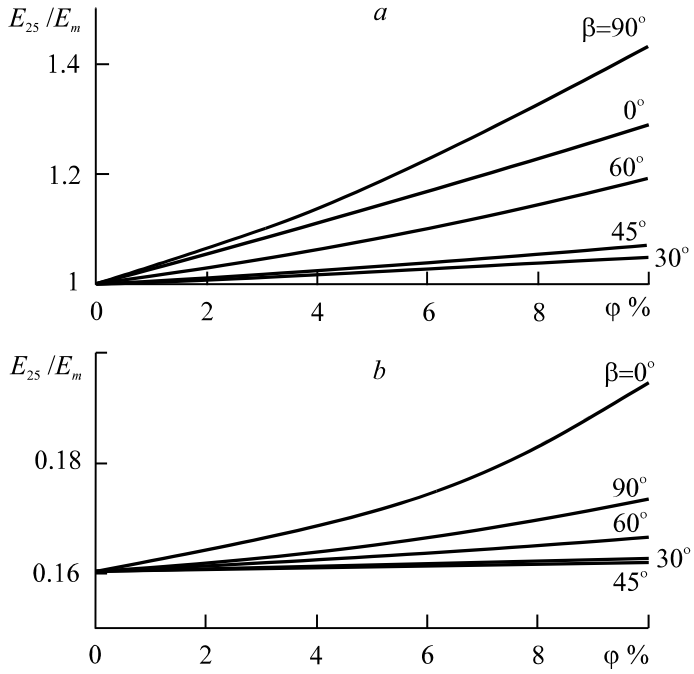

Figure 5: Concentration dependence of the secant modulus E_{25} on the angle of orientation of the inclusion β: a — in a composite cell with elastic matrix, b — elastic-plastic. E_m –the initial elastic modulus of the matrix. $\varepsilon = 25\%$

Acknowledgements

Work is executed at financial support of Russian fund of basic researches (Grants 09-08-00339, 09-06-00402) and Program of Presidium RAS (Program RAS 09-C-1-1008).

References

[1] Fengge G. Clay/polymer composites: the story // Materials Today, (2004). N 11, P. 50–55.

[2] Sheng N., Boyce M.C., Parks D.M., Rutledge G.C., Abes J.I., Cohen R.E. Multiscale micromechanical modeling of polymer/clay nano-composites and the effective clay particle // Polymer, (2004), V. 45, P. 487–506.

[3] Chvalun S. N. Polymer nanocomposites // Priroda, (2000), N 7, P. 22–30.

[4] Shepherd P.D., Golemba F.J., Maine F.W. Clay layers // Adv. Chem. Ser., (1974), V. 41, P. 134–141.

[5] Gerasin V.A., Zubova T.A., Bakhov F.N., Barabbikov A.A., Merekalov N.D., Korolyov Yu.M., Antipov E.M. The structure of nanocomposites polymer/montmorillonit gained by merging in melt // Rossyiskie nanotechnologyi, (2007), N 1-2, P. 90–105.

[6] Gerasin V. A, Guseva M. A, Merekalova N.D., Garishin O. K, Svistkov A.S., Antipov E.M. Making polymer-silicate nanocomposites. // IV International is

scientific(scientifically)-practical conference “New polymeric composites”: Proceedings, Nalchik, (2008), P. 97–100. (in Russian)

[7] Xie W., Gao Z., Liu K., Pan W.-P., Vaia R., Hunter D., Singh A. Thermal characterization of organically modified montmorillonite // Thermochimica Acta, (2001), V. 367-368, P. 339–350.

[8] Garishin O.K., Svistkov A.L., Gerasin V.A., Guseva M.A. Simulation of the elastic-plastic behavior of polyolefin-based nanocomposites with a different structure of layered filler // Polymer Science, Ser. A., (2009), V. 51, N 4, P. 407–415.

[9] Garishin O.K., Korlyakov A.S. Modeling of mechanical interaction between filler particles and binder in polymer-silicate nanocomposites under finite macrodeforma-tion // Computational continuum mechanics, 2009, V. 2, N 3, P. 25–33. (in Russian)

[10] Pechkovsky K.A. Black as the caoutchouck amplifier. M: Chemistry, (1968), 215 p. (in Russian)

Oleg K. Garishin, Institute of Continuous Media Mechanics, Perm, Russia
Sergey N. Lebedev, Institute of Continuous Media Mechanics, Perm, Russia

Simulation of failure processes of coarse grained elastomeric composites using a structural model

Lyudmila A. Golotina
golotina@icmm.ru

Abstract

This study concerns simulation of the behavior coarse-grained polymeric composites and their failure. One of the approaches to the structural analysis of these materials suggests using a structural cell capable of representing the peculiarities of the macroscopic behavior of materials. In this study, the structural cell is taken in the form of an isometric elastomeric cylinder with a spherical rigid inclusion in its center. The inclusion is assumed to be not only absolutely rigid but also unfractured. Thus, the failure of the cell can only occur inside the matrix or at the interface of its adhesion to the sphere. As a strength criterion for the matrix, the rupture deformation of the matrix under uniaxial stretching is used. The inclusion-matrix adhesion strength is characterized by the inclusion-matrix bond energy. The developed method allowed us to study some peculiarities of the character of failure of the examined materials with respect to their structure. The sample's rupture deformation was studied as a function of solid-phase concentration. The character of failure of filled composites is mainly specified by the degree of heterogeneity of the material structure. The failure of homogeneous materials proceeds via the brittle failure mechanism. If the material is heterogeneous, the failure is a consequence of the gradual accumulation of damage. Investigation in the framework of a simplified model shows that the proposed approach holds promise for studying deformation and fracture of coarse grained elastomeric composites.

In this paper, we study the mechanical behavior of coarse-grained polymeric composites and their failure using the known approach developed for structural investigation of this class of materials [1]. For a more reliable simulation, it is necessary to take account of the individual properties of structural cells. To this end, a structural cell is taken in the form of an isometric cylinder (matrix) with a rigid spherical inclusion (particle) in its center. The inclusion is assumed to be not only absolutely rigid but also unfractured. Thus, the failure of the cell can only occur inside the matrix or at the interface of its adhesion to the sphere. As a strength criterion for the matrix, we use the rupture deformation of the matrix ε_m under uniaxial tension. The inclusion-matrix adhesion strength is characterized by the inclusion-matrix bond energy T_d.

Based on experimental data [2], three types of the failure of cells can be distinguished: 1) transverse interpolar cracking of the uneasily deformable matrix firmly bonded to the filler; 2) detachment of the matrix from the filler particles accompanied either by pore formation or by displacement along the interface; 3) rupture of the strands detached from the matrix.

Let us suppose that the appearance of transversal cracks in the matrix leads to an immediate failure of the cell. We consider composites in which pore formation precedes composite failure. The presence of small unbounded regions, which are technologically

inevitable, at the matrix-filler particle interface provokes matrix detachment. The detachment begins to propagate when the energy accumulated in the matrix under tension reaches the value sufficient to create a new interface [3, 4]. This condition is usually expressed as

$$\frac{dU}{dS} = T_d \tag{1}$$

where dU is the increment of the elastic energy of a cell necessary to detach the interfacial area dS, and T_d is the energy per surface unit, which determines the adhesion level between the inclusion and matrix.

Calculations of the stress-strain state of a structural cell are executed using the finite-element method. A computer program has been developed to simulate cell stretching in increments. At each load step, the accumulated deformation energy is calculated and the fulfillment of condition (1) is verified. When the condition is met, the detachment zone increases due to the change in boundary conditions. Using boundary conditions, inhomogeneous normal stresses at the ends and sides of the cell are replaced by the average values of σ_r, σ_z , which are considered to be the ordinary stress at the boundary of an element of a continuous medium. The cell deformation, ε_z , is calculated as the ratio of the cell ends to the initial cell height.

Owing to the accepted geometric shape, cells can be easily arranged into macroscopic specimens meant for uniaxial tensile testing, which is the most common way of primary evaluation of the mechanical behavior of materials. The model takes into account the fact that the inevitable structural inhomogeneity of materials is peculiar to cells. As the most important accidental parameter, we have chosen the inclusion-matrix bond energy T_d and rupture deformations of the matrix ε_m. Examination of the model specimens allows us to study the mechanical properties of coarse-grained polymeric composites in relation to structural parameters such as the mean volume fraction of inclusions and the average size of rigid inclusions. Figure 1 presents a tension diagram for the polyurethane specimen with $60\mu m$ glass balls comprising 24 % of the specimen content, in which the calculation results are compared with the available experimental data [4]. This diagram supports our observations that the developed techniques can be successfully employed in predicting the properties of composites.

The proposed approach allowed us to study the peculiarities of the failure of tested materials taking into account their structure. The rupture deformation of the specimen was investigated as a function of rigid phase concentration. The rupture deformation of the matrix ε_m was assumed to be a random quantity uniformly distributed over the interval (0.5 –1.5). Calculations were performed using relative quantities and the following values of constants $G = 1.0, \nu = 0.49$, and T_d - the accidental quantity with the uniform distribution over the interval (0.3 – 1.0).

Tension diagrams were plotted for specimens representing the composite with the rigid phase volume fraction $\varphi = 20, 30$ and 40%. Deformation values obtained for the failure of the specimen were compared with the rupture deformations calculated by the formula for composites with “good” adhesion given in work [5]

$$\varepsilon_r = \varepsilon_m(1 - \varphi^{1/3}) \tag{2}$$

A comparison shows that the examined dependences agree qualitatively. The results of comparison are summarized in the table:

$\varphi, \%$	20	30	40
ε_r	0,39	0,29	0,21
ε_r *by* (2)	0,41	0,33	0,26

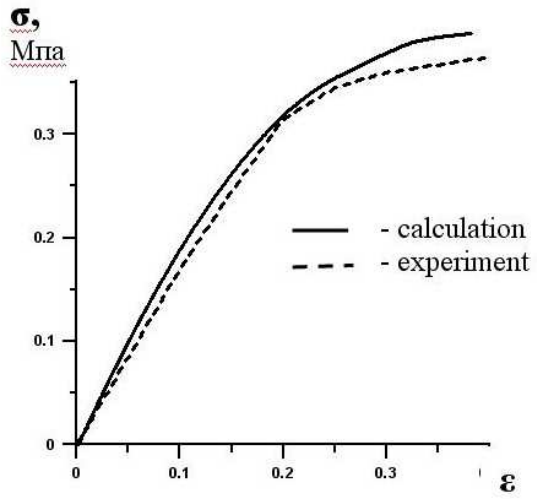

Figure 1: Calculation results in comparison with experimental data

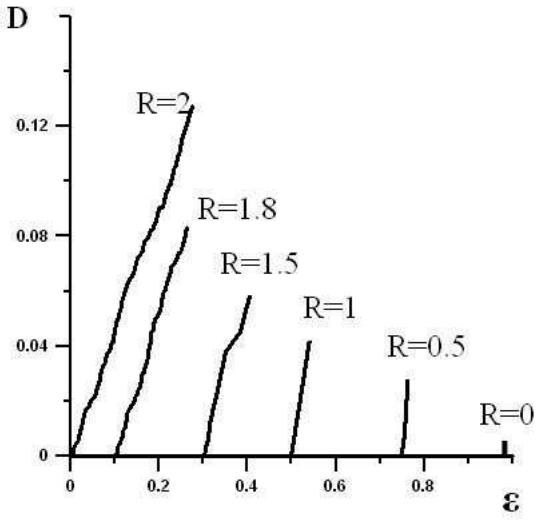

Figure 2: D versus ε for different values of R

The character of failure of the filled composite is mainly specified by the degree of structural heterogeneity of the material. The failure of homogeneous materials proceeds via the brittle failure mechanism. If the material is heterogeneous, the failure is a consequence of the gradual accumulation of damages. The specimens composed of 2000 structural cells (50 layers, each contains 40 cells) and simulating the composite with the rigid phase equal to 20% were stretched to failure. The width of the distribution interval R for rupture deformations$\varepsilon_m¿$ varied with its mean value kept constant. To evaluate the accumulated failure, we use the quantity D that is equal to the ratio of the amount of cells damaged at each step to their primary number. The obtained results are shown in Figure 2 as the plot of D versus ε for different values of R.

For $R = 0$, the specimens exhibited an instantaneous failure while approaching rupture deformation. At small values of R, the failure of a single cell in some cross-section causes the failure of this cross-section and, as a consequence, the whole sample. The appreciable accumulation of fractured cells before the sample failure takes place at $R \geq 0.5$ only. Using a simple model, we deduce from our results that the proposed approach provides a convenient way of studying deformation and failure processes in coarse grained elastomeric composites.

Acknowledgements

This study was supported by the Fundamental Research Program of the Department of Power Engineering, Mechanical Engineering, Mechanics and Control Processes of RAS 09-T-1006.

References

[1] Broberg K.B. The cell model of materials. Computation Mechanics, 1997, v.19, p. 447-452.

[2] Gent A.N., Park B. Failure process in elastomers at/or near rigid spherical inclusion. J. Ma-ter. Sci .,1984, v.19, p.1947-1956.

[3] Gent A. N. Detachment of an elastic matrix from a rigid spherical inclusion . J. Mater. Sci., 1980., v.15., p.2884-2888.

[4] George J. Dvorak, Jian Zhang. Transformation field analysis of damage evolution in com-posite materials. J. of the Mechanics and Physics of Solids, 2001, v. 49, p. 2517-2541.

[5] Polymeric composite materials. Research edition /S.L. Bazhenov, A.A. Berlin et al.- Intel-lect Publ.: Dolgoprudnyi, 2010, P.352.

Lyudmila A. Golotina, ICMM UB RAS, Perm, Russia

Soils in terms of nonlinear elastic reduced Cosserat medium: small perturbations near a spherical prestressed state

Elena F. Grekova
elgreco@pdmi.ras.ru

Abstract

In this work we formulate a nonlinear elastic reduced Cosserat theory in order to model consolidated soils, rocks, and granular materials. We consider a prestressed state, a nonlinear homogeneous stress state with spherical symmetry, reached quasistatically from the natural configuration.

In statics and zero external torques, the reduced Cosserat theory yields in symmetric stress tensor. Therefore it has to be almost symmetric for the triaxial test while the critical force is not reached. However, rotational degrees of freedom can be important when we consider small deviations from this prestressed state. In experiments it is shown that when the material fails in the triaxial test under quasi-static loading, there are fast dynamic processes where particles rotate strongly. When the material does not fail, particle rotation may be important for wave propagation. In this work, we consider small perturbations from a nonlinear prestressed state and write down the equations for deviations. For isotropic materials and certain domain of stresses the wave propagation near spherical presstressed state can be similar to that one for the isotropic linear elastic reduced Cosserat medium: it has a prohibited frequency band for the shear wave, where localisation is possible, and strong dispersion near this zone is present. For large class of strain energies under large pressure the materials becomes unstable, it fails under small shear perturbations, and for large tension it fails via rotation perturbations under certain frequency.

1 Introduction

Rotation of grains is always present in shear bands. Rotational degrees of freedom of grains are important in shear processes, avalanches, stability of granular systems, flowability, and influence general behaviour of the material: “Unlike most metals, soils undergo significant plastic volume changes. An element can dilate or contract depending on the current void ratio and pressure. A major cause of dilation in granular materials is due to the fact that individual grains must ride up over each other in order to accommodate shear strains, as was graphically demonstrated by Reynolds” [1]. Local (induced) anisotropy, one of the characteristic features of granular materials, also may be explained in terms of Cosserat continuum.

On large scale and for enough low or high frequencies, usually rock or soil seem to be an isotropic material where rotational degrees of freedom do not play role. However, for some frequencies a propagating wave may induce a proper rotational dynamics of a typical heterogeneity (Fig. 1). Even for earthquakes rotations may be important in the near field (e.g. see http://rotational-seismology.org, or the special issue on the rotational seismology of the Bulletin of the Seismological Society of America [2]). Though it may seem that in quasistatics rotational degrees of freedom are not important, it is not really so: they

are important when we talk about stability. In many problems with quasistatic loading, for instance, in typical tests for granular materials, the material behaves as non-polar until its structure changes, for instance, under shear stress (Fig. 2). Experiments show that despite quasistatic loading, the process of restructurisation of soil is dynamic and particle rotation does take place (discussion with S. Slotterback at 7th Euromech Solid Mechanics Conference). We interpret this as follows: the medium reaches quasistatically a certain nonlinear state, where the instability with respect to shear-rotation occurs. This rotational-shear unstable motion yields in rearrangement of system of contacts in the medium, and may cause dilatation or compression due to repacking.

Though many authors treat rocks and granular materials as full Cosserat continuum, we believe that the model of the reduced Cosserat continuum is more physically appropriate. In the reduced Cosserat continuum, couple stresses are zero, and the medium does not react to the relative rotation of neighbouring particles. We model a rock with heterogeneities as a homogeneous continuum, where each particle may rotate and move, and the medium resists to its rotation relative to the background, but not to the gradient of rotation. For the linear isotropic case, this theory was suggested by L.M. Schwartz,

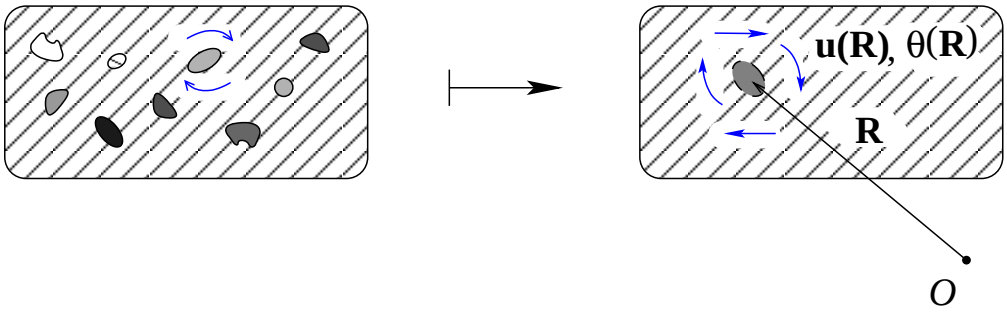

Figure 1: Heterogeneous rock modelled as reduced Cosserat continuum

D.L. Johnson, S. Feng [3]. In previous works [4], [5] we investigated waves in the linear

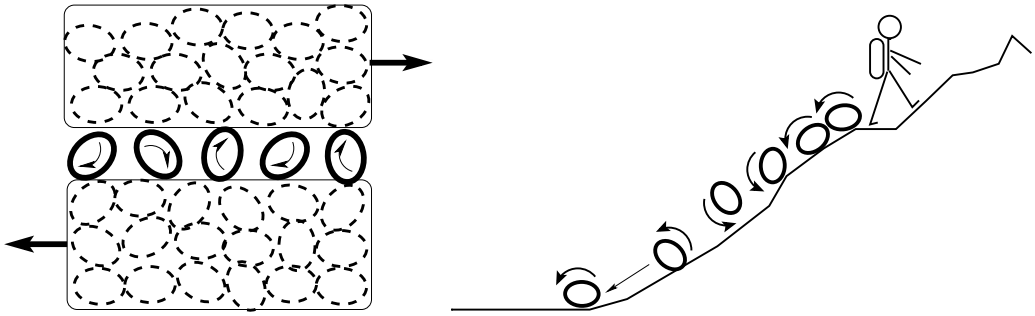

Figure 2: Importance of rotation in shear and avalanches

reduced Cosserat continuum. We have also formulated nonlinear reduced Cosserat continuum and investigated small perturbations near a certain nonlinear prestressed state. Nonlinearity is very important in granular materials due to their ability to rearrange the structure easily [6]. We shall see that a nonlinear reduced Cosserat continuum, resisting to the deformation described by the Cosserat deformation tensor, may have a loss of stability under quasistatic loading.

2 General equations

Strain energy U in the full elastic Cosserat medium depends on two strain tensors: $\mathbf{A} = \overset{\circ}{\nabla}\mathbf{R}\cdot\mathbf{P}$ and $\mathbf{G} = -(\overset{\circ}{\nabla}\mathbf{P}\cdot\mathbf{P}^\top)\cdot\cdot(\mathbf{E}\times\mathbf{P})/2$, $\mathbf{R}$ and $\mathbf{P}$ are the radius vector and rotation tensor in the actual configuration, respectively, $\overset{\circ}{\nabla}$ is the gradient in the reference configuration, $\mathbf{E}$ is the unit tensor. In the reduced Cosserat continuum, by its definition, the strain energy does not depend on the $\nabla\mathbf{P}$. Therefore, U is not function of $\mathbf{G}$, $U = U(\mathbf{A})$. The constitutive equations for the nonlinear elastic Cosserat medium (following from the balance of energy) [7] give us that the couple stress tensor $\boldsymbol{\mu} = 0$, and the stress tensor

$$\boldsymbol{\tau} = \rho\,\overset{\circ}{\nabla}\mathbf{R}^\top\cdot\frac{\partial U(\mathbf{A})}{\partial\mathbf{A}}\cdot\mathbf{P}^\top, \tag{1}$$

where ρ is the mass density. The stress tensor is not symmetric. The balance of force and balance of torque in this case look as

$$\nabla\cdot\boldsymbol{\tau} + \rho\,\mathbf{K} = \rho\,\ddot{\mathbf{u}}, \tag{2}$$

$$\boldsymbol{\tau}_\times + \rho\,\mathbf{L} = \rho\,(\mathbf{I}\cdot\boldsymbol{\omega})^{\cdot}, \tag{3}$$

$\boldsymbol{\omega}$ is the angular velocity, $\mathbf{I}$ is the density of the tensor of inertia, $\mathbf{K}$ and $\mathbf{L}$ are the external volume force and torque, respectively, $\mathbf{Q}_\times \overset{\text{def}}{=} Q_{mn}\,\mathbf{i}^m\times\mathbf{i}^n$. . Note that in absence of volume torques and in (quasi)statics the stress tensor $\boldsymbol{\tau}$ is symmetric, this follows from (3). However, when we consider small perturbations from this state, leading or not to instability, rotational degrees of freedom are very important.

For convenience, let us write down the laws of balance in another form using first Piola-Kirchoff stress tensor $\mathbf{T} \overset{\text{def}}{=} \overset{\circ}{\nabla}\mathbf{R}^{-\top}\cdot\boldsymbol{\tau}\det\overset{\circ}{\nabla}\mathbf{R}$:

Laws of dynamics (balance of force and torque)

$$\overset{\circ}{\nabla}\cdot\mathbf{T} + \rho_0\mathbf{K} = \rho_0\dot{\mathbf{v}}, \tag{4}$$

$$[\overset{\circ}{\nabla}\mathbf{R}^\top\cdot\mathbf{T}]_\times + \rho_0\mathbf{L} = \rho_0\mathbf{I}\cdot\dot{\boldsymbol{\omega}}. \tag{5}$$

The constitutive equation:

$$\mathbf{T} = \rho_0\frac{\partial U}{\partial\mathbf{A}}\cdot\mathbf{P}^\top.$$

3 Small deviations from a nonlinear equilibrium in a material with strain energy twice differentiable with respect to the strain tensor.

Let us consider a certain nonlinear equilibrium state $\boldsymbol{\tau} = \boldsymbol{\tau}_s$, $\mathbf{T} = \mathbf{T}_s, \mathbf{A} = \mathbf{A}_s$, $\mathbf{R} = \mathbf{R}_s$ and small deviations from this state: $\mathbf{R} = \mathbf{R}_s + \mathbf{u}$, $\quad\mathbf{P} = (\mathbf{E} + \boldsymbol{\theta}\times\mathbf{E})\cdot\mathbf{P}_s$. In this section we will write in black constant magnitudes determined by the stress state, and in blue the deviations and differential operators acting upon them. We obtain

$$\mathbf{A} = \mathbf{A}_s + (\overset{\circ}{\nabla}\mathbf{u} + \overset{\circ}{\nabla}\mathbf{R}_s\times\boldsymbol{\theta})\cdot\mathbf{P}_s + o^2(1), \tag{6}$$

$$\mathbf{T} = \mathbf{T}_s - \mathbf{T}_s\times\boldsymbol{\theta} + \rho_0((\left[\frac{\partial^2 U}{\partial\mathbf{A}^2}\right]_s\cdot{\mathbf{P}_s}^\top)\cdot\cdot(\overset{\circ}{\nabla}\mathbf{u} - \boldsymbol{\theta}\times\mathbf{F}_s))\cdot{\mathbf{P}_s}^\top + o^2(1), \tag{7}$$

where

$$\mathbf{F}_s = [\overset{\circ}{\nabla}\mathbf{R}]_s{}^{\top}, \quad \mathbf{T}_s = \rho_0 \left[\frac{\partial U}{\partial \mathbf{A}}\right]_s \cdot \mathbf{P}_s{}^{\top}. \tag{8}$$

The first law of dynamics of Euler (2) can be written as follows:

$$\overset{\circ}{\nabla} \cdot (\rho_0((\left[\frac{\partial^2 U}{\partial \mathbf{A}^2}\right]_s \cdot \mathbf{P}_s{}^{\top}) \cdot\cdot (\mathbf{u}\overset{\circ}{\nabla} - \boldsymbol{\theta} \times \mathbf{F}_s)) \cdot \mathbf{P}_s{}^{\top}) - \overset{\circ}{\nabla} \cdot \mathbf{T}_s \times \boldsymbol{\theta} = \rho_0 \ddot{\mathbf{u}} \tag{9}$$

The second law of dynamics of Euler (balance of torque) (3) gives us

$$\mathbf{u} \times (\overset{\circ}{\nabla} \cdot \mathbf{T}_s) + \boldsymbol{\theta}\, \mathbf{F}_s \cdot\cdot \mathbf{T}_s - \boldsymbol{\theta} \cdot \mathbf{F}_s \cdot \mathbf{T}_s + [\rho_0((\mathbf{F}_s \cdot \left[\frac{\partial^2 U}{\partial \mathbf{A}^2}\right]_s \cdot \mathbf{P}_s{}^{\top}) \cdot\cdot (\mathbf{u}\overset{\circ}{\nabla} - \boldsymbol{\theta} \times \mathbf{F}_s)) \cdot \mathbf{P}_s{}^{\top}]_{\times} = \rho_0 \mathbf{I} \cdot \ddot{\boldsymbol{\theta}} \tag{10}$$

4 Spherical deformation in an arbitrary elastic reduced Cosserat material: dynamic equations for small deviations

Equations (9), (10) are valid for any type of twice differentiable with respect to $\mathbf{A}$ near the equilibrium state strain energy U and nonlinear equilibrium state and can be used, for instance, to model instability and rearrangement of the soil structure in the critical state. Let us consider a spherical nonlinear deformation:

$$\mathbf{A}_s = \overset{\circ}{\nabla}\mathbf{R}_s = A\mathbf{E}, \quad \mathbf{P}_s = \mathbf{E}. \tag{11}$$

Then equation (9) can be written as

$$\overset{\circ}{\nabla} \cdot (\rho_0 \left[\frac{\partial^2 U}{\partial \mathbf{A}^2}\right]_s \cdot\cdot (\mathbf{u}\overset{\circ}{\nabla} - A\,\boldsymbol{\theta} \times \mathbf{E})) - \overset{\circ}{\nabla} \cdot \mathbf{T}_s \times \boldsymbol{\theta} = \rho_0 \ddot{\mathbf{u}} \tag{12}$$

and equation (10) as

$$\mathbf{u} \times \overset{\circ}{\nabla} \cdot \mathbf{T}_s + A\boldsymbol{\theta} \cdot (\operatorname{tr} \mathbf{T}_s \mathbf{E} - \mathbf{T}_s) + [\rho_0(A\left[\frac{\partial^2 U}{\partial \mathbf{A}^2}\right]_s \cdot\cdot (\mathbf{u}\overset{\circ}{\nabla} - A\,\boldsymbol{\theta} \times \mathbf{E}))]_{\times} = \rho_0 \mathbf{I} \cdot \ddot{\boldsymbol{\theta}} \tag{13}$$

5 Spherical prestressed state in an isotropic reduced Cosserat material: dynamic equations for small deviations

Now consider an isotropic material. Let us choose the natural configuration (with zero stresses) as a reference one. Then, if we reach quasistatically a spherical stress state, the deformation is also spherical: $\mathbf{A}_s = \overset{\circ}{\nabla}\mathbf{R}_s = A\mathbf{E}$, $\mathbf{P}_s = \mathbf{E}$, $\mathbf{T}_s = T\mathbf{E}$, $\boldsymbol{\tau}_s = \tau\mathbf{E} = (T/A^2)\mathbf{E}$.

Using arguments of symmetry, we obtain that $\left[\frac{\partial^2 U}{\partial \mathbf{A}^2}\right]_s$ for any isotropic material must have the same form as the corresponding tensor of elastic constants in the linear elastic Cosserat medium, but its constants $\lambda_s, \mu_s, \alpha_s$ are determined by the equilibrium stress state under consideration:

$$\left[\frac{\partial U}{\partial \mathbf{A}^2}\right]_s = \mathbf{X} = \lambda_s \mathbf{E}\mathbf{E} + 2\mu_s(\mathbf{i}_m\mathbf{i}_n)^S(\mathbf{i}^m\mathbf{i}^n)^S + 2\alpha_s(\mathbf{i}_m\mathbf{i}_n)^A(\mathbf{i}^n\mathbf{i}^m)^A. \tag{14}$$

Denote $\boldsymbol{\varphi} = A\,\boldsymbol{\theta}$. Then equations (12),(13) take form

$$\begin{aligned}(\lambda' + 2\mu')\overset{\circ}{\nabla}\overset{\circ}{\nabla}\cdot\mathbf{u} - (\mu' + \alpha')\overset{\circ}{\nabla}\times(\overset{\circ}{\nabla}\times\mathbf{u}) + 2\alpha'\overset{\circ}{\nabla}\times\boldsymbol{\varphi} &= \rho_0\ddot{\mathbf{u}}\\ 2\alpha'\overset{\circ}{\nabla}\times\mathbf{u} - 4\alpha'\boldsymbol{\varphi} &= (\rho_0/A)\mathbf{I}\cdot\ddot{\boldsymbol{\varphi}}\\ \text{(for spherical tensor of inertia)} &= (\rho_0 I/A)\ddot{\boldsymbol{\varphi}}\end{aligned} \tag{15}$$

where

$$\alpha' = \alpha_s - T/(2A), \quad \mu' = \mu_s + T/(2A), \quad \lambda' + 2\mu' = \lambda_s + 2\mu_s. \tag{16}$$

These equations by form coincide with the equations for the isotropic linear reduced Cosserat continuum investigated by us (see, for instance, [4]), and therefore if all the "effective elastic parameters" are positive, they inherit all their properties: dispersion curves with strong dispersion and apparent attenuation for the shear-rotation wave, forbidden band of frequencies for the shear-rotation wave, localisation in this forbidden band on small inertial heterogeneities, a resonant frequency etc. Here and further we consider the case of the spherical inertia tensor $I\mathbf{E}$. Dispersion curves for this medium are shown in Fig. 3. The shear dispersion relation is:

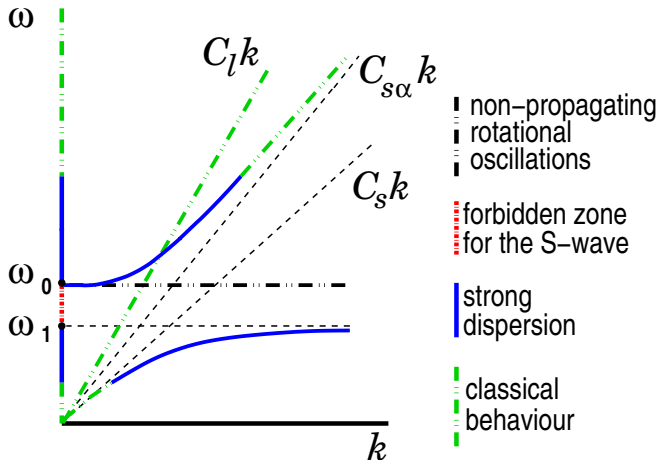

Figure 3: Dispersion curves for the linear reduced isotropic elastic Cosserat continuum. $\omega_0^2 = 4\alpha/I, \quad \omega_1 = \omega_0/(1+\alpha/\mu)$, $C_s^2 = \mu/\rho$, $C_{s\alpha}^2 = (\mu+\alpha)/\rho$, $C_l^2 = (\lambda+2\mu)/\rho$.

$$k_S^2 = \frac{\omega^2}{C_S^2}\cdot\frac{1-\omega^2/\omega_0^2}{1-\omega^2/\omega_1^2}. \tag{17}$$

Note that the only supposition about the strain energy we made until now is that it is twice differentiable in $\mathbf{A}$, and that the material is isotropic.

We may consider this as an "effective" linear reduced Cosserat continuum with an "effective" strain energy

$$\rho_s U = \frac{1}{2}(\overset{\circ}{\nabla}\mathbf{u} + \boldsymbol{\varphi}\times\mathbf{E})\cdot\cdot\,\mathbf{X}\,\cdot\cdot(\overset{\circ}{\nabla}\mathbf{u} + \boldsymbol{\varphi}\times\mathbf{E})^{\top}. \tag{18}$$

6 Physically linear, geometrically nonlinear Cosserat medium

It is easy to suggest a simple kind of strain energy which makes effective constant α' to be negative at certain strain A, and therefore gives an unstable solution for the shear-rotation wave determined by (15). Physically, this would mean that at a certain tension the medium changes its structure via rotation and shear.

Indeed, consider the simplest example of the strain energy, an isotropic geometrically nonlinear but physically linear material with natural state $\mathbf{A} = \mathbf{E}$. The strain energy for such a continuum is determined by expression

$$\rho_0 U = \frac{1}{2}(\mathbf{A} - \mathbf{E}) \cdot\cdot \mathbf{X} \cdot\cdot (\mathbf{A} - \mathbf{E})^{\top}, \tag{19}$$

where

$$\mathbf{X} = \lambda \mathbf{E}\,\mathbf{E} + 2\mu(\mathbf{i}_m\mathbf{i}_n)^S(\mathbf{i}^m\mathbf{i}^n)^S + \alpha(\mathbf{i}_m\mathbf{i}_n)^A(\mathbf{i}^n\mathbf{i}^m)^A. \tag{20}$$

In this case elastic parameters do not depend on the prestressed state. Now, calculating $\boldsymbol{\tau}_s$ at the prestressed state $\mathbf{A}_s = A\mathbf{E}$, we have $T = 3(A-1)(\lambda + 2\mu)$, $\alpha' = \alpha - \frac{A-1}{A}(\lambda + 2\mu)$, $\mu' = \mu + \frac{A-1}{A}(\lambda + 2\mu)$, $\lambda' + 2\mu = \lambda + 2\mu$. This gives us that if $\lambda + 2\mu > \alpha$ and $A > (\lambda + 2\mu)/(\lambda + 2\mu - \alpha)$, we have $\alpha' < 0$. The "effective" strain energy is not non-negatively defined any more, and this leads to instability. The frequency ω_0 becomes imaginary, and the mechanism of the stability loss in this case is via rotations.

Under enough strong compression, when $A < 1 - \mu/(\lambda + 2\mu)$, we have $\mu' < 0$, the shear wave becomes instable, material fails under small shear perturbation (at rather low frequencies). At strong expansion, when $\alpha' < 0$, mechanism of failure is via rotations (at frequency ω_0'). This can be a possible way to describe restructurization in the material (private communication by M.A.S. Quintanilla confirms that we see the first phenomenon in experiments on granular materials; in experimental work by Yu.I. Mescheryakov et al., presented at APM 2010, both phenomena were observed). Of course, if we wish to describe a certain type of soil, we have to think on the strain energy which would describe in the best way its properties. Our example illustrates that nonlinear elastic reduced Cosserat model gives a possibility to describe material restructurization under quasistatic loading as well as its stable state. One can prove that this result is also valid for a wide class of strain energies.

Acknowledgements

The author is very grateful to Prof. A. Kiselev and Prof. A. Castellanos for valuable discussions. This work was partially supported by Spanish government (Project FIS2006-03645) and by Shell International E.&P. (Project "Advanced modelling of mechanical behaviour of rocks and soils").

References

[1] I.F. Collins. Elastic/plastic models for soils and sands. *International Journal of Mechanical Sciences*, 47(4-5):493–508, 2005.

[2] Bulletin of the seismological society of america, 99(2b), 2009.

[3] L.M. Schwartz, D.L. Johnson, and S. Feng. Vibrational Modes in Granular Materials. *Physical Review Letters*, 52(10):831–834, 1984.

[4] E.F. Grekova, M.A. Kulesh, and G.C. Herman. Waves in linear elastic media with microrotations, part 2: Isotropic reduced Cosserat model. *Bulletin of the Seismological Society of America*, 99(2B):1423, 2009.

[5] M.A. Kulesh, E.F. Grekova, and I.N. Shardakov. The problem of surface wave propagation in a reduced Cosserat medium. *Acoustical Physics*, 55(2):218–226, 2009.

[6] M. Oda and K. Iwashita. *Mechanics of Granular Materials*. Balkema, 1999.

[7] E. Grekova and P. Zhilin. Basic equations of Kelvin's medium and analogy with ferromagnets. *Journal of elasticity*, 64(1):29–70, 2001.

Elena F. Grekova, Institute for Problems in Mechanical Engineering of Russian Academy of Sciences, Bolshoy pr. V.O., 61, 199178, St. Petersburg, Russia

Elastic reduced Cosserat continuum by eyes of a "rotation blind" person

Elena F. Grekova
elgreco@pdmi.ras.ru

Abstract

We discuss the equations of the reduced Cosserat continuum expressing rotations in terms of translations via the law of balance of torque. We try to understand how we can interpret the behaviour of the medium if we do not measure rotations and see only translations in the medium. For the linear case under certain conditions it is possible to express explicitly the rotational displacement as a functional of the translation gradient. Substituting the rotation by this expression in the law of balance of force, we obtain the equation of motion in translational displacements. This equation can be interpreted as an equation of motion of a classical history-dependent medium with symmetric stress tensor. The stress tensor of the real medium is not symmetric, but a "rotation blind" person cannot see this.

1 Introduction

Reduced Cosserat continuum could be a good model to describe soils, rocks and powders in the solid state, since rotational degrees of freedom can be very important in wave propagation and loss of stability. However, for the time being the equipment measuring rotational degrees of freedom of particles in soils and rocks is rather in the stage of development. Usually we measure only translational strains and force stress tensor. In this short work we wanted to see how the linear reduced isotropic Cosserat continuum, suggested by L.M. Schwartz, D.L. Johnson, S. Feng [1] and investigated in [2], [3], would look in eyes of a person who cannot see rotations.

2 General equations

The equations of motion in displacements for the homogeneous linear elastic isotropic Cosserat medium with the density of tensor of inertia $I\mathbf{E}$ are [2]

$$\begin{aligned}&(\lambda+2\mu)\nabla\nabla\cdot\mathbf{u}-(\mu+\alpha)\nabla\times(\nabla\times\mathbf{u})+2\alpha\,\nabla\times\boldsymbol{\theta}+\rho\mathbf{K}=\rho\ddot{\mathbf{u}},\\&2\alpha\,\nabla\times\mathbf{u}-4\alpha\,\boldsymbol{\theta}+\rho\mathbf{L}=\rho\,I\ddot{\boldsymbol{\theta}}.\end{aligned}\tag{1}$$

Here $\mathbf{u},\boldsymbol{\theta}$ are translational and angular infinitesimal wave displacements, $\mathbf{K}$ and $\mathbf{L}$ are the densities of external volume force and torque, respectively, ρ is the mass density. Denote $\omega_0=2\sqrt{\alpha/I}$. We express $\boldsymbol{\theta}$ via $\mathbf{u}$ and its derivatives using the second equation of system (1):

$$\boldsymbol{\theta}=\boldsymbol{\theta}_0e^{i\omega_0t}-\frac{\rho}{2\pi I}\int\limits_{-\infty}^{+\infty}\int\limits_{-\infty}^{+\infty}\frac{\mathbf{L}(\tau)e^{i\omega(t-\tau)}}{\omega^2-\omega_0^2}d\omega\,d\tau-\frac{\omega_0^2}{4\pi}\nabla\times\int\limits_{-\infty}^{+\infty}\int\limits_{-\infty}^{+\infty}\frac{\mathbf{u}(\tau)e^{i\omega(t-\tau)}}{\omega^2-\omega_0^2}d\omega\,d\tau.\tag{2}$$

Here we supposed that we were allowed to change the order of integration. Using the causality principle, we suppose $\tau < t$ and calculate the integral

$$\int_{-\infty}^{+\infty} \frac{e^{i\omega(t-\tau)}}{\omega^2 - \omega_0^2}\, d\omega = -\frac{2\pi}{\omega_0} \sin\omega_0(t-\tau), \tag{3}$$

and we have

$$\boldsymbol{\theta} = \boldsymbol{\theta}_0 e^{i\omega_0 t} + \frac{\rho}{I\omega_0} \int_{-\infty}^{t} \mathbf{L}(\tau) \sin\omega_0(t-\tau) d\tau + \frac{\omega_0}{2} \nabla \times \int_{-\infty}^{t} \mathbf{u}(\tau) \sin\omega_0(t-\tau) d\tau \tag{4}$$

Then from the first equation of (1) we obtain

$$(\lambda + 2\mu)\nabla\nabla\cdot\mathbf{u} - (\mu+\alpha)\nabla\times(\nabla\times\mathbf{u}) + \alpha\omega_0\nabla\times(\nabla\times\int_{-\infty}^{t}\mathbf{u}(\tau)\sin\omega_0(t-\tau)\,d\tau)$$
$$+ 2\alpha\nabla\times\boldsymbol{\theta}_0 e^{i\omega_0 t} + \nabla\times\frac{\omega_0}{2}\int_{-\infty}^{t}\rho\mathbf{L}\sin\omega_0(t-\tau)\,d\tau + \rho\mathbf{K} = \rho\ddot{\mathbf{u}}. \tag{5}$$

We see that if rotational degrees of freedom are "invisible" for an observer, their presence changes the "effective" constitutive equation, making the medium be history-dependent. Also, "new external volume forces" appear if $\nabla\times\mathbf{L}$ and $\boldsymbol{\theta}_0$ are not equal to zero. Let us consider the case when $\nabla\times\mathbf{L} = \mathbf{0}$, and due to inital conditions $\boldsymbol{\theta}_0 = \mathbf{0}$. Then (5) can be written as

$$\nabla\cdot\mathbf{T} + \rho\,\mathbf{K} = \rho\,\ddot{\mathbf{u}}, \tag{6}$$

where

$$\mathbf{T} = \boldsymbol{\tau}_c - \alpha\omega_0\ \mathrm{Dev}\int_{-\infty}^{t}(\nabla\mathbf{u}(\tau))^S \sin\omega_0(t-\tau)\,d\tau, \tag{7}$$

$\boldsymbol{\tau}_c$ is a stress tensor in the classical isotropic linear elastic medium with Lamé constants $\lambda' = \lambda - 2\alpha$, $\mu' = \mu + \alpha$.

We see that equation (7) is a constitutive equation for an effective history-dependent continuum with stress tensor $\mathbf{T}$. The peculiar thing is that while the real stress tensor $\boldsymbol{\tau}$ has an antisymmetric part, the stress tensor $\mathbf{T}$ for the effective medium is symmetric, and its deviator is history dependent. Thus we have to ask ourselves: what stress tensor do we measure in experiments if we do not measure rotations?

Acknowledgements

This work was partially supported by Spanish government (Project FIS2006-03645) and by Shell International E.& P. (Project "Advanced modelling of mechanical behaviour of rocks and soils").

References

[1] L.M. Schwartz, D.L. Johnson, and S. Feng. Vibrational Modes in Granular Materials. *Physical Review Letters*, 52(10):831–834, 1984.

[2] E.F. Grekova, M.A. Kulesh, and G.C. Herman. Waves in linear elastic media with microrotations, part 2: Isotropic reduced Cosserat model. *Bulletin of the Seismological Society of America*, 99(2B):1423, 2009.

[3] M.A. Kulesh, E.F. Grekova, and I.N. Shardakov. The problem of surface wave propagation in a reduced Cosserat medium. *Acoustical Physics*, 55(2):218–226, 2009.

Elena F. Grekova, Institute for Problems in Mechanical Engineering of Russian Academy of Sciences, Bolshoy pr. V.O., 61, 199178, St. Petersburg, Russia

Fatigue of fillet-welded joint assessment by the FEA simulation of damage accumulation

Ruslan V. Guchinskiy Sergei V. Petinov
ruslan239@mail.ru sergei.petinov@gmail.com

Abstract

Fatigue strength evaluation of non-continuous incomplete penetration fillet-welded joints transferring stress flow by the S-N criteria incorporating the "Hot-spot stress" or "Notch-stress" approaches is dubious since the characteristic stress at the crack initiation location is not established by the rules for fatigue design. Application of the linear fracture mechanics (LMF) technique meets a problem of numerical modeling the crack three-dimensional shape and front extension, which becomes insoluble when the crack approaches the outer surface of weld bead and propagates along the seam. Apart from that, considering material plasticity beyond the initial phase of crack extensions from the cavity is off the frames of the principles of the LMF.

An approach based on the FEA simulation of fatigue damage accumulation is suggested and applied to evaluate the crack initiation at the cavity and propagation in the non-continuous fillet-welded joint. The crack initiation at the cavity, its three-dimensional shape formation and evolution are simulated taking into account the elastic-plastic cyclic deformation of weld material until almost complete failure of the joint. The results of analysis are in good agreement with published experimental data.

1 Introduction

Fillet-welded joints are frequent in steel structures applied in civil engineering, in ship and marine structures. Through recent decades, a design principle of welded structures, known as "friendly for manufacturing" assumed application of fillet-welded joints without machining the edges needed to provide complete filling of the joint, has been manifested.

Of special interest are the non-continuous part-penetration joints where the load flow passes via the weld material. A typical example is the welded joints of brackets in connection of outer shell stiffeners and transverse components of welded bridge and ship hull structures. The load flow due to axial deformation and bending of stiffeners is concentrated in the weld material at the bracket ending causing local stress elevation capable of initiating fatigue crack, Fig.1.

Another example is the "friendly for manufacturing" cruciform part-penetration load-carrying welded joints when machining of plate edges is not applied. Depending on the relative width of cavity (compared to plate thickness) and shape of weld bead fatigue failure in these joints may initiate at the weld toe or, alternatively, from the weld root, the cavity tip.

In uniformly loaded continuous fillet-welded joints the first problem, i.e. initiation of fatigue process at the weld toe, can be solved by following the International Institute of Welding (IIW) instructions, e.g. [6, 11], and the rules of International Association of Classification Societies (IACS), e.g. [7], for fatigue design of hull structures.

Figure 1: Fatigue crack (re-welded) at the bracket ending on the flange of longitudinal stiffener. A tanker ship bottom structure. Courtesy of Lloyd's Register

In case the crack is expected at the weld root fatigue strength can be assessed by applying the Fracture mechanics technique [2, 3, 12, etc.].

Since the continuous uniformly loaded joints are considered in above references, the stress analysis can be reduced to the generalized plane stress problem. The crack path is approximately predicted by the FEA as the maximum principal stress planes passing through the weld throat. Respectively, the strength intensity factor (SIF) values along the crack path should be calculated. Further, the crack extensions are found by integrating the Paris-Erdogan equation, e.g. [3]. It should be immediately noted that the crack (SIF) analysis in this case is limited by the properties of stress field at the crack tip: the stress singularity vanishes as the crack traverses approximately 0.7 of the weld throat; apart from that increasing stress in the ligament actuates material plasticity, again, limiting applicability of the Linear fracture mechanics and the prospects of analysis.

Fatigue analysis is seen essentially more complicated when the crack initiation is expected at the weld root of the non-continuous and non-uniformly loaded joints. In such cases, planning fatigue and FE analysis of the joint, one has to foresee the crack initiation location and the three-dimensional crack progress until it would reach the outer surface of the weld bead. The mesh should be re-arranged following the crack front evolution and extensions. Again, the stress field singularity range may be limited and material plasticity would prevent the feasibility of analysis well before the crack might have approached the outer surface of the weld.

An attempt to approximate fatigue properties of non-continuous part-penetration fillet welded joint was made in [14] exemplified by the bending loaded cantilever plate, Fig.2.

The intact weld bead stress field was used to approximately estimate the crack trace and the stress intensities, mostly at the weld ending. The results of analysis were in reasonable agreement with the experimentally obtained fatigue lives [8]. However, the agreement was found at relatively low stresses in the joint. At high stresses in the weld material the Linear fracture mechanics format was not applicable because of development of plasticity at the weld root. All in all, since the crack extensions were modeled rather conditionally, the approach developed could not be regarded a general technique of fatigue strength evaluation.

Recently [9] it was shown that crack initiation and growth in case of elastic-plastic deformation of material might be simulated aided by the FEA using the technique of "damage accumulation", even in polycrystalline silicon components. The idea of the approach is not a new one: it was suggested, e.g., in [1], [2], [5] and in earlier publications. However, modeling of the fatigue process in [9] as in other publications as well, was applied to the plane stress conditions, crack analysis in thin plane elements. In the present analysis the three-dimensional crack progress caused by exhausting of cyclic plasticity is simulated by applying the elements of the above approach. The results of simulation are in good agreement with the experimental data [8] obtained at large load excursions causing cyclic plasticity of weld material.

2 Procedure of analysis

According the present version of the approach, the volume of detail analyzed is modeled by the mesh, the finite elements in which are assumed "material elements", deemed representative of clusters of grains with approximately close slip resistance. This principle allows for statistical modeling of properties of slip resistance in "material elements" providing by this assessment of scatter in fatigue lives [9, 15]. Progressing damage of "material elements" is estimated by the linear damage summation (Palmgren-Miner) rule; the stress field and the damage evolution is accounted in the course of crack extensions. The "failed" elements where the damage reaches the "critical unity" are defined further by the infinitesimal stiffness, thus allowing for the crack initiation and extensions simulation.

In present analysis the elements of this technique are applied for the numerical simulation of fatigue process in non-continuous non-uniformly loaded fillet-welded joint, where the crack is assumed initiated in cavity, at the weld root. The damage accumulation is based on considering elastic-plastic behavior of material; the crack shape and extensions are simulated until almost complete failure of the joint, when the crack approaches the outer surface of the weld and propagates along the weld in the throat plane.

Fatigue resistance of material, a low-carbon structural steel electrode material, is characterized by the Strain-life Manson's criterion [10, 13]:

$$\Delta\varepsilon = \Delta\varepsilon_p + \Delta\varepsilon_e = CN^{-\alpha} + BN^{-\beta} \tag{1}$$

parameters of which, experimentally obtained, are: $C = 0.480$, $B = 0.011$, $\alpha = 0.653$, $\beta = 0.140$[13]; $\sigma_y = 290\ MPa$, $\sigma_u = 450\ MPa$, $\Delta\varepsilon$ is the total cyclic strain range, $\Delta\varepsilon_e$, $\Delta\varepsilon_p$ are the elastic and plastic strain range components, respectively; N is the number of cycles prior fatigue failure of material, defined by the pre-established decrease of the specimen stiffness. During fatigue tests of specimens the cyclic curves were recorded and generalized diagrams obtained [13].

As a reference, the specimen characteristics and loading mode given in [8], Fig.2, were used to design the FE model of the joint. In designing the FE model of the joint the

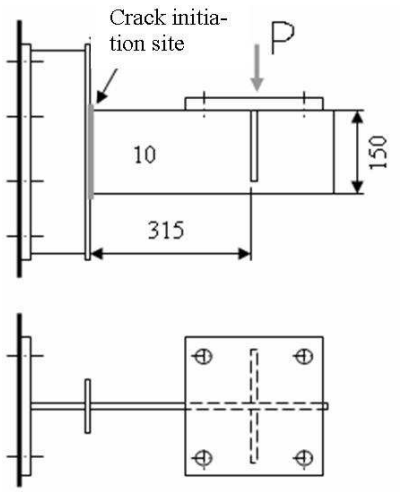

Figure 2: Specimens tested and results reported in [9]

attention was focused solely on the crack initiation at the slit tip circumference and propagation towards the outer surface of the weld bead. It was assumed that crack propagation surface insignificantly deviated from the weld throat plane.

The fracture modes in [8] were indicated only schematically; therefore the fractographic observations revealed in testing of similar fillet-welded joints where fatigue cracks propagated from the weld root [4] were used to support the above assumption, Fig. 3.

Respectively, the mesh was designed reasonably fine in the expected growth plane to provide the necessary cyclic stress and strain resolution (10 elements through the weld thickness in the throat plane); otherwise, it was coarsened, as shown in Fig.4, to reduce the processing time.

In the first load application, the elastic-plastic behavior of elements of the model was characterized by the static tensile diagram. In unloading, the elements, which exhibited plasticity in the initial phase, were further provided with generalized cyclic curve. On assumption of cyclic stability of material (observed in experimental studies), calculated strain range was used to obtain the initial fraction of damage in affected "material elements".

The number of load cycles corresponding to estimated strain range is found from (1) by using maximum strain range in elements located, in the first step, at the circumference of the slit tip. This number is attributed to "failure" of these (or the only, if appropriate) elements. So far, if this number is N_0, then damage accumulated at this step in every of remaining affected elements is:

$$d_{initial} = N_0/N_i \tag{2}$$

So that $n_i = N_0$ is the initial fragment of the "fatigue process", N_i is the number of load cycles to failure in every of the strain range conditions, in every of "material elements" where plasticity occurred in the initial and sequential loadings, which develop due to "failure" of consequential elements. The "failure" is controlled by condition:

$$d = d_{initia}l + \sum_i n_i/N_i = 1 \tag{3}$$

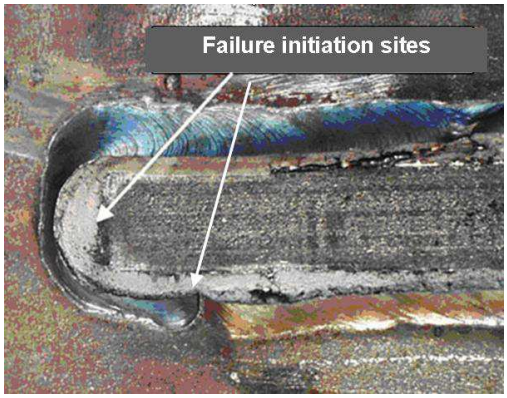

Figure 3: Fracture of weld material initiated at the front and lateral edge of cavity [4]

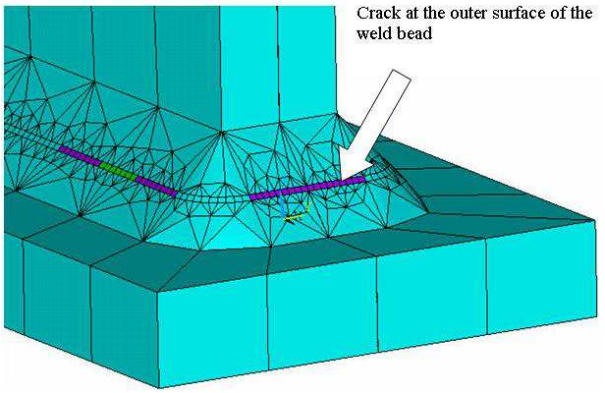

Figure 4: FE model of the weld ending where crack initiation and growth is anticipated from the cavity caused by the lack of penetration of weld material

Here $n_i = n_i(\Delta\varepsilon_i)$ is the number of load cycles corresponding the strain range $\Delta\varepsilon_i$, which completes the damage accumulation in a particular FE ("material element"), d, at every of the "crack extensions".

3 Results of the fatigue process simulation

The briefly displayed procedure allowed analyzing the crack "initiation" at the cavity circumference and its extensions until almost complete fracture of the joint in the weld throat surface. Fig.5 shows the results of FE simulation of the crack initiated in several locations of the slit circumference and its growth towards the outer surface of the weld. As seen, the crack initiation is predicted not only at the weld ending inner boundary; also, simultaneous crack start is expected at a short distance from the weld ending, at the lateral tips of the cavity.

This corresponds to the findings of experimental investigation [4], Fig.3, and of the previous numerical analysis of the same joint, although the latter limited by the uncracked weld material conditions and assessed at the axial tensile loading of the attachment [14], as seen in Fig.6.

The crack shape evolution shown in Fig.5, corresponds to 32, 57, 85, 94, 98 and 99% of the total fatigue life of the joint when the applied load excursions were equal to $\Delta P = 48.33$ kN. Same were the general crack shape characteristics, although the crack extension steps were dependent on the load range, as occurred fatigue lives under different loading conditions as well.

The results of analysis of fatigue properties of the fillet-welded joint when the crack assumed initiated at the cavity due to incomplete penetration, altogether with the experimental findings are presented in Table 1 and in Fig.7.

It is seen, the results of fatigue process modeling by the damage accumulation in "material elements" procedure fit reasonably well the experimental data.

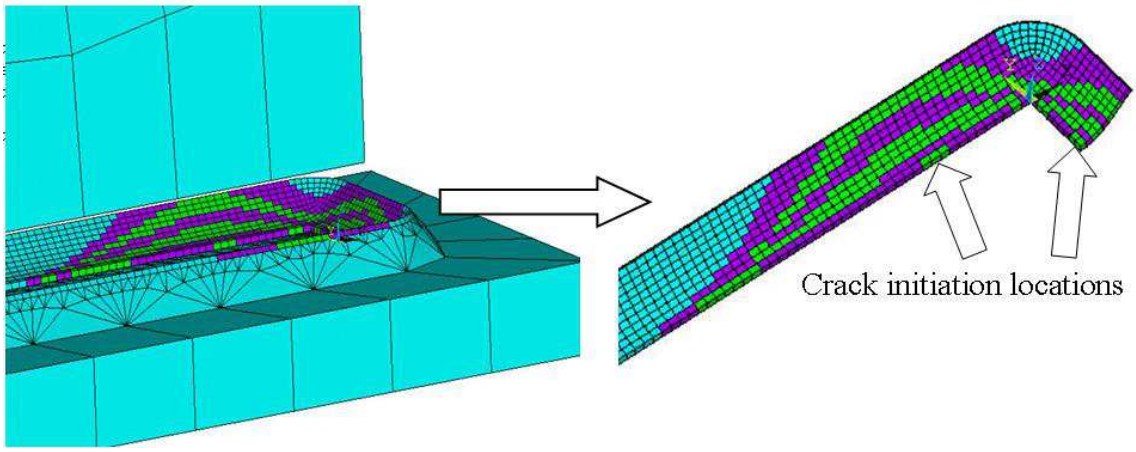

Figure 5: Sequence of "failure" of elements and of the respective "crack extensions" initiated at the slit circumference

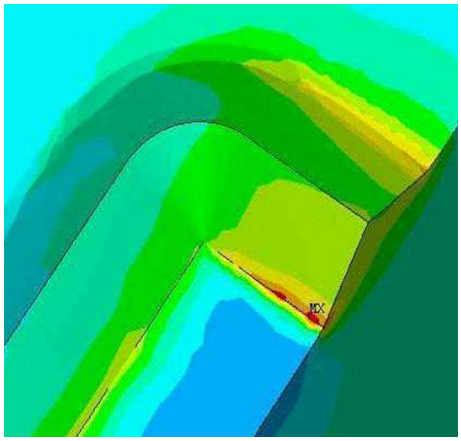

Figure 6: Maximum principal elastic stress field in the weld throat plane; tensile loading of the joint [14]

Table 1. Fatigue life of the joint: test data [8] and results of numerical simulation

Reference stress at the weld toe S, MPa	Load excursion, P, kN	Fatigue life, x 10^6, cycles, experiment [9]	Fatigue life, x 10^6, cycles, simulated, present analysis
188.05	22,748	3.075	9.100
282.14	34,13	1.429	0.877
305.62	36,97	0.819	0.558
329.1	39,81	0.379 - 0.419	0.375
352.58	42,65	0.278	0.269
399.54	48,33	0.084	0.137

Discussing the comparison, it should be noted that repeating of testing of a series of specimens at the same load conditions would result in a scatter of test data. The sources of scatter may be attributed to the difference of the volume and the shape of weld material, especially at the weld ending, to the difference of particular size and shape of cavity in every of tested specimens. Those were uncertain; for the purposes of a more detailed analysis the geometry of the weld and slit should be assessed, e.g., by the means

of ultrasonic scanning.

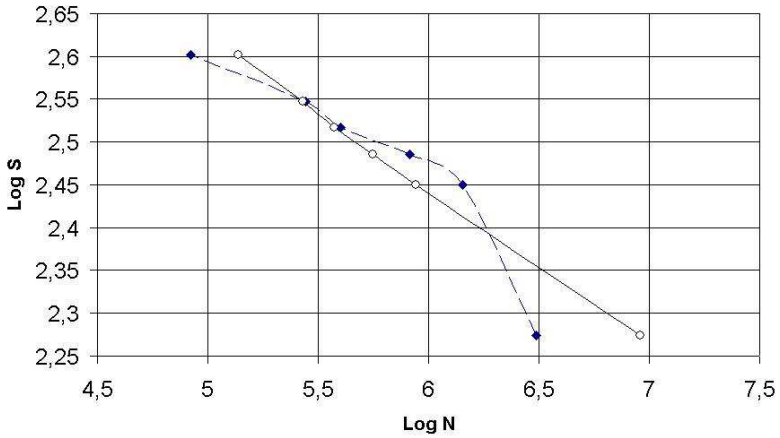

Figure 7: Fatigue lives, comparison of the test data [8], bold diamonds, and of the present numerical modeling results, circles

Also, the present analysis did not consider residual welding stress and its influence on the fatigue process. However, it may be a factor of secondary importance in modeling fatigue of incomplete penetration welding joints: it was shown [16], that the most influential component of welding stress, normal to the expected crack propagation plane, is insignificant at the cavity tip, increasing towards the outer surface of the weld bead. Material cyclic plasticity induced at the crack front and in ligament would result further in the residual stress re-distribution and relaxation, so that total effect of welding stress may be neglected.

Acknowledgements

This work was carried out within the frames of the Program of fundamental research sponsored by the Division of Energy, Mechanical Engineering, Mechanics and Control of Processes of Russian Academy of Science.

References

[1] Boytsov, GV. (1990) A Generalized Analysis of Initiation and Propagation Stages of Fatigue Cracks in Plate Elements of Ship Structures. Proceedings, Gorky Polytechnic, pp.5-11

[2] Ellyin, F, Fakinlede, CO. (1985) Probabilistic Simulation of Fatigue Crack Growth by Damage Accumulation. Engineering Fracture Mechanics, Vol. 22, No. 4, pp. 697-71

[3] Frank, KH, Fisher, JW. (1979) Fatigue Strength of Fillet Welded Cruciform Joints. "Journal of the Structural Division", ASCE, vol.105, No.ST9, pp.1727-1741

[4] Fricke, W, Doerk, O, and Gruenitz, L. (2004) Fatigue Strength Investigation and Assessment of Fillet-Welds around Stiffener and Bracket Toes.// Proc. of Special FPSO Conference of OMAE. Houston, TX

[5] Glinka, G. (1982) A Cumulative Model of Fatigue Crack Growth. "International Journal of Fatigue", April, pp.59-67

[6] Hobbacher, A. (2007) Recommendations for Fatigue Design of Welded Joints and Components. IIW document XIII-2151r1-07 / XV-1254r1-07

[7] IACS (2006) Common Structural Rules for Double Hull Oil Tankers

[8] Kim, WS, Kim, DH, Lee, SG, and Lee, YK. (2001) Fatigue Strength of Load-Carrying Box Fillet Weldment in Ship Structure. Proceedings, 8th International Symposium PRADS-2001, Vol. 2, pp.1161-1167, Shanghai. Elsevier Science Ltd.

[9] Korolev IK, Petinov SV, Freidin AB. (2008) FEM Simulation of Fatigue Damage in a Polycrystalline Silicon Structure. Proc., VI Intern. Conference on Reliability of Materials and Structures "RELMAS-2008". SPb Polytechnic University, St.Petersburg

[10] Makhutov, NA. (1981) Strain-Life Criteria for Fatigue Failure and Strength Analysis of Structural Components. "Mashinostroenie" Pubs, Moscow

[11] Niemi, E. (2000) Structural Stress Approach to Fatigue Analysis of Welded Components. Designer's Guide. IIW Doc. XIII-WG3-06-99

[12] Petinov, SV. (1976) Crack Propagation Period of Fatigue and Prediction of Structure Fatigue Life. Report SK/R-36, Division of Ship Structures, NTH, Trondheim

[13] Petinov, SV. (2003) Fatigue Analysis of Ship Structures. Backbone Publishing Co., P.O. Box 562, Fair Lawn, NJ 07410

[14] Petinov SV, Kim WS, Paik YM. Assessment of Fatigue Strength of Weld Root in Ship Structure: An Approximate Procedure. "Ship and Offshore Structures Journal". Woodhead Publishing, V.1, No.1, 2006, pp.55-60

[15] Petinov, SV, Letova, TI, Yermolaeva, NS. (1998) FEM Modeling of the Aluminium Alloy Microplasticity. In: "Advanced Light Alloys and Composites". NATO ASI Series / Ed. by R. Ciach. Kluwer Academic Publishers, Dordrecht, pp. 427-433

[16] Karzov, GP, Margolin, BZ, Shvetsova, VA (1993) Physical and Mechanical Modeling of the Failure Processes. Polytechnic Publ., St.Petersburg

Ruslan V. Guchinskiy, Sergei V. Petinov, Institute for problems in mechanical engineering, Bolshoy pr., 61, V.O., St. Petersburg, 199178, Russia

Modeling and optimization of vibrational screening process

Kirill Ivanov
ivanoff.k.s@gmail.com

Abstract

Modern analytical approaches to granular medium modelig in vibrational screening processes are sufficiently restricted in its usability, they are applicable in narrow ranges of parameters and dont bring real benefits in new devices development. Numerical modeling methods such as method of discrete elements are quite resource-intensive and don't allow to detect whole process features. The modeling approach presented in the article is aimed at filling emptiness between existing analytical and numerical methods in screening process studying. Because of its computational simplicity the algorithm presented here allows to make an automatic optimization of parameters for screening devices and to estimate its preliminary desirable technical parameters.

1 Introduction

Vibrational screening processes are widely applied in many industrial areas from ore dressing to, for example, waste processing. However, no sufficiently versatile mathematical tools and engineering approaches to the calculation of respective devices have been developed in almost three centuries of application of this technology. Creation of new models was primarily based on experience, tradition and intuition of the developers. Elaboration of new types of devices was governed by natural selection - better designs were replacing less efficient models. Existing analytical approaches were essentially specific and founded on very strong assumptions (applicable in a narrow range of conditions). They might quite accurately describe the existing devices, but were of little use in terms of creation of new designs. A boost in the development of computer technology and computer modeling resulted in the emergence of various discrete element methods for studying such processes. These methods enable an insight into a process, tracing the behavior of each particle of loose material, and detecting weak elements or elements hindering device operation [1]; however, they require substantial computing resources. For example, a computational experiment with a detailed screening model may last up to several months, even upon application of high-performance systems. This fact greatly limits the efficiency of discrete element models in creation of new screens with optimal performance. As a result, there is a gap between effective applicability areas of currently existing computational and analytical models - the first are too resource-intensive, and the latter - not precise enough. When this gap is filled, preliminary screen calculations shall be more efficient. Moreover, in conjunction with stochastic optimization algorithms, appropriate methods in this gap area would allow initially selecting near-optimal parameters for these devices. This, in turn, could become a valuable engineers or designers tool, helping in defining main features of new designs.

2 Screening Model Description

This paper proposes a general model building concept and a specific version of its implementation, allowing both to avoid resource-intensive computations that are inherent in discrete element schemes and to obtain sufficiently accurate results. The main feature of this model is a separate representation of processes occurring in the granular media in contact with the screening surface and in the bulk material flow. Theoretically, it seems possible to also take into account contacts with other surfaces, such as, for example, casing walls. The approach proposed may be considered as a generalization of the methods proposed in a number of analytical studies [2, 3]. In this case, due to the lack of restrictions imposed by an analytical study, it is possible to significantly expand process detailed descriptions. In particular, this approach enables consideration of material separation and mixing during screening. To this end, single separation and mixing models may be created based on data from field and numerical (discrete element) experiments.

Based on this approach, the author has created a program that simulates the behavior of granular media on the vibrational screen. The general algorithm is shown in Fig. 1.

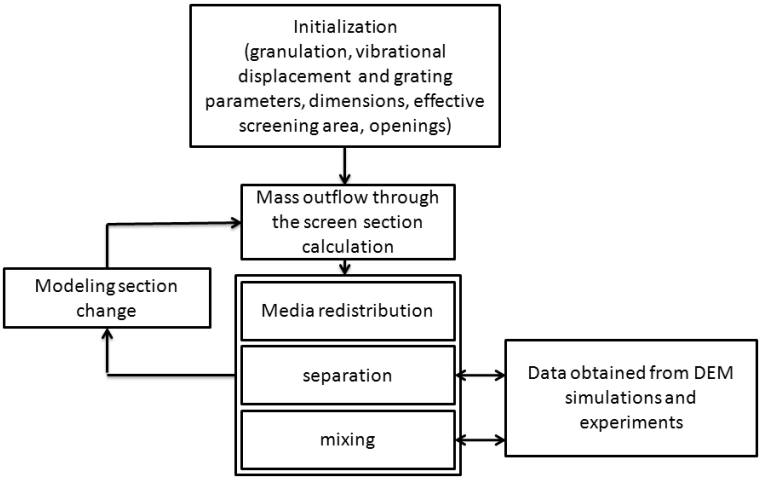

Figure 1: Vibrational Screening Simulation Algorithm Structure

Program input data include: feeding, vibration parameters and the rate of material flow through screen openings, as well as its original particle-size distribution in five narrow ranged grain-size classes (internal grain-size distribution function shall be further set for each class), screen dimensions, screening area and screen opening diameters. Parameters that characterize separation and mixing intensity in a material layer shall be specified separately.

It should be noted that parameters of initial analytical models [2, 3] for the screening process included material vibrational displacement velocity over the screening surface rather than vibration characteristics. Entering these parameters may not be entirely suitable for an engineer. To save program users from having to separately calculate the material flow velocity, a program was developed that simulates loose material displacement with given elastic properties on an inclined vibrating plane [4]. This unit shall be executed first. Vibrational displacement characteristics obtained in this unit shall be then sent to the main part of the program as input data.

An iteration of the basic algorithm includes the following steps:

- Calculation of mass outflows of various material classes through a simulated screen

face segment and interactions in contact areas between the granular media and working surfaces.

- Redistribution of grain-size classes in the material above the simulated screen segment, or modeling of processes occurring in the granular media.

In general, numerous different patterns may be used at the first stage; however, for the sake of simplicity, the program version implemented uses the classical Gaudin formula for a screen with rectangular openings:

$$\varphi(1 - D/d_0)^2$$

where φ - is screening area, D - is narrow ranged grain-size class, d_0 - is screen opening size. As demonstrated by the program tests, this formula ensures more than just a qualitative agreement with the actually observed phenomena. However, this formula turns out a bit "optimistic" results when the modell applied to classes that are similar in size to the opening size.

Separation and mixing processes, considered in the second iteration phase, were simulated as uniform processes by setting specific process flow rates. These parameters may be estimated by simulating the behavior of a loose material with appropriate grain-size distribution on a vibrating surface using, for example, the discrete element method or molecular dynamics [5]. It should be noted that the architecture of the program developed allows easily replacing units covering the representation of individual process elements and even introducing new ones to simulate other processes both in the loose material and in its contact areas with various surfaces.

The program output provides extractions for each of the restricted classes, performance values and other parameters characterizing the screening process flow (Fig. 2).

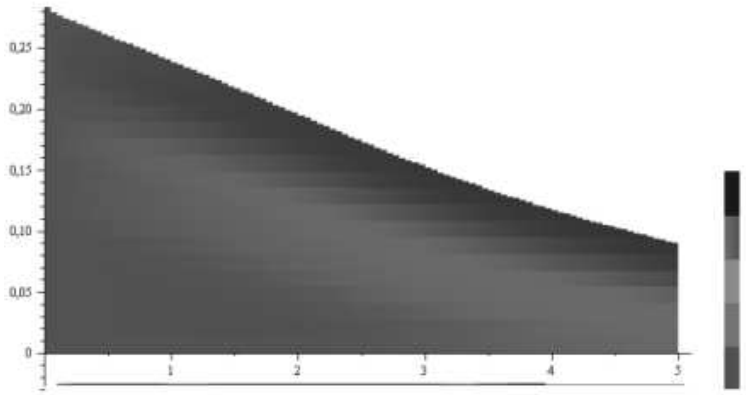

Figure 2: Program Execution Result: Material Layer Lateral Section on the Screen. The cell color characterizes the grain-size distribution of its contents and represents a proportional mixing of the colors given to the right of the scale, where red corresponds to the smallest size class, green – to the middle size class, and blue – to the largest grain-size class

The general algorithm, thus obtained, implements a simple granular media continuum model and simulates the screening process under the main process parameters. The program requires significantly less computing resources as compared to the known discrete element products.

3 Optimization

Computational simplicity of the model proposed allows for a series of experiments for different parameter values in limited time, enabling the application of numerical optimization methods. For an arbitrarily given target function, depending on screening characteristics, such as outputs, extractions etc., a set of maximizing or minimizing parameters may be found. For example, a program was implemented, which offers optimal process screening parameters to maximize the extraction efficiency of a given restricted class. The device parameter space is multidimensional; therefore, it was decided to apply the stochastic optimization algorithm - particle swarm optimization [6]. This method simulates the behavior of a swarm of midges - the parameter space is randomly filled with a swarm of points, where each point is given a random "current" velocity vector. Then the target function is calculated for coordinates of each point - a set of screening process model parameters. Based on the calculation results, individual (memory of the best own position of each individual midge) and collective (memory of the best position in the swarm) knowledge database is updated, and the rates of its individual members are recalculated. The process continues until stopping criteria occurs, for example, until an approximately steady state is achieved by the swarm or until a sufficient number of iterations have taken place. When the given algorithm parameters describing the influence of the individual and collective knowledge are successful, a swarm rapidly gathers near an optimal point in search space. These parameters were selected using the method proposed in [7]. A method similar to differential evolution [8] could be more efficient; however, due to the high performance of the simulation algorithm, calculation of extra intermediate data would not so much slow down the overall algorithm as provide information that may be used to assess the specific nature of effects device parameter variations produce on the target function (Fig. 3, 4).

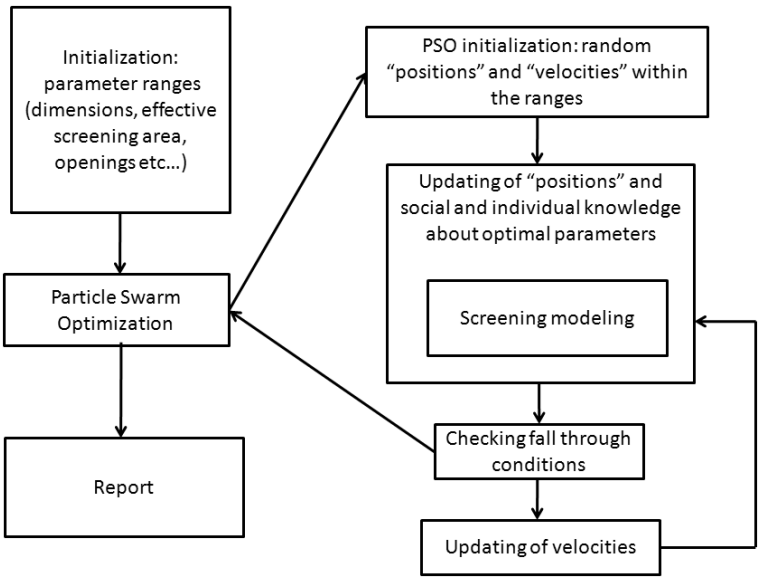

Figure 3: Screening Process Particle Swarm Optimization for the Model Proposed

And yet, a product to be provided to engineers shall be connected to an optimization module and shall apply the differential evolution method.

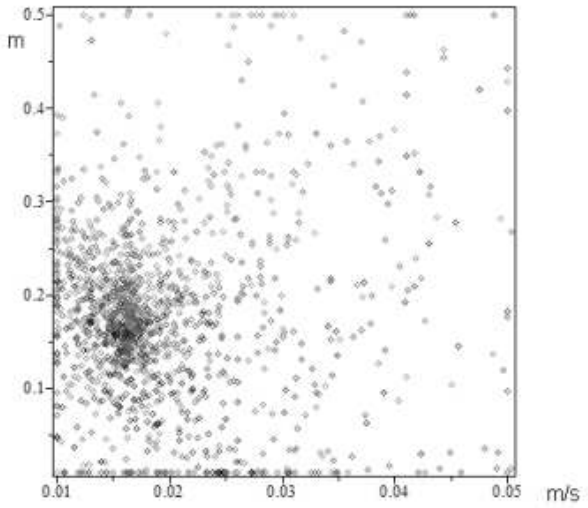

Figure 4: Search Results for Determining Optimal Vibrational Displacement Rate (Along Axis X) and Optimal Material Layer Thickness at Feeder (Along Axis Y) Using the Particles Swarm Method

4 Method Verification

The data obtained by the program described above examinations were compared with results of a series of field experiments. And, despite the fact that, formally, the available experimental data were obtained for grain-size compositions that were slightly different from the program target composition type, the numerical simulation results appeared to be in good agreement with the experimental data. The accuracy of the results obtained in accordance with this algorithm was quite close to the accuracy of discrete element simulations.

test 1		
	extraction	
granulation	natural exp. Data	numerical exp. Data
+0,630	0,000	0,000
-0,630+0,315	0,000	0,000
-0,315+0,180	0,847	0,884
-0,180+0,071	0,989	0,976
-0,071+0,000	0,972	0,978
test 2		
	extraction	
granulation	natural exp. Data	numerical exp. Data
+0,630	0,000	0,000
-0,630+0,315	0,516	0,824
-0,315+0,180	0,971	0,989
-0,180+0,071	0,989	0,992
-0,071+0,000	1,000	0,993

5 Conclusion

The algorithms and calculation methods presented herein may significantly speed up early development stages of new devices. This shall be achieved by providing preliminary near-optimum parameters for standard screens with account of grain-size compositions of the material screened.

Acknowledgements

The work is carried out with financial support of Russian Foundation of Basic Research, Grant 09-08-00620

References

[1] The Theoretical Basis of the Discrete Element Method. NUMETA 1985, Numerical Methods of Engineering, Theory and Applications, A.A. Balkema, Rotterdam

[2] Modelling of screening operations. Intern. J. of Mineral Processing. 22, 1-4, 1988, pp. 193-222

[3] Vibrational screening of granular media (in Russian). Mekhanobr, 1994

[4] Vibrational Displacement (in Russian). Nauka, 1964, pp. 410

[5] Computer simulation of mechanical properties for powder particles using Molecular Dynamics. Proceedings of the XXX Summer School "Advanced Problems in Mechanics", St.-Petersburg, Russia, 2003

[6] Particle Swarm Optimization. Proceedings of IEEE International Conference on Neural Networks. IV, 1995, pp. 1942-1948

[7] Good parameters for particle swarm optimization. Technical Report HL1001 (Hvass Laboratories). 2010

[8] Differential evolution - a simple and efficient heuristic for global optimization over continuous spaces. Journal of Global Optimization. 11, 1997, pp. 341-359

Generalized models of sliding and spinning friction

Alexey A. Kireenkov
kireenk@ipmnet.ru

Abstract

It is presented generalized three-dimensional models of the sliding and spinning friction. The proposed dry friction models generalizing permits to take into account, simultaneously, both the dynamics coupling of the components defining force state and the more realistic representations about dry friction characteristics and the normal contact stresses distributions in the case of combined kinematics for circle contact spots. The procedure of the models constructing consists of the two parts. In the first part, the exact integral expressions for the net vector and torque are formed with the assumption that Coulomb's friction law in classical forms or generalized differential forms is valid at each point of the contact area. In addition, in process of the exact integral models construction there are is used well known results from the theory of elasticity that tangent stresses lead to shift in the symmetric diagram of the normal contact stresses in the direction of the instantaneous sliding velocity. To use the theory of elasticity results in the dynamics problems, it is proposed the simple asymptotic representations for the contact stresses distributions based on their general properties known from the theoretical results of the theory of elasticity. In the second part the exact integral models are replaced by appropriate Pade expansions. The approximate models preserve all properties of the models based on the exact integral expressions and correctly describe the behaviour of the net vector and torque of the friction forces and their first derivatives at zero and infinity. Moreover, one does not have even to calculate the integrals to determine the coefficients of the Pade approximations. The corresponded coefficients can be identified from experiments. Consequently, the models based on Pade expansions may be considered as phenomenological models of combined dry friction.

1 About friction models

One of the first models describing the relation between the sliding friction and the whirling friction in the case of nonpoint contact between the moving bodies was proposed by in [1]. A principally new development of the theory was given by in [2], where exact analytic expressions for the resultant vector and the frictional moment for circular contact sites were obtained under the assumption that the distribution of contact stresses in the contact spot obeys the Hertz law. In [2], to apply the obtained dependencies to problems of dynamics, the linear-fractional Pade approximations of these dependencies were constructed. The developed in [2] theory was used in [3] to study the dynamics of a homogeneous circular disk sliding with rotation on a plane. Under the assumption that the distribution of contact stresses obeys the Galin law, exact analytic expressions for the resultant vector and the frictional moment were obtained and their linear-fractional Pade approximations were constructed.

The convenience in the use of the Pade approximations, which permit describing the effects of combined dry frictions for the entire range of angular and linear velocities, allowed

one to construct principally new the two-dimensional coupled models of the sliding and spinning friction on the basis of these approximations [4].

The two-dimensional friction model was constructed under supposition that the classical Coulomb law in differential form is validated for an infinitesimal area inside of contact spot. Its generalizing for the case of more realistic dry friction characteristic (validity of Coulomb law in generalized differential form) was given in [5]. It was shown that in the case of combined kinematics using of the Coulomb law in generalized differential form leads to new qualitative properties of the friction force dependence on the sliding and spinning velocities, but does not change the model dimension. All these models of the sliding and spinning friction were constructed in the assumption that, in the case of circular contact sites, the distributions of normal contact stresses depend only on the position vector with origin at the contact spot center. But, it is known [6] that in the case of the rigid solids sliding it is appears tangent stresses that leads to shifting in the symmetric diagram of the normal contact stresses in the direction of the instantaneous sliding velocity. This distortion in the symmetry of the normal contact stresses distribution leads to appearing of the friction force component which is perpendicularly directed to the velocity of the instantaneous sliding. In results, the dry friction model became three-dimensional. Moreover, it is arising the dynamics coupling between components defining the force state of rubbed solids [7].

Proposed below the dry friction models generalizing permits to take into account, simultaneously, both the dynamics coupling of the components defining force state and the more realistic representations about dry friction characteristics and the normal contact stresses distributions in the case of combined kinematics.

2 Coupled Models Of The Sliding And Spinning Friction

The combined model of sliding and rolling friction is constructed for circular contact sites under the assumption that the Coulomb law in differential form holds for the small surface element dS in the interior of the contact spot, according to which the differentials of the resultant vector $d\mathbf{F}$ and the moment of friction dM_C with respect to the disk center are determined by the formulas:

$$\begin{aligned} d\mathbf{F} &= -f\sigma\frac{\mathbf{V}}{|\mathbf{V}|}\left(1+\mu_1|\mathbf{V}|^3-\mu_2\,|\mathbf{V}|\right)dS,\\ dM_C &= -f\sigma\frac{\mathbf{r}\times\mathbf{V}}{|\mathbf{V}|}\left(1+\mu_1|\mathbf{V}|^3-\mu_2\,|\mathbf{V}|\right)dS,\\ \mathbf{V} &= (v-\omega y,\omega x),\ \mathbf{r}=(x,y) \end{aligned} \tag{1}$$

where f is the coefficient of friction, $\mathbf{r}=(x,y)$ is the position vector of an elemental area in the interior of the contact spot with respect to its center (Fig. 1), ω is the angular velocity of rotation of the contact spot center, but μ_1 and μ_2 are the coefficients which can be defined in practice from experiments.

To use the theory of elasticity results in the dynamics problems, a simple linear approximation of the normal contact stresses distribution is proposed:

$$\sigma(x,y)=\sigma_0\,(1+k_x x/R) \tag{2}$$

where $\sigma_0=\sigma_0(r)$ distribution of normal contact stresses at absence of motion having the properties of central symmetry, R radius of contact spot, x axe of the restangular coordination systems with origin in the center of contact circle (Fig. 1) which is directed parallelly to vector of the instantenious sliding. To calculate coefficient k in the formula

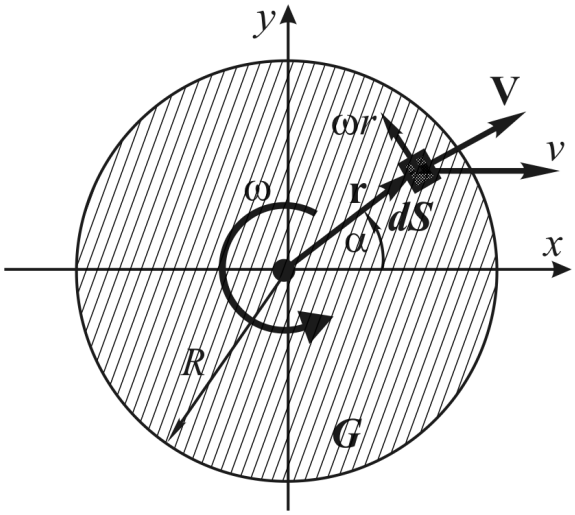

Figure 1: Kinematics inside of contact spot

(1) it is used the condition of equality of the external force F torque to the normal reaction force N torque which is appears from the shifting of the center of gravity of the contact spot in the direction of sliding on the value s:

$$Fh = Ns \tag{3}$$

where h distance from the moving solid center mass to the plane of sliding. On the other hand the shifting s of the gravity center relatively of the contact spot center can be defined by the following formula:

$$s = \iint\limits_G x\sigma(x,y)\,dxdy \Big/ \iint\limits_G \sigma(x,y)\,dxdy \quad G = \left\{(x,y) : x^2 + y^2 \le R^2\right\} \tag{4}$$

Substitution of the representation (2) to the (4) yields:

$$s = \frac{\pi k}{R} \int\limits_0^R \sigma_0(r) r^3 dr \tag{5}$$

Equalization values s calculated from the formulas (3) and (5) allows to calculate coefficient k which is characterized the dynamical coupling of the components defining the force state inside of contact spot. If the distribution of normal contact stresses $\sigma_0(r)$ at the moving absence are obeyed by the Hertz $\sigma_0 = 3N\sqrt{1 - r^2/R^2}\Big/(2\pi R^2)$ or Galin $\sigma_0 = N\Big/\left(2\pi R^2\sqrt{1 - r^2/R^2}\right)$ laws then $k = 5Fh/(NR)$ or $k = 3Fh/(NR)$, correspondently.

2.1 Integral model

To obtain the resultant vector and the moment of friction, it is necessary to integrate the expressions (1) over the contact spot. The obtained dependencies, where $F_{\parallel}$ and $F_{\perp}$ denote the respective components of the resultant vector directed along the tangent and the normal to the trajectory of motion, present an exact combined integral model of sliding and spinning friction

$$
\begin{aligned}
F_{\|}(\omega,v) &= -f\iint\limits_G \frac{(v-\omega y)\sigma_0\,dxdy}{\sqrt{\omega^2(x^2+y^2)+v^2-2\omega vy}}+\\
&\quad -f\iint\limits_G(\mu_1v^3-\mu_2v+2\mu_1v\omega^2(x^2+y^2))\sigma_0\,dxdy\\
F_{\perp}(\omega,v) &= -\frac{fk_x}{R}\iint\limits_G \frac{\omega^2x^2\sigma_0\,dxdy}{\sqrt{\omega^2(x^2+y^2)+v^2-2\omega vy}} \qquad (6)\\
M_C(\omega,v) &= -f\iint\limits_G \frac{(\omega(x^2+y^2)-vy)\sigma_0\,dxdy}{\sqrt{\omega^2(x^2+y^2)+v^2-2\omega vy}}+\\
&\quad -f\iint\limits_G((2\mu_1v^2-\mu_2)\omega(x^2+y^2)+\mu_1\omega^3(x^2+y^2)^2)\sigma_0\,dxdy
\end{aligned}
$$

After introducing dimensionless variables: $x=\hat{x}R,\ y=\hat{y}R$ and $\sigma(\hat{x},\hat{y})=\hat{\sigma}(\hat{x},\hat{y})N\big/R^2$ it is convenient to calculate the modulus of integrals (6) in the polar coordinates: $x=r\cos\alpha,\ y=r\sin\alpha,\ r\in[0,1],\ \alpha\in[0,2\pi]$ (Fig. 1) in which the functions (6) take the form

$$
\begin{aligned}
F_{\|} &= F_0\int\limits_0^{2\pi}\int\limits_0^1 \frac{(v-ur\sin\alpha)r\sigma_0(r)}{\sqrt{u^2r^2+v^2-2uvr\sin\alpha}}drd\alpha+\\
&\quad +2\pi F_0\left((\mu_1v^3-\mu_2v)\int\limits_0^1 r\sigma_0(r)dr+2\mu_1vu^2\int\limits_0^1 r^3\sigma_0(r)dr\right)\\
F_{\perp} &= k_xF_0\int\limits_0^{2\pi}\int\limits_0^1 \frac{ur^3\sigma_0(r)\cos^2\alpha}{\sqrt{u^2r^2+v^2-2uvr\sin\alpha}}drd\alpha,\quad u=\omega R, F_0\equiv fN,\ M_0\equiv fNR \qquad (7)\\
M_C &= M_0\int\limits_0^{2\pi}\int\limits_0^1 \frac{(ur^2-vr\sin\alpha)r\sigma_0(r)}{\sqrt{u^2r^2+v^2-2uvr\sin\alpha}}drd\alpha+\\
&\quad +2\pi M_0\left((2\mu_1v^2-\mu_2)u\int\limits_0^1 r^3\sigma_0(r)dr+\mu_1u^3\int\limits_0^1 r^5\sigma_0(r)dr\right)
\end{aligned}
$$

where the "hat" symbol is omitted for brevity

If the distributions of the normal contact stresses are described by Hertz or Galin lows then integrals in equalities (7) can be calculated in the elementary function with the aid of transition of the polar coordinate system origin to the instantaneous center of velocities. Corresponded expressions for tangent friction force component $F_{\|}$ and for friction torque M_C are fully the same as that were calculated in work [6] and for perpendicular friction force component $F_{\perp}$ they are following:

$$
\begin{aligned}
\frac{F_{\perp}}{F_0} &= k_x\begin{cases}\pi(4-k^2+8)\big/32, & k\le 1\\ (4-k^2)\arcsin(1\big/k)+(2\big/k^2+1)\sqrt{k^2-1}\big/16, & k\ge 1\end{cases}\\
\frac{F_{\perp}}{F_0} &= k_x\begin{cases}3\pi(k^4-4k^2+8)\big/256, & k\le 1\\ (3k^4-12k^2+24)\arcsin(1\big/k)+(8\big/k^2+10-k^2)\sqrt{k^2-1}\big/128, & k\ge 1\end{cases}
\end{aligned}
$$

The first expression in formulas above correspond to Galin distribution and the second to Hertz distribution, but parameter $k = v/u$.

If $k_x = 0$, then model (7) is fully agree to the model, investigated in [3]. Thus, we have substantial approximation to the real situation in dependence on the general properties of the normal contact stresses distribution. At the supposition that external forces are absence, the coefficient k in formula (1), (5), (6), (7) is defined by the friction force component $F_{\parallel}$ from the first expressions in the relations (6-8) and, consequently, the dynamically coupled integral friction model is

$$
\begin{aligned}
F_{\parallel} &= F_0 \int\limits_0^{2\pi}\int\limits_0^{1} \frac{(v - ur\sin\alpha)r\sigma_0(r)drd\alpha}{\sqrt{u^2r^2 + v^2 - 2uvr\sin\alpha}} + 2\pi F_0\left((\mu_1 v^3 - \mu_2 v)I_1 + 2\mu_1 v u^2 I_3\right) \\
F_{\perp} &= \frac{fhF_0R}{\pi I_3} \int\limits_0^{2\pi}\int\limits_0^{1} \frac{(v - ur\sin\alpha)r\sigma_0(r)drd\alpha}{\sqrt{u^2r^2 + v^2 - 2uvr\sin\alpha}} \int\limits_0^{2\pi}\int\limits_0^{1} \frac{ur^3\sigma_0(r)\cos^2\alpha drd\alpha}{\sqrt{u^2r^2 + v^2 - 2uvr\sin\alpha}}, \qquad (8) \\
M_C &= M_0 \int\limits_0^{2\pi}\int\limits_0^{1} \frac{(ur^2 - vr\sin\alpha)r\sigma_0(r)drd\alpha}{\sqrt{u^2r^2 + v^2 - 2uvr\sin\alpha}} + 2\pi M_0\left((2\mu_1 v^2 - \mu_2)uI_3 + \mu_1 u^3 I_5\right)
\end{aligned}
$$

where coefficients of polynomials terms in formulas (3) are the first moments of the normal contact stresses distribution: $I_1 = \int\limits_0^1 r\sigma_0(r)dr$ – moment of the first order, $I_3 = \int\limits_0^1 r^3\sigma_0(r)dr$ – moment of the third order and $I_5 = \int\limits_0^1 r^5\sigma_0(r)dr$ – moment of the fifth order. They can be calculated in elementary functions for the most used functions of the normal contact stresses distributions [5].

If the distribution of normal contact stresses is obeyed to the Hertz law: $\sigma(r) = 3\sqrt{1-r^2}\Big/(2\pi)$ then: $I_1 = 1/2\pi,\ I_3 = 1/5\pi,\ I_5 = 4/35\pi$.

If the distribution of normal contact stresses is obeyed to the Galin law: $\sigma(r) = (2\pi\sqrt{1-r^2})^{-1}$ then: $I_1 = 1/2\pi,\ I_3 = 1/3\pi,\ I_5 = 4/15\pi$.

In the case of thin circle, the distribution of normal contact stresses can be described by the following function: $\sigma(r) = \delta(r-1)/(2\pi)$, where $\delta(r-1)$ – Dirac delta function in the point $r = 1$ and $I_1 = I_3 = I_5 = 1/4\pi$.

Plots of the tangent $F_{\parallel}$ (left figure) and normal $F_{\perp}$ (right figure) friction force components normalized on the their maximum values as function of velocity of sliding v at the constant velocity of whirling $u = 1$ are presented on the Fig. 2. As concerned friction torque then, qualitatively, its behavior is the same as case of using classical form Coulomb law: there are only small quantitative distinctions.

The expressions for the components of the resultant vector and the moment of friction in relations (8) have several important properties as functions of u and v.

Property 1. The distortion in symmetric diagram of the normal contact stresses distribution results in the appearance of the resultant vector component $F_{\perp}$ directed along the normal to the trajectory of motion. The resultant vector is not directed opposite to the velocity of sliding.

Property 2. The distortion in the symmetric diagram of distribution of normal stresses does not affect to the moment M_C and the resultant vector component $F_{\parallel}$ directed along the tangent to the trajectory.

Property 3. The first terms of the tangent $F_{\parallel}$ force component and torque M_C, just as normal $F_{\perp}$ force component, are homogeneous functions of the variables u and v of zero

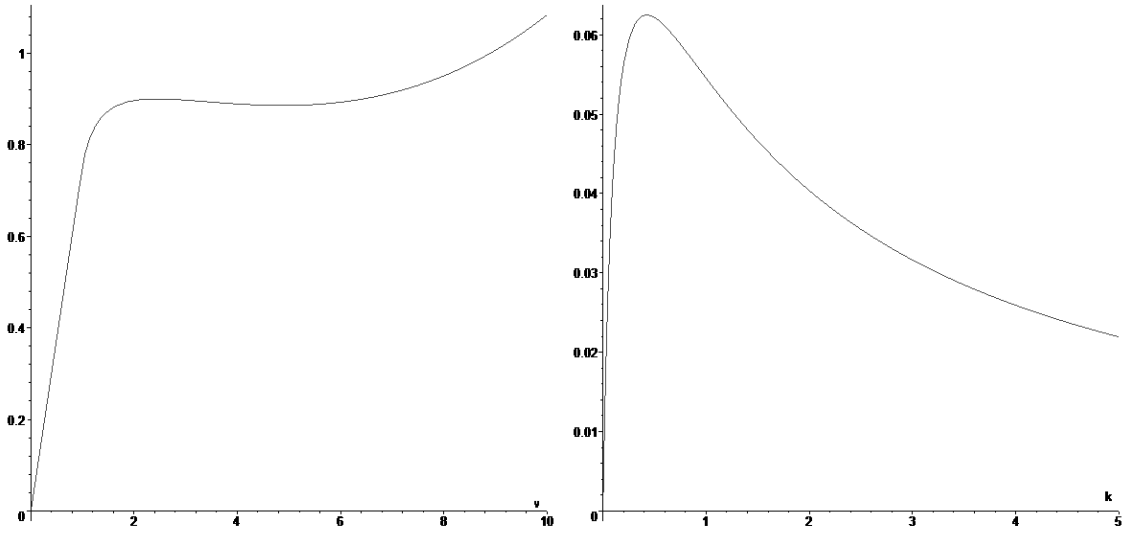

Figure 2: Typical behaviour of the friction force components)

order of homogeneity and hence are invariant under the similarity group:

Property 4. The expressions (9), for the moment and both components of the friction force as functions of u and v have a singularity at the point $(u, v) = (0, 0)$, because they do not have any limit at this point with respect to both of the variables u and v.

Property 5. In the case of pure sliding $u = 0$ or spinning $v = 0$, the moment M_C and the tangential component $F_\parallel$ are homogeneous models corresponding to the usual Coulomb law:

$$F_\parallel(0, v) = F_0 \equiv fN, \;\; M_C(u, 0) = M_0, \; M_0 = 2\pi fNRI_2, \;\; I_2 = \int_0^1 \sigma_0(r) r^2 dr$$

Property 6. In the case of pure sliding, the normal component vanishes: $F_\perp(0, v) = 0$, and hence the friction force is directed opposite to the velocity vector; in the case of pure spinning, it is equal to

$$F_\perp(u, 0) = \mu F_0, \; \mu = fhR/(\pi I_3)$$

Property 7. The moment M_C and both components of the friction force $F_\parallel$ and $F_\perp$ have only one nonzero first partial derivative (the others are zero):

$$\left.\frac{\partial F_\perp}{\partial v}\right|_{v=0} = \frac{\pi hRI_2F_0^2}{I_3 u}, \;\; \left.\frac{\partial F_\perp}{\partial v}\right|_{v=0} = \frac{2\pi hRI_1F_0}{v}, \;\; I_2 = \int_0^1 r^2\sigma_0(r)dr$$

2.2 Models based on Pade expansions

The integral models (8) give a good description of the combined sliding and spinning friction, but are inconvenient to be used in problems of dynamics, because it is required to calculate multiple integrals in the right-hand sides of the equations of motion. This difficult procedure can be eliminated by replacing the exact integral expressions by the corresponding Pade approximations. The simplest of them is the linear-fractional approximation preserving the value at zero and at infinity of both for the torque M_C and for the

tangent force component $F_{\|}$. But, for the normal friction force component, corresponded Pade approximation, naturally, became of the second order.

$$
\begin{aligned}
M_C &= \frac{M_0 u}{u+mv} + 2\pi\left((2\mu_1 v^2-\mu_2)uI_3+\mu_1 u^3 I_5\right),\ \ \frac{1}{m} = \frac{v}{M_0}\frac{\partial M_C}{\partial u}\bigg|_{u=0} \\
F_{\|} &= \frac{F_0 v}{v+au} + 2\pi\left((\mu_1 v^3-\mu_2 v)I_1+2\mu_1 v u^2 I_3\right),\ \ \frac{1}{a} = \frac{u}{F_0}\frac{\partial F_{\|}}{\partial v}\bigg|_{v=0} \\
F_{\perp} &= \frac{\mu F_0 uv}{(u+bv)(v+au)},\ \ \frac{1}{b} = \frac{v}{\mu F_0}\frac{\partial F_{\perp}}{\partial u}\bigg|_{u=0}
\end{aligned}
\tag{9}
$$

The linear-fractional Pade approximations (9) preserve the values of the functions $F_{\|}(u,v)$, $F_{\perp}(u,v)$ and $M_C(u,v)$ at zero, as well as their behavior and the behavior of their first derivatives at infinity. But model of this type cannot completely preserve the values of all first partial derivatives of these functions at zero. To obtain a correct description of the behavior of the first derivatives at zero, it is required to use the second-order Pade approximations, and then the coupled model of sliding and spinning friction takes the form

$$
\begin{aligned}
M_C &= \frac{M_0(u^2+muv)}{v^2+muv+u^2} + 2\pi\left((2\mu_1 v^2-\mu_2)uI_3+\mu_1 u^3 I_5\right), m = \frac{v}{M_0}\frac{\partial M_C}{\partial u}\bigg|_{u=0} \\
F_{\|} &= \frac{F_0(v^2+auv)}{v^2+auv+u^2} + 2\pi\left((\mu_1 v^3-\mu_2 v)I_1+2\mu_1 v u^2 I_3\right),\ \ a = \frac{u}{F_0}\frac{\partial F_{\|}}{\partial v}\bigg|_{v=0} \\
F_{\perp} &= \frac{\mu F_0 uv}{(v^2+buv+u^2)(v^2+auv+u^2)},\ \ b = \frac{v}{\mu F_0}\frac{\partial F_{\perp}}{\partial u}\bigg|_{u=0}
\end{aligned}
\tag{10}
$$

The second-order model (10) completely satisfies all properties 1–7 of the exact integral models (8). But, for the majority of the problems of dynamics, it is sufficient to use the first order model (9). The second-order model (10) is required for a more precise qualitative analysis, for example, for determining the boundaries of the stagnant region and the motion stopping time. The approximations (9) and (10) hold for positive values of u and v. They can be easily generalized to the case of arbitrary (in sign) velocities u and v by a formal change by absolute values in the denominators of the corresponding expressions. The use of the friction models based on the Pade' expansions allows one to avoid calculations of multiple integrals over the contact spot, which significantly simplifies their use in problems of dynamics. The approximate models preserve all properties of the models based on the exact integral expressions and correctly describe the behaviour of the net vector and torque of the friction forces and their first derivatives at zero and infinity. Moreover, the models coefficients can be identified from experiments [8]. Consequently, the models based on Pade expansions may be considered as phenomenological models of the combined dry friction.

3 Conclusion

Proposed in this investigation the three dimensional dry friction models permit to take into account, simultaneously, both the dynamics coupling of the components defining force state and the more realistic representations about dry friction characteristics and the normal contact stresses distributions in the case of combined kinematics for the circle contact spots.

The procedure of the models constructing consists of the two parts. In the first part, the exact integral expressions for the net vector and torque are formed with the assumption that Coulomb's friction law in the generalized differential forms is valid at each point of the contact area. In addition, in process of the exact integral models construction is supposed that there are shift in the symmetric diagram of the normal contact stresses in the direction of the instantaneous sliding velocity. the simple asymptotic representations for the contact stresses distributions based on their general properties known from the theoretical results of the theory of elasticity is proposed to describe this shift. It is shown that the distortion in the symmetry of the normal contact stresses distribution in the case of circular contact sites results to the appearance of the friction force component directed along the normal to the trajectory of the mass center of the rubbed solids and, consequently, the mass center trajectory is inclined from the straight line.

In the second part, to escape the double integrals calculation in the motion equations, the exact integral expressions are replaced by appropriate Pade expansions. The approximate models preserve all properties of the models based on the exact integral expressions and correctly describe the behavior of the net vector and torque of the friction forces and their first derivatives at zero and infinity. Moreover, one does not have even to calculate the integrals to determine the coefficients of the Pade approximations. The corresponded coefficients can be identified from experiments. Consequently, the models based on Pade expansions may be considered as phenomenological models of combined dry friction.

References

[1] P.Contensou, Couplage Entre Frottenmentde Glissementet Frottenment de Pivotement Dans la Theorie de la Toupie. in Kreiselprobleme Gyrodynamics: IUTAM Symp. Celerina, 1962 (Springer, Berlin etc., 1963; Mir, Moscow, 1967), 201 – 216(60 – 77).

[2] V.Ph. Zhuravlev, The Model of Dry Friction in the Problem of the Rolling of Rigid Bodies. Prikl. Mat. Mekh., 62 (5), 762–767, 1998.

[3] A.A. Kireenkov, On the motion of the homogeneous rotating disk alone the plane in the case of combined friction, Izv. Akad. Nauk .Mekh. Tverd. Tela, 1, 60–67, 2002.

[4] V.Ph. Zhuravlev and A.A. Kireenkov, Pade Expansions in the Two-Dimensional Model of Coulomb Friction. Izv. Akad. Nauk. Mekh. Tverd. Tela, 2, 3–14, 2005.

[5] A.A.Kireenkov, Generalized two dimensional model of sliding and spinning friction. Doklady Akademii Nauk, 2010, Vol. 431, No. 4 (Doklady Physics, 2010, Vol. 55, No. 4), 482–486(186–190).

[6] I.G. Goryacheva, Mechanics of friction interaction, Moscow, Moscow, 478, 2001.

[7] A.P. Ivanov, A dynamically consistent model of the contact stresses in the plane motion of a rigid body. Prikl. Math. Mech, 73 (2), 134-144, 2009.

Alexey A. Kireenkov, Institute for Problems in Mechanics RAS, Prospekt Vernadskogo 101, korp.1, 119526 Moscow, Russia

Identification of cracks in composite materials

Alexander Karmazin Evgenia Kirillova Wolfgang Seemann
Pavel Syromyatnikov
kirillova@web.de

Abstract

The application of two methods (genetic and pattern search algorithms) of the reconstruction of the damaged state of constructions' elements produced from the layered composite materials is considered. Layer separation and rupture modeled by the cracks with non-interacting boundaries are studied as such type of damage. The displacements measured on the surface of the body provide additional information for the solution of the inverse problem of the reconstruction of defects. A method based on a solution of boundary integral equations as well as a method based on the finite-element method is used for modeling wave propagation within the structure with damage.

1 Introduction

Lamb waves have high potential for the identification of defects in structures since they are capable of propagating at long distances at a low level of expences for their excitation and measurement. The result of the subtraction of the values of the displacement amplitudes corresponding to the medium without defect from the measured surface amplitudes is wave fields, the use of which significantly increases the accuracy of defect identification by applying well-known methods, for instance a based on calculating Damage Index [1]. However, as a rule, a more precise identification of crack parameters is required for the systems of automatic defect identification during structural (health) monitoring, i.e. the solution of the inverse problems becomes relevant. The reduction of inverse problems to the problems of minimization of objective functionals presenting the residual between the measured and calculated characteristics of static or dynamic behavior of the body (stressedly-deformed state, boundary wave fields of displacements, propagation velocities of elastic waves etc.) imply the existence of a reliable and effective method of solving direct problems.

The methods of quick computation of harmonic wave fields caused by surface sources in multilayered composites consisting of layers with arbitrary anisotropic properties [4, 5, 6] were developed by the authors of this article. These methods are based on the classic technique of the integral Fourier transforms and integral approximations of the Green's functions.

As demonstrated by the results of the solution of the inverse problems of crack reconstruction by reducing them to the problems of minimization of objective functionals, the obtained functionals are non-quadratic and the level surfaces they define in the variation range of the sought-for parameters have complex structure. In the case when the number of unknown parameters is large or the functional has several local minimums or is strongly abounding in ravines, commonly used gradient methods do not achieve a reliable

result. Recently a new prospective class of computational algorithms for the solution of optimization problems has emerged - so called evolutionary or genetic algorithms (GA) applying for its functioning some principles of the development of biological populations. They do not require defining the initial approach, they do not use a priori information on objective function and allow finding global extremums in the case of the complex relief of the function with more probability.

A multilayered structure containing a through-thickness crack located parallel to the layers' boundaries is studied in the given work. A method based on a solution of boundary integral equations [7] as well as a method based on the finite-element method [3] are used for modeling of wave propagation within the structure with damage. The inverse problem is formulated as an optimization problem for the residual functional for the functions depending on the crack parameters. It is possible to use random global search methods (genetic algorithms), as well as other global (diagonal algorithms) or local search methods for solving optimization problem. These methods can also be combined. The advantages and disadvantages of these methods which are employed to solve the identification problem are considered on numerical examples.

2 Mathematical formulation

Let us consider a plane problem about the oscillations of a multilayered medium consisting from N layers with a free bottom base. The medium occupies the following domain $-H \le z \le 0$, $-\infty \le x \le \infty$, H is layer thickness. On the surface of the layer in the domain Ω_1: $x \in [x_0 - a_1, x_0 + a_1]$ a two-component load $\mathbf{q}^{(1)} = \left\{q_1^{(1)}, q_2^{(1)}\right\} \exp(-i\omega t)$ is applied where ω is oscillation frequency, t is time. The structure contains at the depth of $z = -h$ a crack described as domain Ω_2: $x \in [-a, a]$. Solely tunnel (through-thickness) cracks in material the form and location of which are independent from one of the horizontal coordinates (y) are investigated in this work.

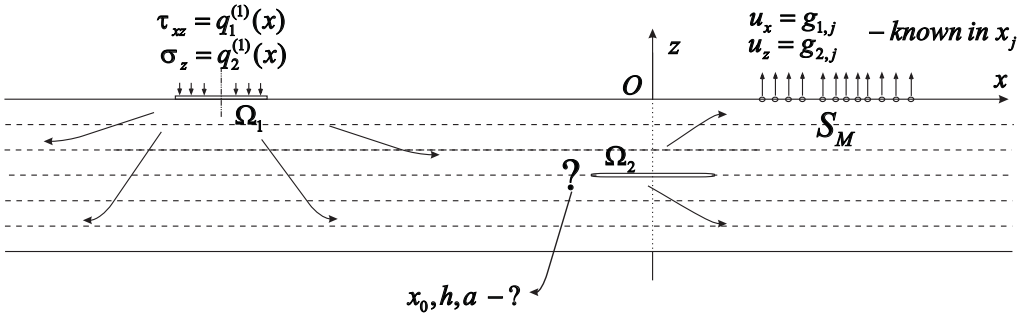

Figure 1: A structure containing crack.

Assuming the independence of the surface load from the same horizontal coordinate y, we can define a problem as a plane problem. The crack is modeled as an infinitely thin cut, the boundaries of which are stress-free and do not interact. The displacements of the medium are described by the elastodynamic equations. The common multiplier $\exp(-i\omega t)$ is hereinafter omitted. In the general case it is necessary to study a mixed boundary problem of the following type:

$$\begin{cases} z = 0, \quad \mathbf{u} = \mathbf{u}^{(1)}(x,z), \quad x \in \Omega_1; \quad \mathbf{q}^{(1)}(x,z) = 0, \quad x \notin \Omega_1, \\ z = -h, \quad \mathbf{q} = \mathbf{q}^{(2)}(x,z), \quad x \in \Omega_2; \quad \mathbf{v}^{(2)}(x,z) = 0, \quad x \notin \Omega_2, \\ z = -H, \quad \mathbf{q}(x,z) = 0, \quad -\infty \le x \le \infty. \end{cases} \tag{1}$$

Here $\mathbf{u}^{(1)}$ is a displacement vector in domain $x \in \Omega_1,\ z = 0$, $\mathbf{q}^{(j)}$ is a stress vector, $\mathbf{v}^{(2)} = \mathbf{u}^{(2)+} - \mathbf{u}^{(2)-}$ is a vector of a displacement jump on the crack boundaries in domain $x \in \Omega_2,\ z = -h$. Let us denote the direct and inverse Fourier transform with symbols $\mathcal{F}$, $\mathcal{F}^{-1}$ and introduce the values:

$$\mathbf{U}(\alpha, z) = \mathcal{F}(\mathbf{u}) = \int\limits_{-\infty}^{\infty} \mathbf{u}(x, z) \exp(i\alpha x) dx,$$

$$\mathbf{u}(x, z) = \mathcal{F}^{-1}(\mathbf{U}(\alpha, z)) = \frac{1}{2\pi} \int\limits_{-\infty}^{\infty} \mathbf{U}(\alpha, z) \exp(-i\alpha x) d\alpha, \tag{2}$$

$$\mathbf{Q} = \mathcal{F}(\mathbf{q}), \quad \mathbf{q} = \mathcal{F}^{-1}(\mathbf{Q}), \quad \mathbf{v} = \mathcal{F}^{-1}(\mathbf{V}), \quad \mathbf{V} = \mathcal{F}(\mathbf{v}).$$

Using the notation of the symbol of the Green's matrix $\mathbf{K} = \mathcal{F}(\mathbf{k})$, corresponding to the surface load for a multilayered strip without cracks [8], it is possible to obtain an extended block matrix $\mathbf{K} = \left\{\mathbf{K}^{(ij)}\right\}$ with a number of blocks N^2, each of whose blocks $\mathbf{K}^{(ij)}$ has a dimension 2×2. The index i in $\mathbf{K}^{(ij)}$ corresponds to the layer number. Blocks $\mathbf{K}^{(i1)}$, $i = 1, \dots N$ describe the action of the surface source $\mathbf{q}^{(1)}$ in layers, blocks $\mathbf{K}^{(ij)}$, $i = 1, \dots N$, $j = 2, \dots N$ describe the influence of the vectors of displacement jumps on the crack boundaries $\mathbf{v}^{(j)}$ (if there are several) located on the boundaries of the layers. For the blocks of the extended Green's matrix we have a following relation:

$$\mathbf{k}^{(ij)} = \mathcal{F}^{-1}(\mathbf{K}^{(ij)}), \quad \mathbf{K}^{(ij)} = \mathcal{F}(\mathbf{k}^{(ij)}). \tag{3}$$

For matrices $\mathbf{k}^{(ij)}$, $i = 1, \dots N$, $j = 2, \dots N$ the notation in the form of the inverse Fourier transform (3) is formal since the corresponding kernels are hypersingular, they do not have an analytic notation and are understood solely as generalized functions. In the case of isotropic media and a small number of layers the symbol of the extended matrix $\mathbf{K}$ can be acquired in an explicit form [7], in the case of anisotropic media it can be acquired numerically [9].

In the case of a two-layer strip (fig. 1) the formalism of an extended Green's matrix allows formulating the corresponding system of integral equations with regard to the unknown vector of surface loads $\mathbf{q}^{(1)}$ and vector of displacement jumps in the crack domain $\mathbf{v}^{(2)}$ with the given displacements on the surface of the strip $\mathbf{u}^{(1)}$ and stresses on the crack boundaries $\mathbf{q}^{(2)}$:

$$\int\limits_{\Omega_1} \mathbf{k}^{(11)}(x - \xi, z)\mathbf{q}^{(1)}(\xi) d\xi + \int\limits_{\Omega_2} \mathbf{k}^{(12)}(x - \xi, z)\mathbf{v}^{(2)}(\xi) d\xi = \mathbf{u}^{(1)},\ x \in \Omega_1,\ z = 0 \tag{4}$$

$$\int\limits_{\Omega_1} \mathbf{k}^{(21)}(x - \xi, z)\mathbf{q}^{(1)}(\xi) d\xi + \int\limits_{\Omega_2} \mathbf{k}^{(22)}(x - \xi, z)\mathbf{v}^{(2)}(\xi) d\xi = \mathbf{q}^{(2)},\ x \in \Omega_2,\ z = -h.$$

The system of integral equations (4) has a most general form and corresponds to the case in which the interaction of the surface source and crack is taken into consideration and the source itself is given by a physically adequate method. The system of equations (4) is considerably simplified in case the distribution of the stresses $\mathbf{q}^{(1)}$ is regarded as given and the stresses on the crack boundaries $\mathbf{q}^{(2)}$ are absent. Then the system of equations comes to a single integral matrix equation:

$$\int\limits_{\Omega_2} \mathbf{k}^{(22)}(x - \xi, z)\mathbf{v}^{(2)}(\xi) d\xi = -\frac{1}{2\pi} \int\limits_{\Gamma} \mathbf{K}^{(21)}(\alpha, z)\mathbf{Q}^{(1)}(\alpha) \exp(-i\alpha x) d\alpha = -\tau_0(x, z), \tag{5}$$

$$x \in \Omega_2,\ z = -h.$$

The right part of this equation is known, the solution of this equation is the vector of displacement jumps on the crack $\mathbf{v}^{(2)}$, $x \in \Omega_2$. Contour Γ in (5) and further on is chosen in accordance with radiation principle [8]. The displacements on the surface of the strip after the solution of the equation (5) can be presented as follows:

$$\mathbf{u}(x,z) = \frac{1}{2\pi}\int\limits_{\Gamma} \mathbf{K}^{(11)}(\alpha,z)\mathbf{Q}^{(1)}(\alpha)\exp(-i\alpha x)d\alpha + \tag{6}$$

$$+\frac{1}{2\pi}\int\limits_{\Gamma} \mathbf{K}^{(12)}(\alpha,z)\mathbf{V}^{(2)}(\alpha)\exp(-i\alpha x)d\alpha,\ -\infty \le x \le \infty,\ z = 0.$$

Hereinafter we consider that at some points x_j on the surface the structures are known from the physical experiment or numerical modelling of the value of displacements $\mathbf{u}(x_j,\omega) = \mathbf{g}_j(\omega)$ for frequencies ω from the range $[\omega_1,\omega_2]$.

In this case the identification problem of unknown parameters of the crack can be reduced to the solution of the equation (5), computation of integrals (6) and minimization of residuals defined at the points of measurements x_j on the surface of the strip:

$$\min \Phi(a,x_0,h) = \sum_j \|\mathbf{g}_j(\omega) - \mathbf{u}(x_j,\omega,a,x_0,h)\| \to 0, \quad z = 0. \tag{7}$$

The equation (7) can be rewritten in a form of a sum of the smallest squares of the residual of displacements where the deviation of the values of displacements is calculated. Naturally the restrictions can be imposed on the range of admissible changes of the parameters of the cracks with regard to the surface source:

$$a_0 \le a \le a_M, \quad x_{0,L} \le x_0 \le x_{0,R}, \quad 0 < h < H. \tag{8}$$

3 Algorithms of computing displacements for given crack parameters

An optimization process (7) can be interpreted as a search for such crack parameters, for whose a difference between known from measurements data $\mathbf{g}(x_j,0)$ and data obtained using a solution of BIEs (5) at the same surface points is minimal. Thus, it is required to solve the system of BIEs (5) many times.

3.1 Galerkin's method

The technique for the solution of the system of BIEs (5), offered in [7], is used for the computation of the displacements on the surface of the structure with given damage parameters. It is assumed that the unknown jump (vector-function) of displacements on the crack can be approximately represented as a sum of a finite number of basis functions with coefficients-vectors

$$\mathbf{v}(x) \approx \sum_{k=0}^{N_p} \mathbf{c}_k p_k(x). \tag{9}$$

Due to the known properties of behavior of a displacement jump function on the crack boundaries [7], we choose Jacobi polynomials with weight functions as basis functions in the form

$$p_k(x) = P_k^{(\delta_1,\delta_2)}(x/a)(1-x/a)^{\delta_1}(1+x/a)^{\delta_2}, k = 0,\dots N_p. \tag{10}$$

In the general case, the indices δ_1, δ_2 must be calculated numerically, but in the case of the internal crack in the isotropic homogeneous material they are equal to $\delta_1 = \delta_2 = 1/2$. According to the standard Galerkin's scheme, the left and right sides of system (4) are subsequently multiplied scalarwise in L_2 by the basis functions $p_l(x)$ $N_p + 1$ times, and the problem is then reduced to the solution of a system of linear equations.

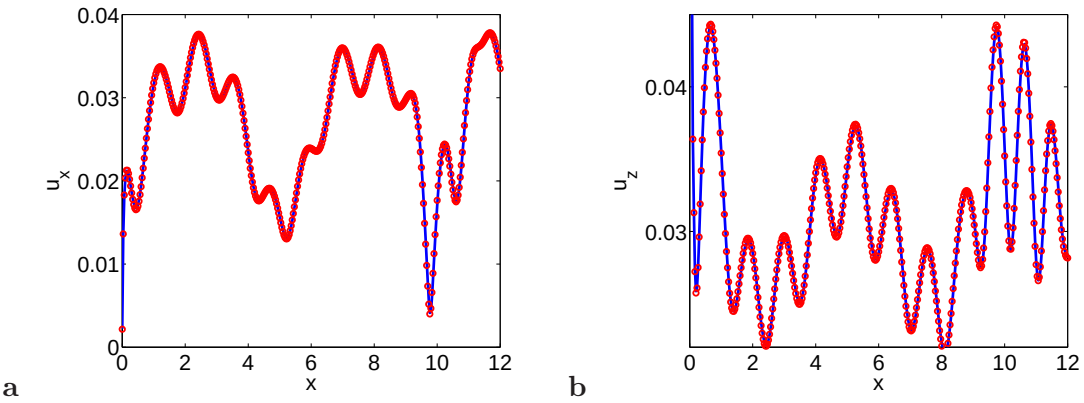

Figure 2: Comparison of in-plane (a) and out-of-plane (b) surface amplitudes for a composite laminate $[C90/G45/G - 45]_s$ containing a crack ($h = 0.5$, $x_0 = 10.3$, $a = 1.2$) (straight lines) with amplitudes obtained for an identified crack ($h = 0.499$, $x_0 = 10.29$, $a = 1.205$) (circles). The laminate is excited at a frequency $\bar{\omega} = \pi$. FEM is used as a forward solver.

3.2 Method of differential factorization and a block element method

For the solution of the problem (5-6) the method of differential factorization [10] and method of block element [11] are also used. These methods allows a consideration of cracks with complex geometry and to obtain an approximate solution of (5-6). An accuracy of these methods can be controlled if it is required. In this case more approariate is a method of block element. However with a comparable accuracy to a method of block element, Galerkin method needs the less computational time and numerical results presented in this paper are obtained using a Galerkin method.

Optim. Method	Meas. error	Errors in h	x_0	a_0	Time [min]
GA	0%	4.2%	1.7%	3.8%	277
GA	1%	2.5%	2.49%	4.4%	332
GA	5%	17.1%	0.6%	6.2%	268
PS	0%	2.6%	2%	1.9%	159
PS	1%	3.3%	2.5%	2.6%	179
PS	5%	6.1%	2.1%	2.5%	209

Table 14: Identification of crack $h = 1/3$, $x_0 = 10.3$, $a_0 = 0.52$ in a composite laminate $[C90/G45/G - 45]_s$. The laminate is excited at a frequency $\bar{\omega} = \pi$. FEM is used as a forward solver.

Optim. Method	Meas. error	Errors in x_0	a_0	Time [min]
PS	1%	0.3%	0.6%	45
PS	5%	0.8%	1.4%	67
PS	7.5%	2.2%	3.5%	82

Table 15: Identification of crack $x_0 = 2.0$, $a = 0.82$, $h = 0.5$ (h assumed to be given) in a steel layer ($\nu = 1/3$) using a pattern search method (PS). Galerkin method is used as a forward solver. The layer is excited at a frequency $\bar{\omega} = 0.97$.

3.3 FEM for a structure with an absorbing non-reflecting boundary

For calculating surface displacements in the medium with a crack of the known configuration was used commercial software ABAQUS. When the problem of wave propagation in the medium infinite along the horizontal coordinate is considered using finite element method (FEM) boundary conditions must be chosen specially, in order to prevent wave reflection. According to the algorithm from [3], it is necessary to supplement the area required for modeling by a damping area with internal friction increasing while moving away from the coordinate center.

4 Numerical examples of crack identification

Local optimization methods are not effective in solving the optimization problem (7-8), since the objective function can have a large number of local maxima and minima and initial approximations of crack parameters are unknown. Genetic algorithms (GA) and pattern search (PS) algorithms have proved their efficiency in problems of global optimization. Genetic algorithms are derived on the principles of natural evolution and are widely used in many optimization problems. Pattern search methods do not require the gradient of the problem and can hence be used for functions that are not continuous or differentiable. The global minimization software DIRECT 2.0 [12], based on the pattern search, is used to the optimization problem (7-8). The DIRECT 2.0 switches to the local search algorithm after a good approximation to the solution is obtained.

In this work the measured data is simulated using calculation of displacements for the given crack parameters at 16 points on the surface of structure. Random errors that are unavoidable during experimental measurement of surface displacements are modeled by adding the uniformly distributed random values to the displacements computed at the measuring points. All computations are carried out on the standard PC.

As a numerical example of application of presented in this paper methods we consider a 2D-problem of identification of parameters x_0, a and h, where as an excitation source a vertical point source is used. In fig. 2 the amplitudes of in-plane (left) and out-of-plane (right) displacements on the surface of symmetrical composite laminate $[C90/G45/G-45]_s$ with layers of carbon-epoxy and graphite-epoxy are presented. Prefix "C" corresponds to the transversally isotropic layers of carbon-epoxy given by $E_1 = 142.17$ GPa, $E_2 = 9.255$ GPa, $G_{12} = 4.795$ GPa, $\nu_{12} = 0.3340$, $\nu_{23} = 0.4862$, $\rho = 1.90$ kg/m^3. Prefix "G" stands for transversally isotropic layers of graphite-epoxy given by $E_1 = 38.49$ GPa, $E_2 = 9.367$ GPa, $G_{12} = 3.414$ GPa, $\nu_{12} = 0.2912$, $\nu_{23} = 0.5071$, $\rho = 2.66$ kg/m^3 [2]. We note, that in numerical implementation all considered values are normalized with respect to the thickness of the structure H and velocity $c_0 = 1$ km/s, so the dimensionless frequency is obtained as $\bar{\omega} = \omega H/c_0$. The values of amplitudes presented in fig. 2 are computed for the true values of crack parameters (marked as straight lines) and for identified crack

parameters, obtained applying GA (marked as circles).

The next tables (Tables. 14, 15) present some results of crack identification if a relative error is introduced in measurement data. As it is clear from the presented tables, both optimization techniques identify a damage with sufficient accuracy. As it is observed, genetic algorithm applied to the optimization problem can quickly give a good approximation of the solution (10-15%), but in the vicinity of the minimum converges slowly. The computational time of DIRECT 2.0 Software is usually about a half of time, needed for the GA.

Acknowledgements

The work has been supported by the Federal Ministry of Education and Research (Germany), Russian Fund for Basic Research and administration of Krasnodar region grants (09-08-96522-r-yug-a, 09-08-00294-a, 09-08-96527-r-yug-a, 09-08-00170-a), the programs of the Presidency of the South Scientific center of Russian Academy of Sciences.

References

[1] W. Ostachowicz, P. Kudela, P. Malinowski, T. Wandowski. Damage localisation in plate-like structures based on PZT sensors. Mechanical Systems and Signal Processing 23, 1805-1829, 2009.

[2] G.R. Liu and Z.C. Xi, *Elastic Waves in Anisotropic Laminates, CRC Press, Boca Raton, 2002.*

[3] G.R. Liu, S.S. Quek Jerry. A non-reflecting boundary for analyzing wave propagation using the finite element method. Finite Elements in Analysis and Design 39, 403-417, 2003.0

[4] A. Karmazin, E. Kirillova, W. Seemann, P. Syromyatnikov. "Investigation of Lamb elastic waves in anisotropic multilayered composites applying the Green's matrix", Ultrasonics 51 (2011), 17-28.

[5] A. Karmazin, E. Kirillova, W. Seemann, P. Syromyatnikov "Methods for computing 3D Steady-state vibrations of composites using Green's functions", Proceedings of The ASME International Mechanical Engineering Congress & Exposition (IMECE 2010) November 12-18, 2010, Vancouver, Canada.

[6] A. Karmazin, E. Kirillova, W. Seemann, P. Syromyatnikov. "Modelling of 3D steady-state oscillations of anisotropic multilayered structures applying the Green's functions", Adv. Theor. Appl. Mech., Vol. 3, 2010, no. 9, 425 - 450.

[7] Ye.V. Glushkov, N.V. Glushkova, M.V. Golub. Diffraction of elastic waves by an inclined crack in a layer. Journal of Applied Mathematics and Mechanics 71, 643-654, 2007.

[8] V.A. Babeshko, Ye.V. Glushkov, Zh.F. Zinchenko. Dynamics of Inhomogeneous Linear Elastic Media. Nauka, Moscow, 1989.

[9] V.A. Babeshko, S.V. Ratner, P.V. Syromyatnikov. On mixed problems for thermoelectroelastic media with discontinuous boundary conditions. Doklady Physics, 2007, Vol. 52, N. 2, pp. 90-95.

[10] V.A. Babeshko, O.V. Evdokimova, O.M. Babeshko, et al., The Differential Factorization Method for a Block Structure, Dokl. Ross. Akad. Nauk 424 (1), 36-39 (2009) 54 (1), 25-28 (2009).

[11] V.A. Babeshko, O.M. Babeshko and O.V. Evdokimova, "On the Method of Block Element," Mech. Solids. 45 (3), 437-444 (2010).

[12] J. M. Gablonsky. DIRECT Version 2.0 User Guide. Technical Report CRSC-TR01-08, Center for Research in Scientific Computation, North Carolina State University, April 2001.

Alexander Karmazin, ITM, Karlsruhe Institute of Technology, Building 10.23, Kaiserstrasse 11, 76131 Karlsruhe, Germany
Evgenia Kirillova, DCSM, RheinMain University of Applied Sciences, Kurt-Schumacher-Ring 18, 65197 Wiesbaden, Germany
Wolfgang Seemann, ITM, Karlsruhe Institute of Technology, Building 10.23, Kaiserstrasse 11, 76131 Karlsruhe, Germany
Pavel Syromyatnikov, South Scientific Center of Russian Academy of Sciences, Chekhov Avenue 41, 344006 Rostov-on-Don, Russia

Weakly-compressible SPH for viscous fluid flow

Vladimir A. Kocheryzhkin
vladimir@kocheryzhkin.com

Abstract

An implementation of weakly-compressible smoothed particle hydrodynamics (WCSPH) method is presented to treat viscous fluid flow based on the Tait equation. Test cases are presented to illustrate the accuracy of the method. The Poiseuille problem is studied by SPH approach and results of calculation are compared with analytical solution. The classical dam-break problem which involves free surface flow is simulated and results are compared with experimental data set.

1 Introduction

Smoothed Particle Hydrodynamics (SPH) is one of meshfree computational method. It works by replacing problem domain with a set of particles containing individual material properties and moving according to the general conservation equations. SPH was originally developed for use in astrophysical gas dynamics. But due to the absence of mesh, SPH was adapted and applied to solve different complex problems such as free surface flow, large deformations, fluid-structure interaction etc.

This paper is devoted to the investigation of modified SPH method. For this purpose two problems are considered: Poisuille flow [1] and Dam Break [2]. Weakly compressible formulation employs Tait equation of state to handle density variation. Following equations with appropriate boundary and initial conditions were used in current work:

$$\begin{cases} \dot{\rho} + \rho \nabla \mathbf{v} = 0; \\ \dot{\mathbf{v}} = -\nabla P + \rho \mathbf{g} + \mu \Delta \mathbf{v}; \\ P = B\left(\left(\frac{\rho}{\rho_0}\right)^{\gamma} - 1\right), \end{cases}$$

where $B = \rho_0 c_0^2/\gamma$, $\mathbf{v}$ - denotes velocity, P - the pressure and $\mathbf{g}$ - external force, c_0 - denoting speed of sound in the fluid, ρ_0 - initial density, γ - adiabatic exponent.

For more comprehensive overview of SPH [4, 5] can be found. Also impressive work are done by SPH European Research Interest Community (http://bit.ly/e7oJGG).

2 Poiseuille flow

Poiseuille flow between parallel infinite plates was simulated to check the accuracy of the WCSPH method. Initial parameters were the same as those used by Morris [1]. The solid walls were modelled using virtual type II particles [4]. The periodic boundary condition was applied to treat infinite plates. The problem domain is consisted of 16x64 particles (see Figure 1(a)). The smoothing length was 1.5 times more than initial particle spacing. Comparison of velocity profile for analytical solution and numerical results is displayed on Figure 1(b).

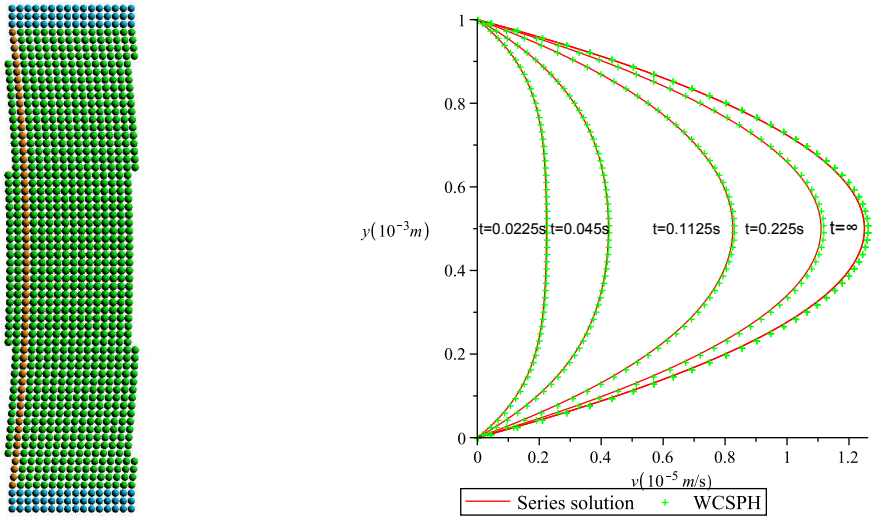

(a) Particles positions in the flow domain (t=2.5s) (b) Velocity profiles comparing SPH simulation results with analytical solution at different time frames.

Figure 1: Poiseuille flow

The maximum relative error at steady flow (1.0s) is less then 0.8%. Morris et al. (0.7%) and Afanasiev et al. (0.8%) obtained the same results [1, 3].

3 Dam Break

As a next test, the classical dam break 2D problem was considered. Due to deficiency of neighbours particles on a free surface, normalised forms of the kernel approximation were used (Shepard interpolant) [4]. Monaghan suggested to use continuity equation to derive density field, but it was not found stable at present work [2]. Initially particles were placed on cartesian grid. The solid walls were modelled using virtual type I particles [4]. Results obtained using 1024 particles were in close agreement with [3]. But, new fluid flow patterns were discovered using more then 16K particles (see Figure 2).

Also a comparison with experimental data was done (right wall was excluded) [6]. It is displayed on Figure 3.

4 Conclusions

An efficient Lagrangian method for handling viscous fluid flow is investigated. WCSPH was used to simulate Poiseuille flow problem and results were compared with analytical solution. WCSPH simulation of the dam break flow and impact against a vertical wall showed that method can be incorporated to solve complex problem. Qualitatively new fluid flow patterns were obtained. Comparison with experimental data is provided. Source code is available on http://bit.ly/kvapm11.

References

[1] Morris J.P., Fox P.J., Zhu Y. Modeling low Reynolds number incompressible flows using SPH // J. of Comp. Phys. 1997 V. 136. P. 214-226.

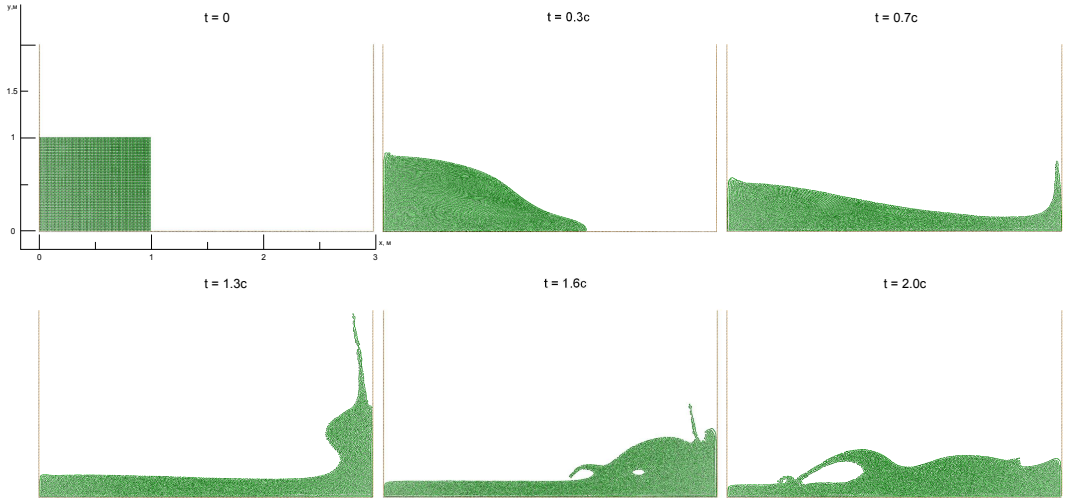

Figure 2: Particle positions for dam break problem at different time frames(16385 particles)

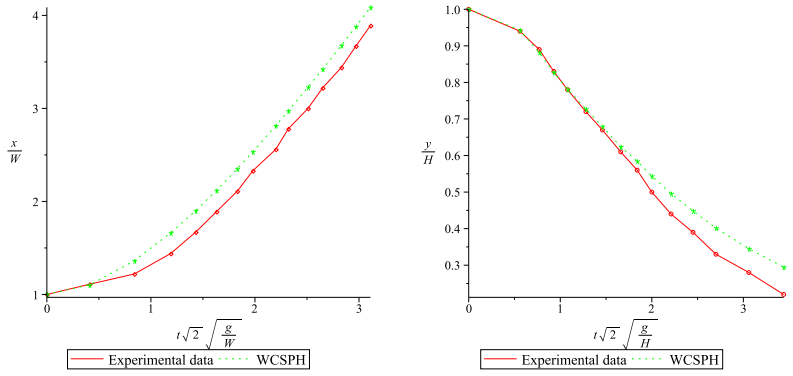

(a) Surge front (b) Height of fluid column

Figure 3: Comparison of experimental data with SPH

[2] Monaghan J.J. Simulating free surface flows with SPH // J. of Comp. Phys. 1994. V. 110 2, P. 399-406.

[3] Afanasiev K.E., Iliasov A.E., Makarchuk R.S., Popov A.Y. Numerical simulation of free boundary flows using SPH and MPS // Comp. Tech. 2006. V. 11. Special issue. P. 26-44

[4] Liu G.R., Liu M.B. Smoothed Particle Hydrodynamics: a Meshfree Particle Method. World Scientific, 2003.

[5] Li S., Liu W.K. Meshfree Particle Methods. Berlin: Springer Verlag, 2004

[6] Martin J.C., Moyce W.J. And experimental study of the collapse of liquid columns on a rigid horizontal plane. // Philos. Trans. Roy. Soc. London. 1952. Ser. A, V. 244 P. 312-324.

Vladimir A. Kocheryzhkin, St.Petersburg State University, Petrodvoretz, Universytetskii prospect, 28, 198504, Russia

Radial deformation of cylindrical membrane

Alexei M. Kolesnikov
Alexei.M.Kolesnikov@gmail.com

Abstract

In this work a thin shell of revolution is considered. The shell is subjected by an axisymmetric deformation. The material of shell is hyperelastic and incompressible. We assume that the bending stiffness is neglected. The problem is solved within framework of the nonlinear theory of membrane. The membrane is free of surface loads. It is subjected to a radial edge load only. The equilibrium equations are derived for an arbitrary axisymmetric membrane. The analytical solution is obtained for a cylindrical membrane made of Bartenev–Khazanovich material.

1 Equilibrium equations

Let $\{\mathbf{i}_1, \mathbf{i}_2, \mathbf{i}_3\}$ be the standard set of orthonormal base vectors in the fixed Cartesian reference frame and let (r, ϕ, z) be a set of circular cylindrical coordinates in this frame with associated orthonormal base vectors $\{\mathbf{e}_r, \mathbf{e}_\phi, \mathbf{e}_z\}$, where

$$\mathbf{e}_r = cos(\phi)\mathbf{i}_1 + sin(\phi)\mathbf{i}_2, \quad \mathbf{e}_\phi = -sin(\phi)\mathbf{i}_1 + cos(\phi)\mathbf{i}_2, \quad \mathbf{e}_z = \mathbf{i}_3.$$

Denote s and ϕ the Gaussian surface coordinates. The position of a point on the membrane of revolution is given by

$$\mathbf{r}(s, \phi) = \rho(s)\mathbf{e}_r + \zeta(s)\mathbf{e}_z, \quad s \in [s_1, s_2], \quad \phi \in [0, 2\pi]. \tag{1}$$

We introduce the covariant base vectors $\mathbf{r}_1$, $\mathbf{r}_2$ and the unit normal $\mathbf{n}$ associated with the surface as

$$\mathbf{r}_1 = \frac{\partial \mathbf{r}}{\partial s} = \rho'(s)\mathbf{e}_r + \zeta'(s)\mathbf{e}_z, \quad \mathbf{r}_2 = \frac{\partial \mathbf{r}}{\partial \phi} = \rho(s)\mathbf{e}_\phi,$$
$$\mathbf{n} = \frac{\mathbf{r}_1 \times \mathbf{r}_2}{|\mathbf{r}_1 \times \mathbf{r}_2|} = \frac{\rho'(s)\mathbf{e}_z - \zeta'(s)\mathbf{e}_r}{\sqrt{\rho'^2(s) + \zeta'^2(s)}},$$

where a prime ($'$) denotes differentation with respect to the Gaussian surface coordinate s.

The covariant components $g_{\alpha\beta}$ $(\alpha, \beta = 1, 2)$ of the first metric tensor $\mathbf{g}$ of axisymmetric surface are functions of s only and are given by [2]

$$\begin{aligned} g_{11} &= \mathbf{r}_1 \cdot \mathbf{r}_1 = \rho'^2(s) + \zeta'^2(s), \\ g_{12} &= g_{21} = \mathbf{r}_1 \cdot \mathbf{r}_2 = 0, \\ g_{22} &= \mathbf{r}_2 \cdot \mathbf{r}_2 = \rho^2(s). \end{aligned} \tag{2}$$

The covariant components $b_{\alpha\beta}$ of the second metric tensor (the curvature tensor) $\mathbf{b}$ of axisymmetric surface are functions of s only and are given by [2]

$$b_{11} = \mathbf{n} \cdot \frac{\partial \mathbf{r}_1}{\partial s} = \frac{\rho'(s)\zeta''(s) - \rho''(s)\zeta'(s)}{\sqrt{\rho'^2(s) + \zeta'^2(s)}},$$
$$b_{12} = b_{21} = \mathbf{n} \cdot \frac{\partial \mathbf{r}_1}{\partial \phi} = \mathbf{n} \cdot \frac{\partial \mathbf{r}_2}{\partial s} = 0, \tag{3}$$
$$b_{22} = \mathbf{n} \cdot \frac{\partial \mathbf{r}_2}{\partial \phi} = \frac{\rho(s)\zeta'(s)}{\sqrt{\rho'^2(s) + \zeta'^2(s)}}.$$

If the deformed membrane is axisymmetric then similarly described above we can be described the surface of the deformed membrane. We will denote the quantities associated with deformed membrane by the capital letters. For example, the position vector $\mathbf{R}(s, \phi)$ has the form similar to (1)

$$\mathbf{R}(s, \phi) = P(s)\mathbf{e}_r + Z(s)\mathbf{e}_z. \tag{4}$$

The axisymmetric deformation of membrane of revolution is one-dimentional deformation, i. e., the static problem reduces to ordinary differentional equations [1]. We assume that the external load is an axisymmetric radial edge load only.

We introduce the Chauchy stress resultant tensor $\mathbf{L} = L^{\alpha\beta}\mathbf{R}_\alpha\mathbf{R}_\beta$ [1] and the Christoffel symbols of the second kind $\Gamma^\mu_{\alpha\beta}$ associated with the deformed surface [1]

$$\Gamma^1_{11} = \frac{1}{2G_{11}}\frac{dG_{11}}{ds}, \quad \Gamma^1_{22} = -\frac{1}{2G_{11}}\frac{dG_{22}}{ds}, \quad \Gamma^2_{12} = \Gamma^2_{21} = \frac{1}{2G_{22}}\frac{dG_{22}}{ds}, \tag{5}$$
$$\Gamma^1_{12} = \Gamma^1_{21} = \Gamma^2_{11} = \Gamma^2_{22} = 0.$$

Here $G_{\alpha\beta}$ are the covariant components of the first metric tensor of the deformed surface similar to (2).

The equilibrium equations of the axisymmetric membrane in the absent of surface loads can be written in the form [1]

$$\frac{dL^{11}}{ds} + L^{11}(2\Gamma^1_{11} + \Gamma^2_{21}) + L^{22}\Gamma^1_{22} = 0, \tag{6}$$
$$L^{11}B_{11} + L^{22}B_{22} = 0. \tag{7}$$

Here $B_{\alpha\beta}$ are the covariant components of the second metric tensor of the deformed surface similar to (3).

We introduce the true stress resultants T_s, T_ϕ and the principal curvatures [2]

$$T_s = L^{11}G_{11}, \quad T_\phi = L^{22}G_{22}, \quad \frac{1}{R_s} = \frac{B_{11}}{G_{11}}, \quad \frac{1}{R_\phi} = \frac{B_{22}}{G_{22}}. \tag{8}$$

From (2), (3), (5) and (8) the equilibrium equations (6) and (7) may be rewritten in the form

$$\frac{dT_s}{ds} + \frac{T_s - T_\phi}{P} \cdot \frac{dP}{ds} = 0, \tag{9}$$
$$\frac{T_s}{R_s} + \frac{T_\phi}{R_\phi} = 0. \tag{10}$$

We introduce the slope of the tangent $\Psi(s)$ to the deformed surface along a coordinate curve $\phi = const$

$$\tan(\Psi(s)) = \frac{Z'(s)}{P'(s)} = \frac{dZ}{dP}.$$

Divide the membrane into two parts along the coordinate curve $s = const$ and consider the equilibrium of one part. If the external load is an axisymmetric radial edge load then its resultant equals to zero. From equilibrium equations we have [3]

$$2\pi T_s P \sin(\Psi) = 0. \tag{11}$$

To solve the problem, the equation (11) can be used instead the equation (9).

The function $P(s)$ can vanish at some points only. Therefore, to satisfy the equilibrium equation (11) at least one of the following conditions must be satisfied

$$T_s = 0, \tag{12}$$
$$\sin(\Psi) = 0. \tag{13}$$

If the condition (12) is satisfied then $T_\phi = 0$, i.e., the membrane is stress free:

$$T_s = 0, \quad T_\phi = 0. \tag{14}$$

For an elastic membrane this conditions means that the part of membrane in the current configuration is undeformed, i.e., taking into account a rigid displacement we have $\mathbf{R}(s,\phi) = \mathbf{r}(s,\phi) + a_1\mathbf{e}_z$ $(a_1 = const)$.

If the condition (13) is satisfied then the part of deformed membrane must be a flat [4], i.e., $Z(s) = c_1 = const$. In this case the equilibruim equation (10) is satisfied. If we define the constitutive relations then we obtain the equation for unknown function $P(s)$ from (9).

Thus, the equilibrium equations of the membrane of revolution, which is subjected by uniformly radial edge loads only, reduce to the form

$$P_1(s) = \rho(s), \quad Z_1(s) = \zeta(s) + a_1, \tag{15}$$
$$Z_2(s) = c_1, \quad P_2(s) : \frac{dT_s}{ds} + \frac{T_s - T_\phi}{P_2} \cdot \frac{dP_2}{ds} = 0. \tag{16}$$

The fuctions $P_1(s)$ and $Z_1(s)$ correspond to the conditions (14), $P_2(s)$ and $Z_2(s)$ correspond to the condition (13).

The equation (16) has the first integral for the uncompressible isotropic elastic material [5]. Consider the strain energy density $W(\lambda_1, \lambda_2)$, the true stresses has the form [1] ($h = const$ is the initial thickness of membrane)

$$T_s = \frac{h}{\lambda_2}\frac{\partial W}{\partial \lambda_1}, \quad T_\phi = \frac{h}{\lambda_1}\frac{\partial W}{\partial \lambda_2}, \tag{17}$$

where λ_1 and λ_2 are the principal stretches, which are defined by

$$\lambda_1 = \sqrt{\frac{P'^2(s) + Z'^2(s)}{\rho'^2(s) + \zeta'^2(s)}}, \quad \lambda_2 = \frac{P(s)}{\rho(s)}. \tag{18}$$

The first integral of (16) may be written in the following form [5]

$$W - \lambda_1 \frac{\partial W}{\partial \lambda_1} = const. \tag{19}$$

2 Circular cylindrical membrane

The similar problem of the deformation tube of finite lenght to annulus was consider by Wu [6], where the numerical results and the asymptotic behavior of the solution are presented for neo-Hookean and Mooney–Rivlin materials. In this study we consider the semi-infinite tube made of Bartenev–Khazanovich material. Only part of tube is deformed. The Lagrangian coordinate of the boundary between undeformed and deformed parts is unknown.

The semi-infinite cylindrical membrane is described by the equations

$$\rho(s) = 1, \quad \zeta(s) = s, \quad s \in (-\infty, 0]. \tag{20}$$

The covariant components of the first metric tensor of the undeformed membrane (20) have the form

$$g_{11}(s) = 1, \quad g_{22}(s) = 1. \tag{21}$$

We consider Bartenev–Khazanovich strain energy density [7]

$$W = 2\mu(\lambda_1 + \lambda_2 + \frac{1}{\lambda_1\lambda_2} - 3). \tag{22}$$

In case (16) the principal stretches are defined by

$$\lambda_1 = P_2'(s), \quad \lambda_2 = P_2(s). \tag{23}$$

We assume that $P_2'(s) > 0$.

In view of (22) and (23), the equation (19) may be written in the form

$$P_2'(s) = -\frac{2}{P_2(s)(P_2(s) - c_2)}. \tag{24}$$

From the above, we obtain the restriction $1 \leq P_2(s) < c_2$. Integrating (24), we obtain

$$s = -\frac{1}{6}P_2^3 + \frac{1}{4}c_2P_2^2 + c_3. \tag{25}$$

Thus, the solutions of problem may be expressed as

$$P_1(s) = 1, \quad Z_1(s) = s + a_1, \tag{26}$$

$$Z_2(s) = c_1, \quad s(P_2) = -\frac{1}{6}P_2^3 + \frac{1}{4}c_2P_2^2 + c_3. \tag{27}$$

The solution (26) corresponds to the undeformed part of membrane. Let s_C denote the boundary between the solutions (26) and (27).

We shall give the edge displacement instead of the radial edge load. The boundary conditions at $s = 0$ can be written in the following form

$$Z_2(0) = 0, \quad P_2(0) = A. \tag{28}$$

Then we obtain

$$c_1 = 0, \quad c_3 = \frac{1}{6}A^3 - \frac{1}{4}c_2A^2. \tag{29}$$

The constant a_1 and the unknown boundary s_C are determined by the continuity of the functions $Z(s)$ and $P(s)$

$$Z_1(s_C) = Z_2(s_C), \quad P_1(s_C) = P_2(s_C). \tag{30}$$

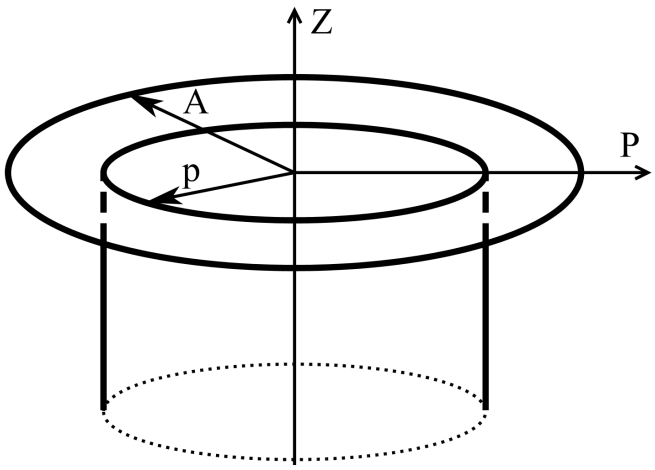

Figure 1: The cylindrical membrane under radial edge stretches.

We have

$$a_1 = -s_C, \quad s_C = \frac{1}{6}(A^3 - 1) + \frac{1}{4}c_2(1 - A^2).$$

By the continuity of the stress resultants we shall determine the constant c_2. In case (27), using (22)–(24), the stress resultants (17) can be expressed as the function of P_2 in the following form

$$T_s(P_2) = \frac{\mu h}{2P_2}\left(4 - P_2(c_2 - P_2)^2\right), \tag{31}$$

$$T_\phi(P_2) = \frac{\mu h}{2}(c_2 - P_2)\left(3P_2 - c_2\right). \tag{32}$$

It follows from (26) and (30) that $P_2(s_C) = 1$. Using (31) and (32) from $T_s(1) = 0$ and $T_\phi(1) = 0$, we have

$$c_2 = 3.$$

Thus, the membrane in the current configuration (fig. 1) is given by the equations containing the parameter A

$$P_1(s) = 1, \quad Z_1(s) = s - \frac{1}{6}A^3 + \frac{3}{4}A^2 - \frac{7}{12}, \tag{33}$$

$$Z_2(s) = 0, \quad s(P_2) = \frac{1}{6}(A^3 - P_2^3) + \frac{3}{4}(P_2^2 - A^2). \tag{34}$$

$$s_C = \frac{1}{6}A^3 - \frac{3}{4}A^2 + \frac{7}{12}. \tag{35}$$

This solution is defined in the interval $P_2 \in [1, 3]$. If $P_2 > 3$ then the solution in the form (16) does not exist for Bartenev-Khazanovich material.

The stress resultants T_s and T_ϕ depend on P_2 only. The plots of the stress resultants (31) and (32) are shown in figure 2. The X-axis is P_2. The Y-axis is the dimensionless stress resultants ($T_s^* = T_s/\mu h$ and $T_\phi^* = T_\phi/\mu h$). The solid curve corresponds to T_s^*. The dotted curve corresponds to T_ϕ^*.

The stress resultants have maximums in the interval $P_2 \in [1, 3]$. T_ϕ^* has a maximum at the point $P_2 = 2$. T_s^* has a maximum at the point $P_2 \approx 2,732$. Thus, it is necessary to investigate the stability of this form of equilibrium for $A \geq 2$.

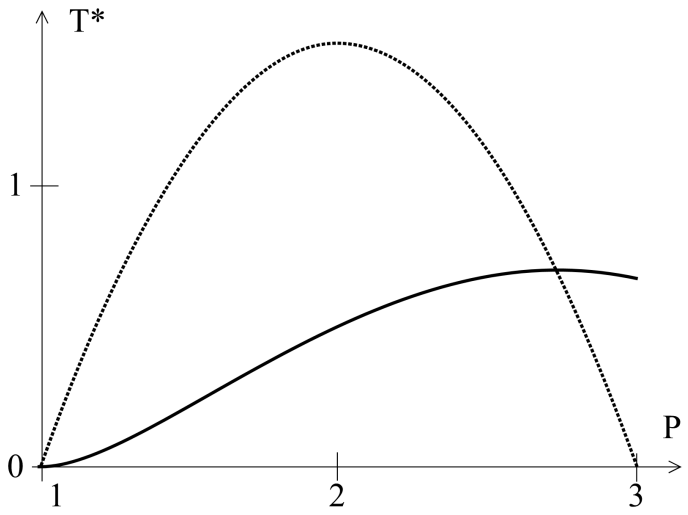

Figure 2: The dimensionless stress resultants T_s^* and T_ϕ^*.

Acknowledgements

This study was supported by the grant of the President of the Russian Federation (MK-439.2011.1).

References

[1] A. M. Kolesnikov, L. M. Zubov, Large bending deformations of a cylindrical membrane with internal pressure. ZAMM, 89, 2009, p. 288–305.

[2] L. M. Zubov, The methods of nonlinear elasticity in the shell theory (in Russian). Rostov. University Press, Rostov-on-Don, 1982.

[3] S. Timoshenko, S. Woinowsky-Krieger, Theory of plates and shells. 2nd Editions, McGraw-Hill BGGK Company, New York, NY, 1959.

[4] W. Flügge, P. M. Riplog, A large deformation theory of shell membranes. Tech. Rept. No. 102, Div. Engr. Mech., Standford Univ. [R, S, T], 1956.

[5] A. C. Pipkin, Integration of an equation in membrane theory. ZAMP, 19 (5), 1968, p. 818–819.

[6] C.-H. Wu, Tube to annulus – an exact nonlinear membrane solution. Quarterly of Applied Mathematics XXVII, 4, 1970, p. 489–496.

[7] G. M. Bartenev, T. N. Khazanovich, Law of highly elastic deformation of grid polymers. Vysokomolekulyarnye Soedineniya, 2, 1, 1960, p. 21–28.

Alexei M. Kolesnikov, ul. Milchakova 8a, Rostov-on-Don, Russia

Dipole interaction of wagon wheels knock at the off-center railway

Vitaliy M. Kolykhalin
cap-007@mail.ru

Abstract

Possibilities of application of methods of acoustical compensation the noise from railway wagon wheels knock at the rail separations are considered. The greatest compensating of the basic and odd oscillations in low frequency range in case of sufficient temporarily difference between impulses coming in point of observation are obtained. The noise corresponding of different distance between a pair of points rail separation registered by the microphone are estimated.

1 Introduction

The most widespread and economic rail transport in the Russian Federation brings the greatest component in an over-all level of a background noise, especially in urban infrastructures. Despite of using a lot of effective methods sound-proofing or absorption in carriages and on rail tracks, the high level of infrasonic and low-frequency vibrations practically is not excluded. The air-slaked noise is oscillated by impacts (and interacting) wheel pairs of carriages about technological joints and rail roughness. The vertical and horizontal rail waviness is as a result of wearing out rail structure, wheel carriages retardation, and a lot of collisions of carriages.

The dipole (compensation) effect was showed in real conditions noticeably enough, as the common noise level and specificity interleaving of maximum and of minimum in the power spectrum with the predominance in the low frequencies.

The maximum noise level generated by the wheel disks, the carriage frames and the bottom carriages is registered in the field of contact and the flange base. So the noise level reaches 110...115 dB(A) that is approximately higher on 20 dB(A) than carriage roof and higher on 10...15 dB(A) than at walls of the carriage, moving with speed 120 km/h [1]. The spectrum of such noise reaches a maximum in frequency band at 31,5 Hz and sharply decreases approximately on 50 dB(A) in frequency band at 8000 Hz. The noise level is increased up to 110 dB(A) with maximum of power spectrum in band 8...50 Hz under overpasses and in tunnels. The level sound pressure 80 dB(A) was registered in low frequency spectrum on distance in 30 meters from highways.

The maximum level noise of an electric train moving with speed 60 km/h achieves 116 dB(A) on the 1 meter distance from wheels. The duration of impact pulses of rail joints reaches approximately 0,03 sec. and reaches approximately 0,06 sec. for carriage collisions when the maximum noise spectral density is corresponded with frequency band up to 33 Hz.

One of radical methods of decrease of shock noise is application lengthy (up to 800 m.) rail with packing on sleepers with the special shock reducers weakening generation of

vibrations and noise. Using lengthy rail leads us to decrease of air-slaked noise up to 10 dB(A) on the open spaces, however the easing noise level is exceeded only 2...3 dB(A) under overpasses, in narrow streets and tunnels. Such rail tape is influenced the changing atmospheric conditions in the air and their manufacturing, installation and repair cost approximately in 3 times more then usual rail tape.

The most effective method of vibration weakening can be method of mutual compensation of a pair sound sources offered H.E. Olson for electro-acoustic systems. It was developed for vibration and acoustic fields in the foreign and domestic scientist works who have received practical application in the further [2].

Moreover the practical implementation dipole effect can be received by formation a noncoherent pair of the strike impulse sources when the direction of acoustical axes is along the railway under small (15...20) angles. The similar effect can be obtained by shift a pair of parallel rail joints on a pair of offset rail joints, for example, the right rail joint is shifted concerning the left rail joint on the certain distance .The distance is depend on the speed of train and promotes the correlation interconnection between excited acoustical pulses.

2 Numerical calculation based on analytical solution of the problem

The total pressure in some point P at the moment of time t will be the algebraic sum of the sound pressure created by each rail joint separately. If f and $f1$- oscillation frequencies, ε and $\varepsilon 1$ - phase constants, A and A1 - complex amplitudes, then the total pressure $p(r,t)$ will be represented in the form

$$p = \frac{A}{r} e^{2\pi i f(t-(r/c))} + \frac{A}{r_1} e^{2\pi i f_1(t-(r_1/c))} \tag{1}$$

were $A = ae^{-2\pi i f\varepsilon}$; $\quad A_1 = a_1 e^{-2\pi i f_1 \varepsilon_1}$

We will consider two sources located on an axis X: one of them we shall place in point of origin, second - on small distance s from the point of origin.

Let's assume, that both of these sources create oscillations with equal valid amplitude and equal frequency and that initial oscillations are opposite on phase.

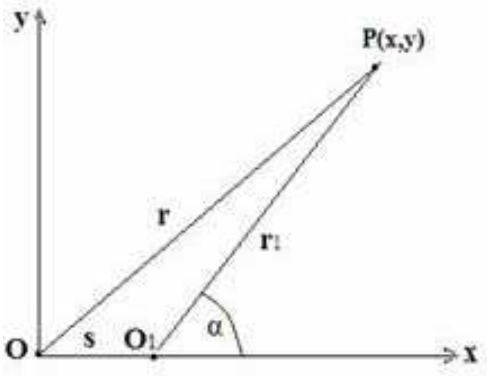

Figure 1: The sound pressure created by double sources.

The case with a pair of rail joints is shown in figure 1. There are following relationships between the magnitudes entering into expressions (1)

$$a = a_1;\ f = f_1;\ \varepsilon = 0;\ \varepsilon_1 = \frac{1}{2f}A = a;\ A_1 = ae^{\pi i} = -a \tag{2}$$

The distance between two sources (a pair of point sources oscillated of wheel knocks at the rail separation) is limiting closed to null, and the valid amplitude *a*of individual oscillation is so great that product *as* is finite value. Such combination of sources with very greater individual amplitudes on very small distance from each other is a double source or a dipole. The double source can be characterized by two magnitudes: the product *as* and the direction (the sources connecting line).

For the dipole the solution (1) must be sought in the form

$$p = \frac{a}{r}e^{2\pi if(t-(r/c))} - \frac{a}{r_1}e^{2\pi if(t-r_1/c)} \tag{3}$$

were $r^2 = x^2 + y^2 + z^2$; $\quad r_1 = (x-s)^2 + y^2 + z^2$ (4)

If $F(r)$ – derivative from r and r ≈ r1 we obtain

$$F(r) - F(r_1) \approx (r - r_1)\frac{dF}{dr} \tag{4}$$

The value $(r - r1)$, taking into account x, s, r, can be calculated

$$r - r_1 = \frac{r^2 - r_1^2}{r + r_1} = \frac{r^2 - r_1^2}{2r};\ r \approx r_1 \tag{5}$$

In accordance with (4) the value $r - r1$ can be equal *sx/r*. The value *dF/dr* can be calculated as follows

$$\frac{dF}{dr} = \frac{\partial F}{\partial x}\cdot\frac{\partial x}{\partial r} + \frac{\partial F}{\partial y}\cdot\frac{\partial y}{\partial r} + \frac{\partial F}{\partial z}\cdot\frac{\partial z}{\partial r} \tag{6}$$

If the point of origin is moved from O to $O1$ and distant is changed from r to $r1$ but the coordinates X and Y of any point do not change. Taking representations (5) and (6) into account the solution (4) must be sought in the form

$$F(r) - F(r_1) = s\frac{\partial F}{\partial x} \tag{7}$$

We right expression (3) in the form

$$p = as_e^{2\pi ift}\frac{\partial}{\partial x}\left[\frac{1}{r}e^{-2\pi if(r/c)}\right] \tag{8}$$

After calculating the derivative from brackets on x taking into account $\partial r/\partial x = x/r$, we shall receive the following expression

$$p = as_e^{2\pi ift}e^{-2\pi if(r/c)}\frac{x}{r^2}\left(\frac{2\pi if}{c} + \frac{1}{r}\right) \tag{9}$$

If α is angle between an X-axis and radius-vector OP, then $x/r = cos\ \alpha$ and the previous expression becomes

$$p = as_e^{2\pi ift} e^{-2\pi if(r/c)} \frac{\cos\alpha}{r} \left(\frac{2\pi if}{c} + \frac{1}{r} \right) \tag{10}$$

When r is so long in comparison with c/f the expression (10) becomes

$$p = \frac{2\pi ifas}{cr} \cos\alpha e^{2\pi if[t-(r/c)]} \tag{11}$$

After replacement as on b we have finally

$$p = \frac{2\pi ifb}{cr} \cos\alpha e^{2\pi if[t-(r/c)]} \tag{12}$$

It is visible from expression (1) that the real amplitude is equal of absolute value complex amplitude. Let a is the real amplitude and equal

$$a = \frac{2\pi fb}{c} \cos\alpha \tag{13}$$

then we obtain real sound pressure from expression (12)

$$p(r, \alpha, t) = a \cos 2\pi f \left(t - \frac{x}{r} \right) \tag{14}$$

So as pressure is sinusoidal changes the average quadric value for full period is equally half of square of amplitude (13) then sound intensity is represented in the form

$$I(r, \alpha) = \frac{1}{r^2} \left(\frac{2\pi fb}{c} \cos\alpha \right) \frac{1}{2\rho_0 c} = \frac{2\pi^2 f^2 b^2}{\rho_0 c^3 r^2} \cos^2\alpha \tag{15}$$

were ρo is air density.

To summarize, the result of numerical simulation lead to the conclusion that dipole created sound intensity directly proportional to square cosine of angle and inversely proportional to square distance from a dipole.

3 Experiment

The relative estimation of changes of a sound intensity for parallel joints and offset joints at rails was obtained using the computer and the sound intensity analyzer type 3360 (B@K). The sound intensity probe was installed on 1 m distance from railway for measuring sound intensity carriages, moving with speed about 15 km/hours [3].The instant intensity is less approximately on 15 dB(A) for offset joints then parallel joints if compare the instant intensity spectrums in octave bands of sound intensity analyzer type 3360 (B@K).

References

[1] The Noise control on manufacture: Directory/E.Y. Yudin, L.A.Borisov, etc. Under ed. E.Y.Judin.-M.: Engineering industry, 1985.

[2] Olson H.E. System Responsive to Energy Flow of the Sound Waves. U.S. Patent. 1.892.644 (1932).

[3] Kolykhalin V.M., Davidov B.B. About an opportunity of easing of air-slaked noise of wheel pairs of rail transport. SPb.: Collected articles. II Rus. scientific conference "Protection of the population from affecting noise", SPbGTU, 2009, p.231-238.

Multilevel approach to description of deformation and fracture of brittle materials with hierarchical porous structure on the basis of movable cellular automaton method

Igor S. Konovalenko Aleksey Yu. Smolin Anton Yu. Nikonov
Sergeu G. Psakhie
igkon@ispms.tsc.ru

Abstract

An approach to multilevel description of deformation and fracture of brittle porous media on the basis of movable cellular automaton method was proposed. The media characterized by pore size distribution function having two maxima were considered. The core of the proposed approach consists in finding the automaton effective response function by means of direct numerical simulation of representative volume of the porous medium. A hierarchical two level model of mechanical behavior of ceramics under compression and shear loading was developed. The ceramics on the basis of zirconium oxide with pore size greater than the average grain size was considered. At the first level of model the small pores (corresponding to the first maximum of distribution bar chart of pore size) were taking into account explicitly as well as representative volume and effective elastic characteristics of the porous medium were evaluated. At the second scale level of the model, big pores were taking into account explicitly (by removing automata from the initial structure) and the parameters of matrix corresponded to the ones of the first level. Simulation results showed, that the proposed multilevel model allows performing correct qualitative and quantitative description of deformation and fracture of brittle media with hierarchical porous structure.

Introduction

Porous materials are characterized by hierarchical pore structure and complex mechanical behavior at fracture [1, 2]. To study and describe these materials the information about their structure and mechanical properties on a few scale levels is needed. One way of getting this information is a numerical simulation. In the framework of one-level approach direct accounting for peculiarities of structure and mechanical behavior of material on each scale level seems to be impossible. As a result, the goal of this investigations is the development of multilevel approach, represented at [3] and corresponding hierarchical model for describing deformation and fracture of nanostructure porous ceramics under compression and shear on the basis of movable cellular automaton method (MCA) [4]. The choice of this method caused by the fact that he has successfully proved itself in the study of mechanical behavior of brittle porous media from the initiation of the first damages until massive fracture [5].The calculations were performed for a model material with mechanical properties of nanocrystalline $ZrO_2(Y_2O_3)$ (yttria-stabilized zirconia) with the average pore size greater than the average grain size and two maxima in its pore size distribution function [2].

Building up a hierarchical model was performed by several stages. At the first stage to find automaton effective response function on macroscopic scale level the calculation were performed with explicit taking into account the structure of material on micro level (this is the scale level where pores structure of model specimens with the size of $20 \div 250$ μm was defined explicitly). The representative volume of porous medium on this scale level was found. At the second stage the calculations performed on the macro-level. At this scale level the porous structure of specimens was taking into account in the same way (explicit manner) as at the previous scale-level. The third stage was a verification of the developed model.

1 Finding the representative volume of porous medium and corresponding effective response functions on the macroscopic scale level

On "micro-scale" level the representative volume was determined by means of convergence analysis of elastic and strength properties of the model porous specimens with their size increase. Mechanical behavior of six groups of porous ceramics specimens under uniaxial compression and simple shear was performed. All specimens in each group had the same geometrical size, but different pore space distribution. Each group consisted of six specimens. Square specimens under consideration had dimension (square side) of 20, 60, 100, 150, 200 and 250 μm according to the groups. It was supposed that all pores in ceramics under investigation, as well as the model material, had spherical shape. The pore size of the model material, according to maximum in ceramics pore size distribution function was 3 μm [2]. Diameter of movable cellular automata, according to the average grain size was 1 μm [2]. Pore structure of model specimens was made by moving away an automaton randomly and its six nearest neighbors. The total porosity in all the samples was 7% [2]. The initial structure of a model specimen is shown in fig. 1, a, b.

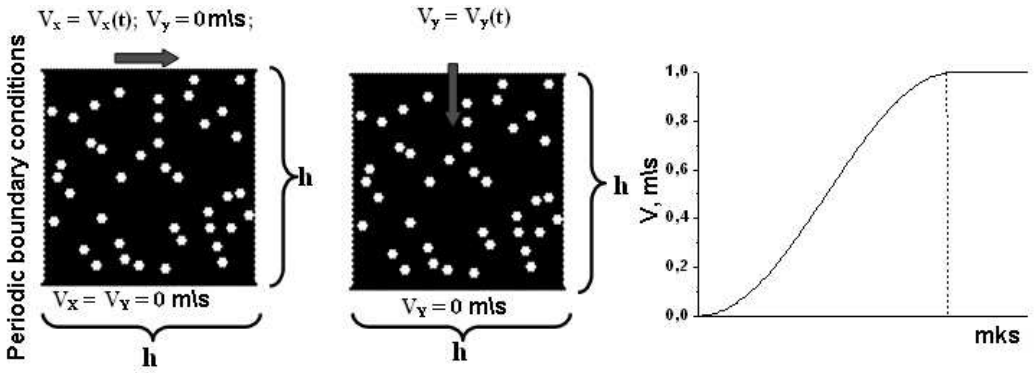

a) b) c)

Figure 1: Initial structure of the model specimen with 60 μm sides and scheme of application of mechanical stress during shear loading (a) and uniaxial compression (b); the law of variation of velocity of the upper automata layer of the specimen (c)

The simple-shear loading was simulated by setting equal velocities in horizontal direction to all automata in the upper layer (fig. 1, a, c). The value of this velocity gradually increased from 0 to 1 m/s in sinusoidal manner and then remained constant. The automata in the bottom layer were fixed. This regime ensured a quasi-static character of loading and allowed dynamic effects to be avoided until the first damage appears. All samples

had periodic boundary conditions in the direction of loading. The uniaxial compression loading was simulated by setting equal velocities in vertical direction (up to 1 m/s) to all automata in the upper layer (fig. 1, b, c). The velocities of automata in the bottom layer were set to zero. Displacement in horizontal direction were allowed to automata in the bottom and upper layers. The lateral surfaces of specimen were free. The problem was solved under plane strain conditions. The response function of automata corresponded to the diagram of loading for nanocrystalline $ZrO_2(Y_2O_3)$ with total porosity of 2% and an average pore size comparable with the grain size [2]. Shear modulus of movable cellular automaton $G = 59.2$ GPa, Poisson ratio $\nu = 0.3$. Inter-automaton bond fracture criterion used for intensity of shear stresses [6].

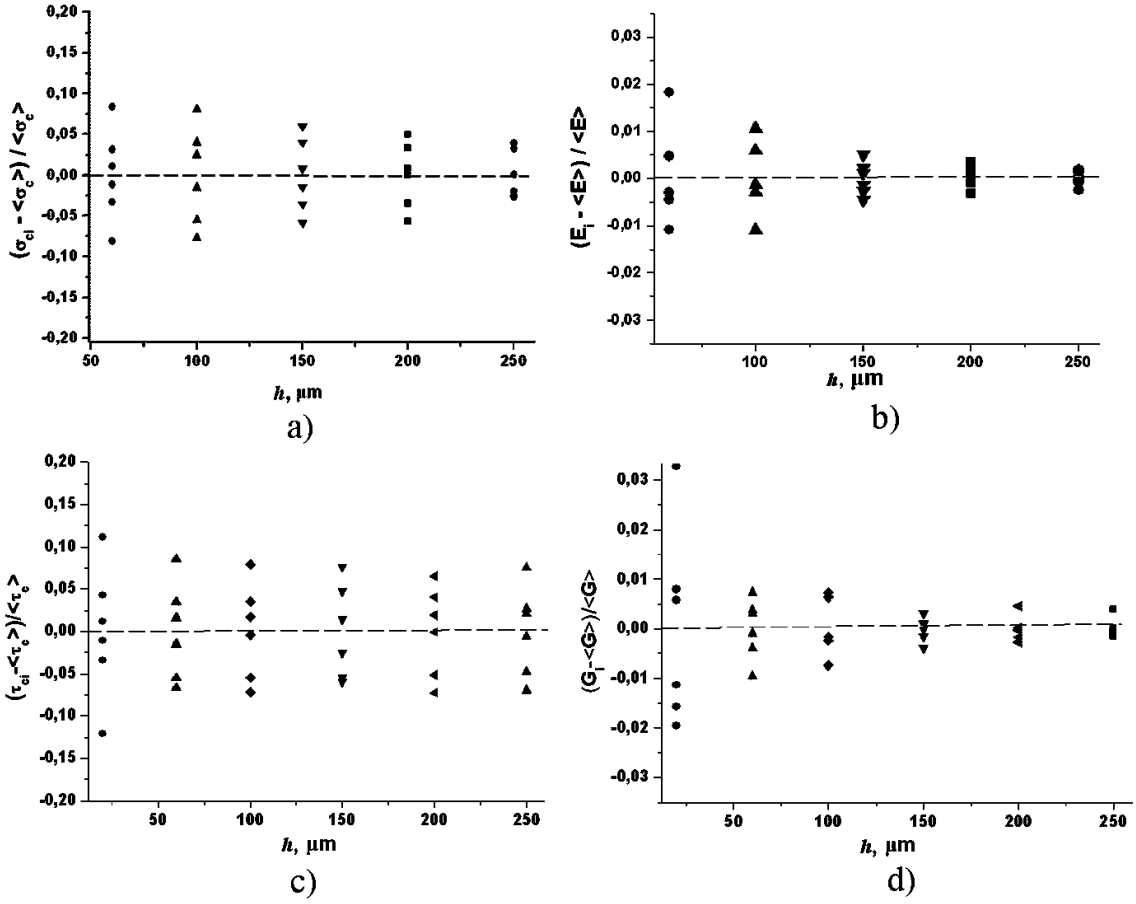

Figure 2: Relative deviation of elastic modulus E_{eff}, shear modulus G_{eff}, compression strength σ_c, shear strength τ_c of model specimens from corresponding mean values $< E_{eff} >$, $< G_{eff} >$, $< \sigma_c >$, $< \tau_c >$ under uniaxial compression (a, b) and shear loading (c, d)

Convergence analysis of mechanical properties for porous model specimens with increase of their size was performed in terms of estimated deviation of effective elastic and strength properties of specimens (modulus of compression-elongation E_{eff}, shear modulus G_{eff}, compression strength σ_c and shear strength τ_c are parameters of diagram of loading) from corresponding mean values in the groups $< E_{eff} >$, $< G_{eff} >$, $< \sigma_c >$ and $< \tau_c >$. The specimen size, for which deviation did not exceed 3% for E_{eff}, G_{eff} and 15% for σ_c, τ_c was accepted as the size of representative volume. Simulation results (fig. 2.) showed nonlinear convergence of strength and elastic properties of model speci-

mens. Relative deviation of E_{eff}, G_{eff}, σ_c and τ_c of model specimens with 150 μm sides from corresponding group average was 0.51, 0.38, 6 and 7.6%. These values did not exceed of the desired limits. Thus, it was shown, that porous specimens with 150 μm sides is the representative volume of the model media under consideration. The values of $< E_{eff} >$ and $< \sigma_c >$ were taken as characteristics of response function of automata on macroscopic level. Slight deviations of these values (-9.5% and 36%) from ones evaluated by experimental way are related with two-dimensional formulation of problem, kind of stress state and incomplete correspondence the pore morphology in the model and in the ceramics. They were corrected (by means of) introducing a correction ratio. The transition from the elastic modulus determined by the calculated diagram of loading under plane strain conditions E_{PSS} to the Young modulus was based on the ratio $E = E_{PSS}(1 - \nu^2)$ [7].

2 Numerical simulations on macrolevel with explicit taking into account porous structure of material

On macrolevel the calculations were performed for nine porous square plane specimens with 22.5 mm side. In according to the size of representative volume the diameter of movable cellular automata was 150 mm. Information about structure and strength properties of material from micro– to macrolevel was transferred by means of response functions with corresponding characteristics of loading diagrams for representative volumes of material on microlevel. The response function of automata corresponded to linear function. Its parameters (the maximal value of specific/unit resistance force to loading and elastic parameter corresponded to Young modulus) were 846 MPa and 112 GPa. The accounting of porous structure of material on macro-scale level (explicit manner), loading conditions and assumption about stress state were similar with that at the first stage. In according to pore size distribution function the porosity of specimens was 28%, and the size of pore 450 μm [2].

3 Model verification

We considered the model as successfully verified (i.e. the model is valid for ceramics under investigation) if the simulation results satisfied the following criteria: 1) Linear loading diagram of model specimens, containing the horizontal section, corresponding to quasi-ductile fracture of porous brittle materials with porosity more than 20%. 2) Qualitative compatibility of the fracture patterns of model specimens and real ceramics. 3) Fall of strength properties of specimens into a certain interval whose limits was found on the basis of processing experimental results.

Loading diagrams typical for all model specimens in case of different types of mechanical loading are presented at figure 3. At these diagrams, you can select several sections. The first linear section, corresponding to elastic deformation of specimen, is typical for brittle materials with any value of porosity. The next section is ascending and not insignificant in extent part of the diagram with multiple stress “oscillations” (just under uniaxial compression fig 3, a). These sections correspond to the repetitive processes of damage generation over the entire specimen, the local cracking and then - the elastic deformation of the material, etc. The last section of the diagram is descending. It corresponds to the macrocracks propagation as well as generating separate multiple damages. Under shear loading (fig. 3, b) at the represented diagram after mentioned sections one can see the ascending section of the curve with breakdowns and then - another drop-down area. As

a results of the straitened deformation conditions the development of macrocracks in the sample corresponds to precisely this part of the diagram, and the first drop-down section of diagram corresponds to a one-time generation of damages over the entire sample and their development without the formation of macrocracks system.

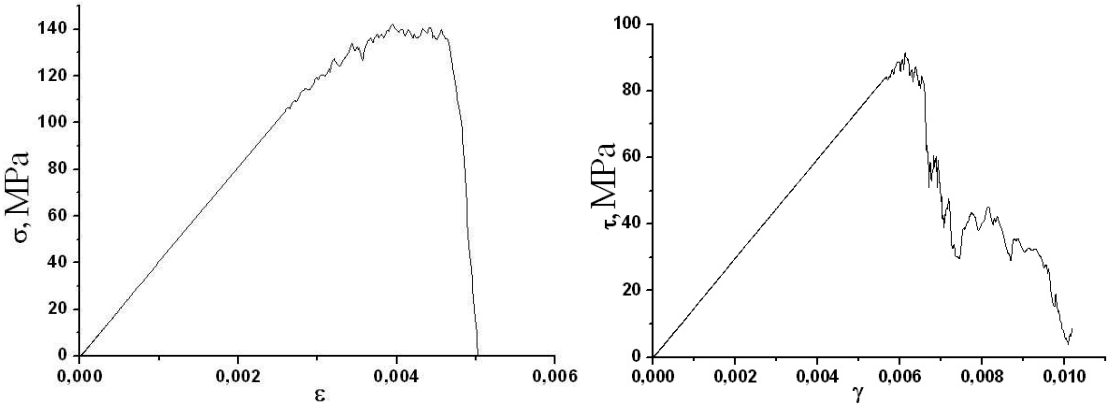

a) b)

Figure 3: Diagram of loading of the model specimens with the side $h = 22.5$ mm under uniaxial compression (a) and shear loading (b)

It should be noted that the horizontal plateau on the compression-test diagram of brittle specimens (fig. 3, a) shows their quasi-ductile fracture, which occurs only when the porosity of the specimen more than 20% [5]. The degree of manifestation of these properties is proportional to the length of this section (plateau) and is different for each model specimens. The reduction of the length of this part of the diagram tell us that fracture is approximate to brittle failure type. It is natural to assume that as the appearance of quasi-ductile character of the sample destruction and the degree of its manifestation is determined by some critical value of the local porosity. The last one is related, in particular, with the value of total porosity, as well as with the form and size of pores. It should be noted that in this case the quasi-brittle fracture is completely due to structural factor, because the model does not take into account any phase transitions, no rearrangement of the lattice of material.

Performed calculations and comparison of simulated diagrams of loading of model specimens with corresponding diagrams of brittle porous bodies under shear and compression loading [2, 5, 8] revealed their good qualitative compatibility. Thus, the first goodness of fit of the model is satisfied.

Typical fracture pattern of model specimens, represented as inter-automaton bond net at the time of first macrocrack propagation, are presented at fig. 4. Under uniaxial compression the specimens were broken-down because of generating therein the asymmetrical system of macrocracks with complex path of crack propagation. In addition, the generation of multiple separated fractures near macrocracks takes place.

In the case of quasi-ductile fracture of specimen (fig. 4, a) the generation of damages and crack growth occur locally, in several places of the sample, characterized by the most-high values of local porosity (and the least web thickness between isolated pores). Until a certain moment some cracks are not merged into main crack - the stage of its growth, as it were “stretched”. It leads to extensive local cracking of the material without losing the integrity of the sample and, consequently, to a substantial dissipation of elastic energy and reduce the effective elastic properties of the material (of the whole sample). Thus, satisfied the second goodness of fit of the constructed model.

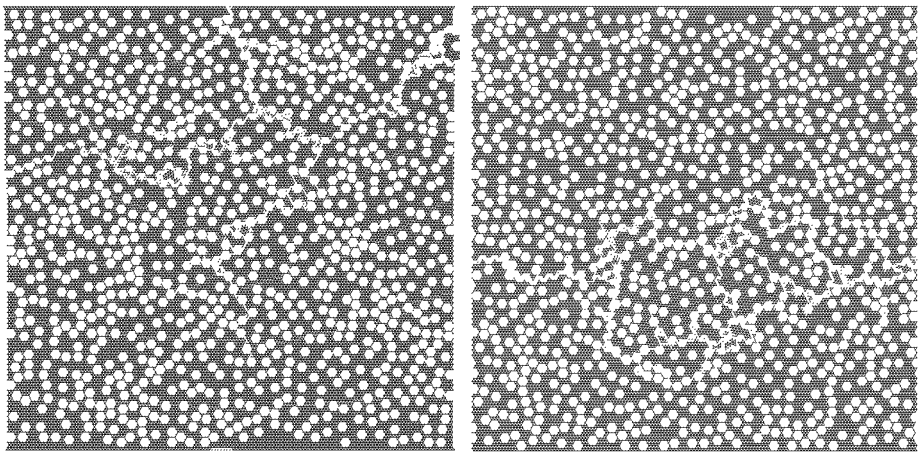

a) b)

Figure 4: Fracture pattern of model specimens with the porosity 28% at the moment of first macrocrack propagation under uniaxial compression (a) and shear loading (b)

To verify the third goodness of fit of the model the average value of the effective elastic modulus ($< E_{eff} >$) and maximum specific resistance force to loading under uniaxial comression were calculated. Then, they were compared with the corresponding values found in natural experiments. It was shown that the deviation of $< \sigma_c >$ and $< E_{eff} >$ model samples from the experimental data does not exceed 30% and 12%, respectively. It is a rather good accuracy in the simulation of highly porous media in plane approximation. This indicates a good quantitative agreement of calculations and experiment and executing the third criterion of the adequacy of the model.

Thus, in this study, the two-level model of porous ceramics with bimodal pore size distribution function, based on a multilevel approach to numerical simulation, was constructed.

Conclusions

Thus, in this study, the multilevel approach to numerical simulation, developed on the basis of movable cellular automaton method, and constructed corresponding hierarchical model can adequately describe the deformation and fracture of porous materials under mechanical loading. Since the proposed approach is sufficiently general, then, if it is necessary, the heterogeneous media containing more than two scale structural level could be simulated on the basis of developed approach.

Acknowledgements

This study was supported by Grant of the President of the Russian Federation for the state supporting young Russian scientists (Project MK-5260.2010.8).

The authors are grateful to Kulkov S.N. and Buyakova S.P. for his interest and helpful comments.

References

[1] Global Roadmap for Ceramics: Proceedings of 2nd International congress on ceramics (ICC2). Edited by Alida Belosi and Gian Nicola Babini. Institute of Science and Technology for Ceramics, National Research Council, Verona (Italy),2008.

[2] Buyakova S.P. Properties, structure, phase structure and laws of formation porous of nanosystems on the basis of ZrO_2. – Diss. doct. Tech. Sci., (2008), Tomsk, 309 p. (Institute of Strength Physics and Materials Science SB RAS).

[3] Ig.S. Konovalenko, A.Yu. Smolin, S.G. Psakhie. Fiz. Mezomekh. 12, 5 (2009) [in Russian].

[4] S. G. Psakhie, G. P. Ostermaier, A. I. Dmitriev, et al., Fiz. Mezomekh. 3 (2), 5 (2000) [in Russian].

[5] Ig.S. Konovalenko. Theoretical investigation of deformation and fracture of porous materials for medical applications and biomechanical constructions. – Diss. cand. Phys.-math. Sci., (2007), Tomsk, 174 p. (Institute of Strength Physics and Materials Science SB RAS) [in Russian].

[6] Kachanov L.M. Basics of fracture mechanics. Moscow: Nauka, 1974.

[7] Sedov L.I. Continuum mechanics. Volume 2. Moscow: Nauka, 1970.

[8] Gogoci G.A. On the classification of difficult-to-deform materials on the specifics of their behavior under loading // Problems of Strength. 1 (1977) [in Russian].

Igor S. Konovalenko, pr. Academicheskii 2/4, *Tomsk,* 634021 *Rissia*
Aleksey Yu. Smolin, pr. Academicheskii 2/4, *Tomsk,* 634021 *Rissia*
Anton Yu. Nikonov, pr. Academicheskii 2/4, *Tomsk,* 634021 *Rissia*
Sergeu G. Psakhie, pr. Academicheskii 2/4, *Tomsk,* 634021 *Rissia*

Molecular dynamics investigation of deformation response of thin-film metallic nanostructures under heating

Ivan S. Konovalenko Konstantin P. Zolnikov Sergey G. Psakhie
ivkon@ispms.tsc.ru

Abstract

Molecular dynamics simulation of nanostructure behavior under impulse heating is carried out. These structures are formed by self-rolling of nano-thickness bilayer crystal films. The interatomic interactions are described by potentials obtained by the embedded atom method. The calculation data are shown that simulated nanostructures can transform the supplied thermal energy into the mechanical oscillations of its free edges. The influence of heating rate and its duration, medium viscosity properties on kinematical characteristics of simulated nanostructures is investigated. The influence of mass and size of oscillating free edges of nanostructures on their behavior under heating is studied. The efficiency estimation of thermal energy transformation, supplied to nanostructures, into mechanical oscillations of their free edges versus nanostructure configuration, chemical composition and rate of impulse heating is carried out. The atomic mechanisms responsible for the peculiarities of local atomic structure transformations in bilayer nanofilm under its detaching from the substrate as well as mechanism of thermal energy conversion into mechanical one by nanostructures are investigated.

Introduction

At present, much attention is paid to the investigation of different properties of nanostructures and its use in nanodevices of different functionalities [1]. Nevertheless, the questions connected with atomic mechanisms responsible for nanostructure formation processes are still urgent. The methods of control over nanostructure motions are not sufficiently investigated as well as over capability of these structures to transform supplied energy. The study of the given subjects is the key stone in solution of many fundamental problems. It is of great importance for the practical use of nano-sized structures, for instance, in nanomachines and when designing the nanorobots and nanodevices.

1 Formulation of the problem

The given paper is aimed at studying the atomic mechanisms of structural changes, determining the behavior of non-closed nanostructures formed of bilayer metallic films during the formation process and under thermal loading.

All the calculations in the given paper were made under the molecular dynamics method [2], using the multiparticle interatomic potentials calculated by the embedded atom method [3].

2 Results of numerical simulation

The subject of the given research is the non-closed nano-sized structures formed on the basis of bilayer metallic films with crystalline structure. The simulation of nano-sized structure formation process composed of inclusions with regular internal structure is described in detail [4]. Each inclusion is composed of atoms of a kind; in particular, one type of inclusions was composed of aluminum atoms, another one - of copper atoms. The final shape of simulated non-closed nanostructures was determined by initial parameters of initial nano-sized films. When varying the geometric sizes of copper inclusions and their mutual arrangement in the initial aluminum film, one can obtain the non-closed nanostructures of different shape. In order to accelerate the rolling process of nanostructures, the etching processes of "victim layer" were neglected in papers [4-8]. It was assumed that initial nano-sized film under stress condition is already separated from substrate. Figure 1 presents the simulation results of non-closed nanostructures, composed of aluminum and copper inclusions.

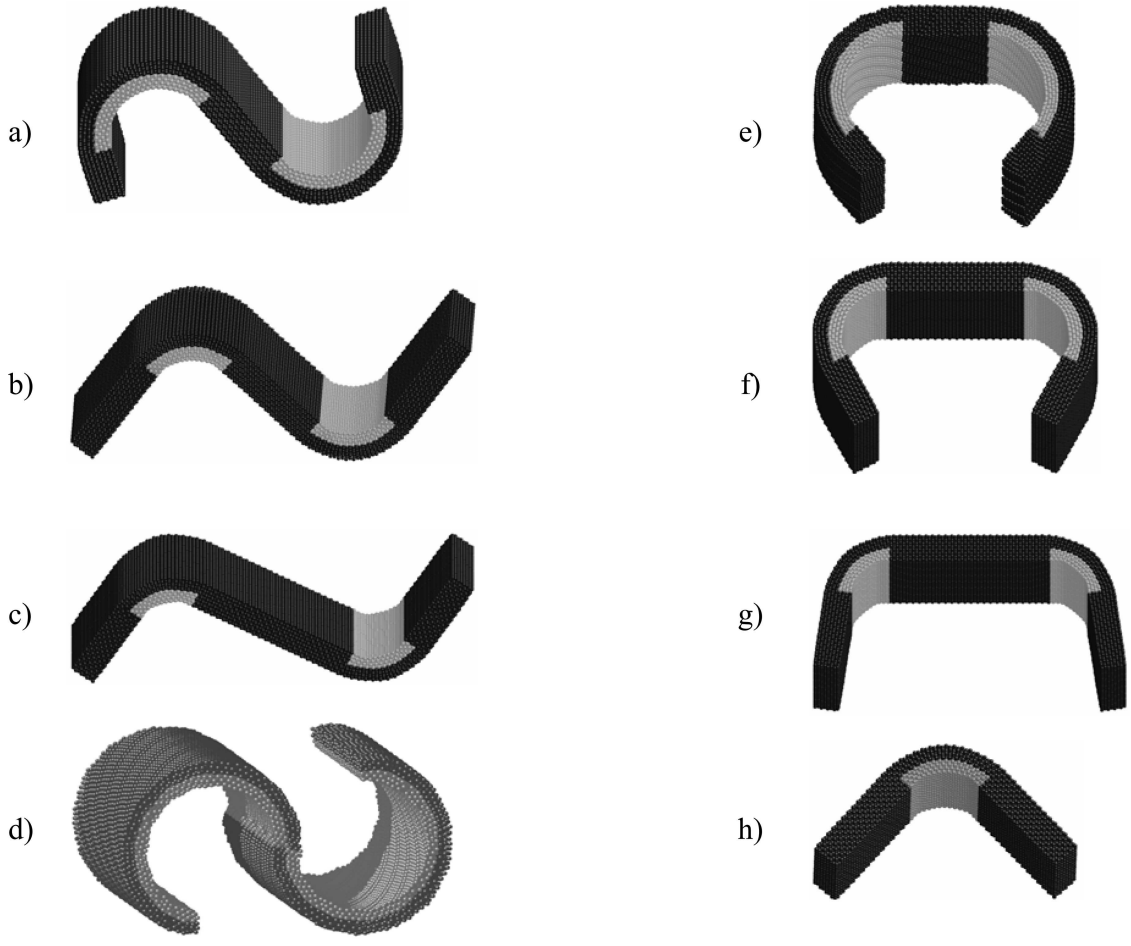

Figure 1: Shapes of non-closed nanostructures. Copper inclusions of different length are found: a-d– on opposite sides of aluminum film; e-g– on one side of aluminum film; h– is the nanostructure with one inclusion. The copper atoms are shown by light grey color; the aluminum atoms are shown by dark-grey color

The behavior of non-closed nanostructures, presented in Fig. 1, was investigated under heating over the temperature interval from 50 to 500 K. The edges of these structures start

oscillating under heating as far as the thermal-expansion coefficients of layers and their temperature dependence differ considerably. The edge oscillation frequencies of simulated nanostructures are essentially independent of heat intensity. At the same time, the length of copper inclusions and their mutual arrangement in the aluminum film affect on frequency and oscillation amplitude. Increase of inclusion length can lead both to the oscillation frequency increase of non-closed nanostructures (inclusions are found on one side of the film (Fig. 1,e-g)), and to the oscillation frequency decrease (inclusions are found on opposite sides of the film (Fig. 1,a-c)).

The calculation results have shown that oscillation amplitude of edges is increased due to the increase in heating temperature and decreased when cooling the non-closed nanostructure. It points to the fact that a part of supplied thermal energy is transformed into the mechanical oscillation energy of free edges. The oscillation frequencies are found in the gigahertz interval for simulated nanostructures. Thus, when varying the arrangement geometry and copper inclusion sizes in films, one can change a response of the simulated non-closed nanostructure under thermal action.

The investigation of questions on supplied thermal energy transformation by the non-closed nanostructures, is not only of scientific interest, but also is very important from the point of view of design and production of nanoengines and energy converters. For this purpose, the simulation of thermal energy transformation into mechanical one by the example of the nanostructure presented in Fig. 1,f.

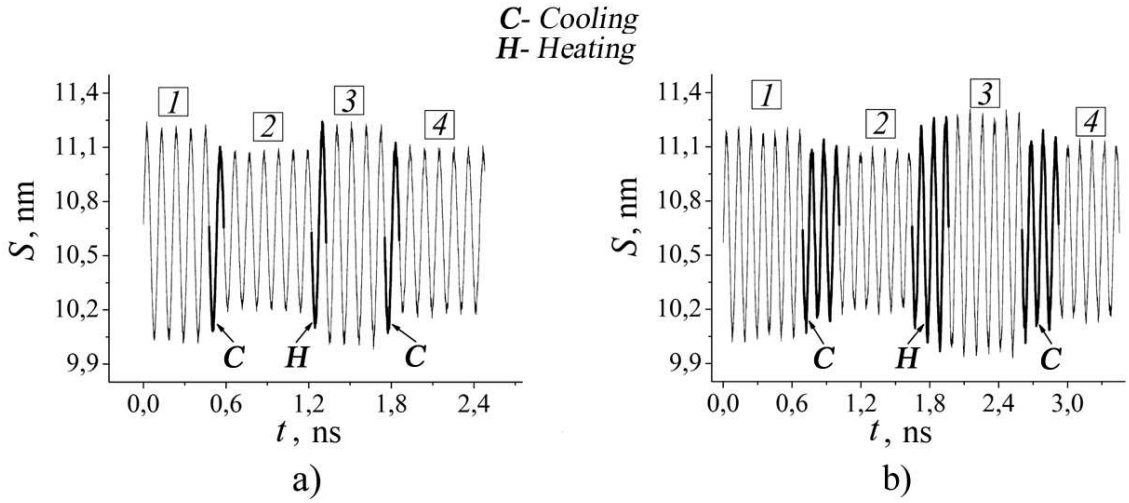

Figure 2: Dependences of distance S between oscillating free edges of the simulated non-closed nanostructure on time. The duration of heating (cooling) made: a – is the one oscillation period; b – is the three oscillation periods

The temperature interval of performed calculations varied over the range of 130 to 230 K. In the model under investigation, the viscosity forces of the medium surrounding the nanostructure was not taken into account, and energy dissipation of mechanical motion (as well as thermal energy supply) was carried out due to the gradual decrease (increase) in nanostructure kinetic temperature by 100 K. Fig. 2,a,b presents the dependences of free edge displacement of the simulated structure on time. The curve sections numbered 1 and 3 correspond to the nanostructure condition with a kinetic temperature of 230 K while the fields numbered 2 and 4, correspond to the nanostructure condition with a kinetic temperature of 130 K. Thus, when varying the temperature of studied nanostructure, it is possible to change the oscillation amplitude of its edges. The influence of heat duration

(cooling) for simulated system on the oscillatory motion behavior was also investigated. Heat (cooling) duration varied from one to three periods of nanostructure oscillation. The calculation results have shown that oscillation frequency of the nanostructure edges poorly depends on thermal action duration over the indicated temperature interval (Fig. 2,a,b).

It should be noted that the viscosity forces affecting the oscillatory edges should be accounted under heating for the more realistic behavior of non-closed nano-sized structures.

In order to take into account the viscosity characteristics of the medium, wherein the simulated nanostructure is arranged, the viscosity force was applied to the surface atoms of oscillatory edges (shown by light grey color in Fig. 3,a). The viscosity force affecting the surface atoms, was determined by the formula: $\overrightarrow{F} = -k\overrightarrow{V}$. Where $\overrightarrow{V}$ is the atom velocity; k is the proportionality coefficient.

For test determination of k in this expression, the oscillation damping behavior of nanostructure was investigated for different viscosity values (k varied over the interval from 0 to $6 \cdot 10^{-11}$ $\frac{N \cdot s}{m}$). The calculation results are presented in Fig. 3, b.

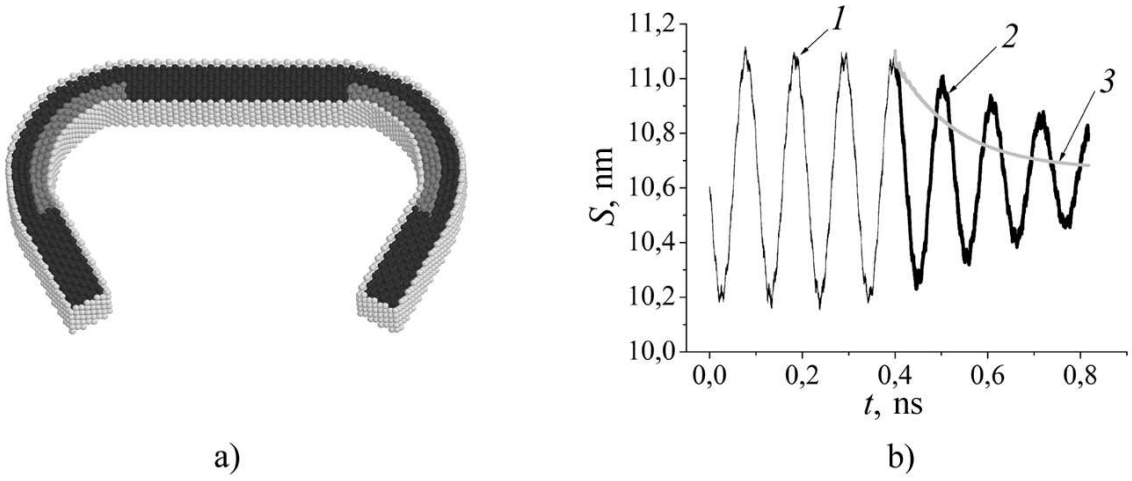

Figure 3: Shape of nanostructure used for studying its behavior in the viscous medium. The aluminum atoms are shown by black color, copper atoms are shown by dark grey color; the surface atoms of nanostructure affected by viscous force are shown by light grey color (a); Dependences of distance S between oscillating free edges of the simulated non-closed nanostructure on time in mediums with different viscosity characteristics. The proportionality coefficient value of viscous force (k) made: *1*– $k = 0$ $\frac{N \cdot s}{m}$ (nanostructure oscillates without viscosity forces); *2*– $k = 26 \cdot 10^{-14}$ $\frac{N \cdot s}{m}$; *3*– $k = 26 \cdot 10^{-12}$ $\frac{N \cdot s}{m}$ (b).

For test calculations on studying the simulated structure response on pulse heating k is set to $k = 26 \cdot 10^{-14}$ $\frac{N \cdot s}{m}$. The test calculations were made in order to investigate the principle possibility of initial amplitude recovery for nanostructure oscillations (see Fig. 4) in the viscous medium by means of periodical pulsed heating. For this purpose in a certain time interval (here in about three oscillation periods) the simulated structure was heated up for one period. Note that, use of pico- or nanosecond lasers can be one of the methods for pulsed heating of the nanostructures in practice. The initial temperature of simulated nanostructure made 140 K. The oscillation amplitude of edges decreased approximately by 50 % over three periods, and kinetic temperature of the whole nanostructure decreased down to 90 K due to the viscous forces. Then due to the uniform artificial heating, the temperature increased up to 400 K. Under this heating, the oscillation amplitude of edges increased approximately by 40 % relative to its value at the previous section (Fig. 4).

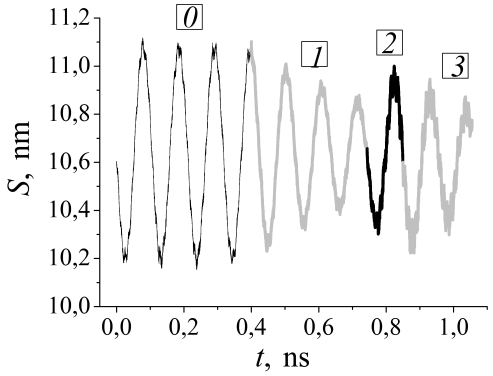

Figure 4: Variation of nanostructural oscillation amplitude in the viscous medium under pulsed heating: *0*– is the nanostructure oscillations disregard of the viscous force; *1*– is the nanostructure oscillations in the viscous medium ($k = 26 \cdot 10^{-14}\ \frac{N \cdot s}{m}$); *2*– is the pulsed heating of the nanostructure for one oscillation period; *3*– is the nanostructure oscillations in the viscous medium ($k = 26 \cdot 10^{-14}\ \frac{N \cdot s}{m}$)

Analysis of using these systems as nanoengines of different functionality is one of the most important aspects of non-closed nanostructure simulation under thermal action. The atomic mechanisms of structural changes in the simulated nanostructures should be investigated, starting from the initial moment of its rolling and finishing with oscillations of the already formed nanostructures. The peculiarities of the atomic system behavior were studied as applied to the Cu-Ni films.

The atomic mechanisms responsible for peculiarities of local atomic structure transformations in bilayer nanofilm under its detaching from the substrate as well as mechanism of thermal energy conversion into mechanical one by nanostructures are reviled. The nanofilms of different thickness are investigated (from 10 to 30 atomic planes). The peculiarities of structural changes of atomic system are studied by analyzing the atomic displacement fields in different points in time for different areas of modeled films. The analysis of the of the atomic displacement fields show that immediately after separation of the film from the substrate, the atomic layers in the film are compressed in direction normal to the free surfaces. The self-rolling of nanofilm involves elastic atomic displacements as vortex collective atomic motion (Fig. 5). The elastic atomic displacements originate at the film edges and are symmetric about the film center. This vortex collective atomic motion is due to the free surfaces and interface between nanofilm layers. The duration of vortex motion of atoms is rather small (for the Cu-Ni system with a thickness of 10 and 30 atomic planes mades not more then several tens of picoseconds), herein the vortex displacement occur at distances from 8 to 15 lattice parameters.

The behavior of non-closed nanostructures under heating is investigated. The initial non-closed nanostructure is relaxed to 200K and then heated up to 300K or up to 500K by means of atom velocities scaling in order to study the transformation of supplied thermal energy into mechanical oscillation energy of its free edges. The efficiency estimation of this transformation is carried out.

The simulation of heating process is carried out for films with following sizes: the lengths are equal to 50, 100, 150 and 200 lattice spacing and the sicknesses are equal to 4, 6, 8, 10 monolayer for each kind of atoms. The efficiency of thermal energy transformation (η) into mechanical oscillation energy of all simulated films is calculated for different temperatures: 300 K (Fig. 6, a), 500 K (Fig. 6, b). This value is estimated as the fraction

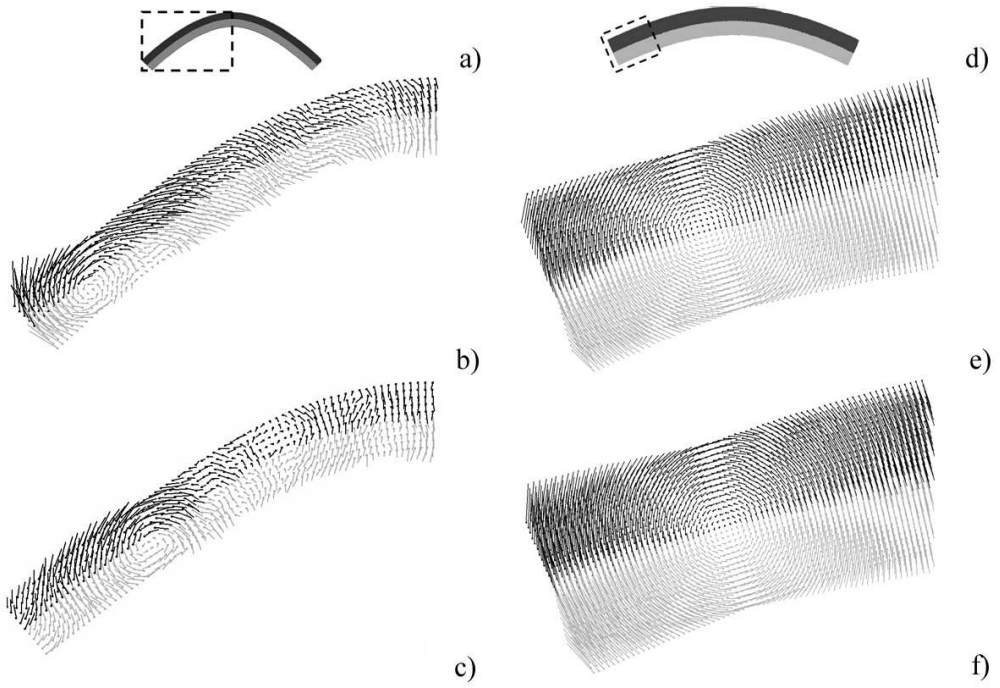

Figure 5: The displacement fields of atoms for fragments (a), (d) of simulated Cu-Ni nanofilms, represented for different time cells: b– (43,54-44,02) ps; c– (44,02-44,50) ps; e– (254-266) ps; f– (268-280) ps. The displacements are represented for nanofilm fragments with length: a– 50 % d– 20 % from initial film length. The film thickness: a– 10 and d– 30 atomic planes

of thermal energy transformed into mechanical oscillations.

As demonstrated in Fig. 6 the transformation efficiency of thermal energy under heating increases with growth of heating temperature. Thus the variation of geometrical parameters of initial film allows purposefully having effect on transformation efficiency of thermal energy into energy of mechanical oscillations.

The behavior of non-closed nanostructure under heating subject to the mass increasing of its oscillated edge is investigated. The mass increasing is performed by applying of additional atomic layers on free edge non-closed nanostructure (Fig. 7, a), which other flat part is rigid fixed.

The resulting nanostructure is heated to about 300 K, which leads to the oscillations of its free edge. The calculations show that increasing the length of the free edge of the nanostructure at the same value of kinetic temperature leads to a decrease of the frequency of its oscillations, Fig. 7, b. Applying of additional atomic layers at the free edge increases the amplitude of their oscillations and virtually no effect on their frequency, Fig. 7, c. An increase in the total mass of the oscillating edge of 4% amplitude increased more than 4 times.

3 Conclusions

Thus, the performed calculations showed an opportunity of using the non-closed nanosized structures as elementary energy converters. By means of matching the corresponding shape and elemental composition of non-closed nanostructure, pulsed heating mode, choice of the medium viscosity characteristics, one can significantly recover the oscillation

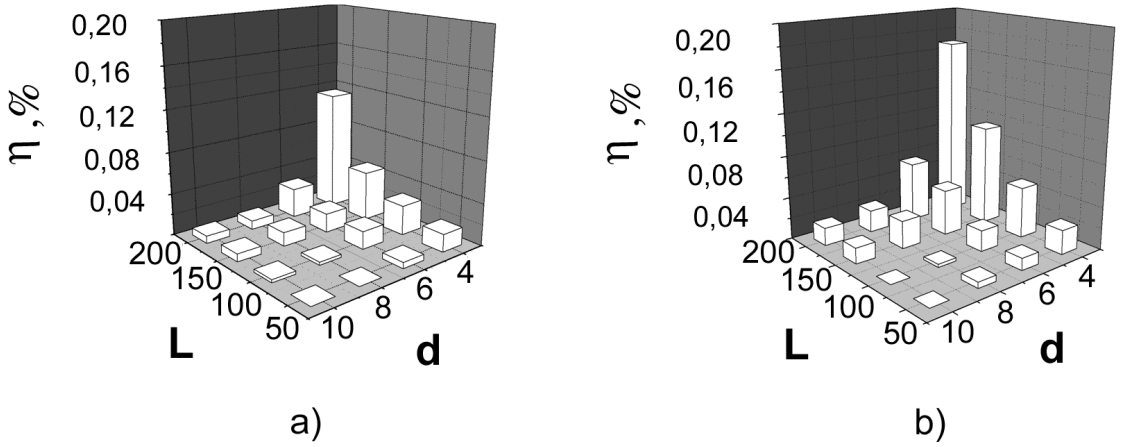

Figure 6: The dependence of transformation efficiency of thermal energy into mechanical one for non-closed nanostructures on different lengths L and thicknesses d of the initial film (d is expressed as atomic plane number, L – as lattice constant number) under heating up to temperatures: a – $T = 300$ K; b – $T = 500$ K

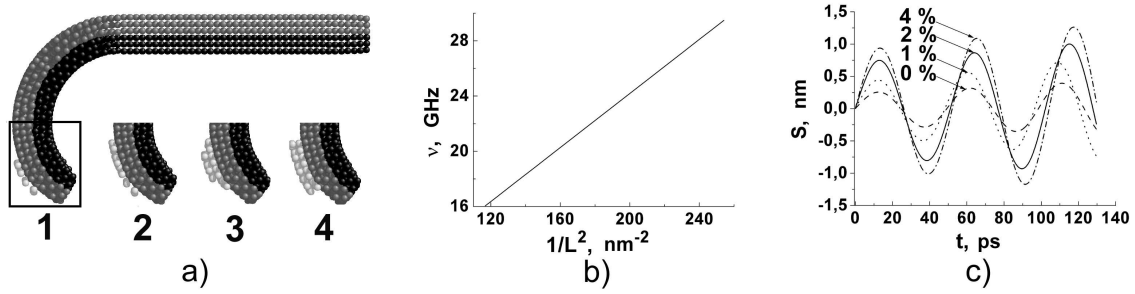

Figure 7: Non-closed nanostructure with applied additional layers of Al atoms: *1*– 1%, *2*– 2%, *3*– 3%, *4*– 4% from weight of free edge of nanostructure (the Cu atoms are shown by black color; the Al atoms– by dark-grey color; the additional applied Al atoms– by light-grey color) (a); the dependence of nanostructure oscillation frequency on the length L of its free edge (b); the dependence of nanostructure free edge displacement S from equilibrium position on time under increasing of edge mass on 1, 2, 4 % (c)

amplitudes of the non-closed nanostructure edges. Relaxation and redistribution of elastic stresses in the initial film at rolling is carried out due to the collective motion of atomic groups. It is shown that there are two types of collective motions of the atomic system, determining the behavior at formation and subsequent oscillations.

Acknowledgements

The work was supported by the Grant of Lavrent'ev competition of young researcher projects of SB RAS 2009-2010 years and the Grant of The Russian Foundation for Basic Research No. 11-08-00817-a.

References

[1] V. Bolzani, M. Venturi, A. Credi, Devices and machines. A Journey into the Nanoworld

(Wiley VCH, Weinheim, 2003).

[2] D.C. Rapaport, The Art of Molecular Dynamics Simulation (Cambridge University Press, Cambridge, 1995).

[3] S.M. Foiles, M.I. Baskes, M.S. Daw, Phys. Rev. B33 (12), 7983 (1986).

[4] K.P. Zolnikov, Iv.S. Konovalenko, S.G. Psakhie, Fiz. Mezomekh. 9 (Special issue) (2), 14 (2004).

[5] S.G. Psakhie, K.P. Zolnikov, S. Blatnik, Fiz. Mezomekh. 6 (4), 125 (2003).

[6] Iv.S. Konovalenko, K.P. Zolnikov, S.G. Psakhie, Izv. visshikh uchebnikh zavedeniy. Fizika 48 (6), 23 (2005).

[7] Iv.S. Konovalenko, K.P. Zolnikov, S.G. Psakhie, Izv. visshikh uchebnikh zavedeniy. Fizika 49 (3), 38 (2006).

[8] S.G. Psakhie, K.P. Zolnikov, Iv.S. Konovalenko, Fiz. Mezomekh. 9 (Special issue), 9 (2006).

Ivan S. Konovalenko, pr. Academicheskii 2/4, Tomsk, 634021 Rissia
Konstantin P. Zolnikov, pr. Academicheskii 2/4, Tomsk, 634021 Rissia
Sergey G. Psakhie, pr. Academicheskii 2/4, Tomsk, 634021 Rissia

Modeling microstructural stresses in polymer-silicate nanocomposite with the influence of spherulitic structures

A. S. Korlyakov
korlaykov@icmm.ru

Abstract

Polymer nanocomposites based on polyolefins and layered clay minerals (smectites) are multi-layered structure. Even unfilled polyolefins (polyethylene, polypropylene, etc.) are structurally heterogeneous environment consisting of amorphous and crystalline phases. Adding filler further complicates the structure of the material. The results of computer simulation of interaction of silicate inclusions, crystalline supermolecular formations in the matrix (spherulites) and its amorphous part. Composite is modeled as a square periodicity cell with inclusion and spherulites. Inclusion was a pack of silica plates separated by thin layers of polymer. Spherulite modeled as "snowflakes" of crystallized lamellae (band areas with an ordered arrangement of polymer molecules). Problem was solved by finite element method in nonlinear-elastic formulation (plane strain).

Introduction

Currently, nanocomposites based on polyolefins and layered clay minerals (smectites) are becoming more common in various industries. In the past decade [1, 2] around the world has seen rapid growth in the number of publications and patents relating to the process of their construction and study of the mechanical properties of a huge increase in the funding of basic and applied research on this issue. For such systems, managed to achieve a substantial increase in elastic modulus, strength, fire resistance, resistance to thermal warpage, improved barrier properties with respect to the diffusing substance. However, despite the obvious achievements, analysis of the known publications shows that this branch of materials science from the standpoint of understanding and explanation of accumulated factual material developed more clearly not enough. Therefore, the task of theoretical study of the formation of the mechanical properties of nanocomposite systems based on the features of their internal structure, is important and relevant.

Polymer nanocomposites based on polyolefins and layered clay minerals (smectites) are multi-layered structure. Even unfilled polyolefins (polyethylene, polypropylene, etc.) are structurally heterogeneous environment consisting of amorphous and crystalline phases. Adding filler further complicates the structure of the material.

Structure of nanocomposites

The structure of these systems is a mixture of many thin silicate plates with thickness of about 1 nm and lateral dimension of 30 nm to several microns, placed in a polyolefin matrix [3]. Filler particles can form individual crystallites (taktoid) from several (several

tens) of parallel plates or placed on the volume of material randomly. In the first case, called intercalated nanocomposites, in the second - exfoliated (Fig. 1).

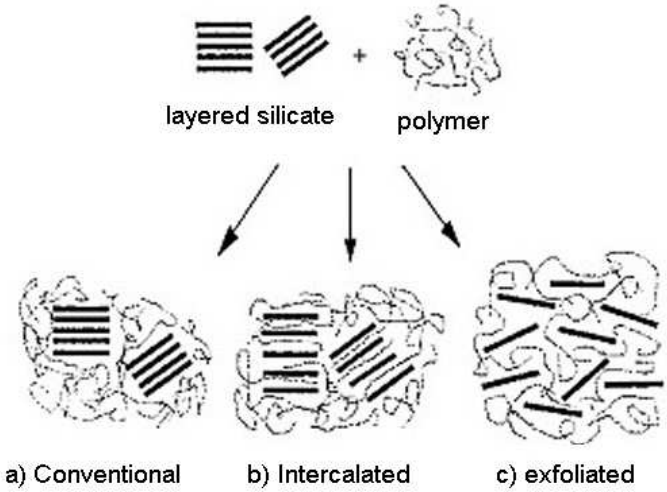

Figure 1: Schematic representation of the dispersion models layered silicate in polymer matrix: (a) conventional, (b) intercalated nanocomposite, (c) exfoliated nanocomposite.

Structural heterogeneity of these systems is not limited to the presence of nanofillers. Matrix itself may also contain a variety of supramolecular structures, in particular the spherulites.

Spherulites - the most common type of morphological formations for crystallize out of melt semi-crystalline polymers.

Spherulite size depends on the supercooling during crystallization. Spherulites have a scale of 0.1 - 1000 microns. For polyethylene in the usual conditions of crystallization of the diameter of the spherulite reaches approximately 100 microns. Spherulites - polycrystalline formations consisting of lamels arranged in a "snowflake". Lamella in the spherulites - a relatively large thin plates (polietilen) separated by amorphous layers. Lamella growing from a common core in the center of the spherulite and embedded in a matrix of amorphous material [4].

Model of the mechanical behavior of nanocomposites

Problem was solved for plane-strain state of the finite element method [5, 6, 7]. Taktoid consisted of ten elastic parallel plates of thickness 1 nm and a length of 80 nm. The distance between the plates in the unloaded state was 1 nm. Spherulite was modeled as a structure in the form of "snowflakes" of crystallized lamellae with the stiffness is much higher than the material in the surrounding matrix. Believed that the matrix material in the gaps tactoid, spherulite and around as incompressible and can be described by Treloar elastic potential:

$$W{=}C_m(tr\,\mathbf{B}-3) \tag{1}$$

where $\mathbf{B}$ - the Cauchy-Green left tensor in the polar decomposition of deformation gradient medium, C_m - elastic constant equal to half the initial shear modulus. For polyethylene,

it corresponds to 80 MPa. It is known that the modulus of the individual plates of silicate (Na^+-montmorillonite) close to the module glass (49000-78000 MPa), which is about two orders of magnitude higher than the module polyethylene. It was therefore decided that the stiffness of the filler particles is 150 times greater than that of the matrix (72,000 MPa). Stiffness of the filler particles is 150 times greater than that of the matrix. Stiffness of the material "branches" of the spherulite is 10 times higher than the filler (matrix).

Seen several cases of the location of the spherulite with respect to taktoid:
- Composite without spherulitic structures;
- Spherulite in the center of the periodicity cell without silicate plates;
- Spherulite in the center of the periodicity cell with silicate plates;
- Spherulite formed on the surface of silicate plates;

On the basis of the solutions were evaluated effective modulus of the nanocomposite depending on the location of the spherulite in the composite. We used a standard method of regularization, widely used in mechanics of composite materials. Composite is regarded as a system with a regular ordered structure, which greatly simplifies the calculations, since all the necessary information can be obtained from the analysis of the periodicity cell. This method has worked well for small and medium filling (10-20 by volume), ie while irregular mutual arrangement of particles and their interactions did not become the determining factor in shaping macroproperties heterogeneous environment (as occurs in highly filled systems) [8].

Results

The results of the calculations showed that the presence of spherulites in the composite is not substantially affect the macro-module as the input composite silicate particles. The greatest increase in modulus was observed when the spherulite is located on the plates taktoid (Fig. 2). In this case, the module compared to the option when the matrix contained only taktoid increased by 12%.

Figure 3 shows the results of the calculation module, depending on the orientation of the plates relative to the axis stretching for two options: a spherulite is formed on the surface taktoida and without spherulites. The appearance of the spherulite leads to some increase in the rigidity of the cell.

Conclusion

Calculations showed that for this case the location and form of spherulites, their presence in the composite is not substantially affect the macro module of the composite as the introduction of silicate particles. The greatest increase in modulus was observed when the spherulite is located on the plates taktoid. In this case, the module compared to the option when the cell had only inclusion, increased by 12%.

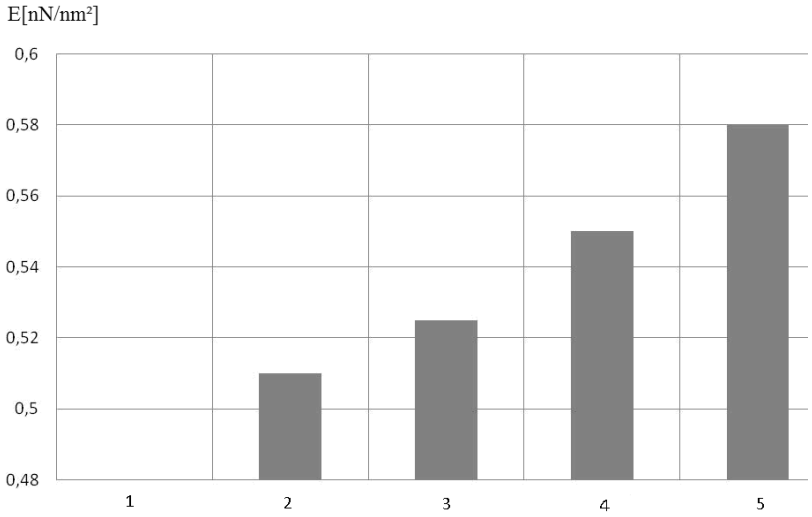

Figure 2: Dependence of the modulus of the nanocomposite depending on the location of the spherulite. 1 - pure polyethylene, 2 - composite without spherulitic structures, 3 - spherulite in the center of the periodicity cell without silicate plates, 4 - spherulite in the center of the periodicity cell with silicate plates, 5 - spherulite formed on the surface of silicate plates.

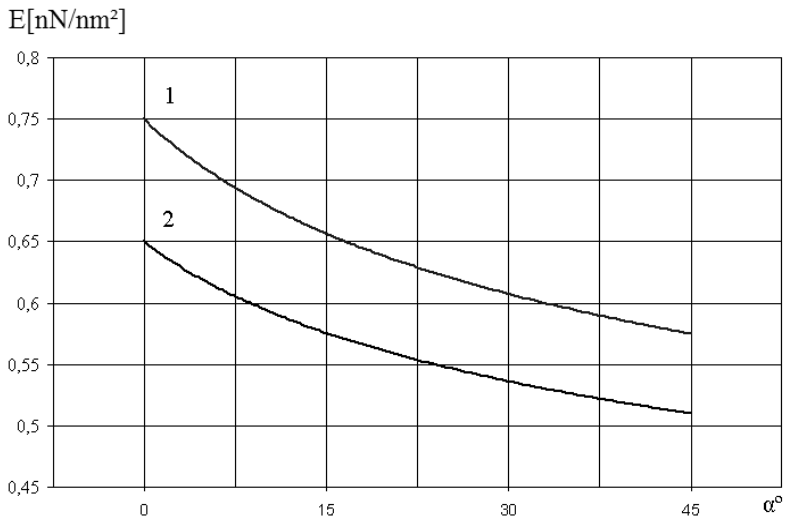

Figure 3: Dependence of the modulus of the nanocomposite depending on the orientation of the plates relative to axis stretching. 1 - spherulite formed on the surface of silicate plates, 2 - composite without spherulitic structures.

Acknowledgements

This work was supported by RFBR (projects No 09-08-00339 and No 09-03-00402).

References

[1] Fengge G. Clay/polymer composites: the story. Materials Today. - 2004. - N 11. - P. 50-55.

[2] Sheng N., Boyce M.C., Parks D.M., Rutledge G.C., Abes J.I., Cohen R.E. Multiscale micromechanical modeling of polymer/clay nano-composites and the effective clay particle // Polymer. - 2004. - V. 45. - P. 487-506.

[3] Guseva M.A. Struktura i fiziko-mehanicheskie svojstva nanokompozitov na osnove nepoljarnogo polimera i sloevogo silikata. Dis.kand. fiz.-mat. nauk, 2005. Moskva, 155 s.In Russia

[4] Oleinik Je. F. Plastichnost' chastichno-kristallicheskih gibkocepnyh polimerov na mikro- i mezo-urovnjah. Vysokomolek. soed. S, 2003, T.45, 10, S.1-129. In Russia

[5] Garishin O.C., Lebedev S.N., Svistkov A.L. Shape distortion of silicate nanoinclusions in dispersly filled polyolefines // XXXV Summer school "Advanced problems in mechanics": Proceedings. - St. Petersburg (Repino), 2007. - P. 118-122.In Russia

[6] Garishin O.K., Lebedev S.N., Korlyakov A.S. Issledovanie mikronaprjazhennogo sostojanija v polimernyh nanokompozitah na osnove glinistogo napolnitelja i poliolefinovoj matricy // Vestnik PGTU: Matematicheskoe modelirovanie sistem i processov. Perm': PGTU, 2007. ? 15. S. 914. In Russia

[7] Garishin O.K., Korlyakov A.S. Modelirovanie mehanicheskogo vzaimodejstvija mezhdu chasticami napolnitelja i svjazujuwim v polimer-silikatnyh nanokompozitah pri konechnyh makrodeformacijah. // Vychislitel'naja mehanika sploshnyh sred. Tom 2. 2009. T. 2, 3. S. 2533. In Russia

[8] Bahvalov N.S., Panasenko G.P. Osrednenie processov v periodicheskih sredah. Matematicheskie zadachi mehaniki kompozicionnyh materialov. M.: Nauka, 1984. 352 s. In Russia

Korlyakov A.S., Institute of continuous media mechanics UB RAS, Perm, Russia

Analytical expressions for bulk moduli and frequencies of volumetrical vibrations of fullerenes C_{20} and C_{60}

Oleg O. Kovalev and Vitaly A. Kuzkin
kovalevoleq@gmail.com, kuzkinva@gmail.com

Abstract

In the present paper simple analytical expressions connecting bulk moduli for fullerenes C_{20} and C_{60} with stiffness of interatomic bond and geometrical characteristics of the fullerenes are derived. Ambiguities related to definition of the bulk modulus are discussed. Nonlinear volumetrical deformation of the fullerenes is considered. Pressure-volume dependence for the fullerenes under volumetrical compression are derived. Simple analytical model for volumetrical vibrations of the fullerenes is proposed. The expression connecting frequencies of volumetrical vibrations for fullerenes C_{20} and C_{60} with parameters of interatomic interactions are obtained.

1 Introduction

The discovery of unique physical and mechanical properties of fullerenes in the end of XXth century [1] have strongly increased scientific interest to these carbon nanostructures. The fullerenes are closed spheroidal surfaces, made of pentagons and hexagon with carbon atoms in tops. During the last several decades a great number of fullerenes have been synthesized [2, 3]. However it is notable that only two of them, C_{20} and C_{60}, have perfect geometrical shape (dodecahedron and truncated icosahedron respectively). Due to the small size of fullerenes experimental investigation of their physical and mechanical properties is still a challenge problem for the modern physics. That is why only few characteristics of fullerenes can be measured. In the case when experimental methods are not applicable, computer simulation becomes almost the only method for investigation. The main methods for computer simulation of nanostructures are classical [4] and *ab initio* [5] molecular dynamics (MD). A great number of papers is devoted to both classical and *ab initio* MD simulation of fullerenes [6, 7]. Though computer simulations allow to overcome many limitations of real experiment, they are still not a "panacea". In particular, results of computer simulations require verification and validation. In this situation simple analytical models allowing to check the quality of the results are very important [8].

In the present paper simple analytical formulas for equivalent bulk moduli of fullerenes C_{20} and C_{60} are a derived. The following definition for bulk modulus is used. A bulk modulus of the fullerene is a proportionality factor between the pressure exerted on the fullerene and relative change of volume in case of small volumetric deformations [8]. The ambiguity of definition for the pressure exerted on the fullerene is discussed. Three definitions of the pressure, differing in the way of calculation of the equivalent surface area of the fullerene, are considered. Analytical expressions connecting bulk moduli of fullerenes C_{20} and C_{60} with micro- parameters (bond stiffness, bond length, etc.) are derived. The expressions are compared with a result of paper [8]. Bulk moduli of the fullerenes are calculated for different values of bond stiffness reported in literature. The

dependence of pressure on volumetrical deformation of the fullerene is derived in the case of large deformations. Linearized equation of volumetrical vibrations of the fullerenes is presented. Corresponding eigenfrequency is calculated. The comparison with experimental data [10] is discussed.

2 Linear volumetrical deformation of fullerenes C_{20} and C_{60}

Let us assume that pressure exerted on the fullerene is carried out by the external forces of magnitude F acting on each carbon atom. Forces are directed to the center of the molecule. Consider the case of small volumetrical deformations. In this case angles between atoms do not change during the deformation. Then forces acting between atoms depend on interatomic distances only. Let us assume that atoms in the fullerene interact via pair central forces proportional to deformation of the bond. From the symmetry reasons all atoms in the fullerene are equivalent. Therefore the reasoning is carried out for one specific atom. Using symmetry one can show that equation of equilibrium for the given atom in a projection to direction of corresponding external force has the following form

$$F = -3ka_0\varepsilon\cos\alpha, \tag{1}$$

where α is an angle between the external force and direction of the bonds (α is identical for all bonds of the given atom); k is a stiffness of the bond; ε is a relative deformation of the bond; a_0 is an equilibrium bond length. It is important to note that the angle α doesn't change in the course of deformation. Let us use the expression connecting deformation of the bond ε and volumetrical deformation $\Delta V/V_0 = (V - V_0)/V_0$, where V and V_0 are volumes of the fullerene in deformed and undeformed states. In the case of small deformations the expression has form

$$\frac{\Delta V}{V_0} \approx 3\varepsilon. \tag{2}$$

Substituting expression (2) into formula (1) one obtains

$$F = -ka_0\cos\alpha\frac{\Delta V}{V_0}. \tag{3}$$

Let us define the pressure acting on fullerene as follows

$$P \stackrel{\text{def}}{=} \frac{NF}{S} \approx -\frac{Nka_0\cos\alpha}{S_0}\frac{\Delta V}{V_0}, \tag{4}$$

where N is a number of carbon atoms in the fullerene (N=20 for C_{20} and N=60 for C_{60}), S_0 is an equivalent surface area of the fullerene in undeformed state. Thus, one have the following expression for bulk moduli of fullerenes C_{20} and C_{60}

$$B = N\frac{a_0k\cos\alpha}{S_0}. \tag{5}$$

Note that equivalent surface are S_0 in formulas (4), (5) is in principle not unique. Therefore in the present paper three different definitions of S_0 are considered: area of the inscribing sphere, area of the circumscribing sphere and the surface area (the area of dodecahedron and truncated icosahedron respectively). Geometrical characteristics of fullerenes C_{20} and C_{60} required for calculation of the bulk modulus are presented in table 1. Using the characteristics, bulk moduli of the fullerenes are calculated for different values of S_0 (see

	C_{20}		C_{60}	
	Formula	Value	Formula	Value
R_c	$a_0\sqrt{3}(1+\sqrt{5})/4$	0.201 nm	$a_0/(2\cos\alpha)$	0.355 nm
R_i	$a_0\sqrt{10(25+11\sqrt{5})}/20$	0.160 nm	$3a_0\sqrt{3}(3+\sqrt{5})/12$	0.325 nm
S_0^c	$4\pi R_c^2$	0.507 nm^2	$4\pi R_c^2$	1.58 nm^2
S_0^i	$4\pi R_i^2$	0.320 nm^2	$4\pi R_i^2$	1.33 nm^2
S_0^p	$3a_0^2\sqrt{5(5+2\sqrt{5})}$	0.424 nm^2	$30\sqrt{3}a_0^2+15a_0^2\mathrm{ctg}\frac{\pi}{5}$	1.49 nm^2
$\cos\alpha$	$\frac{a_0}{2Rc}$	0.357	$\sqrt{\frac{1+2\cos\frac{3}{5}\pi}{10+2\cos\frac{3}{5}\pi}}$	0.202

Table 16: Geometrical characteristics of undeformed fullerenes C_{20} and C_{60}. Here R_c, S_0^c are radius and surface area of the sphere circumscribed around the fullerene, R_i, S_0^i are radius and surface area of inscribed sphere, S_0^p is a surface area of corresponding polygon.

Area	Bond stiffness, N/m	bulk modulus B, GPa	
		fulleren C_{20}	fulleren C_{60}
circumscribed sphere	762	1538	834
	708	1429	775
	672	1356	736
	660	1332	723
	635	1282	695
inscribed sphere	762	2436	997
	708	2263	926
	672	2148	879
	660	2110	863
	635	2030	830
polyhedron	762	1838	887
	708	1708	824
	672	1621	782
	660	1592	768
	635	1532	739

Table 17: Stiffness of the bond and bulk moduli of fullerenes C_{20} and C_{60}

table 2). The following value of bond length is used: $a_0 = 0.1433$ nm. Values of bond stiffness k, presented in table 2, are taken from the paper [8]. Note that maximal difference between values of k is approximately 17%. One can see from table 2 that bulk modulus B of fullerene C_{20} is approximately twice larger than the similar value for fullerene C_{60}. The value of bulk modulus essentially depends on a choice of the equivalent surface area S_0. Maximum difference between values B, calculated for different S_0, is 37% for C_{20} and 16% for C_{60}. Note that the values of bulk modulus of fullerene C_{60}, presented in table 2, do not coincide with results of paper [8]. In paper [8] another definition for pressure acting on the fullerene was used. It was assumed that pressure is carried by normal forces distributed on a surface of the truncated icosahedron. Obviously the given way of loading can not be realized in practice. Therefore physical meaning of the definition used in paper [8] is not clear.

3 Nonlinear volumetrical deformation of fullerenes C_{20} and C_{60}

Let us consider nonlinear deformation of fullerenes C_{20} and C_{60}. Assume that compression of the bond is described by pair potential U. Also assume that pressure is carried out by external forces of value F, acting on all carbon atoms. Forces are directed to the center of the molecule. Then the projection of equilibrium equation for some specific atom on the directions of corresponding external force has the following form

$$F + 3U'(r)\cos\alpha = 0, \tag{6}$$

where r is a distance between the nearest neighbors in the fullerene. Resolving the given equation with respect to F and substituting the result onto definition for pressure (4) one obtains

$$P\left(\frac{V}{V_0}\right) = -\frac{3Na_0\cos\alpha}{S_0}\left(\frac{V_0}{V}\right)^{\frac{2}{3}} U'\left(a_0\left(\frac{V}{V_0}\right)^{\frac{1}{3}}\right), \tag{7}$$

Here the following identities are used $r = a_0\left(V/V_0\right)^{\frac{1}{3}}, S = S_0\left(V/V_0\right)^{\frac{2}{3}}$, where S is a surface area of the fullerene in the deformed state. Formula (7) defines pressure-volume dependence for the fullerene in the case of large volumetrical deformations. For example, let us calculate this dependence for Lennard-Jones potential

$$U(r) = D\left[\left(\frac{a_0}{r}\right)^{12} - 2\left(\frac{a_0}{r}\right)^{6}\right], \tag{8}$$

where D is a bond energy, a_0 is an equilibrium distance between atoms in the fullerene. Substituting (8) into (7) one obtains

$$P\left(\frac{V}{V_0}\right) = \frac{Nka_0\cos\alpha}{2S_0}\left(\frac{V_0}{V}\right)^{3}\left[\left(\frac{V_0}{V}\right)^{2} - 1\right], \tag{9}$$

where the well-known relation between bond energy and stiffness for Lennard-Jones potential $D = ka_0^2/72$ was used. Linearizing formula (9) for the case of small deformations one can obtain the expression for bulk modulus that exactly coincides with formula (5).

4 Volumetrical oscillations of fullerenes C_{20} and C_{60}

Let us calculate the frequency of small volumetrical vibrations of fullerenes C_{20} and C_{60}. Assume that atoms in the fullerene interacts via linear pair central forces. Only interactions between the nearest neighbors are taken into account. Then equation of motion for some specific atom in the fullerene has the following form

$$m\,\ddot{\mathbf{r}}_0 = k\sum_{i=1}^{3}(\mathbf{r}_i - \mathbf{r}_0), \tag{10}$$

where m is a mass of carbon atom, $\mathbf{r}_0$ and $\mathbf{r}_i$ are radius-vectors of the specific atom and its neighbor number i with respect to the center of the fullerene. In the case of volumetrical vibrations radius-vectors can be represented in the following form $\mathbf{r}_i = r_0\mathbf{e}_i, i = 0,..,3$. Substituting these expressions into equation of motion (10) one obtains

$$m\,\ddot{r}_0\,\mathbf{e}_0 = kr_0\sum_{i=1}^{3}(\mathbf{e}_i - \mathbf{e}_0) \Rightarrow m\,\ddot{r}_0 = -3kr_0(\cos(2\alpha) + 1). \tag{11}$$

where the identity $\mathbf{e}_0 \cdot \mathbf{e}_i = -\cos(2\alpha), i = 1..3$ was used. Then equation of motion takes simple scalar form

$$m\,\ddot{r}_0 + 6k\cos^2\alpha r_0 = 0. \tag{12}$$

Therefore the eigenfrequency of volumetrical vibrations of the fullerenes is determined by the following expression

$$\omega = \sqrt{\frac{6k}{m}}\cos\alpha. \tag{13}$$

One can see that the only difference between values of ω for fullerenes C_{20} and C_{60} is in the value of angle α. Let us calculate the frequencies assuming that $m = 1.994 \cdot 10^{-26}$ kg, $k = 635$ N/m [8]. Then one obtains $\omega = 156.0$ THz for C_{20} and $\omega = 88.20$ THz for C_{60}. The experimental value of the frequency of volumetrical vibrations of the fullerenes is not reported in literature. However one can carry out the order of magnitude analysis. In paper [10] the first eigenfrequency of fullerene C_{60} is determined using Raman spectroscopy. It is shown that the frequency is equal to 8.19 THz. Obviously the frequency of volumetrical vibrations should be approximately one order higher then the first eigenfrequency. Thus results of the present paper qualitatively coincide with experimental data [10]. However more accurate comparison is required.

5 Conclusion

In the present paper simple analytical expressions connecting bulk moduli B for fullerenes C_{20} and C_{60} with interatomic bond stiffness and geometrical characteristics of the fullerenes were presented. It was shown that B depends on a choice of the equivalent surface area. Maximum difference between values of B, calculated for different S_0 and identical value of the bond stiffness is 37% for C_{20} and 16% for C_{60}. Nonlinear volumetrical deformation of the fullerene was considered. It was assumed that compression of the bond is described by pair potential of the general form. Simple analytical formula for pressure-volume dependence for the fullerenes under volumetrical compression was derived. For example, Lennards-Jones potential was considered. It was shown that at high compressions the pressure is increasing asymptotically as $(V_0/V)^5$. Volumetrical vibrations of the fullerenes are considered. An analytical expression connecting frequencies of volumetrical vibration for fullerenes C_{20} and C_{60} with parameters of interatomic interactions was derived. The following values of the frequencies were obtained: $\omega = 156.0$ THz for C_{20} and $\omega = 88.20$ THz for C_{60}.

Acknowledgements

Authors are deeply grateful to Prof. A.M. Krivtsov for useful discussions and inspiration.

References

[1] Kroto H.W., Heath J.R., O'Brien S.C., Curl R.F., Smalley R.E. C60: Buckminsterfullerene // Nature, No. 318, 1985, pp. 162163.

[2] Dresselhaus M.S., Dresselhaus G., Eklund P.C. Science of fullerenes and carbon nanotubes: Their Properties and Applications, Academic Press, 1996, p. 965.

[3] Sokolov V.I., Stankevich I.V. Fullerenes — new allotropic carbon forms: structure, an electronic structure and chemical properties // Successes of chemistry, 1993, t.62 (5), p.455, 1993.

[4] Hoover W.G. Molecular dynamics, Lecture Notes in Physics, Vol. 258, (Springer, Berlin, 1986), p. 138.

[5] Marx D., Hutter J. Ab Initio Molecular Dynamics: basic theory and Advanced Methods, Cambridge University Press, New York, 2009.

[6] Wang C.Z., Chan C.T. Structure and dynamics of C60 and C70 from tight-binding molecular dynamics // Phys. Rev. B, Vol. 46, No. 15, 1992, pp. 9761-9762.

[7] Yamaguchi Y., Maruyama S. A Molecular Dynamics Simulation of the Fullerene Formation Process // Chem. Phys. Letters, Vol. 286/3, No. 4, 1998, pp. 336-342.

[8] R.S. Ruoff, A.L. Ruoff. The bulk modulus of C60 molecules and crystals: A molecular mechanics approach // Appl. Phys. Lett., 1991, pp. 15531555.

[9] Sakhaee-Pourand A., Vafai A. Natural frequencies of C60, C70, and C80 fullerenes // Appl. Phys. Lett., Vol. 96, 2010, p. 021903.

[10] Kuzmany H., Pfeiffer R., Hulman M., Kramberger C. Raman Spectroscopy of Fullerenes and Fullerene-Nanotube Composites, "Raman Spectroscopy in Carbons: From Nanotubes to Diamond," // Philosophical Transactions: Mathematical, Physical and Engineering Sciences, Vol. 362, No. 1824, The Royal Society, London, 2004, pp. 23752406.

Oleg O. Kovalev, Saint Petersburg State Polytechnical University, Polytehnicheskaya 29, St. Petersburg, Russia
Vitaly A. Kuzkin, Institute for Problems in Mechanical Engineering RAS, V.O., Bolshoj pr., 61, St. Petersburg, Russia

On the motion of the Oloid toy

Alexander S. Kuleshov Mont Hubbard Dale L. Peterson Gilbert Gede
kuleshov@mech.math.msu.su

Abstract

Analysis and simulation are performed for the commercially available toy known as the Oloid. While rolling on the fixed horizontal plane the Oloid moves very swinging but smooth: it never falls over its edges. The trajectories of points of contact of the Oloid with the supporting plane are found analytically.

1 Introduction

Let us consider the motion of the Oloid on a fixed horizontal plane. The Oloid is a developable surface comprises of two circles of radius R whose planes of symmetry make a right angle between each other with the distance between the centers of the circles equals to their radius R. The resulting convex hull is called Oloid.

The Oloid have been constructed for the first time by Paul Schatz [2,3]. The geometric properties of the surface of the Oloid have been discussed in the paper [1]. The Oloid is also used for technical applications. Special mixing-machines are constructed using such bodies [4]. In our paper we make the complete kinematical analysis of motion of this object on the horizontal plane.

Further we briefly describe basic facts from Kinematics and Differential Geometry which we will use in our investigation.

The Frenet - Serret formulas. Consider a particle which moves along a continuous differentiable curve in three - dimensional Euclidean Space $\mathcal{R}^3$. We can introduce the following coordinate system: the origin of this system is in the moving particle, $\boldsymbol{\tau}$ is the unit vector tangent to the curve, pointing in the direction of motion, $\boldsymbol{\nu}$ is the derivative of $\boldsymbol{\tau}$ with respect to the arc-length parameter of the curve, divided by its length and $\boldsymbol{\beta}$ is the cross product of $\boldsymbol{\tau}$ and $\boldsymbol{\nu}$: $\boldsymbol{\beta} = [\boldsymbol{\tau} \times \boldsymbol{\nu}]$.

Then the Frenet - Serret formulas for the derivatives of $\boldsymbol{\tau}$, $\boldsymbol{\nu}$ and $\boldsymbol{\beta}$ are valid:

$$d\boldsymbol{\tau}/dt = k\dot{s}\boldsymbol{\nu}, \quad d\boldsymbol{\nu}/dt = -k\dot{s}\boldsymbol{\tau} + æ\dot{s}\boldsymbol{\beta}, \quad d\boldsymbol{\beta}/dt = -æ\dot{s}\boldsymbol{\nu}.$$

The tangent $\boldsymbol{\tau}$, the normal $\boldsymbol{\nu}$ and the binormal $\boldsymbol{\beta}$ unit vectors are known as the Frenet - Serret frame.

The Poisson formulas. Let $\boldsymbol{e}_1$, $\boldsymbol{e}_2$, $\boldsymbol{e}_3$ is any moving coordinate system and let $\boldsymbol{\omega}$ be the angular velocity of this system. Then for the derivatives of $\boldsymbol{e}_1$, $\boldsymbol{e}_2$ and $\boldsymbol{e}_3$ the following Poisson formulas are valid:

$$d\boldsymbol{e}_i/dt = [\boldsymbol{\omega} \times \boldsymbol{e}_i], \quad i = 1, 2, 3.$$

According to the Poisson formulas we can rewrite the Frenet - Serret formulas as follows:

$$d\boldsymbol{\tau}/dt = [\boldsymbol{\Omega} \times \boldsymbol{\tau}], \quad d\boldsymbol{\nu}/dt = [\boldsymbol{\Omega} \times \boldsymbol{\nu}], \quad d\boldsymbol{\beta}/dt = [\boldsymbol{\Omega} \times \boldsymbol{\beta}],$$

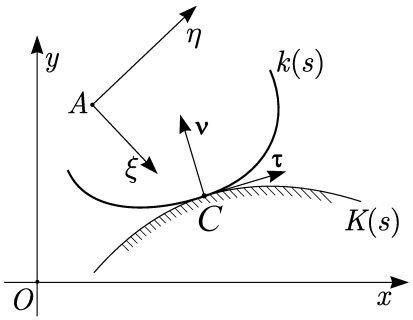

Figure 1: Kinematics of the moving lamina.

where $\boldsymbol{\Omega} = k\dot{s}\boldsymbol{\beta} + æ\dot{s}\boldsymbol{\tau}$ is the angular velocity of the Frenet - Serret frame known also as the Darboux vector. In particular, for the plane curve we have $æ = 0$ and therefore

$$\boldsymbol{\Omega} = k\dot{s}\boldsymbol{\beta}. \tag{1}$$

The law of composition of angular velocities. Consider three coordinate systems: the fixed system $Oxyz$ and two moving systems $A\xi\eta\zeta$ and $Cx_1x_2x_3$. Then the angular velocity of the system $Cx_1x_2x_3$ with respect to $Oxyz$ - system is the sum of the angular velocity of the $Cx_1x_2x_3$ - system with respect to the $A\xi\eta\zeta$ - system and the angular velocity of the $A\xi\eta\zeta$ - system with respect to the $Oxyz$ - system:

$$\boldsymbol{\omega}^{Oxyz}_{Cx_1x_2x_3} = \boldsymbol{\omega}^{Oxyz}_{A\xi\eta\zeta} + \boldsymbol{\omega}^{A\xi\eta\zeta}_{Cx_1x_2x_3}.$$

We will call the angular velocity $\boldsymbol{\omega}^{A\xi\eta\zeta}_{Cx_1x_2x_3}$ of the moving coordinate system $Cx_1x_2x_3$ with respect to another moving system $A\xi\eta\zeta$ as "the relative angular velocity". The angular velocity $\boldsymbol{\omega}^{Oxyz}_{A\xi\eta\zeta}$ will called "the transfer angular velocity" and the angular velocity $\boldsymbol{\omega}^{Oxyz}_{Cx_1x_2x_3}$ will called "the absolute angular velocity".

Angular velocity of the moving lamina. Let us consider the following problem: the rigid lamina bounded by the convex curve of the given curvature $k(s)$ is rolling without slipping on the fixed convex curve of the given curvature $K(s)$ (we assume that the both curves have the same arc parametrization $s = s(t)$). Let us find the angular velocity $\boldsymbol{\Omega}$ of the moving lamina.

For this purpose we introduce three coordinate system: the fixed system $Oxyz$, connected with the fixed curve, the moving system $A\xi\eta\zeta$ rigidly connected with the moving lamina and the Frenet - Serret frame $C\boldsymbol{\tau\nu\beta}$ with the origin at the point of contact of two curves (Fig. 1). We will use the law of composition of angular velocities. The absolute angular velocity of the Frenet - Serret frame with respect to the fixed coordinate system $Oxyz$ is $K\dot{s}\boldsymbol{\beta}$ (according to (1)). But this angular velocity is the vector sum of relative and transfer angular velocities. The relative angular velocity of the Frenet - Serret frame is its angular velocity with respect to the $A\xi\eta\zeta$ - system. This angular velocity is equal $k\dot{s}\boldsymbol{\beta}$ (since in the moving frame $A\xi\eta\zeta$ the motion of the Frenet - Serret frame $C\boldsymbol{\tau\nu\beta}$ is the motion along the bound of the lamina). The transfer angular velocity of the Frenet - Serret frame is the angular velocity of the $A\xi\eta\zeta$ - system with respect to $Oxyz$ - system, i.e. it is the angular velocity of the moving lamina $\boldsymbol{\Omega}$. Finally we have

$$\boldsymbol{\Omega} = (K - k)\,\dot{s}\boldsymbol{\beta}.$$

In particular when the lamina moves along the straight line, its angular velocity equals

$$\boldsymbol{\Omega} = -k\dot{s}\boldsymbol{\beta}.$$

Two contact points. Let us consider the rolling of the body consisting of two similar symmetric laminas in perpendicular planes connected to each other along the common axis of symmetry.This body rolls without slipping on the fixed horizontal plane. Let G be the center of mass of the moving body and K_1, K_2 be two contact points of the body with the plane.

From the rolling conditions for the two contact points follows that the angular velocity is always parallel to the line between the contact points i.e.

$$\left[\boldsymbol{\omega} \times \overrightarrow{K_1K_2}\right] = 0.$$

Now we introduce four coordinate systems. The first coordinate system is the fixed coordinate system $Oxyz$ with the origin at any point O of the fixed plane. The Oz - axis is directed upward. The second coordinate system is $Gx_1x_2x_3$ system with Gx_2 axis directed along the common axis of symmetry of the two laminas. The Gx_3 - axis is perpendicular to the plane of the first lamina and the Gx_1 - axis is perpendicular to the plane of the second lamina. The third coordinate system is the Frenet - Serret frame $K_1\boldsymbol{\tau\nu\beta}$ for the bound of the first lamina: the $\boldsymbol{\tau}$ - vector is the tangent vector to the bound of the lamina, the $\boldsymbol{\nu}$ - vector is in the plane of the lamina and the $\boldsymbol{\beta}$ - vector coincides in the unit vector of Gx_3 axis (i.e. $\boldsymbol{\beta}$ is perpendicular to the plane of lamina). The fourth coordinate system is also the Frenet - Serret frame. The origin of this system is also in K_1, the first unit vector $\boldsymbol{\tau}_1$ of this system coincides with the vector $\boldsymbol{\tau}$ of the system $K_1\boldsymbol{\tau\nu\beta}$. The second vector $\boldsymbol{\nu}_1$ of this system is in the plane of motion and the third vector $\boldsymbol{\beta}_1$ is perpendicular to the plane of motion (i.e. the vector $\boldsymbol{\beta}_1$ coincides with the vector $\boldsymbol{e}_z$ of the system $Oxyz$). Therefore we can conclude that the coordinate system $K_1\boldsymbol{\tau}_1\boldsymbol{\nu}_1\boldsymbol{b}eta_1$ is the Frenet - Serret frame for the curve which is obtained by the motion of the contact point K_1 (i.e. it is a "trace" of the point of contact on the plane).

Let us try to find the angular velocity of the moving body. We will use the law of composition of angular velocities. Let us consider the systems $Oxyz$, $K_1\boldsymbol{\tau\nu\beta}$ and $Gx_1x_2x_3$. The absolute angular velocity of $Gx_1x_2x_3$ system with respect to $Oxuz$ system is the sum of angular velocity of $Gx_1x_2x_3$ with respect to $K_1\boldsymbol{\tau\nu\beta}$ and the angular velocity of $K_1\boldsymbol{\tau\nu\beta}$ with respect to $Oxyz$. But the angular velocity of $Gx_1x_2x_3$ system with respect to $K_1\boldsymbol{\tau\nu\beta}$ system can be found very easy: it is equal $-k\dot{s}\boldsymbol{\beta}$. So we need calculate now the angular velocity of $K_1\boldsymbol{\tau\nu\beta}$ system with respect to $Oxyz$ system.

Let us denote by φ the angle between two unit vectors $\boldsymbol{\beta} = \boldsymbol{e}_3$ and $\boldsymbol{\beta}_1 = \boldsymbol{e}_z$. Then we can represent the angular velocity of $K_1\boldsymbol{\tau\nu\beta}$ system with respect to $Oxyz$ system is the sum of the angular velocity of $K_1\boldsymbol{\tau\nu\beta}$ system with respect to $K_1\boldsymbol{\tau}_1\boldsymbol{\nu}_1\boldsymbol{\beta}_1$ system and the angular velocity of $K_1\boldsymbol{\tau}_1\boldsymbol{\nu}_1\boldsymbol{\beta}_1$ system with respect to $Oxyz$ system. But the angular velocity of $K_1\boldsymbol{\tau\nu\beta}$ with respect to $K_1\boldsymbol{\tau}_1\boldsymbol{\nu}_1\boldsymbol{\beta}_1$ system is equal $\dot{\varphi}\boldsymbol{\tau}$ and the angular velocity of $K_1\boldsymbol{\tau}_1\boldsymbol{\nu}_1\boldsymbol{\beta}_1$ system with respect to $Oxyz$ system is equal $K\dot{s}\boldsymbol{\beta}_1$. Therefore finally we obtain:

$$\boldsymbol{\omega} = \dot{\varphi}\boldsymbol{\tau} - k\dot{s}\boldsymbol{\beta} + K\dot{s}\boldsymbol{\beta}_1.$$

Since $\boldsymbol{\beta} = -\boldsymbol{\nu}_1 \sin\varphi + \boldsymbol{\beta}_1 \cos\varphi$, we have

$$\boldsymbol{\omega} = \dot{\varphi}\boldsymbol{\tau}_1 + k\dot{s}\sin\varphi\boldsymbol{\nu}_1 - k\dot{s}\cos\varphi\boldsymbol{\beta}_1 + K\dot{s}\boldsymbol{\beta}_1.$$

But from the rolling conditions we already obtained that the vector $\boldsymbol{\omega}$ is proportional to $\overrightarrow{K_1K_2}$ vector i.e. $\boldsymbol{\omega}$ is always in the plane of motion

$$\boldsymbol{\omega} = \omega_1\boldsymbol{\tau}_1 + \omega_2\boldsymbol{\nu}_1.$$

This means that

$$K = k\cos\varphi \quad \text{or} \quad \rho\cos\varphi = r, \tag{2}$$

where ρ and r are radii of curvature of the curve on the fixed plane (trajectory of the point K_1) and the bound of the first lamina.

Natural equations of a curve. Let us consider the planar curve, defined by its parametric equations:

$$\boldsymbol{r} = \boldsymbol{r}\,(s) = x(s)\boldsymbol{e}_x + y(s)\boldsymbol{e}_y,$$

with the arc-length s as a parameter. We denote by $\alpha(s)$ the angle between the unit tangent vector $\boldsymbol{\tau}$ to the given curve

$$\boldsymbol{\tau} = \frac{d\boldsymbol{r}}{ds} = \frac{dx}{ds}\boldsymbol{e}_x + \frac{dy}{ds}\boldsymbol{e}_y$$

and the unit vector $\boldsymbol{e}_x$ of the Ox - axis. The initial value of $\alpha(s)$ at $s = 0$ can be chosen within the value divisible by 2π, for other points the angle $\alpha(s)$ is defined explicitly.

Since $\boldsymbol{\tau}(s)$ is the unit vector its projections on the Ox and Oy axes are $\cos\alpha$ and $\sin\alpha$ respectively. From the other side

$$\boldsymbol{\tau}(s) = \cos\alpha\boldsymbol{e}_x + \sin\alpha\boldsymbol{e}_y = \frac{dx}{ds}\boldsymbol{e}_x + \frac{dy}{ds}\boldsymbol{e}_y,$$

and therefore

$$dx/ds = \cos\alpha, \quad dy/ds = \sin\alpha. \tag{3}$$

Moreover, using the first Frenet – Serret formula we have

$$\frac{d\boldsymbol{\tau}}{ds} = (-\sin\alpha\boldsymbol{e}_x + \cos\alpha\boldsymbol{e}_y)\,\frac{d\alpha}{ds}\boldsymbol{\nu} = k(s)\boldsymbol{\nu},$$

and hence

$$d\alpha/ds = k(s). \tag{4}$$

This means that we can find the parametric equations of the curve if we know its curvature $k(s)$.

Thus we derived all the necessary facts for the investigation of the Oloid motion.

2 Motion of the Oloid

Coordinate frames and parametrization. We consider now the motion of Oloid. Let two circles of the same radius R in perpendicular planes be given such that each circle contains the center of the other. Then the convex hull of these circles is called Oloid. Let k_A and k_B be two circles of the same radius R in perpendicular planes Π_1 and Π_2 such that k_A passes through the center M_B of k_B and k_B passes through the center M_A of k_A.

According to the previous theory let us introduce the moving coordinate system $Gx_1x_2x_3$. The origin of this system will be at the midpoint G of M_AM_B (i.e. G is the center of mass of the system). The Gx_3 - axis is perpendicular to the plane Π_1 of the first circle, Gx_1 - axis is perpendicular to the plane Π_2 of the second circle and Gx_2 axis is directed along the common axis of symmetry of two circles (Fig. 2).

We will parametrize the first circle by the angle θ between the negative direction of Gx_2 axis and the direction to the point of contact. Note that this parametrization is proportional to the arc-length parametrization s: $s = R\theta$. We introduce also the angle ψ for the parametrization of the second circle: let ψ be the angle between the positive

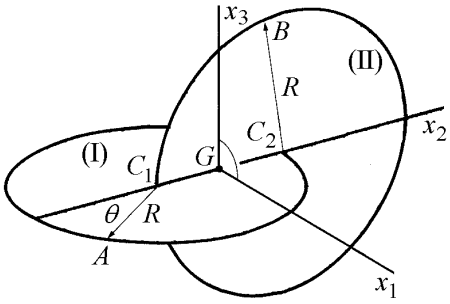

Figure 2: The Oloid.

direction of Gx_2 axis and the direction to the point of contact B. Then the radius - vector of the point A can be written as follows:

$$\overrightarrow{GA} = \boldsymbol{r}_1 = R\sin\theta\boldsymbol{e}_1 - \left(\frac{R}{2} + R\cos\theta\right)\boldsymbol{e}_2.$$

The radius-vector of the point B has the form:

$$\overrightarrow{GB} = \boldsymbol{r}_2 = \left(\frac{R}{2} + R\cos\psi\right)\boldsymbol{e}_2 + R\sin\psi\boldsymbol{e}_3.$$

When Oloid rolling on a fixed plane the three vectors $\boldsymbol{r}_1 - \boldsymbol{r}_2$, $\boldsymbol{r}_1'$ and $\boldsymbol{r}_2'$ should situated in this plane. This condition can be written in the form:

$$\cos\psi + \cos\theta\cos\psi + \cos\theta = 0.$$

Thus we can express

$$\cos\psi = -\frac{\cos\theta}{1+\cos\theta}$$

and obtain the radius – vector $\overrightarrow{GB} = \boldsymbol{r}_2$ in the θ – parametrization:

$$\overrightarrow{GB} = \boldsymbol{r}_2 = \left(\frac{R}{2} - \frac{R\cos\theta}{1+\cos\theta}\right)\boldsymbol{e}_2 - \frac{R\sqrt{1+2\cos\theta}}{1+\cos\theta}\boldsymbol{e}_3. \tag{4}$$

Note here the interesting fact: the length of the vector $\overrightarrow{AB}$

$$\overrightarrow{AB} = \overrightarrow{GB} - \overrightarrow{GA} = -R\sin\theta\boldsymbol{e}_1 + \left(R + \frac{R\cos^2\theta}{1+\cos\theta}\right)\boldsymbol{e}_2 - \frac{R\sqrt{1+2\cos\theta}}{1+\cos\theta}\boldsymbol{e}_3$$

will be a constant $AB = R\sqrt{3}$. This feature is usually used in construction of Oloid.

The expression (4) for the vector $\boldsymbol{r}_2$ should make a sense therefore we should have

$$O \le 1 + 2\cos\theta.$$

Therefore we have the following restrictions for the introduced parametrizations:

$$-2\pi/3 \le \theta \le 2\pi/3, \quad -2\pi/3 \le \psi \le 2\pi/3.$$

Trajectories of the points of contact. Let us obtain now equation for the plane of motion in the $Gx_1x_2x_3$ coordinate system. Points A, B and the tangent vector to the first circle at A are always in this plane. Using this fact we can write equation for the fixed plane in the form:

$$-2\sin\theta X + 2\cos\theta Y + 2\sqrt{1+2\cos\theta}Z + R\,(2+\cos\theta) = 0.$$

The unit vector

$$\boldsymbol{n} = -\sin\frac{\theta}{2}\boldsymbol{e}_1 + \left(\frac{1}{2\cos\frac{\theta}{2}} - \cos\frac{\theta}{2}\right)\boldsymbol{e}_2 + \frac{\sqrt{1+2\cos\theta}}{2\cos\frac{\theta}{2}}\boldsymbol{e}_3.$$

is the normal vector to this plane. Therefore the angle between the plane of the first circle and the fixed plane is defined as follows:

$$\cos\varphi = (\boldsymbol{n}\cdot\boldsymbol{e}_3) = \frac{\sqrt{1+2\cos\theta}}{2\cos\frac{\theta}{2}}.$$

The curvature of a circle at any point is equal to $k = 1/R$. Thus using (2) we can calculate the curvature of a curve drawn by the point of contact A on the fixed plane:

$$K = k\cos\varphi = \frac{\sqrt{1+2\cos\theta}}{2R\cos\frac{\theta}{2}}.$$

Having the expression for K we can find the parametric equations of the trajectory of the point A on the fixed plane.

For this purpose let us introduce the fixed coordinate system $Oxyz$. The origin O of this system coincides with the point of contact of the first circle with the plane at $\theta = 0$. The Ox - axis is tangent to the first circle, the Oz - axis is directed upwards. The Oy - axis forms the right triple with the Ox and Oz axes. Then we get:

$$\frac{d\alpha}{ds} = \frac{d\alpha}{Rd\theta} = K(\theta), \quad \text{i.e.} \quad \frac{d\alpha}{d\theta} = \frac{\sqrt{1+2\cos\theta}}{2\cos\frac{\theta}{2}}.$$

Integration of this equation gives us the following expression for α:

$$\alpha = 2\arcsin\left(\frac{2}{\sqrt{3}}\sin\frac{\theta}{2}\right) - \arcsin\left(\frac{\sin\frac{\theta}{2}}{\sqrt{3}\cos\frac{\theta}{2}}\right).$$

Then

$$\sin\alpha = \frac{\sqrt{3}\sin\frac{\theta}{2}}{9\cos\frac{\theta}{2}}(5+4\cos\theta), \quad \cos\alpha = \frac{\sqrt{3}}{9}\frac{(1+2\cos\theta)^{\frac{3}{2}}}{\cos\frac{\theta}{2}}.$$

Using these formulas together with (3), (4) we find after some trigonometric simplifications

$$x_A(\theta) = \frac{2R\sqrt{3}}{9}\left(\arcsin\left(\frac{2}{\sqrt{3}}\sin\frac{\theta}{2}\right) + \arcsin\left(\frac{\sin\frac{\theta}{2}}{\sqrt{3}\cos\frac{\theta}{2}}\right) + 2\sin\frac{\theta}{2}\sqrt{1+2\cos\theta}\right),$$

$$y_A(\theta) = \frac{8R\sqrt{3}}{9}\sin^2\left(\frac{\theta}{2}\right) - \frac{2R\sqrt{3}}{9}\ln\left(\cos\left(\frac{\theta}{2}\right)\right), \quad -\frac{2\pi}{3} < \theta < \frac{2\pi}{3}.$$

These equations give the parametric representation for the trajectory of the point A on the fixed plane.

We can use the similar ideas in finding the trajectory of point B. But we choose another way. Obviously we have the following vector relation:

$$\overrightarrow{OB} + \overrightarrow{OA} + \overrightarrow{AB} = \overrightarrow{OA} + AB\boldsymbol{e}_{AB} = \overrightarrow{OA} + R\sqrt{3}\boldsymbol{e}_{AB}.$$

We can represent this relation in the scalar form:

$$x_B(\theta) = x_A(\theta) + R\sqrt{3}\cos(\alpha+\gamma), \; y_B(\theta) = y_A(\theta) + R\sqrt{3}\sin(\alpha+\gamma).$$

Here γ is the angle between the vector $\boldsymbol{e}_{AB}$ and the tangent vector $\boldsymbol{\tau}$ to the first circle at A. The tangent vector $\boldsymbol{\tau}$ has the form $\boldsymbol{\tau} = \cos\theta\boldsymbol{e}_1 + \sin\theta\boldsymbol{e}_2$ and therefore its scalar product with $\overrightarrow{AB}$ leads to:

$$\left(\overrightarrow{AB}\cdot\boldsymbol{\tau}\right) = AB\,(\boldsymbol{e}_{AB}\cdot\boldsymbol{\tau}) = AB\cos\gamma = R\sqrt{3}\cos\gamma = R\tan\frac{\theta}{2},$$

$$\cos\gamma = \frac{\sin\frac{\theta}{2}}{\sqrt{3}\cos\frac{\theta}{2}}, \quad \sin\gamma = \frac{\sqrt{1+2\cos\theta}}{\sqrt{3}\cos\frac{\theta}{2}}.$$

Finally in the explicit form we have the following expressions for x_B and y_B:

$$x_B(\theta) = \frac{2R\sqrt{3}}{9}\left(\arcsin\left(\frac{2}{\sqrt{3}}\sin\frac{\theta}{2}\right) + \arcsin\left(\frac{\sin\frac{\theta}{2}}{\sqrt{3}\cos\frac{\theta}{2}}\right) - \frac{2\sin\frac{\theta}{2}}{(1+\cos\theta)}\sqrt{1+2\cos\theta}\right),$$

$$y_B(\theta) = \frac{7R\sqrt{3}}{9} + \frac{2R\sqrt{3}}{9\cos^2\left(\frac{\theta}{2}\right)} - \frac{2R\sqrt{3}}{9}\ln\left(\cos\left(\frac{\theta}{2}\right)\right), \quad -\frac{2\pi}{3} < \theta < \frac{2\pi}{3}.$$

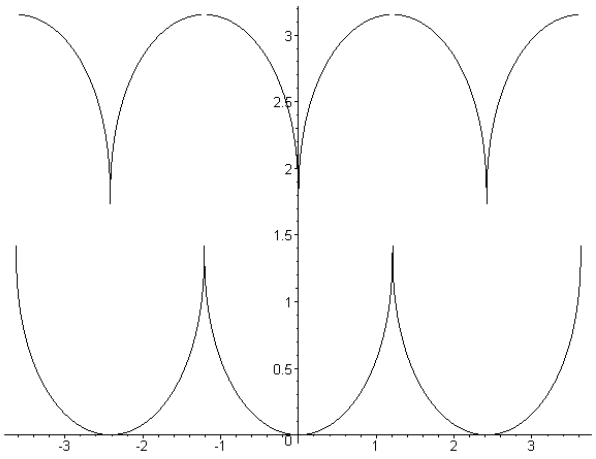

Figure 3: Trajectories of points A and B on the fixed plane Oxy.

These equations give the parametric representation for the trajectory of the point B on the fixed plane. Figure 3 shows the trajectory of point A (bottom curve) and B (upper curve) on the fixed plane Oxy.

References

[1] Dirnbök H., Stachel H. (1997) The Development of the Oloid. *J. Geometry Graphics* **1**:105-118.

[2] Schatz P. (1975) Rhythmusforschung und Technik. Verlag Freies Geistesleben, Stuttgart.

[3] Schatz P. (1933) Deutsches Reichspatent Nr. 589 452 in der allgemeinen Getriebeklasse.

[4] Bioengineering AG (Sagenrainsrt. 7, 8636 Wald, Switzerland).

Alexander S. Kuleshov, Department of Mechanics and Mathematics, Moscow State University, Moscow, Russia
Mont Hubbard, Department of Mechanical and Aerospace Engineering, University of California, Davis, USA
Dale L. Peterson, Department of Mechanical and Aerospace Engineering, University of California, Davis, USA
Gilbert Gede, Department of Mechanical and Aerospace Engineering, University of California, Davis, USA

The influence of cohesion between the materials on stress-strain condition of reinforced composite

G. M. Kuziomkina O. I. Yakubovich A. O. Shimanovsky Yu. M. Pleskachevskii
theor-mech@yandex.ru

Abstract

The stress-strain condition of reinforced composite on the basis of finite element modeling is being investigated. The rectangular cross-section cantilever beam reinforced with five rods has been considered as a test subject. The special feature of the developed model is the presentation of the armature as a 3D deformed solid body. The analysis of the stress-strain condition of the construction has been done with a glance that between the composite materials there is Coulomb's friction. The cohesion between the materials has also been taken into consideration. The analysis of the contact between the contacting surfaces allowed to define the slip areas between the armature and the composite matrix. In addition the gaps between the composite phases were found. The results of the carried out research may be used for the optimization of reinforcement of building and machine building constructions.

1 Studies of Reinforced Composite Deformations

Despite the considerable interest to the analysis of composite deformation in well-known published works there are no computation results for the stress-strain condition of building constructions with the simultaneous glance of the following factors: 1) creep and relaxation effects of matrix material; 2) nonlinear deformation of matrix material; 3) breaking-down and heterogeneity of interfacial relationship in composite; 4) joint deformation of structural elements of reinforced polymers and traditional building materials. Complex analysis of all these factors is possible only within numerical methods of mechanics. Thus, the use of finite-element method allows to describe in details the stress-strain condition of a composite within the boundary between phases. In this case there is the possibility to specify the typical component properties and boundary conditions-load parameters dependences for studied composites.

The implantation of the reinforcement in the composite matrix allows increasing durability and rigidity of engineering and building constructions, the properties of composite material depending on the nature of its contact phases interaction [1, 2]. Among the factors influencing the mechanical bond are the structural elements geometry, the reinforced rod position in cross section and the bond stress distribution along the reinforcement [3].

As a rule, so far the analysis of mechanical bond influence on the construction durability has been carried out by experimental methods. For example, in work [4] there has been examined the concrete-reinforcement cohesion durability where the latter is steel wires twisting. In article [5] during pulling tests there has been established the dependence of bond stress on the reinforced rod-concrete contact length. In paper [2] there has been considered test categories necessary for defining concrete-reinforced fiber composite rods cohesion description and establishing reasonability of their practical application.

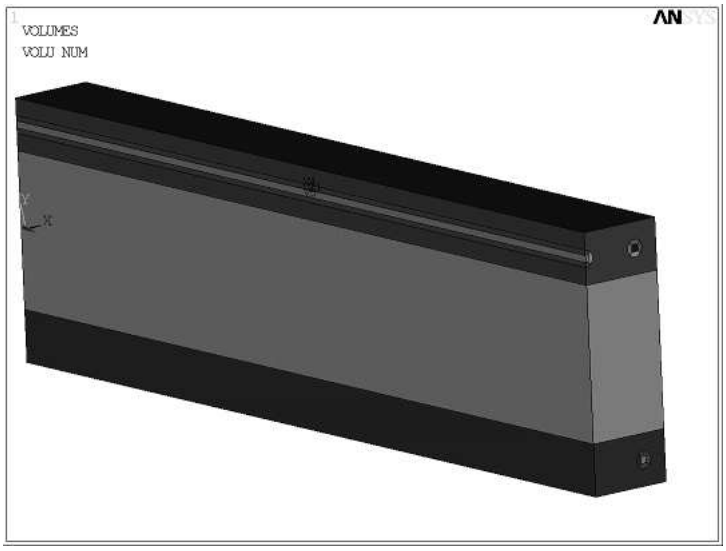

Figure 1: The splitting of a beam into volumes scheme

In recent years a number of theoretical studies analyzing the deformation of reinforced building constructions have appeared [6, 7, 8, 9]. But the authors design the reinforcement as rods accepting only longitudinal loads. Firstly, it doesn't allow to evaluate for sure the stress in reinforcement-composite matrix interaction area because as it doesn't take into account irregularity of stress distribution along the section, secondly, it doesn't allow to take into account the influence of friction between contact phases of the composite on its stress-strain condition and also to reveal distribution of cracks in reinforcement-concrete matrix interaction area. The solution of the problem is possible only when modeling reinforcement by a 3D deformable solid body [10, 11, 12].

2 The Influence of Inner Friction between the Materials on Construction Stresses and Deformations

In the present work the task is to define stress-strain condition of reinforced composite taking into account the contact interactions of reinforcement and matrix. The object of the research is a cantilever beam 1 m long with a rectangular 20-30 sm cross-section the reinforcement of which is done by five steel rods with 2 sm diameter. It is accepted that the coefficients of elasticity for matrix material and reinforced steel are 27 and 200 GPa respectively.

To reduce the amount of calculations under load symmetric to the vertical plane of beam symmetry the model representing half of the real beam cut by the longitudinal vertical plane has been created. Figure 1 shows a scheme of splitting the beam into volumes with the same physical properties. Computating the cases for unbalanced load effects the adhesion of construction symmetrical halves has been carried out.

The reinforcement and composite matrix were designed by prismatic finite elements with twenty nodes. The necessity of defining the location of internal slipping grounds required the usage of contact elements with the size not larger than 2 sm along the reinforcement. It allowed defining with adequate accuracy the location of internal slipping grounds. That's why the general number of model finite elements was equal 144000. The computations were done under the assumption that there was dry friction between the ma-

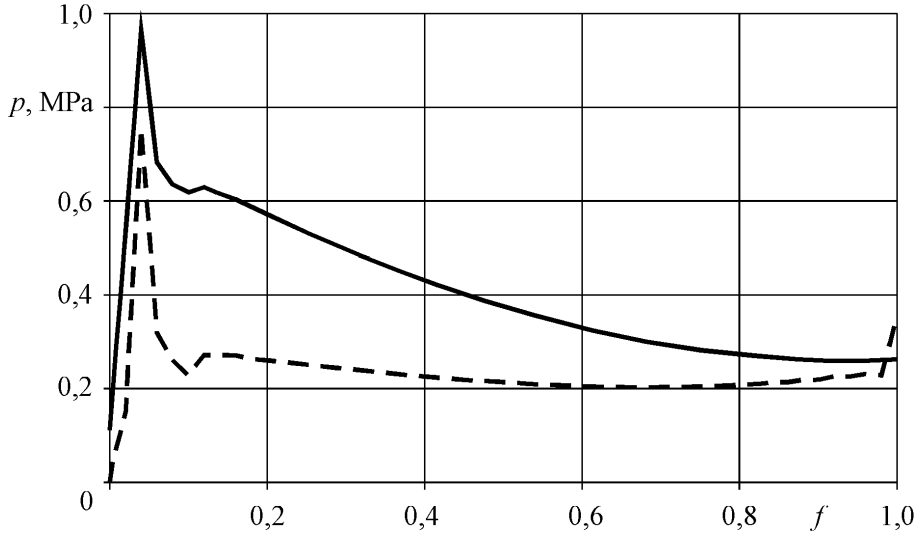

Figure 2: Scheme of distribution of contact stresses along the top generatrix of reinforced rod subject to distance between the section and beam bedding point; upper curve – without friction, lower curve – for friction coefficient f = 1

terials defined by Coulomb law. The friction coefficient values were accepted in the range from 0 to 10 corresponded with different physical properties of composite contact phase surfaces. Taking into account the adhesion between the materials may lead to friction coefficient values over 1.

The loading of beam was carried out by gravity forces of its elements and uniformly distributed pressure of 170 kPa applied to the upper boundary. The analysis of contact condition between the contact surfaces of reinforcement and matrix under the action of transversal forces only showed that slipping motion is absent only in small areas of contact between the reinforcement and composite matrix. These areas are located in the upper parts of reinforced rods at the distance not exceeding five diameters of reinforcement from fixing place.

In the absence of friction the maximal equivalent stresses are observed in embedded cross-section. With increasing friction coefficient the place with the maximal equivalent stresses moves away from the fixed beam end. Figure 2 shows schemes for distribution of contact stresses along the top generatrix of upper reinforced rod subject to distance to the fixed beam end when the internal friction is absent and for friction coefficient f = 1. From these schemes it is seen that the maximal contact stresses appear at the distance equivalent to two diameters of the reinforced rod from the bedding point. In the absence of friction the contact stresses are gradually decreasing towards the free beam end. Friction taken into account allowed to reveal that at the free end of the reinforced rod there is a contact pressure jump.

Analysis of Mises' maximal equivalent stresses in reinforcement material showed that they are steadily increasing as the friction coefficient is increasing. The similar dependence was found for the first principal stress as well (figure 3). The rigidity of the construction is gradually increasing as the cohesion between the composite materials is increasing. And the gradient of deformation decrease is gradually falling down as the friction coefficient is increasing. The deformation values under the friction between the composite phases decrease by 15% and more. The installation of reinforcement in matrix with tension may maximize this effect.

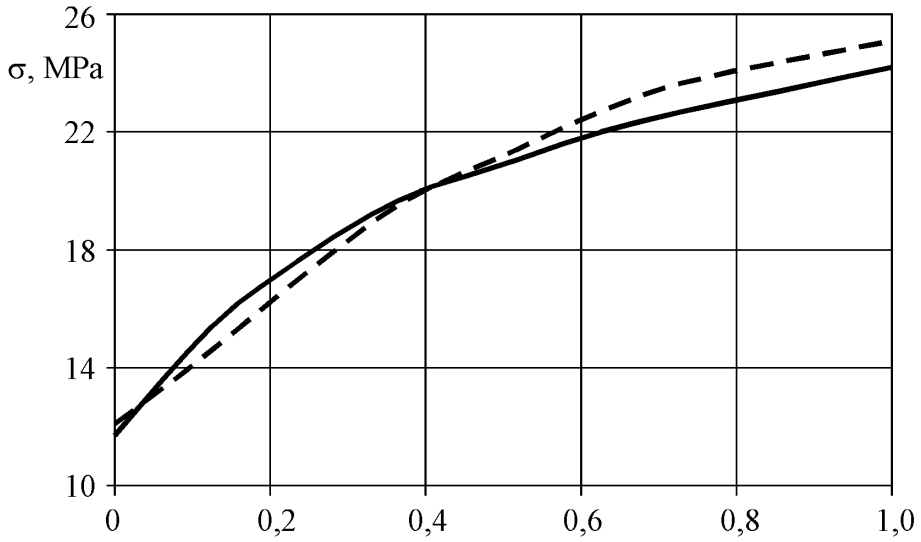

Figure 3: The dependence of maximal principal (firm line) and equivalent (dotted line) stresses in reinforcement material on the coefficient of friction between the components

There made some computations to determine the influence of cohesion between the reinforcement and composite matrix on the stress-strain condition of the construction. Figures 4–8 show a number of dependences obtained in multi-choice calculations.

The analysis of the received results shows when the cohesion doesn't exceed 10 kPa its changes hardly influence the durability and rigidity of the construction. By analogy the increasing of cohesion over 100 kPa doesn't lead to the significant change in the stress-strain condition.

The performed computations showed that in the range from 10 to 100 kPa there is a significant change in the composite stress-strain condition: the stress in reinforcement increases to 30%, the stress in concrete matrix decreases by 12-20%, maximal construction deformations increase by 20%.

The differences in the coefficients of elasticity of composite materials result in the creation of gap between the reinforcement and matrix. The maximal gap between the reinforcement and matrix increases by 15%, the contact pressure increases by 30% for cohesion changing from 10 to 100 kPa.

The received results allow to develop the recommendations to ensure the durability of reinforced constructions by changing the location of strain-hardening reinforcement in the concrete matrix. They may be used in design agences for the development of new bearing structures or modifications of some elements of the existing ones.

Acknowledgements

The work is supported by Foundation for Fundamental Research of the Republic of Belarus Fund, Grant T10-100.

References

[1] M. F. Aiello, M. Leone, L. Ombres. Modeling of behavior of concrete structural elements reinforced by fiber composite rods and work in tension, Mechanics of Composite Materials, 39, N 4, (2003) 431–444. (in Russian)

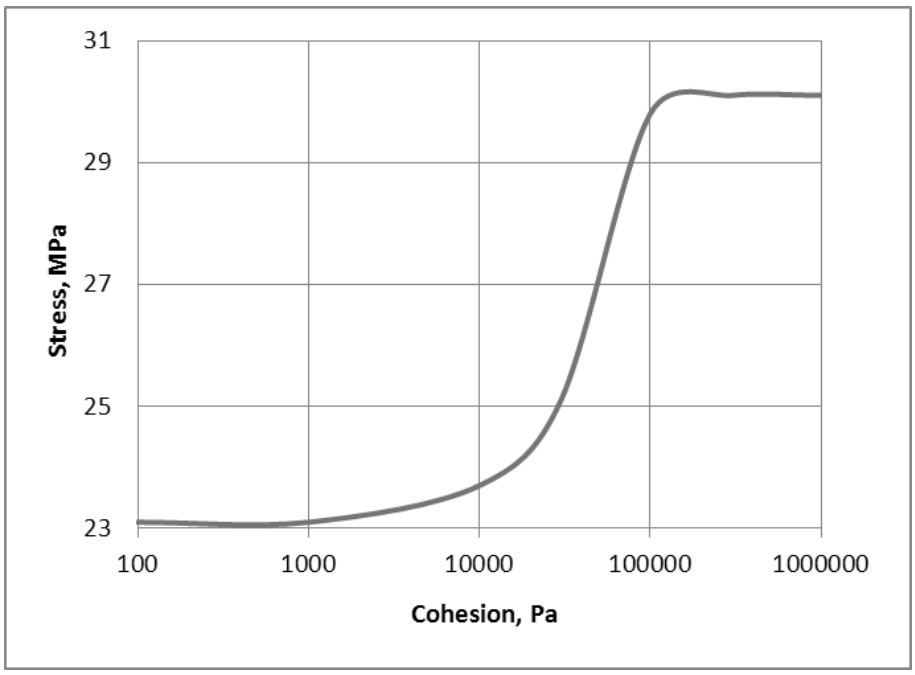

Figure 4: The dependence of reinforcement stresses on the cohesion between the reinforcement and matrix

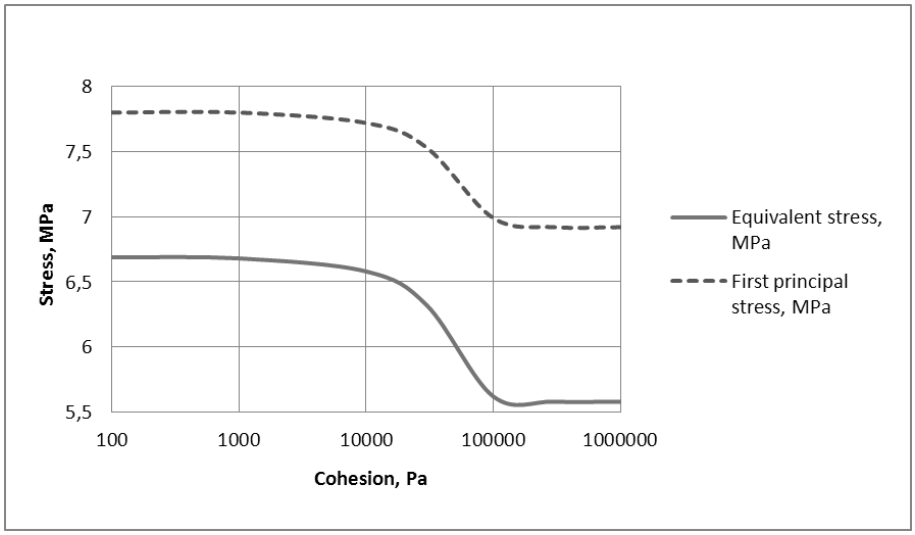

Figure 5: The dependence of concrete stresses on the cohesion between the reinforcement and matrix

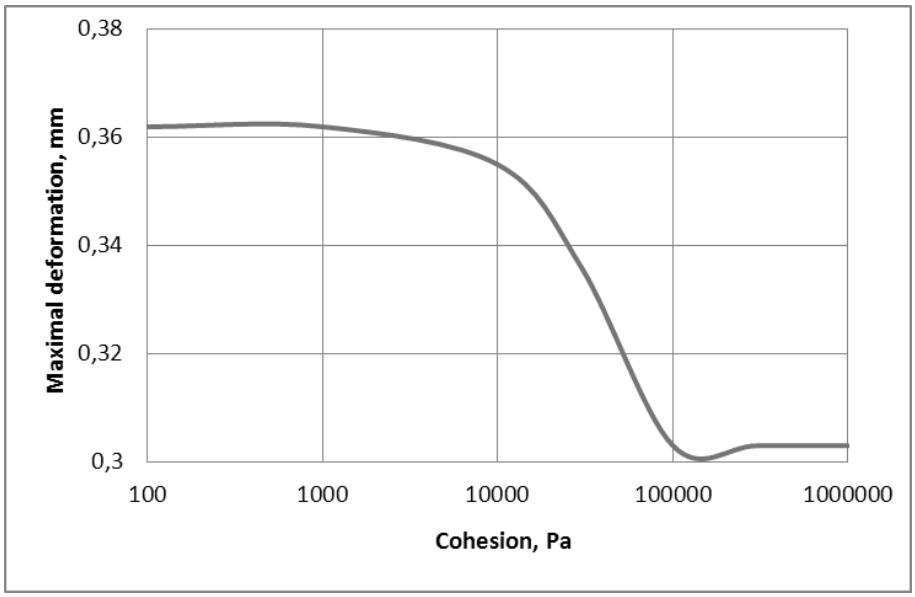

Figure 6: The dependence of beam point maximum displacement on the cohesion between the reinforcement and matrix

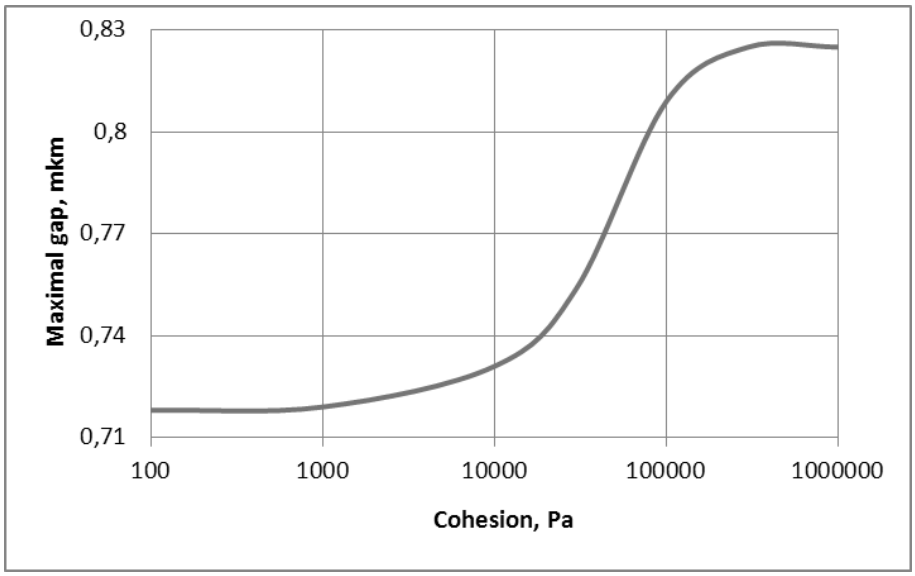

Figure 7: The maximum gap between the reinforcement and composite matrix dependence

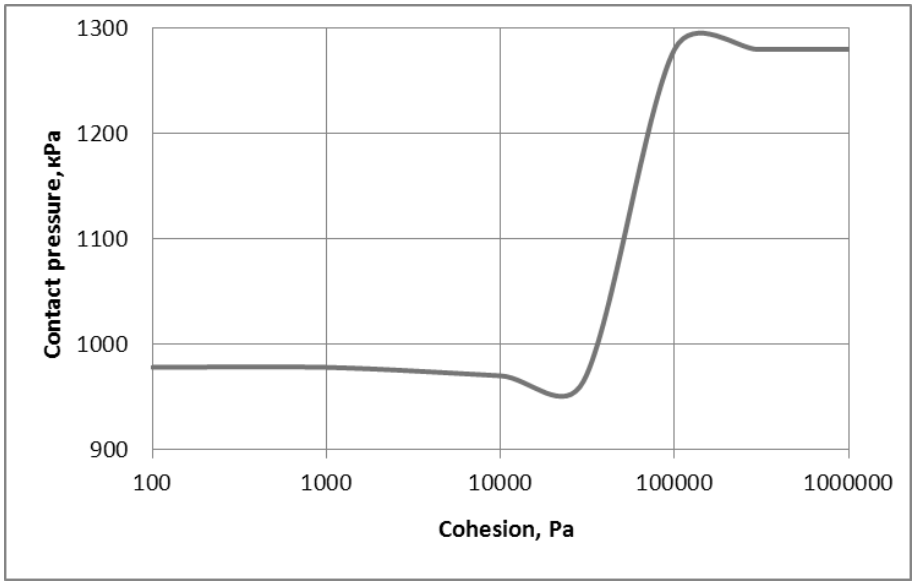

Figure 8: The dependence of contact pressure on the cohesion between the reinforcement and matrix

[2] R. Tepfers, L. De Lorenzis. Adhesion of fiber composite reinforcement in concrete – an actual problem, Mechanics of Composite Materials, 39, N 4, (2003) 477–496. (in Russian)

[3] V. Tamuzs et al. The performance of bond of FRP reinforcement in concrete, SAMPE, Long Beach, California, May 6-th – 10 th., (2001) 1738–1748.

[4] Tepfers R. Bond stress along lapped reinforcing bars, Magazine of Concrete Research, 32, N 112, (1980) 135–142.

[5] R. Tepfers. Craking of concrete cover along anchored deformed reinforcing bars, Magazine of Concrete Research, 31, N 106, (1979) 3–12.

[6] D. Kachlakev et al. Finite element modeling of reinforced concrete structures strengthened with FRP laminates: Final Report, United States Department of Transportation, Federal Highway Administration, 2001, 34 p.

[7] P. Fanning. Nonlinear models of reinforced and post-tensioned concrete beams, Electronic Journal of Structural Engineering, N 2, (2001) 111–119.

[8] S. Limkatanyu, E. Spacone. Reinforced concrete frame element with bond interfaces. Part 1: Displacement-Based, Force-Based and Mixed Formulations, Journal of Structural Engineering, 128, N 3 (2002) 346–355.

[9] J. Broovsk. Modelovn fizikln nelinernino chovn elezobetonovych konstrukci: Teze disertačni prace. Brno, 2001. 44 p.

[10] Yu. M. Pleskachevskii, A. O. Shimanovskii, G. M. Kuzemkina. Finite element Modeling of the Integration of Reinforcement with Concrete Matrix, Mechanics of Composite Materials, 44, N 3, (2008) 209–214.

[11] Yu. M. Pleskachevskii et al. Modeling of reinforcement-composite matrix mechanical interaction, Mechanics of machinery and materials, N 1 (2009) 67–71. (in Russian)

[12] G. M. Kuziomkina et al. Stress-strain condition of reinforced composite under complex loading. Proceedings. International scientific conference The strength of materials and structural elements, Kiev, 2010, Vol. 1, pp. 192–194. (in Russian)

Galina M. Kuziomkina, Educational Center Gomeluchcentrstroy, 30, 8th Pereulok Il'icha, Gomel, 246042, Belarus
Olga I. Yakubovich, Alexandr O. Shimanovsky, Belarusian State University of Transport, 34 Kirova str., Gomel, 246653, Belarus
Yuri M. Pleskachevskii, Presidium of Gomel Branch of NAS Belarus, 4 Fedyuninskogo str., Gomel, 246007, Belarus

On numerical simulation of hydraulic fracturing

Alexander M. Linkov
linkoval@prz.edu.pl

Abstract

The paper concerns with numerical modeling of hydraulic fracture. It is shown that proper using of the mass balance leads to the local speed equation, which may serve for employing well-developed methods of the theory of propagating interfaces. It appears that existence of the speed equation, which is additional to a prescribed boundary condition at the liquid front, can make a problem ill-posed and complicate numerical simulation. It is also shown how the very source of the difficulty gives the key to overcome it. To this end, a method of ε-regularization is suggested. It consists in using the speed equation together with a prescribed boundary condition to formulate a new boundary condition at a small distance behind the front rather than on the front itself. Specially designed numerical experiments reveal the peculiarities of the problem. They evidently show (i) strong deterioration of the solution near the liquid front if the regularization is not employed, (ii) high accuracy and stability of the solution obtained by using the suggested regularization. We conclude that the ε-regularization presents an efficient means for numerical simulation of hydraulic fracturing.

1 Introduction

Hydraulic fracturing is widely used with the purpose to increase surface to or from which a fluid flows in rock. It is applied to enhance oil, gas and thermal heat production, to control rock pressure, to provide efficient CO_2 sequestration and to isolate contaminants. A similar process of fracturing occurs in natural conditions when pressurized magma fractures earth crust leading to formation of veins. Numerous papers have been published on mathematical modeling of hydraulic fracture starting from the works [1], [2], [3], [4],[5]. To date, authors have employed *global* mass balance to trace the liquid front propagation (e.g. [6], [7], [8], [9], [10]). In this paper, we derive and use the *local* consequence of the balance. It gives us general equation specifying the speed function for problems of hydraulic fracturing. The speed function, being the basis of the well-developed theory of propagating interfaces, it may serve for employing level set methods and fast marching methods for hydraulic fracture simulation. Its employing also shows that when we fix the liquid contour in iterations of numerical simulation, a problem may become over-determined and consequently ill-posed. A way to overcome the difficulty and to obtain accurate and stable results follows from the very source of the difficulty. The speed equation together with a prescribed boundary condition gives us an asymptotic equation, which may be efficiently used for the problem regularization by imposing a new boundary condition at a small distance behind the front rather than on the front itself. Results of numerical experiments demonstrate the computational features of the problem and the efficiency of the regularization method.

2 Speed function and speed equation for hydraulic fracturing

For flow of incompressible liquid in a narrow channel, the global mass balance reads

$$\frac{dV_e}{dt} = \int_{S(t)} \frac{\partial w}{\partial t} dS + \int_{L(t)} q_*(x_*) dL,$$

where V_e is the volume of liquid entering/leaving the channel from/to external sources/sinks; $S(t)$ is the middle surface of the channel; w is its width (opening); $L(t)$ is the contour of the liquid at the time t; x_* is a point on the liquid front; $q_{n*}(x_*) = w_* v_{n*}$ is the total flux through the front cross section with the external normal n to the liquid front L; $w_* = w(x_*)$; $v_{n*} = dx_*/dt$ is the normal component of the front velocity. From the expression for q_{n*} we have

$$v_{n*} = \frac{q_{n*}}{w_*}. \tag{1}$$

In cases when a lag between the liquid front and the crack tip is neglected (e.g. [5], [6], [7], [8], [9], [10]), both q_{n*} and w_* are zero at the liquid front, which in these cases coincides with the tip of a crack where the flow occurs. Then the r. h. s. of (1) becomes uncertainty $\frac{0}{0}$, and equation (1) takes the form:

$$v_{n*} = \lim_{\mathbf{x} \to \mathbf{x}_*} \frac{q_{n*}}{w_*}. \tag{2}$$

The limit on the r. h. s. of (2) should be finite to exclude instant fracture propagation with infinite velocity.

The flow of viscous incompressible liquid in a narrow channel is described by partial differential equations (PDE) by Poiseuille and Reynolds. The Poiseuille equation connects the flux $\mathbf{q}$ through a cross-section with the pressure gradient as

$$\mathbf{q} = -D(w,p) grad p, \tag{3}$$

where $D(w,p)$ is a prescribed function or operator, p is the pressure. Substitution of (3) into the continuity equation gives the Reynolds equation:

$$\frac{\partial w}{\partial t} - div[D(w,p) grad p] - q_e = 0, \tag{4}$$

where q_e is the intensity of external sources per unit area of the middle surface of the channel. Note that the PDE (3) and (4) contain the flux $\mathbf{q}$ through a cross-section rather than the particle velocity $\mathbf{v}$. The latter enters only the speed equation (1) or its limit form (2). This implies that the r.h.s. of (1) defines the so-called speed function [11] for problems of hydraulic fracturing. The speed function may serve to employ the well-established theory of propagating interfaces and methods developed in this theory, such as level set methods and fast marching methods, to simulate hydraulic fracturing.

Using (3) in (1) gives the explicit form of the speed function of hydraulic fracture:

$$v_{n*} = -\frac{1}{w_*} D(w,p) \frac{\partial p}{\partial n} \lfloor_{x=x_*}. \tag{5}$$

The speed equation (1) or its explicit form (5) is additional to a boundary condition (BC) imposed at the liquid front by considering a physical state ahead of the front. In

cases when a lag between the liquid front and the crack tip is taken into account, the pressure $p_0(x_*)$ is commonly prescribed (e. g. [12]):

$$p(x_*) = p_0(x_*). \tag{6}$$

In cases, when the lag is neglected, the opening at the crack tip is set zero:

$$w(x_*) = 0. \tag{7}$$

The opening being unknown, a solid mechanics equation is used to connect it with the pressure. Besides, a fracture mechanics condition is imposed to let the fracture surface change in time. Because of using these equations, the condition (7), like (6), actually involves the pressure. For certainty, in further discussion, we consider the BC (6).

In view of (6) and (5), we have two rather than one BC for the PDE (4) at the points of the liquid front. The first of them is the prescribed BC (6), while the second is the speed equation (5). Note now that the operator $div[D(w,p)gradp]$ is elliptic in spatial coordinates. Thus, when solving numerically a problem involving (4) under a fixed contour $L(t)$ at a time step, we have a Cauchy (initial value) problem for an elliptic operator. Consequently, a problem may appear ill-posed [13], [14]. This strongly complicates obtaining accurate and stable numerical results. To overcome the difficulty, it is reasonable to have an appropriate method of regularization.

3 Regularization method

We suggest the regularization method based on employing the very cause of the difficulty. Specifically, the equations (5) and (6) are used together to formulate a new BC at a small distance behind the front rather than on the front itself.

Consider a point x_* at the front and introduce the local Cartesian coordinates $x_1'O'x_2'$ with the origin O' at the point x_*, the axis x_1' opposite to the direction of the normal to the front and the axis x_2' in the tangent direction. The flux $\mathbf{q}$ is normal to the front, hence, its tangential component is zero, while according to (3) its normal component is $q_{n*} = D(w,p)\frac{\partial p}{\partial x_1'}$. Then (5) yields the approximate equation for points at a vicinity of the front:

$$\frac{1}{w}D(w,p)\frac{\partial p}{\partial x_1'} \approx v_*, \tag{8}$$

where $v_* = dx_*/dt$ is the absolute value of the front velocity. Integration of (8) and accounting for (6) gives:

$$\int_{p_0}^{p} \frac{1}{w}D(w,p)dp \approx v_* x_1'. \tag{9}$$

By using (9) we may impose the BC at a small distance $x_1' = \varepsilon'$ behind the front:

$$\int_{p_0}^{p_\varepsilon} \frac{1}{w}D(w,p)dp = v_*\varepsilon', \tag{10}$$

where p_ε is the pressure at the point ε'. Thus instead of using the BC (6) at the front, we suggest to employ the regularized condition (10) behind the front. It is obtained by integrating the speed equation in the local coordinates and by using a prescribed BC when evaluating the lower limit of the integral. Besides, in numerical calculations, taking into

account that the distance ε' is small, the equation (8) is written as the equality at the point ε':

$$\frac{1}{w}D(w,p)\frac{\partial p}{\partial x_1'}\lfloor_{x_1'=\varepsilon'}= v_*. \tag{11}$$

Equation (11) may serve for iterations in v_* when employing finite differences to numerically simulate fracture propagation.

4 Numerical tests without and with regularization

We tested the regularization method by revisiting the Nordgren problem [5] in the case when there is no leak-off ($q_e = 0$). In the model used by Nordgren, 1-D flow of incompressible Newtonian liquid occurs along the interval $[0, x_*(t)]$ of the x-axis; the pressure p is proportional to the opening w and the lag is zero, so that both the opening and the flux are zero at the liquid front (the pressure is also zero at the front because it is proportional to the opening). There is a prescribed flux q_0 at the inlet $x = 0$. After normalizing variables, the mathematical problem is formulated as follows [5]: we need to solve the Reynolds PDE, which takes the form

$$\frac{\partial^2 w^4}{\partial x^2} - \frac{\partial w}{\partial t} = 0 \tag{12}$$

under the boundary conditions at the inlet

$$\frac{\partial w^4}{\partial x}\lfloor_{x=0}= q_0 \tag{13}$$

and at the liquid front

$$w(x_*, t) = 0. \tag{14}$$

The opening $w(x,t)$ is assumed positive behind the front and zero ahead of it:

$$w(x,t) > 0 \ \text{ for } 0 \le x < x_*; \ \ w(x,t) = 0 \ \text{ for } x > x_*. \tag{15}$$

Note that the last equations actually serve to find the front velocity as a part of the solution.

At the initial moment $t = 0$, the opening is zero along the entire x-axis:

$$w(x, 0) = 0. \tag{16}$$

Nordgren solved the problem (12)-(16) by using the Crank-Nicolson scheme and linear approximation for w^4. The results obtained are given in [5] to the accuracy of some one percent. Our attempts to reach higher accuracy without regularization failed: *by no means could we obtain more than two significant digits.* Using various variables (w, w^3, w^4) and employing various formulations of the problem, including the self-similar formulation, made not good. Remarkable is that when using fine meshes, the results always strongly deteriorated near the liquid front. This evidently confirms the theoretical proposition that the problem is ill-posed and needs proper regularization to get accurate and stable numerical results. As noted above, the reason is that the speed equation is additional to a prescribed boundary condition at the liquid front.

In the case considered the speed equation reads:

$$-\frac{4}{3}\frac{\partial w^3}{\partial x}\lfloor_{x=x_*}= v_*(t). \tag{17}$$

Following the line sketched in the previous section, we use (14) and (17) together to impose the boundary condition at a small distance ε' behind the front:

$$w^3\lfloor_{x=x_*-\varepsilon'}= \frac{3}{4}v_*(t)\varepsilon'. \tag{18}$$

Equation (11), serving for iterations in v_* at a time step, becomes:

$$\frac{\partial w^3}{\partial x}\lfloor_{x=x_*-\varepsilon'}= -\frac{3}{4}v_*(t). \tag{19}$$

We solved the regularized problem (12), (13), (18) by Crank-Nicolson method with iterations in non-linear terms and in v_* (according to (19)). In contrast with the solution without regularization, the results obtained with regularization are accurate and stable. Specifically, we have at least five correct significant digits when taking the relative distance $\varepsilon = \varepsilon'/x_*$ from the front as small as 10^{-3}, 10^{-4}, the spatial step $\Delta\zeta = \Delta x/x_*$ in the range $10^{-6} \le \Delta\zeta \le 10^{-3}$ and sufficiently small time step ($\Delta t < t_0$, where t_0 is the starting time). No signs of instability were observed in specially designed numerical experiments with the number of time steps exceeding 20000. The method deteriorated only when the spatial step $\Delta\zeta$ and the regularization parameter ε were very small *simultaneously*: $\Delta\zeta = \varepsilon = 10^{-6}$. Actually, in this case, to the employed accuracy of double precision, there is no regularization (ε is too small), while the mesh is very fine ($\Delta\zeta$ is too small); according to the discussion above, calculations without regularization deteriorate when using very fine meshes. The time expense on a conventional computer never exceeded 15 seconds. We conclude that the suggested regularization is efficient.

5 Acknowledgment

The author appreciates the support of the EU Marie Curie IAPP program (Grant # 251475).

References

[1] Khristianovic S. A., Zheltov Y. P. Formation of vertical fractures by means of highly viscous liquid. In: Proc. 4-th World Petroleum Congress, Rome, 1955, 579-586.

[2] Perkins T. K., Kern L. R. Widths of hydraulic fractures. J. Pet. Tech., 1961, 13 (9), 937-949.

[3] Geertsma J., de Klerk F. A rapid method of predicting width and extent of hydraulically induced fractures. J. Pet. Tech., 1969, 21, 1571-1581.

[4] Haward G. C., Fast C. R. Hydraulic fracturing. Monograph series, v. 2, Richardson, Soc. Petroleum Eng., 1970.

[5] Nordgren R. P. Propagation of a vertical hydraulic fracture. SPE J., 1972, 12 (8), 306-314.

[6] Spence D. A., Sharp P. W. Self-similar solution for elastodynamic cavity flow. Proc. Roy. Soc. London, Ser A, 1985, 400, 289-313.

[7] Adachi J. I., Detournay E. Self-similar solution of plane-strain fracture driven by a power-law fluid. Int. J. Numer. Anal. Meth. Geomech., 2002, 26, 579-604.

[8] Jamamoto K., Shimamoto T., Sukemura S. Multi fracture propagation model for a three-dimensional hydraulic fracture simulator. Int. J. Geomech., ASCE, 2004, No 1, 46-57.

[9] Adachi J., Siebrits E. et al. Computer simulatiion of hydraulic fractures. Int. J. Rock Mech. Min. Sci., 2007, 44, 739-757.

[10] Hu J., Garagash D. I. Plane-strain propagation of a fluid-driven crack in a permeable rock with fracture toughness. J. Eng. Mech., ASCE, 2010, 136 (9), 1152-1166.

[11] Sethian J. A. Level set methods and fast marching methods. Cambridge, Cambridge University Press, 1998.

[12] Garagash D. I. Propagation of a plane-strain hydraulic fracture with a fluid lag: Early time solution. Int. J. Solids Structures, 2006, 43, 5811-5835.

[13] Hadamard J. Sur les problemes aux derivees partielles et leur signification physique. Princeton University Press, 1902, 49-52.

[14] Tychonoff A. N. Solution of incorrectly formulated problems and the regularization method. Soviet Mathematics, 1963, 4, 1035-1038.

Alexander M. Linkov, IPME, Saint-Petersburg, Russia; Rzeszow University of Technology, Rzeszow, Poland

Evolution of nonstationary waves in the condensed medium

T. A. Khantuleva A. V. Litvinov
khan47@mail.ru, lit43848@gmail.com

Abstract

The problem on the shock-induced wave propagating in solid is solved in the framework of the nonlocal theory. An approximate solution to the problem describing all regimes of the pulse propagation in between the elastic and hydrodynamic limits is obtained.

1 Introduction

Propagation of moderate intensity shock-induced waves in condensed matter is followed by the momentum and energy exchange between degrees of freedom at several scale levels. Essential difference in rates of exchange processes for spherical and shear degrees of freedom determining the elastic precursor relaxation, makes a wave nonstationary. In transient regime the two-wave front is formed. An information about the inner processes and changes of the medium properties behind the front is encrypted in the waveform. Such nonequilibrium process cannot be described in scope of the conventional continuum mechanics and only nonlocal transport theory valid through all the range of regimes [1-2] can be used to describe the wave fronts evolution.

2 Formulation of the problem and approximate solution to it

The medium response to the shock loading is the stress relaxation and inertia effects that characterized by their time and space scale parameters. For the short pulses in condensed matter 3 scale parameters characterize the nonstationary wave propagation.

$$\tau = \frac{t_r}{t_R} \geq 1$$

t_r - relaxation time, t_R - loading time, θ - retardation time

$$\varepsilon = \frac{Ct_r}{L} << 1$$

L - target width, C = *const* - longitudinal sound velocity

In the transition regime momentum transport on the conditions $V_o << C$ - - shock velocity is a multi-scale group of nonlinear damping plane waves propagating along the x axis at the sound velocity for the elastic precursor.

In a reference system connected to the elastic precursor new wave variables are introduced

$$\zeta = t - \frac{x}{C}, \xi = x; \quad \tau\frac{\partial}{\partial\zeta} << \varepsilon\frac{\partial}{\partial\xi}$$

The mass and momentum balance equations in new variables take a form

$$\frac{\partial\rho_1}{\partial\zeta} - \frac{\rho_0}{C}\frac{\partial\nu}{\partial\zeta} + \frac{\varepsilon}{\tau}\frac{\partial\rho_0\nu}{\partial\xi} = 0 \tag{1}$$

$$\frac{\partial\rho_0\nu}{\partial\zeta} - \frac{\rho_0}{C}\frac{\partial\Pi}{\partial\zeta} + \frac{\varepsilon}{\tau}\frac{\partial\rho_0\Pi}{\partial\xi} = 0 \tag{2}$$

According to the nonlocal theory [1-2] longitudinal stress tensor component is Π expressed as an integral

$$\begin{aligned}\Pi = C\nu = -\int_0^{C_t} d\xi' \int_0^{\omega} R(\zeta,\zeta')\delta(\zeta,\zeta')\left[-\frac{1}{C}\frac{\partial C\nu}{\partial\zeta'} + \frac{\varepsilon}{\tau}\frac{\partial C\nu}{\partial\xi}\right]d\zeta' = \\ = C\int_0^{\omega} R(\zeta,\zeta')\left[\frac{\partial\nu}{\partial\zeta'} + \frac{\varepsilon}{\tau}\frac{\partial\nu}{\partial\xi}\right]d\zeta', \;\; \omega(\zeta) = \begin{cases}\zeta, & \zeta < 1\\ 1, & \zeta \geq 1\end{cases}\end{aligned} \tag{3}$$

Nonequilibrium correlation function determining the collective interaction effects on the macroscopic medium response to an intensive external loading is used

$$R(\zeta,\zeta';\tau) = exp\left[-\frac{\pi(\zeta-\zeta'-\theta)^2}{\tau^2}\right], \;\; \theta - the\ model\ parametr \tag{4}$$

Eqs(1) -(3) under the condition $\frac{\varepsilon}{\tau} << 1$ take a form

$$\nu - \int_0^{\omega} R(\zeta,\zeta';\tau)\frac{\partial\nu}{\partial\zeta'}d\zeta' = 0 \tag{5}$$

An approximate solution to Eq (5) had been obtained by iteration method [2]. Supposing the strain-rate during the shock to be constant $\frac{\partial\nu}{\partial\zeta} = \kappa$ one can get an explicit form of the solution in the 1-st iteration.

$$\Pi = C\begin{cases}\frac{\kappa\tau}{2}\left(erf\frac{\sqrt{\pi}(\zeta-\theta)}{\tau} + erf\frac{\sqrt{\pi\theta}}{\tau}\right), & \zeta < 1\\ \frac{\kappa\tau}{2}\left(erf\frac{\sqrt{\pi}(\zeta-\theta)}{\tau} + erf\frac{\sqrt{\pi}(1-\zeta+\theta)}{\tau}\right), & \zeta \geq 1\end{cases} \tag{6}$$

The calculated longitudinal stress (6) depends on strain at the initial elastic regime and on strain-rate at final hydrodynamic stage. In the transition regime in between the elastic and hydrodynamic limits the stress depends simultaneously both on strain and strain-rate 3. In this case the solution depends also on the loading conditions and initial medium parameters. Information on the shock parameters and the medium state written down in the shape of the non-stationary wave front has been obtained.

Retardation parameter θ corresponds to maximum of the plastic front and relaxation parameter τ connected to the elastic precursor amplitude.

$$h = exp(-\frac{\pi\theta^2}{\tau^2})$$

3 Back front based on inertia process

In conventional models of shock-induced wave propagating in solid the back front is ignored as far as the impactor considers being semi-infinite. Supposing the stress to be constant after the maximum point for a finite time until the unloading wave comes one can include the inertia effects depending on the impactor's length. The waveforms for the mass velocity for different values of the relaxation τ, and retardation θ parameters are presented on Fig.1-2

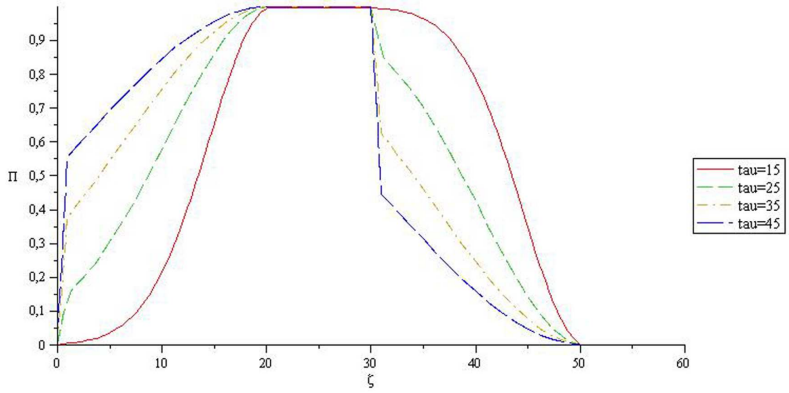

Figure 1: Waveforms for different relaxation parameters τ at fixed $\theta = 20$

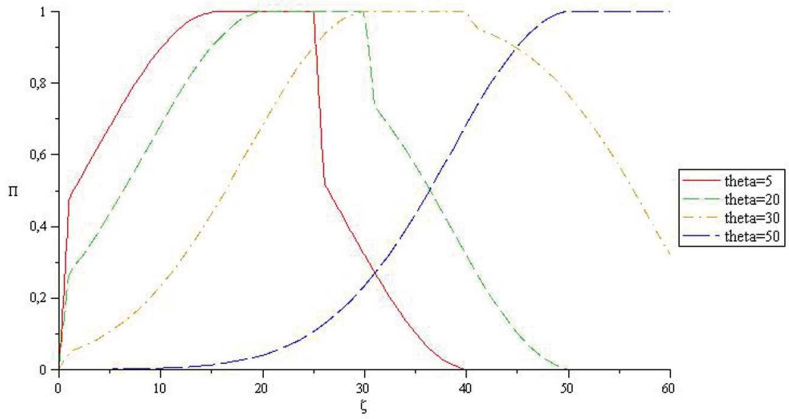

Figure 2: Waveforms for different relaxation parameters θ at fixed $\tau = 20$

4 Back front based on relaxation process

If we consider relaxation process to take place immediately after the maximum of the plastic front without the inertia effects then unloading should subtracted from relaxing velocity profile. The waveforms for the mass velocity for different values of the relaxation τ, and retardation θ parameters are presented on Fig.3-4

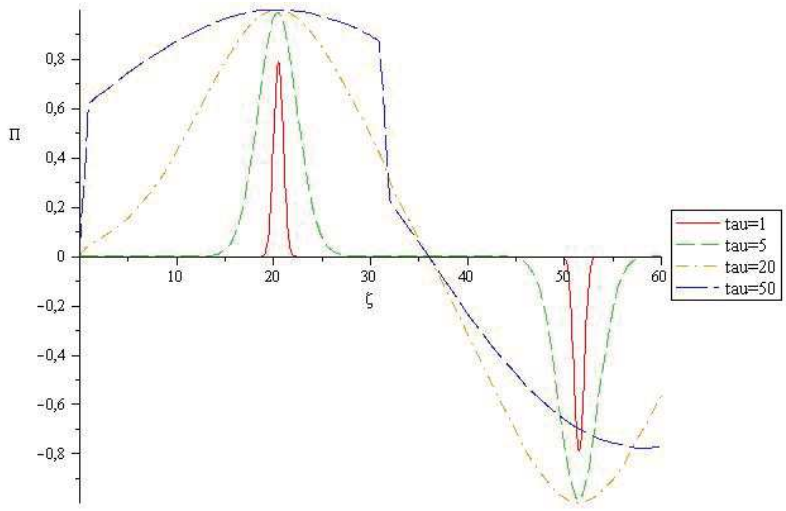

Figure 3: Waveforms for different relaxation parameters τ at fixed $\theta = 20$

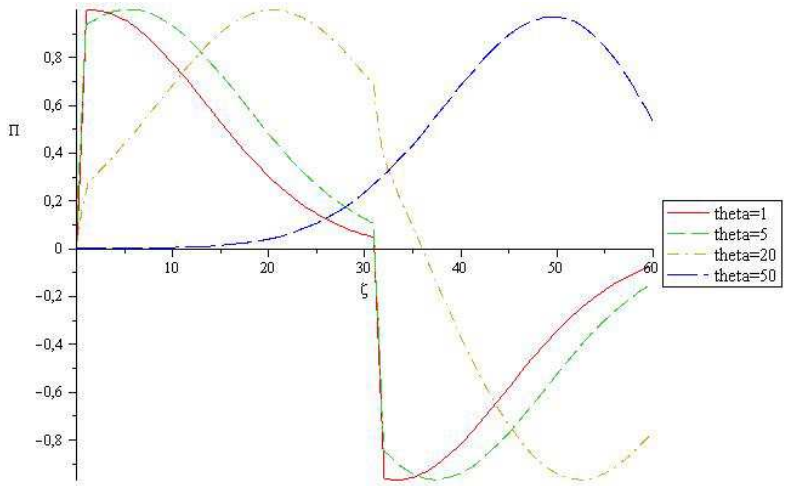

Figure 4: Waveforms for different relaxation parameters θ at fixed $\tau = 30$

5 Internal structure evolution and adaptive control with feedback

The nonlocal model parameters evolve according to the adaptive control theory [4]. Goal function - minimum of the integral entropy production in the wave.

$$\frac{\partial S}{\partial \xi} = \rho_0 C \int_0^\infty \frac{\partial \nu}{\partial \zeta}(\zeta, \xi) \int_0^\infty exp\left[-\frac{\pi(\zeta - \zeta' - \theta(\xi))^2}{\tau(\xi)^2}\right] \frac{\partial \nu}{\partial \zeta'}(\zeta', \xi) \partial\zeta' \partial\zeta \tag{7}$$

Speed gradient algorithm determines the parameters evolution on the integral entropy production surface. According to the evolution equation the model parameters tend to move down the surface along the speed gradient trajectories to reach stable state.

The structure evolution is connected to the nonstationary mass velocity waveforms by feedback through the model parameters. As a result a change of dynamical properties of a medium occurs. Integral entropy production surface with descending trajectories in case

of the back front based on inertia process and based on the relaxation process is presented on Fig.4-5 respectively.

The negative entropy values correspond to the energy storied in the medium after the wave front propagation.

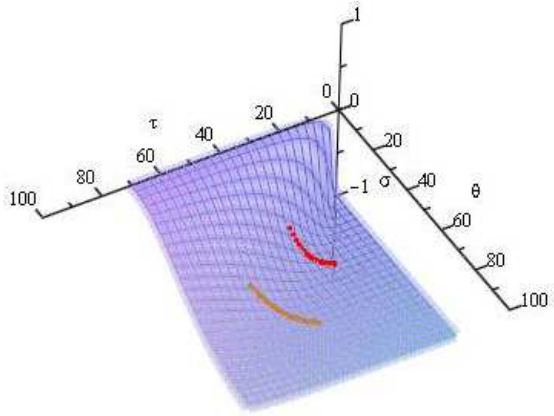

Figure 5: Entropy production surface and trajectories descending from the points (tau47=;theta=31) and (tau=25;theta=16)

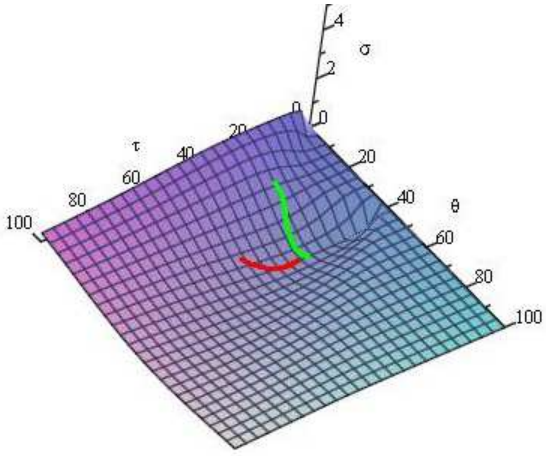

Figure 6: Entropy production surface and the trajectories descending from points (tau47=;theta=31) and (tau=25;theta=16)

6 Projection of descent trajectories on the parameters plane

On the plane (τ-θ) one can see that direction of the waveform evolution depends on the back front conditions.

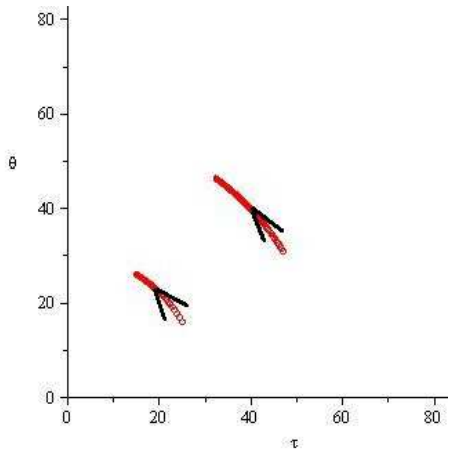

Figure 7: Projection of descent trajectories from points (tau=47;theta=31) and (tau=25;theta=16)in case of the back front based on the inertia effects

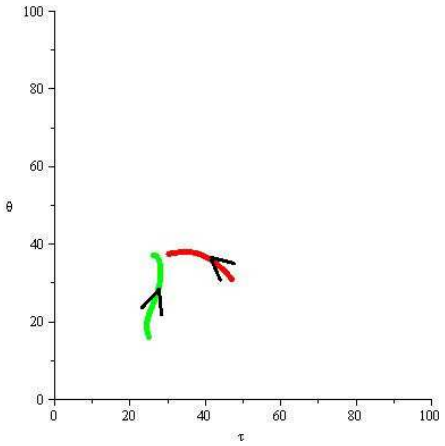

Figure 8: Projections of descent trajectories from points (tau=47;theta=31) and (tau=25;theta=16) in case of the back front based on the relaxation effects

7 Conclusion

A comparison of the obtained results based on the nonlocal model with experimental data for the shock loading of solids (5) shows that the real waveforms differ from the both situations considered above at the same parameters (Fig. 8). The real velocity profile has a plateau lower than in the inertia case but the unloading begins as in the relaxation case. It means that in the real process both effects take place. At present it is not clear what a mechanism is responsible for the plateau formation. It is possible that it is connected to the momentum exchange at mesoscale.

References

[1] Khantuleva T.A. The shock wave as a nonequilibrium transport process // "High-pressure compression of solids VI: old paradigms and new challenges"(Y.Horie,

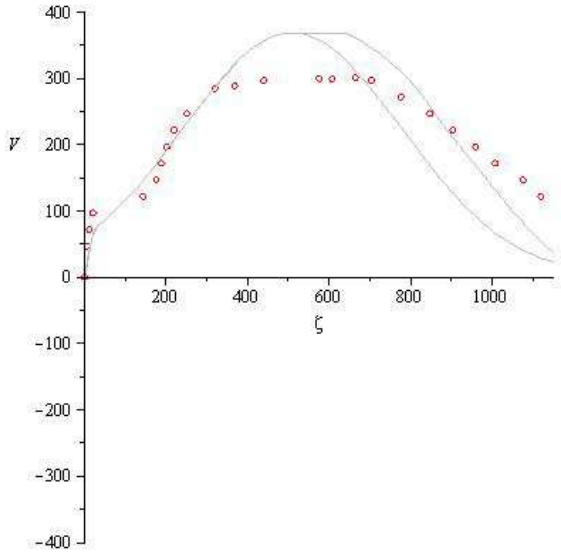

Figure 9: Experimental data and approximate solutions in 2 cases

L.Daison, N.N.Thadhani, Eds.). Berlin. Springer. 2003. P215-254.

[2] Khantuleva T.A. Chemical Physics. 2005. Vol.24. N.11. P36-47.

[3] Khantuleva T.A.,Litvinov A.V. Effect of strain rate on the plastic properties of solids. // Proc. of the conf. Part 2. P309-312.

[4] Khantuleva T.A. //. Proc. the 2nd International Conference "Physics and Control 2005" IEEE 05EX1099C ISBN 0-7803-9235-3.05. P 41.

[5] Yu.I. Meshcheryakov, A.K. Divakov, N.I. Zhigacheva, I.P. Makarevich, B.K. Barakhtin. //Dynamic sttructures in shock loaded copper.// Physical Review B Vol.78, p.064301-064318, (2008).

T.A. Khantuleva, Saint-Petersburg, Russia
A.V. Litvinov, Saint-Petersburg, Russia

Ratchetting of spherical vessels

H. Mahbadi M. R. Eslami
h_mahbadi@iauctb.ac.ir

Abstract

In this paper, cyclic loading behavior of thick spherical vessels under mechanical and thermal cyclic loads is investigated. The kinematic hardening theory based on the Chaboche model with von Mises associated flow rules is used to predict the ratcheting, reverse plasticity, or shakedown behavior of the vessel. Results based on this model are compared with the Armstrong-Frederick model. A numerical iterative method is proposed and used to analyze the structural behavior under cyclic loading condition.

1 Introduction

Cyclic loading behavior of structures is related to the developed stress category imposed by cyclic loads. Due to the ASME boilers and pressure vessel code [1], the sum of primary and secondary stresses are responsible for ratchetting or shakedown behavior of structures. According to this code, a primary stress is a normal or shear stress developed by the imposed loading which is necessary to satisfy the simple laws of equilibrium of external and internal forces and moments. The basic characteristic of the primary stress is that it is not self-limiting. A secondary stress is a normal or shear stress developed by the constraint of the adjacent structure. The basic characteristic of the secondary stress is that it is self-limiting. Eslami and Shariyat[2] proposed a technique to distinguish the primary and secondary stresses. Eslami and Mahbadi, [3, 4] classified the cyclic loading of structures to load controlled and deformation controlled types. They showed that the load controlled cyclic loading of structures results to ratchetting, while the deformation controlled cyclic loading of structures result into shakedown behavior.

Accurate prediction of ratchetting and shakedown behavior may depend on the hardening model assumed to obtain the results. The bilinear Prager [5] model, cannot represent the experimental hysteresis curve during the initial nonlinear part. Multilinear and nonlinear kinematic hardening models are two categories of models which are utilized to improve linear kinematic hardening model. A number of multilinear models, such as Mroze [6] and Besseling [7], which are proposed to improve the linear kinematic hardening model are used by Bari [8] to investigate the cyclic loading behavior of structures. All these models divide the uniaxial stress-strain curve into many linear segments. Armstrong and Frederick [9] introduced a kinematic hardening rule containing a 'recall' term which essentially makes the stress-strain curve nonlinear in nature. This model attempts to simulate the experimental stress-strain curve by a single exponential equation and since this curve is not essentially exponential in nature, the model does not yield a good fit. To improve the model, a series of nonlinear models, such as Chaboche [10, 11] and Guionnet [12] models, are proposed which utilize several superposed Armstrong-Frederick models.

In this article, the Chaboche kinematic hardening model with three decomposed Armstrong-Frederick model is used to evaluate cyclic loading behavior of thick spheri-

cal vessels under various mechanical and thermal loads. The vessel's material is assumed to be isotropic and homogeneous and obey a nonlinear strain hardening law in the plastic range. Results obtained using the Chaboche model are compared with those obtained using the proposed method in Ref. [13] for Armstong-Frederick model. Since the Chaboche model needs six material constants to model the stress-strain curve, more accurate results are expected compared to the Armstrong-Frederick model.

2 MATHEMATICAL FORMULATION

Consider a thick spherical vessel of inside radius a and outside radius b, under internal and external pressures p_i and p_o and radial temperature distribution $T(r)$. The axisymmetric condition is assumed for the thick sphere. The following differential equations together with the stress-strain relations and incompressibility conditions for plastic deformation in the spherical coordinates are solved to obtain the thermoelastic-plastic stress and strain distributions in the thick sphere. The dimensionless quantities are:

$$\begin{array}{llllll} S_r = \frac{\sigma_r}{\sigma_0} & S_\theta = \frac{\sigma_\theta}{\sigma_0} & S_\phi = \frac{\sigma_\phi}{\sigma_0} & e_r = \frac{\epsilon_r}{\epsilon_0} & e_\theta = \frac{\epsilon_\theta}{\epsilon_0} & e_\phi = \frac{\epsilon_\phi}{\epsilon_0} \\ e_r^p = \frac{\epsilon_r^p}{\epsilon_0} & e_\theta^p = \frac{\epsilon_\theta^p}{\epsilon_0} & e_\phi^p = \frac{\epsilon_\phi^p}{\epsilon_0} & e_r^{Res} = \frac{\epsilon_r^{Res}}{\epsilon_0} & e_\theta^{Res} = \frac{\epsilon_\theta^{Res}}{\epsilon_0} & e_\phi^{Res} = \frac{\epsilon_\phi^{Res}}{\epsilon_0} \\ p_i = \frac{P_i}{\sigma_0} & p_o = \frac{P_o}{\sigma_0} & \tau = \frac{E\alpha T}{(1-\nu)\sigma_0} & \rho = \frac{r}{a} & \beta = \frac{b}{a} & \end{array}$$

where $\sigma_r,\ \sigma_\theta$, and σ_ϕ are the radial, tangential, and meridian stresses, respectively. Similarly, $\epsilon_r,\ \epsilon_\theta,\ \epsilon_\phi$ are the total strains, $\epsilon_r^p,\ \epsilon_\theta^p,\ \epsilon_\phi^p$ are the plastic strains, and $\epsilon_r^{Res},\ \epsilon_\theta^{Res},\ \epsilon_\phi^{Res}$ are the residual strains in the radial, tangential, and axial directions, respectively, σ_0 is the yield stress and ϵ_0 is the yield strain. The Poisson's ratio is denoted by ν. The inclusion of the residual strains in the stress-strain relations is unique and important, as the relations are capable to be used for the cyclic loading analysis. The equilibrium equation is:

$$\frac{dS_r}{d\rho} = \frac{2(S_\theta - S_r)}{\rho} \tag{1}$$

The compatibility equation is:

$$\frac{de_\theta}{d\rho} = \frac{e_r - e_\theta}{\rho} \tag{2}$$

From the spherical symmetry

$$S_\theta = S_\phi \tag{3}$$

From the incompressibility condition The boundary conditions are:

$$\begin{aligned} \sigma_r(1) &= -p_i \\ \sigma_r(\beta) &= -p_o \end{aligned} \tag{4}$$

$$e_r^p = -2e_\theta^p \tag{5}$$

The same relation exist between the residual strains, provided the previous load cycles are spherically symmetric

$$e_r^{Res} = -2e_\theta^{Res} \tag{6}$$

Solving the governing equations, the radial and tangential stresses are

$$S_r = \frac{1}{1-\nu}\int_1^\rho \frac{e_r^p}{\rho}d\rho + \frac{1}{1-\nu}\int_1^\rho \frac{e_r^{Res}}{\rho}d\rho - \frac{2}{\rho^3}\int_1^\rho \tau\rho^2 d\rho + \frac{C_2}{\rho^3} + C_1 \tag{7}$$

$$S_\theta = \frac{1}{1-\nu}\int_1^\rho \frac{e_r^p}{\rho}d\rho + \frac{e_r^p}{2(1-\nu)} + \frac{1}{1-\nu}\int_1^\rho \frac{e_r^{Res}}{\rho}d\rho + \frac{e_r^{Res}}{2(1-\nu)} + \frac{1}{\rho^3}\int_1^\rho \tau\rho^2 d\rho - \tau - \frac{C_2}{2\rho^3} + C_1 \tag{8}$$

where the constants of integration are given as

$$C_1 = -p_i - C_2$$

$$C_2 = \frac{\beta^3}{\beta^3-1}(p_o - p_i) - \frac{1}{1-\nu}\int_1^\beta \frac{e_r^p}{\rho}d\rho - \frac{1}{1-\nu}\int_1^\beta \frac{e_r^{Res}}{\rho}d\rho - \frac{2}{\rho^3}\int_1^\beta \tau\rho^2 d\rho \tag{9}$$

3 Hardening Model

Different kinematic hardening models are available for the plastic analysis of structures. The Prager [5] kinematic hardening model is proposed for the linear strain hardening materials. The Frederick and Armstrong [9] modified the Prager model so that the transformation of yield surface in the stress space is different during loading and unloading. Chaboche [10, 11] proposed a model which was composed from three Frederick-Armstrong models. Based on this assumption better approximation can be found for the uniaxial stress-strain curve. The von Mises yield criterion for the kinematic hardening model is in the following form:

$$f(\sigma_{ij} - \alpha_{ij}) = [\frac{3}{2}(s_{ij} - a_{ij}) \cdot (s_{ij} - a_{ij})]^{\frac{1}{2}} = \sigma_0 \tag{10}$$

where σ_{ij} and α_{ij} are the stress and back stress tensors, and s_{ij} and a_{ij} are the stress and back stress deviatoric tensors in the stress space. The flow rule to obtain the plastic strain components increment is defined as follow:

$$d\epsilon_{ij}^p = \frac{1}{H} < \frac{\partial f}{\partial \sigma_{ij}} \cdot d\sigma_{ij} > \frac{\partial f}{\partial \sigma_{ij}} \tag{11}$$

where in Eq. (5) H is the plastic modulus. The back stress tensor in the Armstrong-Frederick model is defined as follow:

$$da_{ij} = \frac{2}{3}C d\epsilon_{ij}^p - \gamma a_{ij}\,|d\epsilon_p| \tag{12}$$

where C and γ are material constants for the Armstrong-Frederick model. The back stress tensor in the Chaboche model is defined by the following equation:

$$da_{ij} = \sum_{i=1}^{3}(\frac{2}{3}C_i d\epsilon_{ij}^p - \gamma_i a_{ij}^i\,|d\epsilon_p|), \quad i = 1\ldots 3 \tag{13}$$

In this equation a^i are the back stress tensors for the Frederick-Armstrong kinematic hardening models, C_i and γ_i are the material constants for these models which are found

from the experimental tests and best fit the uniaxial stress-strain curve. The equivalent plastic strain and equivalent stress are defined as:

$$|d\epsilon_p| = \sqrt{\frac{2}{3} d\epsilon_{ij}^p d\epsilon_{ij}^p} \tag{14}$$

$$|\sigma_e| = \sqrt{\frac{3}{2} s_{ij} s_{ij}} \tag{15}$$

4 Numerical Method

Due to the complexities incurred by the assumed kinematic hardening theories, the proposed method is quite capable and unique to handle the cyclic loading calculations. This method may be used for the analysis of uniaxial as well as multiaxial state of loadings. Solution procedure is as follow: 1 - The elastic analysis of structure is obtained and the critical load to bring the structure to plastic yielding is calculated. 2 - The difference of the final and critical load is divided into steps. 3 - The accumulated plastic strain for the first increment of load in the plastic region is set to zero. 4 - A value is assumed as the first guess for the current value of equivalent plastic stain. 5 - Calculate the current value of the plastic strain, using the flow rule. 6 - Calculate the total plastic strain ϵ_{ij}^p. 7 - Calculate the increment of current value of back stress tensor Δa_{ij}. 8 - Calculate the total value of the back stress tensor a_{ij}. 9- Calculate the stress components from the solution of the differential equations using the current value of the assumed plastic strain components. 10 - Calculate the new values of the current plastic components with stress components found from step 9, using the flow rule. 11 - Calculate a new value for the current increment of the equivalent plastic strain. 12 - Repeat the procedure from step 5 through 11, until the current value of the increment of equivalent plastic strain converges. 13 - Add the converged value of the increment of current equivalent plastic strain to the accumulated plastic strains. 14 - The load is increased one step and the procedure is repeated from step 4 through 14, until the final value of load is reached. For unloading, we may define two different coordinate axes showing the loading and unloading behavior of the structure. A coordinate system is initially fixed at the origin, showing the loading curve. At the end of the loading curve, we may fix the second coordinate system with opposite coordinate directions showing the unloading curve. In the second coordinate system the effective stress, as the result of unloading, is always positive and is increasing. The final residual stresses are obtained by adding up the stresses in the second coordinate system to those in the first system, where proper change of sign are considered (Jiang [14]). It should be noted that if during loading the value of $d\epsilon_p$ is negative, then $|d\epsilon_p|$ in Eqs. (6) and (7) is equal to $-d\epsilon_p$.

5 Results and Discussion

To check the numerical algorithm, results obtained from the proposed numerical method are compared with the uniaxial test of Hassan [15]. The Chaboche kinematic hardening model is used for uniaxial cyclic loading of $CS1026$ material. The specimen material data are: modules of elasticity $E = 181\ GPa$, yield stress $\sigma_0 = 131 MPa$, Poisson's ratio, $\nu = 0.3$, thermal expansion coefficient $\alpha = 10.8E-6\ ^oC^{-1}$. Due to the reports given by Hassan [14] on uniaxial cyclic loading of $CS1026$, Bari [8] proposes the following values for the Chaboche model: $C_1 = 413.4$, $C_2 = 88.6$, $C_3 = 3.14\ GPa$, and $\gamma_1 = 20000$, $\gamma_2 = 800$, $\gamma_3 = 9$. Figure (1) shows axial stress versus axial strain and as it may be seen from

this figure, close agreement with the experimental data is obtained using the Chaobche model. Axial strain range of stress-strain hysteresis loop is -1% to 1%. In the next

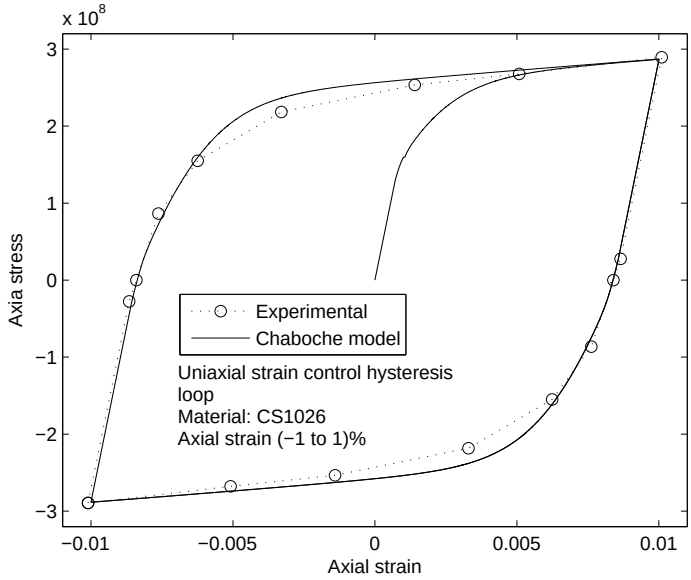

Figure 1: Comparison the experimental uniaxial hysteresis loop with the Chaboche model

example a thick sphere made of $CS1026$ material, with the ratio of outside to inside radius $b/a = 1.5$, and the same data of the first example is considered. The inside pressure of the thick sphere is cycled between 0 to 300 MPa. Figure (2) shows normalized equivalent stress versus normalized equivalent strain at inside surface of the thick cylinder, using the Chaboche kinematic hardening model. The yield pressure, where the inside surface yields, is $P_c = 114\ MPa$. The mean pressure cycle is $P_m = 150\ MPa$. The figure shows ratchetting for inside pressure cyclic loading of the thick sphere. The same thick sphere under thermal cyclic loading is considered in the next example. The inside temperature cycle is ($T_i = 0$ to 380^oC, $T_o = 0$). The mean inside temperature is $T_m = 180^oC$ and the inside temperature which brings the inside surface to yield is ($T_c = 144^oC$). Figure (3) shows the plot of normalized stress versus normalized strain at inside surface of the thick sphere and transient ratchetting to reversed plasticity behavior is obtained as it may be seen from this figure. The case where the thick sphere experiences cyclic pressure of ($P_i = 220\ MPa$, $P_o = 0$) and ($P_i = 0$, $P_o = 80\ MPa$) is the next example. In this case, the thick sphere is under nonproportional inside and outside pressure cyclic loadings. The behavior of normalized equivalent stress versus equivalent strain at inside surface of the sphere is shown in Fig. (4), where ratchetting to reversed plasticity is observed. The same problems (1) through (4) are solved using the Armstrong-Frederick kinematic hardening model and the results are shown in figures (5) through (8). According to the experimental data of Hassan [12], the Armstrong-Frederick model parameter which are used in cyclic loading simulation of the structures made of CS1026 material are as follow in this paper: $C = 47\ GPa$, $\gamma = 280$. Comparing plots of Fig. (5) with Fig. (1) shows that more accurate results are obtained for the stabilized hysteresis loop under uniaxial cyclic loading using the Chaboche model rather than the Armstrong-Frederick model. Comparing results of Fig. (6) with Fig. (2) shows that both models predict ratchetting behavior for cycling of mechanical loads, while the Armstrong-Frederick model

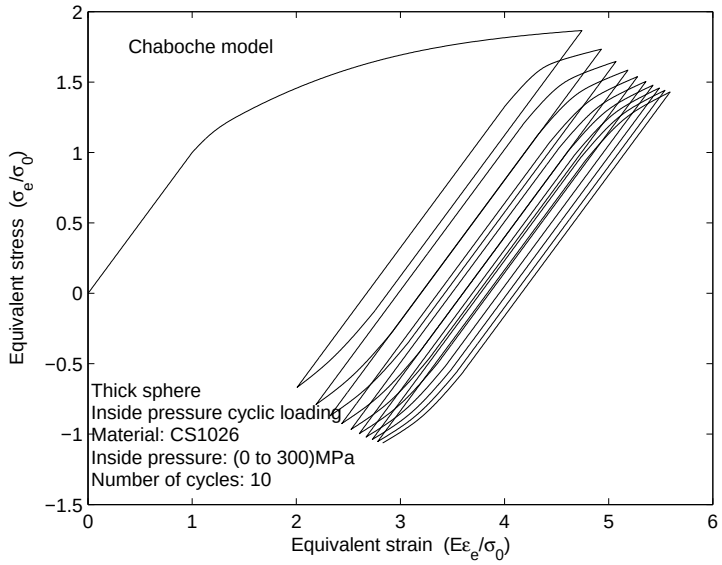

Figure 2: Inside pressure cyclic loading of thick sphere based on the Chaboche kinematic hardening model

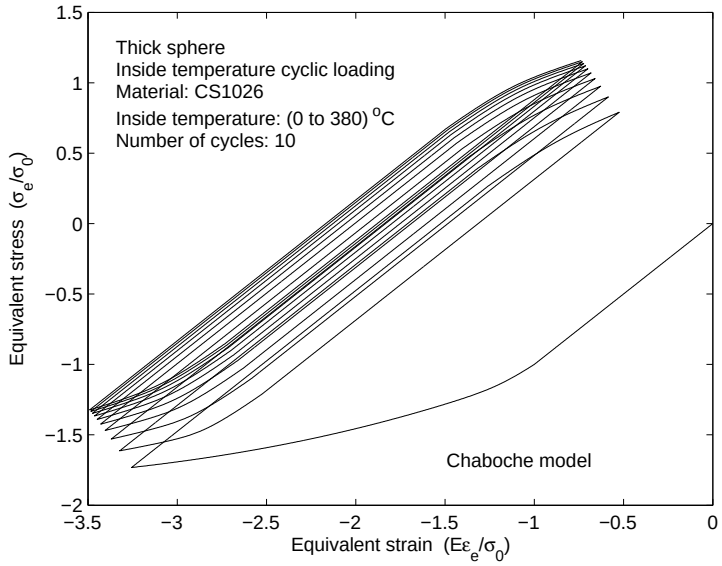

Figure 3: Inside temperature cyclic loading of thick sphere based on the Chaboche kinematic hardening model

over predicts the ratchetting behavior with respect to the Chaboche model. Figure (7) shows ratchetting to reversed plasticity (shakedown) for cyclic loading of thermal loads using the Armstrong-Frederick model. The same results are obtained , As discussed in Fig. (3). Comparing the ratchetting rate of both models, shows that the ratchetting rate in transient part is larger using the Armstrong-Frederick model with respect to the Chaboche model.

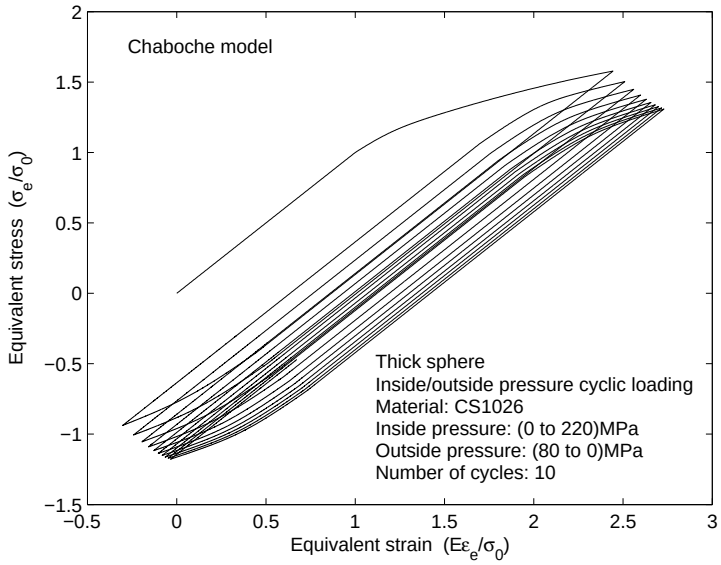

Figure 4: Inside, outside pressure cyclic loading of thick cylinder based on the Chaboche kinematic hardening model

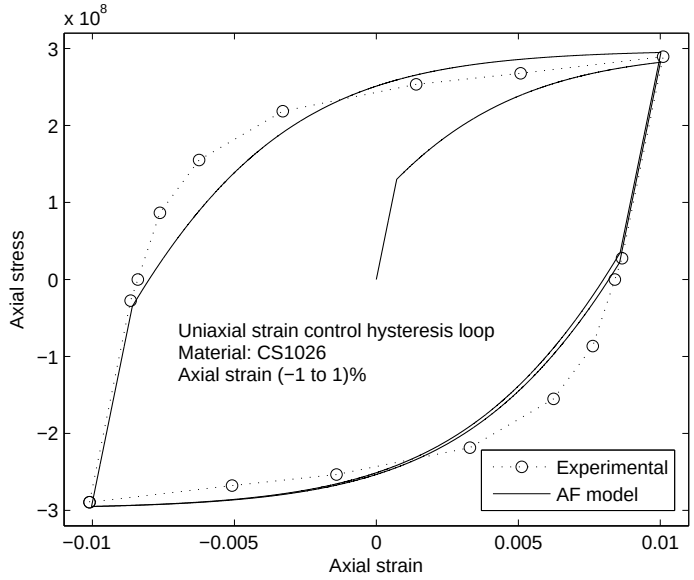

Figure 5: Comparison the experimental uniaxial hysteresis loop with the Armstrong-Frederick model

Finally, as it may be seen by comparing the results of Fig. (8) using the Armstrong-Frederick model with those which are obtained in Fig. (4), the Armstrong-Frederick model over predicts ratchetting behavior of a thick sphere under nonproportional mechanical cyclic loading with respect to the Chaboche model. Comparing the ratchetting rate of both models, shows that the ratchetting rate in transient part is larger using the Armstrong-Frederick model with respect to the Chaboche model.

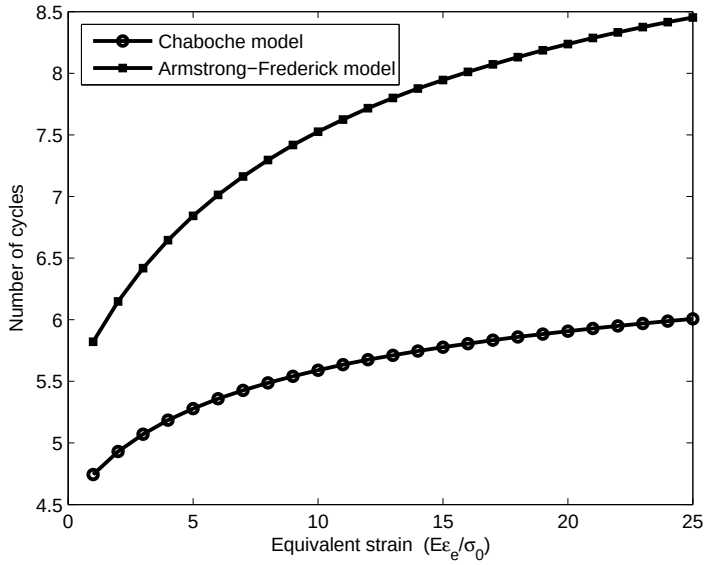

Figure 6: Comparison the inside pressure cyclic loading behavior of thick sphere using A-F and Chaboche models

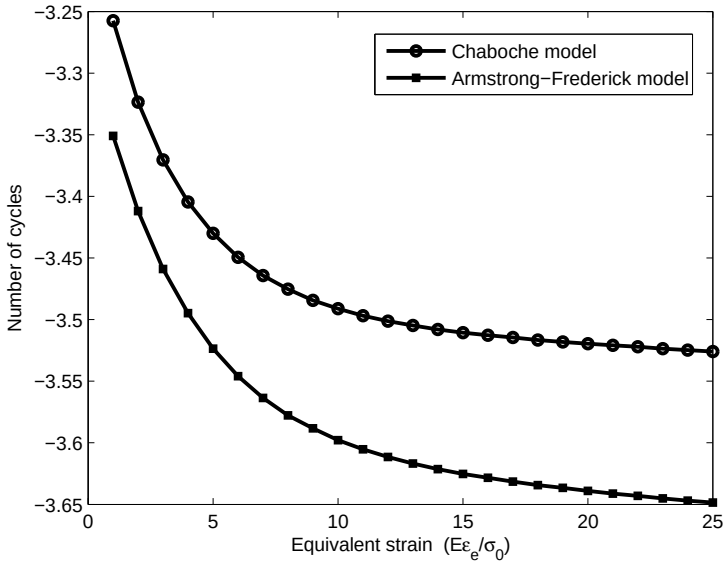

Figure 7: comparison the inside temperature cyclic loading behavior of thick sphere based using A-F and Chaboche models

6 Conclusion

In this article, the cyclic loading behavior of thick spherical vessels under different types of mechanical and thermal loads is obtained. The Armstrong-Frederick and Chaboche kinematic hardening models are employed to evaluate the results of cyclic loadings. It is concluded that when the vessel is subjected to the cyclic mechanical loads, both models

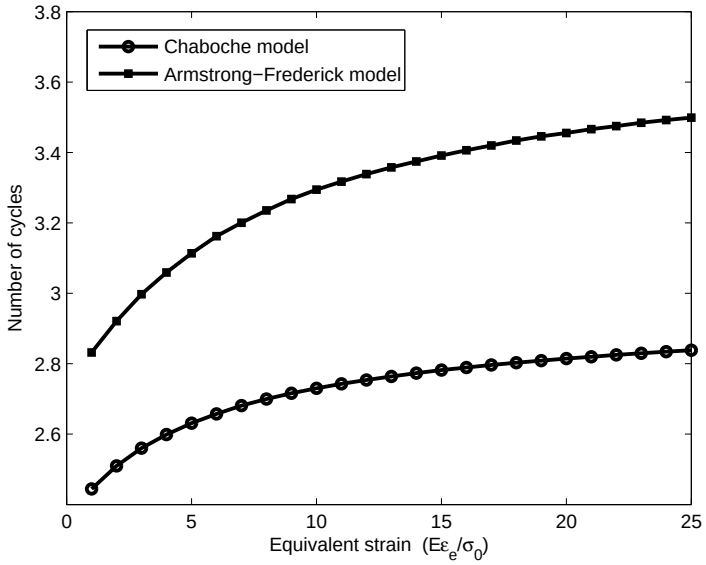

Figure 8: Comparison the inside, outside pressure cyclic loading of thick sphere using A-F and Chaboche models

predict ratchetting behavior while, the Armstrong-Frederick model over predicts the ratchetting rate. On the other hand when the vessel is subjected to the thermal cyclic loads, both models predict ratchetting to reversed plasticity behavior, while the Armstrong-Frederick model predicts larger ratchetting rate in transient part of cyclic loading with respect to the Chaboche kinematic hardening model. Verification of experimental data for uniaxial test shows that more accurate result obtains using the Chaboche model rather than Armstrong-Frederick model, since Chaboche model needs six parameter in comparison with the Armstrong-Frederick model which needs two parameters. This specification makes the longer simulation time for the Chaboche model with respect to the Armstrong-Frederick model, due to the complexity of the Chaboche model.

References

[1] ASME Boiler and Pressure Vessel Code, Article 4-1, "Terms relating to stress analysis", Section VIII, Division 2, American Society of Mechanical Engineers, New York, NY., 1998 Edition.

[2] Eslami, M.R., and Shariyat, M., A Techinque to Distinguish the Primary and Secondary Stresses, ASME Journal of Pressure Vessel Technology, Vol. 117, pp. 1-7, August 1995.

[3] Mahbadi, H., and Eslami, M.R., Cyclic Loading of Beams Based on the Prager and Frederick-Armstrong Kinematic Hardening Models, International Journal of Mechanical Sciences, Vol. 44, pp. 859-879, 2002.

[4] Mahbadi, H., and Eslami, M.R., Cyclic Loading of Thick Vessels Based on the Prager and Armstrong-Frederick Kinematic Hardening Model, IMechE, International Journal of Pressure Vessels and Piping, Vol. 83, pp. 409-419, 2006.

[5] Prager, W., A New Method of Analyzing Stresses and Strains Work-Hardening Plastic Solids, Journal of Applied Mechanics, pp. 493-496, December 1956.

[6] Mroz, Z. On the Description of Anisotropic Work Hardening, J. of the Mechs and Phys of Solids, Vol. 15, pp. 163-175, 1967.

[7] Besseling, J.F., A theory of elastic, plastic and creep deformations of an initially isotropic material. J. of Appl. Mechs. Vol. 25, pp. 529-536, 1958.

[8] Bari, S. and Hassan, T., Anatomy of coupled constitutive models for ratchetting simulation, Int. J. of Plasticity, Vol. 16, pp. 389-409, 2000.

[9] Armstrong, P.J. and Frederick, C.O., "A Mathematical Representation of the Multiaxial Bauschinger Effect", CEGB Report No. RD/B/N 731, 1966.

[10] Chaboche, J.L., Dang-Van, K. and Cordier, G. Modelization of the Strain Memory Effect on the Cyclic Hardening of 316 Stainless Steel. Proceedings of the 5th International Conference on SMiRT, Div. L, Berlin, Germany, 1979.

[11] Chaboche, J.L. Time-Independent Constitutive Theories For Cyclic Plasticity. International Journal of Plasticity, Vol. 2, pp. 149-188, 1986.

[12] Guionnet, C. "Modeling of Ratchetting in Biaxial Experiments", Journal of Engineering Materials and Technology, Vol. 114, 1992, pp. 56-62.

[13] Eslami and Mahbadi, Cyclic loading of thick pressure vessels, Proceedings, Int. Conference on pressure vessel and piping, ICPVT11-AORC-F-022, 2006.

[14] Jiang, Y., and Sehitoglu, H., "Modeling of Cyclic Ratchetting Plasticity, Part I: Development of Constitutive Relations", Journal of Applied Mechanics, Vol. 63, pp. 720-725, 1996.

[15] Hassan, T. and Kyriakides, S., "Ratchetting in Cyclic Plasticity, Part 1: Uniaxial Behavior, International Journal of Plasticity", Vol. 8, pp. 91-116, 1992.

H. Mahbadi, ME Dept., Islamic Azad University, Central Tehran Branch, IRAN
M.R. Eslami, ME Dept., Amirkabir University of Technology, Tehran, IRAN

Relation between structural parameters and abrasion in multiphase matrix–cement materials

Natalya.V. Makarova
maknat@bk.ru

Abstract

Different series of cement-matrix materials have been investigated about correlation of their speci?c structural parameters — especially volumetric coast aggregate distribution — with GOST-13087 abrasion wear rates. For this study, the concrete surfaces after abrasion wear test have been characterized by structural parameters, such as mean inter-particle distance; mean coast aggregates diameter, its area fraction, and matrix hardness. To generate quantitative values for the inter-particle distances a particular method was developed. From regression analyses, it has become evident that wear effects arising from coast aggregate fraction, particle diameter and inter-particle distance surpass the influence of matrix hardness.

Introduction

In the modern projects of hydraulic engineering and transport reinforced concrete structures, sufficient attention should be given to the abrasion durability of concrete. Such abrasion causes loss of effective thickness and of constructive elements.

Another very important problem is how to provide requirements to abrasion strength characteristics of constructional building materials for maintenance of reliability and safety of hydraulic engineering constructions during the whole exploitation period.

The mechanics of friction interaction enables the analysis of wear failure process and phenomena which occur in friction interaction of moving components resulting in the energy and material losses in constructions. It allows determining serviceability of a construction during its destruction. Application of theoretical and experimental contact mechanics methods to an estimation of strength and durability of concrete constructions is hampered as against designs from metal, ceramics and other materials because of concrete structure singularities.

The model of wear failure process of concrete due to sea ice is developed in [1, 2]. In those papers the process of destruction is divided into 3 stages. But the structure of concrete is not taken into account.

Concrete is a stochastically heterogeneous material with brittle cement stone matrix. Thus the softening near-surface layer zone attains the considerably size. Different models can predicts that its abrasion strength depend on technological, physical and geometrical characteristics of concrete mix. But only experimental researches support and specify these theoretical predictions.

1 Modelling for Wear Failure of Concrete

A simple model for wear failure of concrete is proposed thus, takes into account heterogeneity of material at micro-, meso- and macro-levels. To consider the modeled process of destruction the following hypotheses are accepted: mechanical forces of friction are considered only; adhesive is ignored, and erosive deterioration is ignored too.

Let's consider wear process of a concrete surface at various structural levels. Thus the choice of criteria of destruction is difficult; therefore the wear can be divided into the following stages:

Stage 0 — the new stage. Near-surface layer is submitted by the following structural components: a surface of concrete; a grain of a coarse aggregate; solvation sphere of a coarse aggregate; a fine grain; solvation sphere of a fine grain; the hardened cement paste.

Stage I — the initial stage. In this stage of the wear process: the abrasion of solvation sphere of fine grains; the destruction of solvation sphere of fine grains; the abrasion of a surface of fine grains. At a micro-level only the cement-sand stone is wear out by break of bonding between cement paste and a fine grain.

Stage II — the normal operating stage. In this stage of the wear process: the abrasion of coarse aggregates surface; the abrasion of a cement-sand stone surface. In meso-level the grains surface of a coarse aggregates and the cement-sandy stone between them is abraded. As soon as volumetric degradation (softening) of near-surface layer zone of concrete is beginning, the stage II is finished.

Stage III — the destruction stage. Two cases of destruction near-surface layer zone of concrete are possible. The case 1 is characteristic for concrete which includes a fragile cement-sandy stone. In this stage of the wear process: the volumetric degradation (softening) of cement-sand stone; the shaking and falling of coarse aggregates grains. The case 2 is characteristic for concrete which includes a strong cement-sandy stone. In this stage of the wear process: the fatigue macrocrack propagates on border between a coarse aggregates grains and a cement-sand stone.

In a stage I modeling is not difficult; concrete can be accepted as homogeneous solid. The wear rate can be presented as dW/dt , which depends from speed V, pressure p, materials hardness H and also from the parameters having certain value for each mechanism of wear process and used for its studying model.

Stage I is finished, when a grains of coast aggregates is exposed on surface. The materials hardness H is different for coarse aggregate and a cement-cand stone, therefore the application of previous model to stage II incorrectly. In a stage II the wear process should be considered simultaneously on micro- and meso-levels. At a meso-level there is a abrasion of coarse aggregates surface. At a micro-level there is a destruction of a cement-sand matrix, it results in change of the form of a surface.

In [4] the model of a surface with the strengthened areas [3] is used for modeling of concrete surfaces wear process. The surface of concrete can be presented as elastic half-space with the area, in which strengthened inside circular areas of the radius r, in nodes of a square mesh with step l. The parameter m characterizes a strengthening of surface as hardness relations between cement-sand stone and coarse aggregates grains. The parameter $a = r/l$ characterizes geometrical parameters of strengthening of a surface. By varying parameters m and a it is possible to optimize the concrete structure [5].

However, only experimental researches will allow estimating the degree of idealization of the accepted modelling parameters.

2 Experimental Procedure

Dependencies of concrete abrasion strength on technological parameters of a concrete mix are experimentally established. As varied factors are chosen: the volume fraction of coarse aggregate, volume fraction of silica and superplasticizer (4 series of samples). The maximal size of coarse aggregate, the water-cement ratio and the charge of cement were used for manufacturing of the testing specimens as a constant.

The test method meets the requirements of GOST 13087-81 [6]. Abrasion resistant is estimated as loss of weight at abrasion of concrete cubes on a rotating circle. The total way of the sample - 600 m, consists of 20 cycles on 30 m everyone. In addition the height of deterioration was determined.

After test the received surfaces of samples were investigated. Hardness of coarse aggregates and of each sample hardness of a cement-sand matrix was experimentally determined by use of Poldi device. The parameter of surface strengthening m has been certain as relation between average diameters of imprints on a reference bar at test accordingly matrixes and coast aggregate.

For definition of geometrical parameters the received surfaces have been photographed after tests. Quantitative image parameters (maximum and minimum diameter, area fraction and centroid coordinates) were determined by using the standard method of GetData.Graph.Digitizer.v.2.24 software and used for further statistical analysis. Statistical calculations were done with Statgraphics statistical package. In the described way, all relevant material parameters for wear loss in abrasive environment could be defined for each received surface. Correlation between abrasion (loss of weight and height of deterioration) and relevant structural parameters of received surfaces were investigated using multiple regression analysis.

3 Results and Discussion

Macrostructure analyses of typical concrete surface after abrasion test were carried out. Predominantly, the almost spherical sand particles are homogeneously distributed within the surface, but the distribution of polygonal coast aggregates particles is inhomogeneous. Quantitative wear rates on weight and height loss for the four series of samples are shown that the hardness of cement matrix depends from silica and superplasticizer volume fractions.

Statistical analysis was used in this study to determine linear effects and regressions coefficients of the quantitative image parameters on the abrasive wear resistance predicted by model [4, 5]. Two dependent parameter models (loss of weight and height of deterioration) were considered for the fourteen variables (hardness, area fraction, diameter, inter-particle distance and their parities). It has to be pointed out that these variables are not independent; however, for simplification of modelling they were set independent. Variance and regression coefficients for any of the linear functions are documented.

The parameter model based on total area fraction shows with p-value = 0,029 higher correlation than the model based on equivalent particle diameter with p-value = 0,10. It means that wear resistance can be much more addressed to particle area fraction than to equivalent diameter. The model based hardness shows the low fitting with p-value = 0,126. The model based on inter-particle distance shows the lowest fitting with p-value = 0,51. Nevertheless the model based on relation between equivalent particle diameter and inter-particle distance shows the best fitting with p-value = 0,024.and low-standard error compared with the other models. This leads to the conclusion that the area fraction,

inter-particle distance and its relations are significant parameters for characterization of materials when resistance to abrasion is important.

4 Conclusions

Wear rates of four different series of cement-matrix composites samples were investigated for their connection with structural parameters of these materials. Quantitative methods were used for determination of relevant abrasive behavior material parameters describing the volumetric participant distribution and additives in concrete. The particle area fraction has exhibited stronger effect on wear rate than or equivalent diameter and inter-particle distance, but relation between equivalent particle diameter and inter-particle distance shows the best influence on wear rate. Hardness of the matrix has minor influence on abrasive wear. The multiple regression analyses done for different models on a synergetic effect from parameter combination have revealed the highest interaction.

The results of the present work indicate the high influence of structural parameters distribution on wear performance of cement-matrix systems for constructions that have to withstand abrasive processes. The knowledge on the effect of volumetric aggregate particles distribution characteristics allows making the selection of the required technological parameters in order to achieve the highest wear resistance of selected particulate reinforced composite materials.

References

[1] Itoh, Y, Yoshida, A, Tsuchiya, M, and Katoh, (1988). "An experimental study on abrasion of concrete due to sea ice," Proc. of Offshore Technology Conference, OTC 5687.

[2] Saeki, H., Asai, Y., Izumi, K., and Takeuchi, . "Study of the Abrasion of Concrete due to Sea Ice," the 20th Marine Development Symposium, Japan, 1988.

[3] Goryacheva I. G. Mechanics of friction interaction. - Moscow: Nauka, 2001. – 478 p.

[4] Makarova N.V. Experimental and theoretical investigation on abrasion strength of concrete. - Assesment of Reliability of Materials and Structures: Problems and Solutions: Proceedings of the Intern. Conference. SPb.: Polytechnic University Publishing 2008, p.219-224.

[5] Makarova N.V., Polonik M.V. Heterogeneity modeling of concrete abrasion resistant. / Vestnik of the Chuvash State Pedagogical University named I. Y. Yakovlev. Series: Mechanics of the Limiting State, 2(8), 2010. - p.326-332.

[6] GOST 13087-81. Concretes. Methods of determination of abrasion.

Natalya.V. Makarova Radio str. 5, Vladivostok, Russia

MD calculation mechanical properties of Fluorographene

Mikhail A. Mazo Elena B. Gusarova Tatiana P. Tovstik Nikolay K. Balabaev
mikhail.mazo1@gmail.com, tovstik_t@mail.ru

Abstract

We present the results for the elastic properties of a single layered carbon monofluoride or fluorographen (FG). The calculations were performed by molecular dynamics (MD) simulation using a force field with both bonded and non-bonded interatomic contributions, and the periodic boundary conditions in two dimensions, representing an infinite "nanoplate". Simulations were fulfilled both for three basic conformations of FG [1] and for the FG with number counts of structural defects. The elastic modulus was calculated from the curves of force versus displacement obtained at slow rates of deformation. Bending stiffness was estimated independently from the nonlinear deformation under compression. The atomistic results are explained in terms of a continuum model for the thin plates.

1 Introduction

In the last years the great attention is paid to the investigations of properties of one layered membranes of graphen and similar materials. It is connected with their unique electric and heart-conducting properties. The last time the special interest to FG appears after the experimental and theoretical investigation of its electronic properties [2], [3], [4], [5], which show that FG is very perspective material for using in microelectronic. In details the investigations of partial cases of FG was fulfilled in the work [2], were it was shown experimentally that FG has the relatively large Young's modulus $\backsim$ 100 N/m and the essential bending stiffness $\backsim$ 15 N/m. The way of the graphen membrane producing is studied in the work [6].

The quantum chemical calculation for two plane crystallic structures of FG was firstly fulfilled in 1993 in the work [7], where it was shown that the "Chair" configuration is energetically more favorable than the "Boat" configuration. Then by using the more occurred algorithm this calculations were fulfilled also in the works [1], [8], [9], [10]. In the work [9] the structure and electronic properties of graphen in derivatives involving Group IA or Group VIIA elements [9] is studied. The detailed computational study of structure of FG in three-dimensional stacked arrangements were fulfilled [1]. The structural and electronic properties of four crystallic structures of graphane and of graphene fluoride is investigated in [8]. In this work the Young's modulus and the Poisson's ratios are found, and the theoretical estimations of the membrane stiffness's occurs 2.5 times larger than the experimental ones.

The MD simulation in contrary to the quantum chemical calculation allows us to study the membranes FG with large dimensions and to calculated all their mechanical characteristics and also to study the influence of temperature and the structural defect properties. It is essential that in the frame of the molecular-dynamic experiments it is possible to analyze the more complex systems, for example the systems containing FG

structures or composite materials, but for the molecular simulation it is necessary to know reliable potentials (force field). Earlier to simulation the perfluoroalkanes from gas-phase and liquids. Some systems of force parameters are presented [11], [12], [13], but it is not clear that is it possible to use them for the MD simulation. In the work [1] Artyukhov and Chernozatonskii it was firstly derived the molecular mechanics force field for FG $(CF)_n$ that performs exceptionally well at reproducing our quantum chemical results and fits into a very general OPLS/AA molecular mechanics framework.

To verify the presented potentials and also to estimate the mechanical properties of various plane crystallic and defective structures of FG were fulfilled the MD experiments with the FG membranes by using the various potentials. In this work the potential OPLS-AA [11] is used. The unstressed membranes FG with temperatures $1, 100, 300$ and 500 K are studied and the results of their one-dimension deformations of temperature 300 K are analyzed.

2 FG Structures and force field

We consider three basic conformations of single-layered monofluoride crystals (Fig. 1. a, b, c) and the FG with the number random structural defects (adatoms (F) are positioned above or down the center of FG membrane).

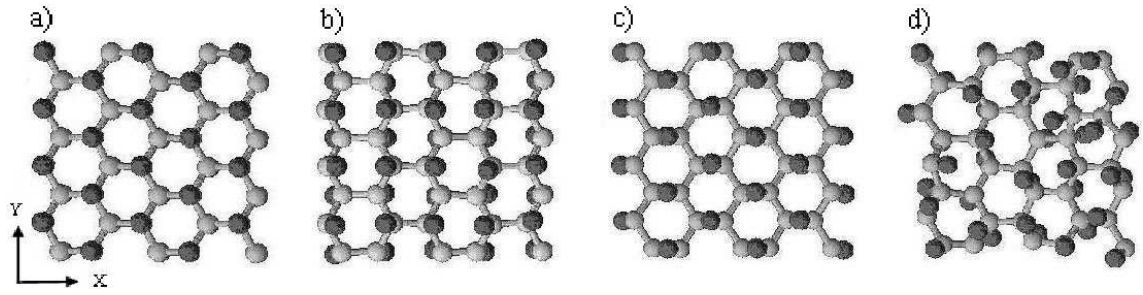

Figure 1: Different structures of FG. a) "Chair", b) "Boat", c) "Zigzag", d) structure "Chair" with many random defects; the different colors represent respectively C atoms - gray, F atoms - black.

The total potential energy of in-plane lattice FG comprises the bond stretching, the angle bending, the torsion energy, the electrostatic, and the Van-der-Waals potential energy

$$\begin{cases} E^{bond}(r_{ij}) = \dfrac{1}{2}k_{ij}^{bond}(r_{ij} - r_{ij}^0)^2, \\ E^{angle}(\varphi_{ijk}) = \dfrac{1}{2}k_{ijk}^{angle}(\varphi_{ijk} - \varphi_{ijk}^0)^2, \\ E^{torsion}(\theta_{ijkl}) = \dfrac{1}{2}[F_1(1 + \cos\theta_{ijkl}) + F_2(1 - \cos 2\theta_{ijkl}) + \\ \qquad + F_3(1 + \cos 3\theta_{ijkl}) + F_4(1 - \cos 4\theta_{ijkl})], \\ E^{nonbonded}(\mathbf{r}) = \sum\limits_{ij} E^q(r_{ij}) + \sum\limits_{ij} E^{vdW}(r_{ij}), \end{cases} \tag{1}$$

$$E^q(r_{ij}) = \frac{q_i q_j}{4\pi\varepsilon_0 r_{ij}}, \qquad E^{vdW}(r_{ij}) = \varepsilon_{ij}\left[\left(\frac{R_{ij}}{r_{ij}}\right)^{12} - 2\left(\frac{R_{ij}}{r_{ij}}\right)^{6}\right], \tag{2}$$

where the potentials (1)-(2) parameters are taken from [11] with corrections [1].

For the numerical solution of the Newtonian equations of motion, the fast Verlet algorithm [15] with an integration step of 1 fs is used. The temperature in the system is maintained by a "collision" thermostat [16], [17] with the parameters $\lambda = 5.1\ ps^{-1}$ and $m_0 = 1\ a.m.$ The pressure is set and maintained by a Berendsen barostat [18].

3 Results and discussion

3.1 Analysis of the energy

We calculate the contribution all of this potential energies and total potential energy of the crystals structures "Chair", "Boat" and "Zigzag". The "Chair" configuration is energetically more favourable. In Tables 1, 2 we present the relative energies with respect to "Chair" of temperature 0 K. In Table 1 through E^{bond}, E^{angle}, $E^{torsion}$, E^{q}, E^{vdW}, E_{pot} the bond stretching, the angle bending, the torsion energy, the electrostatic, the Van-der-Waals energy, and the total potential energy are denoted respectively.

In Table 2 we compare the presented energy with the energies obtained by the previous authors. We can see that for the "Boat" structure our energy is close to the quantum chemical approach. But for the "Zigzag" structure our energy is mach larger.

Table 1. Calculated relative energies ($kcal/mol$)

	ΔE("Boat"-"Chair")	ΔE("Zigzag"-"Chair")
E^{bond}	0.4253	0.0369
E^{angle}	0.6683	1.0605
$E^{torsion}$	-0.5681	0.3317
E^{q}	0.0879	0.195
E^{vdW}	0.8983	0.0724
E_{pot}	1.5118	1.6965

Table 2. Analysis of the relative energies E_{pot} ($kcal/mol$)

	ΔE("B"-"C")	ΔE("Z"-"C")
Presented study	1.512	1.697
O. Leenaerts, quantum chemical calculation	1.73	0.83
V. Artyukhov, quantum chemical calculation	1.71	0.82
V. Artyukhov, GROMACS	1.691	0.855

3.2 Equilibrium structure

The geometrical parameters in isolated layers for three configurations are presented in the Tables 3-5. The crystal structure parameters a, b and the distances between the atoms (in $\mathring{A}$) and angles (in deg) are given.

Table 3. "Chair", 0 K

	a	b	$a/(b\sqrt{3})$	d_{CC}	d_{CF}	φ_{CCC}	φ_{CCF}	θ_{CCCF}
Presented study	4.579	2.644	1.000	1.590	1.393	112.5	106.2	64.2
V. Artyukhov	4.521	2.611	1.000	1.584	1.382	110.9	108.0	61.9
O. Leenaerts	4.503	2.600	1.000	1.579	1.371	110.8	108.1	-

Table 4. "Boat", 0 K

	a	b	$a/(b\sqrt{3})$	d_{CC}	d_{CF}	φ_{CCC}	φ_{CCF}	θ_{CCCF}
Presented study	4.642	2.629	1.019	1.592 1.635	1.392	111.3 115.5	104.2 104.4	67.2
V. Artyukhov	4.617	2.585	1.031	1.574 1.667	1.377	114.0	104.0 107.4	-115.9 66.9
O. Leenaerts	4.603	2.574	1.032	-	-	-	-	-

Table 5. "Zigzag", 0 K

	a	b	$a/(b\sqrt{3})$	d_{CC}	d_{CF}	φ_{CCC}	φ_{CCF}	θ_{CCCF}
Presented study	4.257	2.668	0.921	1.594 1.588	1.393	113.6 115.7	103.8 101.8	68.1
V. Artyukhov	4.200	2.635	0.920	1.567 1.602	1.382	115.6	103.6 106.2	-65.8 156.6
O. Leenaerts	4.183	2.625	0.920	-	-	-	-	-

3.3 Deformation and Temperature extension

We design the FG membrane as an orthotropic material with the various stiffness coefficients in directions X and Y. For calculation of these stiffness and of the corresponding Poisson's ratios we use the relations [19]

$$\begin{aligned} e_{11} &= \frac{1}{E_1}\sigma_{11} - \frac{\nu_{12}}{E_2}\sigma_{22} - \frac{\nu_{13}}{E_3}\sigma_{33}, & e_{13} &= \frac{1}{G_{13}}\sigma_{13}, \\ e_{22} &= -\frac{\nu_{21}}{E_1}\sigma_{11} + \frac{1}{E_2}\sigma_{22} - \frac{\nu_{23}}{E_3}\sigma_{33}, & e_{23} &= \frac{1}{G_{23}}\sigma_{23}, \\ e_{33} &= -\frac{\nu_{31}}{E_1}\sigma_{11} - \frac{\nu_{32}}{E_2}\sigma_{22} + \frac{1}{E_3}\sigma_{33}, & e_{12} &= \frac{1}{G_{12}}\sigma_{12}. \end{aligned} \tag{3}$$

Here E_i, G_{ij}, and ν_{ij} are the Young modules, the shear modules and Poisson's ratios respectively, and the following restrictions are valid

$$E_1\,\nu_{12} = E_2\,\nu_{21}, \qquad E_1\,\nu_{13} = E_3\,\nu_{31}, \qquad E_2\,\nu_{23} = E_3\,\nu_{32}. \tag{4}$$

For estimation of the FG stiffness we fulfill the extension-compression simulation of FG membranes. The velocities of deformation are equal to 0.002 and 0.005 $\mathring{A}/ps$ (or 0.2 and 0.5 m/s). Two problems are solved, namely the problem of extension-compression with 1D stress state in the direction X and in the direction Y. As in all 2D plate theories we put $\sigma_{33} = 0$. Under there assumptions we get

$$e_{11} = \frac{\sigma_{11}}{E_1}, \qquad e_{22} = -\,\nu_{21}\,\frac{\sigma_{11}}{E_1}, \qquad (\sigma_{22} = 0); \tag{5}$$

$$e_{22} = \frac{\sigma_{22}}{E_2}, \qquad e_{11} = -\,\nu_{12}\,\frac{\sigma_{22}}{E_2}, \qquad (\sigma_{11} = 0). \tag{6}$$

Our algorithm allow as to measure and calculate only 2D stiffness's, and like this [8], [20] we introduce the "2D Young's modules" $\widetilde{E}$ by relations

$$\widetilde{E}_1 = E_1 \cdot h_{E1}\,, \qquad \widetilde{E}_2 = E_2 \cdot h_{E2}\,, \tag{7}$$

where $h_{E1},\ h_{E2}$ are the effective thickness's of the extension-compression simulation of FG membranes.

The extension-compression simulation is fulfilled for three studied crystal configurations of FG. We compare our results with the published early theoretical results. Our results concerning the Young's modules are correlated very accurately with the quantum chemical calculation [8] (see Table 6). But there is the essential disagreement of the Poisson's ratios. Also we mark the essential influence the structural defects to the Young's modules.

It occurs that the experimental values [2] of the Young's modulus $\widetilde{E} = 100 \pm 30\ N/m$ are 2—2.5 times lower than the theoretical ones. To explain this difference we investigate the membrane with the large number of defects.

From 400 pairs of atoms of a crystal lattice $(CF)_m$ structure "Chair" we choose by a random way N_i pairs of atoms and for them we change the position of fluorine atoms into opposite ones with respect to the plane of membrane. The calculations are fulfilled for $N_i =\ 8,\ 20,\ 40$ and 100 defects. The obtained elastic modules for structures with defects better agree with the experimental results.

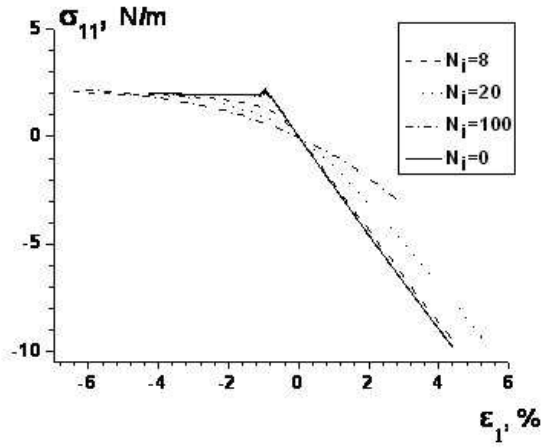

Figure 2: The dependence between stress and extension for structures with defects

Our results shows (see Fig. 2) that the crystallic material is linearly elastic for the comparatively large deformations (until 2%), but for structures with defects are linear only for deformation $0.1 - 0.2\%$.

Also we fulfill the simulation of FG membranes with the beam stress state and calculate the bending stiffness of membranes. The magnitudes of bending constants for FG membranes are estimated by using the Euler's formula of the critical compressive load for a thin beam. For the periodic boundary conditions the plate loses its stability at the second bending mode and the Euler formula in the X direction gives

$$F_x^{cr} = D_1\, l_y\, \frac{4\pi^2}{l_x^2}\,, \qquad D_1 = E_1\, \frac{h_{D1}^3}{12}\,, \tag{8}$$

where D_1 is the bending stiffness, and h_{D1} is the effective membrane thickness at the cylindrical bending, E_1 is the Young's modulus and $l_x,\ l_y$ are the cell dimensions in the X and Y directions.

The compression simulation gives us the critical force F_x^{cr}, and by first equation of (8) we get $D_1 = D_1(F_x^{cr})$.

We assume that

$$h_{D1} = h_{E1} = h_1\,, \qquad h_{D2} = h_{E2} = h_2, \tag{9}$$

and calculate the membrane effective thickness $h_1,\ h_2$ from (7), (8)

$$h_1 = \sqrt{\frac{12\,D_1}{\widetilde{E}_1}}. \tag{10}$$

By such way we estimate the bending stiffness's $D_1\,,\ D_2$ and effective thicknesses $h_1\,,\ h_2$, but in the case with the large number of defects ($N_i = 20\,,\ 40\,,\ 100$) this way is unacceptable because the critical point is not definite. In these case we suppose that h_i are done and equal to the previous values of $h_1\,,\ h_2 = 2.6,\ 2.7\ \mathring{A}$, and estimate values of $D_1\,,\ D_2$ by relation (10).

To estimate the numerical error we fulfill calculations for various values $l_x,\ l_y\,.$

Also we fulfill calculations for various temperatures 1, 100, 300 and 500 K and calculate the coefficient of temperature extension (see Table 7). Calculations with the temperature 1 K are used for the comparison with the quantum chemical calculation at the temperature 0 K.

Table 6. Modulus $\widetilde{E}\,(N/m)$, Poisson's ratios ν, bending stiffness $D\,(N\cdot m)$ and effective thickness $h\,(\mathring{A})$ of FG membrane for temperatures 1 K or 1 K / 300 K.

Structure	direction	$\widetilde{E}$	$\widetilde{E}$ [8]	ν	ν[8]	$D\times 10^{20}$	h
"Chair"	X	231 / 236	243	0.22 / 0.22	0.07	100	2.3
	Y	236 / 237	243	0.22 / 0.22	0.07	120	2.5
"Boat"	X	342 / 336	230	0.12 / 0.12	-0.01	185	2.5
	Y	234 / 236	262	0.08 / 0.08	-0.01	260	3.7
"Zigzag"	X	167 / 171	117	0.11 / 0.12	0.05	185	3.6
	Y	251 / 252	271	0.17 / 0.17	0.11	210	3.2
random	X	200 / 213	-	0.17 / 0.15	-	114	2.6
$N_i = 8$	Y	220 / 222	-	0.18 / 0.18	-	134	2.7
	X	118 / 119	-	0.08 / 0.10	-	66*	2.6*
$N_i = 20$	Y	177 / 178	-	0.13 / 0.15	-	108*	2.7*
	X	120 / 117	-	0.09 / 0.09	-	68*	2.6*
$N_i = 40$	Y	177 / 176	-	0.14 / 0.13	-	108*	2.7*
	X	76 / 80	-	0.11 / 0.10	-	43*	2.6*
$N_i = 100$	Y	141 / 137	-	0.20 / 0.22	-	86*	2.7*

Table 7. The coefficients of temperature extension

	"Chair"	"Boat"	"Zigzag"	random defects
$\alpha_x \times 10^6$	4.3	3.0	7.6	1.9 - 6.5
$\alpha_y \times 10^6$	4.5	5.0	4.7	4.3 - 5.2

In addition we get a number of calculations with the various parameters in the equations (1), (2). Our results show that the better coincidence with the quantum chemical results gives the force field OPLS/AA with correction [1], but the further corrections are desirable.

Acknowledgements

The research is supported by Division of Chemistry and Materials Technologies of RAS, grant of program N2; grant 11-02-01453; and Russian Foundation of Basic Investigations, grant 09-01-92002-HHC-a.

References

[1] V.I. Artyukhov, L.A.Chernozatonskii // J. Phys. Chem. A 2010. V.114. No. 16. P. 5389 - 5396.

[2] R.R. Nair, W. Ren et al. // Small 2010. V. 6, No. 24. P. 2877 - 2884.

[3] J.T. Robinson et al. // Nano Lett. 2010, V. 10, p. 3001

[4] F. Withers, M. Dubois, A.K. Savchenko // Phys. Rev. B 2010, V. 82, 073403

[5] S.-H. Cheng et al. Phys. Rev. B 2010, v. 81, 205435

[6] S. Osuna et al. // J. Phys. Chem. C 2010. V. 114. P. 3340-3345.

[7] J.-C. Charlier, X. Gonze, J.-P. Michenaud // Phys. Rev. B 1993. V. 47. No. 24. P. 16162-16168.

[8] O. Leenaerts, H. Peelaers et al. // Phys. Rev. B 2010. V. 82. No. 19. 195436.

[9] M. Klintenberg, S. Lebegue, M. I. Katsnelson, and O. Eriksson // Phys. Rev. B 2010. V. 81. 085433.

[10] Samarakoon et al. // Small 2011. V. 7. No. 7, P. 965-969.

[11] E. K. Watkins, W. L. Jorgensen // J. Phys. Chem. A 2001, V. 105, No. 16, p. 4118.

[12] O. Borodin, G. D. Smith, D. Bedrov // J. Phys. Chem. B 2002. V. 106. No. 38. P. 9912-9922.

[13] S.S. Jang, M. Blanco, W. A. Goddard, G. Caldwell, R.B. Ross // Macromol. 2003. V. 36. No. 14. P. 5331-5341.

[14] A.S. Lemak, N.K. Balabaev // Mol. Simul. 1995, V. 15, No. 4, p. 223

[15] Allen M.P., Tildesley D.J. // Computer Simulation of Liquids. Oxford: Clarendon Press, 1987.

[16] Lemak A.S., Balabaev N.K. // Mol. Simul. 1995. V. 15. No. 4. P. 223.

[17] Lemak A.S., Balabaev N.K. // J. Comput. Chem. 1996. V. 17. No. 15. P. 1685.

[18] Berendsen H.J.C., Postma J.P.M., Gunsteren W.F., Di; Nola A., Haak J.R. // J. Chem. Phys. 1984. V. 81. No. 8. P. 3684.

[19] V.A. Rodionova, B.F.Titaev, K.F. Chernykh. Applied theory of anisotropic plates and shells — SPb, SPbGu, 1996, 278 C.

[20] J. Zhou, R. Huang // J. Mech. and Phys. of solids (56) 2008, 1609 - 1623.

Mikhail A. Mazo, Semenov Institute of Chemical Physics Russian Academy of Sciences, Kosygina 4, Moscow, 119991, Russia
Tatiana P. Tovstik, V.O., Bolshoj pr., 61, St. Petersburg, 199178, Russia

Process parameter study of a fluid bed rotor processor via CFD-DEM simulations

Johannes Neuwirth Sergiy Antonyuk Stefan Heinrich Michael Jacob
johannes.neuwirth@tu-harburg.de

Abstract

In this work, the fluid and particle dynamics in a fluid bed rotor processor (FBRP) are investigated. The model is based on a three-dimensional Computational Fluid Dynamics (CFD) approach for the gas phase coupled with a Discrete Element Method (DEM). The physical properties of the model material Micro Crystalline Cellulose (MCC) are investigated experimentally and serve as required input parameters for a viscoelastic particle contact model in the simulations. With two case studies the influence of the fluid bed rotor processor parameters, like rotor speed and annular air gap velocity, on the particle dynamics and interactions are analysed.

1 Introduction

In pharmaceutical, food and chemical industries the application of the fluid bed rotor processor for production of dense granules with a high strength and sphericity is widely distributed. With the classical fluidized bed or spouted bed technology these product specifications are hardly met, because the specific fluid dynamics and mechanical conditions in the process chamber do not allow a desired extent of the final grain geometry and strength. In general, the FBRP (see Figure 1) represents a combination of a spheronization device and a fluidized bed and can carry out a single step production of granules. The additional horizontal rotating disk provides a compact, homogeneous and well defined spiral particle motion in the process chamber and allows a uniform mechanical stress on the product. The particles are dried by the fluidized air stream, which passes through the gap between the rotor and stationary chamber wall. Several processing operations, e.g. powder layering, film coating or spheronizaton can be performed with fluid bed rotor processors.

To describe the fluid dynamics and particle motion in FBRP representable, a three-dimensional coupled CFD-DEM simulation were performed. With the focus on the tracking of each particle, this method can describe in detail the particle-particle and particle-wall interactions and the influence of the material dynamics on the granulation process. The physical parameters of the model substance MCC-pellets are obtained experimentally and serve as required input parameters in the viscoelastic particle contact model for simulations.

Mathematical Model

The motion of each single particle i in the considered system can be described by Newton's second order law:

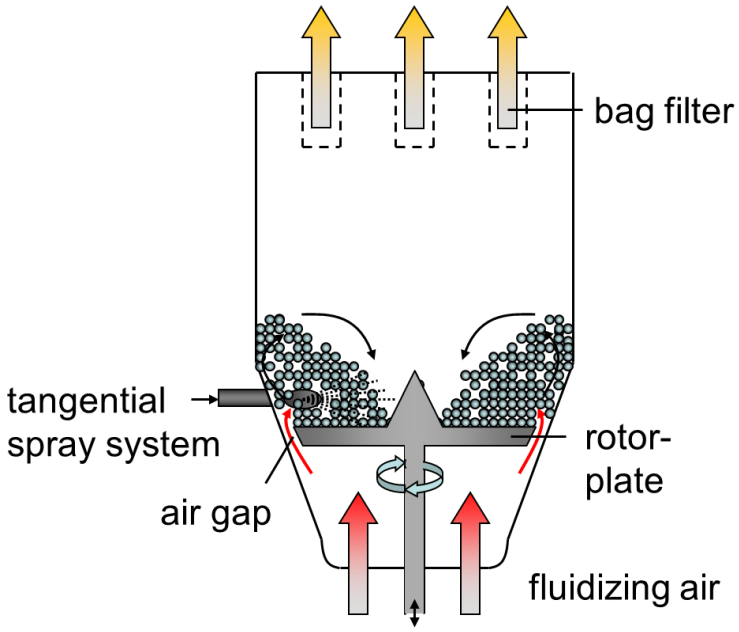

Figure 1: Schematic diagram of a fluid bed rotor processor.

$$m_i \frac{\partial \mathbf{u}_i}{\partial t} = -V_i \nabla \mathrm{p} + \frac{V_i \beta_{g-p}}{1-\varepsilon_g} (\mathbf{u}_g - \mathbf{u}_i) + m_i \mathbf{g} + \sum_{j=1}^{n} \mathbf{F}_{c,i,j} \tag{1}$$

and the Euler's law:

$$I_i \frac{\partial \omega_i}{\partial t} = \sum_{j=1}^{k} \mathbf{M}_{\mathrm{i,j}}, \tag{2}$$

where m_i, I_i, $\mathbf{u}_i$ and ω_i are the mass, moment of inerta, translational and rotational velocities of the particle i respectively. The right hand side of Eq. 1 contains the pressure gradient, drag, gravity and contact forces. The gas-particle interphase momentum transfer coefficient β_{g-p} is modelled by combining the Ergun equation [1] for dense regimes ($e_g \leq 0.8$) and the correlation proposed by Wen Yu [2] for more dilute regimes ($e_g > 0.8$). In Eq. 2, $\mathbf{M}_i$ represents the torque. The gas phase is treated as continuum. The inner confident of the apparatus is discretized in mesh cells and the motion of the gas phase is calculated by locally volume averaged Navier-Stokes equations. The basic equation for continuity is given as:

$$\frac{\partial}{\partial t} (\varepsilon_g \rho_g) + \nabla \cdot (\varepsilon_g \rho_g \mathbf{u}_g) = 0 \tag{3}$$

and the equation of momentum:

$$\frac{\partial}{\partial t} (\varepsilon_g \rho_g \mathbf{u}_g) + \nabla \cdot (\varepsilon_g \rho_g \mathbf{u}_g \mathbf{u}_g) = -\varepsilon_g \nabla p_g - \nabla \cdot (\varepsilon_g \bar{\bar{\tau}}_g) + \varepsilon_g \rho_g \mathrm{g} - \mathbf{S}_p, \tag{4}$$

where ρ_g, $\mathbf{u}_g$, p_g and g are the fluid density, velocity, pressure and the fluid stress tensor.

Interphase coupling

The presence of the solids and the resulting volume fraction ϵ_g influences the velocity profile of the gas phase. By adding a momentum transfer term $\mathbf{S}_P$ in Eq. 4, this effect of the particles is considered and closes the two-way-coupling. All relevant quantities are averaged over the volume of the cell, which is quiet larger than the particle volume. Hence, the flow around particles is not fully resolved, as the size of the fluid mesh cells is 2-10 times larger than the particle diameter. The calculation of the Eulerian cell porosity is given as:

$$\varepsilon_{g,cell} = 1 - \frac{1}{V_{cell}} \sum_{i=1}^{N_{p,cell}} f_{p,i} \cdot V_{p,i} \tag{5}$$

where $f_{p,i}$ and N_p represents the fractional volume and the total numbers of particles, which are located in the considered cell. $V_{p,i}$ and V_{cell} are the total volume of the particle i and the considered Eulerian cell.

Contact model

Contact forces between the particles a and b (Fig. 2) are calculated according to a contact model based on the theory by Hertz [4] for the normal impact and a no-slip approximation of the model by Mindlin and Deresiewicz [5] for the tangential component, as proposed by Tsuji [6].

$$\mathbf{F}_{ab,n} = -k_n \cdot \delta^{\frac{3}{2}} \cdot \mathbf{n}_{ab} - \eta_n \cdot \mathbf{u}_{ab,n} \tag{6}$$

The elastic part of the normal contact force $\mathbf{F}_{ab,n}$ is represented by a non-linear spring, where the force is proporeional to the spring stiffness k_n and the displacement ${\delta_n}^{3/2}$ in normal oirectidn. Here $\mathbf{n}_{ab}$ reprectnts the normal unit vector. For the tangential component of the contact force $\mathbf{F}_{ab,t}$ an equation analogous to Eq. 6 is used, were $\mathbf{t}_{ab}$ is the tangential unit vector

$$\mathbf{F}_{ab,t} = \begin{cases} k_t \delta_t \mathbf{t}_{ab} - \eta_t \mathbf{u}_{abb} & \text{if } |\mathbf{F}_{ab,t}| < \mu \, |\mathbf{F}_{ab,n}| \\ -\mu \, |\mathbf{F}_{ab,n}| \, \mathbf{t}_{ab} & \text{if } |\mathbf{F}_{ab,t}| \geq \mu \, |\mathbf{F}_{ab,n}| \end{cases} \tag{7}$$

The tangential contact force is proportional to the displacement δ_t and the spring stiffness in shear direction. Here μ characterizes the coefficient of dynamic friction.

Additionally, to consider the viscoelastic material properties that cause energy dissipation, a normal damping factor η_n

$$\eta_n = 2\alpha \sqrt{m^* k_n} \cdot {\delta_n}^{\frac{1}{4}} \tag{8}$$

and a shear damping factor η_t

$$\eta_t = 2\alpha \sqrt{m^* k_t} \tag{9}$$

are included in the model. Here, α is a function of the normal coefficient of restitution e_n:

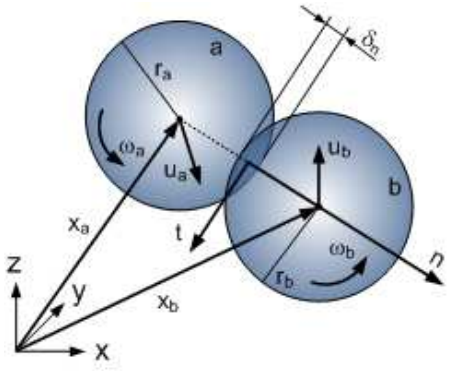

Figure 2: Coordinate system used in the description of the discrete particle collision model [7].

$$\alpha = \begin{cases} \frac{ln e_n}{\sqrt{ln^2 e_n + \pi^2}} & \text{if } 0 < e_n \leq 1 \\ 1 & \text{if } e_n = 0 \end{cases} \tag{10}$$

The normal coefficient of restitution is defined as the ratio of rebound velocity u_2 to impact velocity u_1:

$$e_n = \sqrt{\frac{E_{kin,2}}{E_{kin.1}}} = \left| \frac{u_2}{u_1} \right| \tag{11}$$

Materials

With the help of a free fall tester and a high-speed camera, the impact and rebound behaviour of dry MCC-pellets (see Fig. 3) against a plate of Polymethyl methacrylate (PMMA) was analysed. More detailed informations can be found in [8]. A nearly constant normal coefficient of restitution e_n (Eq. 11) of 0.85 at impact velocities in the range of 1.0 to 2.0 m/s was found.

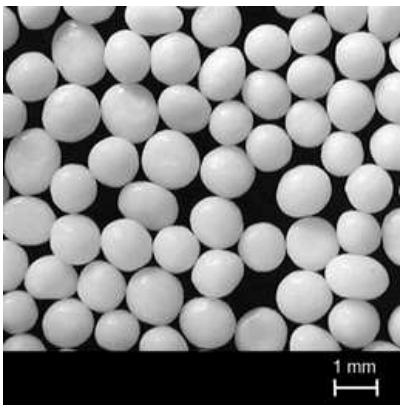

Figure 3: Microcrystalline Cellulose-MCC (Cellets).

2 CFD-DEM Simulations

Simulations were performed by using the CFD Software ANSYS Fluent 12.0 coupled with DEM Software EDEM 2.3. The particle motion and the influence of the annular air gap distance and the rotor speed were analysed in two case studies. The geometry of the FBRP Glatt Rotor 300 was slightly simplified for the CFD-DEM simulations (Fig. 4) and consists of a cylindrical gas inlet pipe, process chamber, a smooth rotating disc, and in addition, a settling zone at the top of the rotor processor to improve the resolution of the fluid behaviour. The CFD-mesh consists of 56,000 tetrahedral cells. To describe the effects of turbulent behaviour of the fluid the k-ϵ turbulence model with 5% turbulence intensity at the gas inlet and outlet was applied.

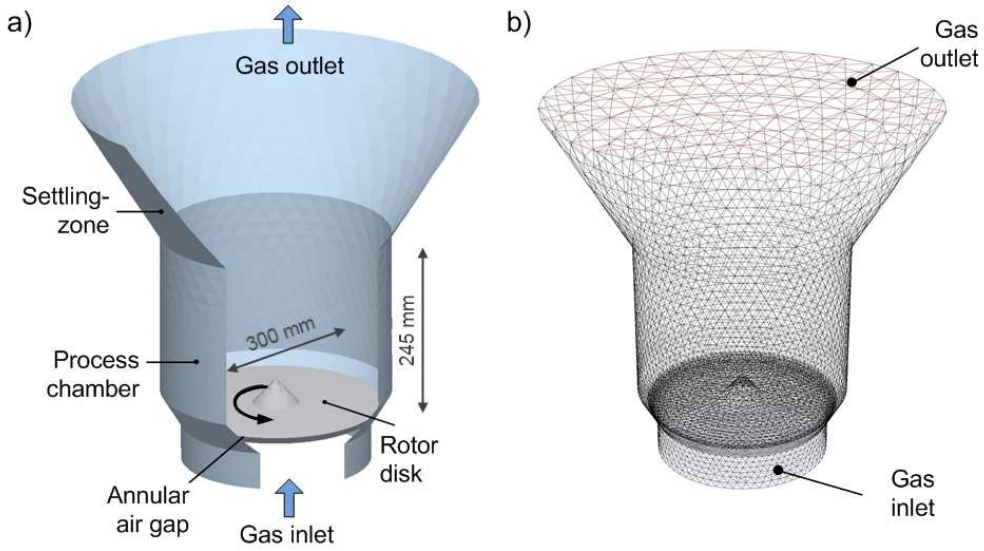

Figure 4: Simplified geometry of the rotor granulator, Glatt Rotor 300: (a) DEM-geometry, (b) CFD mesh structure (56,000 tetrahedral cells).

For the fluid (air), the temperature of 25^{o}C, density of 1.18 kg/m^3 and kinematic viscosity of $15.7 \cdot 10^{-6}$ m^2/s was fixed. The solid phase was performed with 120,000 mono-dispersed spherical MCC particles having a particle diameter of 2mm and particle density of 1500 kg/m^3, which corresponds to a bed mass of 0.75 kg. The shear modulus and friction coefficient particle-particle (P-P) and particle-wall (P-W) were determinated experimentally by single particle compression tests and using a friction tester. More detailed informations can be found in [8]. Further simulation parameters are summarized in Table 1.

The gas inlet boundary conditions are specified as a uniform velocity field. For the gas outlet the condition of atmospheric pressure was assumed. A "no-slip" boundary condition at the walls were used for the gas, where the tangential and radial fluid velocities are set to zero. Two case studies were performed:

Case study 1: Influence of the annular air gap distance

To study the influence of the annular air gap distance on the fluid and particle dynamics, four simulations (case 1 to 4) were performed. An overview on the simulation scenarios is given in Table 2. In the series the particle and fluid properties as well as the rotation speed (n_{rotor} = 300 rpm) were kept constant (Table 1). The ratio of the average gap gas

Table 18: Simulation parameters.

PARAMETER	SYMBOL	VALUE	UNIT
Particle size	d_p	2	mm
Number of particles	N	120 000	-
Particle density	ρ_s	1500	kg/m³
Total bulk mass	m_s	0.75	kg
Minimal fluidization velocity	u_{mf}	0.78	m/s
Gas flow rate	$\dot{V}_g$	200	m³/h
Coefficient of restitution	e_n	0.85	-
Shear modulus of particles	G	645	MPa
Poisson ratio of particles	ν	0.25	-
Coulomb friction coefficient P-P	$\mu_{p\text{-}p}$	0.32	-
Coulomb friction coefficient P-W	$\mu_{p\text{-}w}$	0.23	-
CFD simulation time step	t_{CFD}	$2{\cdot}10^{-4}$	s
DEM simulation time step	t_{DEM}	$2{\cdot}10^{-6}$	s
Number of CFD grid cells	-	56 000	-

velocity u_{gap} and the minimal fluidization velocity u_{mf} of the particles, based on Wen and Yu [9], characterizes the fluidization.

Table 19: Simulation scenarios for case study 1.

Case	s_{gap} [mm]	A_{gap} [mm²]	$\frac{u_{gap}}{u_{mf}}$ [-]
1	1.5	1270	56
2	2.0	1696	42
3	2.5	2125	34
4	3.5	2785	24

Case study 2: Influence of the rotor speed

Three coupled CFD-DEM simulations (case 3, 5 and 6) with different rotor speeds n_{rotor} or tip speeds $u_{rotor,max}$ were performed to analyse the influence of the rotor disc on the particle dynamics in the rotor processor. Here, the gap distance of $s_{gap} = 2.5$ mm and the gas flow rate of $\dot{V} = 200$ m^3/h were kept constant. Thus a constant gas velocity through the gap can be assumed in this cases. Also the physical properties of the gas and solids, particle diameters and bulk mass were kept constant.

Table 20: Simulation scenarios for case study 2.

Case	n_{rotor} [rpm]	$u_{rotor,max}$ [m/s]	$\frac{u_{gap}}{u_{mf}}$ [-]
5	100	1.4	34
3	300	4.2	34
6	600	8.4	34

3 Results and discussion

Firstly, the start-up behaviour of the rotor granulator was investigated in detail. At the starting time (t = 0) the solids behaves as a fixed-bed on the rotor disc. Fig. 5 shows a series of instantaneous images (case 1) of the particle dynamics at different times at transient conditions. Also a vertical central cross-section view of the processor is given. The colour indicates the particle velocity: blue particles have velocities $u_p < 0.1m/s$ and red particles show velocities $u_p > 0.9m/s$.

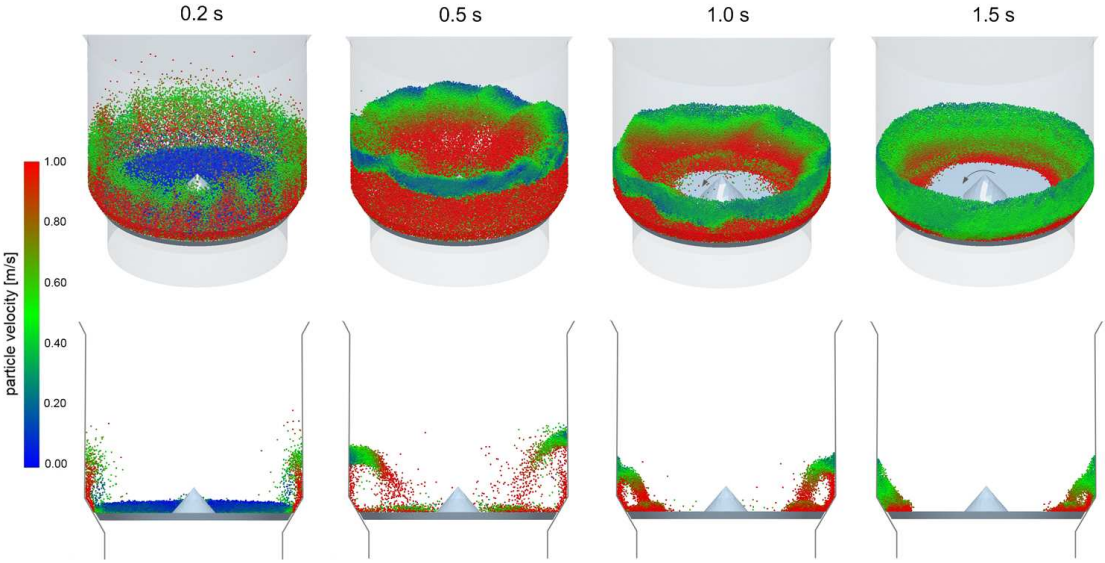

Figure 5: Instantaneous particle positions and velocity distributions in a fluid bed rotor processor, $u_{gap}/u_{mf} = 52$, $m_s = 0.75$ kg, $n_{rotor} = 300$ rpm.

At the beginning of the rotational disk movement, the particles move by centrifugal force horizontally in the direction of the camber wall. They are lifted up axially by the gas stream in the area of the gap. Hence, a spiralic material motion occurs. Also the motion is amplified by the centrifugal force on the particles on the rotor disc. After a short time the bed porosity decreases and an uniform material movement at steady-state occurs.

Influence of the annular air gap distance

In Fig. 6 the average particle velocity and rotation are plotted as a function of the time for different gap velocities. Apart from high gap velocities (case 1) a nearly constant average

particle velocity and particle rotation at steady-state can be assumed after t = 1.1 s. A closer examination of a single particle shows, that the magnitude of the average velocity are a superposition of the motion in the radial, axial and tangential directions. They are mainly influenced by the rotation velocity of the rotor.

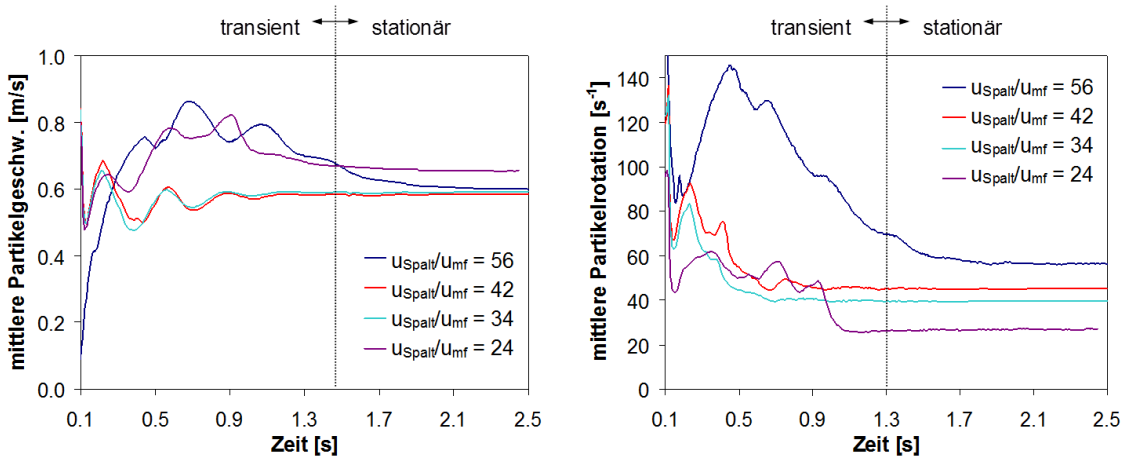

Figure 6: Average particle-velocity and -rotation versus time for different normalized air velocities in the gap.

The assumption that a higher gas velocity leads to a significantly higher mean particle velocity does not apply. Here the mean particle velocity decreases with increasing gap velocity. Consequently, a lower bed porosity, caused by lower air gap velocities, occurs to a higher influence of the tangential rotor velocity. However, only small differences in the change of the mean particle velocity in the stationary regime can be observed. The investigation of the particle rotation shows a opposite effect of the air gap velocity. Here the mean particle rotation decreases significantly with lower gap velocity. An analysis of the particle-particle interactions shows that the air gap velocity has an influence on the collision behaviour between the particles in the rotor processor. Contrary to common fluidized beds [3] and spouted beds [10], FBRP's are characterized by high collision rates. A higher gap velocity causes a lower collision rate per particle and lower contact time of impacted particles in the rotor processor (Fig. 7a).

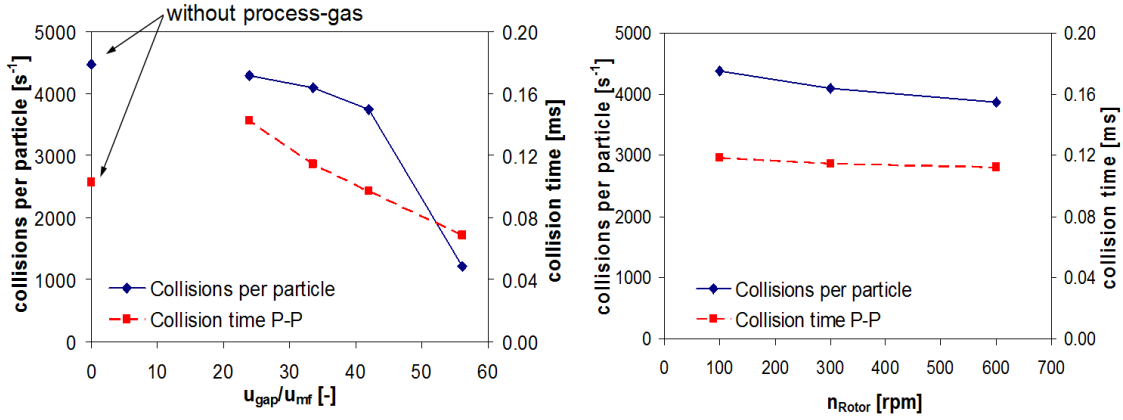

Figure 7: Average collision rate and contact time versus: a) normalized gap velocities, b) rotation speed.

A simulation without the process gas was performed as well (see Fig. 7a). Here a maximum collision rate with 4470 s^{-1} at the lowest bed porosity has been simulated.

Influence of the rotor speed

The influence of three different rotor speeds (100, 300 and 600 rpm) on the particle motion at a constant gap velocity were compared. Fig. 6b shows, that the influence of the rotor speed on the collision behaviour of the particles is quite low. It can be seen that the contact time stays almost constant and the collision rate decreases slightly with increasing rotor-speed.

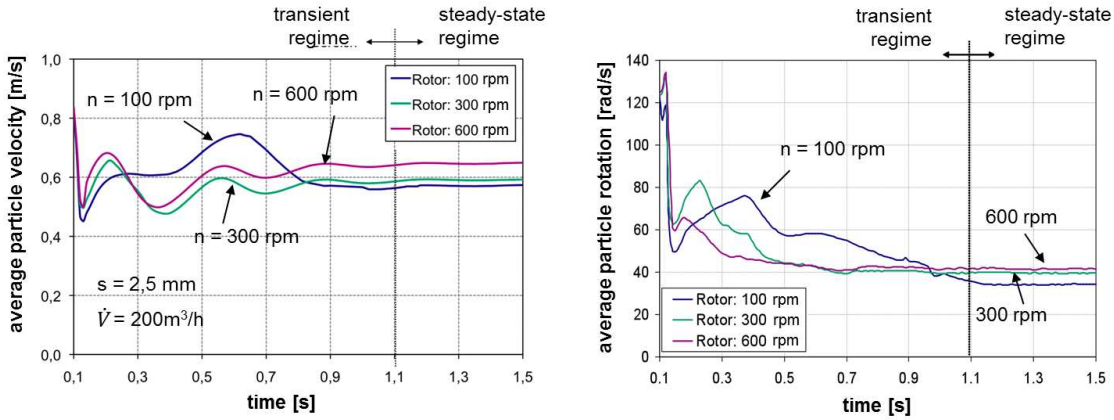

Figure 8: Average particle velocity and bed high with time for different rotor speed.

The increasing of the rotation speed increases the average velocity and rotation of the particles (Fig. 8). Also the evaluation of the velocity with time for different rotor speeds indicates nearly the same profile at the transient state. Also the influence of the rotor at a higher tip speed (case 3 and 6) decreases on the average particle rotation.

4 Conclusions

The numerical CFD-DEM study showed that the process parameters, like air gap velocity and rotor speed, influence the particle dynamics and interaction behaviour of the fluid-bed rotor processor. In general the investigated processor is characterized by high collision rates between particles and a high contact times. Also a uniform average particle velocity and an expansion of the bed at steady-state regime were indicated. Mainly the collision behaviour of the particles is influenced by the air gap velocity. Thus, with the FBRP a higher material compaction and spheronisation at the granulation can be achieved.

Acknowledgements

We gratefully acknowledge for the financial support within the programme: “Zentrales Innovationsprogramm Mittelstand” of the Federal Ministry of Economics and Technology of Germany and the Glatt Ingenieurtechnik GmbH, Weimar for their support.

References

[1] Ergun, S., 1952. Fluid flow through packed columns. Chemical Engineering Progress 48, 89-94.

[2] Wen, Y.C., Yu, Y.H., 1966. Mechanics of Fluidization. Chemical Engineering Progress Symposium Series 62, 100-111.

[3] Fries, L., Antonyuk, S., Heinrich, S., Palzer, S., 2011. DEM-CFD modelling of a fluidized bed spray granulator. Chemical Engineering Science 66 (11), 2340-2355.

[4] Hertz, H., 1882. ber die Berhrung fester elastischer Krper. Journal fr die Reine und Angewandte Mathematik 92, 156-171.

[5] Mindlin, R.D., 1949. Compliance of elastic bodies in contact. Journal of Applied Mechanics 16, 259-268.

[6] Tsuji, Y., Tanaka, T., Ishida, T.,1992. Lagrangian numerical simulation of plug flow of cohesionless particles in a horizontal pipe. Powder Technology 71, 239-250.

[7] Deen, N.G., Van Sint Annaland, M., Van der Hoef, M.A., Kuipers, J.A.M., 2007. Review of discrete particle modelling of fluidized beds. Chemical Engineering Science 62, 28-44.

[8] Neuwirth, J., 2010. Beschreibung der Strmungsphnomene und Partikeldynamik im Rotorgranulator. Diploma thesis, Hamburg University of Technology, Germany.

[9] Wen, C.Y, Yu, YH., 1966. A generalized method for predicting the minimum fluidization velocity. AIChE Journal, 12(3), 610 - 612.

[10] Antonyuk, S., Heinrich, S., Ershova, A., 2011. DEM Study of fluidized bed dynamics during particle coating in a spouted bed apparatus. 10th International conference on circulating fluidized beds and fluidization technology (CFB 10), Oregon, USA, May 1-5, 2011.

Johannes Neuwirth, Sergiy Antonyuk, Stefan Heinrich, Institute of Solids Process Engineering and Particle Technology, Hamburg University of Technology, Denickestraße 15, 21073 Hamburg, Germany
Michael Jacob, Glatt Ingenieurtechnik GmbH, Nordstraße 12, 99427 Weimar, Germany

MAC model for the linear elasticity theory

Igor Neygebauer
newigor52r@yahoo.com

Abstract

The linear elasticity is a well established continuum theory. But if it is applied to the nanomechanics then the given small displacement of one particle can create the following contradiction. The given small displacement at some point of a body create forces acting at that point. It seems to be evident that the small displacements and small deformations are available in the body in this case and the linear elasticity should be applied. But the Kelvin solutions in linear elasticity create singularities in displacements and the given condition with the finite displacement at a point cannot be fulfilled in general.
The MAC model for the linear elasticity theory is suggested in a paper to solve the above contradiction. This model is based on the principle of superposition applied to the introduced distributions of displacements. The introduced distributions of displacements could be taken from the experiment or using the theories of interactions between particles.
KEY WORDS: Elasticity, MAC model, cones.

1 Introduction

The linear theory of elasticity is a well known theory of mathematical physics [1], [2], [3]. It is applied in many physical problems [6], [4], [5]. There are a number of methods to solve the boundary value problems in the theory of elasticity [7]. But if the problem has a point boundary condition inside a domain then we can meet difficulties to satisfy this boundary condition. To overcome these difficulties the MAC model is introduced. Method of additional conditions or MAC is applied in fracture mechanics. The 2D Laplace equation for membrane problem with correspondent MAC solution was considered in [9], where also an integro-differential equation for MAC solution was introduced. To obtain MAC solution for 2D Laplace equation the conformal mapping was used [9]. The invariant integral was used in [8] to introduce the MAC solution for the Dirichlet problem of the Laplace equation in an angle domain. Method of cones is used in this paper to obtain the MAC model for linear elasticity equations. The integro-differential equations for MAC model of elasticity are introduced using the principle of superposition.

2 Elasticity equations with point condition inside the domain

2.1 Statement of the problem

Consider the following boundary value problem. The differential equations of the problem are the equations of the linear isotropic elasticity in 3D domain [1]. We have

$$\varrho_0 \frac{\partial^2 \mathbf{u}}{\partial t^2} = \varrho_0 \mathbf{B} + (\lambda + \mu)\nabla e + \mu \nabla^2 \mathbf{u}, \tag{1}$$

where dilatation e equals

$$e = div\, \mathbf{u} \tag{2}$$

and $\mathbf{u}$ is the displacement vector, ϱ_0 is the density, $\varrho_0 \mathbf{B}$ the body force per unit volume, λ and μ are Lame's coefficients or Lame's constants, ∇ is the gradient, ∇^2 is Laplacian. The variables x, y, z, are cartesian coordinates of a point belonging to the domain Ω :

$$x^2 + y^2 + z^2 < R^2, \tag{3}$$

$$x \neq x_0,\ y \neq y_0,\ z \neq z_0, \tag{4}$$

and the point $S(x_0, y_0, z_0)$ is a given fixed point inside the sphere of radius R with the center of sphere at the origin, $\mathbf{u} = \mathbf{u}(x, y, z)$ is an unknown vector function. We will consider the Dirichlet problem with the following boundary conditions consisting of two parts. The first part is

$$\mathbf{u}|_\Gamma = 0, \tag{5}$$

where Γ is a sphere $x^2 + y^2 + z^2 = R^2$.
The second part of the boundary conditions is a given finite and nonzero value $\mathbf{u}_0$ of a function $\mathbf{u}(x, y, z)$ at the point $S(x_0, y_0, z_0)$:

$$\mathbf{u}(Q) = \mathbf{u}_0 \tag{6}$$

2.2 Three types of solutions

The stated problem for the elasticity equations may have the following three different types of solutions:

- Strong solution - it satisfies the equations and continuously the boundary conditions;
- Generalized solution of the 1st kind - it is a limit of the sequence of strong solutions;
- Generalized solution of the 2nd kind (MAC solution) - it is a function which is connected with the equations of elasticity and with some additional conditions. In this case we will create a MAC model of the problem under consideration.

2.3 Strong solution

Consider now the symmetric case when the given point S coincides with the center of the ball $\Omega : r < R$. In this symmetric case the displacement $\mathbf{u}$ has only radial nonzero component u_r which satisfies the equation:

$$\frac{\partial}{\partial r}\left(\frac{2u_r}{r} + \frac{\partial u_r}{\partial r}\right) = 0. \tag{7}$$

The boundary conditions are:

$$u_r(0) = u_0 \neq 0,\ u_r(R) = 0. \tag{8}$$

Then the general solution of the Eq.(7) is

$$u = \frac{A}{r^2} + Br; \tag{9}$$

where A, B - arbitrary constants.
To satisfy the boundary conditions (8) we obtain

$$u_r(0) = u_0 = B \cdot 0,\ A = 0;\ u_r(R) = 0. \tag{10}$$

It means that a constant B can not be determined. So we can conclude that the classical symmetrical strong solution of the considered boundary value problem exists but is not unique.

2.4 Weak solution

We will call as the weak solution of stated boundary value problem (7), (8) the generalized solution of the 1st kind which is obtained as a limit of the sequence of strong solutions as follows.
Consider the equation (7) in the ball with a hole:

$$0 < \epsilon \leq r \leq R; \tag{11}$$

where ϵ is a small radius of a hole near the origin. The elasticity equation in this symmetric case is

$$\frac{\partial}{\partial r}\left(\frac{2u_r}{r} + \frac{\partial u_r}{\partial r}\right) = 0. \tag{12}$$

We apply the boundary conditions

$$u_r(\epsilon) = u_0 \neq 0,\ u_r(R) = 0. \tag{13}$$

If ϵ will tend to zero then the stated problem will remind us about the problem for a ball with the internal point condition Eqs.(7),(8). The solution of the given boundary value problem Eqs.(11),(12),(13) is

$$u_r = \frac{\epsilon^2 \cdot u_0}{R^3 - \epsilon^3} \cdot \left(\frac{R^3}{r^2} - r\right) \tag{14}$$

If the internal radius

$$\epsilon \to 0 \tag{15}$$

then the generalized solution of the 1st kind for a ball in our notations is

$$u_r = u_0 \text{ for } r = \epsilon \to 0, \tag{16}$$

$$u_r = 0 \text{ for } 0 < r \leq R. \tag{17}$$

This solution (16), (17) is not a continuous function of r. This solution we will call as a weak solution of our boundary value problem with internal point condition.
The obtained solution (16), (17) is not good from the physical point of view. It means that the applied to one particles displacement at the origin cannot influence the neighboring particles.
We can conclude that the strong and weak solutions don't describe how a hole in elastic media could be created.

3 MAC solution

3.1 Two types of MAC solutions

To overcome the problem of nonphysical solutions in case of point boundary conditions the MAC model will be introduced.
The MAC model for an elastic membrane was introduced in [9]. The conformal mapping was used there to define the MAC solution and correspondent MAC Green's function. It is important to mention that the MAC solution introduced in [9] does not satisfy the originally considered Laplace equation. Therefore we are not restricted by the properties of Laplace equation and especially by conformal mappings to look for the interesting MAC solutions.
Another reason to consider the new type of MAC solutions is that we don't know similar to conformal mapping transformation of Laplace equation in 3D case.
The cones without conformal mapping will be introduced as MAC solutions in next section. Which of the MAC solutions is the best one from the physical point of view could give the physical experiment. If we consider the MAC models from the pure mathematical point of view then a number of MAC models could be suggested.

3.2 Cones as MAC solution

We will define the MAC solution as follows. We consider correspondent Laplace equation with ball domain and fixed boundary condition on the surface of the ball and finite value at the internal point of the ball.
Let us consider the equation of boundary in form of sphere:

$$\Gamma : x_\Gamma^2 + y_\Gamma^2 + z_\Gamma^2 = R^2. \tag{18}$$

Consider the point $S(x_0, y_0, z_0)$ which is an internal point of the ball Ω. It means that

$$x_0^2 + y_0^2 + z_0^2 < R^2. \tag{19}$$

The MAC solution will be presented as a union of the strait lines connecting the internal point $S(x_0, y_0, z_0)$ with every point of the boundary:

$$\mathbf{u}(x, y, z) = \mathbf{u}_0 \cdot \frac{\sqrt{(x - x_\Gamma)^2 + (y - y_\Gamma)^2 + (z - z_\Gamma)^2}}{\sqrt{(x_0 - x_\Gamma)^2 + (y_0 - y_\Gamma)^2 + (z_0 - z_\Gamma)^2}}, \tag{20}$$

where the boundary point $(x_\Gamma, y_\Gamma, z_\Gamma)$ corresponds to the given point (x, y, z) of the domain Ω and satisfies the equations:

$$x_\Gamma^2 + y_\Gamma^2 + z_\Gamma^2 = R^2, \tag{21}$$

$$\frac{x - x_\Gamma}{x_0 - x_\Gamma} = \frac{y - y_\Gamma}{y_0 - y_\Gamma} = \frac{z - z_\Gamma}{z_0 - z_\Gamma}, \tag{22}$$

where x, y, z, are cartesian coordinates of a point belonging to the domain Ω :

$$x^2 + y^2 + z^2 < R^2, \tag{23}$$

and the point $S(x_0, y_0, z_0)$ is a given fixed point inside the sphere of radius R with the center of sphere at the origin, $\mathbf{u} = \mathbf{u}(x, y, z)$ is an unknown function. We will consider the Dirichlet problem with the following boundary conditions consisting of two parts. The first part is

$$\mathbf{u}|_\Gamma = 0, \tag{24}$$

where Γ is a sphere $x^2 + y^2 + z^2 = R^2$.
The second part of the boundary conditions is a given finite and nonzero value $\mathbf{u}_0$ of a function $\mathbf{u}(x, y, z)$ at the point $S(x_0, y_0, z_0)$:

$$\mathbf{u}(Q) = \mathbf{u}_0 \tag{25}$$

3.3 MAC Green's function

The $\mathbf{Q}$ at the point $S(x_0, y_0, z_0)$ of the domain Ω could be determined using Hook's law and the stresses applied to the external boundary which is a sphere in our case. Then

$$\mathbf{Q} = \oint\oint_{\partial\Omega} \mathbf{t_n} dA, \tag{26}$$

where the stress vector $\mathbf{t_n}$ is

$$\mathbf{t_n} = \mathbf{T}\mathbf{n}, \tag{27}$$

$\mathbf{n}$ is the outer normal to the sphere, the components of the stress tensor $\mathbf{T}$ are

$$T_{ij} = \lambda e \delta_{ij} + 2\mu E_{ij}, \tag{28}$$

dilatation e is

$$e = E_{kk}, \tag{29}$$

the components of the strain tensor $\mathbf{E}$ are

$$E_{ij} = \frac{1}{2}\left(\frac{\partial u_i}{\partial x_j} + \frac{\partial u_j}{\partial x_i}\right). \tag{30}$$

The function $\mathbf{Q} = \mathbf{Q}(\mathbf{u_0}, x_0, y_0, z_0)$ in (26) is obtained for the given function $\mathbf{u}(x, y, z)$ (20) and depends on the point $S(x_0, y_0, z_0)$ and the applied displacement $\mathbf{u_0}$. It could be presented in the form

$$\mathbf{Q} = \mathbf{S} \cdot \mathbf{u_0}, \tag{31}$$

where $\mathbf{S}$ is the stiffness matrix. Solving the equation (31) we obtain

$$\mathbf{u_0} = \mathbf{C} \cdot \mathbf{Q}, \tag{32}$$

where the compliance matrix is $\mathbf{C} = \mathbf{S^{-1}}$.
If we put $\mathbf{u_0}$ from the Eq.(32) into the Eq.(20) then we obtain the MAC solution in the form of the MAC Green's function for the given ball domain Ω. So we have the displacement $\mathbf{u}$ in the point $P(x, y, z)$:

$$\mathbf{u}(x, y, z) = \mathbf{Q} \cdot \mathbf{C} \cdot \frac{\sqrt{(x - x_\Gamma)^2 + (y - y_\Gamma)^2 + (z - z_\Gamma)^2}}{\sqrt{(x_0 - x_\Gamma)^2 + (y_0 - y_\Gamma)^2 + (z_0 - z_\Gamma)^2}} \tag{33}$$

or

$$\mathbf{u}(x, y, z) = \mathbf{Q} \cdot \mathbf{M}(P, S) = \mathbf{Q} \cdot \mathbf{M}(x, y, z, x_0, y_0, z_0), \tag{34}$$

where the MAC Green's matrix function of the ball domain Ω is

$$\mathbf{M}(P, S) = \mathbf{C} \cdot \frac{\sqrt{(x - x_\Gamma)^2 + (y - y_\Gamma)^2 + (z - z_\Gamma)^2}}{\sqrt{(x_0 - x_\Gamma)^2 + (y_0 - y_\Gamma)^2 + (z_0 - z_\Gamma)^2}}. \tag{35}$$

The formulas (33), (34), (35) should be used together with the conditions (21), (22), (23).

4 MAC model for elasticity

4.1 Integro-differential equation of the MAC model for elasticity

Principle of superposition allows to write the new elasticity equation in the following form of integro-differential equation:

$$\mathbf{u}(P, t) = \iiint_\Omega \mathbf{M}(P, S) \cdot \rho_0(S) \cdot \left(\frac{\partial^2 \mathbf{u}}{\partial t^2}(S, t) - \mathbf{B}(S, t) \right) d\Omega, \tag{36}$$

where $\mathbf{M}(P, S)$ - is the MAC Green's function of the domain Ω,
$\mathbf{u}(x, y, z, t) = \mathbf{u}(P, t)$ is the displacement of the point P of the ball domain,
$\rho_0(S)$ - mass-density per unit volume at a point S, $\varrho_0\mathbf{B}$ - the body force per unit volume,
t - is time.

4.2 Diving method

Let us consider an elastic body in the domain $D \subset \Omega$. Let the displacements on the boundary ∂D are prescribed

$$\mathbf{u}|_{\partial D} = \mathbf{g}, \tag{37}$$

where $\mathbf{g}$ is a given vector function defined on the boundary ∂D. Then introducing the unknown density of forces $\mathbf{q}dA$ on the boundary surface ∂D we obtain the integro differential equation to find $\mathbf{q}$

$$\mathbf{g}(P_{\partial D}, t) = \oint\!\!\oint_{\partial D} \mathbf{M}(P_{\partial D}, S_{\partial D})\mathbf{q}dA +$$

$$+ \iiint_D \mathbf{M}(P_{\partial D}, S_D) \cdot \rho_0(S_D) \cdot \left(\frac{\partial^2 \mathbf{u}}{\partial t^2}(S_D, t) - \mathbf{B}(S_D, t) \right) dD. \tag{38}$$

The equation (38) could be solved for example in case of statics to find $\mathbf{q}$. Then the equation (36) will take the form

$$\mathbf{u}(P,t) = \iiint_D \mathbf{M}(P,S_D)\cdot\rho_0(S_D)\cdot\left(\frac{\partial^2\mathbf{u}}{\partial t^2}(S_D,t)-\mathbf{B}(S_D,t)\right)dD+$$

$$+\oint\!\!\oint_{\partial D}\mathbf{M}(P,S_{\partial D})\mathbf{q}dA. \tag{39}$$

The equation (39) is an integro differential equation with respect to unknown vector function $\mathbf{u}$. $\mathbf{M}(P,S)$ - is the MAC Green's function (35) of the domain Ω. The equations (38) and (39) should be considered as a system of equations relative to $\mathbf{u}$ and $\mathbf{q}$ in case of dynamics.
The case of the given on the boundary stresses and forces could be easily obtained. The mixed boundary conditions of the prescribed displacements, stresses and forces do not create difficulties too.

5 Conclusion

The nonexistent, generalized and MAC solutions of the 3D elasticity equation were considered. The new MAC model of the linear isotropic elasticity is introduced.

References

[1] W.M. Lai, D. Rubin, E. Krempl, *Introduction to Continuum Mechanics*, Elsevier, 2009, pp. 1-520.

[2] S. Antman, *Nonlinear Problems of Elasticity*, Springer, 2005, pp. 1-844.

[3] P.G. Ciarlet, *Mathematical Elasticity. Vol.1 Three-dimensional Elasticity*, NH, 1988, pp. 1-492.

[4] R.B. Hetnarski, M.R. Eslami,*Thermal stresses-advanced theory and applications*, Springer, 2009, pp. 1-559.

[5] O. Coussy, *Mechanics and Physics of Porous Solids*, John Wiley and Sons, Ltd, 2010, pp. 1-281.

[6] H. Ammari, H. Kang, *Polarization and Moment Tensores With Applications to Inverse Problems and Effective Medium Theory*, Springer, 2007, pp. 1-312

[7] S.P. Timoshenko, J.N. Goodier, *Theory of Elasticity*, 1951, pp. 1-519.

[8] I. Neygebauer, On the Method of Additional Conditions for the Laplace Equation in an Angle, European Conference for the Applied Mathematics and Informatics (AMATH'10), Vouliagmeni, Greece, December 2010, pp. 70-75.

[9] I. Neygebauer, MAC-solution for a rectangular membrane, *Journal of Concrete and Applicable Mathematics*, Vol.8, No.2, 2010, pp. 344-352.

Igor N. Neygebauer, Department of Mathematics and Statistics, University of Dodoma, Tanzania, PO Box 259.

Molecular-dynamic investigation of contact interaction of pure metals

A. Yu. Nikonov A. I. Dmitriev S. G. Psakhie
nikonov@usgroups.com

Abstract

In using the method of molecular dynamics simulation of contact interaction between the copper crystallite and the various pure metals under shear loading was carried out. Shown that the structure of the boundary layer obtained during the shear deformation is determined by the loading conditions and materials of contact pair. In particular, in the interaction of copper with aluminum, soft aluminum material begins to be introduced into the lattice of copper, and in the interaction of copper with iron, this process is not observed. The effect of loading conditions and mode of heat transfer was studied. The research results can be useful for controlling strength properties of interfacial layer coated material, as well as to control the properties of the surface layer in contact problems.

1 Introduction

A large variety of realized micromechanisms interaction under conditions of frictional contact and multilevel nature of the processes of friction and wear leads to the need to develop new tools explicitly take into account features of the studied phenomena [1, 2, 3]. This leads to considerable interest in development, including computational methods to study and analyze a wide range of processes in the surface layers of the solid [3, 4, 5]. The results obtained during the simulation allow better understand the mechanisms of contact interaction, which enable targeted impact on the structure and composition of the surface layers of frictional materials to enhance and improve their performance.

Because the friction and wear processes are accompanied by intensive formation and accumulation of damage in the contact area, mixing the material, cleavage and other processes related to the continuity violation use of computational methods based on the concept of particles [5, 6] is the predominant. Gained by the authors experience in the development and application of particle method for solving various tribological problems on mesoscopic scales [7, 8, 9, 10] allows us to speak about the effectiveness of using of this approach. In particular, the formation in a contact patch "quasi-liquid" layer in which structure differs from the structure in the bulk of both interacting bodies was shown in [8]. The structure and composition of the layer significantly affect on sliding mode of interacting bodies and determine the macroscopic characteristics of friction. Were suggested possible ways to reduce or increase the calculated value of the coefficient of friction by introducing appropriate inclusions in the surface layer of material contacting pair [9], as well as methods of stabilizing a given friction coefficient during the whole process of friction [10], which is particularly important from a practical point of view.

In this study, we attempted to analyze the features of the development processes of deformation and fracture of thin surface layers which are implemented under of conditions

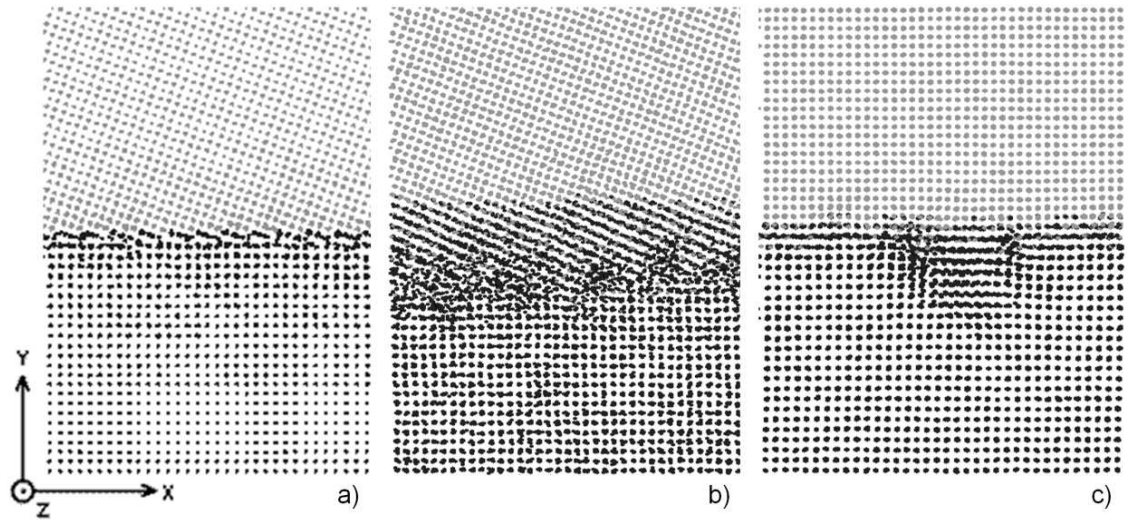

Figure 1: a) The initial structure of interacting crystallites, b) and c) structure of modeled crystallites after 500 ps with different initial relative orientation of the crystal lattices

of frictional contact at the nanoscopic scale. For this purpose, the method of particles on the atomic scale - a method of molecular dynamics [11] was selected.

2 Influence of crystallographic orientation

For calculations within the molecular dynamics method was used the software package LAMMPS [12], which has the possibility of parallel computing. Originally considered frictional contact between two crystalline materials with properties of Cu and Al, whose atomic lattice were oriented so that the axis of the X, Y and Z coincide with the crystallographic directions [100] [010] and [001] for the aluminum crystallite (Fig. 1a). In some calculations, a copper crystal was oriented so that the X, Y and Z coincide with the directions [130], [$\overline{3}$10] and [001], in others it was the same direction as the atomic lattice of the crystallite aluminum. Relative slippage of the crystallites at a speed of 20 m/s along the X axis was simulated by setting the extra velocity to the boundary atoms of crystallites, external to the contact plane. The thickness of the loaded layers for each of the grains correspond to two radii of cutoff of the interatomic potential ($R_{cut} = 0,501$ nm for copper), which was described in framework of the embedded-atom method [13]. The choice of potential was determined by the possibility with a high degree of accuracy to describe the elastic and surface properties, and energy parameters of defects of the system. The equations of motion were integrated with time step $\Delta t = 0,001$ ps. The total number of atoms exceeds 200000. In the direction of X and Y axes periodic boundary conditions were simulated, and in the Z direction the load is not set. In the calculations the following characteristics of the contact have changed: the conditions of loading and the crystallographic orientations of the atomic lattices. In addition, by varying the profile of the contacting surfaces have changed the conditions of conjugation implemented at the junction.

According to the results of molecular dynamic study the features of the behavior of crystalline materials strongly depend on the conditions implemented at the junction. In particular, in the area of tribological contact may occur effects associated with the loss of crystalline order of the interacting materials. This is followed by formation of

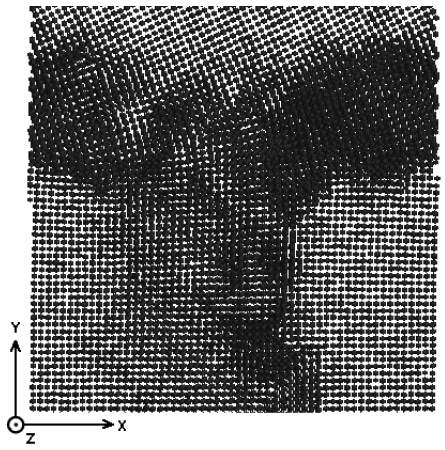

Figure 2: The structure of simulated crystallites after 450 ps, characterized by the movement of grain boundaries with the formation of structural defects

a layer in which interdiffusion of atoms belonging to both the crystallites is occurred (Fig. 1b). And this process is mechanically activated, which can significantly improve its dynamic characteristics. Likewise, in the conditions of mechanical activation can be increasing of speed, for example, processes such as oxidation of the materials pair friction pairs. It should be noted that this result was indirectly mentioned in [9], where based on a comparison of the values of coefficient of friction for various contacts was concluded about the rate of formation of oxide films on surface of pure metals. By comparing the simulation results at different scales, also it should be noted analogy of the effect of the formation of the mixed layer that was observed in [8, 9] on the scale of individual grains of nanocrystalline materials obtained by the simulation by movable cellular automata. This suggests a multiscale of studied processes and a commonality of the nature of the observed phenomena.

However, an explicit account of the atomic structure of interacting materials enable identifies and some features of the behavior of crystalline materials during their interaction. In particular, during such interaction, it is possible the formation of disoriented nanoblock structure in aluminum near the interface area, which is clearly seen in Fig. 1c. Individual blocks are nanocrystalline grains. These effects contribute to increase the resistance of the relative sliding surfaces of contacting bodies. It should be noted that the formation of block structure observed experimentally near the surface under conditions of tribological contact. The results of molecular dynamics simulations show that under conditions of straitened shear deformation may occur the growth of one of the contacting grains of nanocrystalline materials at the expense of the structure of the neighboring grain. In this case, the movement of intergrain area is determined by the loading conditions. In addition, the contact area of two interacting bodies could be the place of nucleation of defects such as dislocations, stacking faults, etc., which are distributed from the zone of the interface into the bulk of material (Fig. 2). The intersection of multiple dislocations can also lead to fragmentation of the material.

In spite of the mentioned diversity of results of computer simulation, obtained by the molecular dynamic studies, in all cases may be noted that formation of interface layer with a composition and structure differed from the structure in the bulk material takes place. Features of this layer observed before, but on a different scale level. Formation of interfacial layer at the atomic level changes surface properties of interacting materials, lowers energy barriers to form new phases (including metastable) and the initiation of

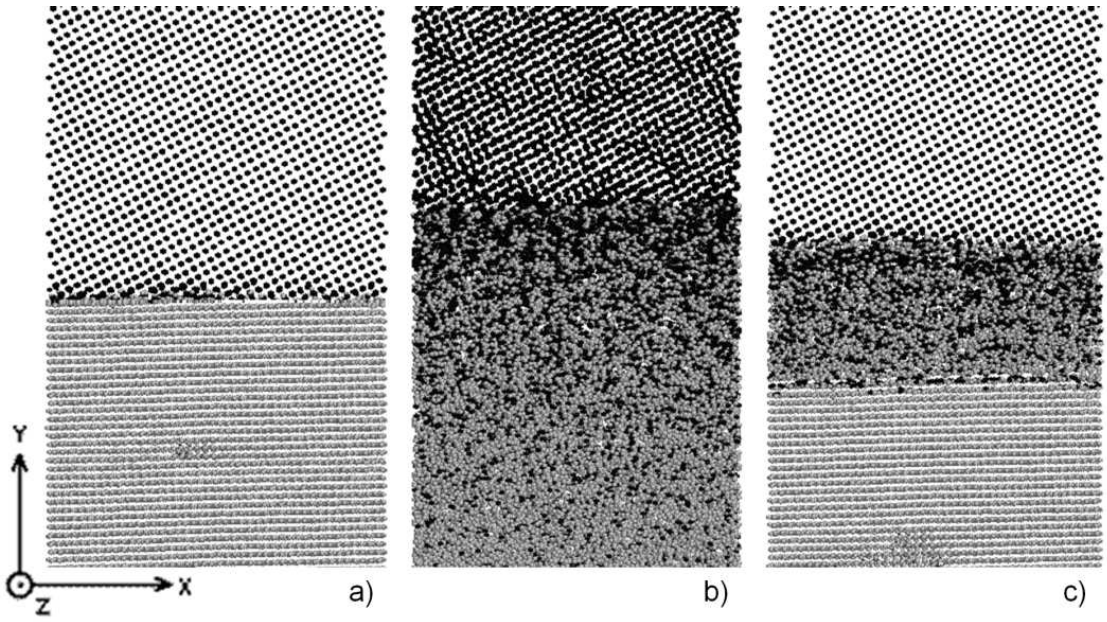

Figure 3: The structure of simulated crystallites: a) original, b) the final structure in case without the heat removal and c) the final structure in case with the heat removal.

chemical reactions.

3 Accounting for the effects of frictional heating

It is obvious that the intensive shear strain realized in conditions of contact interaction can lead to significant heating of material near the surface. So the next step of studying the features of contact interaction at the atomic scale is the explicit account of the effect of termofrictional influence upon changes in physical and mechanical properties and structure of the surface layers of contacting crystallites. In view of the smallness of the time intervals considered in the computer simulation, the steady stage of friction was investigated. the interaction of model materials with the properties of Cu and Ag, the atomic lattice of which were oriented so that the axis of the X, Y and Z corresponded to the crystallographic directions [100], [010] and [001] for the copper crystallite and the [120], [$\overline{2}$10] and [001] for the silver crystal (Fig. 3a), was simulated. Relative slippage of the crystallites at a speed of 20 m/s along the X axis was simulated by setting the extra velocity to the boundary atoms of crystallites, external to the contact plane. In the direction of X and Y axes periodic boundary conditions were simulated, and in the Z direction the load is not set. Here we consider two options for loading. In the first case, all energy imparted to the system due to external shear, redistributed within the simulated pair. In the second case, near of the loaded areas a special layer of atoms was simulated, within which was set additional dissipation of kinetic energy, thereby simulated the removal of heat from the contact area into the inner layers of extended contacting materials. Thus, the first option corresponds to the interaction of two thin films, and the second version can be viewed as a local contact of two bulk crystalline materials.

The results showed that the behavior of materials in the contact region for the options under consideration is markedly different. In the case of the interaction of two crystalline thin films occurred heating the contact area with the achievement of the melting temper-

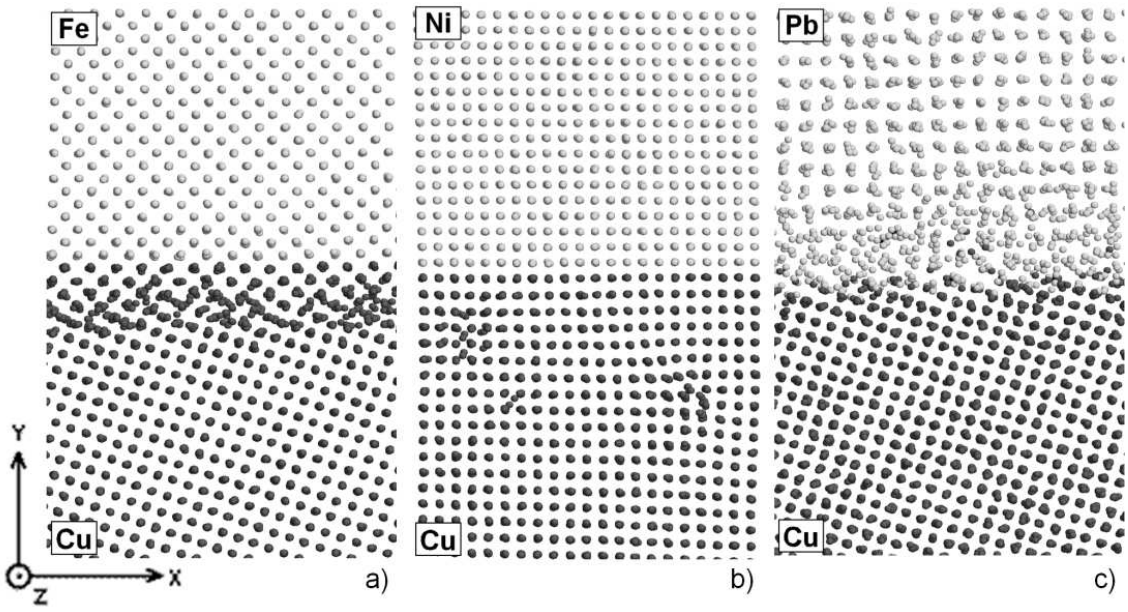

Figure 4: Structure of sample in case of modeling the interaction of copper a) with iron, b) with nickel, a) with lead.

ature of the copper crystallites. Fig. 3b clearly shows violation of the order of the atomic lattice in the bulk of simulated crystallite. In this case, a refractory material retained crystalline structure. Characteristically, the relative slippage of interacting material is accompanied by the mixing of atoms in the contact zone with a pronounced gradient nature of the implementation of the Ag atoms in the copper crystal is almost the entire depth of the modeled fragment. In the case of simulation of contact with the heat removal there is the preservation of crystal lattices of the two interacting materials under the same other conditions of loading, as in the first embodiment. Meanwhile zone of mixing of atoms of both substances is localized near the contact area, and the distribution of atoms in area of interface has uniform in character (Fig. 3c). The results of the simulation should take into account in various practical applications where the mechanisms are contact interactions are determining.

4 Accounting for the influence of type of material

It is obvious that not only the orientation and temperature, but the type of contacting materials affect on the features of contact interaction. This is primarily due to the difference between the phase diagrams of interacting agents. Thus, the next stage of the study was simulation of contact interaction of copper with different metals. The relative orientation of the crystals was selected so that the axes coincide with the directions [130], [$\bar{3}$10] and [001] for copper [100] [010] and [001] for the second crystallite (Fig. 1a). Loading conditions corresponded to the task of adapting frictional heating. Addressed the following metals: iron, nickel and lead.

The simulation results showed that the behavior of metals in the contact area varies greatly. In the interaction of copper with iron a few atomic layers of copper transformed from the fcc structure into the bcc and incorporated into lattice of iron (Fig. 3a). Upon further loading, the restructuring does not occur, only region with disrupted structure at the interface between the bcc and fcc copper increases.

According to the results of modeling of copper with nickel the contact interaction reduces to a complete reorientation of the copper atoms and incorporating on the lattice of nickel (Fig. 3b). This is probably due to the fact that the lattice parameters for copper and nickel are very similar (3,615 Å and 3,524 Å, respectively). High in comparison with other metals the rate of restructuring has suggested that the reorientation of the lattice will occur without an external load, but that has not been confirmed in the further study.

In the interaction of copper with lead, the simulation results are similar to the case of interaction between copper with aluminum. During the loading the atomic structure of lead near the interface starts to break down (Fig. 3c). With further load the width of the layer with structure similar to the irregular increases.

5 Conclusions

The main results can be formulated as follows. With the help of computer simulation revealed some features of contact interaction occurring at the level of individual atoms. It is shown that, during the relative sliding in the contact area a special interface layer formed, whose structure differs from the structure of the material in bulk. Conditions of formation of interfacial layer and its parameters are determined by various factors, such as: matter of contacting pairs, loading conditions, the degree of misorientation of atomic planes, conjugation conditions, etc. Thus, under certain conditions, atoms of one material can penetrate into the crystal lattice of another material, replacing the atoms in it basis. Because this process is a mechanically activated, then the rate of such diffusion is much higher traditional process. Change the crystallographic orientation of the contacting crystallite significantly affects the speed of the process of structural change.

The results of these studies can be used to understand the processes determining the strength properties of interfacial layer of the coated materials, as well as to control the properties of the surface layer in contact problems.

Acknowledgements

The work was supported by fundamental research program of the Department of Energy, Engineering, Mechanics and Control Processes of RAS No. 13.13.3, and integration project of SB RAS No. 127.

References

[1] Gorjacheva I.G. The mechanics of frictional interaction. M.: Nauka, 2001. 478 p.

[2] Panin V.E., Elsukova T.F., Grinyaev Yu.V. Mechanism of the effect of grain size on resistance to deformation of polycrystals in the concept of structural levels of deformation of solids. Part I. The need to incorporate mesoscopic structural levels of deformation in the analysis of the Hall-Petch equation. Phys. Mesomech., 6, No. 3 (2003) 63.

[3] Persson B.N.J., Bucher F., Chiaia B. Elastic Contact Between Randomly Rough Surfaces: Comparison of Theory with Numerical Results // Phys. Rev. B. 64, No.18 (2002) 184106/1 – 184106/7.

[4] Iordanoff I., Berthier Y.: First steps for a rheological model for the solid third body. Tribology Series 36 (1999) 551-559.

[5] Krivtsov A.M., Volkovets I.B., Tkachev P.V., Tsaplin V.A. Application of the method of particle dynamics to describe the high-speed fracture of solids // Third All-Russian Conference "Mathematics, Mechanics and Informatics 2002".

[6] Ostermeyer G.P.: The mesoscopic particle approach. Tribol.Intern. 40 (2007) 953-959.

[7] Dmitriev A.I., Oesterle W.: Modeling of brake pad-disc interface with emphasis to dynamics and deformation of structures. Trib. Int., Vol.43 Issue 4, (2010) P.719-727.

[8] Popov V.L., Psakhie S.G., Shilko E.V., Dmitriev A.I. Quasi-fluid nano-layers at the interface between rubbing bodies: simulation by movable cellular automata // Wear., 254, No. 9 (2003) 901 – 906.

[9] Dmitriev A.I.; Oesterle W.; Kloss H.: Numerical simulation of typical contact situations of brake friction materials. Tribology International 41 (2008) 1–8.

[10] Dmitriev A.I., Oesterle W., Kloss H.: Numerical simulation of mechanically mixed layer formation at local contacts of an automotive brake system. Tribology Transactions 51 (2008) 810–816.

[11] Guld H. Tobochnik Ja. Computer Simulation in Physics. – M.: Mir, 1990. – V.1. – 350 p.

[12] Plimpton, S.J. Fast Parallel Algorithms for Short-Range Molecular Dynamics // J. Comp. Phys. 1995. V. 117. No. 1, P. 1–19.

[13] Foiles S.M. Embedded-atom and related methods for modeling metallic systems // MRS Bull, 1996. V. 21, 2, P. 24–28.

Nikonov A.Yu., Akademichesky 2/4, 634021, Tomsk, Russia
Dmitriev A.I., Akademichesky 2/4, 634021, Tomsk, Russia

Stability of 2D triangular lattice under finite biaxial strain

Ekaterina A. Podolskaya Artem Yu. Panchenko Anton M. Krivtsov
katepodolskaya@gmail.com

Abstract

Stability of 2D triangular lattice under finite biaxial strain is investigated. In this work only diagonal strain tensor is regarded. The lattice is considered infinite and consisting of particles which interact by pair force central potential. Dynamic stability criterion is used: frequency of elastic waves is required to be real for any real wave vector. Two stability regions corresponding to horizontal and vertical orientations of the lattice are obtained. It means that a structural transition, which is equal to the change of lattice orientation, is possible. The regions' boundaries are explained: wave equation coefficients change their signs at the border, as well as Young modulae and shear modulae. The results are proved by direct numerical simulation.

1 Introduction

In this work stability of plane triangular lattice under finite biaxial strain is investigated. This problem and its possible solutions have been considered earlier in [1]. Then in [2] a qualitatively new result, that is proved and discussed in detail in this work, was obtained. In spite of the fact that real objects with such lattice have not been discovered, triangular lattice is convenient for both constructing the theory and carrying out numerical simulations. Finite strain may lead to discontinuities, so in this work analysis and modeling based on discrete atomistic methods [3] is proposed. The medium is represented by a set of particles interacting by a pair force central potential, in particular Lennard-Jones and Morse. Direct tensor calculus [4] is used.

Let us introduce the following notation to describe the geometry:

$$\underline{a}_k = \underline{r}_k - \underline{r}_0, \tag{1}$$

where $\underline{r}_k$ is radius vector of a particle k, $\underline{r}_0$ is radius vector of reference particle. If a lattice is simple, then any particle can be named "reference", each particle k has a pair $-k$ and $\underline{a}_{-k} = -\underline{a}_k$. Triangular lattice is simple and close-packed, which means that it coincides with its Bravais lattice and possesses maximum concentration of nods in elementary volume V_0 with the given minimum distance between the nods. Let us refer to the geometry which is described by $\underline{r}_k$ and $\underline{a}_k$ as reference configuration.

Let $\overset{\circ}{\nabla}$ and ∇ be Hamilton's operators in reference and current configurations [4]:

$$\overset{\circ}{\nabla} = \underline{e}_i \frac{\partial}{\partial x_i}, \qquad \nabla = \underline{e}_i \frac{\partial}{\partial X_i}. \tag{2}$$

Vectors $\underline{e}_i$ form an orthonormal basis. If vector $\underline{r}$ has projections x_i in reference configuration, then in current configuration $\underline{r}$ will turn into $\underline{R}$ with projections X_i in the same basis.

Suppose that the lattice is subject to strain characterized by $\overset{\circ}{\nabla}\underline{R}$. According to long-wave approximation [3, 5]

$$\underline{A}_k = \underline{R}\,(\underline{r} - \underline{a}_k) - \underline{R}\,(\underline{r}) \approx \underline{a}_k \cdot \overset{\circ}{\nabla}\underline{R}. \tag{3}$$

Long-wave approximation takes into account those wave lengths that are much greater than the interatomic distance. The thermal motion is neglected.

Morse and Lennard-Jones potentials are used in this work to describe the interaction between particles

$$\mathit{\Pi}(r) = D\left[e^{-2\theta\left(\frac{r}{a}-1\right)} - 2e^{-\theta\left(\frac{r}{a}-1\right)}\right], \quad \mathit{\Pi}_{LJ}(r) = D\left[\left(\frac{a}{r}\right)^{12} - 2\left(\frac{a}{r}\right)^{6}\right]. \tag{4}$$

Here a is equilibrium distance in the system of two particles, D is the depth of potential well, θ characterizes the width of the well. If $\theta = 6$, these potentials coincide in the elastic zone. If $r \to 0$, then $\mathit{\Pi}_{LJ} \to \infty$, but Morse potential remains finite. This is very important for numerical simulations of strong compression. If $r \to \infty$, then Morse potential decreases faster, so less particles may be taken into consideration. That is why Morse potential is preferable in this work.

Let $F_k = F(A_k) = -\Pi'(A_k)$ be interaction force and $C_k = C(A_k) = \Pi''(A_k)$ be the bond stiffness, both calculated in current configuration. Then we can introduce

$$\begin{aligned}
&\underline{\underline{A}}_k = \underline{A}_k\underline{A}_k, \quad {}^4\underline{\underline{A}}_k = \underline{A}_k\underline{A}_k\underline{A}_k\underline{A}_k, \quad \underline{\underline{a}}_k = \underline{a}_k\underline{a}_k, \quad {}^4\underline{\underline{a}}_k = \underline{a}_k\underline{a}_k\underline{a}_k\underline{a}_k \\
&\Phi_k = -\frac{F_k}{A_k}, \quad \mathcal{B}_k = \frac{1}{A_k^2}(C_k - \Phi_k), \quad \underline{\underline{\Phi}} = \frac{1}{2}\sum_k \Phi_k \underline{\underline{A}}_k, \quad {}^4\underline{\underline{\mathcal{B}}} = \frac{1}{2}\sum_k \mathcal{B}_k\, {}^4\underline{\underline{A}}_k.
\end{aligned} \tag{5}$$

2 Stability criterion

Following [1, 2], let us write the equation of motion in Piola form [4]

$$\rho_0 \ddot{\underline{u}} = \overset{\circ}{\nabla} \cdot \underline{\underline{P}}, \tag{6}$$

where ρ_0 is density in the reference configuration, $\underline{u} = \underline{R} - \underline{r}$ is displacement vector, $\underline{\underline{P}}$ is Piola stress tensor. According to [3]

$$\underline{\underline{P}} = \frac{1}{2V_0}\sum_k \Phi_k \underline{a}_k \underline{A}_k. \tag{7}$$

To investigate the stability of current configuration the first variation of (6) is found [1]

$$\rho_0 \delta\ddot{\underline{u}} = \overset{\circ}{\nabla} \cdot \delta\underline{\underline{P}}. \tag{8}$$

If initial deformation characterized by $\overset{\circ}{\nabla}\underline{R}$ is uniform, the following equation is obtained from (8) using (5)

$$m\ddot{\underline{v}} = {}^4\underline{\underline{C}} \cdots \nabla\nabla\underline{v}, \tag{9}$$

where $m = \rho_0 V_0$, $\underline{v} = \delta\underline{u}$, ${}^4\underline{\underline{C}} = \underline{\underline{E}}\,\underline{\underline{\Phi}} + {}^4\underline{\underline{\mathcal{B}}}$.

The solution of (9) can be represented in the following form

$$\underline{v} = \underline{v}_0 e^{i\omega t} e^{i\underline{K}\cdot\underline{R}}, \tag{10}$$

where ω is frequency, $\underline{K}$ is wave vector. Substitution of solution (10) into equation (9) leads to a system of homogeneous linear equations for amplitude v_0. This system has non-trivial solution, if

$$\det\left[\underline{\underline{D}} - \Omega\underline{\underline{E}}\right] = 0, \tag{11}$$

where $\Omega = m\omega^2$, $\underline{\underline{D}} = {}^4\underline{\underline{C}} \cdot\cdot\, \underline{\underline{K}}$, $\underline{\underline{K}} = \underline{K}\,\underline{K}$.

Dynamic stability criterion is: frequency of elastic waves is required to be real for any real wave vector. Thus, the following has to be fulfilled for any real vector $\underline{K}$, so that $\underline{v}$ will remain infinitesimal

$$\Omega > 0. \tag{12}$$

3 Deformation of triangular lattice

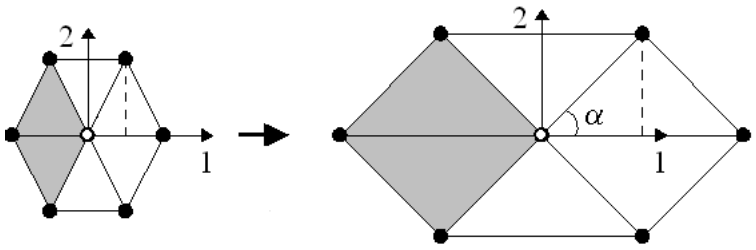

Figure 1: Reference and current configurations

Fig. 1 shows the typical part of triangular lattice before and after deformation. In reference configuration $\alpha = 60°$.

Let $\underline{e}_1$ and $\underline{e}_2$ be the unit vectors of directions 1 and 2 respectively. In 2D case (11) takes the form

$$\Omega^2 - \Omega \operatorname{tr}\underline{\underline{D}} + \det\underline{\underline{D}} = 0. \tag{13}$$

According to (12) roots of equation (13) are positive for stable current configurations. Thus, stability criterion is

$$\operatorname{tr}\underline{\underline{D}} > 0, \qquad \det\underline{\underline{D}} > 0, \qquad 2\operatorname{tr}\underline{\underline{D}}^2 - \left(\operatorname{tr}\underline{\underline{D}}\right)^2 \geq 0. \tag{14}$$

Inequality $2\operatorname{tr}\underline{\underline{D}}^2 - \left(\operatorname{tr}\underline{\underline{D}}\right)^2 \geq 0$ is always true in 2D.

Let $\underline{\underline{G}} = \underline{\underline{E}} \cdot\cdot\, {}^4\underline{\underline{C}}$. The equations (14) yield

$$\begin{aligned} &\operatorname{tr}\underline{\underline{D}} > 0 \Leftrightarrow G_{11}K_1^2 + G_{22}K_2^2 > 0, \\ &\det\underline{\underline{D}} > 0 \Leftrightarrow AK_1^4 + 2BK_1^2K_2^2 + CK_2^4 > 0, \end{aligned} \tag{15}$$

where

$$\begin{aligned} &G_{11} = C_{11} + C_{21}, \qquad G_{22} = C_{12} + C_{22}, \\ &A = C_{11}C_{21}, \quad 2B = C_{11}C_{22} + C_{12}C_{21} - 4C_{44}^2, \quad C = C_{12}C_{22}. \end{aligned} \tag{16}$$

Here C_{ij} are the components of tensor ${}^4\underline{\underline{C}}$ from (9).

The stability regions for Morse potential with $\theta = 6$ are shown in fig. 2.

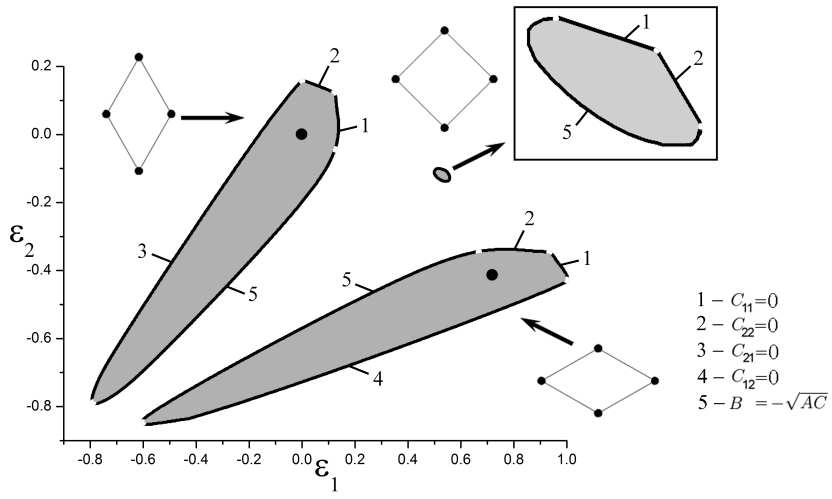

Figure 2: Stability regions

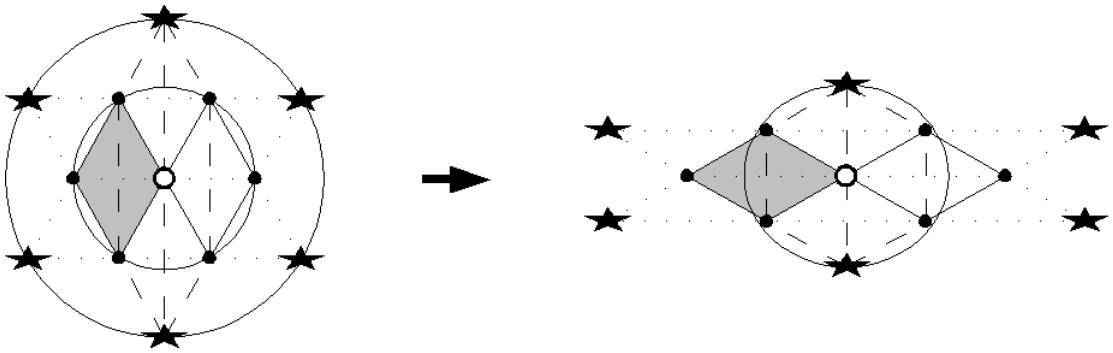

Figure 3: Coordination spheres

Here ε_1 and ε_2 are linear parts of Cauchy-Green tensor. Two coordination spheres are considered, because taking only the first sphere into account is not sufficient in the case of finite strain [2].

Fig. 3 shows the transition from the vertical orientation to the horizontal orientation of the lattice. Particles from first coordination sphere in vertical lattice are marked by circles, stars correspond to second sphere. After deformation that is equal to rotation all particles change their position, and some "stars" occupy the place of "circles" in close vicinity to reference particle. If the second sphere is neglected, there will be no equilibrium at horizontal lattice [1, 2].

Let us draw a series of stress-strain diagrams, e.g. fig. 4. According to [3] Cauchy stress tensor has the form

$$\underline{\underline{\sigma}} = \frac{1}{2V} \sum_k \underline{A}_k \underline{F}_k, \tag{17}$$

where $V = \sqrt{3}/2(1+\varepsilon_1)(1+\varepsilon_2)$. Grey zones in the fig. 4 correspond to stability regions. In the fig. 4 we can see, that the loss of stability is strongly connected with the sign of $d\sigma/d\varepsilon$.

Let us evaluate the signs of Young modulae and shear modulae (the plural is due to anisotropy of the deformed lattice).

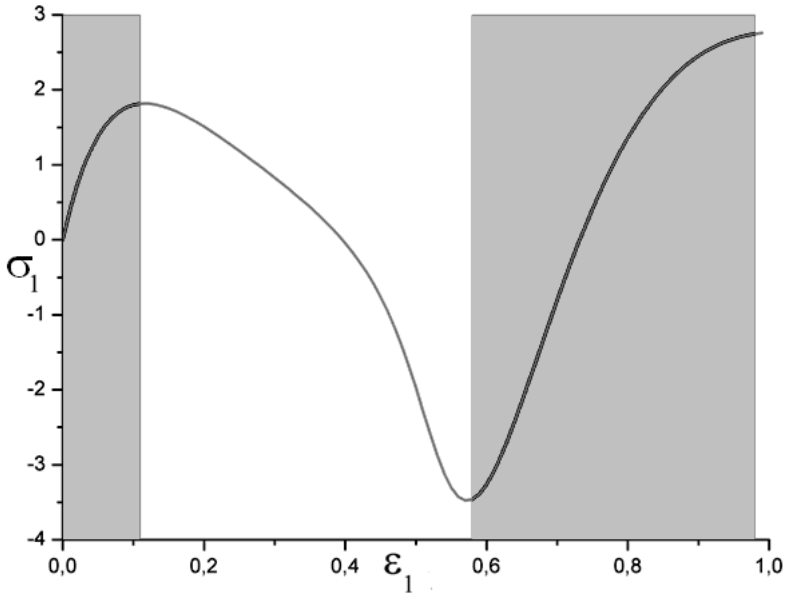

Figure 4: Uniaxial loading ($\sigma_2 = 0$)

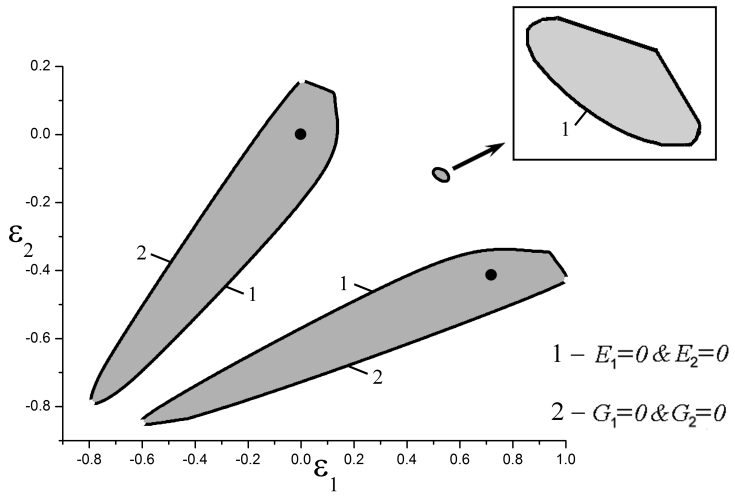

Figure 5: Young modulae and shear modulae

In the fig. 5 we can see, that dynamic and "static" stability (positivity of local elastic modulae) coincide in the case of diagonal stress tensor.

The number and the shape of stability regions strongly depend on the potential (see fig. 6). For example, intermediate small stability area vanishes with the decrease of θ (increase of width of potential well).

4 MD simulation

In order to verify the obtained results, numerical simulation is carried out. The simulation method is based on molecular dynamics (MD) technique and it is described in [3, 6]. A set of current configurations with periodic boundary conditions to model an infinite lattice is exposed to additional minor strains caused by small chaotic velocities, given to each

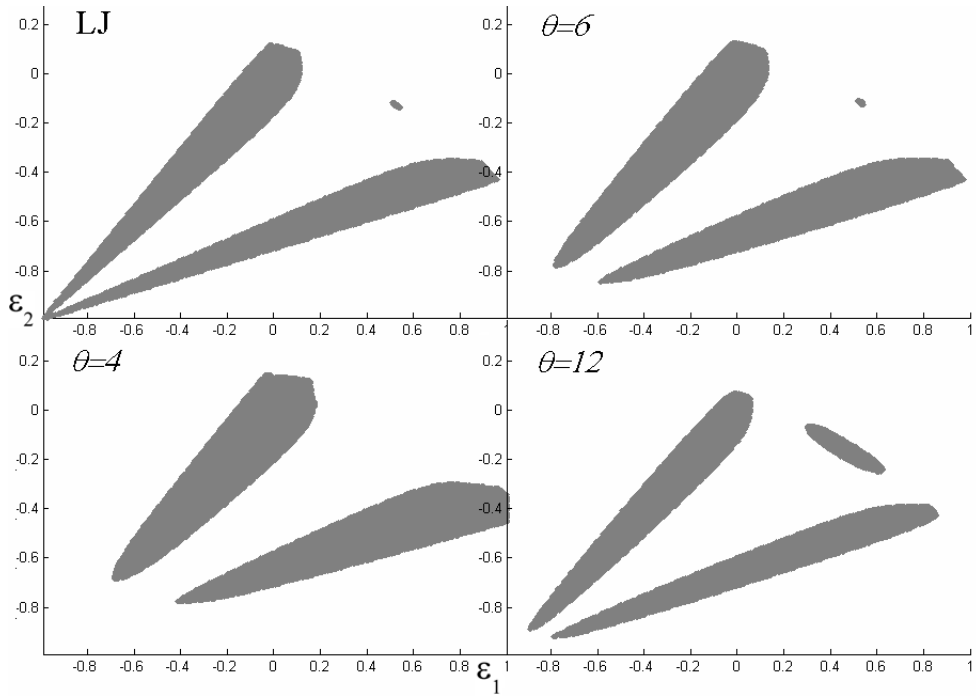

Figure 6: Stability regions for different potentials

particle. At each step the following system is integrated numerically

$$m\ddot{\underline{r}}_k = \sum_{n=1}^{N} F\left(|\underline{r}_k - \underline{r}_n|\right) \frac{\underline{r}_k - \underline{r}_n}{|\underline{r}_k - \underline{r}_n|}, \qquad k = 1 \div N, \tag{18}$$

where N is the total number of particles in the simulation. The total kinetic energy of the system is calculated. If a sudden growth of kinetic energy is observed, the configuration is considered unstable. An example of unstable configuration evolution is presented in the fig. 7. Black ovals mark "crack" initiation zones.

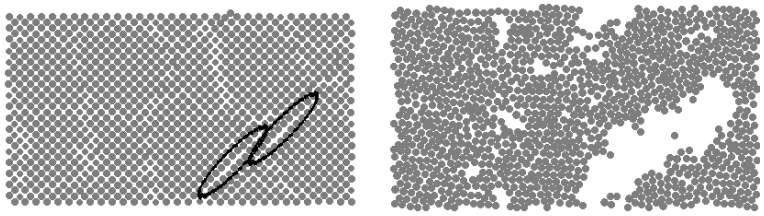

Figure 7: Configuration $\varepsilon_1 = 0.506$, $\varepsilon_2 = -0.108$ after 10^5 and $3{\cdot}10^5$ integration steps

In the fig. 8 the results for diagonal strain tensor are presented. We can see a good agreement between two approaches. Discrepancies at high compression and at the borders are caused by computational errors, perhaps by insufficient number of steps and also by the difference between the number of configurations regarded (10^6 in theoretical analysis and 10^4 in numerical simulation due to big time consumption of the latter).

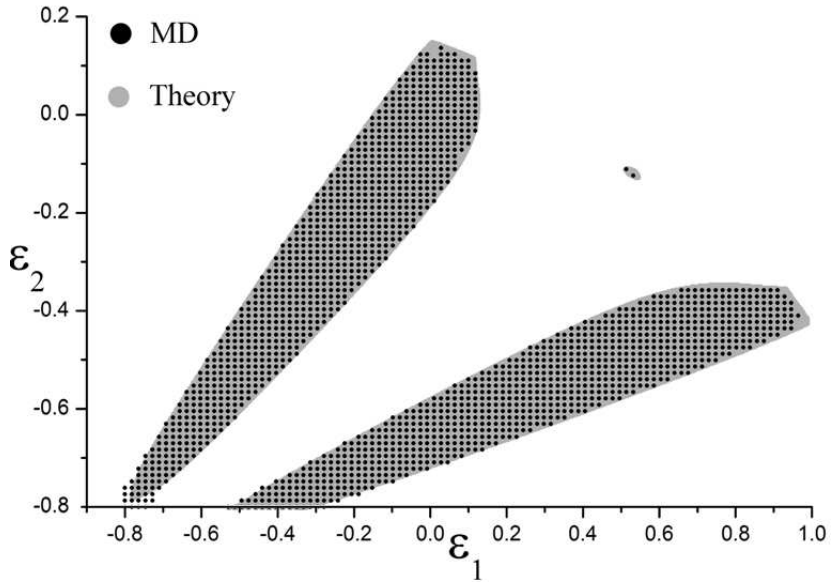

Figure 8: Results of numerical simulation

5 Concluding remarks

Stability of 2D triangular lattice under finite biaxial strain was investigated. Two stability regions, which correspond to vertical and horizontal orientations of the lattice, were obtained both analytically and using MD simulation. It was shown that taking more than one coordination sphere into account leads to a new effect: possibility of structural transition, which is equal to the change of lattice orientation. It was noticed that dynamic and static stability coincide in the case of diagonal strain tensor. It was also shown that stability loss during hydrostatic compression is connected with shear modulus, which coincides with results of [7] obtained for 3D case. To sum up, the analytical approach was proved to be consistent and thus it can be applied to more complex cases, e.g. arbitrary strain of triangular lattice and FCC lattice.

References

[1] P.V. Tkachev, A.M. Krivtsov. Stability criterion of internal structure of the material // XXXIII Science week, St. Petersburg State Polytechnical University. Part V. 2004. P. 4–6. (In Russian).

[2] E.A. Podolskaya, P.V. Tkachev, A.M. Krivtsov. FCC latice stability analysis // XXXIX Science week, St. Petersburg State Polytechnical University. Part V. 2010. P. 111–112. (In Russian).

[3] A.M. Krivtsov. Deformation and fracture of solids with microstructure. Moscow, Fizmatlit. 2007. 304 p. (In Russian).

[4] A.I. Lurie. Nonlinear theory of elasticity. North-Holland. Amsterdam. 1990. 617 p.

[5] M. Born, K. Huang. Dynamical theory of crystal lattices. Oxford: Clarendon Press. 1954. 420 p.

[6] A.M. Krivtsov. Molecular dynamics simulation of plastic effects upon spalling // Physics of the Solid State. 2004. 46(6). P. 1055–1060.

[7] F. Milstein, D. Rasky. Theoretical study of shear-modulus instabilities in the alkali metals under hydrostatic pressure // Phys. Rev. B. 1996. V.54. 10. P. 7016–7025.

Ekaterina A. Podolskaya, 29, Politechnicheskaya str., St. Petersburg, 195251, Russia
Artem Yu. Panchenko, 29, Politechnicheskaya str., St. Petersburg, 195251, Russia
Anton M. Krivtsov, 61, Bolshoj pr., V.O., St. Petersburg, 199178, Russia

Influence of shear strain on stability of 2D triangular lattice

Ekaterina A. Podolskaya Artem Yu. Panchenko Karina S. Bukovskaya
katepodolskaya@gmail.com

Abstract

Stability of 2D triangular lattice under finite arbitrary strain is investigated. The lattice is considered infinite and consisting of particles which interact by pair force central potential. Dynamic stability criterion is used: frequency of elastic waves is required to be real for any real wave vector. Two stability regions corresponding to horizontal and vertical orientations of the lattice are obtained. It means that a structural transition, which is equal to the change of lattice orientation, is possible.

1 Introduction

In work [1] stability of plane triangular lattice under finite biaxial strain was investigated. Two stability regions, which correspond to vertical and horizontal orientations of the lattice, were obtained both analytically and using MD simulation. It was shown that taking more than one coordination sphere into account leads to a new effect: possibility of structural transition, which is equal to the change of lattice orientation. In this work shear strain is added. Modeling based on discrete atomistic methods [2] is proposed. The medium is represented by a set of particles interacting by a pair force central potential, in particular Lennard-Jones and Morse. Direct tensor calculus [3] is used.

Following [4, 5, 1], let us introduce the following notation to describe the geometry:

$$\underline{a}_k = \underline{r}_k - \underline{r}_0, \tag{1}$$

where $\underline{r}_k$ is radius vector of a particle k, $\underline{r}_0$ is radius vector of reference particle. If a lattice is simple, then any particle can be named "reference", each particle k has a pair $-k$ and $\underline{a}_{-k} = -\underline{a}_k$. Triangular lattice is simple and close-packed: it coincides with its Bravais lattice and possesses maximum concentration of nods in elementary volume V_0 with the given minimum distance between the nods. Let us refer to the geometry which is described by $\underline{r}_k$ and $\underline{a}_k$ as reference configuration.

Let $\overset{\circ}{\nabla}$ and ∇ be Hamilton's operators in reference and current configurations [3]:

$$\overset{\circ}{\nabla} = \underline{e}_i \frac{\partial}{\partial x_i}, \qquad \nabla = \underline{e}_i \frac{\partial}{\partial X_i}. \tag{2}$$

Vectors $\underline{e}_i$ form an orthonormal basis. If vector $\underline{r}$ has projections x_i in reference configuration, then in current configuration $\underline{r}$ will turn into $\underline{R}$ with projections X_i in the same basis.

Suppose that the lattice is subject to strain characterized by $\overset{\circ}{\nabla}\underline{R}$. According to long-wave approximation [2, 6]

$$\underline{A}_k = \underline{R}\,(\underline{r} - \underline{a}_k) - \underline{R}\,(\underline{r}) \approx \underline{a}_k \cdot \overset{\circ}{\nabla}\underline{R}. \tag{3}$$

Long-wave approximation takes into account those wave lengths that are much greater than the interatomic distance. The thermal motion is neglected.

Morse and Lennard-Jones potentials are used in this work to describe the interaction between particles

$$\Pi(r) = D\left[e^{-2\theta\left(\frac{r}{a}-1\right)} - 2e^{-\theta\left(\frac{r}{a}-1\right)}\right], \quad \Pi_{LJ}(r) = D\left[\left(\frac{a}{r}\right)^{12} - 2\left(\frac{a}{r}\right)^{6}\right]. \tag{4}$$

Here a is equilibrium distance in the system of two particles, D is the depth of potential well, θ characterizes the width of the well. If $\theta = 6$, these potentials coincide in the elastic zone. Morse potential is preferable in this work, because, firstly, it decreases faster, so less particles may be taken into consideration, secondly, if $r \to 0$ Morse potential remains finite.

Let $F_k = F(A_k) = -\Pi'(A_k)$ be interaction force and $C_k = C(A_k) = \Pi''(A_k)$ be the bond stiffness, both calculated in current configuration. Then we can introduce

$$\begin{aligned} &\underline{\underline{A}}_k = \underline{A}_k\underline{A}_k, \quad {}^4\underline{\underline{A}}_k = \underline{A}_k\underline{A}_k\underline{A}_k\underline{A}_k, \quad \underline{\underline{a}}_k = \underline{a}_k\underline{a}_k, \quad {}^4\underline{\underline{a}}_k = \underline{a}_k\underline{a}_k\underline{a}_k\underline{a}_k \\ &\Phi_k = -\frac{F_k}{A_k}, \quad \mathcal{B}_k = \frac{1}{A_k^2}(C_k - \Phi_k), \quad \underline{\underline{\Phi}} = \frac{1}{2}\sum_k \Phi_k\underline{\underline{A}}_k, \quad {}^4\underline{\underline{\mathcal{B}}} = \frac{1}{2}\sum_k \mathcal{B}_k{}^4\underline{\underline{A}}_k. \end{aligned} \tag{5}$$

2 Stability criterion and deformation of triangular lattice

In the previous works [4, 5, 1] the following stability criterion was applied

$$\Omega > 0, \tag{6}$$

where Ω is determined from equation

$$\det\left[\underline{\underline{D}} - \Omega\underline{\underline{E}}\right] = 0. \tag{7}$$

Here

$$\underline{\underline{D}} = {}^4\underline{\underline{C}}\cdot\cdot\,\underline{\underline{K}}, \quad {}^4\underline{\underline{C}} = \underline{\underline{E}}\underline{\underline{\Phi}} + {}^4\underline{\underline{\mathcal{B}}}, \quad \underline{\underline{K}} = \underline{K}\underline{K}.$$

$\underline{K}$ is a real wave vector. This means that frequency of elastic waves is required to be real for any real wave vector.

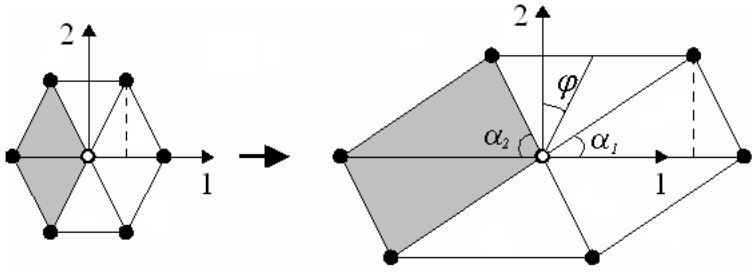

Figure 1: Reference and current configurations

Fig. 1 shows the typical part of triangular lattice before and after deformation. In reference configuration $\alpha_1 = \alpha_2 = 60°$. It is sufficient to take only $0 \le \varphi \le 30°$ in account due to symmetry and infiniteness of the lattice. It was shown in [5, 1] that at least two coordination spheres should be considered.

In 2D case (7) takes the form

$$\Omega^2 - \Omega \operatorname{tr} \underline{\underline{D}} + \det \underline{\underline{D}} = 0. \tag{8}$$

According to (6) roots of equation (8) are positive for stable current configurations. Thus, stability criterion is

$$\operatorname{tr} \underline{\underline{D}} > 0, \qquad \det \underline{\underline{D}} > 0, \qquad 2 \operatorname{tr} \underline{\underline{D}}^2 - \left(\operatorname{tr} \underline{\underline{D}}\right)^2 \geq 0. \tag{9}$$

Inequality $2 \operatorname{tr} \underline{\underline{D}}^2 - \left(\operatorname{tr} \underline{\underline{D}}\right)^2 \geq 0$ is always true in 2D.

Let $\underline{\underline{G}} = \underline{\underline{E}} \cdot\cdot^4 \underline{\underline{C}}$. The equations (9) yield

$$\begin{aligned} &\operatorname{tr} \underline{\underline{D}} > 0 \Leftrightarrow G_{11} K_1^2 + G_{12} K_1 K_2 + G_{22} K_2^2 > 0, \\ &\det \underline{\underline{D}} > 0 \Leftrightarrow A K_1^4 + B K_1^2 K_2^2 + C K_2^4 + D K_1^3 K_2 + E K_1 K_2^3 > 0, \end{aligned} \tag{10}$$

where

$$\begin{gathered} G_{11} = C_{11} + C_{21}, \quad G_{12} = C_{14} + C_{24}, \quad G_{22} = C_{12} + C_{22}, \\ A = C_{11} C_{21} - C_{41}^2, \quad B = 4 C_{14} C_{24} + C_{11} C_{22} + C_{12} C_{21} - 2 C_{41} C_{42} - 4 C_{44}^2, \\ C = C_{12} C_{22} - C_{42}^2, \quad D = 2 C_{11} C_{24} - 4 C_{41} C_{44} + 2 C_{14} C_{21}, \\ E = 2 C_{12} C_{24} + 2 C_{14} C_{22} - 4 C_{42} C_{44}. \end{gathered} \tag{11}$$

Here C_{ij} are the components of tensor ${}^4\underline{\underline{C}}$.

The left part of $\operatorname{tr} \underline{\underline{D}} > 0$ is a quadratic form in the components of the wave vector K_1 and K_2. It is positive definite, if

$$T_{11} > 0, \quad 4 T_{11} T_{22} - T_{12}^2 > 0. \tag{12}$$

The left part of $\det \underline{\underline{D}} > 0$ is a homogeneous polynomial of degree four. In this case, a general analytical criterion cannot be constructed.

Due to the fact that both K_1 and K_2 may be equal to zero, two necessary stability conditions are obtained, which help to narrow down the set of current configurations ε_1, ε_2, φ

$$A > 0, \quad C > 0. \tag{13}$$

Then, there are two ways to obtain sufficient conditions:

1. For each ε_1, ε_2, φ we can construct $\det \underline{\underline{D}}$, and check it for a set of K_1 and K_2 (Monte Carlo method). The inequality is homogeneous and even, so it is sufficient to consider only $-1 \leq K_1 \leq 1$ and $0 \leq K_2 \leq 1$, which increases the efficiency.

2. We can divide $\det \underline{\underline{D}}$ by K_2^4 and look into the problem of determining the coefficients so that a fourth-degree equation has no real roots, again for each ε_1, ε_2, φ. This method is much faster, but it causes a problem of distinguishing between complex and real roots, which leads to inaccurate results at the border.

In the fig. 2 stability regions, obtained by inequalities (12) and (13) and by the second method, are drawn. Here ε_1 and ε_2 are linear parts of Cauchy-Green tensor. There are several points, marked black, which were added by the first method. The stability

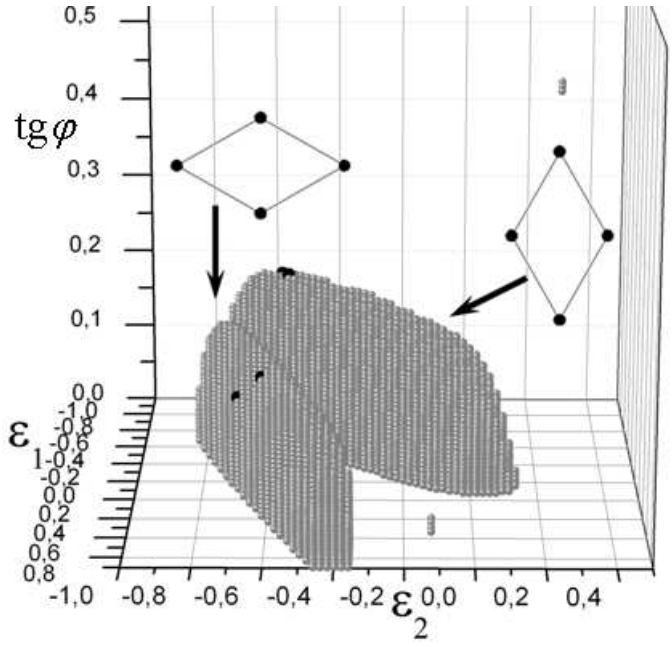

Figure 2: Stability regions

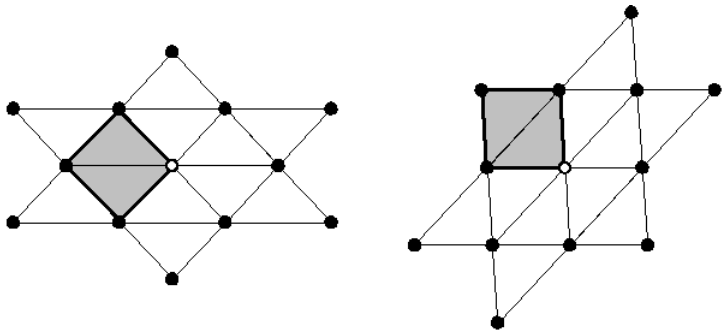

Figure 3: Square lattices at $\varphi \approx 0°$ and $\varphi \approx 26°$

regions are symmetric with respect to the plane $\mathrm{tg}\,\varphi = 0$. Two major areas correspond to horizontal and vertical orientations of the lattice [1]. Two additional small stability areas are connected with square lattices at $\varphi \approx 0°$ and $\varphi \approx 26°$ (see fig. 3).

Let us draw a series of stress-strain diagrams, e.g. fig. 4. According to [2] Cauchy stress tensor has the form

$$\underline{\underline{\sigma}} = \frac{1}{2V} \sum_k \underline{A}_k \underline{F}_k, \tag{14}$$

where $V = \sqrt{3}/2(1+\varepsilon_1)(1+\varepsilon_2)$. Grey zone in the fig. 4 corresponds to stability region, σ_{12} is diagonal component of Cauchy stress tensor. In the fig. 4 we can see, that the loss of stability is strongly connected with the sign of the first derivative.

3 Concluding remarks

Stability analysis of 2D triangular lattice under finite arbitrary strain was carried out. In addition to [1] shear was taken into account. Two stability regions were obtained,

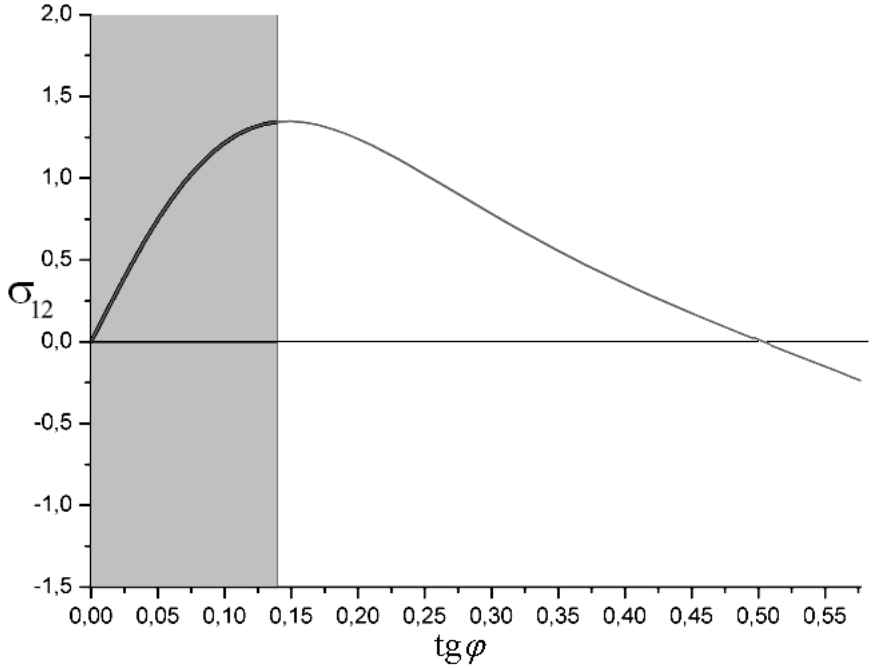

Figure 4: Pure shear ($\sigma_{11} = \sigma_{22} = 0$)

when more than one coordination sphere were regarded, and a possibility of structural transition, which is equal to the change of lattice orientation, was noticed. Monte Carlo and analytical methods were used, and they proved to give practically equal results. Thus, Monte Carlo method can be applied to more complex cases, where it is impossible to accomplish analytical investigation, e.g. 3D lattices.

Acknowledgements

The authors are grateful to professor Anton M. Krivtsov for attention to this work and for useful discussions.

References

[1] E.A. Podolskaya, A.Yu. Panchenko, A.M. Krivtsov. Stability of 2D triangular lattice under finite strain // Proc. of XXXIX Summer School - Conference "Advanced Problems in Mechanics". St. Petersburg. 2011. (In print).

[2] A.M. Krivtsov. Deformation and fracture of solids with microstructure. Moscow, Fizmatlit. 2007. 304 p. (In Russian).

[3] A.I. Lurie. Nonlinear theory of elasticity. North-Holland. Amsterdam. 1990. 617 p.

[4] P.V. Tkachev, A.M. Krivtsov. Stability criterion of internal structure of the material // XXXIII Science week, St. Petersburg State Polytechnical University. Part V. 2004. P. 4–6. (In Russian).

[5] E.A. Podolskaya, P.V. Tkachev, A.M. Krivtsov. FCC latice stability analysis // XXXIX Science week, St. Petersburg State Polytechnical University. Part V. 2010. P. 111–112. (In Russian).

[6] M. Born, K. Huang. Dynamical Theory of Crystal Lattices. Oxford: Clarendon Press. 1954. 420 p.

Ekaterina A. Podolskaya, 29, Politechnicheskaya str., St. Petersburg, 195251, Russia
Artem Yu. Panchenko, 29, Politechnicheskaya str., St. Petersburg, 195251, Russia
Karina S. Bukovskaya, 29, Politechnicheskaya str., St. Petersburg, 195251, Russia

Mechanical properties of polymer nanocomposites based on styrene butadiene rubber with different types of fillers

A. G. Pelevin A. L. Svistkov
pelevin@icmm.ru

Abstract

This article examines the theoretical description of the mechanical behavior of elastomeric nanocomposites based on butadiene styrene polymer, and several species with different filler volume fraction in 30phr and 50phr. To construct the determining equations we use the scheme (Fig. 1), whose points are connected by elastic, viscous, plastic and transmission elements [1]. To describe the properties of each element used well-known equations of nonlinear elasticity theory, the theory of nonlinear viscous fluids, the theory of plastic flow of material in the finite deformation of the medium. To obtain the constants of the model used stepwise algorithm [3]. Used in the experiments (cyclic loading, relaxation and creep) can get more information about the viscoelastic properties of rubber.

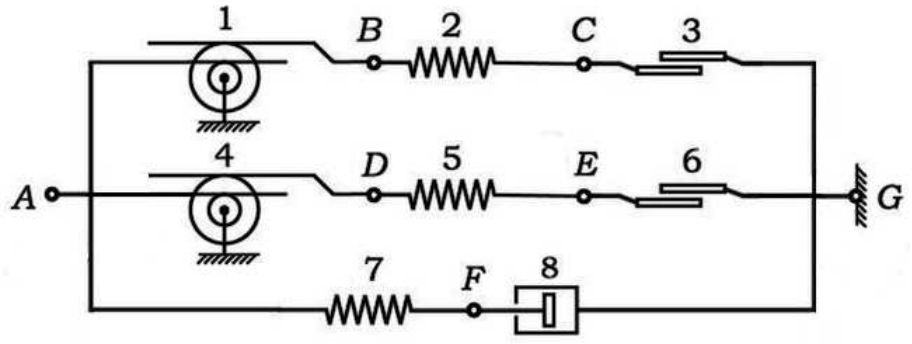

Figure 1: Schematic of the model of the mechanical behavior of rubber

Tested materials and experiments

Experiments were conducted on eight of elastomeric nanocomposites based on butadiene styrene polymer, and three kinds of filler including a carbon black, with surface modification for two fillers (Tab. 21). Volume fraction of filler 30 and 50 phr.

In previous studies, we used the special experiments with a complex cyclic loading condition [3]. Each cycle contained a stretch at a constant rate, stress relaxation under constant tension, unloading at a constant rate and creep. Experiments proposed type give a large amount of information about the mechanical properties of the material. On one sample in one experiment, the data on the softening of the medium on the first

Table 21: Nanocomposite formulation

Nano-composite code name	Polymer S-SBR Buna VSL 5025	filers			
		precip. Silica Aerosil R974	Aerosil 200	Carbon Black N330	Silane TESPT SI69
1	100	30			
2	100	50			
3	100		30		
4	100		50		
5	100		30		2.4
6	100		50		4
7	100			30	
8	100			50	

cycle of deformation (Mullins effect), the viscoelastic properties of the relaxation and creep. Determination of constants of the model can be implemented step by step, using a constant discovery of new information obtained in the previous steps.

In this paper, our experiment consisted of seven cycles. Each cycle consisted of a load at a constant rate to the multiplicity of extensions in this series, stress relaxation under constant tension, unloading of material at a constant rate to zero strain and the rest of the material. Data for each cycle are shown in Tab. 22, and the experiment in Fig. 2. As a result of this experiment, we observed the effect of softening Mullins on the first cycle of deformation of the material. The next two cycles, the strain rate was changed so as to assess the influence of speed on the viscoelastic properties of the materials. In the experiment can be clearly seen (Fig. 2) that there is no difference in mechanical behavior of material at a deformation rate of 20% per minute, and 50% per minute and 100% per minute (see 1,2 and the third cycle in the Tab. 22). The next cycles of deformation had the multiplicity of elongation less than the maximum that we could to construct an equilibrium curve of the material using the bottom points of relaxation. Under the equilibrium curve we mean the limit for experimental stress relaxation with time equal infinite at a given multiplicity of extensions. In this paper, we interpolate the equilibrium curve of the median line between the curve of loading and unloading for the multiplicity of extensions λ <2 and the lower points of relaxation for 4,5,6 and 7 cycles. For the equilibrium curve viscoelastic processes in the material already completed and we can use the model to determine the elastic properties of the material.

Model of the mechanical behavior of rubber

The mechanical behavior of rubber is described by the model schematically represented in Fig. 1, where each point corresponds to a particular set of constitutive equations. The scheme shows how the tensor nonlinear equations are combined into the system of equations used to calculate the complex viscoelastic behavior of the medium deformed in an arbitrary way. The algorithm for constructing constitutive equations consisting of separate groups of equations (elastic, viscous, plastic, transmission) is described in

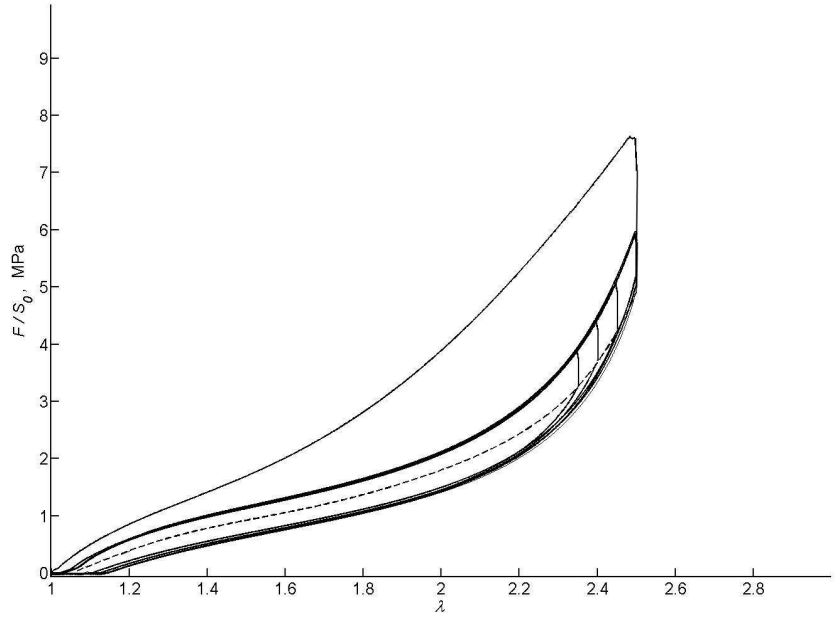

Figure 2: The experimental data - solid line, the equilibrium curve - dotted line

detail in work [1]. The model uses the approach that is based on additive decomposition of the deformation-rate tensor of the medium into the deformation-rate tensors of the scheme elements [2]. The internal scheme points are required to meet the condition of correlation of the Cauchy stress tensors [1]. The scheme for the mechanical behavior of the material involves transmission, elastic, viscous and plastic elements that correspond to the folowing equations. The material is assumed to be incompressible. The deviator of the Cauchy stress tensor of the elastic element is calculated from the equations of the theory of elasticity

$$\operatorname{dev}\mathbf{T}_i = \operatorname{dev}\left(\rho\sum_{k=1}^{3}\lambda_k^{(i)}\frac{\partial f}{\partial\lambda_k^{(i)}}\,\mathbf{n}_k^{(i)}\otimes\mathbf{n}_k^{(i)}\right),$$

in which the mass density of the medium free energy f depends on the extension ratios of elastic elements.

$$f = f(\lambda_1^{(2)},\lambda_2^{(2)},\lambda_3^{(2)},\lambda_1^{(5)},\lambda_2^{(5)},\lambda_3^{(5)},\lambda_1^{(7)},\lambda_2^{(7)},\lambda_3^{(7)}),$$

where $\lambda_1^{(i)}$, $\lambda_2^{(i)}$, $\lambda_3^{(i)}$ and $\mathbf{n}_1^{(i)}$, $\mathbf{n}_2^{(i)}$, $\mathbf{n}_3^{(i)}$ — are the extension ratios and eigenvectors of the stretch tensor $\mathbf{V}_i$ of the i-th elastic element . Time variations in the tensor $\mathbf{V}_i$ are calculated by the evolution equation.

$$\frac{2}{\nu_i}\,\mathbf{Y}_i{}^{0.5}\,\mathbf{D}_i\mathbf{Y}_i{}^{0.5} = \dot{\mathbf{Y}}_i - \mathbf{Y}_i\,\mathbf{W}_{\mathbf{R}}^{\mathrm{T}} - \mathbf{W}_{\mathbf{R}}\,\mathbf{Y}_i, \qquad \mathbf{W}_{\mathbf{R}} = \dot{\mathbf{R}}\,\mathbf{R}^{\mathrm{T}}.$$

The formula uses the following notations:

$$\mathbf{Y}_i = \mathbf{V}_i{}^{\frac{2}{\nu_m}}, \qquad \nu_m > 0,$$

where $\mathbf{R}$ — is the rotation tensor in the polar decomposition $\mathbf{F} = \mathbf{VR}$ of the strain gradient of the medium $\mathbf{F}$ into the left stretch tensor $\mathbf{V}$ and the rotation $\mathbf{R}$; ν_m is the

Table 22: Algorithm of the experiment

number of cicle	loading		relaxation	unloading	rest
	to extensions	deformation rate	time	to zero stress deformation rate	of material time
1	2.5	100% per min	30 min	100% per min	30min
2	2.5	20% per min	30 min	20% per min	10 min
3	2.5	50% per min	10 min	50% per min	10 min
4	2.35	100% per min	10 min	100% per min	10 min
5	2.4	100% per min	10 min	100% per min	10 min
6	2.45	100% per min	10 min	100% per min	10 min
7	2.5	100% per min	10 min	100% per min	10 min

ratio of the m-th transmission element, which is connected on the left to the elastic element under consideration. The rate of work done in the i-th elastic element is determined by the formula

$$\mathbf{T}_i \cdot \mathbf{D}_i = \rho \sum_{k=1}^{3} \frac{\partial f}{\partial \lambda_k^{(i)}} \dot{\lambda}_k^{(i)} - \frac{\rho\, \dot{\nu}_m}{\nu_m} \sum_{k=1}^{3} \frac{\partial f}{\partial \lambda_k^{(i)}} \lambda_k^{(i)} \ln(\lambda_k^{(i)}).$$

The structural deformation of the elastomeric binder fraction and the macroscopic deformation of the rubber differ significantly. This difference is taken into account by the transmission elements. Application of these elements increases the strain rate tensor at the right point of the transmission element by a factor of ν_m in comparison with the corresponding tensor at the left point and simultaneously decreases the Cauchy stress tensor.

$$\mathbf{D}_m^{\text{left}} = \frac{1}{\nu_m} \mathbf{D}_m^{\text{right}}, \qquad \mathbf{T}_m^{\text{left}} = \nu_k \mathbf{T}_m^{\text{right}}.$$

The deviator of the Cauchy stress tensor $\mathbf{T}_j$ of the viscous element is calculated from the equations of the theory of nonlinear viscous fluid using the appropriate strain rate tensor $\mathbf{D}_j$:

$$\operatorname{dev} \mathbf{T}_j = 2\,\eta_j\, \mathbf{D}_j,$$

For the n-th plastic element, the Cauchy stress tensor deviator is determined by the equations of the theory of plastic flow

$$\mathbf{D}_n = \sqrt{\frac{\mathbf{D}_n \cdot \mathbf{D}_n}{\operatorname{dev}\mathbf{T}_n \cdot \operatorname{dev}\mathbf{T}_n}}\, \operatorname{dev}\mathbf{T}_n,$$

To complete the system of equations, the proportional relation between the strain rate tensors of the plastic element $\mathbf{D}_n$ and that of the material is used $\mathbf{D}$.

$$\sqrt{\mathbf{D}_n \cdot \mathbf{D}_n} = \kappa_n \sqrt{\mathbf{D} \cdot \mathbf{D}},$$

where the term κ_n is the non-negative function obtained from the relation

$$\kappa_n = \begin{cases} 0, & \text{when } \Phi_n(\mathbf{T}, ...) < g_n, \\ \zeta_n(g_n), & \text{when } \Phi_n(\mathbf{T}, ...) = g_n. \end{cases}$$

The flow function Φ_n that is used to formulate the criterion for the development of plastic deformations in the medium is the function of the Cauchy stress tensor $\mathbf{T}$ of the medium. The plastic deformation of the medium takes place only in the case when the flow function Φ_n reaches its maximum value over the entire history of the medium development.

$$g_n = \max \Phi_n.$$

Results

In this article we have simulated the behavior of the elastic properties of the material, which are described by 1, 2, 3, 4, 5 and 6 elements of scheme. Elastic properties of the material describes the equilibrium curve, since at these points viscoelastic processes in the material over. Therefore, the constants in the desired elements were chosen from the best convergence of theoretical calculations and the equilibrium curve

First, we searched for the constants for 1, 2 and 3 of the circuit elements. Constants for the third plastic element found with the residual strain after the first cycle of loading. Further modeled the elastic properties described by the first and second elements of the scheme. Potential of the medium takes the form:

$$w = w_2 = c_1^{(2)} \left(\sum_{i=1}^{3} (\lambda_i^{(2)})^2 - 3 \right) + c_2^{(2)} \left(\sum_{i=1}^{3} (\frac{1}{\lambda_i^{(2)}})^2 - 3 \right).$$

Simulation results for 1, 2 and 3 elements are shown in Fig. 3 for sample 8 (carbon black with a mass fraction 50phr). Next, we model the elastic properties of fibers, which are described using 4, 5 and 6 of the first elements of the scheme.

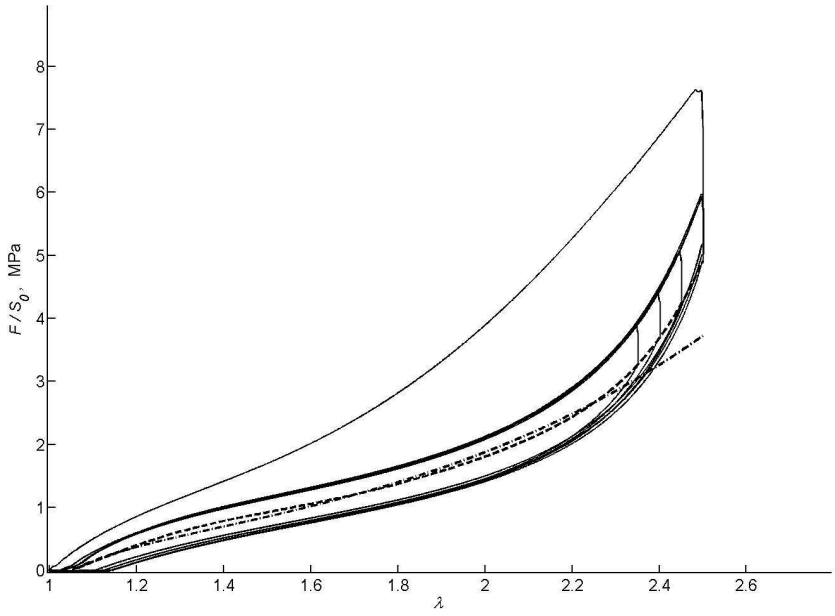

Figure 3: Solid line - experimental data for the sample 8; bar dotted line - theoretical calculation for the 1, 2, 3 elements; dotted line - the equilibrium curve

The potential of the fifth elastic element is expressed as:

$$w_5 = \begin{cases} 0, & \text{where } \xi_5 < 0, \\ c_1^{(5)}\xi_5, & \text{where } \xi_5 \geq 0. \end{cases}$$

and

$$\xi_5 = (\lambda_1^{(5)} - 1)(\lambda_2^{(5)} - 1)(\lambda_3^{(5)} - 1).$$

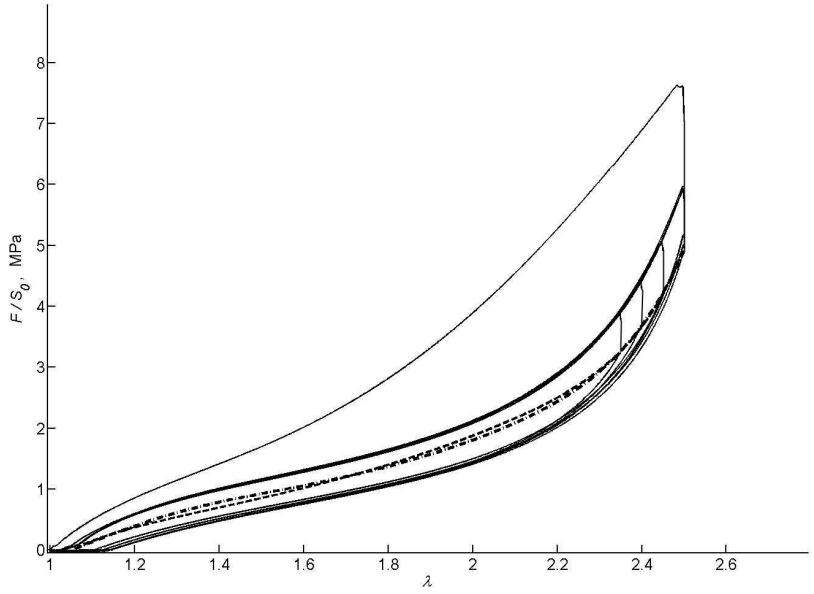

Figure 4: Solid line - experimental data for the sample 8; bar dotted line - theoretical calculation for the 1, 2, 3, 4, 5 and 6 elements; dotted line - the equilibrium curve

Then the potential free-energy environment in the form sum. In Fig. 4, resulted in the simulation results for sample 8 (carbon black with a mass fraction 50phr).

Conclusion

Proposed in the experiments provide information on the mechanical behavior of materials with which to determine the equilibrium curve of the material under loading. With the help of the model we have described (Fig. 3, 4) the elastic properties of the materials. Using the experimental data and simulation results for the materials, we found a correlation between the amount of energy spent on the softening of the material and the constants for 5, 6, 7 element model. The experiments revealed that virtually no difference in mechanical behavior of material at a deformation rate of 20% per minute, and 50% per minute and 100% per minute.

Acknowledgements

This work was supported by RFBR (projects 09-08-00530 and 11-08-00178-a) and Integration Project of basic scientific research carried out jointly by UB RAS, SB RAS, FEB RAS software, RAS 09-C-1-1008.

References

[1] Svistkov A. L., Lauke B., Heinrich G. Modeling of viscoelastic properties and softening of rubber materials // Proceedings of 5th European conference "Constitutive models for rubbers" Paris, 2007. P. 113-118.

[2] Palmov V. A. Comparison of different approaches in viscoelastoplasticity for large strain // ZAMM. 2000. V. 80. P. 801-806.

[3] Pelevin A.G., Lauke B., Heinrich G., Svistkov A.L., Adamov A.A. Algorithm of constant definition for a visco-elastic rubber model based on cyclic experiments, stress relaxation and creep data // Proceedings of the sixth European conference on Constitutive models for rubber - Dresden, Germany, 2009 - P. 79-84.

Pelevin A.G., Svistkov A.L. Institute of continuous media mechanics UB RAS, Perm, Russia

Mechanical modelling of nanotube-polymer adhesion

Mikhail Perelmuter
perelm@ipmnet.ru

Abstract

The modelling of the shear strength of nanotubes based nanocomposites is considered. To model the shear strength of nanocomposites it is assumed that the zone of the adhesive interaction between nanotubes and a polymeric matrix is a thin interface layer which has resistance only in the relation to action of shear stresses and has the given curve of deformation. The stress state of nanotubes and a polymeric matrix is determined in the assumption, that the nanotube is a cylindrical fibril with the straight axis, embedded in a infinite polymeric matrix and the displacement along the axis of the nanotube under the action of the external loading along this direction are much more than others components of the nanotube and matrix displacements. The analytical solutions for the axial displacement and normal stress in the nanotubes and the shear stresses in the interface layer for a case of the bilinear deformation curve of an intermediate layer with elastic and hardening or softening branches are obtained.

1 Introduction

Composites based on polymers or ceramics matrix and filled by nanosized particles or nanotubes are materials with very strong and tough mechanical properties. The mechanisms of toughening these materials by nanoparticles investigated experimentally and theoretically [1]-[4]. From the experimental observations ([1]-[2], [5]) it has been found: 1) the main parameter which defines the nanocomposite strength is the adhesion between matrix and nanofiller; 2) the crack bridging mechanisms is very important during nanocracks formations and fracture of nanocomposites. Noted also that in the most observed cases the size of the nanocrack bridged zones were comparable with the whole crack size. These cases need special consideration during the bridged zone and crack tip growth. Below the mechanical model to describe the nanotubes-polymer matrix adhesion (which is the basis for formulation of the bridged crack problem for nanocomposites) is considered.

2 Model of nanotube-polymer adhesion

The model of nanotube-polymer adhesion based on the shear-lag approach was proposed previously in [6] and discussed in the frame of nanomechanics in [7]. In the frames of our approach, it is assumed that the nanotube is a straight cylindrical fiber of length L_c embedded in an infinite polymer matrix (Fig.1). The nanotube under the external normal loading has only the displacements along its axis and the thin layer of the polymer matrix adjacent to the nanotube is bearing only shear stresses. It is also supposed that the interfacial shear stresses between the polymer matrix and the nanotube depend on the interface layer thickness (H) and the fiber (nanotube) axis displacement (u)

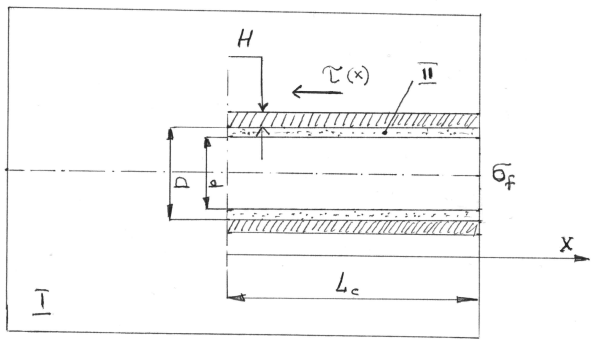

Figure 1: Nanotube (II) embedded in a polymer matrix (I) under the action of the external normal stresses, H is the interface layer thickness

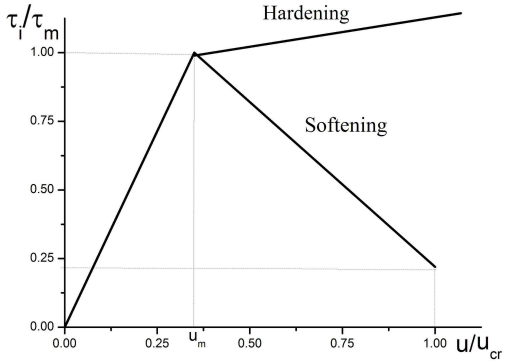

Figure 2: Bilinear shear stress-displacement law for the interface layer

$$\tau_i = \kappa_1 u, \quad \kappa_1 = \frac{G_1}{H}, \tag{1}$$

We will also suppose, if the shear stresses τ_i exceed the given value $\tau_m = \kappa_1 u_m$ then shear stresses in the interface layer between the fiber and the matrix are described by the equation

$$\tau_i = \tau_2 \pm \kappa_2 u, \quad \kappa_2 = \frac{G_2}{H} \tag{2}$$

where G_2 is the shear modulus of the interface layer on the hardening/softening parts of the deformation law curve, $u > u_m$.

If the displacements of the nanotube axis attain the critical value u_{cr} then the detachment of the nanotube from the matrix occurs.

Note, that the interface layer thickness (H) may depend, in general, on the position along the nanofiber (coordinate x) and the shear stresses at the detachment state (τ_{cr}) may be nonzero.

Combining equations (1) and (2) we can write the interface deformation law as follows

$$\tau_i(x) = \begin{cases} \kappa_1 u(x), & 0 < u(x) \le u_m \\ \tau_2 \pm \kappa_2 u(x), & u_m < u(x) \le u_{cr} \\ 0 & u(x) > u_{cr} \end{cases} \tag{3}$$

where $\kappa_{1,2}$ are the stiffness on the hardening/softening parts of the shear-displacement law

$$\kappa_1(x) = \frac{G_1}{H} = \frac{\tau_m}{u_m}, \quad \kappa_2 = \frac{G_2}{H} = \frac{|\tau_{cr} - \tau_m|}{u_{cr} - u_m}, \quad \tau_2 = u_m \left(\kappa_1 \mp \kappa_2\right) \tag{4}$$

and the value u_{cr} is the critical elongation of the nanofiber (see Fig. 2).

In dependence on the values τ_m and τ_{cr} the deformation with the softening ($\tau_{cr} < \tau_m$), the bottom sign in (3-4), or with the hardening ($\tau_{cr} \ge \tau_m$), the upper sign in (3-4), can be considered, see Fig.2.

Next, we will write the equilibrium equation for an infinitely small part of the nanotube embedded in the polymer matrix. This equation has the following form

$$0.25\pi \left(D^2 - d^2\right) \frac{d\sigma(x)}{dx} = \pi D \tau_i(x) \tag{5}$$

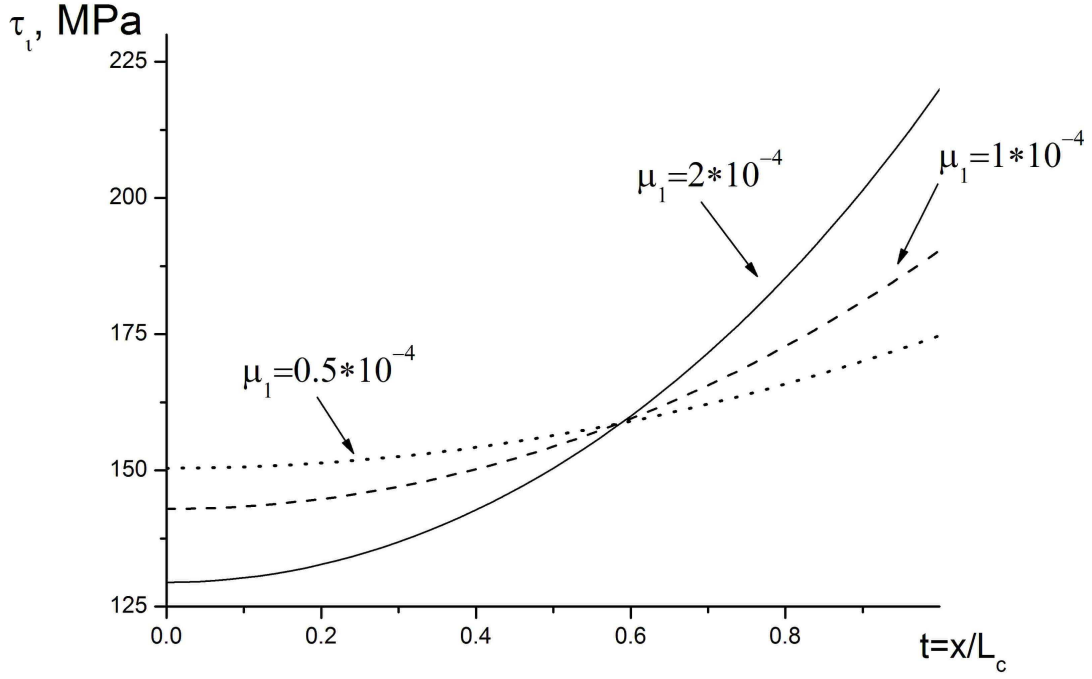

Figure 3: Distributions of the shear stresses over the nanotube length for different values of the relative stiffness of the interface layer, μ_1

Suppose that the axial deformation of the nanotube fiber is elastic, then, taking into account the temperature difference during the cure, ΔT, we can write

$$\sigma(x) = E_f \left(\frac{du(x)}{dx} - \alpha_f \Delta T \right) \tag{6}$$

where E_f and α_f are the elastic modulus and the thermal expansion coefficient of the nanotube, respectively.

Finally, substituting equations (3) and (6) into the equilibrium equation (5), taking into attention the changing of the shear stress law along the nanotube and the possibility of the nanotube detachment, we obtain the following system of the differential equations for the axial displacements of the nanofiber:

$$\begin{cases} \frac{d^2u_1}{dx^2} - \beta_1^2 u_1 = 0, & 0 < x \le x_m \\ \frac{d^2u_2}{dx^2} + \beta_2^2 u_2 = R_2, & x_m < x \le x_{cr} \\ \frac{d^2u_3}{dx^2} = 0, & x_{cr} < x \le L_c \end{cases} \tag{7}$$

where

$$\mu_{1,2} = \frac{G_{1,2}}{E_f}\frac{D}{H}, \quad \beta_{1,2} = \frac{2\delta\sqrt{\mu_{1,2}}}{D} \quad R_2 = \frac{4\tau_2\delta^2}{E_f D}, \quad \delta = \frac{D}{\sqrt{D^2 - d^2}} \tag{8}$$

The point x_m in (7) is the position along the axis of the nanotube where the deformation law is changed according to Eq. (2) and the point x_{cr} is the detachment point position. This system of the differential equations solves together with the appropriate boundary conditions and the additional conditions of continuity and compatibility at the point of changing the deformation law x_m where $u = u_m$

$$u_m = u_1(x_m) = u_2(x_m), \quad \left.\frac{\partial u_1}{\partial x}\right|_{x=x_m} = \left.\frac{\partial u_2}{\partial x}\right|_{x=x_m} \tag{9}$$

and the conditions at the detachment point x_{cr} where $u = u_{cr}$

$$u_{cr} = u_2(x_{cr}) = u_3(x_{cr}), \quad \left.\frac{\partial u_2}{\partial x}\right|_{x=x_{cr}} = \left.\frac{\partial u_3}{\partial x}\right|_{x=x_{cr}} \tag{10}$$

Note, that if the interface layer thickness (H) depends on the coordinate then equations (7) can only be solved numerically, for instance, by finite difference method.

We initially have considered the simple case of the constant thickness of the interface layer thickness (H). The equations (8) in this case have the analytical solution. Based on the analytical solution of the equations (8) we considered different types of the boundary conditions for the embedded nanotube model and have got the shear stresses distributions along of a nanotube axis.

3 Estimation of nanocomposites shear strength

Let's define the average shear stress τ_a along of a nanotube part of the length L_c as follows

$$\tau_a = \frac{1}{L_c}\int_0^{L_c} \tau_i(x)dx \tag{11}$$

For a case when the shear stresses $\tau_i(x)$ are dependent on the axis displacements u linearly in the whole range of the external loading and at the nanotube sections $x = 0$ and $x = L_c$ (see Fig. 1) are adopted the following boundary conditions

$$\sigma(L_c) = E_f \left.\frac{\partial u_1}{\partial x}\right|_{x=L_c} = \sigma_f, \quad \sigma(0) = E_f \left.\frac{\partial u_1}{\partial x}\right|_{x=0} = 0 \tag{12}$$

we can obtain the dependence of the shear stresses over the nanotube axis:

$$\tau_i(t) = \frac{\sigma_f}{2\delta}\sqrt{\mu_1}\frac{\cosh\left(\frac{2\delta L_c\sqrt{\mu_1}}{D}t\right)}{\sinh(\lambda_1)}, \quad \lambda_1 = \beta_1 L_c, \quad t = x/L_c; \tag{13}$$

By using formula (13) we can write

$$\tau_a = \frac{\sigma_f\sqrt{\mu_1}}{2\delta L_c \sinh(\lambda_1)}\int_0^{L_c} \cosh(\beta_1 x)\, dx = \frac{\sigma_f D}{4L_c\delta^2} = \sigma_f\left[\frac{D}{4L_c}\left(1 - \frac{d^2}{D^2}\right)\right] \tag{14}$$

Let's note, that the average value of the shear stresses (14) coincides with the value of the shear stress for an ideally-plastic matrix [6, 7].

The dimensionless shear stresses (the shear stress concentration factor, SCCF) can be defined as follow

$$\tau_R(t) = \frac{\tau_i}{\tau_a} \tag{15}$$

By incorporating Eqs. (13) and (14) we obtain for the linear deformation law

$$\tau_R(t) = \frac{\tau_i}{\tau_a} = \lambda_1\frac{\cosh(\lambda_1 t)}{\sinh(\lambda_1)} = \frac{2\delta L_c}{D}\sqrt{\mu_1}\frac{\cosh\left(\frac{2\delta L_c\sqrt{\mu_1}}{D}t\right)}{\sinh(\lambda_1)} \tag{16}$$

Within the framework of the linear deformation law the maximal value of the shear stresses is observed on loaded end of the nanotube ($x = L_c$). Let's evaluate the physical-mechanical parameters in (8)-(16). According to the data presented in [7] the wall thickness ($h = 0.5(D-d)$) of single-wall nanotubes is $h = 0.34nm$ and the external diameter is about $D = 2-5\,nm$. Supposing that $D = 5\,nm$ then the internal diameter is $d = 4.32\,nm$ and

$$\delta = \frac{D}{\sqrt{D^2 - d^2}} \approx 1.986 \tag{17}$$

According to [7] the critical length of a nanofiber is about $L_c \approx 100 - 500\,nm$ and the critical external stress σ_f vary between 20 and $150\,GPa$. The elastic modulus of the nanotubes is in the range $E_f = 0.8 - 1,8\,TPa$ [6, 8].

Information regarding other parameters of the model is rather undetermined. The thickness of the interface layer H strongly depends on the types of adhesion. There are several methods to improve interaction between nanotubes and polymeric matrix. For example, chemical attachment or cross linking of nanotube walls and polymeric matrix (functionalization) has been proposed as one of the techniques to improve the interfacial bonding. Based on molecular dynamics simulation it was shown [9-11] that the shear strength of nanotubes-matrix interface and the critical length for load transfer are essentially improved by chemical cross-linking the nanotubes and matrix. The length of a functionalization group is about $0.1 - 0.2\,nm$ [9]. Therefore, the lower bound of the thickness of the interface layer is $H = (0.04 - 0.1)\,D$ and the upper reasonable bound of this parameter is not more than the nanotube diameter $H \approx D$. Let's proceed to the determination of other parameters of the deformation law.

We can evaluate the bounds for the shear modulus G_1 supposing that the distance between the functionalize attached groups is not more then the nanotube diameter as in the numerical simulation [9-11] and the thickness of the functionalize group is less than the nanotube wall thickness $h = 0.34nm$. In this case the upper bound for the elastic modulus of the interface layer is

$$E_1 < \frac{h}{D+h} E_f \tag{18}$$

If Poisson's ratio for the interface layer equals $\nu = 0.25$ and $D = 2 - 5\,nm$ we obtain

$$G_1 < \frac{0.5h}{(D+h)} \frac{E_f}{(1+v)} \approx 0.05E_f \tag{19}$$

The elastic modulus of the polymer matrix is about $E_m = 2 \div 3.5\ GPa$, therefore the bounds for the shear modulus of the interface layer are

$$\psi G_m \le G_1 \le \frac{\varepsilon E_f}{2(1+\nu)}, \quad \varepsilon < \frac{h}{D+h} \tag{20}$$

where the parameter $\psi < 1$ is determined by the equality of the adhesion without the functionalization and is the shear modulus of the matrix.

We also can choose the parameter (G_2) of the hardening part of the deformation law supposing that $0 \le G_2 \le G_1$. The case $G_2 = 0$ corresponds to the ideal plastic flow. Finally, we will use the following parameters for the computation: 1) the nanotube external diameter - $D = 5\,nm$; 2) the nanotube internal diameter - $d = 4.32\,nm$; 3) the wall thickness of single-wall nanotube - $h = 0.34\,nm$; 4) the critical length of the nanofiber - $L_c = 100\,nm$; 5) the elastic modulus of the nanotubes - $E_f = 1\ TPa$; 6) the Poisson ratio - $\nu = 0.25$; 7) the critical external stress is $\sigma_f = 50\,MPa$ [9-11]; 8) the thickness of the intermediate layer - $H = D$.

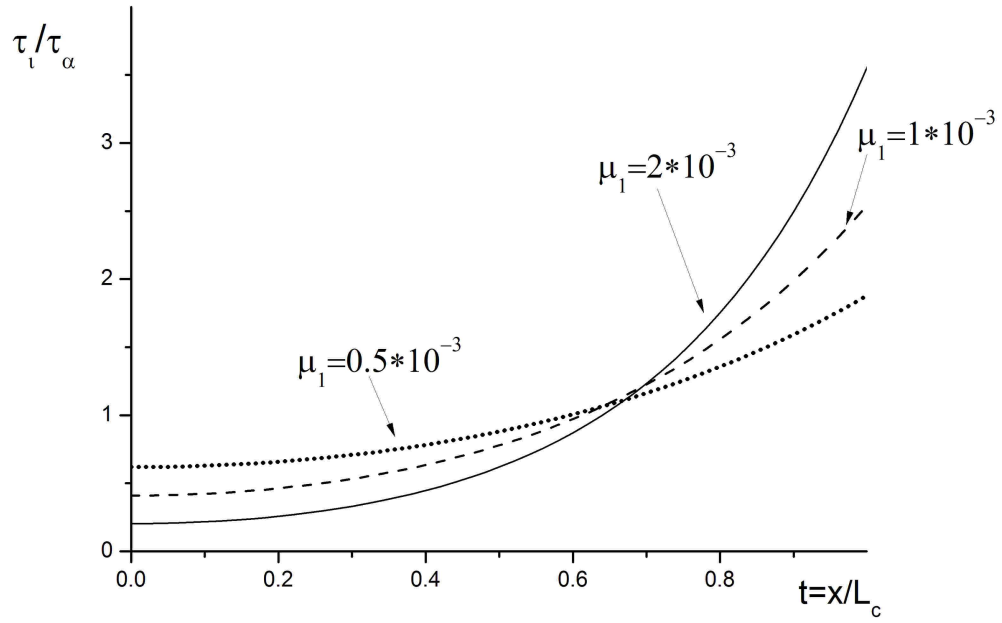

Figure 4: Distributions of the relative shear stresses along nanotube axis for different values of the relative stiffness of the interface law, $\mu_{1\alpha} = 10\mu_1$

The values of the parameter ε in (20) are chosen as $\varepsilon = 0.0005,\ 0.00025,\ \ 0.000125$ and the shear modulus of the interface layer is calculated according to

$$G_1 = \frac{\varepsilon E_f}{2(1+\nu)} \tag{21}$$

The values of the relative stiffness of the interface layer for the given values of D, H, E_f and ε are determined as follows

$$\mu_1 = \frac{G_1}{E_f}\frac{D}{H} = 2.0 \cdot 10^{-4}; 1.0 \cdot 10^{-4}; 0.5 \cdot 10^{-4} \tag{22}$$

The average shear stresses for linear deformation law and given above values of parameters σ_f, L_c, D, d is equal to $\tau_a \approx 158.44\ MPa$.

The dependencies of the shear stresses over the nanotube length for different values of the relative stiffness of the layer, are given in Fig.3. Note, that the results in Fig.3 are close to the experimental results [9-10] where the shear stresses for nanotube based composites were investigated: $138MPs$ (epoxy matrix) and $186MPa$ (polystyrene matrix). One can also see in Fig.3 that when the relative stiffness of the interface layer is decreasing then the distribution of the shear stresses tends toward the uniform state.

For a small parameter μ_1 we can write

$$\lambda_1 = \frac{2\delta L_c\sqrt{\mu_1}}{D} \approx 1$$

and therefore we obtain

$$\tau_i(t) \to \sigma_f \left[\frac{D}{4L_c}\left(1-\frac{d^2}{D^2}\right)\right], \quad \tau_R = \frac{\tau_i}{\tau_a} \to 1 \tag{23}$$

this is similar to ideally-plastic case [6,7].

The distributions of the dimensionless shear stress (SCCF) along the nanotube axis for the values of relative stiffness $\mu_{1\alpha} = 10\mu_1$ (μ_1 from (22)) are shown in Fig.4. Noted, when the relative stiffness of the interface layer is increasing by 10 times then the distribution of the shear stresses tend toward more non-uniform state. For example, if $\mu_1 = 0.5 \cdot 10^{-4}$ then $\tau_R(1)/\tau_R(0) \approx 1.085$ and for $\mu_{1\alpha} = 2 \cdot 10^{-3} = 40\mu_1$ (see Fig. 4) we obtain $\tau_R(1)/\tau_R(0) \approx 17.75$. Noted, that if the stiffness of polymer matrix is decreasing then the shear stresses are tending to uniform state.

Above results can be use for the formulation of the bond deformation law in the frame of the crack bridging model, [11].

4 Acknowledgements

This work was supported by the RFBR, the project number is 11-08-01243-a

References

[1] Qian D., Dickey E.C., Andrews R., Rantell T. Load transfer and deformation mechanisms on carbon nanotube-polystyrene composites, App. Phys. Let., 2000 (76), **20**, 2868

[2] Xia Z. at al. Direct observation of toughening mechanisms in carbon nanotube ceramic matrix composites, Acta Materiala, 2004, **52**, 931-944

[3] Srivastava D., Wei C., Cho K., Nanomechanics of carbon nanotubes and composites, App. Mech. Rev., 2003, 2, **56**, 215-230

[4] Wanga J., Pyrzb R., Prediction of the overall moduli of layered silicate-reinforced nanocomposites, part I, II: Composites Science and Technology, 2004, **60**, 925-9544

[5] Watts P.C., Hsu W.K., Behaviours of embedded carbon nanotubes during film cracking, Nanotechnology, 2003, **14**, L7-L10

[6] Kelly A., Tyson W.R., Tensile properties of fibre-reinforced metals: copper/tungsten and copper/molybdenum, J. Mech. Phys. Solids, 1965, **13**, 329-350

[7] Wagner H.D., Nanotube-polymer adhesion: a mechanical approach, Chemical Physics Letters, 2002, **361**, 57-61

[8] Lau K.T., Interfacial bonding characteristics of nanotube/polymer composites, Chemical Physics Letters, 2003, **370**, 399-405

[9] Wong M. et al., Physical interaction at carbon nanotube-polymer interface, Polymer, 2003, **44**, 7757-7764

[10] Frankland S.J.V., Caglar A., Brenner D.W., Griebel M., Molecular Simulation of the Influence of Chemical Cross-Links on the Shear Strength of Carbon Nanotube-Polymer Interfaces, Journal of. Physical Chemistry B, 2002, **106**, 3046

[11] Goldstein R.V., Perelmuter M.N. Fracture toughness modelling of composite materials, Computational continuum mechanics, 2009, **2**, 22-39

Perelmuter Mikhail
A. Ishlinsky Institite for Problems in Mechanics of RAS,
pr. Vernadkogo, 101-1, 119526, Moscow, Russia

Nonlinear dynamic variations in internal structure of a complex lattice

A. V. Porubov B. R. Andrievsky
alexey.porubov@gmail.com

Abstract

Essentially nonlinear model of a crystalline bi-atomic lattice described by coupled nonlinear equations, is considered. Its nonlinear wave solutions account for dynamic variations in an internal structure of the lattice due to an influence of a dynamic loading. Numerical simulations are performed to study evolution of a kink-shaped dynamic variations in an internal structure of the lattice. Special attention is paid on the transition from kink-shaped to bell-shaped variations. It is shown how predictions of the known exact traveling wave solutions may help in understanding and explanation of evolution of localized waves of permanent shape and velocity in numerical solutions.

Introduction

The cardinal, qualitative variations of the cell properties, lowering of potential barriers, switching of interatomic connections, arising of singular defects and other damages, phase transitions require development of essentially nonlinear models of a crystalline lattice taking into account deep variations in the structure. Recently such a nonlinear model of a crystalline bi-atomic lattice has been developed in Refs. [1, 2]. The variations in the internal structure are described by coupled nonlinear equations which are derived for the vectors of macro-displacement U and relative micro-displacement u for the pair of atoms with masses m_1, m_2,

$$\mathbf{U} \;=\; \frac{m_1\mathbf{U_1}+m_2\mathbf{U_2}}{m_1+m_2},\;\; \mathbf{u} \;=\; \frac{\mathbf{U_1}-\mathbf{U_2}}{a}$$

where a is a period of sub-lattice. The first variable allows us to describe macro-dispalcements, while the second variable accounts for the reference displacement of the atoms in the lattice. In the one-dimensional (1D) case, the coupled governing equations read [1, 2]

$$\rho U_{tt} - E\,U_{xx} \;=\; S(\cos(u)-1)_x, \tag{1}$$

$$\mu u_{tt} - \kappa u_{xx} \;=\; (SU_x - p)\sin(u). \tag{2}$$

Nonlinearity is introduced via the trigonometric functions that ensures description of translational symmetry in the crystalline lattice. The 1D formulation allows some analytical solutions to account for dynamic variations in the internal structure governed by function u while the strain function $v \;= U_x$ accounts for an external loading of the lattice. Of

Table 23: Wave shapes for $\sigma = 0$

V^2	$(0; c_L^2 - c_0^2)$	$(c_L^2 - c_0^2; c_L^2)$	$(c_L^2; c_L^2 + c_0^2)$	$> c_L^2 + c_0^2$
Shape of v	Tensile (4)	Tensile (4)	Compression (5)	Compression (4)
Shape of u	Kink	Bell-shaped	Kink	Kink
Choice of $Q_\pm$	Q_+	Q_-	Q_+	Q_+

special interest are bell-shaped and kink-shaped localized solutions [3, 4, 5, 6, 7]. However, they belong to the traveling wave solutions, hence they cannot account for arising of localized internal variations. In particular, existence of the bell-shaped or kink-shaped dynamic structure depends on the phase velocity as follows from exact solutions [3]. However, how one or another velocity may be achieved from rather arbitrary input for u and v? Only numerical simulations may answer this question. Previously the domain of the wave velocities has been studied where both macro- and micro- bell-shaped strain waves co-exist [4, 5, 6]. Only some preliminary results obtained for the kinks in Ref. [7]. Now we consider the kink-shaped waves for u. Like in Refs. [4, 5, 6] the use of particular exact solution to design and describe numerical results is studied.

1 Exact kink-type solution

The function u may be found from Eq.(1) when all functions depend only on the phase variable $\theta = x - V\ t$,

$$\cos(u) = 1 - \frac{(E - \rho V^2)U_\theta - \sigma}{S}, \tag{3}$$

where σ is a constant of integration. It is known that only bell-shaped exact localized traveling wave solutions exist for the macro-strain v [3]:

$$v_1 = \frac{A}{Q\ \cosh(k\ \theta) + 1}, \tag{4}$$

$$v_2 = -\frac{A}{Q\ \cosh(k\ \theta) - 1}. \tag{5}$$

whose parameters are defined for two values of σ, $\sigma = 0$ and $\sigma = -2S$ [3]. Thus, for are $\sigma = 0$ we obtain

$$A = \frac{4\ S}{\rho(c_0^2 + c_L^2 - V^2)}, Q_\pm = \pm\frac{c_L^2 - V^2 - c_0^2}{c_L^2 - V^2 + c_0^2}, k = 2\sqrt{\frac{p}{\mu(c_l^2 - V^2)}} \tag{6}$$

where $c_L^2 = E/\rho$, $c_l^2 = \kappa/\mu$, $c_0^2 = S^2/(p\ \rho)$.

Depending on the value of the phase velocity, see Table 1, Eq.(3) gives rise to the solution for u in the kink-shaped or in the bell-shaped form [3, 4, 5, 6]. In this paper we consider only the former solution which reads

$$u = \pm \arccos\left(\frac{(\rho V^2 - E)U_x}{S} + 1\right) \text{ for } \theta \leq 0, \tag{7}$$

$$u = \pm\pi \mp \arccos\left(\frac{(\rho V^2 - E)U_x}{S} + 1\right) \text{ for } \theta > 0, \tag{8}$$

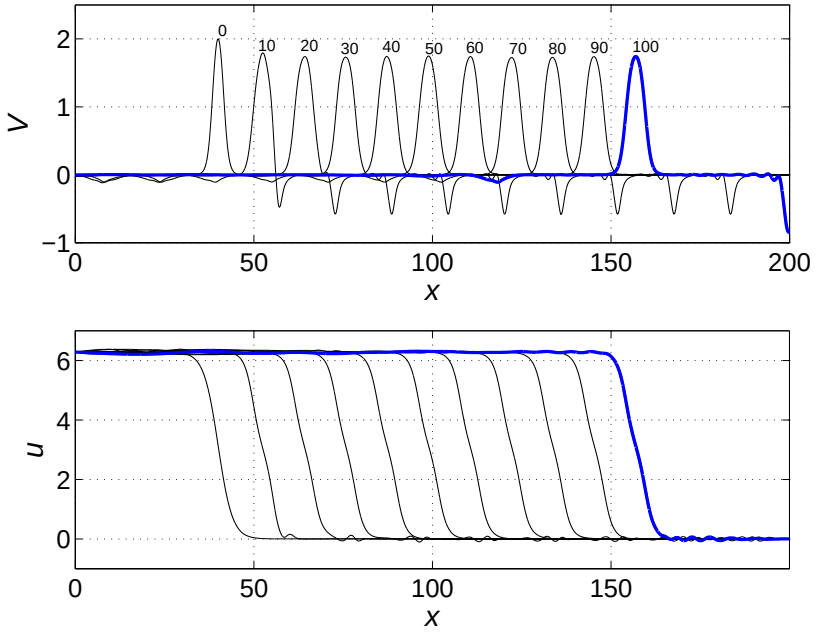

Figure 1: Simultaneous propagation of localized bell-shaped macro-strain wave v and the kink-shaped wave u in the interval of velocities prescribed by the exact solution. Points of time correspond to the neighboring peaks. Final wave profiles are allocated in bold.

In particular, the kink-shaped solution exists in the interval $(0; c_L^2 - c_0^2)$ as follows from Table 1. while the bell-shaped solution for u [3]

$$u \;=\; \pm \arccos\left(\frac{(\rho V^2 - E)U_x}{S} + 1\right) \;, \tag{9}$$

exists in the neighboring interval of velocities $(c_L^2 - c_0^2; c_L^2)$. Previously we have obtained in [7] that moving kink-shaped wave of internal variations u may arise in a lattice even if its initial velocity lies within the neighboring interval $(c_L^2 - c_0^2; c_L^2)$. The kink velocity is changed due to variations in the amplitude of the input of external loading v. Now we call attention to the waves evolution caused by variation in the relative position of the inputs for u and v.

2 Transition from kink to bell-shaped moving variations in the structure

To solve Eqs. (1), (2) numerically the standard MATLAB routine *ode45* is used [8]. The parameters chosen are $S = 1$, $p = 1$, $\rho = 1$, $c_0 = 1$, $c_L = 1.6$, $c_l = 2$, then the suitable for kinks values of V lie in the interval $(0, 1.25)$. The initial condition for v is chosen in the form (4) with $Q = Q_+$ and with initial velocity V. The condition for u is used in the form slightly differing form that of described by Eqs.(7), (8), namely, $u = \pi(1 - \tanh(kx))$ where $k = 0.25$ is chosen to be as close as possible to the shape of the solution (7), (8).

First the case is considered when initial positions x_{11} of the input for v and x_{12} of that of u coincide and equal to 40 units. Shown in Fig. 1 is rather fast transition of the input u to that of the exact solution (7), (8) and further simultaneous stable propagation

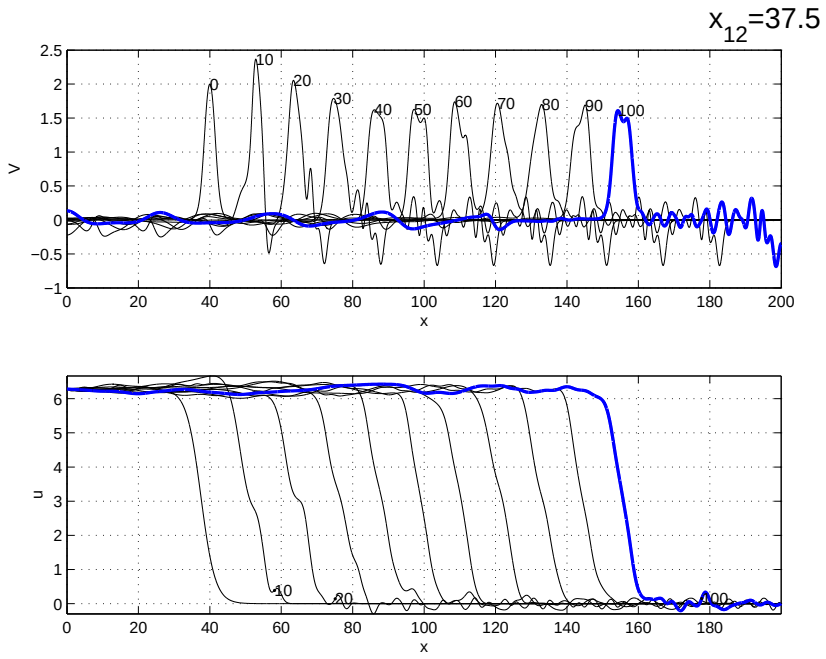

Figure 2: Perturbations on the profiles of moving localized bell-shaped micro-strain wave and kink-shaped wave u when its initial position is slightly shifted behind that of v. Points of time correspond to the neighboring peaks. Final wave profiles are allocated in bold.

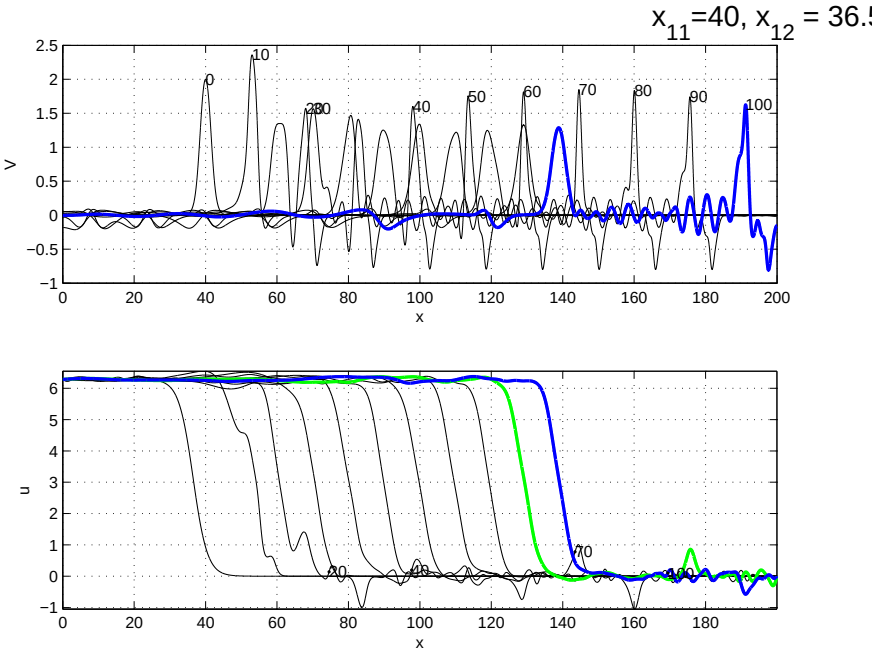

Figure 3: Splitting of moving localized bell-shaped micro-strain wave v when the kink-shaped input for u is shifted more behind that of v. Points of time correspond to the neighboring peaks. Final wave profiles are allocated in bold.

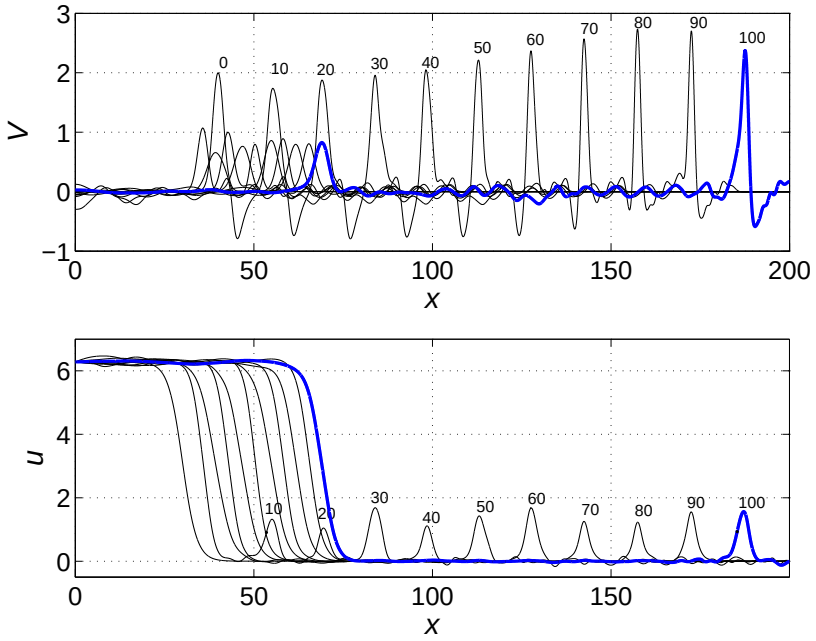

Figure 4: Generation of moving localized bell-shaped micro-strain wave in a lattice from the kink-shaped input for u whose initial position is shifted behind that of v. Points of time correspond to the neighboring peaks. Final wave profiles are allocated in bold.

of this kink with the bell-shaped wave of v or an external loading. The velocity of the waves propagation lies in the interval $(c_L^2 - c_0^2; c_L^2)$ prescribed by the exact solution.

The initial position of the inputs should coincide according to the exact solution. Small difference in the relative position, $x_{11} = 40$, $x_{12} = 37.5$, yields perturbations on the profiles of the waves propagating with the velocity from the interval $(0; c_L^2 - c_0^2)$, see Fig.2. Further increase in the relative initial positions, $x_{11} = 40$, $x_{12} = 36$, gives rise to a splitting of the wave v into two localized bell-shaped parts what is clearly seen at the final bold curve in Fig.3. One can see that one part continue to move together with the kink-shaped wave u while the second one propagates faster. The last wave gives rise to an appearance of perturbations in the shape of u trapped by this part of v. Finally, at larger relative initial distance, $x_{11} = 40$, $x_{12} = 35$, the initial condition for u also splits into two parts as shown in Fig. 4. The kink-shaped part propagates with corresponding part of v like in Fig. 3 while the new bell-shaped part moves faster together with corresponding bell-shaped wave v with the velocity from the interval $(c_L^2 - c_0^2; c_L^2)$ prescribed by the bell-shaped exact solutions.

3 Conclusions

It is shown that exact kink-shaped solution prescribes well the velocity interval required for propagation of the kink-shaped wave accounting for variations in the internal structure of the lattice. However, variation in the initial positions of the inputs for u and v gives rise to their splitting into two parts. These parts yield two pairs of the waves u and v propagating with different shapes and velocities. However, correspondence between the wave shape and its velocity is in an agreement with the analysis following from the traveling wave exact solution.

Acknowledgements

The work has been supported by the Russian Foundation for Basic Researches, grants No 09-01-00469a and 10-01-00243-a.

References

[1] Aero, E.L. Micromechanics of a double continuum in a model of a medium with variable periodic structure. J. Eng. Math. **55**, 81–95 (2002)

[2] Aero, E.L., Bulygin, A. N. Strongly Nonlinear Theory of Nanostructure Formation Owing to Elastic and Nonelastic Strains in Crystalline Solids. Mechanics of Solids. **42**, 807–822 (2007)

[3] Porubov, A.V., Aero, E.L., Maugin, G.A. Two approaches to study essentially nonlinear and dispersive properties of the internal structure of materials. Phys. Rev. E. **79**, 046608 (2009)

[4] Porubov, A.V., Aero, E.L., Andrievsky, B.R. Dynamical properties of essentially nonlinear generalized continua. In: G.A. Maugin. A.V. Metrikin (eds), Mechanics of Generalized Continua,p. 161–168, Springer, Berlin (2009).

[5] Porubov, A.V., Andrievsky, B.R., Aero, E.L Nonlinear dynamic processes in media with internal structure. In: Mechanics of Generalized Continua, H.Altenbach, G.A. Maugin, V.I. Erofeyev (Eds.), P. 245–254, Springer, New York, (2011).

[6] Porubov, A.V., Andrievsky, B.R. Influence of coupling on nonlinear waves localization. CNSNS (2011) 8 pages,in press, .

[7] Porubov, A.V., Andrievsky, B.R. Localized nonlinear strain waves in media with internal structure. In: Proceedings of 10th biennial International Conference on Vibration Problems, Springer, Berlin, (2011), 6 pages, in press.

[8] Shampine, L. F. and Reichelt, M. W.: SIAM Journal on Scientific Computing, **18-1** (1997).

A.V. Porubov, IPME RAS, Saint-Petersburg, Russia
B.R. Andrievsky, IPME RAS, Saint-Petersburg, Russia

Influence of the dispersion in nonequilibrium models for continuous mechanics

Evelina V. Prozorova
prozorova@niimm.spbu.ru

Abstract

Present investigation develops theory of continuous mechanics for formulation general laws of equilibrium as laws of equilibrium angular momentum in gas-solid interaction and influence cross flux on fluctuation normal shock waves. Usually the equilibrium conditions for forces are postulated in spite of that it is special case interpretation. The new model for solution the problem of flow rarefied gas near bodies is suggested. Layer closed to surface is order of some radius of interaction molecules. The modified Navie-Stokes for remainder can be used and conjugate conditions at surface can be written without the Knudsen layer. You will be able to count friction and heat flow to the surface by solution the Boltzmann equation without collision integral in thin layer and by solution the Navie-Stokes equations with addition new terms. The Chapman-Enskog distribution function as boundary condition for external boundary of thin layer is used with macroscopic parameters are determined from the Navie-Stokes equations. It is discussed the influence of distribution function structure on interaction gas-solid. The inertial N. A. Kolmogorov region in boundary layer is analyzed.

Keywords: angular momentum, conservation laws, nonsymmetrical stress tensor, Boltzmann equations, Chapman-Enskog method, conjugate problem the Navie-Stokes

1 Introduction

Any movement of an elementary volume of liquid today can be considered as a result of the following motion: quasisolid motion that is translation with selecting pole, rotating motion around this pole and deformation motion. This theorem was proved by Gelmholtz H. Prandtl L. formulated conception of hardplastic body as the theory of ideal plasticity. Usually we do not take into account twist velocity. Instability of shock waves for Mach number M $\approx$1 is well known. For other M experimental data shows instability of shock waves for plasma and reacting gases with endothermic reactions. The explanation of these effects we have not at present. Some experimental facts tell us about importance of gradients of physical values. This paper reports on influence the angular momentum variation in an elementary volume and cross flux through the sides of an elementary volume on continuous equations. At present used of continuous mechanics equations were received, as we see it, from insufficiently full physical laws and, hence, these laws would be revised. Present investigation attempts to formulate the equilibrium conditions as equilibrium conditions of angular momentum but usually the laws of equilibrium are postulated as equilibrium of force. In the classical Newton mechanics we have four conservation laws: masses, liner momentum, energy, angular momentum. In continuous mechanics we use only three first laws. Last law degenerates in symmetric tensor P. The kinetic theory does not save the situation. The law of angular momentum does not implement in the

Boltzmann equation. The numerical solution of the Boltzmann equation does not contain this mistake if it was solved without employment of the conservation laws. In this paper the relationships between the Boltzmann equation and hydrodynamics are discussed. The modified equations of hydrodynamic follow from the modified Boltzmann equation [1,2]. The modified laws of conservation were received for the particles without structure. The angular momentum does not contain the new dimension constants. So the similar solution for classic equations are similar for modified equations. For elasticity theory equations did not change but were proposed another interpretation and added the angular momentum equation to the classic equations. Essential that continuity for solid is fulfilled. Taking into account the angular momentum law nonsymmetrical stress tensor is received. The method for calculation of nonsymmetrical part is suggested. Besides usually convective flows the cross flux performed. As example for density was take into consideration only the flows of density across the surface of an elementary volume. Conclusion of the equation with the more full physical idea as classical was done by S.V. Vallander in 1951 year (for the cross effects) [3]. The self- diffusion, energy and linear momentum were considered for the perfect continuous gas in supposition about internal energy $E = c_v T$. Here c_v is the coefficient of thermal capacity under constant volume. For great gradients of physical values colliding molecules are belonging to different distribution functions can have different macroparameters (density, temperature, velocity) . The influence variation of the distribution function over times of the mean time τ between collisions of particles was suggested B.V.Alexeev [4]. We suggest that the second term R. Taylor series in collision integral necessary to take into account. It received after expansion the distribution functions in collision integral over space coordinates near the point x. Differentiating the equilibrium distribution function of collision integral the structure of formulas by S.V.Vallander can be received for interacting molecules with hard potential. In other case it is necessary to take averaged cross section. In general case (nonstationary) the collision integral can be written in form suggested by B. Aleexeev. Constants are defined by the species of concrete potential. Always in spite of that concrete time for two molecules we will be exploit average time which is proportional to inverse value of frequency. For numerical solution can be used the average values of collision integral for concrete velocity. Classical theory predicts the existence of the second viscosity but usually we assumed that it should be take into account for molecules with inner degree of free or for dense gas. The modified kinetic theory gives the second viscosity. The modified Boltzmann and Navier-Stokes equations are needed boundary conditions. Another problem for the solving of the Boltzmann equation is the asymptotical methods. It is essential that selecting the local equilibrium distribution function f_0 as the basis in solution of the Boltzmann equation by the Chapman-Enskog method exploits macroscopic parameters in f_0 from the Euler equations [5]. Macroscopic parameters are determined the Chapman-Enskog distribution function leads to the Euler equations parameters and tensor P is symmetric. Formally in that way we have values (density, linear momentum, energy) with mistake of the first order. This fact was noted by Hilbert without further use and correction. So for the equilibrium in collision integral [5,6]

$$f\left(t,x,\xi\right) \equiv f_0\left(t,x,\xi\right) = n\left(\frac{m}{2\pi kT}\right)^{3/2} \exp\left\{-\frac{m}{2kT}c^2\right\}, \quad \left(c^2 = c_1^2 + c_2^2 + c_3^2\right) = \left(\xi - u\right)^2$$

and for nonequilibrium distribution

$$f = f_0\left[1 + \frac{p_{ij}m}{2pkT}c_i c_j - \frac{q_i m}{pkT}c_i\left(1 - \frac{mc^2}{5kT}\right)\right]$$

has the same macroparameters in f_0. The nonequilibrium distribution function is such that integral of it contains only the integral of equilibrium function $f_0$and gives containing in f_0 macroscopic parameters. The remaining term gives null. Besides it is essentially for the value of viscosity. So it is necessary to do iteration all values (density, linear momentum, energy). It is possible for equation with angular momentum. In classic thus tensor P is entering as the value p in the Euler equations and as symmetric tensor in the Navier-Stokes equations. Consequently the theory value p for the Navie-Stokes equations is not equal to value p for the macroscopic Euler equations.

The order of the new equations (for the density and for the linear momentum, energy) is more than in classical case. If we deal with continual medium the external boundary condition for boundary layer can be determined as the value of rotor velocity or as of value normal velocity. That is for the vertical velocity. For the longitudinal velocity it is need to put friction. In turbulence layer we need to set a friction too [7,8]. For the rarefied gas the boundary conditions would be included the value gas flow besides the classical boundary conditions [1,2]. At present the theory of description turbulence does not clear in spite of existence a large number theories. Usually we consider the following theory for turbulence streams: Direct Numerical Simulation, Large Eddy Simulation, Reynols-Averaged Navie-Stokes and some others. In the previous papers we investigated numerically and analytical method the modified Blasius problem, the Falkner-Skan problem, the flow near infinite plate. For the last case the motionless thin film was detected and the Prandtl formula was received. It has been shown that longitudinal velocity profile for these problems has fluctuations near upper boundary. For the boundary layer turbulence is beginning here.

Essentially that the tasks about the flow in tube, flow among two plates are formulated in our textbook as hydrotechnical tasks (middle change is constant).

Gas-surface interaction plays an essential role in processes connected with atmosphere re-entry vehicles [5]. It is necessary to know aerodynamic characteristics. These conditions are known badly for rarefied gas and for turbulence streams. To solute the Boltzmann equation is more difficult than Navier-Stokes equations. So better to solute Navier-Stokes equations. Usually for the classical case near the surface the Knudsen layer is considered [9]. This layer has the length of order free path. M. Lunc, J. Luboncki, V.C.Liu , R.G. Patterson, W. Bule, F.O.Goodman, H.Y.Wachman, R G. Barantsev, Yu. A.Ryzhev, G.V. Dubrovskii and the others investigated the interaction molecules with surface near freely-molecular simulations. Another type of works are investigation of nanostructures, but we do not discuss this problem. The analytical study of weak shock waves with cross flows across the surface of an elementary volume has been investigated for gas without structure [10]. For structure gas with threshold energy of destruction was received possibility for movement it in reverse direction if Mach number is near the unit. The aim of this paper is to find the reason for appearing the second viscosity for cross flow at large gradients of the physical values, to investigate the self- diffusion which gives additional diffusion for normal shock waves where angular momentum does not work but the self- diffusion give additional diffusion. The convective flow has the same value as diffusion flow for the Mach number M$\approx$1. It will be received in our work. The boundary conditions for rarefied gas near the surface make more accurate than early. Boltzmann equation and hydrodynamics are discussed. The modified equations of hydrodynamic follow from the modified Boltzmann equation [1,2].

2 Equations

Our results can be summarized as follows for all continuous mechanics : in phenomenon theory we have four equilibrium equations but if we choose equilibrium of force the three equilibrium equations and symmetric tensor are received; so our interpretation bases on traditional theory. The degree of asymmetric stress tensor we can received from momentum equation (in projections) [11]

$$y\left(\frac{\partial\sigma_{xz}}{\partial x}+\frac{\partial\sigma_{yz}}{\partial y}+\frac{\partial\sigma_{zz}}{\partial z}\right)-z\left(\frac{\partial\sigma_{xy}}{\partial x}+\frac{\partial\sigma_{yy}}{\partial y}+\frac{\partial\sigma_{zy}}{\partial z}\right)+\tau_{zy}-\tau_{yz}=0,$$
$$x\left(\frac{\partial\sigma_{xz}}{\partial x}+\frac{\partial\sigma_{yz}}{\partial y}+\frac{\partial\sigma_{zz}}{\partial z}\right)-z\left(\frac{\partial\sigma_{xx}}{\partial x}+\frac{\partial\sigma_{yx}}{\partial y}+\frac{\partial\sigma_{zx}}{\partial z}\right)+\tau_{zx}-\tau_{xz}=0$$
$$x\left(\frac{\partial\sigma_{xy}}{\partial x}+\frac{\partial\sigma_{yy}}{\partial y}+\frac{\partial\sigma_{zy}}{\partial z}\right)-y\left(\frac{\partial\sigma_{xx}}{\partial x}+\frac{\partial\sigma_{yx}}{\partial y}+\frac{\partial\sigma_{zx}}{\partial z}\right)+\tau_{yx}-\tau_{xy}=0$$

The angular momentum does not contain the new dimension constants and nonstationary contains in density and velocity but not have the nonstationary term for the angular momentum equation. Then we received the modified Navier-Stokes equations

$$\frac{\partial\rho}{\partial t}+\frac{\partial\rho u_i}{\partial x_i}+\frac{\partial}{\partial x_i}\left(x_i\frac{\partial\rho u_i}{\partial x_i}\right)=0.$$

$$\frac{\partial\rho u_i}{\partial t}+\frac{\partial}{\partial x_i}\left(\rho u_i u_j+P_{ij}+x_i\frac{\partial P_{ij}}{\partial x_i}\right)-\frac{X_i}{m}\rho=0.$$
$$\frac{\partial}{\partial t}\rho\left(\frac{3}{2}RT+\frac{1}{2}u^2\right)+\frac{\partial}{\partial x_j}\left[\rho u_j\left(\frac{3}{2}RT+\frac{1}{2}u^2\right)+u_kP_{kj}+q_j\right]+$$
$$+\frac{\partial}{\partial x_i}x_i\frac{\partial}{\partial x_j}\left[\rho u_j\left(\frac{3}{2}RT+\frac{1}{2}u^2\right)+u_kP_{kj}+q_j\right]=0$$

We obtain the equation for angular momentum from the modified Boltzmann equation.

$$\frac{\partial\vec{r}}{\partial x}\times\vec{p}_x+\frac{\partial\vec{r}}{\partial y}\times\vec{p}_y+\frac{\partial\vec{r}}{\partial z}\times\vec{p}_z+x_j\frac{\partial}{\partial x_j}\left(\vec{P}_j\right)=M_I$$

We should use this equation for definition of value nonsymmetric tensor in gas. Besides the second viscosity can be received from collision integral and formulas suggested by S.V. Vallander

$$\tilde{f}'\tilde{f}_1'-\tilde{f}\,\tilde{f}_1=f'f_1'+\Delta t\left\{\xi'\frac{\partial f'}{\partial x}(t,x,\xi')\cdot f_1'(t,x,\xi_1')+f_1(t,x,\xi')\,\xi_1'\frac{\partial f_1'}{\partial x}(t,x,\xi_1')\right\}-$$
$$-f\,f_1-\Delta t\left\{\xi\frac{\partial f}{\partial x}(t,x,\xi)\cdot f_1(t,x,\xi_1)+\xi_1\frac{\partial f_1}{\partial x}(t,x,\xi_1)\,f(t,x,\xi)\right\}+O(\Delta x)$$

$$\frac{df^{(0)}}{dt}|_{t=0}=f^{(0)}\left\{\frac{m}{kT}\left(c_ic_j-\frac{1}{3}c^2\delta_{ij}\right)\frac{\partial u_i}{\partial x_j}+\right.$$
$$\left.+\frac{1}{2T}\frac{\partial T}{\partial x_i}c_i\left[\left(\frac{m}{kT}\right)c^2-5\right]+\frac{m}{kT}\left(c_ic_j-\frac{1}{3}c^2\delta_{ij}\right)\frac{\partial}{\partial x_j}x_i\frac{\partial u_i}{\partial x_i}\right\}$$

3 Beam

Consider protozoa task about beam. Closer definition of equilibrium will be obtained if angular momentum would take into attention.

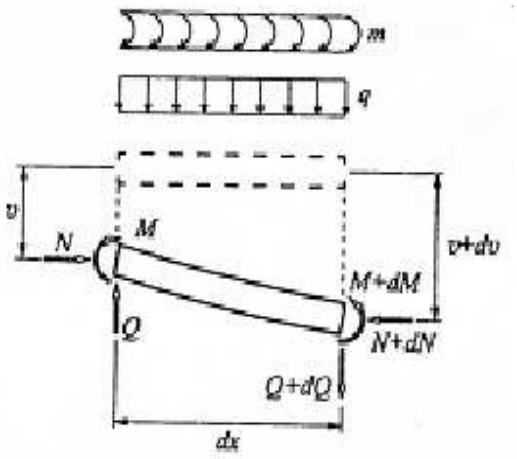

Figure 1: Elementary beam section.

$$-M'' = q - m' - (Nv')'$$
$$dM - Qdx - mdx - Ndv = 0,$$
$$dQ + qdx = 0,$$
$$-M'' = q - m' - ((Nv)')'.$$

For this problem the solution for general case and without N' (for N=Const) is the same. Consequently we can choose the beam of variable cross-section. For beam on elastic foundation results distinguish. For another problem the solutions can be different too.

4 Blasius problem

The Blasius problem was considered in [12] by numerical and analytical.

Some results for infinite plate will be formulated here. The equation for this case is

$$\frac{d}{dy}\left(\mu\frac{du}{dy}\right) + \frac{d}{dy}\left(\mu y\frac{d^2u}{dy^2}\right) = 0.$$

Boundary conditions are

$$u = 0, \quad \mu\frac{du}{dy} = \tau_w, \quad y = 0,$$
$$u = U_\infty, \quad y \to \infty.$$

Integrating gives

$$\mu\frac{du}{dy} + \mu y\frac{d^2u}{dy^2} = Const = \tau_w.$$

There are t-time, y-coordinate, ρ-density, $P_{i,j}$– stress tensor, u-velocity, μ-viscosity. Index "w" is relative to surface. From boundary condition we have $Const = \tau_w$. τ_w is skin friction. Integral of the equation is

$$u = C * \ln y + \tau_w/\mu * y + Const.$$

Possible variant to satisfy boundary conditions is that under the $y = \dfrac{\nu}{v_*}$, where $\nu = \dfrac{\mu}{\rho}$, $v_* = \left(\dfrac{\tau_w}{\rho_w}\right)^{1/2}$ we have $ln = 0$. Later on diminution velocity takes place up zero, derivative can be very large but zero velocity observes between surface and y. So layer of the rest liquid is formed. Thickness of this layer is 10^{-3}cm. We have not reliable measurements there. Probably for laminar layer there is no layer with zero velocity. Near the edge the gradient of the velocity tends to work. It works near the rebuilding region too. Far from edge friction strives to zero. It does not follow from the theory for semi-infinite plate that the value of the friction is finite but if we suggest zero friction in the first integral we can get the Karman formula for the mixture length. Equality $\tau_w = 0$ provides $u = 0$ as $y = 0$ and $u = U_\infty$ as $y \to \infty$ and leads to rebuilding of the flow. The profile of the velocity becomes more completed than near the edge. The region with $\tau_w = 0$ formulated the inertial layer(N.A. Kolmogorov). This case relies to logarithm profile for boundary layer. It is interesting that asymptotic friction for half- infinite plate has not the value for infinite plate. In my opinion we have similar situation for tubes.

5 Shock wave

The classical structure normal shock waves can be found in [13]

$$\rho u = \rho_0 D = a, \quad p + \rho u^2 + w = p_0 + \rho_0 D^2 = p_{00}, \quad w = -\mu \frac{du}{dx},$$

$$\frac{\gamma}{\gamma - 1}\frac{p}{\rho} + \frac{1}{2}u^2 + \frac{1}{\rho_0 D}(S + uw) = h_0 + \frac{D^2}{2} = h_{00}, \quad S = -k\frac{dT}{dx}, \quad \frac{p}{\rho} = RT$$

Here ρ is the density, μ is the viscosity, internal energy $E = c_v T$, p is the pressure, u is the velocity.

To investigate the weak shock wave for Mach number M = 1 is very difficult. The front of shock wave is not stability for this regime in experiments. The cause of instability is not clearly. In my opinion the cause is in the next. Influence of self- diffusion (only of density) leads to

$$\frac{d\rho u}{dx} = \frac{d}{dx}\frac{\mu\alpha_1}{\rho}\frac{d\rho}{dx},$$

$$\rho u\frac{du}{dx} + u\frac{d}{dx}\frac{\mu\alpha_1}{\rho}\frac{d\rho}{dx} + \frac{dp}{dx} - \frac{d}{dx}\frac{4}{3}\mu\frac{du}{dx} = 0,$$

$$\rho\frac{d}{dx}c_V T + \left(c_V T - \frac{u^2}{2}\right)\frac{d}{dx}\frac{\mu}{\rho}\alpha\frac{d\rho}{dx} = \frac{4}{3}\mu\left(\frac{du}{dx}\right)^2 + \frac{d}{dx}\lambda\frac{dT}{dx} + \frac{d}{dx}\frac{\mu c_V T}{\rho}\frac{d\rho}{dx}$$

$$\frac{\gamma}{\gamma - 1}\frac{p}{\rho} + \frac{1}{2}u^2 + \frac{1}{\rho_0 D}(S + uw) = h_0 + \frac{D^2}{2} = h_{00}, \quad S = -k\frac{dT}{dx}, \quad \frac{p}{\rho} = RT$$

Here ρ is the density, μ id the viscosity, internal energy $E = c_v T$, p is the pressure, u is the velocity.

From R.Becker solution (for η) $\dfrac{\dfrac{\mu_0\alpha_1}{\rho_0}\dfrac{d\eta}{dx}}{\rho_0 D_0} \approx 1$ for $M = 1$, $\eta = \dfrac{\rho_0}{\rho}$.

In our case for gas without structure we have equation for η [14,15]

$$\frac{d\eta}{dx} - \frac{D\rho_0}{\mu\alpha_1}\eta + \frac{u\rho_0}{\mu\alpha_1} = 0.4$$

Consider the influence of the new terms (self-diffusion) on changing ρ, u, p, T. Transfer new terms on the right side of equation as in the first equation. In shock wave we have growth of density. Hence after integration of x we have larger zero increment density. So for small growth of density velocity should increased, pressure increased and for small reduction of density we have opposite situation. For $M \approx 1$ velocity can change and shock wave can modify to wave of compression. So we can tell about unstable shock waves for some special parameters of flows. After decrease of density in shock wave the process go to opposite side. For pressure we have similar process. If gas is mixture and it contains the light components we can have tongue of light component at two side of shock wave.

6 Conclusions

We discuss the problems that can be appearing to consider the angular momentum variation in an elementary volume near the surface and influence the cross flows through the sides of an elementary volume for great gradients of the physical values.

The unstable shock wave for M≈1 is investigated.

References

[1] E.V. Prozorova, *Influence of dispersion in mechanics*. Seventh International Workshop on Nondestructive testing and Computer Simulations in Science and Engineering, edited by Akexander I. Melker, Proceedings of SPIE Vol.5400 (SPIE, Bellingham, WA, 2004) pp.212-219.

[2] E.V.Prozorova. Influence of the dispersion in nonequilibrium models for continuous mechanics. Proceedings of XXXVIII Summer School "Advanced Problems in Mechanics", pp.568-574, Spb. 2010.

[3] S. V. Vallander. The equations for movement viscosity gas. DAN SSSR. 1951. V. LXXIII, N 1.

[4] Alexeev. Generalized Boltzmann Physical Kinetics. Elsevier, Amsterdam, 2004. 5.

[5] M.N. Kogan. The dynamics of the rarefied gases. M.: Nauka, 1967.(Russian)

[6] C. Cercignani, Mathematical methods in kinetic theory Macmillan. 1969.

[7] L.G.Loyotinskiy. Mechanics of fluids and gas. M.: Nauka. 1970 (in Russian)

[8] Handbook of turbulence. Ed. W Frost,T.H. Moulden Plenum Press: New York, London 1980

[9] F. O. Goodman, H. Y. Wachman. Dynamics of gas-surface scattering. Academic press. New York. 1976. 423pp.

[10] Prozorova E.V. Influence of dispersion on cross flux in gas mechanics. Material Physics and Mechanics No 2, 2010 pp. 105-110.

[11] A.Ya. Ishlinsky, D.D. Ivlev, "The mathematical theory of plasticity", M.: Feezmatleet, 2003.

[12] A. .I. Voronkova, E.V. Prozorova, "Influence of the dispersion on the perturbations in the some problem of mechanics" *Mathematical Modeling,* 2006. No 10. P. 3 –10 (in Russian).

[13] R.Becker. Stosswelle und Detonation, Zeitschr.fur Phys. N 8. 321-322

[14] V.A.Kononenko, E. V. Prozorova, A.V. Shishkin. Influence dispersion for gas mechanics with great gradients. 27-th international symposium on Shock waves. . St. Peterburg. pp.406-407, 2009.

[15] Prozorova E.V. Influence of dispersion and cross flows on shock wave. 19-th International Shock Interaction Symposium. Moscow, 2010. p.123

Evelina V. Prozorova, Mathematics Mechanics Faculty, St. Peterburg State University, University av. 28 , Peterhof, 198904, Russia

Asymptotics of fields near common apex of functionally graded wedge(s)

Alexander Linkov Liliana Rybarska-Rusinek
rybarska@prz.edu.pl

Abstract

The paper aims to work out a method to evaluate the characteristics of singular fields near an apex of functionally graded wedges. It is shown that the efficient method, previously developed for homogeneous wedges, may be immediately extended to graded wedges by using appropriate eigenfunctions. An approximate solution may be obtained without evaluation the eigenfunctions: it is sufficient to represent an inhomogeneous wedge as the sum of homogeneous wedges with sufficiently small angles. Numerical experiments confirm high efficiency of the approximate method.

1 Introduction

Regions with continuously changing mechanical, thermal or optical characteristics are produced artificially to obtain materials with desired properties or appear in manufacturing processes like crystallization, thermal treatment, fogging, etc. In a polycrystalline structure, such functionally graded regions may arise in structural elements near their common apex. This strongly influences the concentration of physical fields near the apex, which presents a singular point at which fluxes (stresses), or at least their spatial derivatives tend to infinity. Therefore, studying the concentration influenced by continuously changing physical properties is important from scientific and practical points of view. The paper aims to work out a method to evaluate the characteristics of singular behavior and fields near an apex of functionally graded wedges. The method is based on the technique previously used for systems of homogeneous wedges with a common apex ([1], [2], [3]). It takes into account that eigenvalues and eigenfunctions, corresponding to a functionally graded wedge, are rarely presented by analytical formulae, while their numerical calculation requires considerable computational effort. To overcome the difficulty in the general case, we suggest the simplest way: to represent an inhomogeneous wedge by a system of homogenous wedges with sufficiently small angles. This means piece-wise constant approximation of the continuously changing physical properties. Then employing the well-developed technique and computer codes to solve the problem for systems of homogeneous wedges with quite small angles (degrees and even minutes), we obtain an approximate solution of the problem under consideration. The method was implemented and tested for the potential problems (steady liquid, heat or current flow, antiplane strain). To check the accuracy we made numerical experiments of two kinds. One of them uses the straightforward approach, which consists of successive increase of the number of thin wedges representing the graded wedge. Then comparing the results for systems with growing number of thin wedges, we may see whether and when they actually converge. Another approach is more sophisticated and consists in looking for and studying particular cases when eigenvalues

and eigenfunctions may be found analytically. We could see that the numerical results obtained in experiments of the both types match quite well and confirm high efficiency of the method suggested.

2 Problem formulation

Consider antiplane strain of a system of m elastic wedges. The system may be open (Fig 1a) or closed (Fig. 1b). The angle of a wedge is denoted Θ, its shear modulus is μ. One of the wedges, marked by the subscript 0, is functionally graded (FG). Its angle is Θ_0 and the shear modulus $\mu_0(\vartheta)$ changes as a continuous function of the polar angle ϑ.

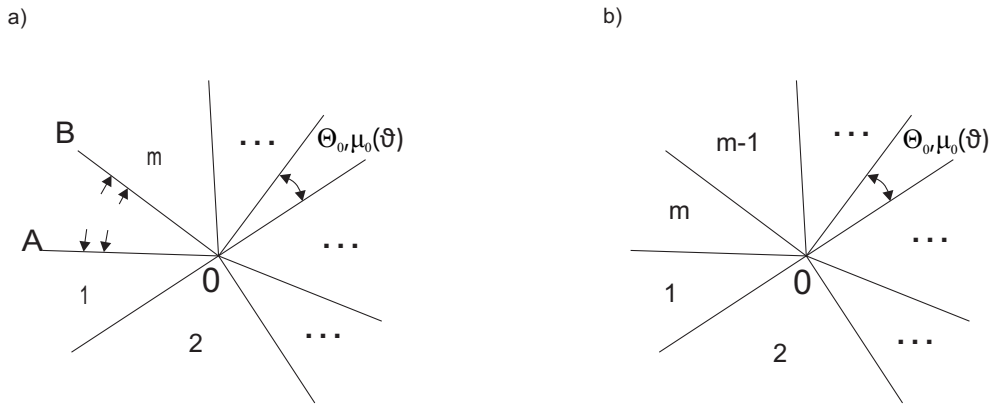

Figure 1: a system of m wedges a) open, b) closed with a functionally graded wedge

In each of the wedges, the component $u_z(r,\vartheta)$ of the displacement vector, considered in polar coordinates (r,ϑ), satisfies the equation:

$$\frac{\partial^2 u_z}{\partial r^2}+\frac{\partial u_z}{r\partial r}+\frac{\partial^2 u_z}{r^2\partial\vartheta^2}+\frac{1}{r^2}\frac{d\mu}{\mu d\vartheta}\frac{\partial u_z}{\partial\vartheta}=0 \tag{1}$$

The stresses $\sigma_{\vartheta z}$ and σ_{rz} are expressed via the displacement as $\sigma_{\vartheta z}=\mu\frac{1}{r}\frac{\partial u_z}{\partial\vartheta}$, $\sigma_{rz}=\mu\frac{\partial u_z}{\partial r}$. For a homogeneous wedge we have $\mu=const$, and (1) becomes the Laplace equation.

Assume for simplicity that both displacements and tractions are continuous across a contact:

$$u_z^+(r)=u_z^-(r),\ \sigma_{\vartheta z}^+(r)=\sigma_{\vartheta z}^-(r), \tag{2}$$

Herein, the superscript plus (minus) refers to the limiting value from the wedge, for which the external normal is directed clock-wise (counter clock-wise). For a closed system, we have m pairs of the conditions (2). For an open system, there are $m-1$ pairs, and two additional equations are given by boundary conditions at the external boundaries OA and OB of the system. In a sufficiently general case, these boundary conditions may be written as

$$a_u u_z(r)+a_\sigma r\sigma_{\vartheta z}(r)=b_u f_u(r)+b_\sigma r f_\sigma(r), \tag{3}$$

where a_u, a_σ, b_u, b_σ are prescribed constants; $f_u(r)$, $f_\sigma(r)$ are prescribed functions. Obviously, equation (3) includes the case of prescribed displacements, then $a_\sigma=0$, $b_\sigma=0$, and the case of prescribed tractions, when $a_u=0$, $b_u=0$.

3 Method of solution for a system with a functionally graded wedge(s)

As usual, we employ the Mellin's transform for each of the wedges:

$$u_z(s,\vartheta) = \int_0^\infty u_z(r,\vartheta) r^{s-1} dr, \tag{4}$$

It reduces the equation (1) to the linear ordinary differential equation

$$\frac{d^2 u_z(s,\vartheta)}{d\vartheta^2} + \frac{d\mu(\vartheta)}{\mu d\vartheta}\frac{du_z(s,\vartheta)}{d\vartheta} + s^2 u_z(s,\vartheta) = 0. \tag{5}$$

Its general solution is:

$$u_z(s,\vartheta) = C_1(s) f_1(s,\vartheta) + C_2(s) f_2(s,\vartheta), \tag{6}$$

where $f_1(s,\vartheta)$, $f_2(s,\vartheta)$ are two linearly independent eigenfunctions. In particular cases, eigenfunctions have a simple analytical case. Specifically,

(i) for a homogeneous ($\mu = const$) wedge, the eigenfunctions are $f_1(s,\vartheta) = \sin(s\vartheta)$, $f_2(s,\vartheta) = \cos(s\vartheta)$,

(ii) for a FG material with the shear modulus changing exponentially as $\mu(\vartheta) = \exp\{-2a\vartheta\}$ with $a > 0$, the eigenfunctions are:

$$f_1(s,\vartheta) = \exp\{a[1 + \sqrt{1-(\tfrac{s}{a})^2}]\vartheta\},\ f_2(s,\vartheta) = \exp\{a[1 - \sqrt{1-(\tfrac{s}{a})^2}]\vartheta\} \ \text{ if } s \neq a$$

and

$$f_1(s,\vartheta) = \exp\{a\vartheta\},\ f_2(s,\vartheta) = \vartheta\exp\{a\vartheta\} \ \text{ if } s = a.$$

In other cases of a FG material, the eigenfunctions $f_1(s,\vartheta)$ and $f_2(s,\vartheta)$ may be found in the form of power series (for instance, when the function $\frac{d\mu(\vartheta)}{\mu d\vartheta}$ is analytical), or numerically. When having the eigenfunctions, the solution (6) may be re-written in terms of the boundary values of displacements and tractions rather than in terms of the constants $C_1(s)$ and $C_2(s)$:

$$\begin{pmatrix} u_t(s) \\ u_b(s) \end{pmatrix} = R(s) \begin{pmatrix} p_t(s) \\ p_b(s) \end{pmatrix}, \tag{7}$$

where $u_t(s) = u_z(s, +\frac{\Theta_0}{2})$ is the displacement of the "top" boundary of the wedge; $u_b(s) = u_z(s, -\frac{\Theta_0}{2})$ is the displacement at its "bottom" boundary; $p_t(s) = \sigma_{\vartheta z}(s, \frac{\Theta_0}{2})$, $p_b(s) = \sigma_{\vartheta z}(s, -\frac{\Theta_0}{2})$, and the matrix $R(s)$ is defined as

$$R(s) = \begin{pmatrix} R_{tt} & R_{tb} \\ R_{bt} & R_{bb} \end{pmatrix} = \tag{8}$$

$$\begin{pmatrix} f_1(s,\frac{\Theta_0}{2}) & f_2(s,\frac{\Theta_0}{2}) \\ f_1(s,-\frac{\Theta_0}{2}) & f_2(s,-\frac{\Theta_0}{2}) \end{pmatrix} \begin{pmatrix} \mu(\frac{\Theta_0}{2}) f_1'(s,\frac{\Theta_0}{2}) & \mu(\frac{\Theta_0}{2}) f_2'(s,\frac{\Theta_0}{2}) \\ \mu(-\frac{\Theta_0}{2}) f_1'(s,-\frac{\Theta_0}{2}) & \mu(-\frac{\Theta_0}{2}) f_2'(s,-\frac{\Theta_0}{2}) \end{pmatrix}^{-1}. \tag{9}$$

This form allows us to use the efficient method suggested for multi-wedge systems in [1] and successfully employed in [2], [5], [6]. The only (non-principal) difference consists in

expressions for the shear modulus and eigenfunctions: for a FG material, μ changes with the polar angle, while eigenfunctions are not given by sine and cosine.

The method is very accurate and stable; many numerical examples evidently show that it is applicable even for very thin wedges (of some minutes) and in cases of wedges with highly contrast elastic modules. This suggests using piece-wise linear approximation of $\mu(\vartheta)$ for an inhomogeneous wedge and employing well-developed codes for multi-wedge systems of homogenous wedges (e.g.[2], [5]).

4 Approximate solution

The piece-wise linear approximation of $\mu(\vartheta)$ may be used when we do not have analytical expressions for the eigenfunctions $f_1(s,\vartheta)$ and $f_2(s,\vartheta)$ or when avoiding numerical evaluation of these functions. Actually, it corresponds to representation of an inhomogeneous wedge by the sum of homogeneous wedges with ideal contacts.

We take n wedges with sufficiently small angles to represent the FG wedge. Each of the thin wedges is assumed homogeneous with a constant shear modulus equal to

$$\mu_i = \mu\left(-\frac{\Theta_0}{2} + (2i-1)\frac{\Theta_0}{2n}\right),\ i = 1,..n. \tag{10}$$

By using procedures developed in [2], [5] for arbitrary systems of homogeneous wedges, we find parameters, which characterize the singular behavior of physical fields near the common apex of the total system of wedges. Below the accuracy of this simple straightforward approach is checked by (i) comparing the results with those, obtained without the approximation in particular cases when the eigenfunctions are available and (ii) increasing the number of thin wedges (decreasing their angles) and inspecting the convergence of evaluated parameters.

5 Numerical examples

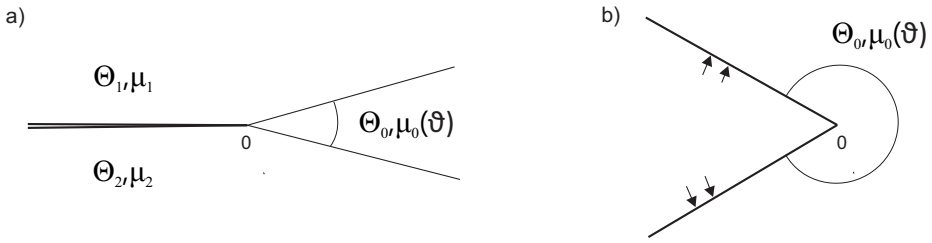

Figure 2: a) plane with a crack and functionally graded wedge, b) a functionally graded wedge

Example 1. Consider a system of three wedges with a crack between the first and last wedges (Fig 2a). The middle wedge is inhomogeneous with the angle $\Theta_0 = \frac{\pi}{6}$ and the shear modulus changing as $\mu(\vartheta) = \exp\{-2a\vartheta\}$, $a = 2$. For the latter, the matrix $R_0(s)$ is:

$$R_{tt} = \frac{a}{s^2}\exp\{a\Theta_0\}\left(1 - \sqrt{1 - \left(\frac{s}{a}\right)^2}\coth\tilde{s}\right),$$

$$R_{bb} = \frac{a}{s^2}\exp\{-a\Theta_0\}\left(1+\sqrt{1-\left(\frac{s}{a}\right)^2}\coth\tilde{s}\right),$$

$$R_{tb} = -R_{bt} = \frac{a}{s^2 sinh\tilde{s}}\sqrt{1-\left(\frac{s}{a}\right)^2},$$

where $\tilde{s} = a\sqrt{1-\left(\frac{s}{a}\right)^2}\Theta_0$.

The external wedges are located symmetrically, they have the same angle $\Theta_1 = \Theta_2 = \frac{11\pi}{12}$ and the same shear module $\mu_1 = \mu_2 = 1$. Thus for the external wedges, the matrices $R_i(s),\ i = 1, 2$, are:

$$R_i(s) = \begin{pmatrix} R^i_{tt} & R^i_{tb} \\ R^i_{bt} & R^i_{bb} \end{pmatrix} = \begin{pmatrix} -\frac{1}{\mu_i s}\cot(s\Theta_i) & \frac{1}{\mu_i s}\frac{1}{\sin(s\Theta_i)} \\ -\frac{1}{\mu_i s}\frac{1}{\sin(s\Theta_i)} & \frac{1}{\mu_i s}\cot(s\Theta_i) \end{pmatrix}.$$

Having the matrices, we employ algorithms and procedures developed in [5] to find the roots s^* of the characteristic determinant in the interval $(-1, 0)$. In the example considered, there are two such roots. Their bench-march values, obtained by using the exact expressions of the matrices, are: $\lambda_1 = 0.5081675034,\ \lambda_2 = 0.0176036428$.

Compare these accurate results with those obtained by using approximate approach based on the piece-wise approximation of the shear modulus. We represent the inhomogeneous wedge as the sum of n thin homogeneous wedges with the shear modules $\mu_i = \exp\{-2a(-\frac{\Theta_0}{2} + (2i-1)\frac{\Theta_0}{2n})\}$, and angles $\frac{\Theta_0}{n},\ i = 1, ..n$. We change the number of the thin wedges $n = 1, (3, 10, 30, 60)$ to see how the accuracy depends on the approximation parameter. The results are summarized in Table 1. It contains the values of $\lambda = 1+s^*$ found for various angles of thin homogeneous wedges approximating the inhomogeneous wedge. We see that, as could be expected, the accuracy grows with decreasing angles of thin wedges. When the angles equal to 3^o, the accuracy is three significant digits.

Table 24: Values of $\lambda = 1 + s^*$ for Example 1

n	1	3	10	30	60
λ_1	.5000000000	.5071533824	.5080750093	.5081572141	.5081649308
λ_2		.0153494258	.0173973088	.0175806826	.0175979019

Example 2. Consider an inhomogeneous wedge with the angle $\Theta_0 = \frac{5\pi}{3}$ and the shear modulus changing as $\mu(\vartheta) = \exp\{-2a\vartheta\}$, where $-\frac{5\pi}{6} \le \vartheta \le \frac{5\pi}{3}$, $a = 1.5$ (Fig 2b). The exact value of the characteristic determinant $D(s) = R(s)$ is $\frac{1}{s^2}$ and it is the same for an arbitrary angle Θ_0 and for an arbitrary real a. Hence, there is no roots in the interval $(-1, 0)$. Compare this exact result with approximate solution obtained by using the piece-wise linear approximation.

We again represent the inhomogeneous wedge as the sum of n thin homogeneous wedges: $n = 2\ (3, 4, 5, 6, 7, 8, 9)$. Their shear modules are $\mu_i = \exp\{-2a(-\frac{\Theta_0}{2} + (2i - 1)\frac{\Theta_0}{2n})\}$, $i = 1, ..n$. Table 2 contains the approximate values of λ for various n. In accordance with the analytical result, the value of λ decreases; for $n = 9$, in complete agreement with the analytical solution, there are no roots in the interval $(-1, 0)$.

Example 3. Consider a plane with a crack: $\Theta_0 = 2\pi$. The plane is inhomogeneous with the shear modulus changing linearly as $\mu(\vartheta) = a\vartheta,\ 0 \le \vartheta \le 2\pi,\ \ a = 2$. We use the approximate method to find λ. Data of Table 3 show that, as could be expected, the

Table 25: Values of $\lambda = 1 + s^*$ for Example 2

n	2	3	4	5
λ	.4000000000	.2457976326	.1691462578	.1274067962
n	6	7	8	9
λ	.1026334451	.0868760453	.0762927013	-

Table 26: Values of $\lambda = 1 + s$ for Example 3

n	2	3	4	6	8	9
λ	.5000000000	.4440310977	.4195693767	.4023856984	.3967859769	.3953338662
n	12	24	36	72	100	180
λ	.3930082168	.3908571164	.3904707276	.3902411396	.3902044647	.3901772099

results tend to converge with decreasing angles of thin homogeneous wedges. The results are reproduced with three significant digits when $n \geq 24$.

Many other examples confirm the efficiency of the approximate approach for systems of various geometry and with various mechanical properties of wedges.

References

[1] V. Blinova, A. Linkov. A method of finding asymptotic forms at the common apex of elastic wedges, J. Appl. Math. Mech. 59: 187-195, 1995. (Transl. Prikl. Mat. Mekh. 59: 199-208, 1995).

[2] A. Linkov, V. Koshelev. Multi-wedge points and multi-wedge elements in computational mechanics: evaluation of exponent and angular distribution, IJSS 43: 5909-5930, 2006.

[3] A. Linkov, V. Koshelev. Multi-wedge singular points in materials: theory, numerical techniques and applications, Proc. 4-th Int. Conference "Mathematical Modeling and Computer Simulation of Materials Technologies,MMT-2006". The College of Judea and Samaria, v. 1: I-48 - I-56, 2006.

[4] M. Paggi, A. Carpinteri. On the stress singularities at multimaterial interfaces and related analogies with fluid dynamics and diffusion, Applied Mechanics Reviews 61. 020801-22, 2008.

[5] A. Linkov, L. Rybarska-Rusinek. Numerical methods and models for anti-plane strain of a system with a thin elastic wedge, Arch. Appl. Mech. 78: 821-831, 2008.

[6] A. Linkov, L. Rybarska-Rusinek. Plane elasticity problem for a multi-wedge system with a thin wedge, IJSS 47: 3297-3304, 2010.

[7] A. Sutradhar, G. H. Paulino, L. J. Gray. Transient heat conduction in homogeneus and non-homogeneus materials by the Laplace transform Galerkin boundary element method, Eng. Analysis with Boundary Elements 26: 119-132, 2002.

Alexander M. Linkov, Liliana Rybarska-Rusinek, Rzeszow University of Technology, W. Pola 2, 35-959 Rzeszow, Poland

Mathematical model of dynamics of micropolar anisotropic elastic thin bars with free rotation

Lilit M. Margaryan Samvel H. Sargsyan
m.liloo@mail.ru, slusin@yahoo.com

Abstract

In the present paper on the basis of mathematical (asymptotic) confirmed hypotheses method, depending on the values of dimensionless physical parameters, mathematical model of dynamics of micropolar anisotropic (orthotropic) elastic thin bars with free rotation is constructed. Transverse shifts and related to them deformations are completely taken into account in the constructed model of micropolar orthotropic bars.

Key words: dynamics, micropolar, orthotropic, elastic, thin, bar, mathematical model.

1 Introduction

Current achievements in micropolar elastic thin bars, plates and shells are presented in papers [1], [2]. The main problem of the general theory of micropolar elastic thin bars, plates and shells is in approximate, but adequate reduction of initial-boundary problem of the micropolar theory of elasticity to applied two-dimensional or one-dimensional model. In papers [3], [4], on the basis of the asymptotically confirmed hypotheses method, the models of dynamics of micropolar isotropic elastic thin plates and shells are constructed, when transverse shifts and related to them deformations are completely taken into account. In paper [5] the asymptotic behavior of the solution of the plane initial-boundary problem of the micropolar theory of elasticity is studied for orthotropic material in a thin domain of rectangle. The internal problem, boundary layers of coordinates and time are constructed by the asymptotic method, the problem of jointing of internal problem and boundary layers is studied. In this paper, having in consideration the qualitative aspects of the asymptotic solution of the initial-boundary problem of plane micropolar theory of elasticity [5], the approach of papers [3], [4] is developed: hypotheses are formulated and applied one-dimensional theory of micropolar orthotropic elastic thin bars with free rotation is constructed.

2 Basic equations, boundary and initial conditions of plane dynamic problem of micropolar theory of elasticity for orthotropic rectangle

Micropolar orthotropic elastic parallelepiped of constant height , length and constant thickness, equal to 1, is considered. Coordinate plane is placed in the middle plane of the parallelepiped. Axis x_2 is directed along the height and axis x_1 - along the length of the parallelepiped, which will divide the height in half. It is assumed that plane stress state

is effected in the parallelepiped in direction of the axis x_2. The basic equations of the plane dynamic problem of the micropolar theory of elasticity for orthotropic material are as follows [6]:

Motion equations:

$$\frac{\partial\sigma_{11}}{\partial x_1}+\frac{\partial\sigma_{21}}{\partial x_2}=\rho\frac{\partial^2 u_1}{\partial t^2},\quad \frac{\partial\sigma_{12}}{\partial x_1}+\frac{\partial\sigma_{22}}{\partial x_2}=\rho\frac{\partial^2 u_2}{\partial t^2},\quad \frac{\partial\mu_{13}}{\partial x_1}+\frac{\partial\mu_{23}}{\partial x_2}+\sigma_{12}-\sigma_{21}=I\frac{\partial^2\omega_3}{\partial t^2}. \tag{2.1}$$

Elasticity relations:

$$\sigma_{11}=A_{11}\varepsilon_{11}+A_{12}\varepsilon_{22},\ \ \sigma_{22}=A_{12}\varepsilon_{11}+A_{22}\varepsilon_{22},\ \ \sigma_{12}=A_{77}\varepsilon_{12}+A_{78}\varepsilon_{21},$$

$$\sigma_{21}=A_{78}\varepsilon_{12}+A_{88}\varepsilon_{21},\quad \mu_{13}=B_{66}\chi_{13},\quad \mu_{23}=B_{44}\chi_{23} \tag{2.2}$$

or

$$\begin{aligned}
\varepsilon_{11}&=\frac{A_{22}}{A_{11}A_{22}-A_{12}^2}\sigma_{11}-\frac{A_{12}}{A_{11}A_{22}-A_{12}^2}\sigma_{22},\\
\varepsilon_{22}&=\frac{A_{11}}{A_{11}A_{22}-A_{12}^2}\sigma_{22}-\frac{A_{12}}{A_{11}A_{22}-A_{12}^2}\sigma_{11},\\
\varepsilon_{12}&=\frac{A_{88}}{A_{77}A_{88}-A_{78}^2}\sigma_{12}-\frac{A_{78}}{A_{77}A_{88}-A_{78}^2}\sigma_{21},\\
\varepsilon_{21}&=\frac{A_{77}}{A_{77}A_{88}-A_{78}^2}\sigma_{21}-\frac{A_{78}}{A_{77}A_{88}-A_{78}^2}\sigma_{12},\\
\chi_{13}&=\frac{1}{B_{66}}\mu_{13},\quad \chi_{23}=\frac{1}{B_{44}}\mu_{23}.
\end{aligned} \tag{2.3}$$

Geometric relations:

$$\varepsilon_{11}=\frac{\partial u_1}{\partial x_1},\ \varepsilon_{22}=\frac{\partial u_2}{\partial x_2},\ \varepsilon_{12}=\frac{\partial u_2}{\partial x_1}-\omega_3,$$

$$\varepsilon_{21}=\frac{\partial u_1}{\partial x_2}+\omega_3,\ \chi_{13}=\frac{\partial\omega_3}{\partial x_1},\ \chi_{23}=\frac{\partial\omega_3}{\partial x_2}. \tag{2.4}$$

Here σ_{11}, σ_{12}, σ_{21}, σ_{22} are the power voltages, μ_{13}, μ_{23} - the moment voltages, u_1, u_2 are the displacements, ω_3 is the free rotation of the points of the rectangle around the axis x_3, ρ is the density of the material, I is the measure of inertia during the rotation, ε_{11}, ε_{12}, ε_{21}, ε_{22}, χ_{13}, χ_{23} are deformations and bending-torsions, A_{11}, A_{12}, A_{22}, A_{77}, A_{78}, A_{88}, B_{66}, B_{44}, are the elastic constants of the orthotropic body. Corresponding boundary and initial conditions should be added to the determining equations (2.1) - (2.4) of the plane dynamic problem of the micropolar theory of elasticity. The power and moment boundary conditions are given on the front sides $x_2=\pm h$ of the rectangle (the problem of bending is considered):

$$\sigma_{21}\,|_{x_2=\pm h}=\frac{1}{2}(X^+-X^-),\ \sigma_{22}\,|_{x_2=\pm h}=\pm\frac{1}{2}(Y^++Y^-),\ \mu_{23}\,|_{x_2=\pm h}=\pm\frac{1}{2}(M^++M^-). \tag{2.5}$$

The following variants of the boundary conditions of the asymmetric theory of elasticity are considered on the lateral edge $x_1=0$ of the rectangle (analogically on the $x_1=a$):
the first boundary value problem:

$$\sigma_{11}\,|_{x_1=0}=\varphi_1(x_2),\quad \sigma_{12}\,|_{x_1=0}=\varphi_2(x_2),\quad \mu_{13}\,|_{x_1=0}=\varphi_3(x_2) \tag{2.6}$$

the second boundary value problem:

$$u_1\,|_{x_1=0} = 0, \quad u_2\,|_{x_1=0} = 0, \quad \omega_3\,|_{x_1=0} = 0 \tag{2.7}$$

the third boundary value problem:

$$\sigma_{11}\,|_{x_1=0} = \varphi_1(x_2), \quad u_2\,|_{x_1=0} = 0, \quad \mu_{13}\,|_{x_1=0} = \varphi_3(x_2). \tag{2.8}$$

Initial conditions are the followings:

$$u_i\,|_{t=0} = f_i(x_1, x_2), \quad \left.\frac{\partial u_i}{\partial t}\right|_{t=0} = F_i(x_1, x_2)(i = 1, 2),$$

$$\omega_3\,|_{t=0} = \varphi_3(x_1, x_2), \quad \left.\frac{\partial \omega_3}{\partial t}\right|_{t=0} = \Phi_3(x_1, x_2). \tag{2.9}$$

Hamilton's variation principal for the stated problem can be introduced in the following form:

$$\delta \int_{t_0}^{t_1} (\Pi - K)\, dt = 0, \tag{2.10}$$

where Π is the complete potential energy of the system, K is the kinematic energy:

$$\Pi = \int_S\int \left(\frac{1}{2}A_{11}\varepsilon_{11}^2 + \frac{1}{2}A_{22}\varepsilon_{22}^2 + A_{12}\varepsilon_{11}\varepsilon_{22} + \frac{1}{2}A_{77}\varepsilon_{12}^2 + \right.$$

$$\left. + \frac{1}{2}A_{88}\varepsilon_{21}^2 + A_{78}\varepsilon_{12}\varepsilon_{21} + \frac{1}{2}B_{66}\chi_{13}^2 + \frac{1}{2}B_{44}\chi_{23}^2\right) dS -$$

$$- \int_0^a \left[X^+u_1 + Y^+u_2 + M^+\omega_3\right]_{x_2=h} dx_1 + \int_0^a \left[-X^-u_1 - Y^-u_2 - M^-\omega_3\right]_{x_2=-h} dx_1 +$$

$$+ \int_{-h}^{h} \left[\varphi_1u_1 + \varphi_2u_2 + \varphi_3\omega_3\right]_{x_1=0} dx_2 - \int_{-h}^{h} \left[\varphi_1u_1 + \varphi_2u_2 + \varphi_3\omega_3\right]_{x_1=a} dx_2, \tag{2.11}$$

$$K = \int_S\int \left[\frac{\rho}{2}\left(\frac{\partial u_1}{\partial t}\right)^2 + \frac{\rho}{2}\left(\frac{\partial u_2}{\partial t}\right)^2 + \frac{I}{2}\left(\frac{\partial \omega_3}{\partial t}\right)^2\right] dS.$$

Motion equations (2.1) and corresponding boundary conditions (2.5), (2.6) are obtained from variation equation (2.10) by the known way.

3 Mathematical Model of Micropolar Orthotropic Elastic Thin Bar with Free Rotation

As it is shown in paper [5], the asymptotics of the initial-boundary problem (2.1)-(2.9) in a thin domain of the rectangle depends on the following dimensionless physical parameters:

$$\frac{A_{11}A_{22}}{A_{11}A_{22} - A_{12}^2}, \quad \frac{A_{11}^2}{A_{11}A_{22} - A_{12}^2}, \quad \frac{A_{11}A_{12}}{A_{11}A_{22} - A_{12}^2}, \quad \frac{A_{11}A_{88}}{A_{77}A_{88} - A_{78}^2},$$

$$\frac{A_{11}A_{77}}{A_{77}A_{88} - A_{78}^2}, \quad \frac{A_{11}A_{78}}{A_{77}A_{88} - A_{78}^2}, \quad \frac{a^2A_{11}}{B_{66}}, \quad \frac{a^2A_{11}}{B_{44}}. \tag{3.1}$$

When dimensionless physical parameters (3.1) have the following values [5]

$$\frac{A_{11}A_{22}}{A_{11}A_{22}-A_{12}^2}\sim 1,\quad \frac{A_{11}^2}{A_{11}A_{22}-A_{12}^2}\sim 1,\quad \frac{A_{11}A_{12}}{A_{11}A_{22}-A_{12}^2}\sim 1,\quad \frac{A_{11}A_{88}}{A_{77}A_{88}-A_{78}^2}\sim 1,$$

$$\frac{A_{11}A_{77}}{A_{77}A_{88}-A_{78}^2}\sim 1,\quad \frac{A_{11}A_{78}}{A_{77}A_{88}-A_{78}^2}\sim 1,\quad \frac{a^2A_{11}}{B_{66}}\sim 1,\quad \frac{a^2A_{11}}{B_{44}}\sim 1, \tag{3.2}$$

components of the vector of rotation are free from the components of the vector of displacement in asymptotic approximations of the initial-boundary problem (2.1)-(2.9) of the plane dynamic micropolar theory of elasticity. Taking into consideration the qualitative results of the asymptotic solution of the initial-boundary problem (2.1)-(2.9) of the plane dynamic micropolar theory of elasticity, in the basis of the following proposed theory of micropolar orthotropic elastic thin bars with free rotation the following rather general assumptions (hypotheses) are put [3-5]:

a) during the deformation initially straight and normal to the axis of symmetry x_1 element is rotated freely at an angle as a whole rigid body, without changing its length and without remaining perpendicular to the deformed axis of symmetry. While the free rotation ω_3 of the rectangle's points doesn't depend from transverse coordinate x_2.

The accepted hypothesis is mathematically written as follows:

$$u_1 = x_2\psi(x_1,t),\ \ u_2 = w(x_1,t),\ \ \omega_3 = \Omega_3(x_1,t). \tag{3.3}$$

Thus, normal to the axis x_1 displacement u_2 and free rotation Ω_3 are constant functions along the thickness of the rectangle, and the displacement u_1 is changed by a linear law along the thickness of the rectangle. It should be noted that from the point of view of displacements the hypothesis (3.3), in essence, is Timoshenko's kinematic hypothesis in the classical theory of elastic bars. As in papers [3], [4] the hypothesis (3.3) is called Timoshenko's generalized kinematic hypothesis in the micropolar theory of bars;

b) in elasticity relations (2.3) power voltage σ_{22} can be neglected in relation to power voltage σ_{11};

c) in determining the deformations, bending-torsions, force and moment stresses, first for the force stress σ_{21} we'll take:

$$\sigma_{21} = \overset{0}{\sigma}_{21}(x_1,t). \tag{3.4}$$

After determining of mentioned quantities, value of σ_{21} will be finally defined as a sum of (3.4) and a result of integration of first motion equation from (2.1), for which the condition, that quantity averaged along the rectangle's thickness is equal to zero, will be required.

Following formulas are obtained for deformations, bending-torsions, force and moment stresses:

$$\varepsilon_{11} = K_{11}x_2,\ \ \varepsilon_{22}=0,\ \ \varepsilon_{12}=\Gamma_{12},\ \ \varepsilon_{21}=\Gamma_{21},\ \ \chi_{13}=k_{13},\ \ \chi_{23}=0,$$

$$K_{11} = \frac{\partial\psi(x_1,t)}{\partial x_1},\ \Gamma_{12} = \frac{\partial w(x_1,t)}{\partial x_1} - \Omega_3(x_1,t),$$

$$\Gamma_{21} = \psi(x_1,t) + \Omega_3(x_1,t),\ k_{13} = \frac{\partial\Omega_3(x_1,t)}{\partial x_1}, \tag{3.5}$$

$$\sigma_{11} = \frac{A_{11}A_{22}-A_{12}^2}{A_{22}}K_{11}x_2,\ \ \sigma_{22} = \frac{(Y^+ + Y^-)}{2h}x_2,\ \ \sigma_{12} = A_{77}\Gamma_{12} + A_{78}\Gamma_{21},$$

$$\sigma_{21} = \overset{0}{\sigma}_{21} + \left(\frac{A_{11}A_{22}-A_{12}^2}{A_{22}}\frac{\partial K_{11}}{\partial x_1} - \rho\frac{\partial^2\psi}{\partial t^2}\right)\left(\frac{h^2}{6} - \frac{x_2^2}{2}\right),$$

$$\mu_{13} = B_{66}k_{13}, \ \ \mu_{23} = \frac{(M^+ + M^-)}{2h}x_2.$$

In order to bring the two-dimensional problem (2.1) - (2.9) to applied one-dimensional problem, which is already done for force and moment stresses, deformations, bending-torsion, displacements, rotation (formulas (3.3), (3.5)), instead of components of the tensors of force and moment stresses equivalent to them integral above the height of rectangle features forces N_{12}, N_{21} and moments L_{13}, M_{11} are introduced in the theory of micropolar bars:

$$N_{12} = \int\limits_{-h}^{h} \sigma_{12}dx_2, \ \ N_{21} = \int\limits_{-h}^{h} \sigma_{21}dx_2, \ \ L_{13} = \int\limits_{-h}^{h} \mu_{13}dx_2, \ \ M_{11} = \int\limits_{-h}^{h} \sigma_{11}x_2dx_2. \tag{3.6}$$

The basic system of equations of the dynamic bending deformation of micropolar orthotropic elastic thin bars with free rotation is the following:

Motion equations:

$$\frac{\partial M_{11}}{\partial x_1} - N_{21} = -h(X^+ - X^-) + \frac{2h^3}{3}\rho\frac{\partial^2\psi}{\partial t^2}, \quad \frac{\partial N_{12}}{\partial x_1} = -(Y^+ + Y^-) + 2\rho h\frac{\partial^2 w}{\partial t^2},$$

$$\frac{\partial L_{13}}{\partial x_1} + N_{12} - N_{21} = -(M^+ + M^-) + 2Ih\frac{\partial^2\Omega_3}{\partial t^2}. \tag{3.7}$$

Elasticity relations:

$$M_{11} = \frac{2h^3}{3}\frac{A_{11}A_{22} - A_{12}^2}{A_{22}}K_{11}, \ \ N_{12} = 2h(A_{77}\Gamma_{12} + A_{78}\Gamma_{21}),$$

$$N_{21} = 2h(A_{78}\Gamma_{12} + A_{88}\Gamma_{21}), \ \ L_{13} = 2hB_{66}k_{13}. \tag{3.8}$$

Geometric relations:

$$K_{11} = \frac{\partial\psi(x_1,t)}{\partial x_1}, \ \Gamma_{12} = \frac{\partial w(x_1,t)}{\partial x_1} - \Omega_3(x_1,t),$$

$$\Gamma_{21} = \psi(x_1,t) + \Omega_3(x_1,t), \ k_{13} = \frac{\partial\Omega_3(x_1,t)}{\partial x_1}. \tag{3.9}$$

The boundary conditions on the edge $x_1 = 0 (x_1 = a)$ of the bar are as follows:

$$M_{11} = M_{11}^* \ \text{ or } \ \psi = \psi^*, \ \ N_{12} = N_{12}^* \ \text{ or } \ w = w^*, \ \ L_{13} = L_{13}^* \ \text{ or } \ \Omega_3 = \Omega_3^*. \tag{3.10}$$

Initial conditions at $t = 0$ must be set for

$$w, \ \frac{\partial w}{\partial t}, \ \Omega_3, \ \frac{\partial\Omega_3}{\partial t}, \ \psi, \ \frac{\partial\psi}{\partial t}.$$

As the asymptotic method of integration of initial-boundary problem (2.1)-(2.9) shows, some simplification is possible in the system of one-dimensional equations (3.7)-(3.9) of micropolar bars: in the first motion equation from (3.7) the member connected with bending moment M_{11} and inertial force $\frac{2h^3}{3}\rho\frac{\partial^2\psi}{\partial t^2}$ are neglected (it should be noted that beside of bending moment M_{11} bending moment L_{13} acts in the transverse sections of the bar). We call this model a simplified model of micropolar bars.

The system of equations (3.7)-(3.9) can be reduced to the system of equations for w, ψ, Ω_3:

$$A_{88}\psi + A_{78}\frac{\partial w}{\partial x_1} + (A_{88} - A_{78})\Omega_3 - \frac{h^2}{3}\frac{A_{11}A_{22} - A_{12}^2}{A_{22}}\frac{\partial^2\psi}{\partial x_1^2} + \frac{h^2}{3}\rho\frac{\partial^2\psi}{\partial t^2} = \frac{(X^+ - X^-)}{2},$$

$$A_{78}\frac{\partial\psi}{\partial x_1}+A_{77}\frac{\partial^2 w}{\partial x_1^2}+(A_{78}-A_{77})\frac{\partial\Omega_3}{\partial x_1}-\rho\frac{\partial^2 w}{\partial t^2}=-\frac{(Y^+ + Y^-)}{2h}, \tag{3.11}$$

$$(A_{78}-A_{88})\psi+(A_{77}-A_{78})\frac{\partial w}{\partial x_1}-(A_{77}+A_{88}-2A_{78})\Omega_3+$$

$$+B_{66}\frac{\partial^2\Omega_3}{\partial x_1^2}-I\frac{\partial^2\Omega_3}{\partial t^2}=-\frac{(M^+ + M^-)}{2h}.$$

Transverse shifts and related to them deformations are completely taken into account in the model (3.7)-(3.10) of micropolar bars with free rotation. Hamilton's variation principal for one-dimensional initial-boundary problem (3.7)-(3.10) can be introduced in the form (2.10), where:

$$\Pi=\int\limits_0^a\left[\frac{h^3}{3}\frac{A_{11}A_{22}-A_{12}^2}{A_{22}}K_{11}^2+hA_{77}\Gamma_{12}^2+hA_{88}\Gamma_{21}^2+2hA_{78}\Gamma_{12}\Gamma_{21}+hB_{66}k_{13}^2\right]dx_1-$$

$$-\int\limits_0^a\left[h(X^+-X^-)\Psi+(Y^++Y^-)w+(M^++M^-)\Omega_3\right]dx_1\pm \tag{3.12}$$

$$\pm\int\limits_{-h}^{h}\Big[\,\varphi_1\Psi x_2+\varphi_2 w+\varphi_3\Omega_3\Big]_{\substack{x_1=0\\x_1=a}}dx_2,$$

$$K=\int\limits_0^a\left[\frac{h^3}{3}\rho\left(\frac{\partial\Psi}{\partial t}\right)^2+\rho h\left(\frac{\partial w}{\partial t}\right)^2+Ih\left(\frac{\partial\Omega_3}{\partial t}\right)^2\right]dx_1.$$

If in the model (3.7) - (3.10) transverse shifts are neglected, i. e.:

$$\Psi=-\frac{\partial w}{\partial x_1}, \tag{3.13}$$

a model of micropolar bars will be obtained, when the normal element is rotated, remaining perpendicular to the bar's deformed axis. Formula (3.13) means that instead of Timashenko's generalized kinematic hypothesis a), Bernoulli's generalized kinematic hypothesis is accepted for micropolar bars (i. e. we take the formula (3.3) as a whole, taking into account (3.13)). The basic system of equations of the dynamic bending deformation of micropolar orthotropic elastic thin bars with free rotation, when Bernoulli's generalized hypothesis is accepted, is the following:

Motion equations:

$$\frac{\partial M_{11}}{\partial x_1}-N_{21}=-h(X^+-X^-)-\frac{2h^3}{3}\rho\frac{\partial^3 w}{\partial x_1\partial t^2},\quad \frac{\partial N_{12}}{\partial x_1}=-(Y^++Y^-)+2\rho h\frac{\partial^2 w}{\partial t^2},$$

$$\frac{\partial L_{13}}{\partial x_1}+N_{12}-N_{21}=-(M^++M^-)+2Ih\frac{\partial^2\Omega_3}{\partial t^2}. \tag{3.14}$$

Elasticity relations:

$$M_{11}=\frac{2h^3}{3}\frac{A_{11}A_{22}-A_{12}^2}{A_{22}}K_{11},\ N_{12}=2h(A_{77}\Gamma_{12}+A_{78}\Gamma_{21}),$$

$$N_{21}=2h(A_{78}\Gamma_{12}+A_{88}\Gamma_{21}),\ L_{13}=2hB_{66}k_{13}. \tag{3.15}$$

Geometric relations:

$$K_{11} = -\frac{\partial^2 w(x_1,t)}{\partial x_1^2},\ \Gamma_{12} = \frac{\partial w(x_1,t)}{\partial x_1} - \Omega_3(x_1,t),$$

$$\Gamma_{21} = -\frac{\partial w(x_1,t)}{\partial x_1} + \Omega_3(x_1,t),\ k_{13} = \frac{\partial \Omega_3(x_1,t)}{\partial x_1}. \tag{3.16}$$

Boundary conditions (3.10), with consideration (3.13), should be added to the system of equations (3.14)-(3.16) of micropolar bars with free rotation. The initial conditions are given accordingly.

The system of equations (3.14)-(3.16) can be reduced to the system of equations for w, Ω_3:

$$-\frac{2h^3}{3}\frac{A_{11}A_{22}-A_{12}^2}{A_{22}}\frac{\partial^4 w}{\partial x_1^4} + 2h(A_{77}+A_{88}-2A_{78})\frac{\partial^2 w}{\partial x_1^2} - 2h(A_{77}+A_{88}-2A_{78})\frac{\partial \Omega_3}{\partial x_1} +$$

$$+\frac{2h^3}{3}\rho\frac{\partial^4 w}{\partial x_1^2 \partial t^2} - 2\rho h\frac{\partial^2 w}{\partial t^2} = -h\frac{\partial (X^+ - X^-)}{\partial x_1} - (Y^+ + Y^-), \tag{3.17}$$

$$(A_{77}+A_{88}-2A_{78})\left(\frac{\partial w}{\partial x_1} - \Omega_3\right) + B_{66}\frac{\partial^2 \Omega_3}{\partial x_1^2} - I\frac{\partial^2 \Omega_3}{\partial t^2} = -\frac{(M^+ + M^-)}{2h}.$$

Hamilton's variation principal for one-dimensional initial-boundary problem (3.14)-(3.16) can be introduced in the form (2.10), where:

$$\Pi = \int_0^a \left[\frac{h^3}{3}\frac{A_{11}A_{22}-A_{12}^2}{A_{22}}K_{11}^2 + hA_{77}\Gamma_{12}^2 + hA_{88}\Gamma_{21}^2 + 2hA_{78}\Gamma_{12}\Gamma_{21} + hB_{66}k_{13}^2\right]dx_1 -$$

$$-\int_0^a \left[-h(X^+ - X^-)\frac{\partial w}{\partial x_1} + (Y^+ + Y^-)w + (M^+ + M^-)\Omega_3\right]dx_1 \pm$$

$$\pm \int_{-h}^{h} \left[-\varphi_1 \frac{\partial w}{\partial x_1}x_2 + \varphi_2 w + \varphi_3 \Omega_3\right]_{\substack{x_1=0 \\ x_1=a}} dx_2, \tag{3.18}$$

$$K = \int_0^a \left[\frac{h^3}{3}\rho\left(\frac{\partial^2 w}{\partial x_1 \partial t}\right)^2 + \rho h\left(\frac{\partial w}{\partial t}\right)^2 + Ih\left(\frac{\partial \Omega_3}{\partial t}\right)^2\right]dx_1.$$

References

[1] Sargsyan S. H. Micropolar Theory of Thin Bars, Plates and Shells// Izvestiya NAS RA. Mechanics. (in Russian). Vol. 58. N2. PP. 84-95. 2005.

[2] Altenbach H., Altenbach J., Eremeyev V.On generalized Cosserat-type theories of Plates and Shells: a short review and bibliography// Arch. Appl. Mech. Special Issue. Doi 10. 1007/s 00419-009-0365-3. Springer-Verlag. 2009.

[3] Sargsyan S.H. General Dynamic Theory of Micropolar Elastic Thin Shells// Doklady Physics. Vol. 56. N1. PP. 39-42. 2011.

[4] Sargsyan S. H., Sargsyan A. A. General Dynamic Theory of Micropolar Thin Plates with Free Rotation and Features of Their Free Vibrations//Acoustical journal. Vol. 57. N4. 2011.

[5] Margaryan L. M. Dynamic Problem of Bending of Micropolar Elastic Orthotropic Thin Bars// Actual Problems of Continuum Mechanics. (in Russian). Vol 2. PP. 13-17 2010.

[6] Iesen D. The plane micropolar strain of orthotropic elastic solids// Archives of Mechanics. Vol. 5. N3. PP. 547-561. 1973.

[7] Timoshenko S. Vibration Problems in Engineering. Toronto-New York-London. D Van Nostrand Company. 444p. 1955.

Lilit M. Margaryan , Gyumri State Pedagogical Institute, Armenia.
Samvel H. Sargsyan , National Academy of Sciences of the Republic of Armenia, Gyumri State Pedagogical Institute, Armenia.

Localization of bending vibrations in the single-wall carbon nanotubes

V. V. Smirnov D. S. Shepelev L. I. Manevitch
vvs@polymer.chph.ras.ru

Abstract

The main result of this work is that the small-amplitude long wavelength bending oscillations of carbon nanotubes (CNT) become localized ones if the intensity of initial excitation exceeds some threshold which depends on the CNT length. This localization results from the intensive resonant interaction of zone-boundary and nearest modes in the weakly nonlinear regime that leads to loss of stability of the zone-boundary mode as to the first step. The further development of resonant interaction leads to effective confinement of energy in the part of the system only. We study this process in the terms of Limiting Phase Trajectories and demonstrate the usefulness of transition from "modal" to "effective particles" representation for description of the system under consideration. We also show that the similar tendency to localization of oscillation is the common property of the systems, the eigenvalue spectra of which are non-equidistant ones near their edges.

1 Introduction

The carbon nanotubes (CNTs) are of great interest not only as the objects that can have large potential use in nanotechnology processes and devices, but also as ideal model systems to check the many physical principles. This work deals with the analysis of localization of bending vibrations of single-walled carbon nanotubes. Such an analysis has to demonstrate both a new phenomenon – localization of bending vibrations of CNTs – and the efficiency of the used approach for description of specific strongly nonlinear behavior which cannot be adequately understood in terms of nonlinear normal modes.

2 The model

To consider the nonlinear localization of CNTs vibrations we should to reduce the description of CNT to that of some effective one-dimensional system. Keeping in mind this objective we consider a single-wall carbon nanotube of a finite length and cut it ideally into the N rings by planes which are perpendicular to the tube axis. (Fig. 1). The actual choice of the ring width has to reflect the real properties of the CNT (in particularly, its chirality). From the other side the width has not to be too large, because the deformation of the ring along the axis is regarded as a constant one.

It is known that the mechanical properties of single-wall carbon nanotubes are well described within the continuum approach, when the tube is replaced by a cylinder shell with an effective thickness δ. In this framework the potential energy of the CNT can be

represented as the sum of deformation energy of the individual rings

$$U_n = \int\limits_0^{2\pi} \left[\frac{1}{2} ESR\varepsilon^2 + \frac{1}{2} EJR\kappa^2 \right] d\theta \tag{1}$$

and the interaction energy between neighbor rings, which should be described as

$$V_n = \int\limits_0^{2\pi} \left[\frac{1}{2} EJ'R\kappa_{||}^2 + \frac{1}{2} E\varepsilon_{||}^2 \right] d\theta \tag{2}$$

Here ε – deformation of the contour length, κ – flexural deformation of the ring (curvature), $\kappa_{||}$ – bending strain along the tube axis, $\varepsilon_{||}$ – longitudinal strain (along the tube axis), E, J, J' – Young's modulus, moment of inertia of the ring and the moment of inertia in the plane passing through the axis of the tube, $S = R\delta$ – effective square of the element of the section of the ring. Because we deal with the small-amplitude vibrations, the energy of the Van der Waals interactions is negligible. To obtain the total potential energy of the CNT we should sum the expressions (1, 2) along the tube axis.

One of the main types of nanotube deformation is bending one. In particular, the action of concentrated external forces which are perpendicular to the axis of the CNT leads to a strain that can be represented as a pure bending in the plane perpendicular to the axis of CNTs in combination with a bend along the cylinder. In the first approximation we can ignore the deformation of the middle surface and consider only the bending deformation. (Accounting for the average tensile strain of the surface somewhat complicates the calculations but does not lead to qualitatively new results.) Thus, the observed deformation is a combination of two modes along the CNT axis (a homogeneous deformation with the wave vector $k_z = 0$ and the mode with $k_z = 2\pi/N$), the ring being changed its form into elliptical one (see fig.1).

Then we can characterize the deformation of carbon nanotubes by a single variable – the amplitude of the elliptical deformation. Indeed, assuming that the bending strain in each section of the CNT is presented as $X \cos 2\theta$, where θ – the azimuth angle, and X – the amplitude, after integration over the angle θ, we obtain the following expression for the strain energy:

$$U_{tot} = \pi \sum_{n=1}^{N} \left[\frac{1}{2} EJR\kappa_n^2 + \beta\kappa_n^4 + \frac{1}{2} EJ'\kappa_{||,n}^2 \right], \tag{3}$$

$$\kappa_n = \frac{X_n}{R}, \quad \kappa_{||,n} = \frac{X_{n+1} - 2X_n + X_{n-1}}{R}, \tag{4}$$

where κ_n is the deformation of the n-th ring and $\kappa_{||,n}$ – corresponds to inter-ring interaction. The strain energy (3) contains also the anharmonic terms ($\sim \beta\kappa_n^4$), which must be taken into account when calculating the dynamics of carbon nanotubes. First of all, it concerns to the vibrations of the ring profile. From symmetry considerations it follows that the anharmonic contribution is the fourth-order strain. Its exact form can be derived directly from the atomic interaction potentials. When the flexural deformation of the ring contour occurs, the main part of the deformation energy corresponds to angular component of interatomic potentials, which is characterized by the nonlinearity of soft type. So the coefficient β should be negative.

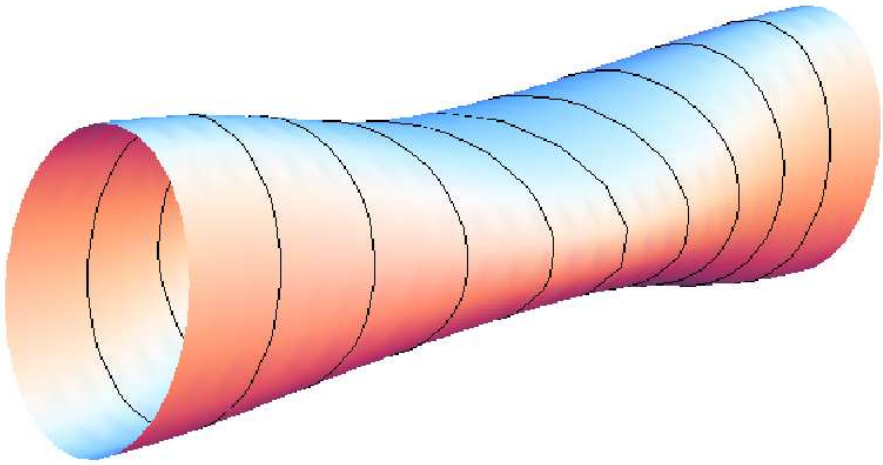

Figure 1. CNT under external forces applied in the center of CNT in the direction which is perpendicular to the tube axis. Thin lines show the boundaries of the effective rings.

It is easy to see that the potential energy in the form of (3) reduces the problem of small-amplitude oscillations of carbon nanotubes to a system of ordinary differential-difference equations for the variables X_n. The significant characteristic feature of the eigenvalue spectrum of such a system is the existence of a gap determined by the bending oscillations of the ring with a frequency $\omega_2 \sim EJR/a^2$, where a – "lattice constant", i.e. effective width of the ring, and the second one – the spectrum crowdling near its edges corresponding to the wave numbers $k_z = 0$ and $k_z = \pi$.

$$\omega^2 = \omega_0^2 + 16c^2 \sin^4 \frac{k_z}{2}, \quad \omega_0^2 = \frac{\pi EJR}{a^2}; \quad c^2 = \frac{\pi ERJ'}{a^2}$$

Such peculiarities of the spectrum make it to be similar to that of the one-dimensional chain (involving longitudinal bonds), on an elastic support (i.e. the model of the Klein-Gordon or the Frenkel-Kontorova). A similar model with periodic boundary conditions was recently considered by us [1], where the asymptotic analysis of the equations of motion was discussed in detail. It was shown that while the amplitude of excitation increases the significant role of resonant interaction between closely spaced modes can be revealed (it relates especially the interaction between zone-boundary mode and the nearest to it). In the present case it corresponds to the modes with wave numbers $k_z = 0$ and $k_z = 2\pi/N$ along the CNT , which describe the deformation of carbon nanotubes as a result of the excitation (Fig. 1). The influence of resonant interaction of non-linear normal modes leads to a loss of stability of the boundary mode ($k_z = 0$), and eventually to the emergence of the energy localization in the system. Qualitatively, this process can be described as follows: a resonant interaction of two closely spaced modes with small amplitudes leads to periodic redistribution of energy with a characteristic time which is inversely proportional to the frequency difference. This process can be naturally regarded as the beats between the "effective" particles, each of which contains about half of the system's atoms. Such a behavior is specific for the harmonic system, where the period does not depend on the amplitude. The effect of nonlinearity leads to the nonlinear beats. At a certain critical level of excitation the zone-boundary mode becomes unstable in the systems with soft nonlinearity ($\beta < 0$). The loss of stability of the boundary mode leads to the emergence of new stationary solutions and a separatrix passing through the unstable stationary point. At the same time the behavior of the trajectories corresponding to the

beats remaines without qualitatively changes. The fundamental change occurs when the excitation energy reaches the value, at which the energy of the beating becomes equal to that of the separatrix. In this case, the beats in the system are generally prohibited and the energy is "trapped" in the domain of initial excitation. Of course, such localization covers large areas corresponding approximately to a half of the chain (in the framework of two-mode approach, we have not the tools to describe a higher degree of localization, because it requires a participation of the shorter nonlinear modes). Therefore, we have a qualitative picture, so to say the manifestation of the nucleing of the localization, that clarifies the origin of the breathers formation. As the result of computer simulations, we can accurately estimate in this model the threshold of localization, and the profile of the localized solutions. The energy contribution ot other modes to this process does not usually exceed 10-20% of the initial excitation energy.

The procedure for analysis of dynamic equations and the determination of thresholds in the asymptotic approach are discussed in detail in [1], [2]. In this case, we want to obtain an estimate of the localization threshold, without resorting to complex analytical calculations. We represent the variable X_n as a combination of the two modes (this representation adequately describes the deformation of CNTs, as it is shown in Figure 1):

$$X_n(t) = \chi_0(t) + \chi_1(t) \cos \frac{2\pi n}{N} \tag{5}$$

where $\chi_0(t)$ and $\chi_1(t)$ are the amplitudes of the modes, which are the periodic functions with period $2\pi/\omega_0$ and $2\pi/\omega_1$ in the harmonic limit; ω_0 and ω_1 – the smallest eigenvalues (see eq.(4)). However, the above-mentioned "effective particles" are described by a linear combination of normal modes:

$$\varphi_1 = \frac{\chi_0 + \chi_1}{\sqrt{2}}, \quad \varphi_2 = \frac{\chi_0 - \chi_1}{\sqrt{2}}, \tag{6}$$

and each of the "effective particles" corresponds to specific function φ. For these variables, the total "number of excitations" $Y = |\varphi_1|^2 + |\varphi_2|^2 = |\chi_0|^2 + |\chi_1|^2$ is preserved. As it becomes apparent from expression (6), the beats realizing the energy transfer from one "effective particle" to another correspond to transition from one "pure" state (in the terms of effective particles φ_j) to another "pure" state, while the zone-boundary normal mode corresponds to some "mixed" state. The "pure" states bound the attraction domains of χ_0 and they are the limiting phase trajectories (LPTs) [1]. The cessation of energy transfer from one "effective" particle to another one occurs when the energy of "effective" particles becomes equal to that of normal mode χ_0. At that the LPT coincides with the separatrix that leads to the prohibition of the transition from "particle" φ_1 to the "particle" φ_2. After substitution of expressions (5-6) into equation (3) and performation of some simple algebra we obtain the expression for threshold level of excitation:

$$|\chi_0|^2 + |\chi_1|^2 = \frac{4N(\omega_0^2 - \omega_1^2)}{3\beta} \sim -\frac{64N \sin^4 \frac{\pi}{N}}{3\beta} \sim -\frac{1}{\beta N^3}, \quad (\beta < 0) \tag{7}$$

The above estimates (7) (with an accuracy about 10%) are in a good accordance with the threshold of localization observed in computer simulations (Fig. 2). In the following example, the numerical estimate of the threshold amplitude according to (5) gives a value of $\chi_0 = \chi_1 \sim 0.1258$ while the localization is observed even at $\chi_0 = \chi_1 \sim 0.1258$.

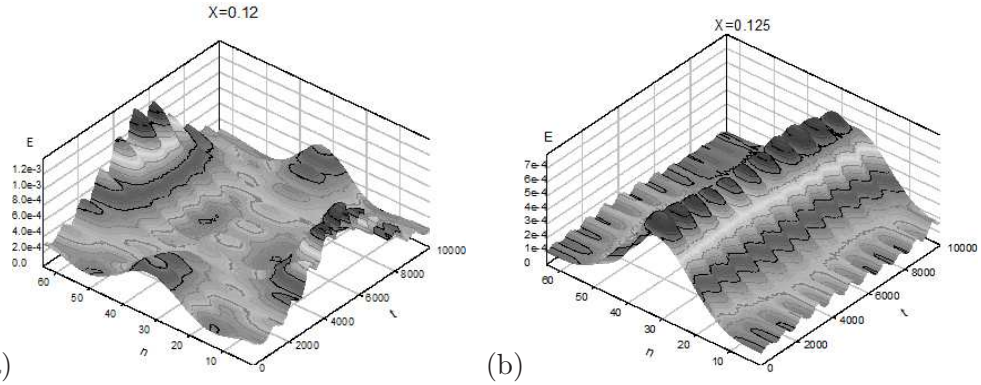

(a) (b)

Figure 2. 3D surface of energy distribution in the CNT with $N = 64$: (a) before and (b) after localization threshold. The beating corresponds to energy transfer from the central part of CNT ("particle" φ_1) to the edge parts of it ("particle" φ_2) and inversely. When the localization occurs the energy is confined in the central part of the CNT. n is the ring number; the time t is measured in the periods of zone-boundary mode $T_0 = \frac{2\pi}{\omega_0}$.

3 Conclusion

The brief qualitative analysis of the bending vibrations of CNT allows us to reveal the origin of non-linear behavior of the system under consideration. First of all, we observed the new nonlinear modes, which do not exist in the linear system and are created from the resonant interaction of the normal modes. The accurate asymptotic analysis which is similar to that made in [1, 2] leads to the clear manifestation of new normal modes. The transformation of the phase space originated from these new modes appearence leads to topological structure of phase space with some domains corresponding to the states with energy localization. We describe adequately the transition from intensive energy exchange between "pure" bending states to energy localization in terms of LPTs. And finally, the comparison with the previous papers [1], [2] allows us to conclude that such a behavior is a specific one for the system with unstable zone-boundary mode and the non-equidistant spectrum of linearized system. We suppose that the approach developed in the paper will be useful for investigations of the nonlinear systems of very different nature.

Acknowledgements

References

[1] V. V. Smirnov and L. I. Manevitch, Acoustical Physics, v. 57, n 2, p. 279 (2011).

[2] L. I. Manevitch and V. V. Smirnov, Phys Rev E 82, 036602 (2010).

V.V. Smirnov, D.S. Shepelev, L.I. Manevitch, N.N.Semenov Institute of Chemical Physics, RAS 199991, 4 Kosygin str.,Moscow, Russia

Computer modeling of liquid sloshing in road tanker reservoirs

Alexandr O. Shimanovsky Marina G. Kuznetsova Yuri M. Pleskachevskii
tm.belsut@gmail.com

Abstract

The computer model of the road tanker for liquid transportation dynamics has been developed. This model is used for the determination of liquid sloshing parameters, vehicle displacement, velocity and acceleration. The computation of forces acting on the vehicle when braking has been made for the installation of vertical cross partitions. A new approach for the definition of optimal design of partitions in the road tanker reservoirs is being suggested. It is based on the energy dissipation analysis of the transported liquid for the first sloshing cycle. The computation of the energy dissipation has been made for several variants of installation of perforated partitions and the analysis of the tanker braking has allowed to determine the optimal hole sizes in partitions for gasoline-filled reservoir.

1 Liquid Sloshing in Tanker Reservoirs

Nowadays in order to increase tank traffic safety there is being developed a number of actions to reduce the influence of liquid oscillations inside the tank on the dynamics of the vehicle. The main method to limit the liquid mobility in the tank is the installation of internal partitions. Their purpose is to introduce liquid longitudinal and transverse oscillation damping.
The devices for liquid oscillation damping have got different installation set ups. There are proposals when the partitions are suggested to install horizontally, vertically or at the angle to the tank longitudinal axis.

The longitudinal liquid motion in road tanker when speeding-up or braking result in additional redistribution of vehicle axle loads reducing its stability and steerability. Therefore for limiting the longitudinal liquid motion inside the tanker the vertical transversal partitions are installed.

The main drawback of vertical transversal partitions is that they have practically no influence on the transversal oscillations of liquid when maneuvering the vehicle which may lead to the significant body roll because of heavy hydrodynamic loads on side frames of the tank. Road tanker field experience determined that the tankers with the installed systems of longitudinal and transversal breakwaters inside the reservoirs have got the best dynamic properties.

However the technical maintenance of reservoirs is complicated because of large number of internal partitions. Therefore the suggestions for the supporting liquid oscillation damping by installing just a few additional elements are worked out.

As shown above at present the key enabler for reducing the influence of liquid oscillation on road tanker dynamics is the installation of breakwaters and partition of the tank into separate sections.

The works performed by many researchers showed that the maximal oscillating ability of liquid is in the tanks without breakwaters with filling by 40-80% [1]. The installation of flat longitudinal transversal breakwaters leads to the rapid liquid oscillation damping. When filling is over 70% the frequency of liquid oscillations may coincide with the frequency of car spring-mounted part oscillations. The probability of coincidence increases with the installation of longitudinal transversal breakwaters. To avoid the effect described above it is suggested to install the longitudinal horizontal plates on the tank side frames with the tank height division into equal segments.

The authors of work [2] point out that for the parts of movement where the damping during a short period of time is necessary it is more efficient to use kerbing rings and for a long period – radial ones. For the constant or slightly changing level the oscillation damper composed of one ring set close to the free liquid surface is the most efficient.

In the work of Wang Z. and others [3] the analysis of longitudinal forces acting in partially filled ellipsoid road tanker during its rectilinear braking was carried out. The dynamic properties of a vehicle equipped with the reservoir with sections are estimated by the forces acting on the reservoir, distance to the stopping, breaking time and delays between the stopping of front and rear wheels. The analysed object of the research is the aerodrome fuel tank equipped with the reservoir of 3 m long and two movable separating partitions. The results of analytical solution are compared with the experimental data under natural condition. The difference in braking lengths when the vehicle is not huge is relatively small. But the dynamic properties of the tank can become much worse because of the big size of partially filled reservoirs used, for instance, for semitrailers [4].

The new modeling concept for vehicles with liquid we suggest is to present it as two subsystems: the system of solid bodies modeling the tank construction and the liquid flowing inside the reservoir of a vehicle. The subsystem interaction is taken into account. Having solved the differential equation of structural element motion the radius-vectors and velocities for the reservoir points at the current instant of time are defined. The received values of coordinates and velocities of the reservoir points are the input information for the computation of liquid flowing in the reservoir. In turn, the dynamic equations of liquid motion based on the information about the displacement of reservoir partitions allow to get parameters of flowing inside the reservoir liquid including its pressure distribution p along the internal surface of the reservoir (figure 1). The defined pressure is the output information on the base of which the computation of hydrodynamic forces and moments acting on the reservoir is made.

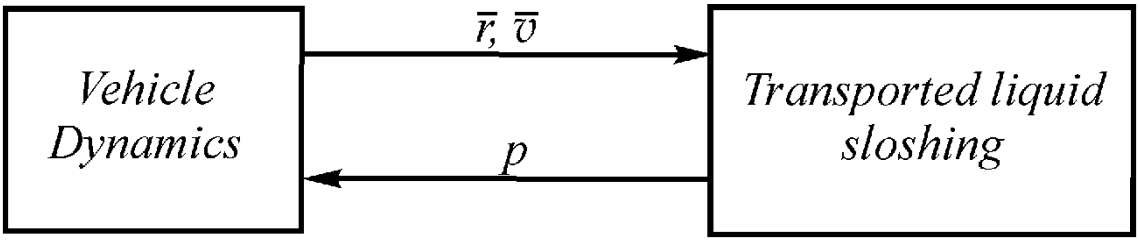

Figure 1: "Vehicle – liquid" system modeling

2 Hydrodynamic Loading of the Reservoir with Partitions

The finite element modeling of liquid flow inside the road tanker reservoir when braking has been carried out on basis model from paper [5]. The aim is to define the influence of

partition geometrical parameters on the hydrodynamic loading of the reservoir structural components. The considered road tanker reservoir is a rectangular parallelepiped. Its length is 5m, height is 2m. In the middle of the reservoir there is the possibility of the partition installation of l height (figure 2).

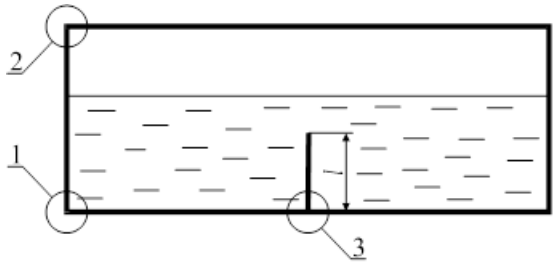

Figure 2: Scheme of road tanker reservoir

For the description of liquid flow in the reservoir the standard turbulence model (k–ε) is used. It is the most widelyspread model and it is based on two equations: turbulent kinetic energy k and the turbulent energy dissipation velocity ε [6, 7]. When designing the geometrical model of liquid flow the detailed finite element mesh has been used since because of the great mesh sizes the loss of accuracy of the solution in the areas of greater pressure and velocity gradients is possible. Since the simplified (no access door and suction compartment) geometrical shape of the reservoir has been considered it is reasonably to use quadrangular finite elements with regular partition of liquid. The application of the latter is more preferable than the application of the triangular ones because it results in a more stable solution. The received finite element model includes for about 10000 elements.

It has been accepted that at the initial time the liquid is at relative rest and its free surface is flat. The adhesion condition is used as the kinematic boundary condition. Time interval is equal 0,003 sec. The computations of liquid flow inside the road tanker reservoir have been made during its braking with 0,6g deceleration. The analysis of hydrodynamic loading for partially filled (60%) reservoir has been carried out. The results of numerical task solution show the most loaded areas of the reservoir are bottom/top chord-bottom joint areas where the pressure values are 32,9 kPa and 24,3 kPa respectively, and these maximal values are reached after a short period of time just after the road tanker starts braking.

To reduce the hydrodynamic loading and amplitudes of liquid oscillation the analysis for the influence of partition sizes on the values of liquid pressures and kinematic parameters of its oscillatory motion has been carried out. The dependences of maximal values of liquid pressure acting on different parts of the reservoir on partition height are shown in figure 3.

While computation it has been ascertained that when the partition is not very high (to 20 % of reservoir height) the values of liquid pressures are slightly reduced (by 2 %) in the area 1 (figure 2), and the pressure maximums are at time 0,72-0,74 sec. At the same time the pressure values in the bottom-top chord joint area (area 2) are slightly reduced at first but then they increase by 9 % at time 0,45 sec. In turn, the loading of the partition-bottom chord joint area (area 3) slightly increases.

The interval of 0,4-1,15m partition heights being taken under the consideration establishes that the values of liquid pressures in these areas are decreasing: area 1 – by 21,7 %, area 2 – by 21,2 %, area 3 – by 11,6 %.

At 1,15-1,4m interval in the studied areas the pressure values are increasing, and in areas 1 and 3 the significant height gradient is observed. So in area 1 the pressure

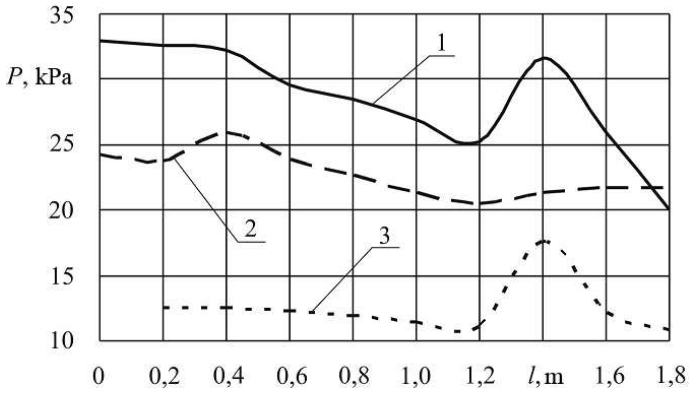

Figure 3: Maximal pressures on the partition height: 1 – bottom-bottom chord joint area; 2 – bottom-top chord joint area; 3 – partition-bottom chord joint area

increases by 21 %, in area 2 by 4 %, in area 3 by 36,7 %. Besides, the dependences of liquid pressure values on time for areas 1 and 3 have several strong marked extremums (figure 4) and maximal values coincide with the second wave of the liquid flow.

With the following increase of partition height the loading of areas 1 and 3 is decreasing, and the loading of area 2 is slightly increasing. Thus the developed mathematical model of liquid flow allows defining the values of hydrodynamic pressure on the structural components of the vehicle reservoir with partitions when it is partially filled. It has been estimated in terms of the criterion for minimum values of liquid load pressure on the reservoir construction that the optimal partition height is within 55-60 % of its height.

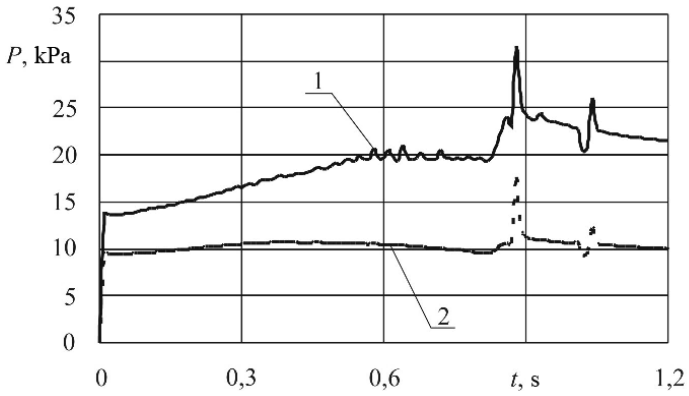

Figure 4: Time dependences of liquid pressures: 1 – bottom-bottom chord joint area; 2 – partition-bottom chord joint area

3 Analysis of Liquid Oscillation Damping Efficiency

Despite the great variety of installation of damping devices there are no techniques allowing to realize the complex efficiency evaluation of this or that kinds of partitions and also to optimize their design.

In the presented work the technique allowing estimating effectiveness of oscillation damping based on the energy approach. The realization of standard k–ε turbulence model means the computation of kinetic energy for each liquid finite element at each time interval.

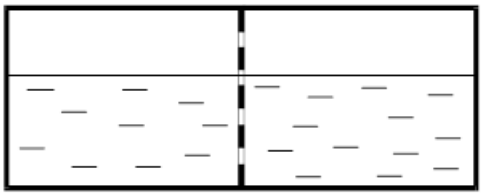

Figure 5: Scheme of partition installation in a reservoir

The summing up of these energies allows to receive the kinetic energy of the whole system. The presence of dissipation leads to the decrease of the kinetic energy. For tank traffic conditions when the liquid effect on tank movements is maximal the most important indicator defining liquid oscillation damping is the decrease of total kinetic energy of the liquid (energy dissipation) during one oscillation. It is the period when there is the development of the phenomena causing heavy dynamic loads on the structural elements or tank overturning.

There have been made the computations for defining energy dissipation-time dependence for different levels of tank filling when there is the change of the hole size in the centre of the partition located in the middle of the tank reservoir. Calculations show, that the energy dissipation turns to be the maximal when the partition diameter is about 10 sm. The detailed analysis of the dissipation curves enables structural optimization of damping devices. Thus, the energy dissipation per one sloshing cycle of liquid in the reservoir must be used as the efficiency criterion of liquid oscillation damping in tank reservoirs. The more the absolute value of this energy the more efficient is the work of damping devices.

With the help of the described technique there has been carried out the computer modeling of liquid flow in the tank when braking with taking into account the installation of the transversal perforated partition. The scheme of its installation is shown in figure 5. The computations for the dependence of energy dissipation on the partition hole sizes have been made. Its results show that there is some value of the perforation diameter when the energy dissipation over the first sloshing cycle is maximal.

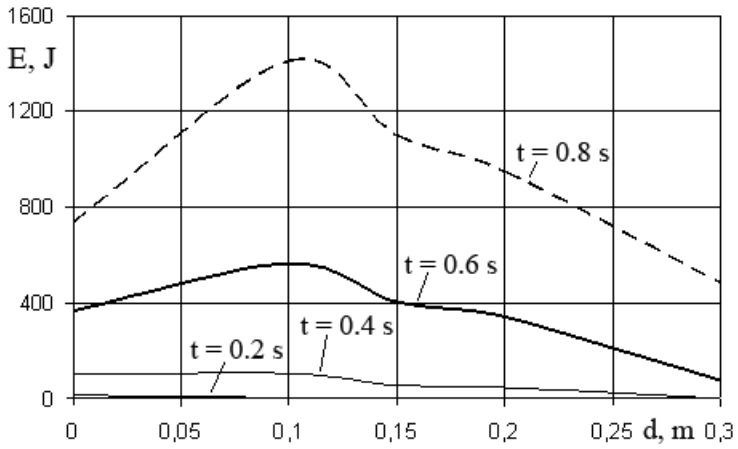

Figure 6: Dependence of liquid energy dissipation on the diameter of perforation

Figure 6 shows the scheme for the dependence of kinetic energy loss when passing through the partitions on the perforation diameter for 2×5 m container. It is seen from the scheme that for the studied situation the liquid oscillation damping is maximal if

the holes are of 11mm diameter and the diameter of holes is 60% in total of the whole partition area. In this case the liquid effect on the tank dynamics will be the least essential compared to the other variants of the partitions.

The similar analysis can be performed for the reservoirs of various shapes under different schemes of partition installations and different variants of perforation taken into account. Besides various schemes of reservoir movements relevant to the specific features of rail and road tanker operations can be considered. The criterion for the efficiency of liquid oscillation damping must be kinetic energy loss per dissipation.

Acknowledgements

The work was supported by the Belarusian State Program of Scientific Research (Project Mechanics 1.15).

References

[1] A. O. Shimanovsky. Tank vehicles safety movement designs (review), Problems of mechanical engineering and automation N 1, (2009) 44-59. (in Russian)

[2] V. V. Gavrilenko, O. Ye. Sokulsky. Methods for determination the features of damping devices in vehicle reservoirs partially filled with liquid. In System Management, Technology and Organization of Production, Repair and Maintenance of Vehicles. Kiev: NAU. 2002. Issue 15, pp. 56-58. (in Russian)

[3] Z. Wang, S. Rakheja, S. Cunzhen. Influence of partition location on directional stability performance of a partially-filled tank truck, Journal of Commercial Vehicles, Transactions of Society of Automotive Engineers, Section 2 (1995) 592–601.

[4] M. S. Vysotsky, Yu. M. Pleskachevskii, A. O. Shimanovsky. Dynamics of road and rail tankers. Minsk: Belavtotraktorostroenie, 2006. 320 p. (in Russian)

[5] A. Shimanovsky, A. Putsiata, O. Kolomnikova. Modeling of vehicle dynamics considering load relative movement, Acta Mechanica Slovaca, N 3-B, (2008) 691–703.

[6] S. Aliabadi, K. Shujaee. Free-surface flow simulations using parallel finite element method, Simulation, 76, N 5, (2001) 257–262.

[7] S. Rebouillat, D. Liksonov. Fluid-structure interaction in partially filled liquid containers: A comparative review of numerical approaches, Computers & Fluids, 39, N 5, (2010) 739–746.

Alexandr O. Shimanovsky, Marina G. Kuznetsova, Belarusian State University of Transport, 34 Kirova str., Gomel, 246653 , Belarus
Yuri M. Pleskachevskii, Presidium of Gomel Branch of NAS Belarus, 4 Fedyuninskogo str., Gomel, 246007, Belarus

Quasi-static and dynamic studies of cracks dynamics in plates of PMMA

Ivan!V. Smirnov Yuri V. Sudenkov
ivansmirnov@math.spbu.ru, sudenkov@land.ru

Abstract

Results of experiments on studying of crack dynamics in plates of polymethylmethacrylate under quasi-static and dynamic types of loading are presented. Unstable behaviour of crack propagation was obtained in both cases of loading. A correlation between the oscillations in the velocity of the crack tip and the structure of the fracture surface is shown. It is established that the time of crack propagation in the case of dynamic loading can greatly exceed the duration of a pulse action.

1 Introduction

A maximum velocity of crack propagation is limited by material nature [1], but change in the crack velocity depends on the type of loading.

Dally et al. [2] have shown that the crack velocity at quasi-static tensile tests of solid polymer specimens increases rapidly up to some value and then remains constant. Ravi-Chandar and Knauss [3] also tested solid polymer specimens, but the loading of the crack was dynamic. It was found that crack propagation occurs only with a constant velocity.

The results [2, 3] can be represented by the solutions of the elasto-dynamic problems [4]. In formulations of these problems it is assumed that the crack velocity is a monotonic function of time. However Fineberg [5] and Kostandov [6] have demonstrated unstable, jumping crack propagation under methods of loading similar to [2, 3].

Hereupon, the studies of the crack front dynamics in solid polymers due to the quasi-static and dynamic loads and comparison of the results, which obtained on the same material at a uniform method of crack registration, are interesting.

2 Experiment

The experimental studies were carried out on specimens of PMMA with density $\rho = 1180$ kg/m^3, longitudinal sound velocity $C_L = 2750 \pm 25$ m/s, transverse sound velocity $C_{TR} = 1400 \pm 25$ m/s, elastic modulus $E = 5.9$ GPa.

Dumbbell-shaped plane specimens with dimensions of the test portion $70 \times 18 \times 2.6$ mm were stretched in the quasi-static tests. The velocity of the specimen grips movement was 5 and 10 mm/min. For registration of acoustic signals, which were generated by the crack front, a piezoelectric sensor was installed on the opposite edge of the sample.

Plates of $125 \times 105 \times 8.5$ mm were used for the dynamic tests. To simulate a real crack in the middle of the specimen a notch 40 mm in length and 0.3 mm in width was made. The impact action was obtained by explosion of an electric wire between the notch faces. The wire was located at a distance of 20 mm from the bottom edge of the specimen

and perpendicular to the plane of the plate. The pulse duration was $T = 0.9 \pm 0.1$ microseconds with the rise time $T_{pf} \approx 0.2$ microseconds.

The registration of the crack tip propagation was carried out by means of a streak camera by the method of a slit scan [7]. A stripe of light was directed at an angle to the sample on location of the intended crack propagation. The light was reflected in the lens of the streak camera after the crack propagation.

3 Results

The typical example of the crack trajectory due to the quasi-static loading is shown on Figure 1.

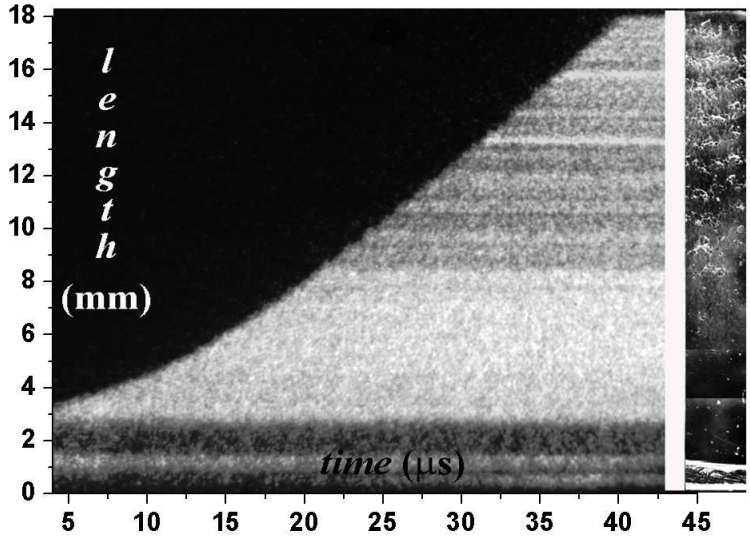

Figure 1: The sweep of the crack front propagation due to the quasi-static loading. The right photo represents the fracture surfaces.

We can observe two characteristic regions of changing the velocity of the crack front after differentiation of the trajectory, see Figure 2. The first region corresponds to a relatively smooth increase of the crack front velocity. In the second region the change of the crack velocity gets oscillatory character. The most pronounced frequencies of the crack front velocity oscillation were in the range of 400-600 kHz. The acoustic emission signal has shown the similar pattern.

The start of the unstable behaviour of the crack corresponds to the start of the ribbed surface structure (see Figure 1) with the distance between the ribs about 1 mm. Considering the period of the acoustic emission fluctuations, we find that the average speed of the crack propagation on the ribbed region is about 500 m/s.

Figure 3 shows the typical plot of the crack propagation in the dynamic tests. During this time period reflected elastic waves had not yet influence on the crack. The stick-slip nature of the crack front propagation is obvious. It is important to note that the time of the crack propagation was much larger than the duration of the pulse action.

The change of the crack velocity in the case of dynamic load is presented in Figure 4. The maximum fluctuations of the velocity, as well as in the quasi-static tests, fall on the rougher region of the fracture surface but have no strictly periodic character. Here, the most pronounced frequencies of the crack front velocity oscillation are in the range of 0.3-1.2 MHz.

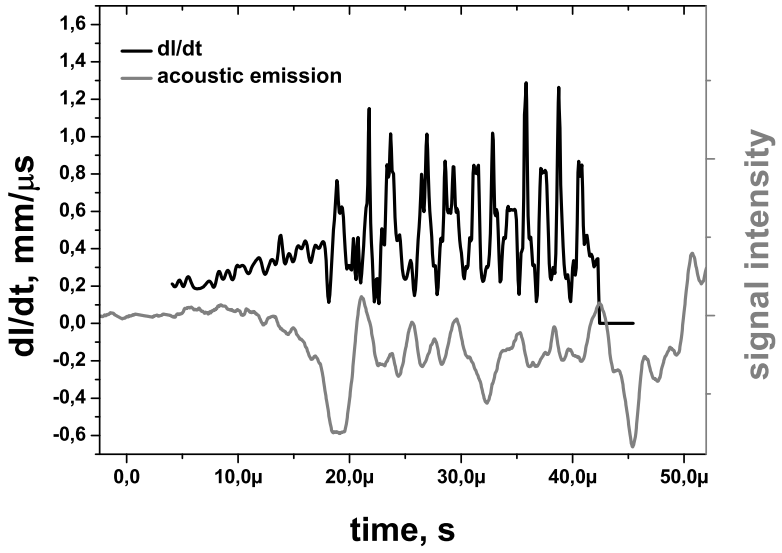

Figure 2: Black curve indicate the velocity of the crack front propagation, gray curve the signal of acoustic emission from a piezoelectric transducer. Zero corresponds to the start time of the crack.

It should be noted that unlike the quasi-static [2, 5] and dynamic [3] tests in this case appearance of the characteristic patterns [8] of the fracture surface are observed in reverse order: roughly-fragmentary, scaly, parabolic, mirror. Also, in our studies, the average velocity of crack propagation in both the quasi-static and dynamic tests did not exceed $0.44C_R$, but it could approach to Rayleigh wave speed C_R on the jumps.

A photo of the prefracture zone in the front of the main crack illustrated in Figure 5 was made after a crack stop in the dynamic tests. According to [9, 10], dynamics of a crack front is associated with this zone. However there is currently no clear, conventional physical model, which connects the original fracture front with the process of propagation of the main crack front.

4 Concluding remarks

The results of the experiments in this paper were obtained by the same technique of registration of the crack. This fact allows us to identify with sufficient reliability the similarities and differences in the stages of fracture in quasi-static and dynamic tests of solid polymers with the unified position.

The experiments demonstrate the general property of quasi-stochastic behavior of the cracks at high speeds of crack front propagation and qualitatively agree to results of other authors [5, 6], which were obtained at other loading rates and significantly longer pulse durations.

The acoustic emission data during the quasi-static tests are well correlated with the velocity of the crack front and allow us to determine the structure of the fracture surface.

In both the quasi-static and dynamic tests the crack tip motion is determined by the interaction of transient stress fields of the original front of micro failures and the stress field generated by the front of the main crack. This process may be the reason that the time of crack propagation is much larger than the duration of a pulse action in dynamic tests.

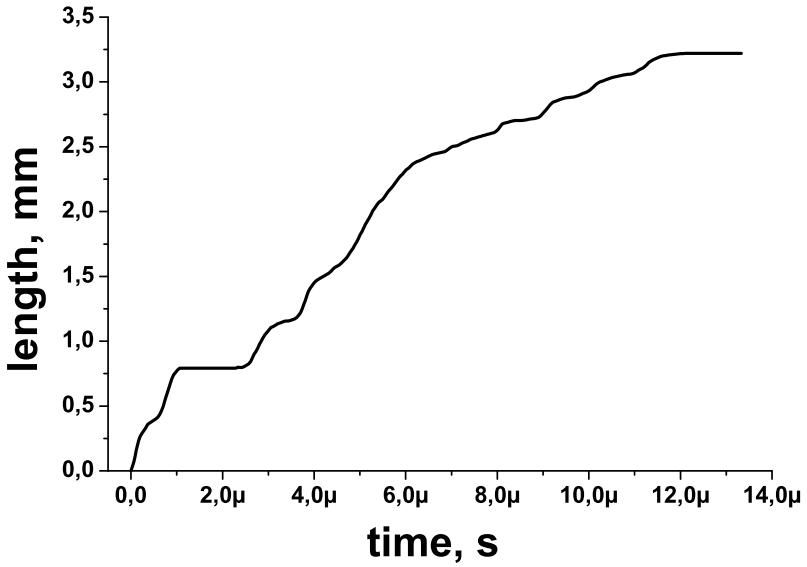

Figure 3: The trajectory of the crack front due to the pulse loading on the notch faces.

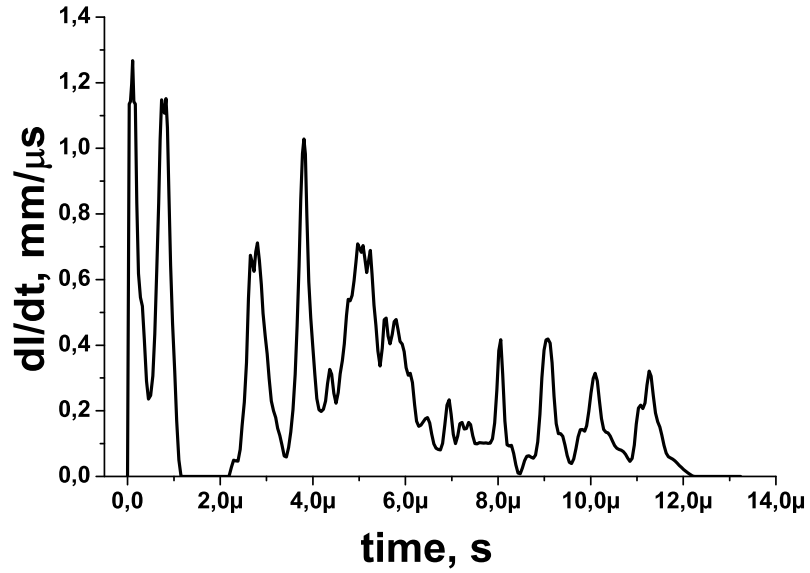

Figure 4: The crack front velocity due to the pulse loading on the notch faces.

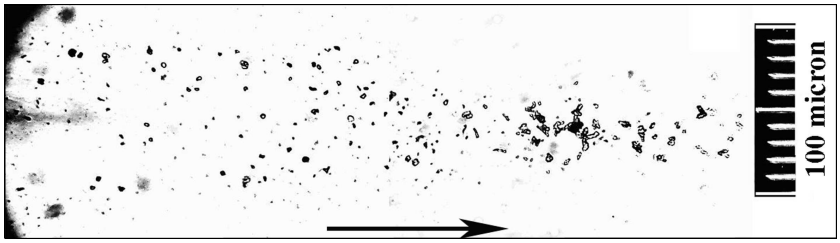

Figure 5: The prefracture region before the front of the main crack.

Acknowledgements

This research was partially supported by RFBR (grants 08-01-92201-GFEN-a, 09-08-

00366-a.)

References

[1] L.I. Slepyan. Mechanics of Cracks. Leningrad, Sudostroenie, 1990. (in Russian)

[2] J.W. Dally, W.L. Fourney and G.R. Irwin. On the uniqueness of the stress intensity factor - crack velocity relationship. International Journal of Fracture 27 (1985) 159-168.

[3] K. Ravi-Chandar and W.G. Knauss. An experimental investigation into dynamic fracture: I. Crack initiation and arrest. International Journal of Fracture 25 (1984) 247-262.

[4] L.B. Freund. Dynamic Fracture Mechanics. Cambridge University Press, 1998.

[5] J. Fineberg, S.P. Gross, M. Marder, and H.L. Swinney. Instability in the propagation of fast cracks. Physical Review B 45 10 (1992) 5146-5154.

[6] Yu.A. Kostandov, A.N. Ryzhakov, and S.I. Fedorkin. Failure of solid polymers under pulse tension. Strength of Materials 24 7 (1992) 444-447 (Translated from Problemy Prochnosti).

[7] A.S. Dubovik. Photographic recording of fast processes. Moscow, Nauka, 1975. (in Russian)

[8] J.P. Berry. The morphology of polymer fracture surfaces. Journal of Polymer Science: Part C 3 (1963) 91-101.

[9] K. Ravi-Chandar and W.G. Knauss. An experimental investigation into dynamic fracture: II. Microstructural aspects. International Journal of Fracture 26 (1984) 65-80.

[10] Yu.A. Kostandov, A.A. Skoblin, S.I. Fedorkin, and Yu.A. Shevlyakov. Fractographic analysis of crack propagation in dynamic loading. Mechanics of Composite Materials 22 6 (1986) 676-684(Translated from Mekhanika Kompozitnykh Materialov).

Ivan V. Smirnov, St. Petersburg State University, Universitetsky pr., 28, St. Petersburg, 198504, Russian Federation
Yuri V. Sudenkov, St. Petersburg State University, Universitetsky pr., 28, St. Petersburg, 198504, Russian Federation

Boundary effects on thin body motion in fluid or gas

M. N. Smirnova A. V. Zvyaguin
wonrims@inbox.ru

Abstract

The two-dimensional problems of thin body motion in fluid parallel to the boundary at a distance comparable with the length of the body were regarded. In particular, resistance and lift forces in thin body motion parallel to free surface and parallel to rigid surface were determined and compared with existing solutions for resistance and lift forces determined in an infinite space. The fluid was assumed occupying infinite semi-space, gravity was neglected as compared with fluid inertia. The solution was obtained for a problem of plate motion in compressible fluid at a definite depth under free surface, constant velocity and inclination angle. The formation of final or infinite length cavity behind the body was taken into account. A different effect on resistance and lift force was produced by a rigid boundary, on approaching to which resistance and lift forces drastically increased. The obtained solutions allowed determining free surface shape, drag and lift forces for moving near free boundary, and resistance and repulsion forces on moving near rigid boundary for both compressible and incompressible fluids. The solution was obtained numerically for all the range of variation of governing parameters. Approximation formulas for numerical solution were developed, which coincide with analytical formulas for the limiting cases. The length of cavity was determined being function of governing parameters.

1 Introduction

The current problem has many practical applications, such as determining resistance and lift forces being the function of the depth in underwater motion of a bullet or shell, which is relevant to evaluation the consequences of in orbit fluid filled containments perforation by small space debris particles [1, 2]. Similar problems arise in evaluating wave-breakers effect on the streaming flow. The problem being relevant to surface or underwater high velocity gliding of thin wing, which is often used to reduce resistance of the glider, it was addressed by many researchers in the past. Many gliding problem statements were done for incompressible fluid because flow velocities were expected to be rather low.

The problem of gliding near the free surface of water of infinite and finite depth was regarded within the frames of linear [3-6] and non-linear [7, 8] statements, and found its generalized classical solution in [9]. Solutions for motions of plates at big attack angles in unbounded incompressible fluid were obtained by V.P. Karlikov and co-workers [10]. High speed streaming flows accounting for fluid compressibility were investigated in [11-13]. The problems regarded in [13] include both cases of positive and negative attack angle, which describe both processes of gliding in the fluid and slicing fluid. However, the solutions relied heavily on the fact that cavity behind the gliding body has infinite length.

The latter approximation being undoubtedly valid for all types of gliding problems, could be hardly used for the conditions of a rather deep underwater motion, under which formation of a final length cavity is more probable [14].

The problem of thin wing motion near rigid surface is relevant to flight close to the bottom of fluid, i.e. flight in an atmosphere above rigid soil or water surface of a planet. Here water surface could be considered as a rigid one due to its inertia surpassing several orders of magnitude gas inertia.

At the beginning of the XX century it was observed that the lift force of a wing moving near flat surface increases strongly in comparison with free flight. An article about screen effect by B.N. Juriev [15] was published in 1923 in the USSR. That fact was used in creation of new flying devices – screen-flights, which got the Russian name "ekranoplan". In 1932 Grohovsky constructed a full-scaled model of a new marine flying device – catamaran. At the same time Finnish engineer T. Kaario proceeded to test his flying apparatus that used a screen effect. Then (1963 – 1976) a Soviet constructor R.L. Bartini created a screen-flight project SVVP-2500 that took off in 1974. The first Soviet manned jet screen-flight SM-1 was created in collaboration with R. Alekseev in 1960 – 1961 [16]. Giant screen-flight KM was finished by 1966 and "Orlyonok" type screen-flights were built from 1974 to 1983. Designing of new flying devices continues in many countries.

L.I. Sedov obtained an analytical solution for the lift force in terms of Weierstrass functions [9] using theory of a complex variable. Approximate analytical solution of the problem of non-steady plane moving near rigid surface was obtained by K.V. Rozjdestvensky [17] using asymptotic expansion. Theoretical investigation of a wing moving near rigid surface was made by A.N. Panchenkov [18, 19], but the obtained solutions incorporated free constants. Experimental results are shown in [20].

The problem of theoretical investigation of a wing's behavior near a motionless surface is still far from being finalized. The present paper provides a theoretical solution for the two-dimensional linearized problem of a thin wing motion near rigid surface in compressible fluid.

2 Mathematical statement of the problem

The two-dimensional problem of fluid streaming thin body in the presence of free and rigid surfaces is regarded. The case of final length cavity formation, which is closed at some distance from the body, is taken into consideration when the body is moving near free surface. Pressure on free surface is assumed to be equal to air ambient pressure. Pressure in the cavity is assumed equal to the sum of partial pressures of saturated vapor at the temperature of fluid and pressure of solute gases. The total cavity pressure value can be determined as a function of cavitation parameter.

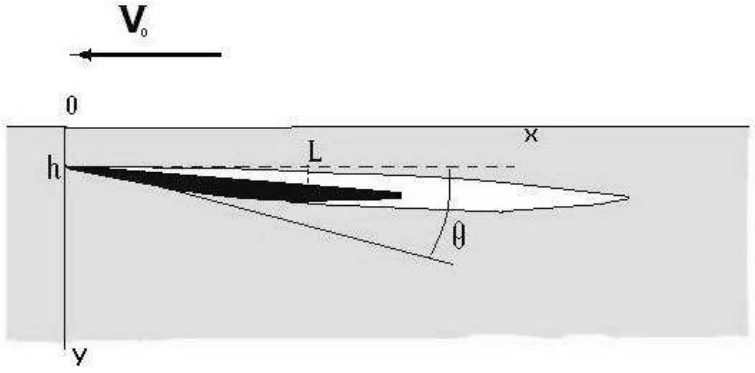

Figure 1: Thin body motion in fluid parallel to free surface with formation of closed cavity.

The coordinate system and flow scheme in case of the presence of free surface are shown in Fig. 1. The coordinate system and flow scheme in case of the presence of rigid surface are shown in Fig. 2. Fluid is assumed to be ideal, depth – infinite, mass forces – negligibly small, flow field – plane. Velocity field in fluid is assumed to be potential. Fluid flow satisfies continuity equation. Fluid pressure is determined by Cauchy-Lagrange integral derived from momentum equation.

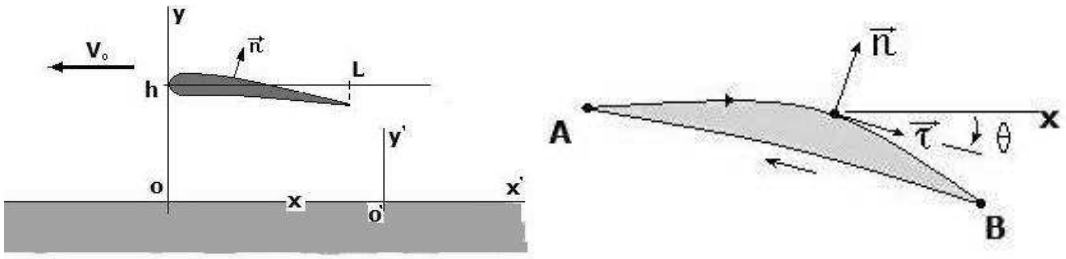

Figure 2: Schematic picture for thin wing motion above rigid surface.

Boundary conditions should be satisfied on the free surfaces, on the rigid surface, on the body surface contacting fluid and in the cavity. On the free surface and in the cavity constant pressure is assumed, on the rigid surface and on the fluid-body contact streaming condition of the equality of normal velocity component.

The obstacle being thin and inclination angle being small all disturbances could be considered small, and boundary conditions could be assigned on the plane parallel to free surface. As it is shown in [11-13] the problem is reduced to developing analytical function in the domain $y > 0$ with a cut $y = \pi, x > 0$, satisfying the following boundary conditions:

for body moving near free surface:

$$y = 0, -\infty < x < \infty : \quad \frac{\partial \varphi}{\partial x} = 0;$$

$$y = h^+, 0 < x < L : \quad \frac{\partial \varphi}{\partial y} = V_0 \sin\theta;$$

$$y = h^-, 0 < x < S; \quad y = h^+, L < x < S : \frac{\partial \varphi}{\partial x} = -\frac{\Delta P}{\rho_0 V_0};$$

$$y = h^\pm, L < x : \quad \frac{\partial \varphi}{\partial x} = 0.$$

for body moving near rigid surface:

$$y = h^\pm, 0 < x < L : \quad \frac{\partial \varphi}{\partial y} = V_0 \sin\theta;$$

$$y = 0, -\infty < x < \infty : \quad \frac{\partial \varphi}{\partial y} = 0,$$

where $\vec{V_0}$ is the mean streaming velocity, $\varphi(x, y, t)$ is the potential of the disturbed flow induced by the relative motion of the body, ρ_0 is the density in quiescent fluid, $\Delta P = C_{cav.min} \frac{\rho_0 V_0^2}{2}$, where $C_{cav.min}$ is the minimal cavitation number, which is determined by the thermo-physical properties of liquid, amount of solute gases, presence of impurities, fluid temperature, etc.

In case of body moving near rigid surface boundary conditions should be supplemented with function behavior at the infinity for the uniqueness of the solution. The demand for function behavior at the infinity is reduced to the following formula, as it is shown in [21]:

$$z \to \infty : \quad \Phi(z) \approx \ln(z) + const.$$

Thus an analytical function satisfying boundary conditions and the conditions at the infinity should be developed.

3 Problem solution

The solution will be developed in the form of a real part for the analytical function of a complex variable $\varphi(x, y) = Re\Phi(z), z = x + iy$. Actually, it is necessary to develop first derivative of the analytical function, which could be denoted as $T(z) = \Phi^{'}(z)$.

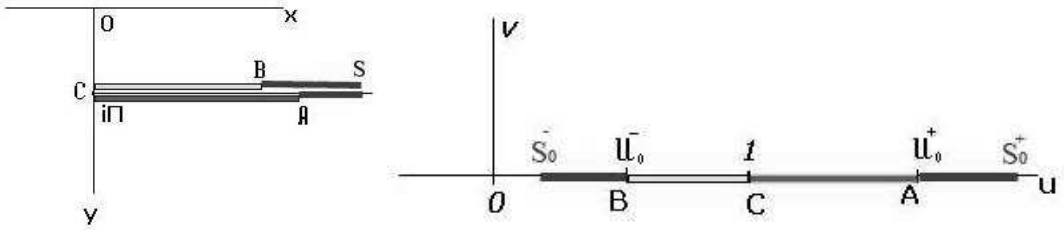

Figure 3: Conformal mapping of the hemi-plane $y > 0$ with a cut $y = \pi, x > 0$ on the upper hemi-plane.

In case of the body moving near free surface the conformal mapping [11] of the hemi-plane $y > 0$ with a cut $y = \pi, x > 0$ on the upper hemi-plane $Imw > 0$ (Fig. 3), which could be performed using function:

$$z = \pi i + w - \ln w - 1, \quad Imw > 0, \quad w = u + iv$$

can be used to obtain a new boundary value problem in the new plane for $T(z(w))$ function. Thus development of the analytical function is reduced to Riemann - Hilbert problem.

The solution could be developed in the following form:

$$T(w) = \sqrt{\frac{u-1}{u_0^+ - 1}} Q(w),$$

where $Q(w)$ tends to zero at infinity. The solution is limited at infinity, and it is equal to zero at the front edge.

The solution for $ReQ(w)$ function is reduced to Dirichlet boundary value problem [11], which is formulated as follows.

It is necessary to develop a harmonic function $ReQ(w)$ in the domain, which takes the following continuous values at the boundary:

$$1 < u < u_0^+ : \quad ReQ(u) = \frac{M\gamma(x(u))}{\alpha} \sqrt{\frac{u_0^+ - u}{u-1}};$$

$$u < 0, 0 < u < s_0^-, s_0^+ < u < \infty : \quad ReQ(u) = 0;$$

$$s_0^- < u < 1: \quad ReQ(u) = -\frac{\Delta P \alpha}{\rho_0 V_0 a}\sqrt{\frac{u_0^+ - u}{1-u}};$$

$$u_0^+ < u < s_0^+: \quad ReQ(u) = -\frac{\Delta P \alpha}{\rho_0 V_0 a}\sqrt{\frac{u - u_0^+}{u-1}},$$

where $\sin\theta = \approx \frac{\gamma}{\alpha}, \alpha = \sqrt{1-M^2}, M = \frac{V_0}{a}$ and $u_0^\pm, s_0^\pm$ are the roots of algebraic equations

$$l = u_0 - \ln u_0 - 1, \quad s = s_0 - \ln s_0 - 1.$$

The solution for the Dirichlet problem for the hemi-plane is given by Schwarz integral:

$$Q(w) = \frac{1}{\pi i}\int_{-\infty}^{\infty} ReQ(t)\frac{dt}{t-w} + iC.$$

In case inclination angle is constant this integral can be taken in elementary functions:

$$Q(w) = -i\frac{\gamma_0 M}{\alpha}(\sqrt{\frac{w-u_0^+}{w-1}} - 1) +$$

$$i\frac{\Delta P \alpha (u_0^+ + 1)}{\rho_0 V_0 a \pi (u_0^+ - 1)} \ln\left|\frac{(1+\sqrt{\frac{s_0^+ - u_0^+}{s_0^+ - 1}})(1-\sqrt{\frac{s_0^- - u_0^+}{s_0^- - 1}})}{(1-\sqrt{\frac{s_0^+ - u_0^+}{s_0^+ - 1}})(1+\sqrt{\frac{s_0^- - u_0^+}{s_0^- - 1}})}\right| +$$

$$+i\frac{\Delta P \alpha (u_0^+ + 1)}{\rho_0 V_0 a \pi (u_0^+ - 1)}\sqrt{\frac{u_0^+ - w}{1-w}} \ln\left|\frac{(\sqrt{\frac{u_0^+ - w}{1-w}} + \sqrt{\frac{s_0^- - u_0^+}{s_0^- - 1}})(\sqrt{\frac{u_0^+ - w}{1-w}} - \sqrt{\frac{s_0^+ - u_0^+}{s_0^+ - 1}})}{(\sqrt{\frac{u_0^+ - w}{1-w}} - \sqrt{\frac{s_0^- - u_0^+}{s_0^- - 1}})(\sqrt{\frac{u_0^+ - w}{1-w}} + \sqrt{\frac{s_0^+ - u_0^+}{s_0^+ - 1}})}\right|$$

The obtained solution makes it possible to develop forces affecting on the plate [14], because pressure distribution in the contact zone is provided by the expression:

$$p(x(u)) = \frac{M}{\alpha} ReT(u), \quad 1 < u < u_0^+$$

$$p(x(u)) = [\frac{M^2 \gamma_0}{\alpha} + i\frac{M \Delta P (u_0^+ + 1)}{\rho_0 V_0 a \pi (u_0^+ - 1)} \ln\left|\frac{(1+\sqrt{\frac{s_0^+ - u_0^+}{s_0^+ - 1}})(1-\sqrt{\frac{s_0^- - u_0^+}{s_0^- - 1}})}{(1-\sqrt{\frac{s_0^+ - u_0^+}{s_0^+ - 1}})(1+\sqrt{\frac{s_0^- - u_0^+}{s_0^- - 1}})}\right|]\sqrt{\frac{u-1}{u_0^+ - u}}.$$

The obtained solution makes it possible to develop velocities on free surfaces. The length of the cavity is determined from the condition of equality of the sum of upper and lower borders of the cavity vertical movements to vertical size of the cavity [14].

The obtained closed form solution is, however, difficult for being used directly in its current form. In case of relatively small depth the following estimates are valid:

$$l = \frac{\pi L}{\alpha h} \to \infty, \quad s = \frac{\pi S}{\alpha h} \to \infty,$$

$$u_0^+ \approx \frac{\pi L}{\alpha h}, \quad s_0^+ \approx \frac{\pi S}{\alpha h}, \quad s_0^- \approx e^{-\frac{\pi S}{\alpha h}} \approx 0.$$

Then the relation between the lengths of the body and cavity takes the form:

$$\frac{L}{S}=\frac{2e^{-\frac{2\pi L}{\alpha h}}}{1+e^{-\frac{2\pi L}{\alpha h}}\frac{(\frac{2}{\alpha}-1)\rho_0 V_0^2\gamma_0\pi}{\Delta P\alpha}\sqrt{\frac{\pi L}{\alpha h}}}.$$

Using this relation the drag and lift forces in case of cavity formation may be estimated for relatively small depth:

$$X=\frac{\rho_0 a^2M^2\gamma_0^2\pi L}{\alpha^3}+\frac{\gamma_0\Delta P\pi L^2}{2h\alpha^2}(\frac{2\pi L}{\alpha h}+\ln(1+e^{-\frac{2\pi L}{\alpha h}}\frac{(\frac{2}{\alpha}-1)\rho_0V_0^2\gamma_0\pi}{\Delta P\alpha}\sqrt{\frac{\pi L}{\alpha h}}))+\frac{M^2\gamma_0^2\Delta PL}{\alpha^3},$$

$$Y=-\frac{\rho_0 a^2M^2\gamma_0\pi L}{\alpha^2}-\frac{\Delta P\pi L^2}{2h\alpha}(\frac{2\pi L}{\alpha h}+\ln(1+e^{-\frac{2\pi L}{\alpha h}}\frac{(\frac{2}{\alpha}-1)\rho_0V_0^2\gamma_0\pi}{\Delta P\alpha}\sqrt{\frac{\pi L}{\alpha h}}))-\frac{M^2\gamma_0\Delta PL}{\alpha^2}.$$

Analysis of the equation for the cavity length shows, that on increasing pressure in the cavity ($\Delta P\to 0$) its length tends to infinity and the solution tends to the solutions obtained for open (infinitely long) cavity. On increasing depth h of the body motion under free surface the length of the cavity decreases.

Formulas for forces' values show that on increasing pressure in the cavity up to ambient value ($\Delta P\to 0$) resistance and lift forces for asymptotic solution tend to the values obtained in [11-13] for infinite cavity length:

$$X=\frac{\rho_0 a^2M^2\gamma_0^2\pi L}{\alpha^3},\quad Y=-\frac{\rho_0 a^2M^2\gamma_0\pi L}{\alpha^2}.$$

In case of the body moving near a rigid surface the solution is reduced to the following boundary problem:

$$y=0,-\infty<x<\infty:\quad Im\Phi^{'}(x)=0;$$

$$y=\pi^{\pm},0<x<l=\frac{\pi l}{\alpha h}:\quad Im\Phi^{'}(x)=\frac{M\gamma}{\alpha}.$$

Boundary conditions should be supplemented with function behavior at the infinity for the uniqueness of the solution. The solution for the problem will be determined in the form of Cauchy integral [22]

$$\Phi^{'}(z)=\frac{1}{2\pi i}\int_0^l\frac{g_{11}(t)-if_{11}(t)}{t-(z-i\pi)}dt+\frac{1}{2\pi i}\int_0^l\frac{g_{11}(t)+if_{11}(t)}{t-(z+i\pi)}dt.$$

This expression satisfies the condition $Im\Phi^{'}(x)=0$ on the axis $y=0,-\infty<x<\infty$. Boundary condition on the body contour still needs to be satisfied. The value of function on the boundary $y=\pi^{\pm},0<x<l$ is

$$\Phi^{'}(x+i\pi^{\pm})=\pm\frac{1}{2}(g_{11}(x)-if_{11}(x))+\frac{1}{2\pi i}\int_0^l\frac{g_{11}(t)-if_{11}(t)}{t-x}dt+$$

$$+\frac{1}{2\pi i}\int_0^l\frac{g_{11}(t)+if_{11}(t)}{t-x-2\pi i}dt,$$

$$Im\Phi^{'}(x+i\pi^{\pm})=\mp\frac{1}{2}f_{11}(x)-\frac{1}{2\pi}\int_0^l\frac{g_{11}(t)}{t-x}dt-\frac{1}{2\pi}\int_0^l\frac{(t-x)g_{11}(t)-2\pi f_{11}(t)}{(t-x)^2+4\pi^2}dt,$$

$$Re\Phi^{'}(x+i\pi^{\pm})=\pm\frac{1}{2}g_{11}(x)-\frac{1}{2}\int_0^l\frac{f_{11}(t)}{t-x}dt-\frac{1}{2\pi}\int_0^l\frac{2\pi g_{11}(t)-(t-x)f_{11}(t)}{(t-x)^2+4\pi^2}dt,$$

$$as - i(t - x + 2\pi i)(g_{11} + if_{11}) = 2\pi g_{11} + (t - x)f_{11} - i((t - x)g_{11} - 2\pi f_{11}).$$

Integrals from the right part of the formula do not depend on the contour side. Therefore the function satisfies the following condition on the contour:

$$y = \pi^{\pm}, 0 < x < l : \quad [Im\Phi^{'}(x)] = -f_{11}(x),$$

$$Im\Phi^{'}(x + i\pi^{\pm}) = \pm\frac{M\gamma}{\alpha} - \frac{1}{2\pi}\int_0^l \frac{g_{11}(t)}{t - x}dt - \frac{1}{2\pi}\int_0^l \frac{(t - x)g_{11}(t) + 4\pi\frac{M\gamma}{\alpha}}{(t - x)^2 + 4\pi^2}dt.$$

Boundary condition on the upper surface of the body should be satisfied for the definition of function $g_{11}(x)$:

$$-\frac{M\gamma}{\alpha} = \frac{M\gamma}{\alpha} - \frac{1}{2\pi}\int_0^l \frac{g_{11}(t)}{t - x}dt - \frac{1}{2\pi}\int_0^l \frac{(t - x)g_{11}(t) + 4\pi\frac{M\gamma}{\alpha}}{(t - x)^2 + 4\pi^2}dt.$$

Finally we get the singular integral equation with Cauchy center [22]:

$$\frac{1}{\pi}\int_0^l \frac{g_{11}(t)}{t - x}dt = 4\frac{M\gamma}{\alpha} - \frac{1}{\pi}\int_0^l \frac{(t - x)g_{11}(t)}{(t - x)^2 + 4\pi^2}dt - 4\frac{M\gamma}{\alpha}\int_0^l \frac{dt}{(t - x)^2 + 4\pi^2}.$$

The determined solution will be limited at the rear edge of the wing (the Chaplygin-Zhukovsky hypothesis [23]). In this case regularizing of the singular equation can be fulfilled that reduces it to Fredholm equation:

$$g_{11}(x) - 2\pi\int_0^l g_{11}(\tau)\sqrt{\frac{1 - x}{x}}K(\tau, x)d\tau = \frac{M\gamma}{\alpha}\sqrt{\frac{1 - x}{x}}(1 + q(x)),$$

where

$$K(\tau, x) = \frac{1}{\sqrt{R}\cos\theta((1 - \tau)^2 + 4\pi^2)}\cdot$$

$$\cdot\frac{R^2(1 - \tau)(1 - x) - R\tau(1 - x)(2\cos 2\theta - 1) - R\tau(1 - x) + x\tau}{R^2(1 - x)^2 + x^2 - 2x(1 - x)R\cos 2\theta},$$

$$q(x) = \frac{1}{\pi}\int_0^l \frac{1}{\sqrt{R}\sin\theta((1 - \tau)^2 + 4\pi^2)}\cdot$$

$$\cdot\frac{R^2(1 - x) + R(1 - x) - x + xR - 2xR\cos 2\theta}{R^2(1 - x)^2 + x^2 - 2x(1 - x)R\cos 2\theta}d\tau,$$

$$R^2 = \frac{\tau^2 + 4\pi^2}{(1 - \tau)^2 + 4\pi^2}, \quad \theta = \frac{1}{2}(\arctan(\frac{2\pi}{\tau}) + \arctan(\frac{2\pi}{1 - \tau})).$$

The Fredholm equation was determined numerically [24]. The obtained solution allows the pressure function and the lift force to be determined:

$$p^{\pm}(x) = \frac{\rho_0 V_0^2}{\alpha}Re[\pm(g_{11}(x) - if_{11}(x))] +$$

$$+\frac{\rho_0 V_0^2}{\alpha}Re[\frac{1}{2\pi i}\int_0^l \frac{g_{11}(t) - if_{11}(t)}{t - x}dt + \frac{1}{2\pi i}\int_0^l \frac{g_{11}(t) + if_{11}(t)}{t - x - 2\pi i}dt]$$

$$F_y = -\int_0^L (p^+ - p^-)dx = \frac{\rho_0 V_0^2}{\alpha}\int_0^l \sqrt{\frac{1 - x}{x}}\frac{1}{\pi}\int_0^l \sqrt{\frac{t}{1 - t}}\frac{g_{11}(t)dt}{t - x}dx.$$

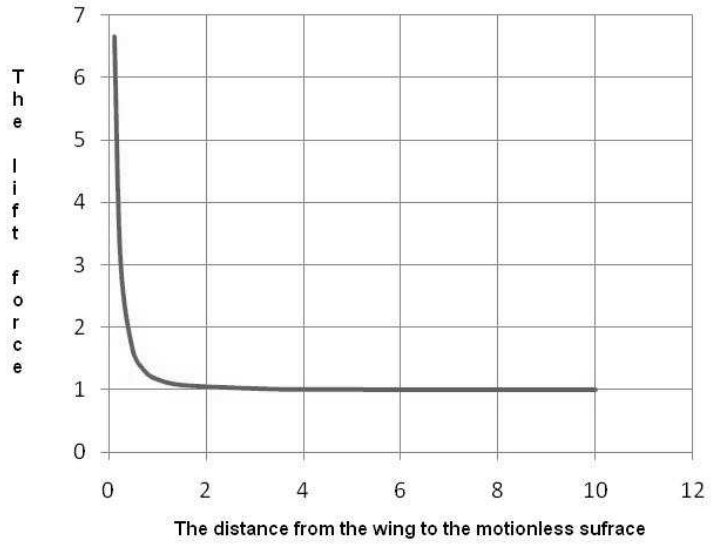

Figure 4: Dependence of dimensionless lift force of a flat wing $\frac{F}{\pi\rho_0\frac{V_0^2}{\alpha^2}\gamma L}$ on the relative distance from the wing to the flat surface $\frac{h}{L}$.

Fig. 4 represents the dependence of the dimensionless lift force of a flat wing $\frac{F}{\pi\rho_0\frac{V_0^2}{\alpha^2}\gamma L}$ upon the relative distance from the wing to the motionless surface $\frac{h}{L}$. It is seen that the screen effect practically disappears for distances equal to two times the length of the wing. The lift force increases greatly when the distance is lower than the length of the wing. If the altitude above the surface surpasses the wing span and the fluid is regarded as incompressible the lift force tends to its value in an unbounded space determined by the classical solution for thin wing lift force in incompressible fluid and unbounded space [23]:

$$F = \pi\rho_0 V_0^2 \gamma L.$$

Fig. 5 represents the dependence of the dimensionless pressure function $\frac{\Delta p}{\rho_0\frac{V_0^2}{\alpha^2}}$ upon the length of the wing $\frac{x}{L}$ for $\frac{h}{L} = 0.1$. The center of applied resultant lift force shifts to the front edge of the wing as the distance $\frac{h}{L}$ decreases because the singularity on the front edge increases. The obtained results fully correspond to the experiment described in [16].

4 Conclusions

The analytical solution was obtained for a problem of body motion in compressible fluid at a final depth with constant velocity and inclination angle. For the case of final length cavity vapor pressure in it is less then the pressure on free surface. The solution allows determining drag and lift forces in the limiting cases. The relation between the body length and the cavity length in the case of small depth or high compressibility was obtained. The forces increase when the pressure in the cavity decreases. When the pressure in the cavity tends to pressure on the free surface the length of the cavity infinitely increases and forces tend to the values obtained in independent solutions with infinite cavities. The increase

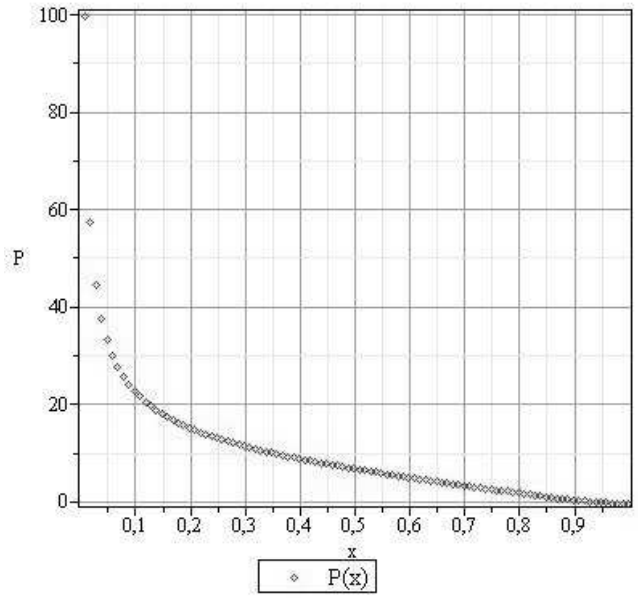

Figure 5: Dependence of dimensionless pressure function $\frac{\Delta p}{\rho_0 \frac{V_0^2}{\alpha^2}}$ upon the length of the wing $\frac{x}{L}$ for $\frac{h}{L} = 0.1$.

of depth under free surface and decrease of compressibility brings to decrease of cavity length.

The theoretical solution for the problem of the wing lift force determination under the conditions of streaming by ideal incompressible fluid in the vicinity of rigid plane is reduced to Fredholm equation, which is developed numerically.

The behavior of the lift force and the point of its application evolution depending on the distance from the rigid surface are examined. It is shown that the lift force increases with the decrease of the wing distance from the plane surface. If the altitude above the surface surpasses the wing span the screen effect practically disappears and the lift force tends to its value in an unbounded space determined by the classical Zhukovsky solution.

The center of applied resultant lift force on the wing profile shifts to the front edge of the wing as the altitude above the rigid plane decreases due to increase of the front edge singularity.

The obtained solution evidently shows, that the increase of lift force near the screen in the orders of magnitude allows developing flying vehicles carrying much more cargo at lower fuel consumption.

The obtained solution would be useful for designing giant screen-flight vehicles, because it is necessary to take into account the essential variation of lift force application center and its value depending on altitude. The effect could be used for developing vehicles for operation on other planets having not very dense atmosphere and relatively smooth surface (like Mars). Flights in such an atmosphere are energy consuming, while using the effect of lift force increase near the surface could be very effective.

Acknowledgements

The research was performed within the frame of joint NSC-RFBR cooperation program 09-08-92002/RP09E11.

References

[1] Smirnov N. N., Kondratyev K.A. Evaluation of craters formation in hypervelocity impact of debris particles on solid structures. Acta Astronautica 65 (2009) No 11-12, pp.1796-1803.

[2] Smirnov N.N., Kiselev A.B., Kondratyev K.A., Zolkin S.N. Impact of debris particles on space structures modeling. Acta Astronautica 67 (2010) No 3-4, pp.333-343, doi:10.1016/ j.actaastro.2010.03.003.

[3] Gurevich M.I., Yanpolskii A.R. On motion of a gliding plate. Techniques of the aviation fleet, 1933, 10.

[4] Haskind M.D. Plane problem on gliding over the surface of heavy fluid. Proc. Acad. Sci. USSR, Tech.Sci. Ser., 1943, 1-2.

[5] Gurevich M.I. Gliding of a circle segment over the surface of heavy fluid. TsAGI Tech. Papers, 1937, 153, 1 - 6.

[6] Chaplyguin Yu.S. Gliding on the surface of fluid of final depth. Journ. Applied Math. and Mech., 1941, 5, 2.

[7] Chaplyguin Yu.S. Gliding of a flat plate of infinite span over the surface of heavy fluid. TsAGI Tech. Papers, 1942, 508.

[8] Green A. E. The gliding of a plate on a stream of finite depth. Proc. Cambridge Phil. Soc., 1935, 31, 4.

[9] Sedov L.I. Plane problems of hydrodynamics and aerodynamics. Moscow: Science Publ., 1980.

[10] Karlikov V.P., Tolokonnikov S.L. On optimal schemes of closing cavities. Fluid Dynamics, A Journal of Russian Academy of Sciences.

[11] Zvyaguin A.V., Smirnova M.N. Motion of a slender body near the free surface of compressible fluid. Moscow University Mechanics Bulletin, 2009, vol. 64, No 2, pp. 5-15.

[12] Smirnova M.N., Zvyaguin A.V. Fluid flow interaction with an obstacle near free surface. Acta Astronautica 64 (2009) 288-294.

[13] M.N.Smirnova, A.V. Zvyaguin, Different flow scenario for thin body subsonic motion in compressible fluid under free surface, Acta Astronautica (2010), vol. 66, pp. 434 - 438. doi: 10.1016/j.actaastro. 2009.07.002

[14] M.N.Smirnova, A.V. Zvyaguin, I.V. Shugan, Ray-Yeng Yang, Hwung-Hweng Hwung. Thin body motion under free surface with formation of final length cavity. Acta Astronautica vol. 68 (2011), No 1-2, 46-51.

[15] Juriev B.N. Earth impact on the aerodynamical characteristics of a wing. “Air fleet herald” No 1. 1923.

[16] Belavin N.I. Screen-flights (ecranoplan). Moscow,“Shipbuilding” Publ. 1977.

[17] Rozjdestvensky K.V. Asymptotic theory of a wing moving on small distances from a rigid wall. Mechanics of liquid and gas, No 6. 1977.

[18] Panchenkov A.N. Hydrodynamics of an underwater wing. Kiev: book printing house No 5. 1964.

[19] Panchenkov A.N. Theory of optimal supporting surface. Novosibirsk: “Science”. 1983.

[20] Serebriisky Y.., Biyachuev S.. The study of horizontal steady wing motion in a pipe. TSAGI papers (Central Aero Hydrodynamic Institute), issue 437. 1939.

[21] Batchelor G.K. An Introduction to Fluid Dynamics. Cambridge University Press. 1970.

[22] Gahov F. D. Boundary problems. Moscow “Science”. 1977.

[23] Kochin N. ., ibel I. ., Roze N. V. Theoretical hydromechanics. Moscow Physmathgys. 1963.

[24] Verlan .F., Sizikov V.S. Methods of solving integral equations with programs for computers. iev “Science”. 1977.

Smirnova M.N., Faculty of Mechanics and Mathematics, Moscow M.V. Lomonosov State University, Moscow 119992, Leninskie Gory 1, RUSSIA

Transition processes in non-uniform media combustion mathematical modeling and computer simulations

N. N. Smirnov V. F. Nikitin V. R. Dushin V. A. Nerchenko N. V. Korolkova
ebifsun1@mech.math.msu.su

Abstract

The paper presents results of computer modeling for the transition processes in homogeneous combustible gaseous mixtures. A new impetus to the increase of interest in deflagration to detonation transition (DDT) processes was given by the recent development of pulse detonation devices. The probable application of these principles to creating the new generation of engines put the problem of pulse detonating devices (PDD) effectiveness on top of current research needs. The effectiveness of the PDD cycle turned to be the key factor characterizing the Pulse Detonation Engine (PDE), which operation modes were shown to be closely related to periodical onset and degeneration of a detonation wave. Thus deflagration to detonation transition processes are of major importance for the issue. Minimizing the pre-detonation length and ensuring stability of the onset of detonation enables to increase effectiveness of PDD. The DDT turned to be the key factor characterizing the PDE operating cycle. Thus, the problem of DDT control in gaseous fuel-air mixtures became very acute.

The paper contains the results of theoretical analysis of the multi-scale combustion processes in technical devices. The processes characterized by three different scales were regarded: the combustion chamber non-uniformity characteristic scale, the turbulent pulsations characteristic scale and the chemistry characteristic scale (laminar flame thickness). In particular, the paper investigates the effect of cavities incorporated in PDD on the onset of detonation in gases.

1 Introduction

In 1881 Mallard et Le Chatelier [1] and Bertelot et Vieille [2] were the first to face deflagration to detonation transition process. On investigating flame propagation in homogeneous gaseous mixtures they unexpectedly detected the onset of a supersonic mode of combustion wave traveling at velocities of thousands meters per second. This combustion mode got the name of "false" or "out of tone" combustion, which sounds in French like "detonation" being originated from the French verb "détonner". The existence of two alternative velocities for the combustion process needed theoretical explanation, which was given in 1893 by an Associate Professor of Moscow University V.A.Mikhelson in his paper "On normal combustion velocity of explosive gaseous mixtures" [3]. Based on having been published by that time papers by Rankine [4] and Hugoniot [5] Mikhelson was the first to explain that the mechanism of flame propagation in detonation was not the heat conductivity, but "adiabatic heating up to the ignition point in shock waves". That was the birth of the classical theory of detonation, which found its further development in the papers by Chapman [6] and Jouget [7].

On analyzing the initiation of detonation by a local energy release in gases one could distinguish three scenarios. The first scenario: the energy release brings to a formation of

a shock wave strong enough to activate chemical reactions in the compressed gas due to temperature increase. Energy release behind the shock due to activated chemistry supports the leading shock preventing its attenuation and keeping its velocity at the level of Chapmen - Jouget detonation. Thus velocity of the wave propagation becomes independent on initiation conditions. This scenario was investigated with great completeness in the papers [8-10] and successive studies by Chernyi, Levin, Markov and co-workers.

The second scenario of detonation initiation takes place under the condition the intensity of the shock wave formed due to initial energy release is too small and its attenuation is too fast to initiate essential energy release in the shock compressed gas, but heating of gas in the zone of energy release is sufficient to initiate chemical reactions. Then a normal combustion wave propagates from the zone of initial energy release. The propagation mechanism of this wave (the mechanism of reaction activation in the neighboring layers of gas) is different from shock wave compression being due to heat conductivity to those layers from the burnt gas. The propagating combustion wave brings to acceleration and turbulization of gas flow ahead of its front, which, in its turn, leads to acceleration of turbulent flame. Compression waves ahead of the flame front converge into one or several shock waves overtaking each other. The flame propagation velocity could either stabilize on reaching some value thus forming a structure of turbulent flame preceded by a shock wave moving with higher velocity and leaving behind the flame zone, or flame acceleration could bring to the onset of detonation thus changing the combustion wave propagation mechanism. The last process got the name of deflagration to detonation transition. The present paper is focused on studying these types of processes.

There could be intermediate scenarios of detonation initiation as a combination of the two limiting cases: creating initial ignition zone and a low intensity shock, which is not strong enough to initiate chemistry, but sufficient to facilitate DDT. Such scenarios could be observed in flame jet ignition [11].

Investigations of deflagration to detonation transition (DDT) in hydrogen – oxygen mixtures [12-16, 76, 77] and later in hydrocarbons - air mixtures [17-19] showed the multiplicity of the transition processes scenario. The various modes of the detonation onset were shown to depend on particular flow pattern created by the accelerating flame, thus making the transition process non-reproducible in its detailed sequence of events. By now, there exist different points of view on the DDT mechanism: the “explosion in explosion” mechanism by Oppenheim [14, 16] and the gradient mechanism of “spontaneous flame” by Zeldovich [20].

The later theoretical analysis showed that micro-scale non-uniformities (temperature and concentration gradients) arising in local exothermic centers (“hot spots”) ahead of the flame zone could be sufficient for the onset of detonation or normal deflagration [21-27]. Analysis and comparison of theoretical and experimental results showed that self-ignition in one or in a number of hot spots ahead of the accelerating flame followed by the onset of either detonation or deflagration waves brings to a multiplicity of the transition scenarios [28, 29]. Shock waves ahead of flame could occur due to initiating energy release and due to the piston effect of expanding flame. Reflection of these compression waves from the walls of the vessels and the contact surface between burnt and unburned gases brings to recirculation of waves its amplitude growing due to wave-flame interaction [30-31]. The common feature of all those scenarios is the formation of local exothermic centers according to stochastic Oppenheim mechanism followed by the onset of detonation at a micro-scale in one of the exothermic centers according to spontaneous Zeldovich mechanism [28]. First numerical DDT investigations carried out using 1-D Navier-Stokes model [70] as well as subsequent analysis [71] also demonstrated this effect. Other investigators explain the

detonation wave onset not by spontaneous flame acceleration within a single exothermic center, but rather restructuring of flow being the result of flame interaction with the zone of elevated temperature ahead, which leads in the long run to ignition delay gradients formation sufficient for spontaneous detonation onset [61, 62]. There is no experimental evidence by nowadays that DDT could take place in an open space without any obstacles and wave reflections, nor has anybody obtained such a DDT in numerical simulations.

There could be distinguished the third mechanism of initiation, which looks like an intermediate one. In the first stage mixture ignition following the second scenario takes place, which gives birth to slow flame propagation in a weak combustion mode, which does not initiate strong enough shock wave ahead of flame zone. Then combustion zone is affected by a strong shock wave formed elsewhere [32, 33, 63]. The intensity of that secondary shock wave is usually less than that necessary for direct detonation initiation in a cold unreacted mixture, but it is sufficient for detonation initiation in interaction with heated layers in the vicinity of flame zone. Experimental and theoretical investigations [32, 33] of the reflected shock - laminar flame interactions bringing to the onset of detonation showed, as well, that the transition to detonation in a hot spot takes place through the gradient mechanism, while the shocks and flames interactions were important for creating the proper conditions for the hot spots to occur.

To promote DDT in tubes effective measures were suggested: introducing the Shchelkin spiral in the ignition section [34], incorporating wider cavities in the ignition section [17, 28], blocking the initial part of the tube with orifice plates [35]. To bring detonation to decay detonation arrestors are used [36]. Wider cavities were discovered to provide for DDT both promoting effect and inhibiting effect depending on their number and location [37]. Combustion wave propagation in tubes incorporating cavities was investigated in papers [37-39, 56-57]. Kinetics of chemical reactions plays an essential role in deflagration to detonation transition as well. It was first demonstrated in the study [40] that contrary to existing opinion ignition of hydrogen - air mixtures at atmospheric pressure near the third limit follows the chain branching mechanism. The competition of chain branching and termination along with self-heating determine the kinetics of the process. Introducing small amounts of additives causing chains termination could essentially inhibit DDT. Experiments on detonation waves formation in a stream of fuel components demonstrated different peculiarities of ignition being the function of initiation energy [64-67]. Rapid flame acceleration was detected in the stream of mixing components ($V = 50 - 150\frac{m}{s}$) and successive formation of detonation exceeding the Chapman-Jouget parameters at a distance of [8-12] diameters with initiation energy not exceeding 20% of the energy for direct initiation.

Theoretical and experimental investigations of DDT were successfully used for evaluating pulse detonation engines and developing prototypes [54, 56-60, 69]. In particular, "Smirnov's cavities" were reported to have been effective for developing research pulse detonation engine [69].

The present investigation was aimed at revealing the effects of wider cavities, mixture composition and temperature in DDT and its control.

2 Physical and mathematical models

At present there exist three basic approaches to DDT modeling and simulation. First, its direct numerical simulation based on Navier-Stokes equations for chemically reacting mixtures, which manifests instability considered to simulate flow turbulence (review paper by Oran, Gamezo, 2007 and sources referred to in the paper [55]). The difficulty of

such modeling, especially in 3-D, brings researchers to a necessity limiting their chemistry simulation by one single stage reaction. It was still impossible to simulate directly DDT caused by flame induced turbulence, which limited the researchers to simulate third (intermediate) regime of detonation initiation: activating DDT by a secondary shock wave colliding flame zone [55]. Besides, such models could not take into account sub grid turbulence, which often brings to simulation results being in conflict with experiment. As it was mentioned in the paper [55] problems of hot spots formation and DDT sensitivity to main gas characteristics, initial temperature, pressure, geometry of the channel were still unresolved and could be a separate research project.

Another approach represents simplified quasi-one-dimensional models [72] and semi-empirical models. A typical example of the last is the supposition on proportionality of turbulent flame area and velocity to the distance from the ignition place [73]. Theoretically allowed for the present statement infinite velocity growth is cut on reaching Chapman-Jouget value, which permits evaluating predetonation length. The empirical model [73] is unable to match experiments in details as it predicts continuous acceleration, while in reality there is a velocity jump in time and space present up to an overdriven mode, and then successive slowing down to Chapman-Jouget regime. Nevertheless, even simplified models supported by proper choice of empirical parameters could be used for engineering applications.

There also exists the third approach, which unifies direct numerical simulations with use of integral turbulence models of *k-epsilon* or *k-omega* types [28, 39, 56-58]. The advantages of such approach stay in possibility to use more detailed kinetic mechanism due to decrease of spatial grid resolution, which is permitted by the use of additional transport equations describing the birth, transport and decay of turbulent energy including the sub grid level. This approach makes it possible to perform direct simulation of DDT beginning from mild ignition, through further flame acceleration due to induced turbulence and leading shock acceleration, and up to detonation onset in a hot spot. Thus we'll concentrate our attention on the last approach.

Numerical investigations of the DDT processes were performed using the system of equations for the gaseous phase obtained by Favre averaging of the system of equations for multicomponent media [57]. The modified *k-epsilon* model was used. To model temperature fluctuations the third equation was added to the *k-epsilon* model to determine the mean squared deviate of temperature [39]. The production and kinetic terms were modeled using the Gaussian quadrature technique [52].

We regarded a model hydrocarbon fuel. The present model allowed to vary hydrocarbon composition and chemical potential being the function of composition. The chemical potential of hydrocarbon fuel h_0^2 was considered to be a problem parameter, along with its composition n and m. The potential depends not only on n and m but also on particular hydrocarbon fractions the fuel consists of. The following brutto reactions between the species were considered:

$$C_nH_m + (\frac{n}{2} + \sigma\frac{m}{4})O_2 \rightarrow nCO + \sigma\frac{m}{2}H_2O + (1-\sigma)\frac{m}{2}H_2$$

$$CO + \frac{1}{2}O_2 \rightarrow CO_2$$

$$CO_2 + M \rightarrow CO + \frac{1}{2}O_2 + M$$

$$H_2 + \frac{1}{2}O_2 \rightarrow H_2O$$

$$H_2O + M \rightarrow H_2 + \frac{1}{2}O_2 + M$$

Here σ is the share of water in hydrocarbon decomposition. This parameter depends on the particular content of fuel (like the hydrocarbon chemical potential). We denote $B = 5$ – reactions number. The rates of species origination are supposed to yield the Arrhenius law and the acting masses law [39].

3 Numerical model and validating experiments

The system of gas-dynamics equations being rewritten in a vector form was split in three parts due to three different physical processes: chemistry, source terms, generalized turbulence production terms formed the "local part" of the equations; convective terms formed the "hyperbolic part" of the equations; and diffusive, viscous and thermo-cunductive terms formed the "parabolic part" of the equations.

The local part was solved implicitly using an iterative algorithm independently for each grid node. The hyperbolic part was solved using explicit FCT techniques [43]. The parabolic part was solved implicitly using 3-diagonal matrix solvers for linear equations [44]. The techniques removed viscosity from the time step criterion and reduced it to the Courant-Friedrichs-Lewy criterion.

To solve the system of equations splitting by coordinates was used according to MacCormack [45].

Following symmetry of boundary conditions simulations were performed for 2-D cylindrical grid. Detonation wave structure is essentially 3-D. Thus one should not expect 2-D simulations to provide detailed matching in terms of microstructure of detonation front. However, these simulations allow to develop macroscopical characteristics of the phenomenon.

Verification of the numerical scheme was performed by comparing the results of test runs with the exact gas-dynamics solutions and with model experiments on turbulent flames propagation in confined volumes.

The mathematical models for simulating turbulent flame acceleration and onset of detonation in chemically reacting gas were validated by comparing the results of numerical simulations for flame propagation in turbulized gaseous combustible mixtures with results of experiments [50], which provided the dependence of turbulent flame propagation velocity as a function of flow turbulence and mixture composition.

The initial values for turbulent kinetic energy and dissipation were introduced to simulate initial flow turbulization prior to ignition. The mean flow velocity was assumed zero. Two dimensional problem of flame propagation in a tube of constant cross-section filled in with $CH_3OH + 1.5\alpha(O_2 + 1.6N_2)$ gaseous mixture was regarded. The kinetic mechanism was based on the one suggested in [51] and incorporated 129 elementary stages. The results were compared with experimental observations summarized in [50].

Results of numerical simulations showed that flame propagation velocity was nearly constant and relatively small in the beginning of the process, but then it rapidly increased, presumably, due to self-turbulization effects. Thus the calculated velocity just before flame acceleration could serve as a reference data for comparison with experimental measurements [50].

Fig. 1 illustrates the experimental dependence of turbulent flame velocity on flow turbulence (solid curves provided in [50]) for two mixture compositions: $\alpha = 1.2$ and $\alpha = 2.0$. Flame velocities obtained in processing the results of our numerical simulations

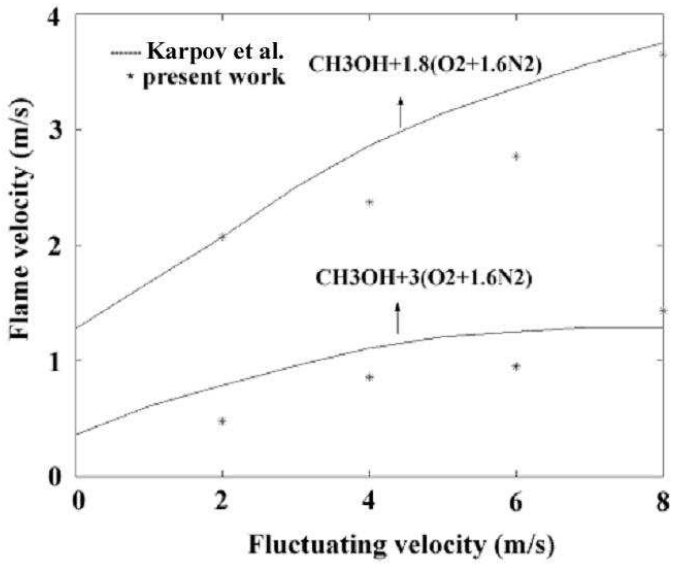

Figure 1: Comparison of numerical and experimental results for flame velocity versus turbulent velocity fluctuations: solid curves – experimental results: upper – $\alpha = 1.2$, lower – $\alpha = 2.0$, dots – numerical results of the present paper.

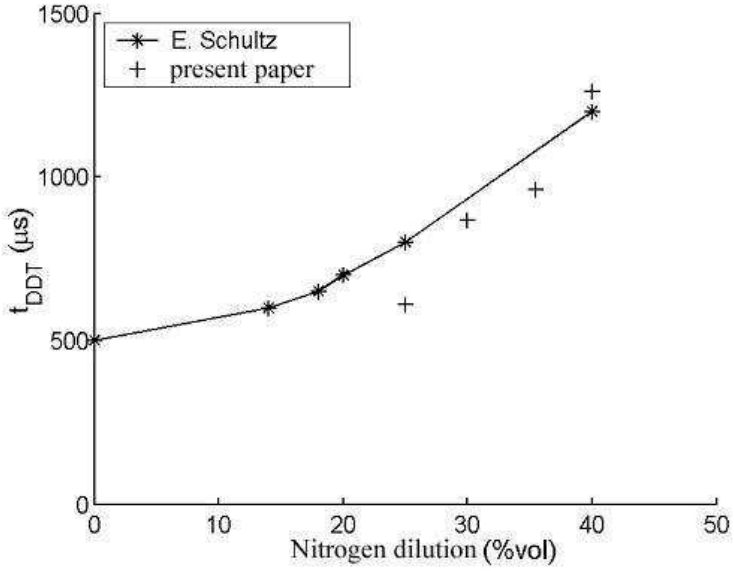

Figure 2: Comparison of numerical and experimental results for pre-detonation time in Hydrogen-oxygen mixture as a function of nitrogen dilution: solid curve – experiment, dots – numerical results of the present paper.

for both mixture compositions and different levels of turbulence are shown by stars in Fig. 1.

Fig. 2 illustrates the experimental dependence of pre-detonation time in DDT in

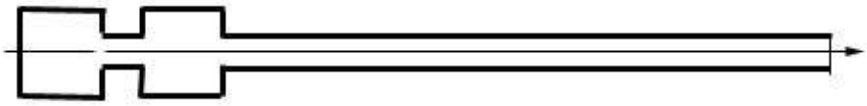

Figure 3: Detonation tube with two cavities in the ignition section.

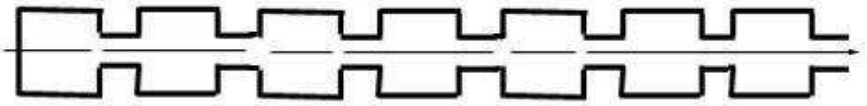

Figure 4: Detonation tube with cavities incorporated into the tube along the whole length.

Figure 5: Detonation tube with two cavities in the far end section of the tube.

hydrogen-oxygen mixtures as a function of nitrogen dilution of the mixture [54]. Numerical simulations [56, 57] performed for validating purposes used kinetic mechanism suggested in the paper [74]. Pre-detonation times obtained in our numerical simulations for four different values of nitrogen content are shown by dots. Comparison of results illustrates a good agreement of theoretical calculations and experimental data.

For further numerical simulations a simpler kinetic model was used described in the present paper and simulating a model hydrocarbon fuel. Numerical modeling was performed with an initial low level of turbulence. That allowed shortening the calculation time without any harm for precision. Numerical simulations described above showed that after mixture ignition the system quickly "forgot" about the initial level of turbulence due to flow induced turbulence in complex confined geometry.

4 Numerical investigations

In numerical simulations the test vessel contained a detonation tube with a number of cavities of a wider cross-section incorporated in different places of the tube filled in with combustible gaseous mixture at ambient pressure (Figs. 3-5). Ignition of mixture was performed by a concentrated energy release in the center of the first cavity or the tube itself in the left hand side near the closed end. The number of cavities was varied from one to twenty. The location of cavities was also the question under investigation: Simulations were performed for the following cases:

1. the initial section had two incorporated turbulizing cavities of a wider cross-section;
2. the far end section had two similar incorporated turbulizing cavities of a wider cross-section;
3. turbulizing cavities were located along the whole tube.

Table 1.

Fuel concentration	**Detonation velocity m/s**	
	Numerical	**Theoretical**
0.009		1694.2 –lean mixture–
0.010		1744.0
0.011	1735-1790	1788.6
0.012	1840-1865	1829.1
0.013		1866.1 –below stoicheometry –
0.014	1880-1920	1900.1 –above stoicheometry –
0.015	1930-1960	1931.5
0.016		1960.5
0.017		1987.0
0.018		2010.9
0.019		2031.4
0.020		2046.6
0.021		2052.7 –detonation velocity maximum–
0.022		2047.2
0.023		2033.1 –rich mixture–

The ratio of tube/cavity cross-section areas was also a parameter under investigation. Additional validation of the code was performed by calculating the parameters for the self-sustained Chapman-Jouget detonation in model gaseous mixture under consideration. The results shown in Table 1 provide theoretical data for detonation velocity as a function of fuel concentration. Velocities, obtained as results of numerical simulations of unsteady state problems using the developed code are provided along with their fluctuations.

Analyzing the results obtained for detonation velocity one could notice that maximal velocity is attained for fuel concentration higher than the stoicheometric one for the regarded model hydrocarbon fuel. The cell size for the regarded model fuel at pressure 1 bar $T_0 = 300K$ was 4-8 mm for $C_{fuel} = 0.015$, and 8-12 mm for $C_{fuel} = 0.012$.

The grid resolution was sufficient for the detonation velocity to be insensitive to further grid refinement (1 mm grid size). The Chapman-Jouget Detonation structure obtained numerically was in a good coincidence with the theoretical one, no signs of under-compressed weak detonation were noticed, which testifies the absence of ignition driven by numerical errors [27, 28].

5 The role of cavities in the ignition section

To investigate the influence of turbulizing cavities incorporated into the ignition section the test vessel contained a detonation tube with two cavities of a wider cross-section filled in with combustible gaseous mixture at ambient pressure. Ignition of the mixture is performed by a concentrated energy release in the center of the first cavity. The tube has 20 mm in diameter with two cavities 100 mm in diameter and 100 mm long incorporated in the ignition section. The bridge between the two cavities is 20 mm in diameter and 50 mm long. The results were obtained for fuel molar concentration $C_{fuel} = 0.015$ (the stoicheometric concentration is $C_{fuel} = 0.014$).

The results show that on mixture ignition in the first cavity the process of flame propagation is rather slow and is determined mostly by initial turbulization of the mixture.

The flame being initially spherical changes its form for cylindrical on approaching the walls of the cavity. The flame accelerates and penetrates the bridge between the two cavities due to a gas flow caused by the expansion of reaction products. Line segments marking gas velocity, show that a high velocity jet penetrates the second cavity prior to flame front, which brings to a very fast flame propagation both due to additional flow turbulization and the piston effect of the expanding reaction products supported by the continuing combustion in the first cavity.

Fast combustion in the second cavity brings to a sharp pressure increase that pushes the flame further into the tube. A shock wave is formed in the tube ahead of the flame zone. Pressure waves generated by continuing combustion in the cavities overtake the flame and the leading shock wave. That causes non-uniformity in the combustion zone and formation of transverse waves. At some place the detonation arises from a hot spot within the combustion zone. For the present scenario of the process the onset of detonation takes place at a distance of about 1 m from the ignition section. Before the onset of detonation hot spots appearing in the combustion zone bring to formation of compression waves irradiated form the reaction zone in all directions. Those waves support the leading shock and propagate backwards as well until the onset of detonation waves in one of successive hot spots gives birth to strong detonation and retonation waves.

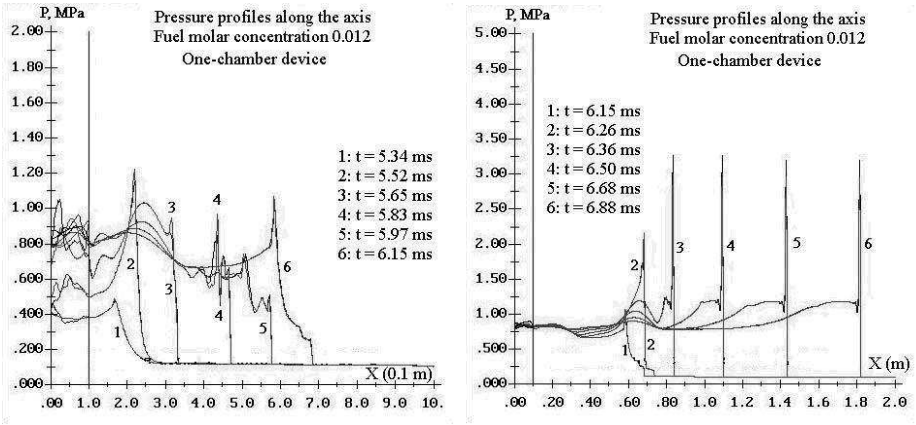

Figure 6: Pressure profiles along the axis for successive times in a device incorporating one cavity in the ignition section. Fuel volume concentration 0.012.

Pressure profiles along the tube axis for successive times are illustrated in Fig. 6. Vertical lines mark the location of cavities in the ignition section. It is seen from the figures that after onset of the detonation takes place in one of exothermic centers detonation wave overtakes the leading shock. Their interaction gives birth to an overdriven detonation, which propagates forward and gradually slows down to a Chapman-Jouget regime, and to a rarefaction wave propagating backward but being blown off by the gas flow. Thus pressure profile behind the detonation in DDT is the result of interaction of two rarefaction waves moving in opposite directions, which introduces some peculiarities as compared with classical Taylor profile.

Computational experiments allowed to explain the multiplicity of scenario for the DDT process in gases as well as experimentally observed phenomenon of the detonation onset on the contact discontinuities in the flow ahead of accelerating turbulent flame as well [27, 28]. Actually, it was observed, that flame acceleration could give birth to several shock waves ahead of the flame zone, overtaking each other. In particular, on interaction of

two shock waves ahead of flame one leading shock is formed and a contact discontinuity existing between the leading shock and flame zone and giving birth to a hot spot.

The onset of detonation on the contact surface being one of the most probable scenarios has the following explanation. In case weak shock waves precede the deflagration wave their interaction gives birth to an advancing leading shock, rarefaction wave moving backward towards the flame front and the contact discontinuity, which exists between the leading shock and the flame zone. The zone between the leading shock and the contact surface has a higher temperature. Thus the induction period in this zone is less than that between the flame front and the contact surface. The first thermal explosion takes place in the layer of gas, which has been exposed at the higher temperature for the longest time, i.e. in the gas layer on the contact surface. Depending on the flow history and induction delay gradients in the vicinity of the contact surface that explosion can bring to either deflagration or detonation waves propagating from the exothermic center. Following the gradient mechanism detonation waves propagating in opposite directions could be formed in this zone. The intensity of the retonation (reverse detonation) wave falls down on entering the reaction products. The detonation wave overtaking the leading shock forms an overdriven detonation in the uncompressed mixture that gradually slows down to the Chapman-Jouget speed.

Normal deflagration waves caused by one or several successive auto-ignitions (thermal explosions) on contact discontinuities in the pre-compressed gas, which propagate in both directions from the place of the origin, cause further compression and heating of the gas thus decreasing the induction period and leading to formation of a detonation wave. Thus the multiplicity of the "hot spots" present in the flow ahead of the accelerating flame can bring to multiplicity of scenario of the deflagration to detonation transition. The decrease of the number of cavities incorporated into the ignition section to one cavity, and then to zero cavities brings to the increase of pre-detonation length. In the absence of turbulizing cavities of wider cross-section in the ignition zone DDT could also take place, but it is very unstable: small variation of parameters could strongly influence the DDT scenario. The onset of detonation in different experiments has a sporadic character.

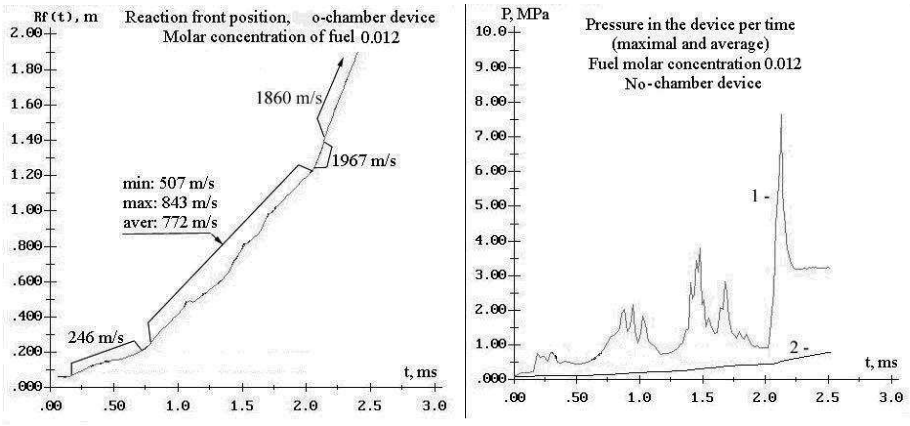

Figure 7: Reaction front trajectories (left) and pressure evolution (right) for DDT in a gaseous mixture (fuel concentration 0.012) in tubes without turbulizing cavities; 1 - maximal pressure in the device, 2 - average pressure in the device.

Fig. 7-9 illustrate flame trajectories and pressure evolution for the DDT in a tube without cavities, and with one and two cavities incorporated into the ignition section for

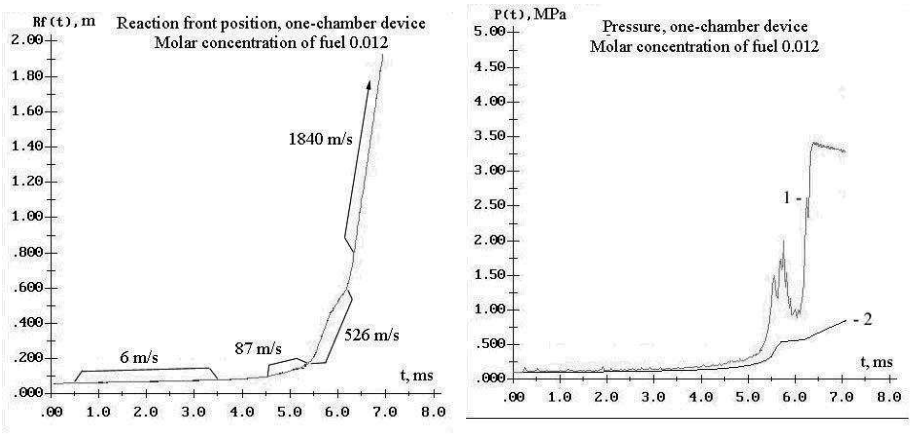

Figure 8: Reaction front trajectories (left) and pressure evolution (right) for DDT in a gaseous mixture (fuel concentration 0.012) in tubes with one turbulizing cavity; 1 - maximal pressure in the device, 2 - average pressure in the device.

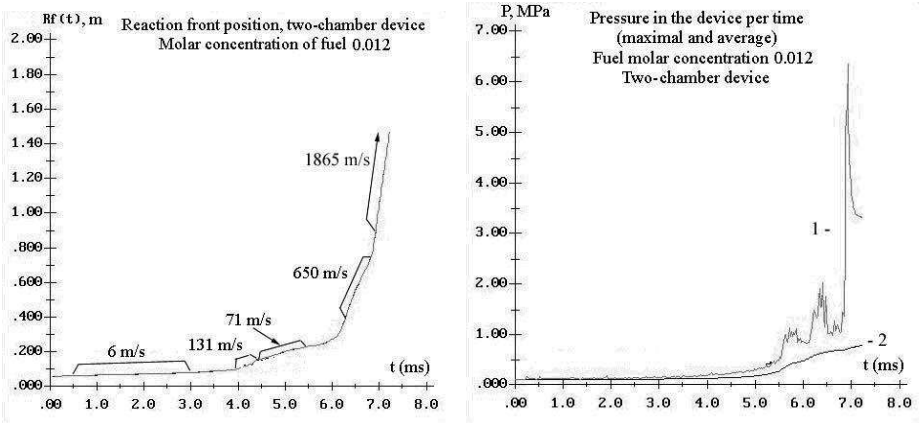

Figure 9: Reaction front trajectories (left) and pressure evolution (right) for DDT in a gaseous mixture (fuel concentration 0.012) in tubes with two turbulizing cavities 1 - maximal pressure in the device, 2 - average pressure in the device.

fuel concentration $C_{fuel} = 0.012$. Comparison of the velocities and trajectories shows that incorporating cavities in the ignition section promotes the DDT. Incorporating turbulizing cavities brings to more slow flame propagation in the very beginning of the process due to an increase of volume, but then leads to a stable detonation initiation and its coming to a self-sustained regime. While in the absence of turbulizing cavities flame propagation is much faster and irregular in the very beginning of the process. That is due to the fact that similar initiation energy is being redistributed within a smaller volume thus providing an initiating piston effect, which is not too strong to cause the onset of detonation, but sufficient to initiate irregular galloping combustion mode. The onset of detonation takes place at a distance of 1.2 m from the beginning of the tube, which is higher than for the case of one or two cavities incorporated into the ignition section. However, shortening the run-up distance could also bring to the increase of the time for DDT, could be important in limiting the maximum PDE operating frequency.

Using cavities in the ignition made the transition more reproducible, which is im-

portant for PDE applications. The onset of detonation in a tube without cavities is an irreproducible stochastic process, and each pulsation of velocity depending on some additional disturbance could result in the onset of detonation. Thus pre-detonation length for such an irreproducible transition processes, as we saw in a tube without cavities in the ignition section, could be less or much larger than the one obtained in the regarded numerical experiment.

6 The influence of wide cavities at the end of the tube

To provide a comparative data here we investigated the role of two cavities of a wider cross-section incorporated in the far end of the tube (Fig. 5). The tube was identical to that used in numerical experiments described in the previous section, but ignition was performed at the opposite side (symmetrical in respect to 180^0 rotation). To have a guaranteed detonation formation the ignition energy was 2.5 times higher than that in the above experiments. The ignition source was located at the tube axis.

Numerical results showed that after ignition in a narrow tube acceleration of flame zone accompanied by a number of oscillations brought to formation of the detonation wave propagating with mean velocity $1850\frac{m}{s}$. On entering the first cavity decoupling of the shock wave and reaction zone took place and the mean velocity of reaction zone propagation decreased to $200\frac{m}{s}$, then in a narrow bridge flame accelerated up to $400\frac{m}{s}$, and slowed down in the second cavity to $100\frac{m}{s}$. The average velocity in the cavities was $140\frac{m}{s}$. Decoupling of shock wave and reaction zone took place due to the fact that geometrical factor, which is the ratio of critical detonation exit diameter to the original tube diameter [29] was more than unity.

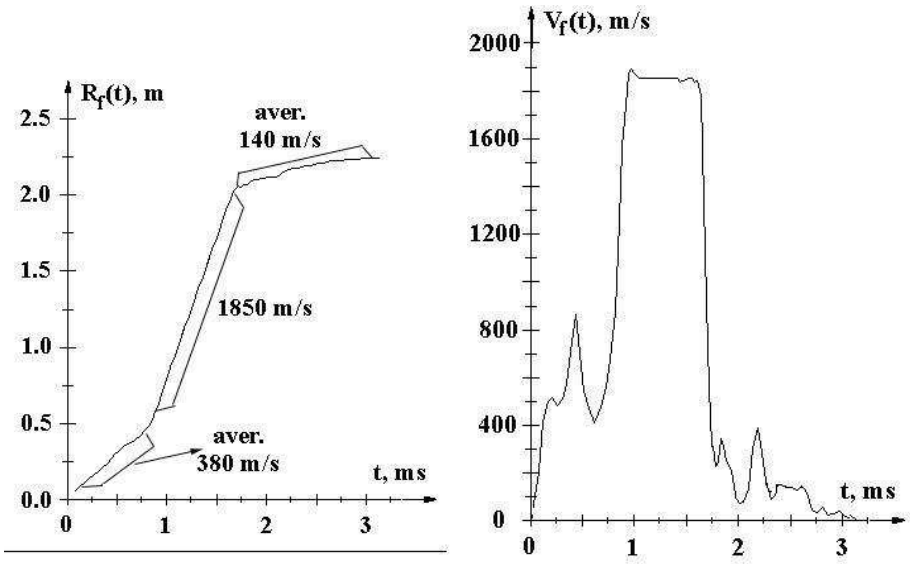

Figure 10: Reaction front trajectory and velocity for fuel volumetric concentration 0.012: in a tube incorporating two turbulizing cavities of a wider cross-section at the end.

Fig. 10 illustrates reaction front velocity variation versus time for the detonation onset and degeneration in a tube with two cavities at the end. Fuel concentration in the mixture was 0.012, which corresponds to results of numerical experiments illustrated in Figs. 6 and 7-9.

The results show, that normal detonation wave propagating close to Chapman-Jouget velocity on entering a set of cavities of a wider cross-section degenerated to a galloping combustion mode (Fig. 10), which was characterized by a low subsonic velocity of reaction front propagation in the axial direction.

7 The influence of wider cavities incorporated into the tube along the whole length

The results of previous investigations showed that incorporating one or two cavities of a wider cross-section into the beginning of the tube, where ignition takes place, stabilize the DDT process and shorten the pre-detonation length. To investigate the influence of the cavities number increase on the onset of detonation numerical experiments were undertaken for the structure (Fig. 4) incorporating 20 similar cavities 100 mm diameter and 100 mm long incorporated into the tube 20 mm diameter with the intervals 50 mm. The length of the structure turned to be 2.95 m.

The results showed that for the fuel concentration $C_{fuel} = 0.012$ the DDT process did not take place at all. The galloping combustion mode was established characterized by velocity oscillations within the range $80-300\frac{m}{s}$, average velocity of flame front being $156\frac{m}{s}$. The results of numerical experiments show, that increasing the number of turbulizing cavities did not promote the DDT for the present configuration, but just the opposite, it prevented from the onset of detonation and brought to establishing of the galloping combustion mode. The effect took place due to very sharp jumps of the cross-section area in the cavities and periodical slowing the flame down due to its expansion (Fig. 11).

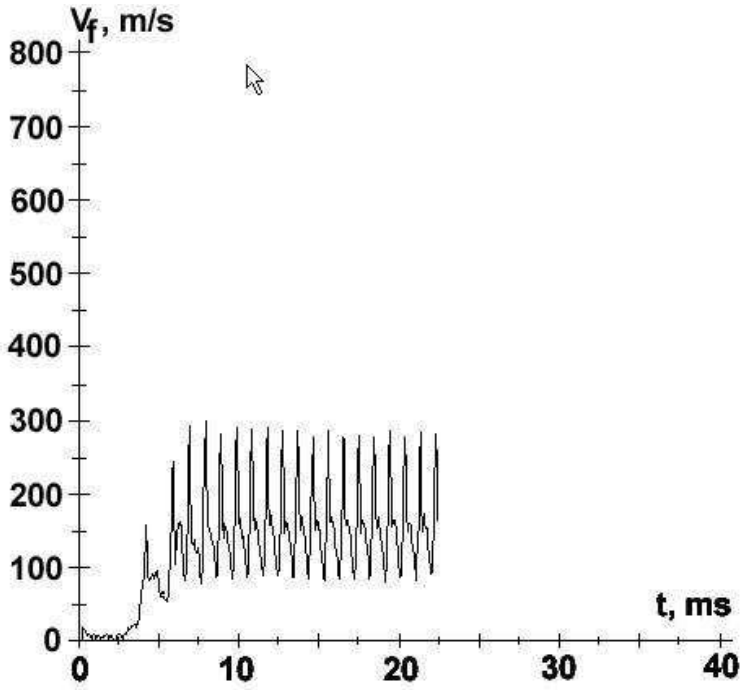

Figure 11: Combustion front velocity versus time for the case of cavities being incorporated along the whole tube $\beta_{ER} = 0.96$.

To characterize the cross-section area jumps within the structures of such type one

could use the expansion ratio parameter and the volume ratio parameter

$$\beta_{ER} = \frac{S_{chamb} - S_{tube}}{S_{chamb}}; \quad \alpha_{ER} = \frac{S_{chamb}L_{chamb} + S_{tube}L_{tube}}{S_{chamb}(L_{chamb} + L_{tube})} = 1 - \frac{\delta\beta_{ER}}{1+\delta};$$

$$\delta = \frac{L_{tube}}{L_{chamb}},$$

where S_{chamb} is a cavity cross-section area, S_{tube} is the cross-section of the tube, L_{tube} is the length of a bridge connecting the two cavities, L_{chamb} is the length of a cavity of a wider cross-section. In our experiment the expansion ratio was very high ($\beta_{ER} = 0.96$), that could promote flame acceleration in the beginning of the tube, but blocked it in other parts.

Evaluating the effect of turbulizing cavities of wider cross-section incorporated into a detonation tube on the DDT process, it should be noted that the presence of fore-cavities in the ignition section of the tube promotes flame acceleration and stabilizes DDT. On the other hand the established detonation wave could degenerate on entering the cavity of large expansion ratio, which brings to the suppression of detonation. What is the optimal number of cavities to be integrated into the ignition section, which could promote DDT? Numerical modeling undertaken for the expansion ratio $\beta_{ER} = 0.96$ shows that two cavities were enough for the adopted values of governing parameters.

Theoretical explanation for the effect is based on the necessary condition for the DDT to be satisfied - the Zeldovich criterion for the so-called coupling of gas dynamics processes (compression waves generation ahead of the flame) and chemical physics and transport phenomena, which govern the flame front propagation [20, 24, 48, 49]. This criterion, actually, means that flame propagation velocity should exceed the speed of sound in the unburned gas mixture. Analysis of results shows that the piston effect of expanding reaction products in fore-cavities brings to a rapid acceleration of the flame on entering a narrow tube. On leaving the first cavity and entering the narrow tube between the two cavities flame accelerates up to velocities $110 - 260\frac{m}{s}$ depending on fuel concentration, which turns to be less then sonic velocity. On leaving the second cavity flame is pushed into the detonation tube at a speed of $435 - 920\frac{m}{s}$, which already surpasses the necessary criterion. Thus further increase of the number of cavities is no longer necessary.

8 Conclusions

Results of investigations show that the onset of detonation wave in DDT process takes place in local exothermic centers ("hot spots") between the accelerating zone of turbulent combustion and the leading shock wave. Those hot spots appear due to flow non-uniformity mostly on the contact discontinuities, formed due to the interaction of flame and shock waves overtaking each other ahead of flame zone.

In case of detonation onset the detonation wave propagates in all directions from the source and finally forms detonation wave propagating ahead and retonation wave propagating backward. The detonation wave overtakes the leading shock and after their interaction a quasi-plane overdriven detonation wave is formed in the unburned mixture, which gradually slows down to a self-sustained Chapman-Jouget mode.

The presence of several cavities of a wider cross-section in the ignition zone shortens the pre-detonation length for hydrocarbon-air gaseous mixtures and makes the onset of detonation more stable.

The increase of the number of similar cavities uniformly distributed along the tube could block the onset of detonation and lead to establishing of galloping highs speed combustion modes for large expansion ratios, or low velocity galloping detonations for small expansion ratios. The increase of the number of turbulizing cavities in the ignition section promotes DDT until flame velocity on leaving the last cavity surpasses sonic velocity. The further increase of the number of cavities inhibits DDT.

Acknowledgments

Russian Foundation for Basic Research (grant 11-03-00213), is acknowledged for financial support.

References

[1] Mallard E., Le Chatelier H.L. Compt. Rend. Acad. Sci. Paris, v. 93, (1883) 145.

[2] Berthélot M., Vieille P. Compt. Rend. Acad. Sci. Paris, v. 93, (1883) 18.

[3] Mikhelson V.A. On normal combustion velocity of explosive gaseous mixtures. Imperial Moscow University Scientific Bulletin. Phys. & Math. Ser., 10, (1893) 1-92.

[4] Rankine W.J.M. On the thermodynamic theory of waves of finite longitudinal disturbance, Phil. Trans. (1870), 277-288.

[5] Hugoniot H. Journ. Liouville. v.3, (1887), 477-492; v. 4, (1888), 153-167.

[6] Chapman D.L. On the role of explosion in gases, Phil. Mag. v. 47, (1899) 90.

[7] Jouget E.J. Mathematics. 1905, p. 347.

[8] Bishimov E., Korobeinikov V.P., Levin V.A., Cherny G.G. (1968) One dimensional unsteady state flows of combustible mixtures accounting for final rate of chemical reactions. Fluid Dynamics, No 6, 7-19.

[9] Levin V.A., Markov V.V. (1975) Onset of detonation in concentrated energy input. Combustion, Explosion and Shock waves, vol. 11, No 4, 623-629.

[10] Levin V.A., Markov V.V., Osinkin S.F. (1992) Direct initiation of detonation in hydrogen - oxygen mixtures diluted by nitrogen. Fluid Dynamics, No 6, 151.

[11] Hayashi A.K., Shimada H., Kenmoku Y., Sato H. Detailed mechanism of flame jet ignition in pulse detonation engines. Application of Detonation to propulsion (Roy, Frolov, Shepherd - Eds.), Moscow: Torus Press Ltd. 2004, 207-211.

[12] Salamandra G.D. On interaction of a flame with a shock wave. In: Physical Gasdynamics, USSR Acad. Sci. Publ., 1959, 163-167.

[13] Bazhenova T.V., Soloukhin R.I. Gas ignition behind the shock waves. Internat. VII Sympos. on Combust., Buttterworths, London, 1959.

[14] Oppenheim A.K., Urtiew P.A. Experimental observations of the transition to detonation in an explosive gas, Proc. Roy. Soc., A295, (1966) 13.

[15] Soloukhin R.I. Methods of measure and main results of experiments in shock tubes. Novosibirsk State University Publ., Novosibirsk. 1969.

[16] Oppenheim A. K., Soloukhin R. I. Ann. Rev. Fluid Mech., 5, (1973) 31.

[17] Smirnov N.N., Boichenko A.P. Deflagration to detonation transition in gasoline-air mixtures, Combustion, Explosion and Shock Waves, 22, 2, (1986) 65 - 68.

[18] Lindstedt R. P., Michels H. J., Deflagration to detonation transition in mixtures of alkane LNG/LPG constituents with, Combustion and Flame, 72, 1, (1988) 63 - 72.

[19] Smirnov N.N., Tyurnikov M.V. Experimental Investigation of Deflagration to Detonation transition in hydrocarbon-air gaseous mixtures, Combustion and Flame, 100, (1995) 661-668.

[20] Zeldovich Ya. B., Librovich V.B., Makhviladze G.M. and Sivashinsky G.I. On the onset of detonation in a non-uniformly pre-heated gas. Sov. J. Applied Mechanics and Technical Physics, 2, (1970) 76.

[21] Merzhanov A.G. On critical conditions for thermal explosion of a hot spot. Combustion and Flame, 10, (1966) 341-348.

[22] Borisov A.A. Acta Astronautica, 1, (1974) 909-920.

[23] Kailasanath K. and Oran E.S. Ignition of flamelets behind incident shock waves and the transition to detonation. Combustion Science Technology, 34, (1983) 345-362.

[24] Zeldovich Ya.B., Gelfand B.E., Tsyganov S.A., Frolov S.M., Polenov A.N. Concentration and temperature non-uniformities of combustible mixture as a reason of pressure waves generation. In: Dynamics of Explosions (A Kuhl et al. Eds.) AIAA Inc., New York, 114, (1988) 99.

[25] Smirnov N.N., Demyanov An.Yu., Panfilov I.I. Deflagration to detonation transition, Chemical Physics of Comb. and Expl.: Detonation. USSR Acad. Sci. Publ., 1989, 52-56.

[26] Wolanski P., Archivum Combustions, 3 - 4, (1991) 143 - 149.

[27] Smirnov N. N., Panfilov I. I., Deflagration to detonation transition in combustible gas mixtures, Combustion and Flame, v. 101, (1995) 91 - 100.

[28] Smirnov N.N., Nikitin V.F., Boichenko A.P., Tyurnikov M.V., Baskakov V.V. Deflagration to detonation transition in gases and its application to pulse detonation devices. In: Gaseous and Heterogeneous Detonations: Science to Applications (G.D.Roy et. al. Eds.) Moscow, ENAS Publ. 1999, pp.65-94.

[29] Smirnov N.N. and V.F.Nikitin, Comb. Exp. Shock Wave 40 (2):186-199, 2004

[30] Gostintsev Yu.A., Istratov A.G., Fortov V.E. Proc. RAS, 1997, 353, 1, 55-57.

[31] Gostintsev Yu.A., Istratov A.G., Kidin N.I., Fortov V.E. Thermophysics of High Temperatures, 1999, 37, 2, 306-312.

[32] Brown C.J., Thomas G.O. Experimental studies of shock-induced ignition and transition to detonation in ethylene and propane mixtures. Combustion and Flame, 117, (1999) 861-870.

[33] Khohlov A.M., Oran E.S. Numerical simulation of detonation initiation in a flame brush: the role of hot spots, Combustion and Flame, 119, (1999) 400-416.

[34] Shchelkin K.I., Troshin Ya.K. Gasdynamics of Combustion. USSR Academy Sci. Publ., Moscow. 1963.

[35] Knystautas R., Lee J.H.S., Shepherd J.E., Teodorczyk A. Flame acceleration and transition to detonation in benzene-air mixtures. Combustion and Flame, 115, (1998) 424-436.

[36] Fischer M., Pantow E., Kratzel T. Propagation, decay and re-ignition of detonations in technical structures. In: Gaseous and Heterogeneous Detonations: Science to Applications (G.D.Roy et. al. Eds.) Moscow, ENAS Publ. (1999) pp.197-212.

[37] Smirnov N.N., Nikitin V.F., The Influence of Confinement Geometry on Deflagration to Detonation Transition in Gases. J. Phys. IV France, 12, Pr7, (2002) 341-351.

[38] Abdullin R.H., Babkin V.S., Borisenko A.V., Senachin P.K. (1997) Combustion of gas in a linear system of connected vessels. Preprint Altay Tecn. UNiv. Barnaul, 3-55.

[39] Smirnov N.N., Nikitin V.F., Tyurnikov M.V., Boichenko A.P., Legros J.C., Shevtsova V.M. Control of detonation onset in combustible gases. In: High Speed Deflagration and Detonation. (G.D. Roy et al. Eds.) Moscow, Elex-KM Publ., (2001) 3-30.

[40] Azatyan V.V. (1996) The role of chain branching mechanism in ignition and combustion of hydrogen-oxygen mixtures near the third limit. Kinetics and Catalysis, vol. 37, No 4, 512-520.

[41] Philip M. Dissertation "Experimentelle und theoretische Untersuchungen zum Stabilitatsverhalten von Drallflammen mit zentraler Ruckstromzone". Karlsruhe University. 1991.

[42] Pironneau O. and Mohammadi B. Analysis of the K-Epsilon turbulence model. Masson Editeur, Paris, 1994.

[43] Oran E.S., Boris J.P., Numerical simulation of reactive flow. Elsevier, New York. 1987.

[44] Smirnov N.N., Nikitin V.F. Unsteady-state turbulent diffusive combustion in confined volumes. Combustion and Flame, 111, (1997) 222 - 256.

[45] Anderson D.A., Tannehill J.C., Pletcher R.H., Computational Fluid Mechanics and Heat Transfer. Hemisphere Publ. Co. 1984.

[46] Laffitte P. Influence of temperature on the formation of explosive waves. Comp. Rendu, 186, (1928) 951.

[47] Bollinger L.E., Fong M.C., Edse R. Experimental measurement and theoretical analysis of detonation induction distance. ARSJ, 31, (1961) 588.

[48] Cheng R.K., Short J.M. Diagnostics of the exothermic process.(1977) Progr. Astronaut. Aeron. N.-Y. AIAA Inc. V. 53, 611.

[49] Dold J.W., Short M. (1991) Compressibility corrections to Zeldovich's spontaneous flame and the onset of an explosion in a non-uniformly pre-heated medium. Proc. 13-th ICDERS, Nagoya, p.63.

[50] Karpov V.P., Politenkova G.G., Severin E.S., Turbulent burning of alcohol. Combustion, Explosion, Shock waves, 22, N 4: 12-14, 1986.

[51] Marinov N.M. A Detailed Chemical Kinetic Model for High Temperature Ethanol Oxidation, Int. J. Chemical Kinetics, 31: 183-220, 1999.

[52] Hamming R.W. Numerical methods for engineers and scientists. Second Ed. New York, Dover: 1986.

[53] Press W.H., Teukolsky S.A., Vetterling W.T., Flannery B.P. Numerical receipts in C. Second edition. Cambridge University Press: 1992.

[54] Schultz E., Wintenberger E., Shepherd J., Investigation of deflagration to detonation transition for application to pulse detonation engine ignition systems,16th JANNAF Propulsion Meeting, 1999.

[55] Oran E.S., Gamezo V.N. (2007) Origins of the deflagration to detonation transition in gas-phase combustion. Combustion and Flame, 148, 4-47.

[56] N. N. Smirnov, V. F. Nikitin, S. Alyari Shurekhdeli. Transitional Regimes of Wave Propagation in Metastable Systems. Combustion, Explosion, and Shock Waves, Vol. 44, No. 5, pp. 517-528, 2008.

[57] N. N. Smirnov, V. F. Nikitin, S. Alyari Shurekhdeli. Investigation of Self-Sustaining Waves in Metastable Systems: Deflagration-to-Detonation Transition. Journal of propulsion and power. Vol. 25, No. 3, 2009 pp. 593-608.

[58] Smirnov N.N., Shemyakin E.I. Combustion to explosion transformation in meta-stable media. Modern problems of Mathematics and Mechanics. Moscow: MSU Publ., 2009, v.1, pp. 245-275.

[59] V.F. Nikitin, V.R. Dushin, Y.G. Phylippov, J.C. Legros. Pulse detonation engines: Technical approaches.Acta Astronautica 64 (2009) 281-287.

[60] Nikitin V.F., Smirnov N.N., Phylippov Yu.G., Shemyakin E.I. Detonation onset in transmission from a ring gap into a chamber. Moscow Univ. Mech. Bull., Allerton Press 2009, 3, 67-72.

[61] M. A. Liberman, M. Kuznetsov, I. Matsukov, A. Ivanov, Restructuring of a flame due to a preheated zone as a mechanism underlying the deflagration-to-detonation transition, (22nd ICDERS, 3), Minsk, 2009.

[62] M. A. Liberman, M. Kuznetsov, I. Matsukov, A. Ivanov, Formation of the preheated zone ahead of a propagating flame and the mechanism underlying the deflagration-to-detonation transition, Physics Letters A 373, 501-510 (2009).

[63] Markstein G.H. (1964) Nonsteady flame propagation. Macmillan, New York.

[64] Bazhenova T.V., Golub V.V. Utilization of gaseous detonation in a controlled high frequency regime (review) Combustion, Explosion, and Shock Waves, Vol. 39, 2003. 4. 3-21.

[65] Baklanov D.I., S.V. Golovastov, L.G. Gvozdeva, A. Kaltayev, N.B. Scherbak, V.V. Volodin. Investigation of Transition of Deflagration to Detonation in Moving Mixtures of Combustible Gases. In: CD of Proceedings of 20th International Colloquium on

Dynamics of Explosions and Reactive Systems, Montreal, Canada, July 31 - August 5, 2005.

[66] Baklanov D.I., Gvozdeva L.G., Scherbak N.B. Pulsed detonation combustion chamber for PDE. In: High-Speed Deflagration and Detonation: Fundamentals and Control. Ed. by G.D. Roy and others. Moscow: ELEX-KM Publishers, 2001, P. 239-250.

[67] Baklanov D.I., S.V. Golovastov, V.V. Golub, V.V. Volodin. Detonation formation in moving detonable mixture flow. Application of Detonation to Propulsion. [Ed. by G. Roy at al.]. - Moscow: TORUS PRESS LTD., 2004. Pp.225-231.

[68] Achasov O.V., Penyazkov O.G. Some gasdynamic methods for control of detonation initiation and propagation. In: High-Speed Deflagration and Detonation: Fundamentals and Control. Ed. by G.D. Roy and others. Moscow: ELEX-KM Publishers, 2001, P. 31-44.

[69] Schauer F., Stutrud J., Bradley R., Katta V., Hoke J. Detonation studies and performance results for a research pulse detonation engine. [Ed. by G. Roy at al.]. - Moscow: TORUS PRESS LTD., 2004, pp. 287-302.

[70] Clarke J. F., Kassoy D. R., Riley N., (1986). On direct initiation of a plane detonation wave. Proceedings of Royal Society, A408, 129 - 148, London.

[71] Kassoy, D.R., Kuehn, J.A., Nabity, M.W., Clarke, J.F., (2006) Detonation initiation on the microsecond time scale: DDTs, Collection of Technical Papers - 44th AIAA Aerospace Sciences Meeting 15, pp. 11453-11512.

[72] Kaltajev A, J. Leblanc and T. Fujiwara. Influence of Turbulence on the Deflagration to Detonation Transition in a Tube. 17th International Coll. on the Dynamics of Explosions and Reactive Systems. Heidelberg, Germany, July 31- August 5, 1999.

[73] Sabdenov K.O. Thermo-physical hydro-gas-dynamical effects in combustion of gases and rocket propellants. Dissertation Doctor of Science (2007) Tomsk, Tomsk State University.

[74] Starik A. M., Titova N. S., Initiation of detonation in a supersonic flow behind a shock wave under non-equilibrium excitation of vibrational degrees of freedom of molecules, In: G. D. Roy et al. (Eds.), Gaseous and Heterogeneous Detonations, ENAS Publ., Moscow, pp.225-240, 1999.

[75] Powell D., Van Tiggelen P.J., Vasatko H., Wagner H.G. Initiation of detonation in various gas mixtures. Combustion and Flame (1970) v.15 p. 173-177.

[76] Oppenheim A.K., Stern R.A. On the development of gaseous detonation. Analysis of wave phenomena. Seventh Sympos (Internat) on Combust. London: Butterworths (1959) p. 837-850.

[77] Salamandra G.D., Bazhenova T.V., Naboko I.M. Journal of Theoretical Physics. 1959. V. 29. Issue 11. P. 1354.

Nikolay N. Smirnov, Faculty of Mechanics and Mathematics, Moscow M.V. Lomonosov State University, Moscow 119992, Leninskie Gory 1, RUSSIA

Simulation of structural transformations in copper nanoparticles under collision

Aleksey Yu. Smolin Nikita V. Roman Konstantin P. Zol'nokov
Sergey G. Psakhie Valery K. Kedrinskii
asmolin@ispms.tsc.ru

Abstract

The copper nano-sized particles collision under various loading condition was studied in the paper. The special attention was paid to changes in structure of the particles. The numerical investigations were performed by molecular dynamics method. The inter-atomic interaction was described within the embedded atom method. The initial particles were of ideal crystal structure, spherical shape, radius of 6–15 nm. The velocity of collision was varied from 200 up to 1000 m/s, rotation of the particles with the speed up to $1.5{\cdot}10^{13}\,\mathrm{s}^{-1}$ was applied in some calculations. It was shown that specific changes in initial ideal crystal structure of the particles took place under interaction, and the shape of the final particle was not symmetric one. The changes in potential energy of the particles, structural transformation from one type of the crystal lattice to another one as well as quasi-amorphous regions formation were studied in detail.

Simulation of nanoparticles collision is an actual problem having many practical applications such as surface treatment, new materials manufacturing, etc. Here it is important to consider the structural transformation in material of the particles. In particular, for the powder coating on the substrate it is required to increase the degree of mechanical activity of both the particles and the substrate. In addition, the collision process of powders in high cumulative flows is one of the most promising techniques for the synthesis of nanoparticles of complex composition, as well as nanoparticles with a block structure having novel properties [1, 2].

3D case of nano-particles collision was studied using molecular dynamics method [3, 4]. Inter-atomic interaction was described within the embedded atom method (Mishin's potential) and corresponded to copper. This approach allows to describe elastic properties, energy of structural defects, surface energy, melting temperature and other properties with high level of accuracy [5, 6, 7].

In [5] calculations were performed for a wide range of collision velocities of copper clusters with a diameter 1 and 2 nm. It was shown that depending on the size and velocity of nanoclusters the two modes of repulsion or association were possible. The conditions of bound state formation and the parameters characterizing the interaction were established. In particular, it was shown that in such nano-objects kinetic temperature in the contact area under collision did not reache melting point and the resulting relationship is determined exclusively by the interaction potential.

In this paper the particle size was much large and varied from 6 up to 15 nm. At that the velocity of each particle varied from 100 up to 1000 m/s. The initial particles had almost spherical shape and ideal crystal structure under zero temperature. The changes in potential energy and crystal structure of the particles, also as transformation from one

type of crystal structure to another one and formation of quasi amorphous region was analyzed.

At the first step central collision of particles was investigated. Calculations showed that the final shape of the particles formed under collision varied from dumbbell to the disk-like depending on the velocity and the size of the initial nanoparticles. In collisions of nanoparticles with velocities ranging from 500 m/s and higher their initial ideal structure undergoes irreversible changes (Fig. 1,c). Nevertheless, after "annealing" at finite temperatures fragments of crystal structure appeared in the resulting nanoparticle. In Fig. 1,d small dots show the atoms not forming any srystal structure, and large gray spheres show atoms, forming a face-centered cubic (fcc) structure.

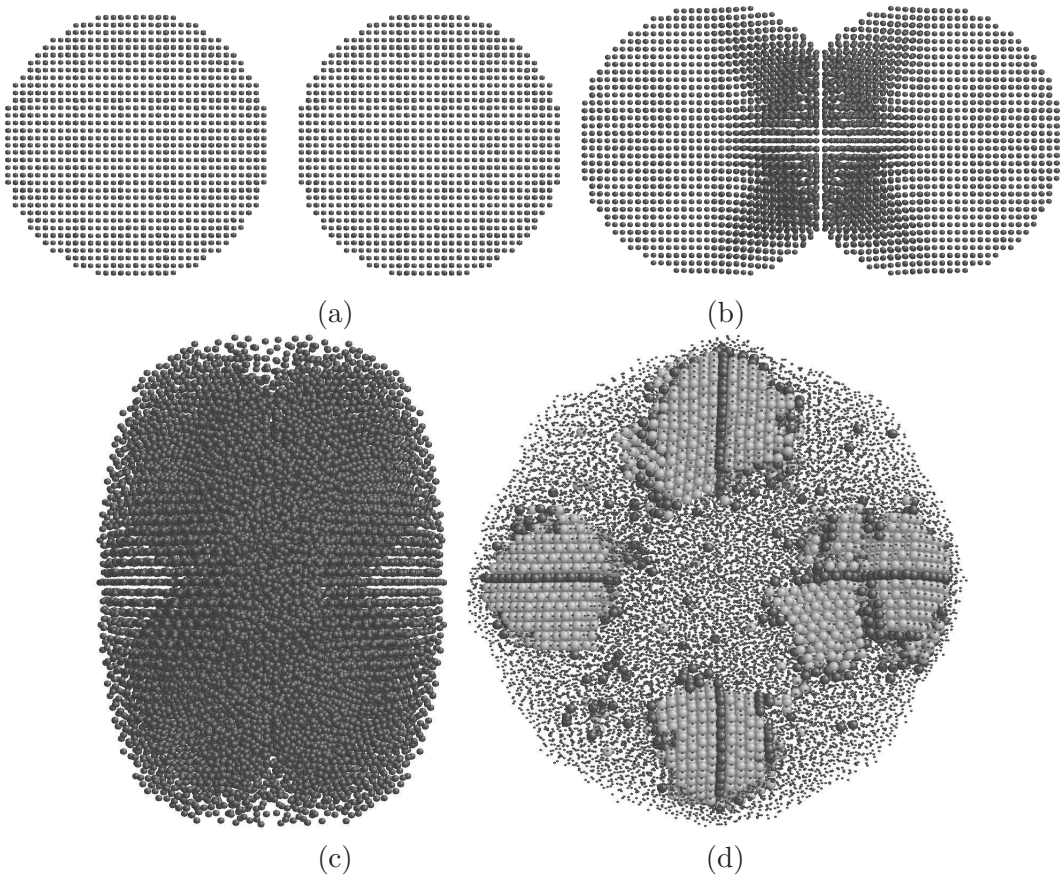

Figure 1: Nanoparticle structure at different times of collision: a) t=0; b) t=1.1 ps; c) t=3.4 ps; and after "annealing" at 100°K and relaxation to $T = 0$°K (d)

It should be noted that because of their crystalline structure the original simulated nanoparticles, strictly speaking, had not perfect spherical shape but regular polyhedra. Therefore, the thresholds velocities at which the nanoparticles are deformed irreversibly, depend on how they touch under collision (by faces, edges, vertices, etc.).

The resulting nanoparticle fragmented after relaxation was rather stable and deffered from initial nanoprticles by redundant potential energy (Fig. 2).

At the second step of the study special attention was paid to the influence of particles rotation on the change in their structure during the impact. Linear velocity of the collision of the particles varied in the range from 200 to 1000 m/s, and their angular velocity from 0 to $1.5{\cdot}10^{13}\,\mathrm{c}^{-1}$.

Fig. 3 shows the calculation results of two particles collision when one (right) is mov-

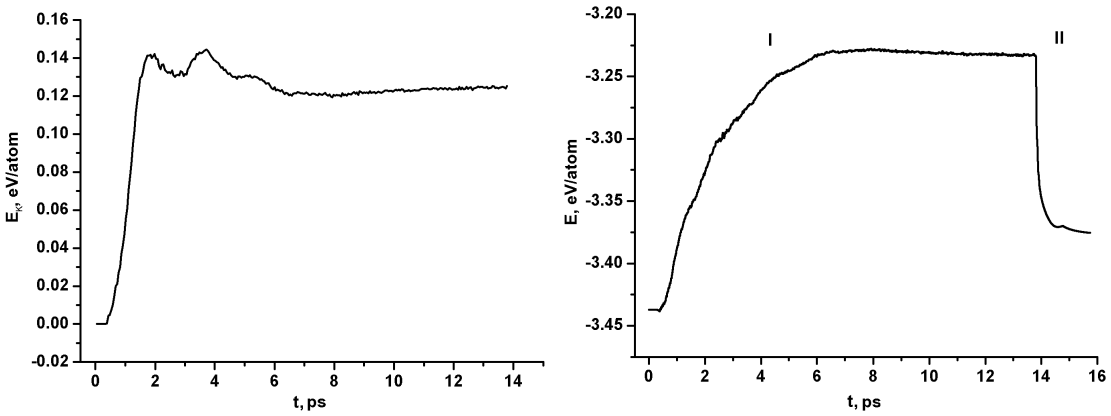

(a) (b)

Figure 2: Plot of kinetic temperature of nanoparticles under collision and further evolution (a) and plot of their potential energy versus time at evolution (I) and relaxation (II) at 100°K with consequent cooling to 0°K (b)

ing steadily with a velocity of 1000 m/s, and the second rotates with angular velocity $1.5{\cdot}10^{13}\,\mathrm{c}^{-1}$. One can see that after the collision structure of nanoparticles degenerates from an ideal fcc crystal structure into a "mixture" of the fcc, hexagonal close-packed (hcp) and quasi-amorphous structure. Moreover, the atoms forming the hcp structure, are located in parallel planes, dispersed in space relatively to each other. The maximum concentration of a quasi-amorphous structure is attained in the zone of direct interaction between the nanoparticles.

Calculations showed that the shape of final nanoparticle can vary significantly depending on the angular and linear velocities of the collision. Obviously, that due to rotation of one of the particles the final shape of the resulting nanoparticle is not symmetric (Fig. 3) in contrast from the collision without rotation (Fig. 1).

Based on calculations conducted, one can conclude that as a result of collisions of copper nanoparticles of 6–15 nm in diameter at velocity above 500 m/s, their structure undergoes irreversible changes. The original crystal structure of nanoparticles is completely destroyed, subsequent relaxation leads to formation of fragmented crystal structure. The resulting nanoparticles after the relaxation processes have redundant potential energy, whose value depends on several factors, such as the geometric dimensions of the initial nanoparticles, the velocity of their collision, the relaxation and annealing temperature. The presence of rotation can play a very important role. For example, such collisions produce a larger part of the amorphous structure, which has a high degree of mechanical activity. In particular, this effect may be useful in the deposition, production of activated powders, etc.

Thus we have shown that as a result of high-velocity collision it is possible to arrange the synthesis of nanoparticles with a blocked crystalline structure having new properties, the production of which by conventional methods is difficult or impossible. The use of such nanoparticles is promising in various directions of high technology, particularly in the chemical processes (e.g. catalysis), and the development of new structural and functional materials with special physical properties (e.g., magnetic). As a further development of the above studies it is interesting to consider the interaction of particles of different material and particles with various defects such as vacancies and interstitial atoms.

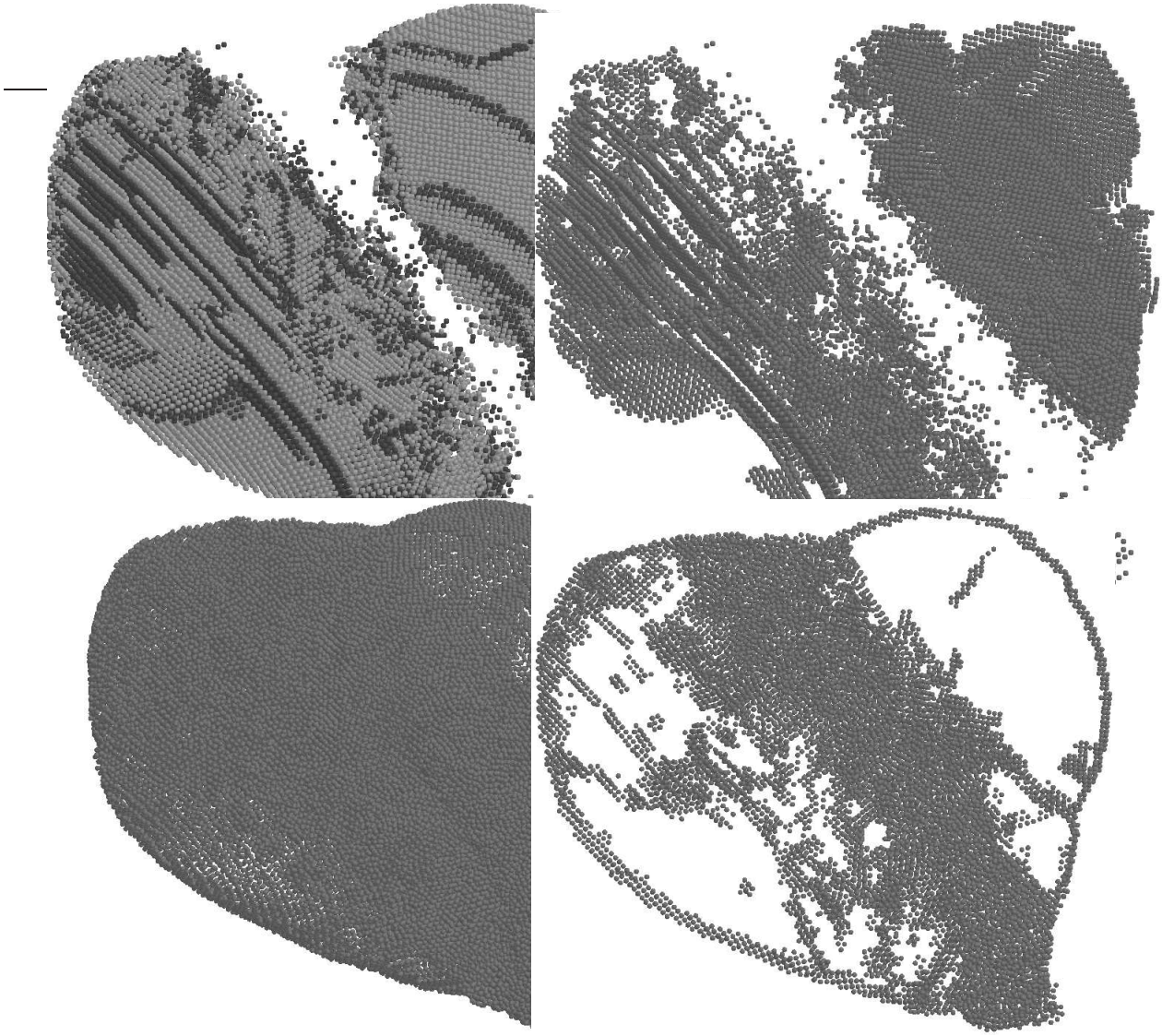

(c) (d)

Figure 3: Atomic structure after collision of two particles. Only atoms forming certain structures are shown: a) fcc and hcp, b) fcc, c) quasi-amorphous structure, d) section of quasi-amorphous structure by YZ-plane.

Acknowledgements

This work was supported by the interdisciplinary integration project No 32 of SB RAS for 2009–2011. The authors thank S.Yu Korostelev and D.S. Kryzhevich for assistance in the calculations.

References

[1] S.A. Kinelovskii, S.A. Gromilov. Fizika gorenia i vzryva 38, No 1. 129 (2002). in Russian

[2] S.A. Kinelovskii, S.A. Gromilov. Zhurnal strukturnoy khimii. 44, No 3. 486 (2003). in Russian

[3] R.W Hockney, J.W Eastwood. Computer Simulation Using Particles. Taylor & Francis. 1989. 540 p.

[4] LAMMPS Molecular Dynamics Simulator URL: http://lammps.sandia.gov/ (access date: 30.03.2011)

[5] A.V. Berch, A.G. Lipnitskii, E.V. Chulkov. Poverkhnost. No 6. 23 (1994). in Russian

[6] G.G. Rusina, A.V. Berch, I. Yu. Sklyadneva, S.V. Eremeyev, A.G. Lipnitskii, E.V. Chulkov. Fizika tvyerdogo tela 38, No 4. 1120 (1996). in Russian

[7] S.V. Eremeev, A.G Lipnitskii, A.I. Potekaev, E.V. Chulkov. Physics of Low-Dimensional Structures. No 3–4. 127 (1997).

[8] I.F. Golovnev, E.I. Golovneva, V.M. Fomin. Physical Mesomechanics, 10, No 3–4. 148 (2007).

Aleksey Yu. Smolin, pr. Academicheskii 2/4, Tomsk, 634021 Russia
Nikita V. Roman, pr. Lenina 36, Tomsk, 634021 Russia
Konstantin P. Zol'nokov, pr. Academicheskii 2/4, Tomsk, 634021 Russia
Serguey G. Psakhie, pr. Academicheskii 2/4, Tomsk, 634021 Russia
Valery K. Kedrinskii, Lavrentyev pr. 15, Novosibirsk, 630090 Russia

Compressibility as the main effect explaining why gas bubbles can sink in an oscillating fluid

Vladislav S. Sorokin
slavos87@mail.ru

Abstract

The present paper generalizes author's recent studies concerned with examination of gas bubbles sinking in vibrating fluid's volume. It is shown that the condition of this effect to occur is strongly dependent on the bubble's own compressibility as well as on the compressibility of the surrounding medium. An approximate expression for the average velocity of bubble motion in gas-saturated viscous fluid layer is derived. Furthermore, an expression for the average velocity of propagation of this fluid layer into the fluid's volume is obtained. The condition of vibrational instability of the two-phase state of the gas-fluid system is formulated. A simple physical explanation of the effects, experimentally observed in the fluid under the action of vibration, is given.

1 Introduction

At present two different mechanisms, two explanations of the effect of gas bubbles sinking in vertically oscillating fluid-filled volume were proposed – "wave" [1, 2, 3] and "nonwave", "vibrational" [4, 5]. For the first explanation key factor is the gradient of the wave amplitude, while for the second – the compressibility of the bubble. In the present paper the joint consideration of these mechanisms is provided – gas bubble motion in vibrating fluid-filled volume is studied with compressibilities of the bubble and of the gas saturated layer, which is generated due to the turbulization of the fluid near its free surface [6], being taken into account. In paper [1], to simplify the analysis, bubble's velocity relative to the fluid was considered to be equal to its velocity relative to the volume; in the present study this supposition is omitted. A nonlinear differential equation, which describes bubble's motion relative to the volume, is derived; for the solution of this equation the method of direct separation of motions is applied. The conditions of bubble sinking in gas saturated fluid layer are determined. An expression for the critical thickness of this layer, starting from which it penetrates deep into the volume, is derived, i.e. the condition of vibrational instability of the separate state of the gas-fluid system is obtained.

An approximate expression for the average velocity of bubble motion in gas saturated layer, which considerably depends on the depth of its submergence and on vibration parameters, and an expression for the average velocity of this layer penetration deep into the volume are derived.

On basis of the obtained correlations a simple physical explanation of the effects, experimentally observed in the fluid under the action of vibration, is given; the results of conducted additional experiments are adduced.

2 Equation of gas bubble translation

Motion of a bubble in vertically oscillating with amplitude A and frequency ω in harmonic law $\alpha = A\sin\omega t$ fluid-filled cylindrical volume is analysed (Fig.1.).

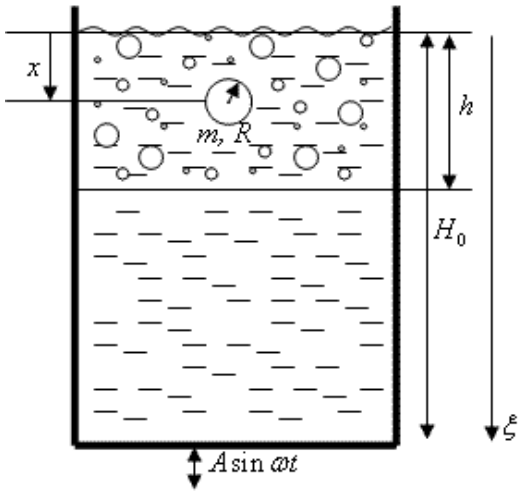

Figure 1: Model of a bubble in gas saturated fluid

It is assumed that the fluid is saturated with gas till the certain depth $h \leq H_0$ (H_0 - the height of the fluid column) and can be considered as an elastic rod; the rest of the fluid is oscillating uniformly with the volume. The absolute displacement of the rod's cross-section, which in undisturbed state is situated at distance x from its free (upper) edge, is designated as $\xi(x,t)$. For boundary conditions $\xi'|_{x=0} = 0$, $\xi|_{x=h} = A\sin\omega t$ this displacement is determined by the expression

$$\xi = \frac{g}{2c^2}(h^2 - x^2) + A\left(\cos\frac{\omega x}{c}\Big/\cos\frac{\omega h}{c}\right)\sin\omega t \tag{1}$$

here c is the sonic speed in gas saturated fluid.

Thereby $\dfrac{\partial\xi}{\partial t}(x,t)$ is velocity of an element of gas saturated fluid, situated at distance x from its free surface, and $\dfrac{\partial^2\xi}{\partial t^2}(x,t)$ - its acceleration. Taking into account these correlations, for the pressure in an oscillating fluid at distance x ($x \leq h$) from its free surface, we obtain the expression

$$P = P_e + \rho x g - \rho\int_0^x \frac{\partial^2\xi}{\partial t^2}(x_1,t)dx_1 \tag{2}$$

here P_e is the external pressure (in the simplest case atmospheric pressure), ρ is the density of gas saturated fluid, g - gravity acceleration.

The equation of gas bubble translation in gas saturated fluid can be written in the form

$$m\ddot{z} + \frac{d\,(m_0 v_{rel})}{dt} = -F(v_{rel}) + mg + F_{Ar} \tag{3}$$

Here $\ddot{z}$ is absolute acceleration of the bubble (dot designates total derivative on time), v_{rel} is bubble's velocity relative to the medium (gas saturated fluid), m is the mass of the

bubble (particles attached to the bubble), m_0 is the added mass of the medium, defined by the formula $m_0 = \chi V_b \rho$, with χ being an added mass coefficient, V_b - current volume of the bubble. $F(v_{rel}) = k_1 R^2 v_{rel}$ is the linearised on velocity v_{rel} resistance force to gas bubble motion. F_{Ar} is "dynamic" Archimedes force, defined by the formula [7]

$$F_{Ar} = -\int\limits_{V_b} \frac{\partial P}{\partial x} \cdot dV_b \tag{4}$$

Considering the bubble to be small (correlation $\frac{\omega R}{c} << 1$ fulfills, R - radius of the bubble) and taking into account expression (2), for the "dynamic" Archimedes force, acting on a bubble situated at distance x from fluid free surface, we obtain the expression

$$F_{Ar} = -\left(\rho g - \rho \frac{\partial^2 \xi}{\partial t^2}(x,t)\right) V_b \tag{5}$$

Absolute velocity of the bubble $\dot{z}$ is the sum of bubble's velocity relative to the volume and absolute velocity of the volume

$$\dot{z} = \dot{x} + \dot{\alpha} \tag{6}$$

Bubble's velocity relative to the medium (gas saturated fluid) v_{rel} is the residual between its absolute velocity $\dot{z}$ and absolute velocity of the medium in the point of its location $\frac{\partial \xi}{\partial t}(x,t)$

$$v_{rel} = \dot{x} + \dot{\alpha} - \frac{\partial \xi}{\partial t}(x,t) \tag{7}$$

Taking into account correlations (5), (7), transform equation (3) to the form

$$m\ddot{x} + \frac{d\left(m_0 \dot{x}\right)}{dt} = -F(v_{rel}) + (m - \rho V_b)\, g + \rho V_b \frac{\partial^2 \xi}{\partial t^2}(x,t) - m\ddot{\alpha} - \frac{d\left(m_0\left(\dot{\alpha} - \frac{\partial \xi}{\partial t}(x,t)\right)\right)}{dt} \tag{8}$$

3 Gas bubble volume pulsations

Gas bubble volume pulsations under the action of fast varying pressure are determined by the following equation [8]

$$\rho R \frac{d^2 R}{dt^2} = -\Delta P - \frac{2T}{R} \tag{9}$$

Here ΔP is difference between ambient pressure in the medium and gas pressure inside the bubble, T is surface tension coefficient.

Assuming that gas bubble volume pulsations are small and isothermal, neglecting tension forces (it is justified for bubbles with radius greater than 2 m^{-6} [1]) and taking into account expression (2), we transform equation (9) to the

$$\rho R_0 \frac{d^2 \Delta R}{dt^2} + 3\frac{\Delta R}{R_0} P_e = -\rho x g - \rho A \omega^2 f(x) \sin \omega t \tag{10}$$

where $f(x) = \frac{c}{\omega}\left(\sin \frac{\omega x}{c} \Big/ \cos \frac{\omega h}{c}\right)$, R_0 is the radius of the bubble near free surface of the fluid, $\Delta R = R - R_0$.

While solving the equation (4), in consequence of correlation $\frac{c}{A\omega} >> 1$ fulfillment, the variable x can be considered as parameter; as a result, for the current volume of the bubble we obtain the following expression

$$V_b = V_{b0}\left(1 - \frac{\rho}{P_e}\left(xg + A\omega^2 f(x)\frac{\lambda^2}{\lambda^2 - \omega^2}\sin\omega t\right)\right) \tag{11}$$

where $\lambda = \frac{1}{R_0}\sqrt{\frac{3P_e}{\rho}}$ is the frequency of bubble's free radial oscillations, V_{b0} is the volume of the bubble near free surface of the fluid.

4 Solution by the method of direct separation of motions

For the solution of the problem we use the concept of vibrational mechanics and the method of direct separation of motions [9]. The solutions to equation (8) are searched in the form

$$x = X(t) + \psi(t, \tau) \tag{12}$$

where X - "slow", and ψ - "fast", 2π- periodic in dimensionless ("fast") time $\tau = \omega t$ variable, with period τ average zero.

For the new variable X the following equation is obtained by averaging equation (8)

$$\begin{aligned} &m\ddot{X} + \left\langle \frac{d}{dt}\left(m_0(\dot{X} + \dot{\psi})\right)\right\rangle = -\left\langle F(v_{rel})\right\rangle + (m - \rho V_{b0})\, g + \\ &+\rho\left\langle V_b \frac{\partial^2 \xi}{\partial t^2}(X + \psi, t)\right\rangle - \left\langle \frac{d}{dt}\left(m_0\left(\dot{\alpha} - \frac{\partial \xi}{\partial t}(X + \psi, t)\right)\right)\right\rangle \end{aligned} \tag{13}$$

Equation for the fast variable ψ is got from equation (8) by subtraction equation (13) from it. The essential advantage of the method of direct separation of motions is a possibility to solve this equation in an approximate manner, if, as is typical, the equation of slow motion (13) is the one of primary interest. In the considered case, taking into account correlations $\Delta V_b << V_{b0}$ and $\frac{c}{A\omega} >> 1$, and neglecting small terms, we write equation of fast motions in the form

$$\ddot{\psi} + \eta\dot{\psi} = \eta A\omega\left(f'(X) - 1\right)\cos\omega t + A\omega^2\left(1 - \delta f'(X)\right)\sin\omega t \tag{14}$$

Here stroke designates spatial derivative,

$$\eta = \frac{k_1 R_0^2}{m + \chi\rho V_{b0}}, \delta = \frac{\chi + 1}{m/\rho V_{b0} + \chi} \tag{15}$$

Periodic solution of equation (14) is

$$\psi = A\left(\frac{\eta^2 + \omega^2\delta}{\eta^2 + \omega^2} f'(X) - 1\right)\sin\omega t + Af'(X)(\delta - 1)\frac{\omega\eta}{\eta^2 + \omega^2}\cos\omega t \tag{16}$$

To compose equation of slow motion (13) it is necessary to determine period τ average value of the resistance force $\langle F(v_{rel})\rangle$ and expressions for vibrational forces

$\left\langle \frac{d}{dt}(m_0(\dot{X}+\dot{\psi})) \right\rangle$, $\rho \left\langle V_b \frac{\partial^2 \xi}{\partial t^2}(X+\psi,t) \right\rangle$, $\left\langle \frac{d}{dt}\left(m_0 \left(\dot{\alpha} - \frac{\partial \xi}{\partial t}(X+\psi,t) \right) \right) \right\rangle$. Carrying this out (corresponding computations are omitted here), we obtain

$$\ddot{X} + \eta \dot{X} = \frac{\rho}{P_e} \frac{\lambda^2}{\lambda^2 - \omega^2} A^2 \omega^4 \left(\frac{1}{2} \frac{\rho V_{b0}}{m + \chi \rho V_{b0}} - \frac{\delta - 1}{3} \frac{\eta^2}{\eta^2 + \omega^2} \right) f(X) f'(X) + \\ + \frac{1}{2c^2} A^2 \omega^4 \left(\frac{\rho V_{b0}}{m + \chi \rho V_{b0}} \left(\frac{\eta^2 + \omega^2 \delta}{\eta^2 + \omega^2} f'(X) - 1 \right) - (\delta - 1) \frac{\eta^2}{\eta^2 + \omega^2} f'(X) \right) f(X) - (\delta - 1) g \tag{17}$$

It is seen from this equation that total vibrational force, induced on the bubble in gas saturated fluid layer, has two components, first of which is conditional on bubble's compressibility, while the second – on the compressibility of the surrounding medium.

5 Condition of bubble sinking in gas saturated fluid layer

Considering the mass of the bubble to be negligibly small in comparison with the mass of the medium in its volume $m << \rho V_{b0}$ (then $\delta = 1 + \frac{1}{\chi}$), we transform equation (17) to the form

$$\ddot{X} + \eta \dot{X} = \\ = \frac{A^2 \omega^4}{2\chi} \left[\frac{1}{c^2} \left(\frac{\omega^2}{\eta^2 + \omega^2} (1 + \frac{1}{\chi}) f'(X) - 1 \right) + \frac{\rho}{P_e} \frac{\lambda^2}{\lambda^2 - \omega^2} \frac{\omega^2 + \frac{1}{3}\eta^2}{\eta^2 + \omega^2} f'(X) \right] f(X) - \frac{1}{\chi} g \tag{18}$$

The conditions of gas bubble sinking (or rising) in gas saturated fluid layer, can be obtained from the form of the equation (18). If the expression written in the right side of this equation has positive value, then bubble sinks, and if it is negative, then bubble rises. So the condition of bubble sinking in gas saturated fluid layer has the form

$$\frac{A^2 \omega^4}{2g} \left[\frac{1}{c^2} \left(\frac{\omega^2}{\eta^2 + \omega^2} (1 + \frac{1}{\chi}) f'(X) - 1 \right) + \frac{\rho}{P_e} \frac{\lambda^2}{\lambda^2 - \omega^2} \frac{\omega^2 + \frac{1}{3}\eta^2}{\eta^2 + \omega^2} f'(X) \right] f(X) > 1 \tag{19}$$

In the present paper motion of bubbles with radius less than 2 sm at frequencies of external excitation $\omega < 250$ 1/s is considered. For such bubbles correlation $\lambda^2 >> \omega^2$ holds true, so ratio $\frac{\lambda^2 - \omega^2}{\lambda^2}$ is believed to be equal to unity.

In general case resistance force to particle motion in a fluid is defined by the expression [10,11]

$$F(v_{rel}) = 4\rho R^2 \Psi(\mathrm{Re}) v_{rel}^2 \mathrm{sgn} v_{rel} \tag{20}$$

Here $\Psi(\mathrm{Re})$ is the resistance coefficient, which dependence on Reynolds number is given by the classical Rayleigh diagram [10,11]. In the case of large Reynolds numbers $\mathrm{Re} > 1000$, examined in the present paper, this coefficient can be considered to be approximately constant

$$\Psi(\mathrm{Re}) \approx 0.2 \equiv \Psi_\infty$$

In the present paper the resistance force is assumed to be linearised on velocity v_{rel}; taking into account that $|v_{rel}|$ is magnitude of order of $A\omega$, the resistance coefficient k_1 is considered to be equal to $k_2 \rho A \omega$, where k_2 is dimensionless parameter of order of unity.

Employing this correlation, we write inequality (19) in the form

$$\frac{A^2\omega^3 c}{4g}\frac{\rho}{P_e}\frac{1+\frac{1}{3}a^2}{a^2+1}\left[1+\frac{P_e}{\rho c^2}\left(\frac{1}{1+\frac{1}{3}a^2}\left(1+\frac{1}{\chi}\right)-\frac{1+a^2}{1+\frac{1}{3}a^2}\frac{\cos\frac{\omega h}{c}}{\cos\frac{\omega X}{c}}\right)\right]\frac{\sin 2\frac{\omega X}{c}}{\left(\cos\frac{\omega h}{c}\right)^2}>1 \tag{21}$$

where $\theta=\dfrac{3k_2}{4\pi\chi}$, $a=\theta\dfrac{A}{R_0}$. To simplify the analysis of inequality (21) the condition of bubble sinking in incompressible viscous fluid is obtained from it (supposing $c\to\infty$)

$$w_*\frac{1+\frac{1}{3}a^2}{a^2+1}\frac{X}{H_0}>1 \tag{22}$$

here $w_*=\dfrac{1}{2}\left(\dfrac{A\omega^2}{g}\right)^2\dfrac{\rho H_0 g}{P_e}$ is characteristic load parameter. Inequality (22) is coincident with condition of gas bubble sinking in oscillating incompressible fluid obtained in paper [5]. Here we reveal how compressibility of the medium affects the conditions of bubble sinking; rewrite inequality (21) in the form

$$w_*\frac{1+\frac{1}{3}a^2}{a^2+1}\frac{X}{H_0}\cdot\zeta\cdot\gamma>1 \tag{23}$$

where $\zeta=1+\dfrac{P_e}{\rho c^2}\left(\dfrac{1}{1+\frac{1}{3}a^2}\left(1+\dfrac{1}{\chi}\right)-\dfrac{1+a^2}{1+\frac{1}{3}a^2}\dfrac{\cos\frac{\omega h}{c}}{\cos\frac{\omega X}{c}}\right)$ and $\gamma=\dfrac{c}{2\omega X}\dfrac{\sin 2\frac{\omega X}{c}}{\left(\cos\frac{\omega h}{c}\right)^2}$. As is seen, the difference between the condition of bubble sinking in compressible medium and (22) is that two supplementary factors ζ and γ are present in its left side.

The influence of medium compressibility on the condition of bubble sinking, reflected by parameter ζ, turns out to be essential only at small values of sound speed in the medium $c<40$ m/s and strongly depends on ratio A/R_0 in that range. At small values of thickness of gas saturated fluid layer $h<5$ sm the influence of medium compressibility on the condition of bubble sinking, reflected by parameter γ, is insignificant. However at values $h\geq 15$ sm and sound speed in the medium $c<25$ m/s this influence turns out to be crucial.

If inequality (21) fulfills at the bound of the fluid-gas phase spreading area $X=h$, then bubbles, generated in the layer with thickness h, will move deep down the fluid, and so gas saturated fluid layer will expand. Thereby the condition of vibrational instability of the separate state of the gas-fluid system has the form

$$w_*\frac{1+\frac{1}{3}a^2}{a^2+1}\frac{h}{H_0}\left[1+\frac{P_e}{\rho c^2\chi}\frac{1-\chi a^2}{1+\frac{1}{3}a^2}\right]\frac{c}{\omega h}\tan\frac{\omega h}{c}>1 \tag{24}$$

6 Velocity of bubble's "slow" motion in gas saturated fluid layer

An approximate expression for the velocity of bubble's "slow" motion in gas saturated fluid layer is defined from the equation (18) with its "slow" acceleration $\ddot{X}$ being considered as small.

$$\dot{X} \approx v(\kappa \frac{\sin 2\frac{\omega X}{c}}{\left(\cos\frac{\omega h}{c}\right)^2} - \kappa_1 \frac{\sin\frac{\omega X}{c}}{\cos\frac{\omega h}{c}} - 1) \tag{25}$$

here $v = \dfrac{\rho V_{b0} g}{k_1 R_0^2}$ - absolute value of nondeformable bubble "slow" floating velocity in incompressible medium, $\kappa = \dfrac{1}{4}\dfrac{A\omega^2}{g}\dfrac{\rho A\omega c}{P_e}\dfrac{1+\frac{1}{3}a^2}{a^2+1}\left[1+\dfrac{P_e}{\rho c^2}\dfrac{1}{1+\frac{1}{3}a^2}\left(1+\dfrac{1}{\chi}\right)\right]$, and $\kappa_1 = \dfrac{1}{2}\dfrac{A\omega^2}{g}\dfrac{A\omega}{c}$.

The velocity of gas saturated fluid layer penetration deep down the volume is equal to the sinking velocity of the bubble, situated at its bound $X = h$.

7 Discussion of the obtained results

Assumptions employed in the analysis, particularly suppositions about character of gas bubble volume pulsations, were verified.

On the basis of the obtained expressions for factors ζ and γ the range of parameters, at which the effect of medium compressibility turns out to be negligibly small in comparison with the influence of bubble's own compressibility, is determined. Corresponding condition is $\gamma \cdot \zeta \approx 1$ (see inequality (23)).

Moreover the range of parameters, at which the influence of medium compressibility turns out to be crucial, is defined.

To verify analytically obtained results a numerical experiment was conducted. Initial equations of gas bubble motion were integrated directly by means of Mathematica 7; the obtained results are in good agreement with the analytical solution.

8 Pilot study

Series of experiments has been conducted on the universal vibrating stand of the Joint laboratory of vibrational mechanics IPME RAS and REC "Mekhanobr-Tekhnika" (Fig. 2).

As it was noted before, vibrational force, acting on a bubble, has two components, first of which is conditional on bubble's compressibility, while the second – on the compressibility of the surrounding medium. Experiments, sustaining existence of both components, were provided before (for example, in [1,3,4,5]); in the present paper series of additional experiments is conducted to study in detail second (wave) force component. Motion of incompressible volatile particle in compressible medium is examined.

Cylindrical vessel with internal diameter 60 mm was filled with water till the level $H_0 =$ 160 mm and fixed at the stand. It was subjected to vertical oscillations with amplitude $A = 4$ mm. A nondeformable ball, whose mass was negligibly small in comparison with the mass of the water in its volume, was attached to the bottom of the vessel by a thread (Fig. 3a). The frequency of the external excitation was increasing from 0 to 200 rad/s.

In the range $0 < \omega < \omega_1 = 170$ s^{-1} the fluid was transparent. A fluid layer, saturated with bubbles of different diameters, arisen near its free surface and gradually grew with increasing of the frequency. At $\omega > \omega_1 = 170$ s^{-1} intensive chaotic oscillations of fluid surface appeared. At frequency $\omega = \omega_2 \approx 190$ s^{-1} gas bubbles sinking from the layer was

Figure 2: Experimental setup

observed. With increasing of the frequency gas content in the fluid gradually grew, and sound speed in it fall in accordance with the formula [7]

$$c \approx \frac{10}{\sqrt{\alpha_g(1-\alpha_g)}} \tag{26}$$

here α_g - gas content of the layer. Thereby, compressible fluid-gas mixture was generated in the vessel.

As soon as frequency of excitation and gas content reach certain values ω_* and α_{g*}, the ball fall on the bottom of the vessel (Fig. 3b). The decreasing of the gas content led to the rising of the ball, i.e. it returned to the initial position. Thereby conclusion about existence of wave force in compressible medium was confirmed by the experiments. It is shown that at some ranges of external excitation parameters this force can lead to volatile rigid particle sinking.

9 Conclusions

Motion of a bubble in vibrating volume with a fluid, saturated with gas till a certain depth, is studied in the paper, with compressibilities of the bubble and of the gas saturated layer being taken into account. The conditions of gas bubble sinking in the layer are determined. The expression for the critical thickness of gas saturated fluid layer, starting form which it penetrates deep into the volume, is derived, i.e. the condition of vibrational instability of the separate state of the gas-fluid system is obtained. The expression for the average velocity of bubble motion in the layer, which considerably depends on the depth of its submergence and on vibration parameters, and the expression for the average velocity of this layer penetration deep into the volume are determined. The reported results are applicable for control and optimization of relevant technological processes.

It is shown that vibrational force, induced on the bubble in oscillating gas saturated fluid, has two components, first of which is conditional on bubble's compressibility, while the second - on the compressibility of the surrounding medium.

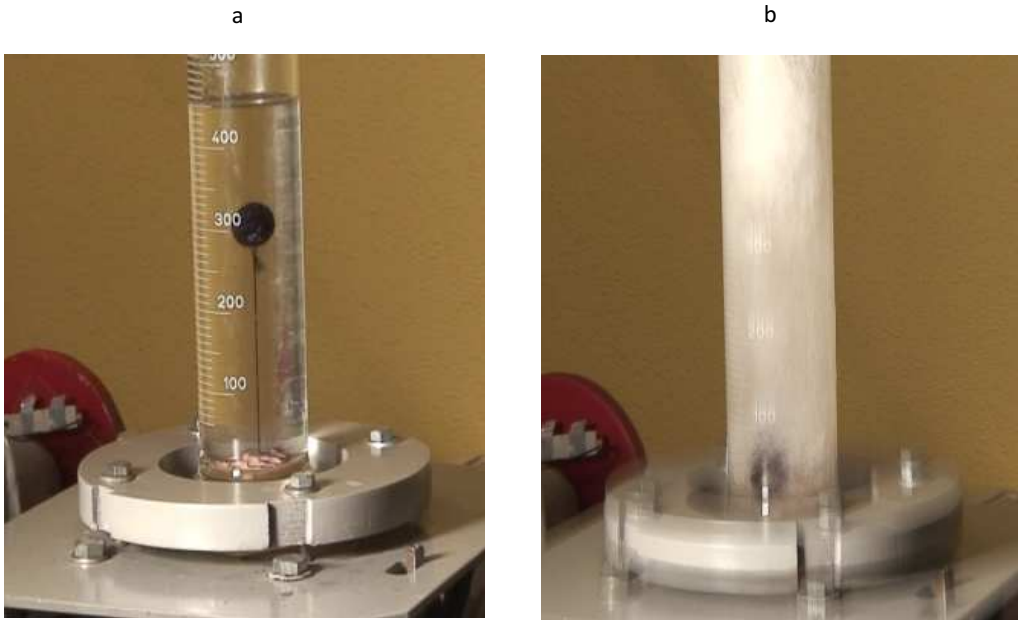

Figure 3: Sinking of the volatile rigid ball in the vibrating vessel with the water: a - the ball in the standing still vessel, b - the ball in the vibrating vessel after the threshold frequency ω_* and gas content α_{g*} are exceeded

Acknowledgements

Work is carried out with financial support from the Russian Foundation of Fundamental Research, grant 10-08-00201.

References

[1] Blekhman, I.I., Vaisberg, L.A., Blekhman, L.I., Vasilkov, V.B., Yakimova, K.S.: "Anomalous" Phenomena in Fluid under Action of Vibration, Doklady Physics, 53, N 10, 2008, pp. 520-524

[2] Crum, L.A., Eller, A.I.: Motion of bubbles in a stationary sound field, The Journal of the Acoustical Society of America, 48, N 1(2), 1970, pp. 181-189

[3] Ganiev, R.F., Ukrainskii, L.E.: Nonlinear wave mechanics and technologies (in Russian), Scientific publishing center "Regular and chaotic dynamics", 2008

[4] Bleich, H.H.: Effect of Vibrations on the Motion of Small Gas Bubbles in a Liquid, Jet Pro-pulsion, Journal of the American Rocket Society, 26, N 11, 1956, pp. 958-964

[5] Sorokin, V.S., Blekhman, I.I., Vasilkov, V.B.: Motion of a gas bubble in fluid under vibration, Nonlinear Dynamics, DOI: 10.1007/s11071-011-9966-9, 2011

[6] Tatevosyan, R.A.: Analysis of the regularities of water-air system vibroturbulisation (in Rus-sian), Theoretical fundamentals of chemical technology, 11, N 1, 1977, pp. 153-155

[7] Loytsyanskiy, L.G.: Fluid and gas mechanics (in Russian), Nauka, 1973

[8] Batchelor, G.K.: Compression waves in suspension of gas bubbles in fluid (in Russian). Mechanics, 3, 65-84, 1968

[9] Blekhman, I.I.: Vibrational Mechanics, World Scientific, 2000

[10] Bogdanov, O.S.: Handbook on enrichment of raw materials (in Russian) 2nd Edition extended and corrected. Nedra, Moscow, 1982

[11] Kisevalter, B.V.: Theory of gravitational enrichment processes (in Russian). Nedra, Moscow, 1979

Vladislav S. Sorokin, Saint-Petersburg, Russia

Newton-Kantorovich method of parametres' characterization of equilibrium of the system which realizes the triaxial strenght of the cube made from the nonlinear material with non-convex potencial

Valeriy V. Struzhanov Natalya V. Burmasheva
nat_burm@mail.ru

Abstract

Search for an initial approximation for Newton-Kantorovich method and equilibria of the system, realizing triaxial tension. The conditions for convergence of this method were obtained.

The problem of stability of the deformation process associated with destruction of structural elements and is therefore a topical. In order for a constructive element lost the stability necessary that at least some of the material passed on an unstable, supercritical stage of deformation (weakening).

In this paper the cubic element, which under triaxial deforming takes the stages of sustainable and unsustainable deforming, is considered. The element is placed in a special mechanical system consisting of three elastic rods offering the element's deforming.

The mechanical system under consideration belongs to a class of gradient systems. The behavior of a gradient system is characterized by its potential function W depending on the parameters of the system state and control parameters [1]. This function is the sum of potential functions to system elements. If we consider the failure as the inability to balance [2], then at least part of the potential functions of system's elements must describe both their stable and unstable states. Such a description is possible only when the designated potential functions are generally non-convex. At the stage of hardening it's convex down function (steady state), at the stage of softening is convex upward functions or non-convex and nonconcavity (resistance is unstable).

To determine the state of stress in the elements of such a mechanical system in equilibrium is necessary to determine all the critical points of the potencial function W from solutions of the system of nonlinear equations $\nabla W = 0$. Here ∇ is the Hamilton operator in the Euclidean space of states. By virtue of the fact that some of potential functions of elements are nonconvex, these equations may have one or more solutions, or no solutions. Degenerate critical point at which the stability matrix $H(W) = \nabla\nabla W$ is singular are of particular importance. Here $H(W)$ is the Hessian matrix consisting of second derivatives [3]. Such points are structurally unstable [1]. Perturbation of the potential function W causes a qualitative change in the behavior of this function. In the Euclidean space of control parameters degenerate critical points form diversity, which are the separatrix of the function W. Outside the region bounded by the separatrix, the mechanical system has only one equilibrium or equilibria do not exist. Within this area there are several equilibria [1]. It is known [1,4] that when a load path lives the region bounded by the

separatrix, the equilibrium of the mechanical system becomes unstable and the system jumps to a new stable equilibrium position (if it exists). In this case we can assume that the mechanical system collapses. Thus, if we know the separatrix of the potential function of a mechanical system we can determine the limiting values of control parameters. To determine the limit loads acting on the discrete gradient mechanical system, the technique of their numerical calculation allowing to avoid of solving of a large number of nonlinear equilibrium's equations is presented.

To find all equilibria for this mechanical system (both stable and unstable) Newton-Kantorovich method is used. An algorithm for choosing the initial approximation to this iterative method depending on the location of the vector of control parameters with respect to the separatrix (or within the region bounded by the separatrix or outside of it) is offered. It is shown that a necessary condition for the applicability of the method is the nondegeneracy of the Hessian of the system's potential function. The proposed algorithm for choosing the initial approximation and iterative method are implemented for the considered mechanical system. The parameters of all equilibria for some characteristic points of the control space were found.

1 The sample, the system, the mapping

The process of triaxial deforming of elementary cube in a special rod system is researched. Cubic element 4 undergoes to triaxial tension in the system, in which tensile forces are transmitted through rods 1,2,3 made of linear elastic material (Fig. 1). In the undeformed length of the edges of a cube is equal to one (reference configuration). Face of the cube with one hand are fastened with absolutely rigid walls, on the other side with the elastic rods 1,2,3 so that in the process of triaxial tensile cube could only take the form of a cuboid. To the points of the free ends of the rods 1,2,3 monotonically increasing displacement u_1, u_2, u_3 (mm) are given (rigid loading). Stiffness of elastic rods under tension are respectively equal $\lambda_1, \lambda_2, \lambda_3$. The loading of the system occurs at a constant temperature and so slowly that its possible to ignore the dynamic effects.

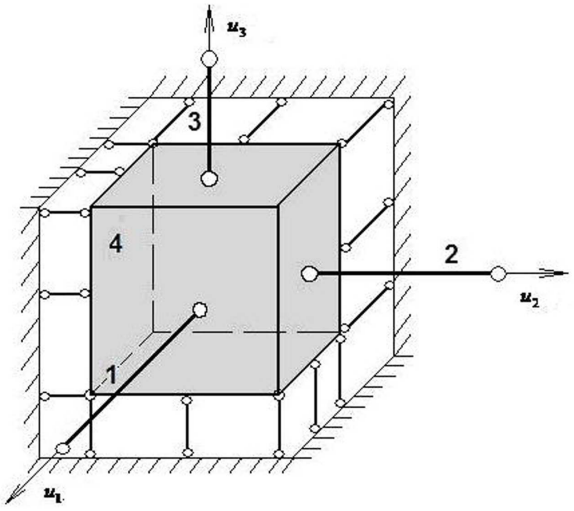

Figure 1: The mechanical system

During the loading of system faces of the cube get extensions $\varepsilon_i (i = 1, 2, 3)$. On the faces of the cube uniformly distributed effort act. $\sigma_i = q_i S_{ia}$, where S_{ia} are areas of the

faces in the actual (current) configuration, are resultants of these efforts.

Values σ_i are nominal stress, defined in the reference configuration by the elementary theory. Values ε_i can be interpreted as deformation, defined by the elementary theory.

Further, we assume that the work of forces on the movement does not depend on the type of trajectory along which the point with coordinates $(\varepsilon_1, \varepsilon_2, \varepsilon_3)$ moves in a Euclidean space of states, ie motion of a point representing the process of stretching the cube, goes in the potential force field with a scalar potential $\Pi(\varepsilon_1, \varepsilon_2, \varepsilon_3)$ having a field concavity, convexity and saddle points.

We take the potential function as [5]

$$\Pi = B\left\{1 - exp(-\frac{1}{4B}[(\frac{\nu E}{(1+\nu)(1-2\nu)}(\varepsilon_1+\varepsilon_2+\varepsilon_3)^2 + \frac{E}{1+\nu}(\varepsilon_1^2+\varepsilon_2^2+\varepsilon_3^2)])\right\},$$

where $B = const$ is the potential's value at the moment of destruction, $E = 2 \cdot 10^4 kg/mm^2$ is Young's modulus, $\nu = 0,3$ is Poisson's ratio (Fig. 2). In the state space level lines of the potencial Π are ellipsoids. For definiteness, we assume $B = 1kg/mm^2$.

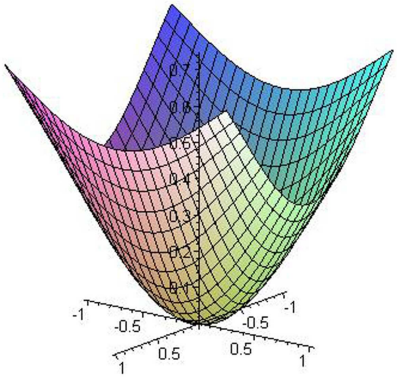

Figure 2: The qualitative behavior of the potential

At the points of state space where the Hessian matrix $H(\Pi)$ is positive definite [3], the potential Π is a function of locally convex downward, which corresponds to the physical (proper) the stability of the material of the cube (hardening). The region of positive definiteness of the matrix $H(\Pi)$, which includes the origin, limits the set of measure zero (the surface in space R_e^3), where the matrix $H(\Pi)$ is singular. At points located beyond this surface, sign of the matrix $H(\Pi)$ is undefined (its eigenvalues have different signs), which corresponds to the softening of the material (intrinsic instability). Thus, the potential function Π describes the material properties of the cube at all stages of deforming, namely the stage of stable deformation (hardening) and the stage of unstable deformation (softening).

Under the active deforming of the above-described mechanical system is gradient and in the case of rigid loading is described by the potential function

$$W = \sum_{i=1}^{3} \frac{\lambda_i}{2}(u_i - \varepsilon_i)^2 + \Pi(\varepsilon_1, \varepsilon_2, \varepsilon_3), \tag{1}$$

where the first three terms are the strain energy of linearly elastic rods 1,2,3, in which, for definiteness, we assume $\lambda_i = 500kg/mm$.

To determine the stress state in the elements of such mechanical system in equilibria it's necessary to determine all the critical points of solutions of nonlinear equations (equilibrium equations) [6]

$$W_{,i} = \Pi_{,i} - \lambda_i(u_i - \varepsilon_i) = 0 (i = 1, 2, 3).$$

The comma denotes the partial derivation with respect to corresponding variable.

We note that this mechanical system belongs to this class of systems, which equilibrium equations can be resolved with respect to control parameters. In this case,

$$u_i = \frac{1}{\lambda_i}\Pi_{,i} + \varepsilon_i. \tag{2}$$

Formula (2) define the mapping $F : R^3_e \to R^3_u$ of strain space to three-dimensional Euclidean space of controls. This differentiable mapping is nonlinear and has features [7], it transforms axis of a Cartesian state space to curves, as well inclined to the bisector of the first octant of the state space (Fig. 3). These curves have such property as, except the origin, they have no common points with the coordinate axes of space R^3_u.

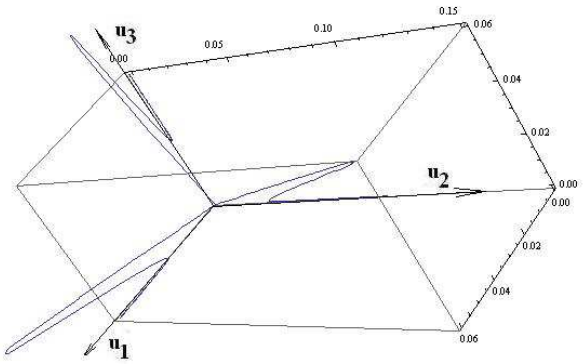

Figure 3: The image of coordinate axes under the action of mapping

The degenerate critical points at which the Hessian matrix $H(W)$ of second derivatives of function W (stability matrix) is singular are of particular importance. Degenerate critical points form a surface in the control space $Ou_1u_2u_3$, which is the separatrix of the function W [7]. Separatrix divides the control space to a qualitatively similar areas in which the equilibrium equations have the same number of solutions. As shown above, by virtue of the nonlinearity of the mapping (2) the image of Cartesian axes are curves. Note that the points in which the surfaces of the degenerate critical points intersect the axis $O\varepsilon_i$, go to the points where the images of axis warp in the space R^3_u. Moreover, these points of curvatures lie on the separatrix (Fig. 4).

If the vector of control parameters lies in the area of 4th type (Fig. 4), the system of equilibrium equations has no solutions. If the vector of control parameters lies in the areas of type 1 (type 3), then a unique solution exists, and it lies in region I (region III, respectively) of the state space. For the control parameters from the area of type 2 there are 3 different solutions (one of the regions I - III deformation space).

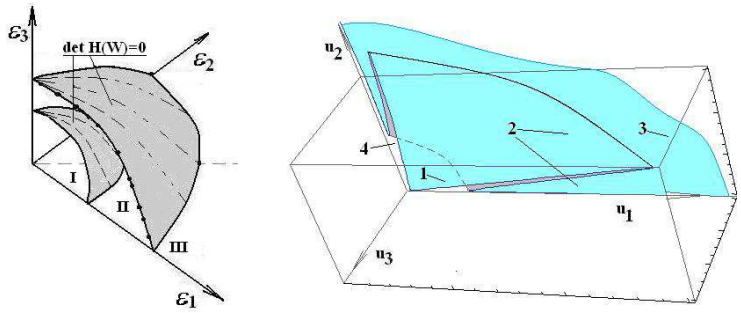

Figure 4: Surface of the degenerate critical points and qualitative character of the mapping

2 The separatrix

The technique of numerical construction of the separatrix is the following. To construct the separatrix we must find all the critical points of the system's potential function in the case of increasing loads, and then select from them the degenerate critical points. Implementing of this scheme requires the solving of a large number of nonlinear equations for finding all the equilibria of mechanical systems under quasi-statically increasing loads. Then we construct the separatrix, and define the limit values of control parameters [7].

To construct the separatrix another approach allowing to avoid of solving systems of nonlinear equations is avaliable. First of all, we shoud break with some small step the Euclidean space $R_e^3 \times R_u^3$ within sufficiently large 6-dimensional cube. Secondly, we find the parameters of state and control in the grid nodes of discretization. Substituting these values in the functions constituting elements of the Hessian matrix, we obtain a set of numerical matrices. Then we compute the determinants of these matrices and select the set L of nodes with their coordinates in $R_e^3 \times R_u^3$ in which the Hessian is close to zero with the desired degree of accuracy. Obviously that the set L in general contains more elements than the set of degenerate critical points of the potential function W.

Substituting the coordinates of the nodes from L to the equilibrium equations, we allocate those that of them which satisfy with the required accuracy. These nodes form a set of degenerate critical points. Now, using the control parameters corresponding to nodes with degenerate critical points, we find in the control space form of the separatrix, with aid of which we already define the limits of control parameters.

Lets apply this approach to the mechanical system under consideration. Critical points of the potential function W are determined by the system (1). In this case the components of the Hessian matrix are functions of the state parameters. We have

$$H(W) = \{\delta_{ij}\lambda_i + \Pi_{,ij}\}_{i,j=1}^{3}.$$

In the case of monotonically increasing parameters u_i state parameters $\varepsilon_i \geq 0$. We select on the set $D = \varepsilon_i \geq$ the cube $0 \leq \varepsilon_i \leq 0,0086$ and will construct within it the mesh of nodes with a step $4,5 \cdot 10^{-4}$. In each node we calculate the value $detH(W)$ and identify those nodes where the determinant is close to zero. We substitute coordinates of these nodes in equations (2) and find the values u_i^s (coordinates of the points of a separatrix). Pulling

the surface on the point(u_1^s, u_2^s, u_3^s), we obtain the approximate form of the separatrix. It consists of two surfaces I and II. Limit values for control parameters determine the points of surface II, after crossing which by load path in the control space a catastrophe happens (sudden loss of stability of the process of the mechanical system's deforming).

Coordinates of points on the separatrix which define limits of control parameters can be represented in tabular form (Table 1).

Table 27: Coordinates of certain points of the separatrix.

u_1^s	0.314	0.342	0.361	0.382	0.31	0.209	0.289	0.242
u_2^s	0.357	0.299	0.202	0.22	0.266	0.353	0.198	0.277
u_3^s	0.18	0.227	0.26	0.31	0.339	0.353	0.386	0.4

3 Newton-Kantorovich method

Thus, to determine the stress state in the elements of the considered mechanical system in equilibrium it's necessary to determine all the critical points. To find solutions to equations of equilibrium for given control parameters we apply Newton-Kantorovich method, a general scheme for which the equation $F(\varepsilon) = 0$ is[8]

$$\overline{\varepsilon}_{n+1} = \overline{\varepsilon}_n - [F'(\overline{\varepsilon}_n)]^{-1} \cdot F(\overline{\varepsilon}_n),$$

here $\overline{\varepsilon}_n$ is a vector with components ε_i, F' is Frechet derivative of the mapping F, and F' is the Hessian matrix of function F ($F' = \dfrac{\partial}{\partial\varepsilon_i}F = \dfrac{\partial^2}{\partial\varepsilon_i\partial\varepsilon_j}W = H(W)$). Hence, a prerequisite condition for the implementation of the method is the nondegeneracy of the Hessian matrix.

Lets consider the algorithm of choosing the initial approximation, based on the location of the vector of control parameters: either outside the region bounded by a separatrix, or within the region bounded by a separatrix. The choice of initial approximation guarantees determination of all parameters of equilibria, both stable and unstable by the Newton-Kantorovich method.

To select a suitable initial approximation, the following algorithm is proposed:
1. Choose the initial and final values $\varepsilon_i^{st}, \varepsilon_i^f (i = 1, 2, 3)$ of the range, in which the coordinates of the state space in the process of finding the initial value for the Newton - Kantorovich method will be change. (Fig. 5).
2. Choose the partition step (on each axis) $h_i = \dfrac{\varepsilon_i^f - \varepsilon_i^{st}}{s} (i = 1, 2, 3)$, where s is the number of partition points.
3. Begin to crawl all nodes of received the grid. Check that the node $(\varepsilon_1^{st} + ih_1, \varepsilon_2^{st} + jh_2, \varepsilon_3^{st} + kh_3)$ belongs to the region under consideration and that $detH(w)$ is different from zero.
4. Consider the image of a node $(\varepsilon_1^{st}+ih_1, \varepsilon_2^{st}+jh_2, \varepsilon_3^{st}+kh_3)$ in the control space $Ou_1u_2u_3$. Define the distance d_{ijk} between the received point and the point $\overline{u}$.
5. If at some stage received point falls in the δ-neighborhood of a point $\overline{u}$, then this point will be an initial approximation to the Newton-Kantorovich method.
6. Otherwise, choose the smallest among all d_{ijk} (we'll note it d).
7. Find the point ε^* with coordinates $(\varepsilon_1^{st} + ih_1, \varepsilon_2^{st} + jh_2, \varepsilon_3^{st} + kh_3)$, an image of which

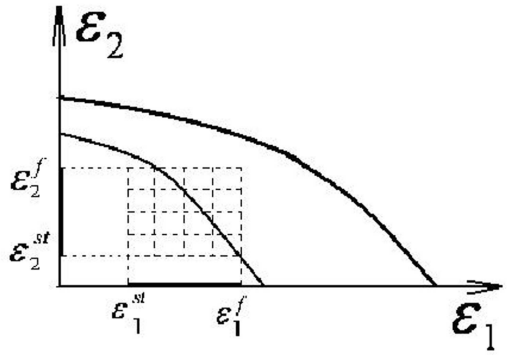

Figure 5: The grid of nodes

lies at a distance d from a given point $\overline{u}$.
8. Further, in the state space we choose eight points closest to the point ε^* so that ε^* was a center of formed parallelepiped . These 8 points have following coordinates(Fig. 6): $(\varepsilon_1^{st} + (i \pm 1)h_1, \varepsilon_2^{st} + (j \pm 1)h_2, \varepsilon_3^{st} + (k \pm 1))h_3)$

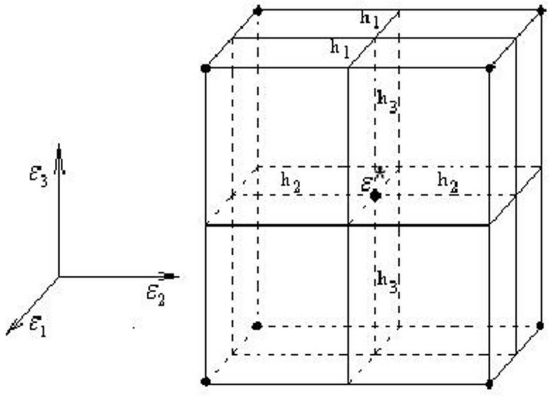

Figure 6: Regions of the best approximation by a given grid of nodes

9. Now narrow down the considered part of the grid, taking the new boundary value of ranges of coordinates:

$$\varepsilon_1^{st} = \varepsilon_1^{st} + (i-1)h_1, \varepsilon_2^{st} = \varepsilon_2^{st} + (j-1)h_2, \varepsilon_3^{st} = \varepsilon_3^{st} + (k-1))h_3,$$
$$\varepsilon_1^{f} = \varepsilon_1^{st} + (i+1)h_1, \varepsilon_2^{f} = \varepsilon_2^{st} + (j+1)h_2, \varepsilon_3^{f} = \varepsilon_3^{st} + (k+1))h_3.$$

Then repeat everything from step number 1.

To implement this algorithm for finding an initial approximation to the Newton-Kantorovich method, it's necessary to determine the area of strain space in wich the current node lies: the area bounded by the surfaces of degenerate critical points, or outside this region.

Let's assume that in this moment the node (Fig. 7) with the coordinates $(\varepsilon_1^*, \varepsilon_2^*, \varepsilon_3^*)$ is under consideration. Let's draw from the origin the straight line l passing through the point ε^*, it intersects the surfaces of I and II of degenerate critical points in the points $\varepsilon^1, \varepsilon^2$ respectively.

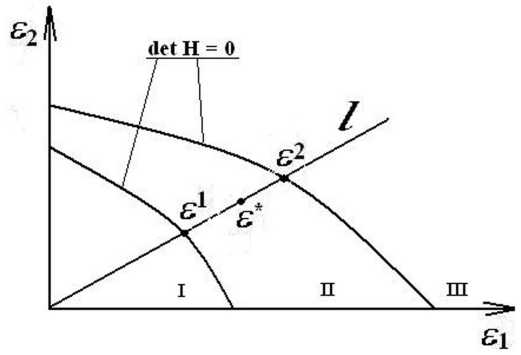

Figure 7:

Parametric equation of a line l can be written easily. And then we can find coordinates of points $\varepsilon^1, \varepsilon^2$. Further, we find the distance from the origin to the points ε^*,ε^1 and ε^2. Depending on inequalities between these three quantities, we can determine in what area of the state space the current node ε^* is situated:

$$\rho(O, \varepsilon^*) < \rho(O, \varepsilon^1), \varepsilon^* \in I,$$
$$\rho(O, \varepsilon^1) < \rho(O, \varepsilon^*) < \rho(O, \varepsilon^2), \varepsilon^* \in II,$$
$$\rho(O, \varepsilon^2) < \rho(O, \varepsilon^*), \varepsilon^* \in III.$$

The proposed algorithm has been implemented for the considered mechanical system. For the values of control parameters chosen as the test values were found initial approximations for all possible equilibria corresponding to a given set of controls. Then, starting from these initial approximations, have been found the equilibria by the aid of the Newton-Kantorovich method.

Depending on the specified accuracy (magnitude neighborhood, which should get the image of the initial approximation under the action of the mapping F) were obtained by different variants of initial approximations. For example, the point $\overline{u} = (0.0005, 0.0004, 0.0003)$ lies outside the region bounded by the surfaces of the separatrix, that's why for thesecontrol values equilibrium equations have only one solution, and it lies in region I of the state space. Proposed algorithm for choosing the initial approximation depending on the accuracy d offers several options:

$$d = 10^{-3} \to \varepsilon^0 = (0, 0, 0)$$
$$d = 10^{-4} \to \varepsilon^0 = (1.62414 * 10^{-5}, 8.12071 * 10^{-6}, 0)$$
$$d = 10^{-5} \to \varepsilon^0 = (1.36348 * 10^{-5}, 7.97033 * 10^{-6}, 1.95499 * 10^{-6})$$

Note, however, that differences in the values of the coordinates of all the found initial approximations begin only in 6th decimal place, and for the problems caused by practical needs, the accuracy of this order is excessive. Therefore to illustrate the problem of choosing an initial value for the other cases of the location of the vector control with respect to the separatrix will restrict ourselves with low accuracy

$d = 10^{-1}$. Thus, for a point $\overline{u} = (0.04, 0.02, 0.03)$ lying between the surfaces of the separatrix, the equilibrium equations have three solutions (one from each region of the state space). As initial approximations to them can take the following points: $(0.00885, 0.00885, 0.00885), (0.0298, 0.0228, 0.0298), (0.0298, 0.0298, 0.0298)$. For the control vector $\overline{u} = (0.2, 0.7, 0.3)$ as an initial approach to the solution we may consider the point (0.223178,0.706622,0.223178) of region III of the state space. Then we apply Newton-Kantorovich method, which allows, for example, to determine for controls $\overline{u} = (0.04, 0.02, 0.03)$ directly the parameters of the equilibrium position. it was found that it will be point $\varepsilon = (1.39561 * 10^{-5}, 7.85856 * 10^{-6}, 1.76099 * 10^{-6})$.

Acknowledgements

The work was supported by RFBR (project 10-01-96018).

References

[1] R. Gilmore. Catastrophe Theory Applied: in 2 books. Book 1.— M.: Mir, 1984. - 350p.

[2] L.I. Sedov. Continuum mechanics. V.1. — M.: Nauka, 1970.- 492p.

[3] R. Horn, Ch. Johnson. Matrix analysis — M.: Mir, 1989. - 655p.

[4] V.V. Struzhanov. On the stability of biaxial tension of a square plate in one gradient mechanical system / / Proceedings of Institute of Mathematics and Mechanics, UB RAS. - 2010. - V.16, No 5. – p.187-195.

[5] V.V. Struzhanov, Ye.Yu. Prosviryakov, N.V. Burmasheva. On one method of constructing of a uniform potencial. Comput. mech. cont. media. - 2009. - Vol.2, No 2. – p.96-107.

[6] T. Poston, I. Stewart. Catastrophe Theory and Its Applications. M.: Mir, 1980. – 608p.

[7] V.I. Arnold,A.N. Varchenko, S.M. Husein-Zade. Singularities of differentiable maps, classification of critical points, caustics and wave fronts. M.: Nauka, 1982.304p

[8] L.V. Kantorovich, G.P. Akilov. Functional analiz.M.: Nauka, 1984. 680p.

Valeriy V. Struzhanov, Institute of Engineering Science Ural Branch Russian Academy of Science, Russia
Natalya V. Burmasheva, Institute of Engineering Science Ural Branch Russian Academy of Science, Russia

Effect of the Higher Order Terms on the Thermal Behaviour of Thin Layer Slab Under the Effect of Hyperbolic Heat Conduction Model

M. A. Al-Nimr S. E. Al-Lubani A. F. Khadrawi
slubani@Huson.edu.jo, malnimr@just.edu.jo, khadrawi99@yahoo.com

Abstract

This work studies the heat transfer mechanisms during rapid heating of one-layer thin slabs from a macroscopic point of view using the hyperbolic heat conduction model. The effect of the order of temperature derivative (**n**) with respsct to time on the thermal behaviour of the slab in the hyperbolic heat conduction model are investigated. Also, a mathematical analysis is achieved to obtain the derivative order importance. It is found that **n** has insignificant effect on the thermal behaviour when it is value is greater than **1**. Also, effect of the thermal realxation time on the thermal behaviour is invistigated in this study.

Keywords: Conduction, derivative order, Hyperbolic Heat Conduction, Thermal Behavior, Thermal relaxation time.

1 Introduction

In the classical theory of diffusion, the heat flux vector (q) and the temperature gradient (∇T) across a material volume are assumed to occur at the same instant of time. Fourier's law of heat conduction:

$$q\left(x,t\right)=-k\nabla T\left(x,t\right), \tag{1}$$

where q is the heat flux vector, k is the thermal conductivity, and t is the physical time, dictates such an immediate response. It results in an infinite speed of heat propagation, implying that the thermal distribution applied at a certain location in a solid medium can be sensed immediately anywhere else in the medium. Because the heat flux vector and the temperature gradient are simultaneous, there is no difference between the cause and the effect of heat flow. However, there are applications in which heat is found to propagate at a finite speed. These applications involving very low temperatures near absolute zero, energy sources such as a laser and a microwave with extremely short duration or very high frequency, very high temperature gradient, and extremely short times. Specific example for one of the above applications is the usage of short-pulse lasers in the fabrication of microstructures, synthesis of advanced materials, measurement of thin-film properties, diagnostic of material's structure transformation, micomachining, laser patterning, laser processing of diamond films from carbon ion-implanted copper substrates and laser surface hardening. To account for the phenomena involving the finite propagation velocity of the thermal wave, the classical Fourier heat flux should be modified. Cattaneo [1] and Vernotte

[3] suggested independently a modified heat flux model in the form

$$q\left(x,t+\tilde{\tau}\right)=-k\frac{\partial T\left(x,t\right)}{\partial x} \tag{2}$$

where $\tilde{\tau}$ is the time delay, called the "relaxation time". The constitution law of Eq. (2) assumes that the heat flux vector (the effect) and the temperature gradient (the cause) across a material volume occur at a different instant of time, and the time delay between the heat flux and the temperature gradient is the relaxation time τ. The first order expansion of q in Eq. (2) with respect to t bridges all the physical quantities at the same time. It results in the expansion:

$$\tau\frac{\partial q\left(x,t\right)}{\partial t}+q\left(x,t+\tau\right)=-k\frac{\partial T\left(x,t\right)}{\partial x} \tag{3}$$

In Eq. (3) it is assumed that τ is sufficiently small so that the first-order Taylor expansion of $q\left(x,t+\tau\right)$ is an accurate representation for the convection heat flux. The equation of energy conservation for such problems is given as:

$$\rho c\frac{\partial T}{\partial t}=-\frac{\partial q}{\partial x}+g \tag{4}$$

where ρ is the density and c is the specific heat and the Taylor expansion of $q\left(x,t+\tau\right)$is givens as:

$$q+\tau\,\dot{q}\,+\frac{\tau^2}{2\,!}\ddot{q}\,+\frac{\tau^3}{3\,!}q+\,\ldots\ldots\ldots=-k\frac{\partial T}{\partial x}$$

or

$$\sum_{n=1}^{n=\infty}\frac{\tau^{(n-1)}}{(n-1)!}\,q^{(n-1)}=-k\frac{\partial T}{\partial x} \tag{5}$$

where $q^{(n-1)}=\frac{dq^{(n-1)}}{dt^{(n-1)}}$

Derive (5) with respect to x:

$$\sum_{n=1}^{n=\infty}\frac{\tau^{(n-1)}}{(n-1)!}\,\frac{\partial q^{(n-1)}}{\partial x}=-k\frac{\partial^2 T}{\partial x^2}\;or\;\sum_{n=1}^{n=\infty}\frac{\tau^{(n-1)}}{(n-1)!}\,q^{(n-1)}=-kT \tag{6}$$

But

$$q^{(n-1)}=\frac{\partial^{(n-1)}}{\partial t^{(n-1)}}\left(q\right)=\frac{\partial^{(n-1)}}{\partial t^{(n-1)}}\left\{\frac{dq}{dx}\right\} \tag{7}$$

Insert (4) into (7) yelds:

$$q^{(n-1)}=\frac{\partial^{(n-1)}}{\partial t^{(n-1)}}\left\{g-\rho\,c\dot{T}\right\}=g^{(n-1)}-\rho\,c\,T^{(n)}$$

Substitute into (6) gives:

$$\sum_{n=1}^{n=\infty}\frac{\tau^{(n-1)}}{(n-1)!}\,\rho\,c\,T^{(n)}=\sum_{n=1}^{n=\infty}\frac{\tau^{(n-1)}}{(n-1)!}\,g^{(n-1)}+kT \tag{8}$$

where

$$g^{(n-1)}=\frac{dg^{(n-1)}}{dt^{(n-1)}}\text{ and }T=\frac{dT^2}{dx^2}$$

The wave model represented in Eq. (7) removes the paradox of the finite speed of heat propagation assumed in Fourier's law. Tzou [3] relates the relaxation time to the thermal wave speed as

$$\tau = \frac{\alpha}{C^2}$$

where α is the thermal diffusivity and$C$ is the thermal wave speed. In the case of C approaching infinity, the relaxation time decreases to zero ($\tau = 0$) and the wave model reduces to Fourier's law.

The Cattaneo [1] and Vernotte [2] (CV) wave model assumes an instantaneous heat flow. The temperature gradient is always the cause for the heat transfer, while the heat flux vector is always the effect. Khadrawi et. all [4] invesitigate the thermal behavior of perfect and imperfect contact composite slab under the effect of the hyperbolic heat conduction model. Also, Transient free convection fluid flow in a vertical microchannel as described by the hyperbolic heat conduction model is investigated by [5].

It is worth mentioning here that the relaxation time $\tau$is of order of picoseconds. The usage of the hyperbolic heat conduction model is essential when the problem time scale, which is the duration of the transient heating process, is comparable with the thermal relaxation time τ.

The hyperbolic heat conduction model as given in Eq. (7) has been receiving increasing attention both for the theoretical motivations (e.g., analysis of thermal waves and second sound in dieletric solids and finite speed of heat transport) and for the analysis of some practical problems involving a fast supply thermal energy as mentioned previously.

2 Analysis

Consider a thin-layer slab of thickness L as illustrated in Fig. 1. Let $\alpha$the thermal diffusivity for the layer. Initially, the region are at temperature $T_i = 0$. For $t¿0$the boundary surface at $x = 0$ is kept at T_w and the boundary surface at $x = L$is kept insolated. Also, there is no heat generation. The thickness of the layer is assumed to be very small relative to the height of the slab, so it is reasonable to assume that the conducted heat is transferred in the x-direction only.

The elementary assumption here is that the heat propagates with a finite speed. Thus, the hyperbolic heat conduction model is suitable for accounting for the phenomena con-

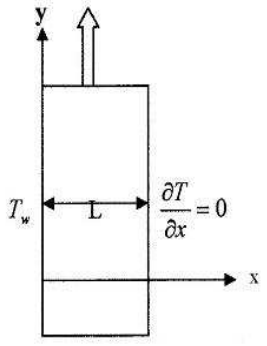

Figure 1: Schematic diagram of the problem under consideration.

cerning the finite propagation speed of the thermal wave. In this case, the energy equation under these assumption is given by:

$$\sum_{n=1}^{n=\infty} \frac{\tau^{(n-1)}}{(n-1)!}\,\rho\,c\,T^{(n)} = kT \tag{9}$$

which assume the following initial and boundary conditions

$$\begin{aligned} &T(0,x) = 0 \\ &T(t,0) = T_w \\ &\frac{\partial T(t,L)}{\partial x} = 0.0 \end{aligned} \tag{10}$$

Now, with the notation that $L\{T(t,x)\} = W(S,x)$, Laplace transformations of Eqs. (9) and (10) yield:

$$\sum_{n=1}^{n=\infty} \frac{\tau^{(n-1)}\rho\,c}{(n-1)!} \left\{ \begin{array}{l} S^n W(S,x) - S^{(n-1)}T_i - \\ S^{(n-2)}\dot{T}_i - S^{(n-3)}\ddot{T}_i - \\ S^{(n-4)}T_i - ..... - T_i^{(n-1)} \end{array} \right\} = kW^{\backslash\backslash}(S,x) \tag{11}$$

Let all initial conditions $T_i = T_i = \ddot{T}_i = T_i = ... = T_i^{(n-1)} = 0$

Equation (11) assume the following solution:

$$W_(S,x) = C_1 e^{M\,x} + C_2 e^{-M\,x} \tag{12}$$

where $M = \sqrt{\frac{\sum_{n=1}^{n=\infty} \frac{\tau^{(n-1)}}{(n-1)!}\,S^n}{\alpha}}$ and$\alpha = \frac{k}{\rho\,c}$

Also, the Laplace transformation of Eq. (10) yields:

$$\begin{aligned} &W(0,x) = T_i = 0.0 \\ &W(S,0) = \tfrac{T_w}{S} \\ &W^{\backslash}(S,L) = 0 \end{aligned} \tag{13}$$

Insert Eq. (11into (12) and solve for C_1 and C_2 to yield

$C_1 = \frac{(T_w/S)\left(e^{-2ML}\right)}{\{1+e^{-2ML}\}}$ and $C_1 = \frac{(T_w/S)}{\{1+e^{-2ML}\}}$

Equations (12) and (13) are inverted using a computer program based on the Riemann-sum approximation as

$$T(x,t) \cong \frac{e^{\gamma t}}{t}\left[\ \frac{1}{2}W(x,\gamma) + Re\sum_{n=1}^{N} W(x,\gamma + \frac{in\pi}{t})(-1)^n\ \right] \tag{14}$$

In Eq. (12), Re represents the real part of the summation and $i = \sqrt{-1}$, and $\gamma\,t =$ 4.7gives the most satisfactory results [3]. Equation (12) yields the exact temperature distribution in the domain.

3 Results and Discussion

Figure 2 shows the effect of derivative order **n** on the spatial temperature distribution. It is clear that **n** has insignificant effect when it s value is greater that **1**. Spatial temperature distribution at different value of τ is shown in Fig. 3. Small values of the thermal relaxation time have insignificant effect on the spatail temperature distribution.

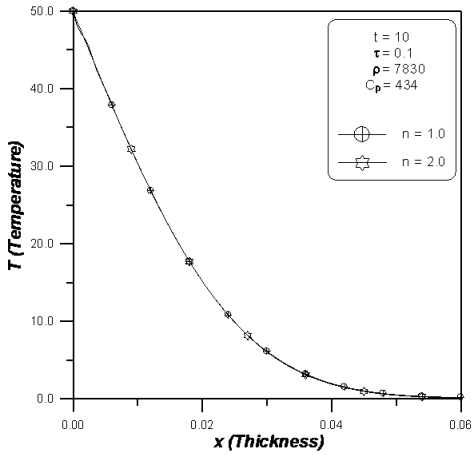

Figure 2: Spatial temperature distribution at diffirent value of **n**.

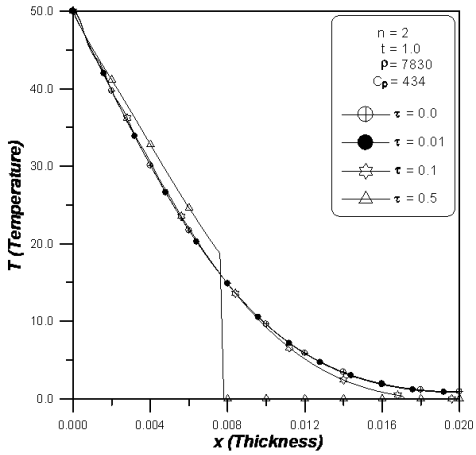

Figure 3: Spatial temperature distribution at diffirent value of τ.

4 Conclusion

The thermal behavior of a thin-layer slab under the effect of the hyperbolic heat conduction model is investigated during rapid heating of one-layer thin slabs. The effect of derivative order (**n**) of the temperature with respsct to time on the thermal behaviour of the slab are investigated. It is found that **n** has insignificant effect on the thermal behaviour when it is value is greater than **1**.

5 Nomenclature

k Thermal conductivity, $W.m^{-1}.K^{-1}$
tTime, s
T Temperature domain , K
T_i Initial temperature of domain, K
T_w Wall temperature, K
WLaplace transformation of the temperature
xx-coordinate

Greek Symbols α Thermal diffusivity, $k/\rho\, c$
ρ Density, $kg.m^{-3}$
τ thermal relaxation time, s
Subscripts
w refers to wall
i refers to initial

References

[1] C. Catteneo, *Comptes Rendus* 247: 431 (1958).

[2] D. Y. Tzou, *Macro- to- Microscale Heat Transfer- The Lagging Behavior* (Taylor and Francis, Washington, DC, 1997) pp. 1-64.

[3] P. Vernotte, *Comptes Rendus*. 252: 2190 (1961).

[4] A. F. Khadrawi, M. A. Al-Nimr and M. Hammad, "Thermal behavior of perfect and imperfect contact composite slab under the effect of the hyperbolic heat conduction model", *International Journal of Thermophysics, Vol. 23(1), pp. 581-598,(2001).*

[5] A. F. Khadrawi, Ali Othman and M. A. Al-Nimr, Transient free convection fluid flow in a vertical microchannel as described by the hyperbolic heat conduction model, *Int. J. of Thermophysics, Vol. 26, no. 3, pp. 905-918,(2005).*

Suleiman E. Al-Lubani, Mohammadieh street, Amman, Jordan

Hybrid algorithms for multiobjective optimization of mechanical and hydromechanical systems

V. D. Sulimov P. M. Shkapov
spm@bmstu.ru

Abstract

In two recent decades approaches with the use of vectorial criteria as mathematical models of choosing find a wide utility in numerous applications. It will suffice to mention some problems of identification and diagnostics of complex systems, optimal design, control, saving of safety. The goal of multiple criteria numerical strategies is to compute a set of non-dominated solutions which constitute Pareto-optimal front approximations. Generally individual criteria are multiextremal not everywhere differentiable functions. Under these conditions searching for a global solution for the criterion is an independent challenging problem. Account must be taken of that the effectiveness of deterministic global optimization algorithms is quickly reduces with increasing the dimension of the search space. On the other hand, stochastic global optimization algorithms are computation-intensive. These considerations motivate a topicality of the development of hybrid methods for solving multiobjective optimization problems with multiextremal nonsmooth criteria. Two novel hybrid vector optimization algorithms combining a Metropolis-based stochastic algorithm and deterministic gradient techniques or a space-filling curve method are introduced. Implementations of the hybrid algorithms are discussed. Results of successful computational experiments are presented to illustrate the efficiency of the approach.

1 Introduction

In many practical cases optimization problems must be formulated as problems with multiple criteria. One of the approaches suggests converting the initial vector optimization problem into a scalarized single-objective problem. More general methods are founded on the concept of Pareto-dominance, where the goal is to find trade-off solutions for criteria being in conflict. When individual criteria are multiextremal not everywhere differentiable functions, the vector optimization problem becomes highly complicated and computationally expensive one [1, 2]. Most problems of this type cannot be solved exactly owing to highly complex and large dimensional search space. The goal is to find the set of non-dominated solutions [3]. The vector linearization method is one of the effective methods for numerical solutions of the multiobjective problems [4]. An introduction of biparametric smoothing approximations makes it possible to extend the method on the class of nondifferentiable problems [5]. In the context of the vector problem under consideraton, it necessary to solve global optimization subproblems for individual criteria. Properties of deterministic global optimization algorithms are well-studied. It is common knowledge that the performance of deterministic algorithms essentially depends on the problem dimension. On the other hand, stochastic global optimization algorithms are generally computation-intensive. A hybrid global optimization algorithm NMPCA that combines the recent stochastic algorithm PCA and Nelder-Mead simplex method is presented in

[6]. The NMPCA algorithm was applied to a nuclear reactor core design optimization problem. During processing two procedures are performing: a wide search in the solution space using the stochastic PCA and a local search in the promising areas with the deterministic simplex algorithm. The local search procedure is performed iteratively until a certain number of fitness function evaluations being reached. It is pertinent to note that the convergence theory for Nelder-Mead simplex method is far from completion; so the method can fail to converge or converge to non-stationary points [7]. By this is meant that the question of reliability of the algorithm as a whole is still an open question. As an alternative to the NMPCA a novel hybrid algorithm may be introduced. In this version of the global optimization algorithm the local search mechanism is a standard deterministic linearization method. Inverse problems are considered to be substantially difficult because of the kinks connected with presence of the repeated or very close frequencies in registered spectra for the computational model under updating. The difficulty motivated the development of algorithms for the solution of the minimization problem via some smooth approximation, which could be minimized by using any of the efficient classical approaches for smooth optimization. Several approximations to smooth out the kinks may be introduced. One of them results in a continuously differentiable approximate fitness function, whereas another one leads to a twice continuously differentiable approximate function. These approximations replace the original function in some neighborhoods of directional differentiability points. Moreover, this approach preserves such important property of the original function as its convexity. It is clear that the approach makes it possible to implement efficient gradient techniques in the solution process [8]. Computational experiments show the principal applicability of the proposed hybrid algorithm PCAHS for solving the global optimization problems. Some powerful algorithms for multiextremal non-convex optimization problem are based on reducing the initial multi-dimensional problem to the equivalent problem of one dimension. This reduction can be executed by applying Peano-type space-filling curves mapping a unit interval on the real axis onto a multi-dimensional hypercube [9]. The approach needs not any derivatives of the function to be minimized with updating parameters.

The plan of the remainder of this paper is as follows. The section following contains statement of the multiobjective optimization problem. Section 3 provides brief description of hybrid vector optimization algorithms for solving problems with multiextremal nonsmooth criteria. In section 4 successful computational experiments for two model multiobjective optimization problems are presented to illustrate peculiarities of the proposed approach. Section 5 gives conclusions and discussion on further work.

2 Formulation of the problem

Assume that the functions $f_i(x)$, $x \in \mathrm{R}^n$, $i = 1, 2, \ldots, m$, constitute a vectorial criterion $f(x) = (f_i(x), \ldots, f_m(x))$ for a multiobjective optimization problem subject to $x \in X = \{x \in \mathrm{R}^n : g_j(x) \leq 0,\ j \in J\}$, where x stands for the vector of control variables; $g_j(x)$ stands for jth function of constraints; the corresponding index set is defined as $J = \{j : j = 1, \ldots, k\}$. It is supposed that in the problem under consideration both individual criteria and constraints are represented by multiextremal nonsmooth functions. In addition to main definitions [3] let introduce two ones.

Definition 1 [4]. For a given vector optimization problem the Pareto-optimal set is defined as $S_P = \{x \in X : \neg\exists x^* \in X,\ x^* \prec x\}$ (here the sign "$\prec$" denotes dominance).

Definition 2 [4]. For a given vector optimization problem and the Pareto-optimal set S_P the Pareto front is defined as $F_P = \{f(x) : x \in S_P\}$.

It should be noted that a Pareto-optimal set is always a non-dominated set. But there may exist non-dominated sets that contain some Pareto-optimal solutions and some non-Pareto-optimal solutions [2]. So it is necessary to realize that the non-dominated solutions found by an optimization algorithm are not certain to be able to present the true Pareto-optimal set.

Let to describe algorithms for solving the multiobjective optimization problem that realize the vectorial optimization method [4].

3 Hybrid multiobjective optimization algorithms

3.1 The hybrid algorithm V-PCALMS

Let introduce biparametric local smoothing approximations for every individual criterion and every constraint function [8]. Let associate with every point $x \in \mathrm{R}^n$ the following auxiliary problem

$$\min_{w,\xi}\left\{\xi + \frac{1}{2}\|w\|^2 : \left(\nabla \tilde{f}_i(p,q,x),\ w\right) \le \xi, \quad i \in I,\right.$$
$$\left.\left(\nabla \tilde{g}_j\,(p,q,x)\,, w\right) + \tilde{g}_j(p,q,x) \le 0, \quad j \in J\right\}, \quad (1)$$

where w is a vector standing for the search direction; ξ is a parameter; $\nabla \tilde{f}_i(p,q,x)$ stands for the gradient of the smoothed approximated criterion $\tilde{f}_i$ which is computed in a admissible point; $I = \{1, \ldots, m\}$; the set J has been defined earlier. Let introduce the following assumptions. Let exists $N > 0$ such that: for $x^0 \in \mathrm{R}^n$ and certain $i \in I$ the set $\Omega_N = \left\{x : \tilde{f}_i(p,q,x) + N\tilde{G}(p,q,x) \le \tilde{f}_i(p,q,x^0) + N\tilde{G}(p,q,x^0)\right\}$ is restricted; $\tilde{G}(p,q,x) = \max\{0, \tilde{g}_1(p,q,x), \ldots, \tilde{g}_k(p,q,x)\}$; gradients of the functions $\tilde{f}_i(p,q,x)$, $i \in I$, $\tilde{g}_j(p,q,x)$, $j \in J$, in Ω_N satisfy the Lipschitz condition with a constant L; there are exist Lagrange multipliers of the problem (1) v_j, $j \in J$, such that $\sum\limits_{j\in J} v_j \le N$, and the problem is solvable with respect to $w \in \mathrm{R}^n$ for each $x \in \Omega_N$. If for certain ε, $0 < \varepsilon < 1$, it is chosen $0 \le \alpha \le 1$, such that $0 \le \alpha \le (1-\varepsilon)/(1+N)/L$, then the following inequality is true [4]

$$\max_{i\in I}\left(\tilde{f}_i(p,q,x+\alpha w) - \tilde{f}_i(p,q,x)\right) + N\tilde{G}(p,q,x+\alpha w) \le$$
$$\le N\tilde{G}(p,q,x) - \alpha\varepsilon\|w\|^2. \quad (2)$$

The algorithm for solving the vector optimization problem consists of the following main steps [4, 5]. Let x^0 be an initial approximation and certain number ε, $0 < \varepsilon < 1$, and parameters of the approximations $p < 0$, $q > 0$ are chosen. Let the current point x^k, is obtained, then:

Step 1. Solve the auxiliary problem (1) when $x = x^k$.

Step 2. Find the first value $s = 0, 1, \ldots$, such that the inequality (2) holds for $\alpha = (1/2)^s$; if the appropriate $s = s_0$ is found, then set $\alpha_k = 2^{-s_0}$, $x^{k+1} = x^k + \alpha_k w^k$.

Optimization of the individual criteria is performed by use of the hybrid global optimization algorithm combining the stochastic algorithm PCA [6] and the linearization method during the local search. For the functions that are not everywhere differentiable the smoothing approximations are introduced. The implementation of the recent stochastic algorithm PCA is based on the analogy with physical processes of absorption and scattering of particles during nuclear reactions. The algorithm PCA uses only one particle

for scanning the search space. The hybrid algorithm for solving a global optimization subproblem for an individual criterion is proposed in [8]. The convergence of the algorithm is proved for the case of simple constraints.

3.2 The hybrid algorithm V-PCASFC

The second hybrid algorithm for multiobjective optimization implements the deterministic space-filling curve method for solving the global optimization subproblem for the individual criterion. The mentioned algorithm is based on the algorithm PCA in combination with the deterministic method of the space-filling curve [9]. Some powerful algorithms for multi-extremal non-convex optimization problem are based on reducing the initial multi-dimensional problem to the equivalent problem of one dimension. This reduction can be executed by applying Peano-type space-filling curves mapping a unit interval on the real axis onto a multi-dimensional hypercube. The Peano curve development maps the segment [0, 1] of the real axis R^1 into the hypercube $X \subset R^n$. Actually, this is the case of continuous single-valued mapping that offers finding point $x(z) = (x_1(z), \ldots, x_n(z))^T \in X$ for each point $z \in [0, 1]$:

$$\min_{x \in X} f_i(x_1, \ldots, x_n) = \min_{0 \le z \le 1} \phi(z).$$

So, the initial multi-dimensional minimization problem is equivalent to the above one-dimensional problem of finding the global minima of the discontinuous multi-extremal function $\phi(z)$. The Hilbert technique is used here for building the development of the Peano space-filling curve depending on parameter m that stands for the number of subdivision levels. The approach needs not any derivatives of the function to be minimized with updating parameters. Some disadvantage of this approach is in the fact that one-dimensional problem obtained by the above reduction leaks some information on the closeness of iteration points in the initial multi-dimensional space.

Algorithm SFC: reduction of the problem dimension using the space-filling curve method.

0. Set formally the point x^* of local minimum. Let two small numbers $\gamma_1 > 0, \quad \gamma_2 > 0$, and the vector of constraints $\beta \in R^n$ be given. Let $k = 0$, $m = 1$.

1. The local minimization phase: find new point x^* (after l sub-iterations); set $k = k + l$. If $f\left(x^k\right) = 0$ then go to step 2. If $f\left(x^k\right) < \gamma_1$ and $x_i^k > \beta_i$ for some $i \in I^x, \quad I^x = \{1, 2, \ldots, n\}$, then build the effective sub-vector x_{eff}^k, reduce the multi-dimensional problem to the one-dimensional form and go to step 2. Else, go to step of stochastic scanning.

2. Set $m = m + 1$. If $m \le m_{\max}$ then go to step 3. Else, go to step 4.

3. Define the current value z_* using the development of the Peano curve and calculate the current approximation of $\phi(z_*)$. If $\phi(z_*) \ge \gamma_2$ then go to step 2.

4. Reconstruct x^* and $f(x_*)$ using z_* and $\phi(z_*)$.

5. Define the point of local minimum $x^{LM} = x^*$, stop.

The pseudo code brief description of the hybrid PCASFC algorithm that combines the PCA and the deterministic space-filling curve method is as follows.

0. Generate an initial solution *Old_Config*
1. For $n = 0$ to # iterations
   Generate a stochastic perturbation of the solution
   If Fitness *(New_Config)* > Fitness *(Old_Config)*
      Old_Config := *New_Config*

```
    Local search ( )
  Else
    Scattering ( )
  End If
End For
2. Local search ( )
  Apply procedure of local search
  using the Space-Filling Curve Method
Return
3. Scattering ( )
  p_scatt = 1 − (Fitness (New_Config))/(Best Fitness)
  If p_scatt > random(0, 1)
    Old_Config := random solution
  Else
    Exploration ( )
  End If
Return
```

4 Computational results

In this section two numerical examples of hybrid algorithms V-PCALMS and V-PCASFC applications to model multiobjective optimizations problems are presented. First example is devoted to the problem of determining the optimal configuration of the rod system. In the second example the updating of the computational model of the coolant two-phase flow dynamics in the primary circuit is carried out.

Example 4.1. The computations were performed in connection with the problem of choosing the optimal parameters for the Π-shaped rod isoperimetric system with a compensator of axial deformations. The system consists of uniform straight rod elements with two fixed lower nodes. Two rods (left and right) are vertical. The middle rod rigidly bounded with them is in a horizontal position. Free oscillations of the system are investigated. The first criterion $f_1(x)$ is a height of the system, and the first (the smallest) eigenfrequency is the second criterion $f_2(x)$. It should be noted that the first criterion is the first variable x_1 in the problem simultaneously. The second variable x_2 is the distant parameter determining a position of the compensator on the horizontal rod. A dependence from the second variable of the lower eigenfrequencies corresponding to plane oscillations and out-of-plane oscillations of the system are shown in Fig. 1.

The lower envelope of the two curves in Fig. 1 represents the second criterion of the problem. The goal is to maximize the criteria being in conflict. It is clear that the second criterion has two local and one global maxima. So it is necessary to solve subproblems for global optimization of the second criterion when solving this multiobjective optimization problem with two criteria. The iteration history for the solution of the current subproblem is shown in Fig. 2.

The solution of the multiobjective optimization problem for normalized criteria in the criterion space is presented in Fig. 3. Exact (theoretical) global Pareto-optimal front and approximated Pareto-optimal front are rather closely related. The maximal computational error here is no more than 3.9%.

Example 4.2. The computations were performed in connection with the problem of identification of the coolant phase constitution in the VVER-1000 primary circuit [10]. Appearance of the second phase is possible: in a coolant heating zone (pressure tank of

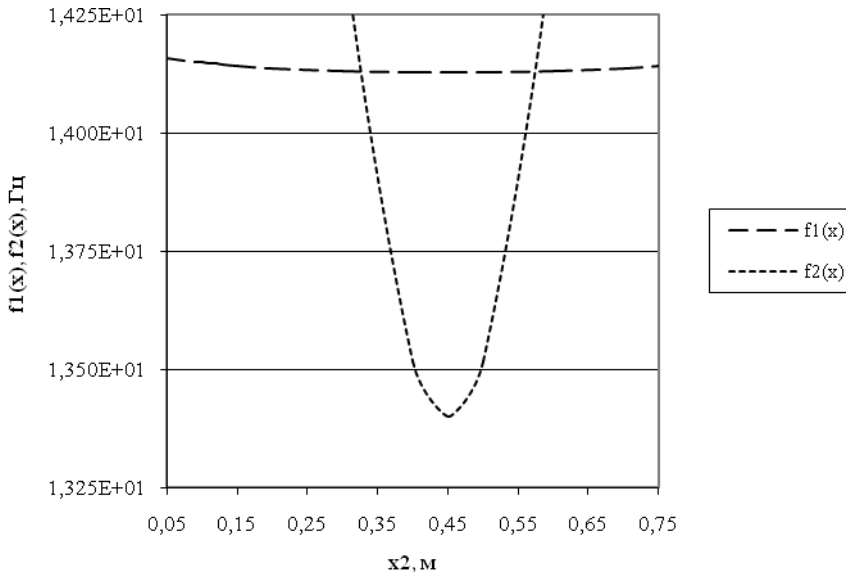

Fig. 1: The second criterion of the multiobjective problem as a lower envelope of eigenfuctions that corresponds to plane and out-of-plane oscillations of the system

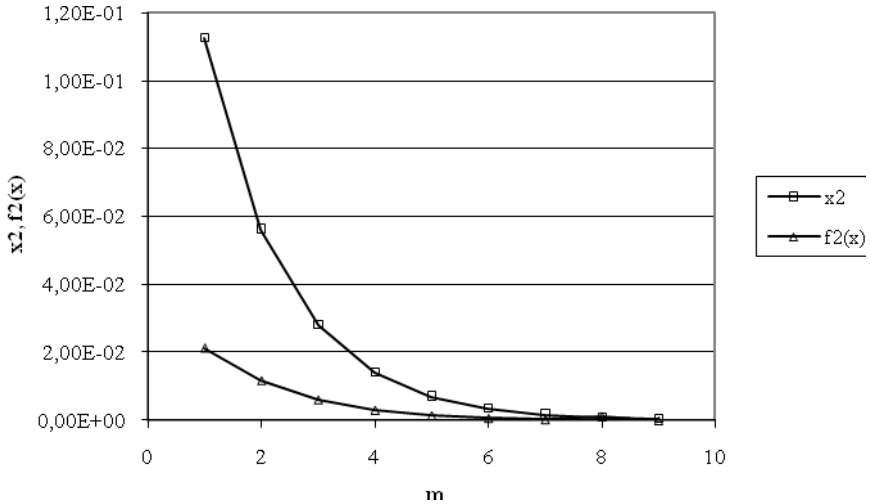

Fig. 2: The convergence of the solution of the current global optimization subproblem when the first criterion is fixed ($x_1 = 0.8$)

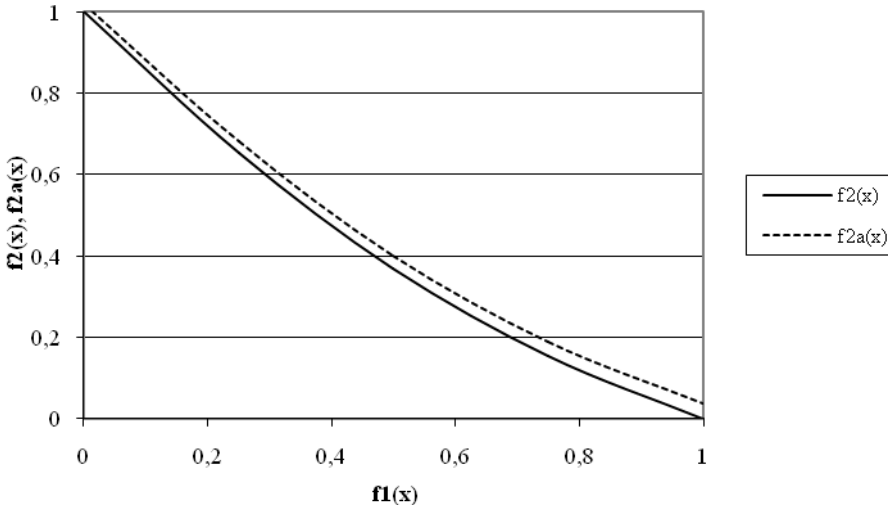

Fig. 3: The exact and approximated global Pareto-optimal fronts

the pressurizer), in an exit volume of the reactor pressure vessel (RPV), in a core barrel of the RPV, in exit volumes of main circulating pumps. In order to formulate the inverse problems two vectors of relative acoustic velocities in a coolant flowing throw the specified zones are introduced. Let now the anomalous coolant state constitution be characterized by the only controlling variables: $x_1 \in [70,\ 100]$ (in %). The error function is determined using ten lower spectral components. The goal to maximize the first spectral component (the first eigenfrequeny of the coolant oscillations) and to minimize the seventh spectral component simultaneously. Both the components are mostly sensitive to the considered state of the coolant constitution. The corresponding bicriterial problem is formulated as the problem of the appropriate correction of the computational model of the two-phase coolant according to current abnormal spectrum. The iteration history for the solution of the current subproblem is shown in Fig. 4.

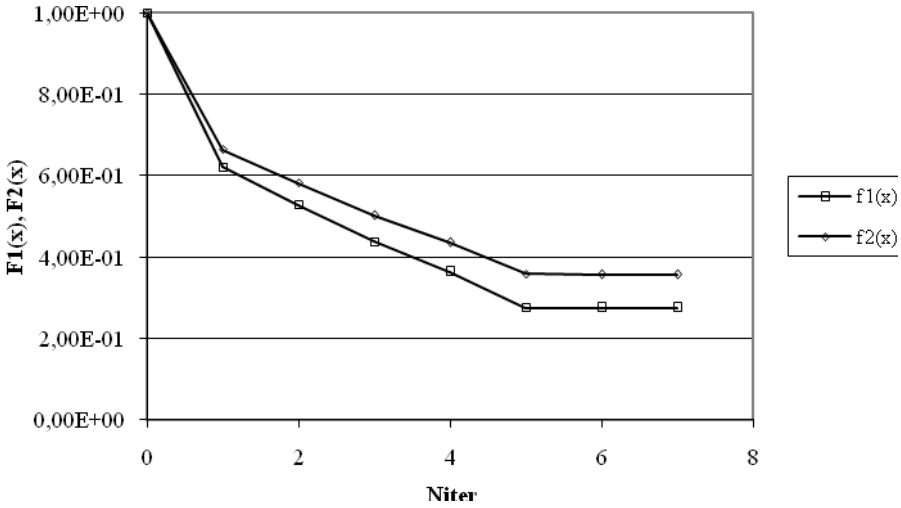

Fig 4: Number of final iterations of the global optimization algorithm vs. the problem criteria values

The solution of the bicriterial optimization problem for normalized criteria in the criterion space is presented in Fig. 5. Exact (theoretical) global Pareto-optimal front and approximated Pareto-optimal front are rather closely related. The maximal computational error here is about 4.0 %.

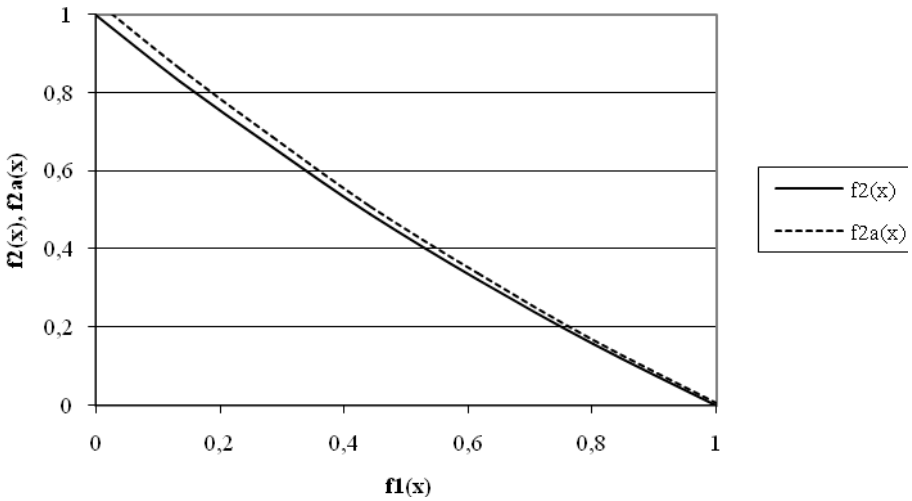

Fig. 5: The exact and approximated global Pareto-optimal fronts

5 Conclusions

Two novel hybrid algorithms for multiobjective optimization problems combining a Metropolis-based algorithm and deterministic gradient technique or space-filling curve method for local search are presented. Smoothing approximations are introduced during the local search that makes it possible to expand the V-PCALMS algorithm on the class of non-differentiable problems. The V-PCASFC algorithm being introduced here does not require any gradient information. Both the algorithms were used for solving bicriterial model problems in connection choosing parameters of Π−shaped rod system with a compensator of axial deformations and with computational model updating for the two-phase coolant flow in the nuclear reactor primary circuit. Numerical experiments show the principal applicability of the proposed hybrid algorithms for solving the above model multiobjective optimization problems. The future work will be devoted to increasing the computational efficiency of tools for solution the model updating problems with regard to noisy data using multiple criteria representation.

Acknowledgements

This research is partially supported by the program "Leading Scientific Schools" of Russian Federation (the grant NSh-5271.2010.8).

References

[1] J. Gao, J. Wang. A hybrid quantum-inspired immune algorithm for multiobjective optimization. Applied Mathematics and Computation 211, 4754-4770, 2011.

[2] C. Gil, A. Márques, R. Baños, M.G. Montoya, J. Gómez. A hybrid method for solving multi-objective global optimization problems. Journal of Global Optimization 38, 265-281, 2007.

[3] V.V. Podinovskij, V.D. Nogin. Pareto-optimal solutions of multicriterial problems. 2^{nd} ed., corr. and suppl. Moscow, FIZMATLIT, 2007 (in Russian).

[4] B.N. Pschenichnyj, R.B. Sosnovskij. A linearization method for multiple criteria problem solution. Kybernetika 6, 107-109, 1987 (in Russian).

[5] V.D. Sulimov, P.M. Shkapov. A smoothing approximation in vector non-differentiable optimization problems for mechanical and hydro-mechanical systems. Vestnik MGTU. Estestvennye Nauki 2 (21), 17–30, 2006 (in Russian).

[6] W.F. Sacco, H.A. Filho, N. Henderson, C.R.E. de Oliveira. A Metropolis algorithm combined with Nelder-Mead Simplex applied to nuclear reactor core design. Annals of Nuclear Energy 35, 861-867, 2008.

[7] K.I.M. McKinnon. Convergence of the Nelder-Mead simplex method to a non-stationary point. SIAM J. Optimization 9, 148–158, 1998.

[8] V.D. Sulimov. A local smoothing approximation in a hybrid algorithm for optimization of hydro-mechanical systems. Vestnik MGTU. Estestvennye Nauki 3 (38), 3–14, 2010 (in Russian).

[9] R.G. Strongin, Y.D. Sergeev. Global optimization: Fractal approach and non-redundant parallelism. Journal of Global Optimization 27, 25-50, 2003

[10] V.G. Kinelev, P.M. Shkapov, V.D. Sulimov. Application of global optimization to VVER-1000 reactor diagnostics. Progress in Nuclear Energy 43, 51–56, 2003.

V.D. Sulimov, Baumanskaya 2nd str. 5, Moscow, 105005, Russia.
P.M. Shkapov, Baumanskaya 2nd str. 5, Moscow, 105005, Russia.

Dynamics of marine stationary platform under action of seismic loading

Vyacheslav A. Shekhovtsov Petr E. Tovstik Tatiana M. Tovstik
a.sheh-411@yandex.ru, peter.tovstik@mail.ru

Abstract

Dynamics of a marine stationary platform under action of the seismic loading is investigated. The structure consists of a tube-like ferroconcrete rod of variable cross-section. To describe the rod vibrations the beam-like model is used. The system of partial differential equation is reduced to the system with 9 degrees of freedom. Some numerical examples are studied. It is established that at design it is necessary to pay the main attention to the concrete strength when the extension deformations appear.

Introduction

Dynamics of a marine stationary platform under action of the seismic loading is investigated. The structure consists of a tube-like ferroconcrete rod. Below the rod is attached to the foundation, the basic platform is attached above the rod. Vibrations in one plane are studied. This structure may be used for the depth until 250 m. At design some excitations are to be taken into consideration. Among them there are the surface gravity waves, the wind acting on the basic platform, the current, the ice loading, and at last the seismic excitation. For this the structure the surface waves excitation was investigated in [1], action of the horizontal seismic excitation was investigated in [2]. Here we study the general case of seismic excitation which has as the horizontal so the vertical components in assumption that in limits of foundation the ground acceleration does not depend on the space co-ordinates.

In linear approximation the longitudinal and the bending vibrations may be studied independently. But due to the nonlinearity of the constitutive relations accepted in the work, these vibrations are connected to each other. As for the bending vibrations so for the longitudinal ones the solution is presented as sums of natural modes with the unknown coefficients depending on time. As an example we use the not a real but a model seismic impulse which allows us to find easy the dependence of the level structure vibrations on the frequency of the seismic excitation. The main result is that at design the main attention is to be paid on the concrete strength in the cases when its extension appear.

The problem of the random seismic excitation is lightly discussed.

1 Mathematical model of structure

Dynamics of a marine stationary platform under action of the seismic loading. The structure consists of a tube-like iron-concrete rod with the variable cross-section. Below the rod is attached to the foundation, which has three degrees of freedom namely the displacements in the horizontal and vertical direction and rotation around the horizontal

axis. The basic platform is attached above the rod. Vibrations in one plane are studied. The attached mass of water and the resistance of water proportional to the square of the rod velocity are taken into account. It is assumed that the water is stationary. Influence of the surface waves and of the current is not studied. The ground acceleration has the horizontal component $a(t)$ and the vertical component $b(t)$, the angle of rotation $(\varphi_0(t))$ is also given. In limits of foundation the ground acceleration does not depend on the space co-ordinates. The used model is described in [1], but here instead the surface waves we study the seismic excitation.

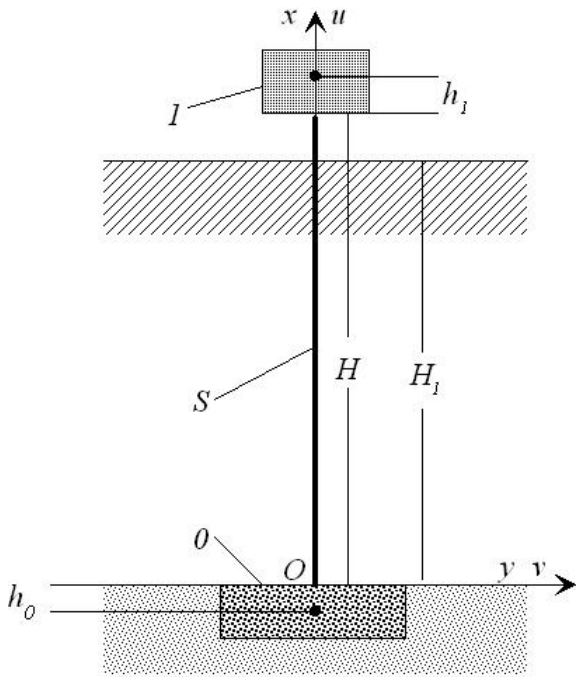

Fig. 1. The sketch of structure.

The foundation and the basic platform are supposed to be the rigid bodies *0* and *1* (see Fig. 1) attached to the rod S, for which the beam model is accepted. The movable co-ordinate system Oxy, which moves forward with the point O of ground with accelerations $a(t)$ and $b(t)$ is introduced.

Equation of the longitudinal rod motions is

$$\frac{\partial P_1}{\partial x} = \rho_0(x)\left(\frac{\partial^2 u}{\partial t^2} + a(t)\right), \tag{1}$$

where $u(x,t)$ is the vertical deflection of the rod cross-section x, $P_1(x,t)$ is the additional extension force appearing due to the seismic impulse, $0 \le x \le H$, H is the rod height, $\rho_0(x)$ is the mass of the rod unit length.

The boundary conditions at the bottom $x = 0$ and at the upper end $x = H$ are the equations of the vertical motion of the bodies *0* and *1*

$$\begin{aligned} m_0\left(\frac{d^2u_0}{dt^2} + a\right) &= -c_u u_0 + P_1(0,t), \quad u_0 = u(0,t), \\ m_1\left(\frac{d^2u_1}{dt^2} + a\right) &= -P_1(H,t), \quad u_1 = u(H,t), \end{aligned} \tag{2}$$

where m_0, m_1 are the bodies *0, 1* mas.

The bending equations of rod are

$$\frac{\partial^2 M}{\partial x^2} - \frac{\partial}{\partial x}\left(P(x)\frac{\partial v}{\partial x}\right) + \rho(x)\left(\frac{\partial^2 v}{\partial t^2} + b\right) = f_v, \tag{3}$$

where v is the lateral deflextion of the rod axis, M is the bending moment, $P = P_0 + P_1$, P_0 is the axial force in the initial state

$$-P_0(x) = \left(m_1 + m_s - \int_0^x \rho_0(x)\,dx\right) g, \quad m_s = \int_0^H \rho_s(x)\,dx, \tag{4}$$

m_s is the rod mass, $g = 9.81$ (m/c^2) is the gravity acceleration, the sign "minus" indicates compression, $\rho(x) = \rho_0(x) + \rho_1(x)$, $\rho_1(x) = \gamma_w S(x)$ is the attached mass of water ($\rho_1 = 0$ for $H_1 \le x \le H$), γ_w is the water density, S is the cross-section area. Here f_v is the resistance force of water per unit height

$$f_v = -C_v \gamma_w R(x) V|V|, \quad V = \frac{\partial v}{\partial t} + V_0, \quad V_0(t) = \int_0^t b(t)\,dt, \tag{5}$$

where C_v os the resistance coefficient, $R(x)$ is the radius of the rod cross-section.

The boundary conditions at the bottom and $x = 0$ at the upper end $x = H$ are

$$\begin{aligned}
&m_0\left(\frac{d^2 v_0}{dt^2} + b\right) = -\frac{dM}{dx} + P\varphi - c_v v_0, \\
&J_0\frac{d^2\varphi}{dt^2} - m_0 h_0\left(\frac{d^2 v_0}{dt^2} + b\right) = M - c_\varphi(\varphi - \varphi_0), \qquad x = 0, \\
&m_1\left(\frac{d^2 v_1}{dt^2} + b\right) = \frac{dM}{dx} - P\varphi, \\
&J_1\frac{d^2\varphi}{dt^2} + m_1 h_1\left(\frac{d^2 v_1}{dt^2} + b\right) = -M, \qquad x = H,
\end{aligned} \tag{6}$$

where

$$v_0 = v(0) - h_0\varphi(0), \quad v_1 = v(H) + h_1\varphi(H), \quad \varphi = \frac{\partial v}{\partial x}, \tag{7}$$

J_0, J_1 are the inertia moments, h_0, h_1 are the distances to the centers of gravity (see Fig. 1) of bodies *0, 1*, c_u, c_v, c_φ are the ground stiffness at the relative displacements of foundation.

2 The rod stiffness at the extension and at the bending

The rod is the three layered ferroconcrete tube with the variable cross-section (see Fig. 2). The outer layers $r_1 \le r \le r_2$ and $r_3 \le r \le r_4$ are steel, and the middle layer $r_2 \le r \le r_3$ is concrete.

$$r_k(x) = r_{k0} - bx, \ k = 1, 2, 3, 4, \quad b = \frac{R_0 - R_1}{H}, \tag{8}$$

where r_{k0} are the layers radii at $x = 0$, $R_0 = r_4(0)$ and $R_1 = r_4(H)$ are the radii of lower and upper tube cross-sections.

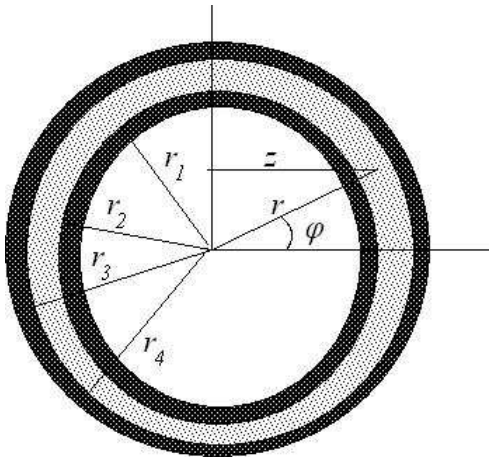

Fig. 2. The cross-section of a three-layered tube.

We accept the following dependences between stresses σ and strains ε (in the vertical direction neglecting the other stresses and strains):
for the steel

$$\sigma = E_s \begin{cases} -\varepsilon_s, & \varepsilon < -\varepsilon_s, \\ \varepsilon, & |\varepsilon| \le \varepsilon_s, \\ \varepsilon_s, & \varepsilon > \varepsilon_s, \end{cases} \qquad \sigma_s = E_s \varepsilon_s, \tag{9}$$

and for the concrete

$$\sigma = E_c \begin{cases} -\varepsilon_c, & \varepsilon < -\varepsilon_c, \\ \varepsilon, & -\varepsilon_c \le \varepsilon \le 0, \\ 0, & \varepsilon > 0, \end{cases} \qquad \sigma_c = E_c \varepsilon_c. \tag{10}$$

Here E_s and E_c are the Young modules for steel and for concrete, ε_s is the yield limit of steel which is accepted identical at extension and at compression, ε_c is the flowing limit for concrete at compression. Relations (9) and (10) correspond to the Prandtl model [3] of an ideal elastic-plastic body, and relation (10) fixes the assumption that the concrete does not resist the extension. In the linear approximation the both materials are linearly elastic ones, and for the steel $\sigma = E_s\varepsilon$ and for the concrete $\sigma = E_c\varepsilon$.

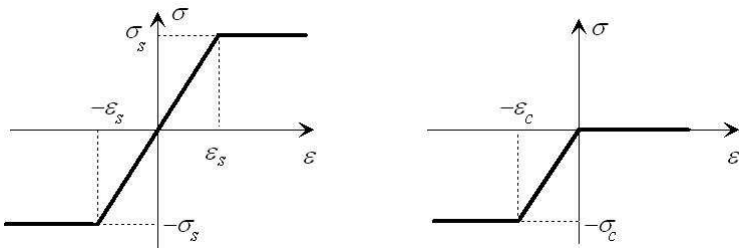

Fig. 3. The Prandtl model for steel (s) and for concrete (c).

In the framework of the plane cross-section hypothesis we study the relations between the axial force P and the bending moment M on the one hand and the axes extension deformation ε_0 and its curvature $\kappa(x) = d^2v/dx^2$ on the other hand. According to this hypothesis the deformation ε of the fiber lying at the distance z from the cross-section axis is a linear function of z (see Fig. 2) namely

$$\varepsilon = \varepsilon_0 + \kappa z. \tag{11}$$

In the linear approximation the mentioned relations are

$$P = c_\varepsilon \varepsilon_0, \quad M = c_\kappa \kappa, \tag{12}$$

where $c_\varepsilon,\ c_\kappa$ are the corresponding stiffness equal to

$$c_\varepsilon = E_s S_s + E_c S_c, \quad c_\kappa = E_s J_s + E_c J_c, \tag{13}$$

$$S_s = \pi(r_4^2 - r_3^2 + r_2^2 - r_1^2), \quad S_c = \pi(r_3^2 - r_2^2),$$
$$J_s = (\pi/4)(r_4^4 - r_3^4 + r_2^4 - r_1^4), \quad J_c = (\pi/4)(r_3^4 - r_2^4).$$

In the accepted designations the weight of the rod unit length is $F_p = g(\gamma_s S_s + \gamma_c S_c)$, where γ_s and γ_c are the densities of steel and of concrete.

For the small enough deformations we get $\varepsilon < 0$, the both materials work in the linear stage and the relations (12) have place. At

$$|\kappa| > \kappa_* = \min\left\{\frac{\varepsilon_0 + \varepsilon_s}{r_4},\ \frac{\varepsilon_0 + \varepsilon_c}{r_3},\ \frac{-\varepsilon_0}{r_3}\right\} \tag{14}$$

one or two materials go in the nonlinear stage and relations (11) are to be revised. The internal stress resultant P and stress couple are equal to integrals of stresses σ

$$P = \iint_S \sigma\, dS, \quad M = \iint_S \sigma z\, dS. \tag{15}$$

3 Natural frequencies and modes of free vibrations

We seek the approximate solution of the non-linear boundary value problems (1), (2) and (3), (6) as a partial sums of series of natural modes with the unknown coefficients $p_k(t)$ and $q_k(t)$ depending on time

$$u(x,t) = \sum_{k=1}^{K_u} U_k(x) p_k(t), \quad v(x,t) = \sum_{k=1}^{K_v} V_k(x) q_k(t). \tag{16}$$

The natural modes may be found as solutions of two separate linear boundary value problems
for the longitudinal vibrations

$$(c_\varepsilon U_k')' + (\omega_k^u)^2 \rho_0(x) U_k = 0, \tag{17}$$

$$\begin{array}{ll} m_0(\omega_k^u)^2 U_k - c_u U_k + c_\varepsilon(0) U_k' = 0, & x = 0, \\ m_1(\omega_k^u)^2 U_k - c_\varepsilon(H) U_k' = 0 & x = H \end{array} \tag{18}$$

and for the bending vibrations

$$(c_\kappa(x) V_k'')'' - (P_0(x) V')' - (\omega_k^v)^2 \rho(x) V_k = 0, \tag{19}$$

$$\begin{array}{ll} (m_0(\omega_k^v)^2 - c_v)(V_{k0} - h_0 V_k') - (c_\kappa V_k'')' + P_0 V_k' = 0, & \\ (J_0 V_k' - m_0 h_0 (V_k - h_0 V_k'))\,(\omega_k^v)^2 + c_\kappa V_k'' - c_\varphi V_k' = 0, & x = 0, \\ m_1(\omega_k^v)^2 (V_k + h_1 V_k') + (c_\kappa V_k'')' - P_0 V_k' = 0, & \\ (J_1 V_k' + m_1 h_1 (V_k - h_0 V_k'))\,(\omega_k^v)^2 - c_\kappa V_k' = 0, & x = H, \end{array} \tag{20}$$

where by sign $'$ the derivative with respect x is denoted, and ω_k^u and ω_k^v are the natural frequencies of the longitudinal and of the bending vibrations.

The eigen functions $U_k(x)$ and $V_k(x)$ satisfy to the orthogonal conditions

$$\int_0^H \rho_0(x)U_k(x)U_n(x)dx + m_0U_k(0)U_n(0) + m_1U_k(H)U_n(H) = 0. \tag{21}$$

$$\int_0^H \rho(x)V_k(x)V_n(x)dx + m_0V_{k0}V_{n0} + J_0V'_{k0}V'_{n0} + m_1V_{k1}V_{n1} + J_1V'_{k1}V'_{n1} = 0, \tag{22}$$

where $V'_{k0} = V'_k(0),\ V_{k0} = V_k(0) - h_0V'_{k0},\ V'_{k1} = V'_k(H),\ V_{k1} = V_k(H) + h_1V'_{k1}$.

We introduce the following designations

$$\begin{aligned}
M_k^u &= \int_0^H \rho_0(x)U_k^2(x)dx + m_0U_k^2(0) + m_1U_k^2(H),\\
\bar{M}_k^u &= \int_0^H \rho_0(x)U_k(x)dx + m_0U_k(0) + m_1U_k(H),\\
M_k^v &= \int_0^H \rho(x)V_k^2(x)dx + m_0V_{k0}^2 + J_0(V'_{k0})^2 + m_1V_{k1}^2 + J_1(V'_{k1})^2,\\
\bar{M}_k^v &= \int_0^H \rho(x)V_k(x)dx + m_0V_{k0} + m_1V_{k1}.
\end{aligned} \tag{23}$$

4 The equations for functions $p_k(t)$ and $q_k(t)$

To deliver the equations for functions $p_k(t)$ we substitute relations (16) in equation (1), then multiply the result by $U_k(x)$ and integrate by x in limits $0 \le x \le H$. Then after integration by parts and some transformations we get the system for $p_k(t)$. By the similar way the system for $q_k(t)$ is delivered.

$$\begin{aligned}
&M_k^u\left(\ddot{p}_k + (\omega_k^u)^2(p_k + \beta_k^u\dot{p}_k/\nu)\right) + \bar{M}_k^u a = Q_k^{(0)}, \quad k = 1,\dots,K_u,\\
&M_k^v\left(\ddot{q}_k + (\omega_k^v)^2(q_k + \beta_k^v\dot{q}_k/\nu)\right) + \bar{M}_k^v = \textstyle\sum_{j=1}^4 Q_k^{(j)},\ k = 1,\dots,K_v
\end{aligned} \tag{24}$$

where the non-linear generated forces are

$$\begin{aligned}
&Q_k^{(0)} = \textstyle\int_0^H (c_\varepsilon u' - P_1)U'_k dx, \quad Q_k^{(1)} = \int_0^H (c_\kappa v'' - M)V''_k dx,\\
&Q_k^{(2)} = -\textstyle\int_0^H P_1V'_k dx, \quad Q_k^{(3)} = \int_0^H f_vV_k dx, \quad Q_k^{(4)} = c_\varphi V_k(0)\varphi_0.
\end{aligned} \tag{25}$$

The derivative with respect time is denoted by dot, $P_1 = P - P_0$, functions $P(u', v'')$ and $M(u', v'')$ are given by formulas (15), and functions $u(x,t)$ and $v(x,t)$ are defined by functions (16).

In equations (24) there are summands with the multipliers β_k^u and β_k^v which integrally take into account the viscous restriction by the Prandtl–Sorokin model [4], [5].

For $Q_k^{(j)} = 0$ equations (24) are linear and are not connected with each other. Nonlinear terms in the right sides of these equations appear if we take into account the non-linear dependences between stresses and strains (see Section 2), and also the water resistance.

5 Model of the seismic ground acceleration

In examples for analytical description of the seismic excitation we accept $\varphi_0 = 0$ and take the vertical and the horizontal components of the ground acceleration in the form

$$a(t) = a_0(t)\cos\gamma, \quad b(t) = a_0(t)\sin\gamma, \quad a_0(t) = At^2e^{-\alpha t}\sin(\nu t + \theta), \tag{26}$$

where γ is the angle of inclination of the seismic wave front. At $\gamma = 0$ the excitation is vertical and at $\gamma = \pi/2$ it is horizontal. The parameters in (26) satisfy to a restriction, which follows from the equality

$$\int_0^\infty a_0(t)dt = 0, \tag{27}$$

because in the opposite case the ground will move when the seismic impulse is finished. From (17) it follows that

$$\alpha(3\nu^2 - \alpha^2)\sin\theta + \nu(\nu^2 - 3\alpha^2)\cos\theta = 0. \tag{28}$$

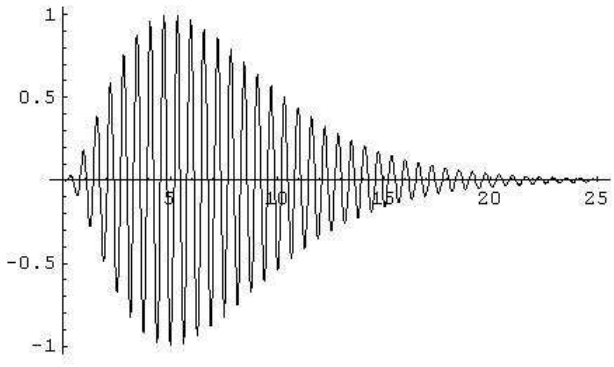

Fig. 4. The seismic impulse.

In Fig. 4 the mode of seismic impulse with parameters $A = 0.295$, $\alpha = 0.4$, $\nu = 10$, $\gamma = 0$ is shown, and value θ is found from relation (28).

6 Numerical results. Discussion

We fix the values of structure parameters and study some values of seismic excitation parameters in (26).

We take the following parameters (given in SI). The structure dimensions and radii of layers are $H = 250$, $H_1 = 235$, $r_{10} = 4.9$, $r_{20} = 4.95$, $r_{30} = 5.95$, $r_{40} = R_0 = 6$, $R_1 = 5$. Densities of water, of steel, and of concrete are $\gamma_w = 10^3$, $\gamma_s = 7.85 \cdot 10^3$, $\gamma_c = 2.2 \cdot 10^3$. The Young modules and yield limits ol steel and of concrete are $E_s = 2.06 \cdot 10^{11}$, $E_c = 0.131 E_s$, $\varepsilon_s = 0.00134$, $\varepsilon_c = 1.16\varepsilon_s$. The mass parameters and the distances to the mass centers of bodies *1, 2* are $m_s = 2.32 \cdot 10^7$, $m_0 = 10^7$, $m_1 = 10^7$, $J_0 = 15\, m_0$, $J_1 = 10\, m_1$, $h_0 = 3$, $h_1 = 3$. The foundation parameters are $c_u = 7.43 \cdot 10^8$, $c_v = 10^7$, $c_\varphi = 10^{12}$. The viscous resistance parameters are $\beta_k^u = \beta_k^v = 0.1$. The resistance coefficient at motion in the water is $C_v = 2.2$.

We take the following numbers of summands in the series (16) $K_u = 3$, $K_v = 6$. In Table 1 the corresponding first natural frequencies of the longitudinal vibrations ω_k^u and of the bending vibrations ω_k^v.

Table 1. The natural frequencies.

k	1	2	3	k	1	2	3	4	5	6
ω_k^u	4.1	29.4	66.4	ω_k^v	0.26	0.69	3.12	8.16	15.9	26.4

We study only the seismic impulses of the identical forms shown in Fig.4 and change only the maximal amplitude $A_{max} = \max_t |a_0(t)|$ and the frequency. We take $\alpha = 0.4$, then in formula (26) $A = 0.295A_{max}$, and the parameter θ is to be found from (28).

We change the frequency ν in the limits $1.5 \leq \nu \leq 30$, and we increase the maximal amplitude A_{max} and fix its values A^c_{max} when at first the extension deformations in concrete appear, and the values A^s_{max} when at first the plastic deformations in steel appear. We study three values of the angle γ, namely $\gamma = 0$ (vertical ground acceleration), $\gamma = \pi/4$ (intermediate case), and $\gamma = \pi/2$ (horizontal acceleration).

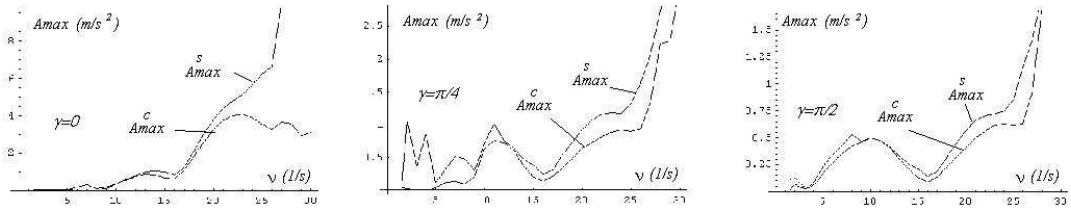

Fig. 5. Comparizon of functions $A^c_{max}(\nu)$ and $A^s_{max}(\nu)$ for three values of γ.

The results of calculations obtained from system (24) are presented in Fig. 5 and in Fig, 6. In Fig. 5 the comparison of functions $A^c_{max}(\nu)$ and $A^s_{max}(\nu)$ for three values of the angle γ is presented. From this Figure it follows that in all cases the extension deformations in concrete appear earlier than the yield deformations in steel. But as a rule the difference between the values $A^c_{max}(\nu)$ and $A^s_{max}(\nu)$ is small.

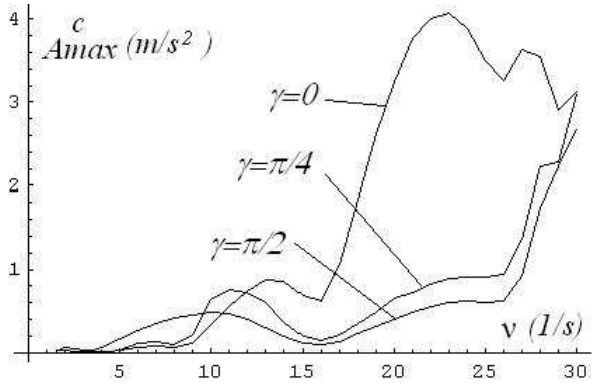

Fig. 6. Comparison of functions $A^c_{max}(\nu)$ for various values of γ.

Fig. 6 demonstrates the comparison of functions $A^c_{max}(\nu)$ for three studied values of the angle γ. From this Figure it follows that for the comparatively small frequency values ν the functions $A^c_{max}(\nu)$ are of the same order, and for the larger ν the rod is less sensitive to the vertical excitations than to the horizontal ones.

7 Remark about the random seismic impulses

The obtained results are based on the analysis of the model impuls (26) action and on the accepted values of the problem parameters. The presented algorithm may be used for any time functions $a(t)$, $b(t)$, $\varphi_0(t)$, describing the seismic excitation.

Now we present the way of simulation for random seismic excitation $a_0(t)$. The random process $a_0(t)$ is non-stationary, but we assume that its spectral density is known [6]. For

simulation we present the process $a_0(t)$ in the product

$$a_0(t) = a_1(t)\zeta(t), \tag{29}$$

where $a_1(t) \geq 0$ is a non-random function describing the process envelope with maximal value equal to unit ($\max a_1 = 1$, in the studied examples is accepted $a_1 = 0.275t^2e^{-\alpha t}$, $\alpha = 0.4$). The process $\zeta(t)$ is a stationary random process with the zero expectation and with the given spectral density $S(\omega)$. The comdition $\max a_1 = 1$ gives the approximate coincidence of the mean square roots of the processes $a(t)$ and $\zeta(t)$ near the point of the seismic excitation maximum.

For simulation of the process $\zeta(t)$ we present it as a sum of a harmonic summands with random amplitudes [7], [8]

$$\hat{\zeta}(t) = \sum_{j=1}^{N} \sqrt{p_j}(\xi_j \cos(\omega_j t) + \eta_j \sin(\omega_j t)), \tag{30}$$

where

$$\omega_j = \Omega_0 + \left(j - \frac{1}{2}\right)\Delta\omega, \qquad \Delta\omega = \frac{\Omega_1 - \Omega_0}{N}, \qquad p_j = 2S(\omega_j)\Delta\omega.$$

Here frequencies ω_j cover the interval $[\Omega_0, \Omega_1]$, which is chosen so that the action on the structure of summands with frequencies outside this interval is negligibly.

In (30) ξ_j and η_j are normal standard independent random values with zero mean and unit dispersion. Assuming that these values have the normal distribution for their simulation we use formulas

$$\xi_j = \sqrt{-2\log\alpha'_j}\cos 2\pi\alpha''_j, \qquad \eta_j = \sqrt{-2\log\alpha'_j}\sin 2\pi\alpha''_j, \tag{31}$$

where α'_j and α''_j are independent random values uniformly distributed in the interval [0,1].

The multipliers p_j give the approximate coincidence of the spectral densities of processes $\zeta(t)$ and $\hat{\zeta}(t)$. This approximation is better with the grows of the number N and of the length of the frequency interval $[\Omega_0, \Omega_1]$.

The constructed realization $\hat{\zeta}(t)$ of the process $\zeta(t)$ does not satisfy to the necessary equality (27). To fulfil it (for the chosen values of the random numbers ξ_j and η_j) we use the following model of the seismic excitation

$$\hat{a}_0(t) = a_1(t)\hat{\zeta}(t+\theta) \tag{32}$$

where the phase shear θ is to be found from equation

$$\int_0^\infty a_1(t)\hat{\zeta}(t+\theta)dt = 0, \tag{33}$$

by the similar way as in the examples above the value θ is found from equation (28).

Acknowledgements

Supported by the Russian Foundation of Basic Researches, grant 10.01.00420 a.

References

[1] V.A.Shekhovtsov. Random nonlinear vibrations of the marine stationary platform. St.Petersburg. 2004. 246 p.

[2] V.A.Shekhovtsov, P.E.Tovstik, T.M.Tovstik. Marine stationary platform under action of horizontal seismic loading. COMPDYN, 2011. Corfu.

[3] A.P.Filin. Applied mechanics of rigid deformable bodies. Moscow. Nauka. V. 1. 832 p.

[4] E.S.Sorokin. To the theory of internal friction at vibrations of elastic systems. Gosstroizdat. 1960.

[5] V.A.Palmov. Vibrations of elasto-plastic bodies. Moscow. Nauka. 1976. 328 p.

[6] A.N.Birbraer. Design of structures at seismic-stability. St.Petersburg. Nauka. 1998. 255 p.

[7] V.S.Pugachev. Theory of random functions. Moscow. Fizmatgiz. 1960. 884 p.

[8] S.M.Ermakov, G.A.Mikhailov. Statistical simulation. Moscow. Nauka. 1982, 206 p.

Vyacheslav A.Shekhovtsov, St.Petersburg Architectural Academy, St.Petersburg, Russia
Petr E.Tovstik and Tatiana M.Tovstik, St.Petersburg State University, St.Petersburg, Russia

Modeling the behavior of the cantilever of the atomic force microscope

Nadezhda Uzhegova Alexander Svistkov
Uzhegova@icmm.ru, Svistkov@icmm.ru

Abstract

In this paper a method for solving dynamic problems of modeling an AFM cantilever motion is offered. Proposed to use a distribution of a displacement axis cantilever in a Fourier series in the coordinate.

1 Introduction

At present, atomic force microscopy is widely used to study a structure and material properties at a nanoscale. But there are still many unresolved issues associated with obtaining quantitative characteristics of a material. We should use mathematical models to decrypt experimental data. A closed contact mode of AFM is most often used. This mode allows us to obtain information not only about a surface topography, but also a phase portrait of a material structure and others characteristics.

One way of solving dynamic problems of modeling an AFM cantilever motion is presented in this paper. In particular, we propose to use a distribution of a displacement axis cantilever in a Fourier series about coordinate. The distributable coefficients are chosen so that an equation of motion of points along a cantilever axis performs always. Therefore boundary conditions must be satisfied at each time step. An example of solving the problem and benefits of the offered approach are in the work.

2 Mathematical formulation

The basis of an AFM is a oscillating cantilever. we simulate a behavior of a cantilever, wich has a constant cross-section.

Consider a cantilever behavior which are based on the following assumptions:

1. Ignored a rotational inertia a short length element of a cantilever relative to a center of mass this element. We take into account only an inertia of a forward movement of a short lenght element of a cantilever.

2. It is believed that we can ignore tangential forces in a cross-section cantilever. Takes into account only normal forces at a cross-section.

3. Use to simulate a linearized equation.

The location of coordinate axes and the cantilever fixing shown on Fig. 1

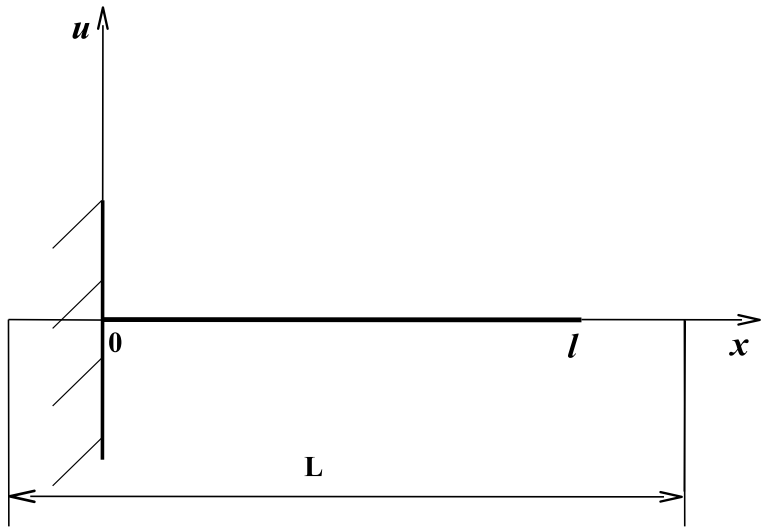

Figure 1: The location of coordinate axes and the cantilever fixing

Thus for the described assumptions we receive following equations the strength of materials theory:

$$q = -\frac{\partial Q}{\partial x},$$

where q is an intensity of forces of inertia of mass and Q is a shear force.

$$Q = \frac{\partial M}{\partial x},$$

where M is bending moment.

$$M = EJ_x \frac{\partial \theta}{\partial x},$$

where E — Young's modulus, J_x — axial moment of inertia about the axis x and theta — rotation angle.

$$\theta = -\frac{\partial u}{\partial x},$$

where u is a displacement in a direction, which is perpendicular x.

D'Alembert force in this problem are defined by:

$$q = -\rho S \frac{\partial^2 u}{\partial t^2},$$

where p — a considered cantilever density, S — a cross-section area.

Thus we obtain the following dynamic equation of cantilever motion:

$$\rho S \frac{\partial^2 u}{\partial t^2} = -\frac{\partial^2}{\partial x^2}\left(EJ \frac{\partial^2 u}{\partial x^2}\right),$$

The cantilever has a constant cross-section so the resulting equation can be rewritten as follows:

$$\frac{\partial^2 u}{\partial t^2} + D\frac{\partial^4 u}{\partial x^4} = 0, \tag{1}$$

where D is

$$D = \frac{EJ}{\rho S}.$$

3 Method of solving the problem

It is proposed to find the solution of equation (1) as Fourier series about a coordinate x. The coefficients of expansion must be set so as to satisfy equation (1). The solution is found step by step over time. The solution can be represented in a interval $[t_j; t_{j+1}]$ as:

$$u = u_1 + u_2 + u_3 + u_4$$

where u_1 is distribution oscillation of cantilever in a direction from the left to the right:

$$u_1 = \text{real}\Big[\sum_{n=1}^{\infty} A_n(t_j)\,\exp\left(\frac{(2\,\pi n)^2\sqrt{D}\,\mathrm{i}\,(t_{j+1}-t_j)}{L^2}\right)\exp\left(\frac{2\,\pi n\,\mathrm{i}\,(x-x_0)}{L}\right)\Big],$$

u_2 is distribution oscillation of cantilever in a direction from the right to the left:

$$u_2 = \text{real}\Big[\sum_{n=1}^{\infty} B_n(t_j)\,\exp\left(-\frac{(2\,\pi n)^2\sqrt{D}\,\mathrm{i}\,(t_{j+1}-t_j)}{L^2}\right)\exp\left(\frac{2\,\pi n\,\mathrm{i}\,(x-x_0)}{L}\right)\Big],$$

u_3 is satisfaction of a left boundary condition

$$u_3 = \text{real}\Big[\sum_{n=1}^{\infty} (C_1\,a_{1n} + C_2\,a_{2n})\,\exp\left(\frac{(2\,\pi n)^2\sqrt{D}\,\mathrm{i}\,(t_{j+1}-t_j)}{L^2}\right)\exp\left(\frac{2\,\pi n\,\mathrm{i}\,(x-x_0)}{L}\right)\Big],$$

u_4 is satisfaction of a right boundary condition

$$u_4 = \text{real}\Big[\sum_{n=1}^{\infty} (C_3\,a_{3n} + C_4\,a_{4n})\,\exp\left(-\frac{(2\,\pi n)^2\sqrt{D}\,\mathrm{i}\,(t_{j+1}-t_j)}{L^2}\right)\exp\left(\frac{2\,\pi n\,\mathrm{i}\,(x-x_0)}{L}\right)\Big].$$

Where coefficients C_1, C_2 ,C_3, C_4 used to satisfy boundary conditions at each step. a_{1n}, a_{2n}, a_{3n}, a_{4n} are Fourier transform coefficients of some functions wich we selected. To satisfy boundary conditions is better to use an interval longer than a length of cantilever which is modelled. So we use L in our solution. But at the same time is satisfied boundary conditions must be at 0 and l (Fig. 1).

Can shown that the coefficients for the next steps in time expressed in terms of the previos steps as follows:

$$A_n(t_{j+1}) = A_n(t_j)\exp\left(\frac{(2\,\pi n)^2\sqrt{D}\,\mathrm{i}\,(t_{j+1}-t_j)}{L^2}\right),$$

$$B_n(t_{j+1}) = B_n(t_j)\exp\left(-\frac{(2\,\pi n)^2\sqrt{D}\,\mathrm{i}\,(t_{j+1}-t_j)}{L^2}\right).$$

The cantilever position at different times shown at Fig. 2

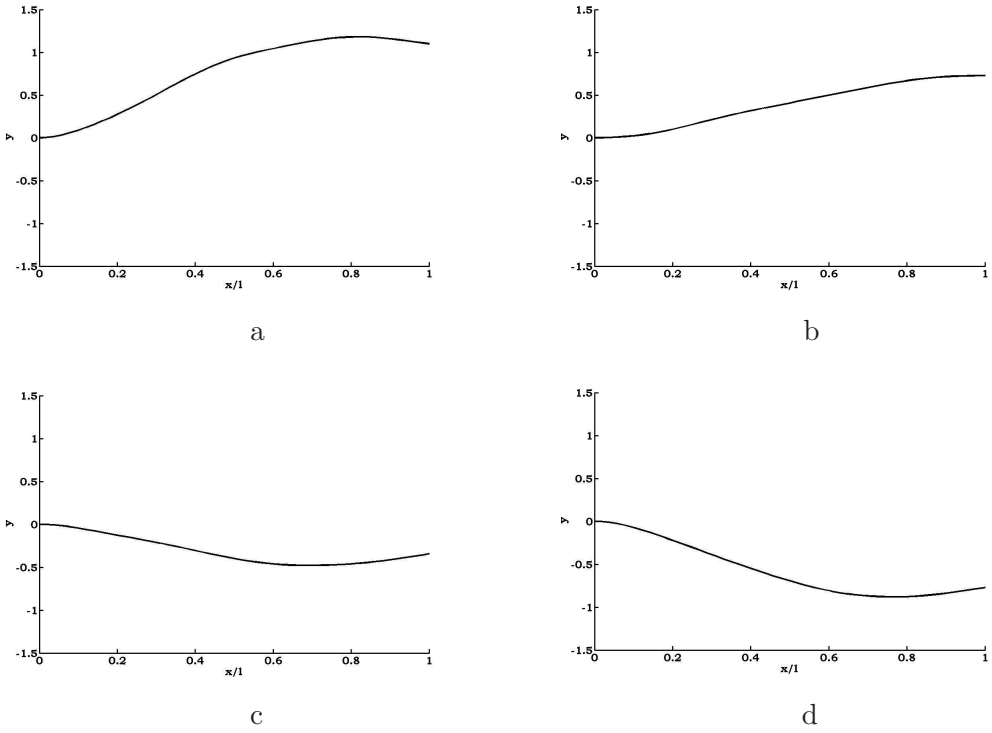

Figure 2: Position of the beam at the moment: (a) t=40; (b) t=50; (c) t=70; (d) t=90

4 Conclusion

To simulation a motion of AFM cantilever is proposed to use the decomposition of the displacement axis of the cantilever in a Fourier coordinate. The advantages of this approach are follows:

1. No need to solve linear equations of large dimentions systems.
2. Oscillation equation is satisfied at each step. Thus the error can accumalate only if we have errors in boundary conditions that we can control easily.

Acknowledgements

This work was supported by the RAS Program 09-T-1-1006 state. contract 02.740.11.0442

Svistkov Alexander, Academic Korolev Street, 1,Perm, Russian
Uzhegova Nadezhda, Academic Korolev Street, 1, Perm, Russian

Numerical simulation of separation from the substrate double nanolayer

E. M. Aryslanova D. N. Vavulin A. V. Alfimov A. V. Panteleev
S. A. Chivilikhin I. Yu. Popov V. V. Gusarov
dima-vavulin@mail.ru

We consider the numerical solution of differential equations describing the mechanics of forming nanoscrolls obtained by hydrothermal synthesis. At the initial stage of the process nanoplates formed, consisting of double-strained layers. Internal stresses due to structural differences nanolayer its constituent layers. Exploring different configurations of nanolayer, we can determine that the most energetically favorable for it is a condition in which it will be twisted in nanoscroll. This twisting of the Van der Waals forces of interaction between the upper layer with the underlying layer nanoplate. Thus, the upper nanolayer will perform thermal vibrations around the equilibrium position until, until its energy exceeds a critical value. If the layer gets from energy from the outside that exceeds a critical value, the balance of the layer is broken and he twisted in nanoscroll - nanotube or nanocones.

We consider interaction of the layer with an infinite substrate, describing the emerging forces of repulsion between the particles with Lennard-Jones potential and the attractive forces of Van der Waals forces, which takes into account many-particle interactions in the system:

$$U_\infty(y) = n^2 e\pi\left(\frac{a^{12}}{5(h_0+h)^{10}} + \frac{a^{10}}{(h_0+h)^4}\right) \tag{1}$$

where $h_0 + h$ - the height above the substrate, $h_0 = \frac{a}{2^{\frac{1}{6}}}$ - the distance to the substrate, according to the minimum potential, h - the height of the deviation from balance, a - the distance at which the force of interaction between two particles is zero, ϵ - the potential well depth, n - concentration of particles in layer, $c = c(n, A)$ - a constant that takes into account the specific type of interaction that occurs in this system because of the dependence of the potential minimum of the interaction on the polarizability of atoms and the applied field, A - polarizability.

In the London approximation for two flat plates, which we shall use later, the interaction energy is equal to:

$$U_\infty(y) = \frac{C_6 n^2 \pi}{12(h_0+h)^2} \tag{2}$$

where C_6 - constant depending on the type of atoms forming the lattice.

Considering the one-dimensional oscillations, we take into account the finiteness of the substrate in a direction along the x and assume its infinite along the coordinate z. Then the potential energy of the layer has the form:

$$U(h,x) = n^2 e\pi \int\limits_{-x}^{L-x} dx' \int\limits_{-\infty}^{\infty} (\frac{a^{12}}{5(h_0+h)^{10}} + \frac{a^{10}}{(h_0+h)^4})dz \tag{3}$$

where L - the size of the layer in the direction of x. Since this expression is unwieldy and inconvenient for the further work proposed approximation model:

$$U(h,x) = U_\infty(h) \cdot F_{APR}(x) \tag{4}$$

where $F_{APR}(x)$ - approximation function of the coordinate dependence of the potential:

$$F_{APR}(x) = \begin{cases} 0.5 + k\frac{x}{a} & 0 \le x < \sigma_{cut} \cdot a; \\ 1 & \sigma_{cut} \cdot a \le x < L - \sigma_{cut} \cdot a; \\ 0.5 + k\frac{L-x}{a} & L - \sigma_{cut} \cdot a \le x < L; \end{cases} \tag{5}$$

where k - the slope of the approximating function and σ_{cut} - coefficient cutoff, constant for any system.

The numerical solution of oscillation equation allows us to observe the spatial configuration of an oscillating layer until ready for separation. Thus, detachment model of the double layer from the substrate can simulate the spatial configuration of the layer, separated from the substrate. Further analysis of the spatial configurations will identify factors that determine the geometry of nanoscroll, in which fold detached layer.

Performance optimization in direct numerical simulation of collisional particle dynamics in heterogeneous flows

Vladimir V. Vinnikov Dmitry L. Reviznikov Andrew V. Sposobin
vvinnikov@list.ru

Abstract

A modification of discrete-element method for direct numerical simulation of heterogeneous flows is presented. The method combines direct simulation of particle collisions, using an approximation for trajectories, with the concept of probe particles.

Introduction

Methods for numerical simulation of two-phase flows based on a combination of Eulerian description of the carrier phase and the Lagrangian description of the dispersed phase receive wide acknowledgement [1-4]. Distinctive feature of a problem for numerical simulation of two-phase flow past an obstacle is the necessity of considering interparticle collisions, that appear even at relatively low particle concentration in the flow and affect significantly the parameters of the integral action of particles on the streamlined surface [5,6]. This effect increases substantially with the rise of admixture concentration.

Highly accurate solutions can be obtained by using a full-scale version of the discrete element method [7]. The algorithm is built on an identical matching of real and computational particles, the solution of motion equations for each computational particle, and calculation of the parameters of particle collisions based on trajectories approximation. These features require considerable computing power and their application is actually limited up-to-date to the two-dimensional problems. This article is concerned with a modified discrete element method, where each computational particle stands for a group of real particles. While retaining high accuracy for the solution, one can significantly reduce the demand for computational resources, improve the efficiency of algorithm parallelization and proceed for solutions of three-dimensional problems.

1 Discrete element method for numerical simulation of dispersed phase dynamics with a consideration for particle collisions

The paper considers the full-scale variant of discrete-element method [7], which is used for numerical simulation of dispersed phase dynamics in a heterogeneous flow past an obstacle. Admixture particles are modeled as homogeneous hard spheres. The motion equations have the form:

$$m_p \frac{d\mathbf{v}_p}{dt} = \mathbf{f}_p, I_p \frac{d\omega_p}{dt} = \mathbf{T}_\omega, c_{mp} m_p \frac{dT_p}{dt} = q_c + q_r$$

where m_p is mass, I_p - moment of inertia, T_p - temperature, $\mathbf{v}_p$ - velocity, ω - angular velocity, c_{mp} - heat capacity of particle's material, T_ω - torque.

Integration of all these equations for all real particles is carried out at each step $\left[t^n, t^{n+1}\right]$ for the gas phase. One constructs a trajectory approximation for each particle as the polynomial $\mathbf{r}(t) = \mathbf{r}_2 t^2 + \mathbf{r}_1 t + \mathbf{r}_0$. The condition for collision of pairs of particles i and j is expressed as an equation $|\mathbf{r}_i(t) - \mathbf{r}_j(t)|^2 = (r_{pi} + r_{pj})^2$, where r_{pi}, r_{pj} are particles' radii.

Parameters of paired interparticle encounters and collisions with an obstacle surface are computed using the polynomial trajectory approximation (see Fig. 1). All particle impacts during this computational step are simulated sequentially in chronological order using the queue of collisions. Calculation of parameters for a pair of particles after collision as well as particle properties after reflection from a surface is carried out according to the model of hard spheres, given in [8].

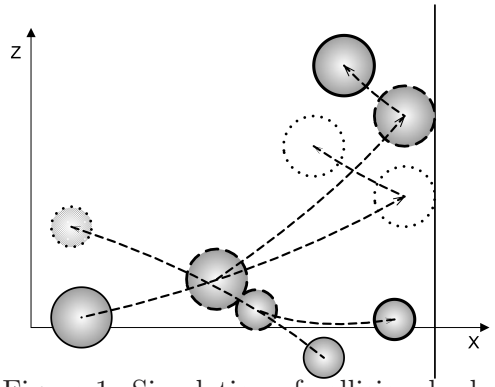

Figure 1: Simulation of collisional admixture

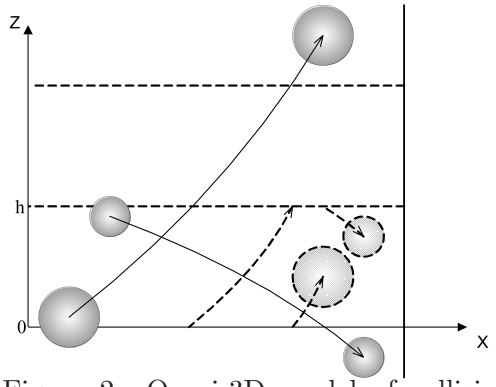

Figure 2: Quasi-3D model of collisional admixture

Processing of each collision event removes all subsequent encounters for this particle from the queue. Then one obtains particle parameters after collision at the instant $\tau \in (t^n, t^{n+1}]$, proceeds to integration of equations of movement and heat exchange on the interval $(\tau, t^{n+1}]$, approximates new trajectory and computes parameters for new collisions. Newly found encounters are placed in the global queue and are treated in a consistent chronological order. It is necessary to put all collisions in the queue, not just the first one, since some of them, including early ones can be removed as not happened. This algorithm continues until the encounter queue becomes empty on the current computational step.

This approach makes possible to simulate complex dynamics of admixture with the best accuracy, including the repeated collisions of particles and their reflection from the obstacle surface. However, the implementation of this method involves considerable computational cost and parallelization of computations is possible only on a stage solving equations of movement and particles' heat exchange. Collisions in the queue are treated in a sequential order.

Numerical solution of the problem of a cross flow past a circular cylinder uses quasi-3D model of collisional admixture, where one considers computational domain bounded along cylindrical axis by periodically boundary conditions. Good accuracy is already achieved at domain layer thickness $z_{max} - z_{min} = 4 \max_i(r_{pi})$, where r_{pi} - particle radius [7].

2 Modified algorithm for direct numerical simulation based on usage of probe particles

To reduce the demands for computational resources every F real particles can be represented by a single probe particle. The probe particle has physical characteristics of a single particle when solving the equations of motion and simulating interactions with other particles. One should take into consideration the factor F for obtaining integral properties, such as an action of admixture on a carrier gas or an obstacle surface, or kinetic energy dissipation due to inelastic collisions. To preserve the properties of the dispersed phase it is necessary to ensure that a probe particle has the same intensity of collisions along the trajectory, as a single real particle has. Therefore, the equation that determines the conditions of collision for a pair of probe particles is $|\mathbf{r}_i(t) - \mathbf{r}_j(t)|^2 = (r_{pi}\sqrt{F} + r_{pj}\sqrt{F})^2$. The results are the moments of time when a distance between centers of mass of the probe particles equals $r_{pi}\sqrt{F} + r_{pj}\sqrt{F}$. Parameters of particle pairs after collision are computed using a normalized vector defining the relative positions of the particles at the instance of the impact:

$$\mathbf{n}_{ij} = (r_{pi} + r_{pj})\frac{\mathbf{r}_j(\tau) - \mathbf{r}_i(\tau)}{|\mathbf{r}_j(\tau) - \mathbf{r}_i(\tau)|}$$

Quasi-3D model for the problem of cross flow past circular cylinder demands that the computational domain thickness should be extended up to $z_{max} - z_{min} = 4\sqrt{F} \cdot \max_i(r_{pi})$. Implementation of probe particles permits to reduce the total number of computational particles in the domain by a factor of $\sqrt{F}$ for the same admixture concentration in the flow.

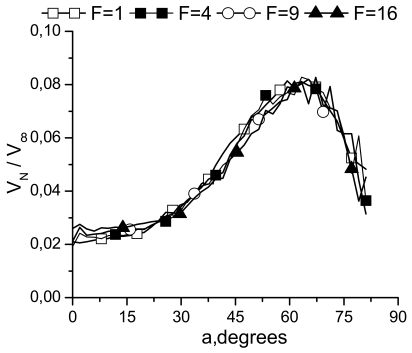

Figure 3: Average value of particle velocity normal to the surface at an instance of impact with the obstacle

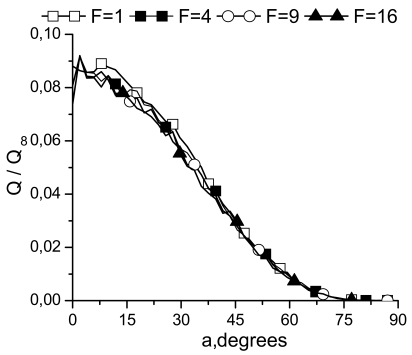

Figure 4: Specific energy flux from admixture to the obstacle surface

The series of computational experiments simulating cross flow of a dusty gas past a circular cylinder with radius of 3 cm were carried out. Admixture is represented by particles 10 μm in diameter of aluminum dioxide Al_2O_3. Motion of a gas phase is governed by a system of modified Euler equations. Gasdynamics equations are integrated numerically via HLL scheme. Boundary conditions are approximated according to ghost-cell immersed boundary method on rectangular grids [9]. Parameters of a gas phase represent the atmospheric conditions at 10 km; Mach number $M_\infty = 6$. Volume concentration for admixture $C_{V0} = 10^4$. Factor F was varying within the range from 1 (full-scale simulation) to 16. Figures 3-4 show dynamical and energy action of admixture on an obstacle surface. One can see good agreement of results, obtained with various values of the factor F.

The distinctive feature of the direct numerical simulation algorithm is an essentially consequent way of processing the queue of collisions. Algorithm parallelization is easy to implement only for integration of equations of movement and heat exchange at each computational time step. At the same time the nonlinear nature of computational costs reduction at the stage of collisions simulation leads to an increase of portion for integration step in overall costs, which means the increase of parallelization efficiency for the problem solution in whole. Figure 5 shows plots of the computer time costs versus the factor F for solving the problem in quasi-3D formulation. One can see that implementation of probe particles in combination with parallel computing reduces runtime up to a factor 10 while retaining the accuracy of full-scale solution (see Fig.6). The problem was solved using PC based on Intel Xeon CPU with 4 cores.

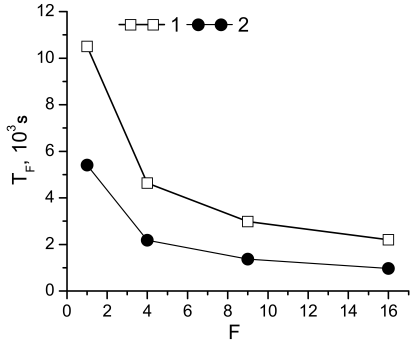

Figure 5: Runtime costs for the algorithms: 1 - successive, 2 - parallel

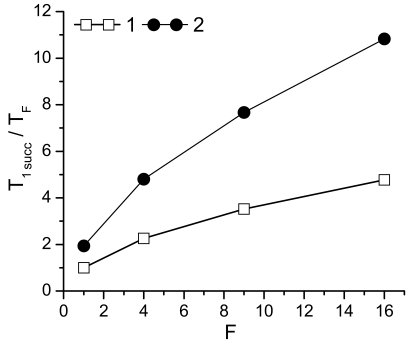

Figure 6: Runtime reduction for the algorithms: 1 - successive, 2 - parallel

There is no need to extend boundaries of computational domain in the case of three-dimensional problems. This circumstance allows to reduce the number of computational particles by F times thus decreasing memory demands. Nonlinear dependence for the number of collisions on the number of particles results in a decrease of runtime at the stage of collisions simulation up to a factor of F^2, which, in turn, increases the efficiency of parallel computations even more.

Conclusions

Implementation of probe particles significantly extends application area of discrete-element method by reducing demands for computer memory and runtime. Algorithm modification for multiprocessor computer systems facilitates problem parallelization and increase efficiency of its solution. Therefore implementation of this modified discrete-element method makes numerical simulation of three-dimensional dusty flows past an obstacle quite plausible.

Acknowledgements

The work is supported by RFBR grant No 09-08-0542 and President's grant for support for young Russian scientists MK-179.2011.8.

References

[1] Nigmatulin R.I. Fundamentals of Mechanics of Heterogeneous Media (Nauka, Moscow, 1978) [in Russian].

[2] Sternin L.E., Maslov B.P., Schreiber A.A. and Podvysotskii A.M. Two-Phase Mono- and Polydisperse Flows of Gas with Particles [in Russian], Mashinostroenie, 1980

[3] Gilinskii M.M. and Stasenko A.L. Supersonic Gas Disperse Jets [in Russian], Mashinostroenie, Moscow. (1990)

[4] Tsirkunov Yu. M. Gas-particle flows around bodies – key problems, modeling and numerical analysis. // Proc. Fourth International Conference on Multiphase Flow (Ed.: E. Michaelides), May 27 – June1, 2001, New Orleans, LA, USA. – CD ROM Proc. ICMF'2001, paper No. 609, 31 p.

[5] Volkov A.N., Tsirkunov Yu.M. and Oesterle B. Numerical simulation of a supersonic gas–solid flow over a blunt body: The role of inter-particle collisions and two-way coupling effects. // Int. J. Multiphase Flow, 2005, Vol. 31, pp.1244–1275.

[6] Reviznikov D.L. and Sposobin A.V. Numerical simulation of the solid phase impact on the blunt body surface in supersonic dusty flow [in Russian], Matem. Mod., 19:11 (2007), p.101–111

[7] Reviznikov D.L. and Sposobin A.V. Direct numerical modeling of disperse phase flow of gas-particle mixture over a body [in Russian]// e-journal "Trudy MAI", 2007, No.26, 13 p.

[8] Crowe C.T., Sommerfeld M. and Tsuji Y. Multiphase flows with droplets and particles. CRC Press LLC, 1998, 471p.

[9] Vinnikov V.V. and Reviznikov D.L. Immersed Boundary Method for Numerical Simulation of Supersonic Flow over Blunt Bodies on Rectangular Grids [in Russian]// e-journal "Trudy MAI", 2007, No.27, 13 p.

Vladimir V. Vinnikov, Moscow Aviation Institute, Volokolamskoe sh. 4, 125993, Moscow, Russia
Dmitry L. Reviznikov, Moscow Aviation Institute, Volokolamskoe sh. 4, 125993, Moscow, Russia
Andrew V. Sposobin, Moscow Aviation Institute, Volokolamskoe sh. 4, 125993, Moscow, Russia

Investigation of vibrations in the multisection cyclic machines including branch and lattice structured systems with variable and nonlinear parameters

I. Vulfson M. Preobrazhenskaya
vujo@rambler.ru

Abstract

In this paper the technique of investigation and dynamic analysis of multisection cyclic machines which form branched and lattice structured vibrating systems with nonlinearities and variable parameters are developed. The conditions of spatial localization wherein the synchronism of actuator's movement is broken and grows the vibroactivity of the drive are established. Analytical criteria of dynamic synthesis and ways of elimination of undesirable dynamic effects are offered.

1 Introduction

To perform the programmed motion of massive actuators of many machines and automatic transfer lines are carried out by long members, which are set in motion by multiply duplicated cyclic mechanisms [1,2]. In such cases the drive consists of many sections forming vibratory systems with spatial dynamic regularity.

The classic theory of regular oscillatory systems is based on the analysis of the chains or lattices consisting of masses and springs [3,4]. The dynamic models of cyclic machines have more complex internal structure of each repeating module, which formed not only a simple connected chain, but also branched and lattice structured vibratory systems with nonlinearities and nonstationary dynamic constraints. Therefore, with reference to the given system the problem has specific features and needs a separate consideration. In the report methods of the analysis and dynamic synthesis of regular vibratory systems of cyclic machines had the further development [1,2,5]. In some cases, regularity conditions are realized only approximately however quite often even small infringements can lead to spatial localization of vibrations on one or several modules of a drive. The effect of spatial localization of vibrations, which breaks in-phase movement of actuator and raises the vibroactivity of machines, should be investigated at the account of variability of parameters.

2 Dynamic models

Figures 1,2,3 illustrate some dynamical models of the branching and lattice structure, where the input link (main shaft) is presented as torsional subsystems and the output link (actuator) is given as a torsional (Figures 1,3) or bending subsystem (Figure 2). Let us assume the following conventions: J are the moments of inertia, m are the masses; c, ψ are the coefficients of rigidity and damping factors reduced to the appropriate elements; Δs is

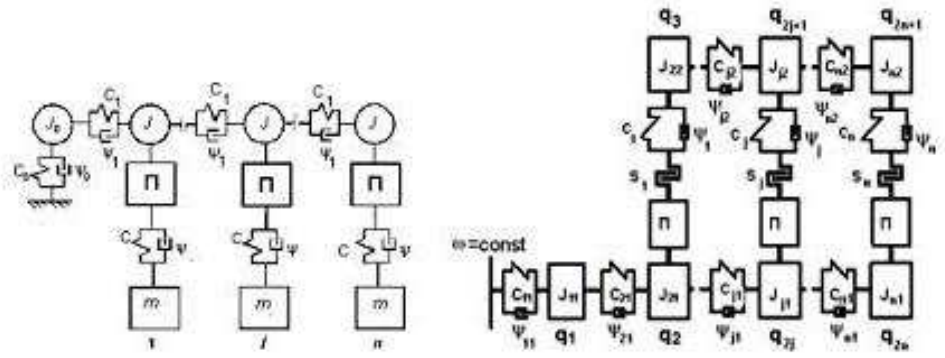

Figure 1: Dynamic models of torsional and longitudinally cyclic vibratory systems

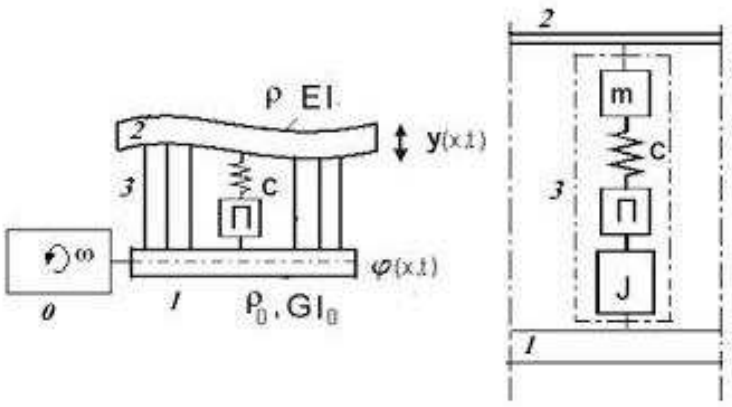

Figure 2: Dynamic model of torsional and bend cyclic vibratory systems

a mechanism clearance reduced to an output link, and Π is a analog of cyclic mechanism corresponding to the transformation of the angular coordinate φ of the mechanism input link into a coordinate of the output link in accordance with the position function $\Pi(\varphi)$. More detailed description of models will be given below.

The rotation angle of the main shaft in the cross section j is $\varphi_j = \varphi_* + q_j$, where $\varphi_* = \omega t$ is the ideal rotation angle; q_j is the oscillatory component (dynamic error). By clearance-free motion after linearizing the position function in the vicinity of the programmed motion, we obtain $\Pi(\varphi_j) \approx \Pi(\varphi_*) + \Pi^{'}(\varphi_*)q_j$, where $\Pi^{'} = d\Pi/d\varphi$ is the first geometric transfer function (an analogue of velocity). Thus, function Π retained their nonlinear properties relative to the gross coordinate φ_* and only small vibrations are included into corresponding expressions linearly.

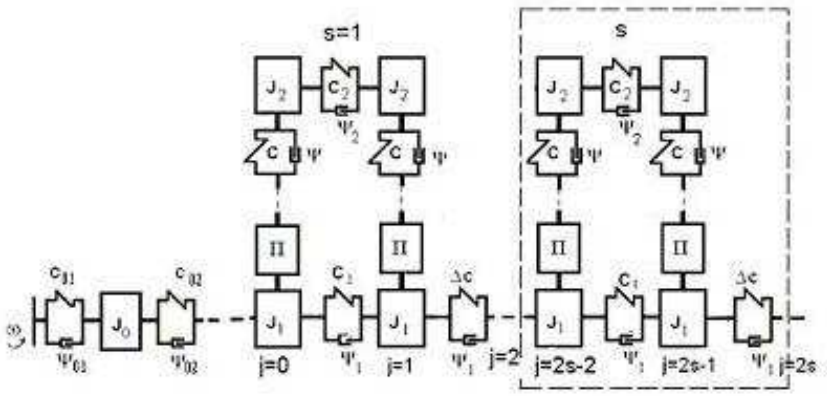

Figure 3: Dynamic model of branch-and-ring cyclic vibratory systems

3 The frequency analysis

At first, it is expedient to perform the frequency and mode analysis of the clearance-free drive. After the transformation to the quasinormal coordinates the original system can be described by differential equations of the form

$$\ddot{\eta}_r + 2n_r(\varphi_*)\dot{\eta}_r + p_r^2(\varphi_*)\eta_r = W_r(t) \qquad (r = \overline{1,H}), \tag{1}$$

where φ_* is "slow time", H is degree of freedom (DOF). According to the method of the conditional oscillator [6], the solution of a homogeneous system for each mode can be supplemented with one additional condition at which $d^2\eta_r/dt^2 = -p_r^2(\varphi_*)\eta_r$, where the function p_r can be considered as a variable eigenfrequency. Let's allocate in dynamic model a repeating module s in which there is a following transformation of state vector $\mathbf{T}_s$=$\mathbf{\Gamma}\mathbf{T}_{s-1}$, where $\mathbf{\Gamma}$ is transition matrix of module. To transition matrix there corresponds a following characteristic equation:

$$\lambda^k + h_1\lambda^{k-1} + h_2\lambda^{k-2} + \ldots + h_2\lambda^2 + h_1\lambda + 1 = 0. \tag{2}$$

Here it is considered that owing to dynamic symmetry of the module at change of an order of numbering of sections its dynamic properties remain the invariable. Thus, the equation (2) is reciprocal. To determine coefficients h_i in the general form, we use the method of D.K. Faddeev:

$$\begin{aligned}
&\mathbf{G}_1 = \Gamma; \quad h_1 = -\mathrm{S}p\mathbf{G}_1; \quad \mathbf{B}_1 = \mathbf{G}_1 - h_1\mathbf{E}^0; \quad \mathbf{G}_2 = \mathbf{G}_1\mathbf{B}_1;\\
&h_2 = -\frac{1}{2}\mathrm{S}p\mathbf{G}_2; \quad \mathbf{B}_2 = \mathbf{G}_2 - h_2\mathbf{E}^0; \quad \mathbf{G}_3 = \mathbf{G}_1\mathbf{B}_2;\\
&h_3 = -\frac{1}{3}\mathrm{S}p\mathbf{G}_3; \quad \mathbf{B}_3 = \mathbf{G}_3 - h_3\mathbf{E}^0; \quad \mathbf{G}_4 = \mathbf{G}_1\mathbf{B}_3;\\
&\ldots\ldots\ldots\ldots\ldots\ldots\ldots\ldots\ldots\ldots\ldots\ldots\ldots\ldots\ldots\ldots\ldots\ldots\ldots\ldots\ldots\ldots\ldots\ldots
\end{aligned} \tag{3}$$

Here $\mathrm{S}p\mathbf{\Gamma}$ is the spur of matrix, $\mathbf{E}^0$ is the unit matrix.

Further, let's consider some typical cases.

Regular vibratory systems with branched structure (k=2). The dynamic model shown on Fig.1a corresponds to a machine camshaft from which branch off n identical cyclic mechanisms. At the account of Eqs.(2), (3) and boundary conditions we have

$$(1+\zeta(p))\cos[(n+0.5)\theta]-\zeta(p)\cos[(n-0.5)\theta]=0, \tag{4}$$

where $\zeta(p)=c_1/R_0(p)$; $\theta=arccos[1+0.5R(p)/R_0(p)]$; $R_0(p), R(p)$ are dynamic stiffness of input-drive and repeating module; n is the number of modules; $p(\varphi_*)$ is slowly changing natural frequency.

If dynamical rigidity at the input does not depend on p we have $\zeta=\text{const}$; consequently, the solution of Eq. (4) can be obtained regardless of the dynamical characteristics of module. Particularly, with $R_0\to 0$ we have $\theta_r=j\pi/n$, where $j=\overline{1,n}$. In the other limiting case, when $\zeta\to 0$, we have $\theta=\pi(2j-1)/(j+1)$.

To derive a formal frequency equation, we should simultaneously consider Eq. (4) and the transition matrix of one module $\mathbf{\Gamma}(p)$. Then, $0.5S_p\mathbf{\Gamma}=\cos\theta(p)$. The number j of the waveform may not coincide with the number r of the frequency. The matter is that each waveform j is fitted by several values r, whose number is equal to the number of "partial" frequencies of the subsystem of one module. Besides, these waveforms are unsteady. In considered model $R(p)=-mp^2/(1-mp^2)-Jp^2$. The variable dimensionless "own" frequencies $\nu=p/p_0$, $p_0=\sqrt{c/m}$ are defined from the biquadratic equation

$$\nu^4-B_1(\varphi_*,\theta_r(p))\nu^2+B_0(\theta_r(p))=0, \tag{5}$$

where $B_0(\theta_i)=2\nu_2^4(1-\cos\theta_i)$; $B_1(\varphi_*,\theta_i)=\nu_2^2[1+\rho^2\Pi'^2(\varphi_*)r_0^{-2}+2(1-\cos\theta_i)]$; $r_0=\Pi'_{max}$;$\rho=\sqrt{m/J}$; $\nu_2=\sqrt{p_0/\omega}$; Π is the number of the main shafts form (to each value i there correspond two values ν).

Regular torsional vibratory systems with lattice structure (k=4). Let us consider a general case of a lattice-structured drive where the dynamic model of a cyclic mechanism consists of an oscillatory circuit of any type formed by sequential connection of inertial, elastic, and kinematic elements (Figure 1,b). The transition matrix looks like [1, 2, 5]

$$\mathbf{\Gamma}=\begin{bmatrix} 1 & c_1^{-1} & 0 & 0 \\ AB^{-1} & A(Bc_1)^{-1}+1 & -B^{-1} & -(Bc_2)^{-1} \\ 0 & 0 & 1 & c_2^{-1} \\ -B^{-1} & -(Bc_1)^{-1} & DB^{-1} & D(Bc_2)^{-1}+1 \end{bmatrix}. \tag{6}$$

For considered model $A=\Pi'-J_{21}p^2(c\Pi')^{-1}$; $B=(c\Pi')^{-1}$; $C=-(\Pi')^{-1}p^2[J_{22}-J_{21}(1-J_{22}p^2/c)]$; $D=(\Pi')^{-1}(1-J_{22}p^2/c)$. Using the substitution $\lambda+\lambda^{-1}=z$, we transform Eq.(2) into two quadratic equations having the roots

$$z_{1,2}=0.5[-h_1^*\pm\sqrt{(h_1^*)^2-4(h_2^*-2)}], \tag{7}$$

where $h_1^*=-[4+A(Bc_1)^{-1}+D(Bc_2)^{-1}]$; $h_2^*=2B^{-1}(Ac_1^{-1}+Dc_2^{-1})+(B^2c_1c_2)^{-1}(C-1)+6$.

It can be shown that $(h_1^*)^2-4(h_2^*-2)=B^{-2}[(A/c_1-D/c_2)^2+4/(c_1c_2)]\geq 0$.

Consequently, z is the real number at any value of "natural" frequency p. It follows that for $|z_k|<2$ we have a pair conjugated roots λ , and real roots for $|z_k|>2$. Hense, the decision is described with trigonometrical, or hyperbolic functions. Using boundary conditions, the frequency equation may be represented as

$$w_{43}(p)[w_{21}(p)+w_{22}(p)\zeta(p)]-w_{23}(p)[w_{41}(p)+w_{42}(p)\zeta(p)]=0, \tag{8}$$

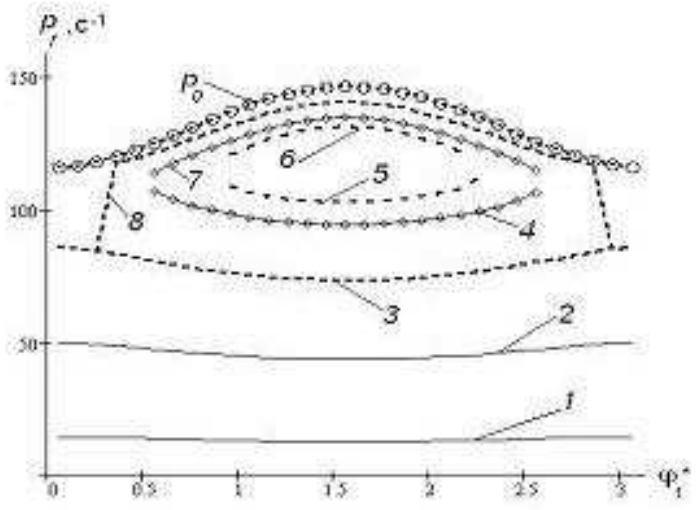

Figure 4: The typical plots $p_r(\varphi_*)$

where w_{ij} are elements of the matrix $\mathbf{W} = \mathbf{\Gamma}^n$.

In Figure 4 the typical plots $p_r(\varphi_*)$ are presented (the number of the curves corresponds to r). A region with an increased density of the frequency spectrum is located in vicinity of the so-called accumulation point $p_0 = \sqrt{c/J_{j2}}$. Based on Eq.(7), we can show that at $p < p_*$ the modes are trigonometric. At particular case $c_1 \to \infty$ we have

$$\nu_r = \sqrt{1 + 2\zeta_2[1 - \cos((r-1)\pi/n)]}, \quad (r = \overline{1,n}; \zeta_2 = c_2/c). \tag{9}$$

The lowest frequency $p(r = 1)$ corresponds to the synchronous movement of an actuator. In this case, the elastic element c_2 is not deformed; therefore, the vibration level is independent of the stiffness coefficient c_2.

Regular torsional-and-bending vibratory systems with lattice structure (k=6). Figure 2 illustrates a lattice structured dynamical model, where the input link (main shaft) is presented in the form of a torsional subsystem and the output link (actuator) is given as a bending subsystem with the distributed parameters. Cyclic mechanisms are schematized in the form of subsystems with discrete parameters. The expediency of such drive schematization is associated with the fact that the acceptable characteristics of the main shaft bending subsystem are usually achieved at the expense of the rational choice of the number of bearing supports and the positions of their arrangement along the shaft length [1]. Here following symbols are in addition accepted: E, G are elasticity and shear modules; I_0, I are the polar and longitudinal moment of inertia of the shaft and actuator cross sections;ρ_0, ρ are the linear moment of inertia of the main shaft and linear masse of actuator. Again using substitution $\lambda + \lambda^{-1} = z$, Eq. (2) is recasting in the form of cubic equation

$$z^3 + h_1 z^2 - (3 - h_2)z - 2h_1 + h_3 = 0. \tag{10}$$

The equation (10) has three real various roots at

$$[-h_1^3/27 + (3 + h_2)h_1/6 - (2h_1 - h_3)/2]^2 - [(3 - h_2) + h_1^2/3]^3/27 = 0. \tag{11}$$

Because $\lambda_{ij} = 0.5z_i \pm \sqrt{0.25z_i^2 - 1}$, Eq.(11) is an insufficient condition of the reality of λ_{ij} . As additional condition serves $|z_i| < 2$. At $|z_i| < 2$ the function λ_{ij} represents the complex conjugate pairs.

Let's accept that the cross-section s=0 of the main shaft rotates with constant angular speed. This assumption allows revealing more accurately the effects arising in regular system. At the account of boundary conditions the frequency equation looks like

$$det \begin{pmatrix} w_{22}(p,\varphi_*) & w_{23}(p,\varphi_*) & w_{24}(p,\varphi_*) \\ w_{52}(p,\varphi_*) & w_{53}(p,\varphi_*) & w_{54}(p,\varphi_*) \\ w_{62}(p,\varphi_*) & w_{63}(p,\varphi_*) & w_{64}(p,\varphi_*) \end{pmatrix} = 0, \tag{12}$$

where w_{ij} are elements corresponding the transition matrix $\mathbf{W} = \mathbf{\Gamma^n}$.

4 Effect of spatial localization by vibrations excitation upon reversal in clearances

The given problem we will consider on an example of dynamic model (Figure 1b) which is described by the following system of nonlinear differential equations

$$\begin{cases} q_1^{''} + 2p_{1,1}\delta_{1,1}q_1^{'} + p_{1,1}^2 q_1 - [2p_{2,1}\delta_{2,1}(q_2^{'} - q_1^{'}) + p_{2,1}^2(q_2 - q_1)]\rho_{2,1} = w_1(\varphi_*); \\ q_{2(j-1)}^{''} + 2\delta_{j,1}p_{j,1}(q_{2(j-1)}^{'} - q_{2(j-2)}^{'}) + p_{j,1}^2(q_{2(j-1)} - q_{2(j-2)}) - [2\delta_{j+1,1}p_{j+1,1}(q_{2j}^{'} - q_{2(j-1)}^{'}) + \\ + p_{j+1,1}^2(q_{2j} - q_{2(j-1)})]\rho_{j+1,1} - \rho_j\Lambda_j[2\delta_j p_j Z_j^{'} + p_j^2 Z_j - 0.5s_j sign Z_j] = w_{2(j-1)}(\varphi_*)); \\ q_{2j-1}^{''} + 2\delta_{j,2}p_{j,2}(q_{2j-1}^{'} - q_{2j-3)}^{'}) + p_{j,2}^2(q_{2j-1} - q_{2j-3}) - [2\delta_{j+1,2}p_{j+1,2}(q_{2j+1)}^{'} - q_{2j-1}^{'})] + \\ + p_{j+1,2}^2(q_{2j+1} - q_{2j-1})]\rho_{j+1,2} + \Lambda_j[2\delta_j p_j Z_j^{'} + p_j^2 Z_j - 0.5s_j sign Z_j] = w_{2j-1}(\varphi_*). \end{cases} \tag{13}$$

Here $()^{'} = d/d\varphi_*$; $p_{j,k}^2 = c_{j,k}/(J_{j,k}\omega^2)$; $p_j^2 = c_j/(J_{j,2}\omega^2)$; $\rho_{j+1,k} = J_{j+1,k}/J_{j,k}$; $\rho_j = J_{j,2}/J_{j,1}$; (at j=2 it is necessary to accept $q_0 = q_1; q_0^{'} = q_1^{'}; p_{2,2} = 0$; if $j = n+1, p_{n+2,1} = 0, p_{n+2,2} = 0$); $Z_j = q_{2j-1} - \Pi^{'}(\varphi_*)q_{2(j-1)}$; $Z_j^{'} = q_{2j-1}^{'} - \Pi^{'}(\varphi_*)q_{2(j-1)}^{'}$; $\delta_i = \psi_i/(4\pi)$; $\Lambda_j = \Lambda_j(|Z_j| - 0.5s_j)$ is the unit function.

On the basis of the set of equations (13) with $\Pi^{'} = r_0 \sin\varphi_*$, the computer simulation was carried out. Thus, have been varied the number n of identical modules, the clearance value, the kinematic, inertial, elastic, and dissipative characteristic. The input data were averaged values of the dynamic parameters of warp knitting machine's actuators. On Figure 5 are shown vibrations some sections of actuators excitation upon reversal in clearances with n=4. At $r_0 = \Pi_{max}^{'} = 0.2$ all sections of the actuator practically move synchronously, and the parameters of the main shaft subsystem have a weak effect. At $r_0 = 0.5$ the vibrations for the first three modules (i = 3, 5, 7) are differ little, however, well-defined undamped vibrations on the coordinate can be observed. Actually, in this case the last module carries out a dynamic damper role.

This effect can be considered as one of manifestation of spatial localization. As has been shown in the theoretical analysis, with increase $\Pi_{max}^{'}$ the dynamic constraint of subsystems grows. It leads to growth of variable components of a frequency spectrum and possibility of the local dynamic instability on final intervals of a kinematic cycle. In this case, the effective value of the logarithmic decrement is determinate by relationship $\tilde{\vartheta} = \vartheta - \vartheta_*$, where $\vartheta_* = (\xi - 0.5\dot{p}/p^2)$, $\xi = 0; 1$ and 2 for vibrations, vibration velocities and vibration accelerations respectively [1,2]. The value $\max|\vartheta_*|$ may be commensurable and

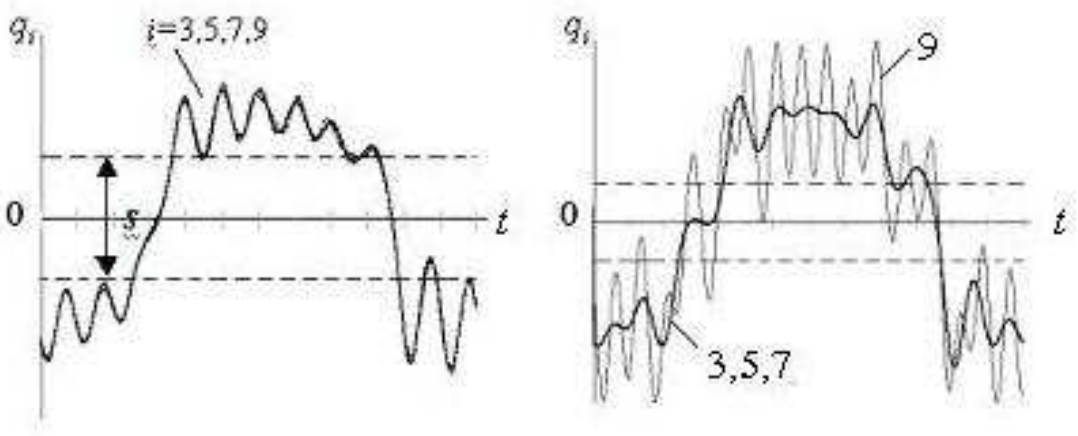

Figure 5: Vibrations excitation upon reversal in a clearance

sometime exceed the initial value the logarithmic decrement ϑ . It can lead to a "negative damping" and to increase in amplitudes.

The big roles also plays the "spatial accumulation" of phase shifts $\Delta\gamma(n)$ in a subsystem of the main shaft at $n \geq 5$ (Figure 6). It is visible on the plots of accelerations (Figure 7) received by computer modeling of free vibrations for s=1 (a curve 1) and s=n (a curve 2; $\gamma_n \to \pi/2$). This leads to spatial localization of actuator's vibrations on the last module. Let us analyze the prerequisites for the loss of the synchronous mode. It is possible to show that the strong additional excitation of the mechanism n involves the specific impact of a subsystem formed by preceding mechanisms, which, in the case of synchronous vibrations, appears as a massive inertial element. This assumption is supported by the result of a numerical experiment for the case of the disruption of the elastic link in an actuator between the mechanism n and the preceding mechanism ($c_{n,2} = 0$) . In this case, curves 1 and 2 practically coincide. Thus, one expedient way of the design solution of the problem of dynamic synthesis is passage to a multimodule structure of the drive, where a long actuator is replaced by indnvidual sections with a limited number of mechanisms. In this case, the sections (modules) are connected with each other only by a shaft. Thus, the dynamic model gets branch-ring structure (Figure 3). The dynamic analysis of this model is resulted in [7].

5 Conclusion

In given article the theory of oscillatory systems with periodic spatial structure is developed with reference to research of dynamic models of cyclic machines with variable and nonlinear parameters. From theoretical analysis and computational modeling the amplitude level of vibrations, the dominant vibration mode, and the conditions of its degeneracy are determined. Analytical criteria of rational dynamic synthesis are proposed. A specific kind of spatial localization is established. It is shown that one of effective ways of elimination of spatial localization in the given class of systems is transition to branch-ring structured drives. In this case practically the coincidence of actuator's vibrations phase is accomplished. Thus, besides the resulted dynamic advantages allow also successfully realizing a economically effective modular principle for the decision of technological and machine's design problems.

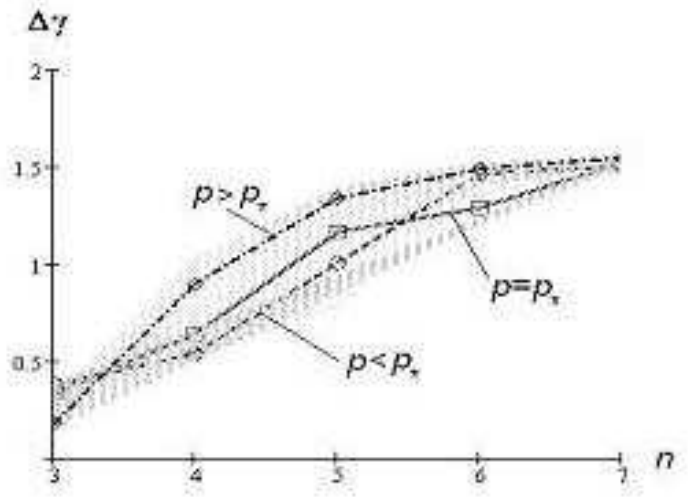

Figure 6: Plots $\Delta\gamma(n)$

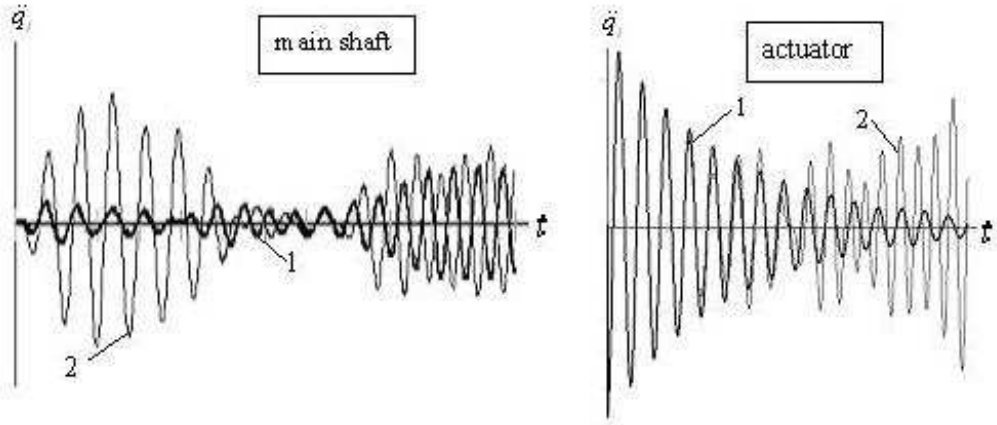

Figure 7: To the analysis of spatial localization

References

[1] Vulfson I.I. Vibrations of machines with cyclic mechanisms [in Russian], Mashinostroenie, Leningrad, 1990. (In Russian).

[2] Vulfson I. Vibroactivity of branched and ring structured mechanical drives. New York, London: Hemisphere Publishing Corporation, 1989.

[3] Landa P.S. Nonlinear oscillations and waves in dynamical systems. Dordrecht-London: Kluwer Academic Publ.,1996.

[4] Indeitsev D.A., Kuznetsov N.G., Motygin O.V., Mochalova Ju.A. Localization of linear waves. St. Petersburg, 2007. (in Russian).

[5] Vulfson I.I.,Preobrazhenskaya M.V. Research of the oscillatory modes arising in clearances of cyclic mechanisms, connected to the common actuator. Journal of Machinery Manufacture and Reliability, 2008. V.37. No1. Pp.29-37.

[6] Vulfson I.I. Vibrations of system with time-dependent parameters. Prikladnaya matematika i mechanika. 1969. V.33. No2. Pp. 331-337. (in Russian).

[7] Vulfson I.I. Investigation of vibrations in multimodule drives of cyclic machines with a branched-ring structure. Journal of Machinery Manufacture and Reliability. 2009. V.38.No2. Pp.22-29.

I.Vulfson, Saint-Petersburg, Russia

Discrete Element Modelling of ceramic/polymer composites

M. F. H. Wolff V. Salikov S. Antonyuk S. Heinrich V. A. Kuzkin
G. A. Schneider
michael.wolff@tuhh.de

Abstract

The structural applications of ceramic materials are often limited by their high brittleness and scatter of mechanical properties resulting in the lack of predictability of the material failure. Therefore, a novel class of composite materials is developed, in which polymer-coated ceramic particles are pressed to high packing densities. The material will have a hierarchical structure with different polymer coatings on different length scales. The polymer acts as a solid bridge binding the ceramic particles together. By varying the type and amount of the soft phase it is expected to obtain customized properties. In order to model the polymer bridges between the ceramic particles we present an enhancement of the linear elastic bonding model in which the geometry of each individual bond is taken into account. Based on this enhancement, results from pressure tests of the mechanical properties using Discrete Element Method (DEM) simulations are presented. We also present an alternative bonding model in which the forces and moments acting on the bond are stringently derived from a potential energy.

1 Introduction

The structural applications of ceramic materials are often limited by their high brittleness and scatter of mechanical properties resulting in the lack of predictability of the material failure. Therefore, a novel hierarchically structured composite material made of densely packed ceramic particles connected by different thin polymer layers is developed [1, 2, 3]. By varying the type and amount of the soft phase as well as the interface strength on different length scales it is expected to obtain customized properties as well as high fracture toughness. By compressing to high packing densities good mechanical properties (high elastic modulus and strength) can be achieved without sintering. In the envisioned material, nanoscale particles are coated by thin polymer layers and densely packed to a building block for the next hierachical level. These building blocks will be coated by another polymer layer etc. (Fig.1). A control and adjustment of the polymeric boundary layers between the building blocks will inhibit crack propagation.

2 Discrete Element Method

The Discrete Element Method (DEM) was introduced by Cundall and Strack in 1979 [4] and has evolved into an important simulation tool within various fields of research, and is particularly suited for the simulation of granular matter due to its mutual discrete character. It is based on the numerical calculation of the equations of motion for the forces and moments acting on each particle (discrete element). The major advantage of the DEM

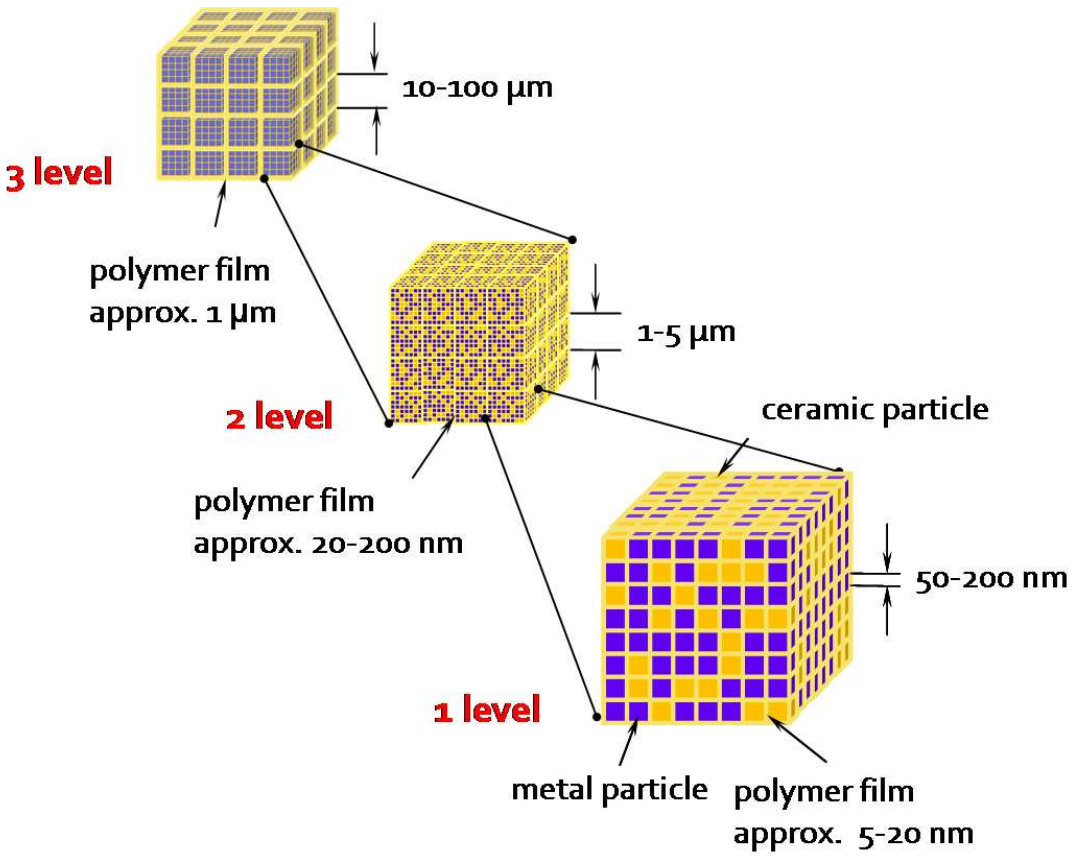

Figure 1: Concept of the hierarchical structure of the ceramic/polymer composites

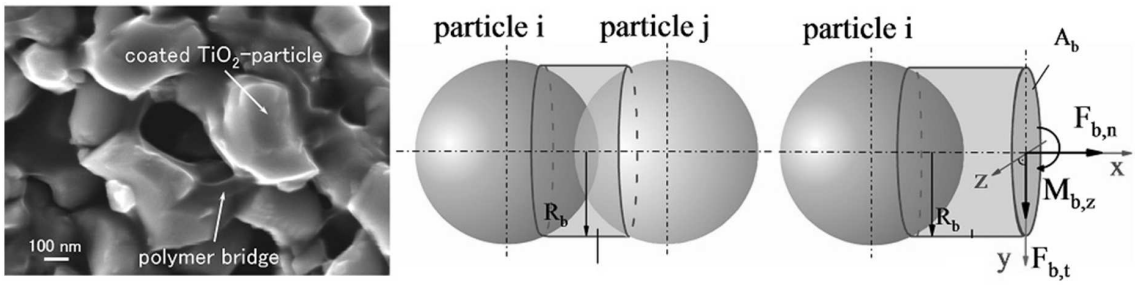

Figure 2: Scanning electron micrograph (left) and DEM solid bridge bond model (right) showing how the ceramic/polymer composite is modelled in DEM.

over continuous simulation methods is that the microstructure and microprocesses, such as deformation of particles and their binding mechanism, fracture propagation etc., are described by solving the actual physical interaction laws governing the processes [4].

3 Bonding model

The bonding model used in this study is based on the linear elastic bonding model introduced by Potyondy et *al.* which is used frequently to model the mechanical properties of agglomerates and granular matter [5, 6, 7, 8, 9, 10, 11]. In this model, the bonds typically act in addition to the standard Hertz-Mindlin contact forces [12], and their contribution to the forces and moments acting on the bonded particles is calculated according to

$$\begin{aligned}
\Delta\vec{F}_{\mathrm{b,n}} &= -k_{\mathrm{n}} A_{\mathrm{b}} \Delta\vec{l}_{\mathrm{n}} \\
\Delta\vec{F}_{\mathrm{b,t}} &= -k_{\mathrm{t}} A_{\mathrm{b}} \Delta\vec{l}_{\mathrm{t}} \\
\Delta\vec{M}_{\mathrm{b,n}} &= -k_{\mathrm{t}} J_{\mathrm{b}} \Delta\vec{\Theta}_{\mathrm{n}} \\
\Delta\vec{M}_{\mathrm{b,t}} &= -k_{\mathrm{n}} I_{\mathrm{b}} \Delta\vec{\Theta}_{\mathrm{t}}
\end{aligned} \tag{1}$$

where $\Delta\vec{F}$ and $\Delta\vec{M}$ are the additional force and moment respectively acting on the bond, $\Delta\vec{l}_{\mathrm{n,t}} = \Delta t \cdot \vec{v}_{\mathrm{n.t}}$ and $\Delta\vec{\Theta}_{\mathrm{n,t}} = \Delta t \cdot \vec{\omega}_{\mathrm{n,t}}$ the relative (rotational) displacement increments, k the stiffness per unit area, Δt the time step, $A_{\mathrm{b}} = \pi {R_{\mathrm{b}}}^2$ the cross section of the bond, $I_{\mathrm{b}} = \frac{1}{4}\pi {R_{\mathrm{b}}}^4$ the moment of inertia and $J_{\mathrm{b}} = \frac{1}{2}\pi {R_{\mathrm{b}}}^4$ the polar moment of inertia of the parallel bond, and R_{b} the radius of the bond [4]. The subscripts n and t denote the normal and tangential direction respectively. The typical criteria for bond breakage are that either the maximum normal ($\sigma_{\mathrm{b,max}}$) or tangential ($\tau_{\mathrm{b,max}}$) stress acting on bond reaches the critical value (strength) of the binder material:

$$\begin{aligned}
\sigma_{\mathrm{b,max}} &= \frac{|\vec{F}_{\mathrm{b,n}}|}{A_{\mathrm{b}}} + \frac{2|\vec{M}_{\mathrm{b,t}}|}{J_b} R_{\mathrm{b}} = \sigma_{\mathrm{b}}^{\mathrm{cr}} \\
\tau_{\mathrm{b,max}} &= \frac{|\vec{F}_{\mathrm{b,t}}|}{A_{\mathrm{b}}} + \frac{|\vec{M}_{\mathrm{b,n}}|}{J_{\mathrm{b}}} R_{\mathrm{b}} = \tau_{\mathrm{b}}^{\mathrm{cr}}
\end{aligned} \tag{2}$$

For the studies presented here, the critical strength of the material was set to a very high value ($\sigma_{\mathrm{b,max}} = \tau_{\mathrm{b,max}} = 10^{20}$Pa) to study the elastic properties and avoid bond breakage. The stresses applied to the structures were small compared to the stresses at which the structures break experimentally (several 100 MPa).

The bonding model is sketched in Fig. 3. The particles (ceramic) are bonded by solid bonds which have elastic properties corresponding to the material of the binder (polymer).

Typically in the linear elastic bonding model values depending on the mechanical behavior and on the geometry of the material bridges are set as parameters for the calculation

of forces and moments acting on each bridge. In particular, the normal (k_n) and tangential (k_t) stiffness per unit area and the bond radius R_B (see eqn. 1) are often used. If one assumes a cylindrical bond, as shown in figure 7, the normal stiffness per unit area k_n is given by Young's modulus E devided by the bond length l_B:

$$\Delta\vec{F}_{\mathrm{n}} = k_{\mathrm{n}}\Delta\vec{l} = \frac{E}{l_{\mathrm{B}}}A_{\mathrm{B}}\Delta\vec{l} \tag{3}$$

However, as the Young's modulus E is a material constant whereas the stiffness per unit area k_n also depends on the geometric properties of the bond (namely on l_B), it is advantageous to consider E is input parameter and calculate the stiffness from it for each bond individually according to

$$k_{\mathrm{n}} = \frac{EA_{\mathrm{B}}}{r_{ij} - \frac{1}{2}z(d_i + d_j)} \tag{4}$$

where r_{ij} is the distance between the center points of particles i and j, d_i (d_j) their diameters, and z an additional parameter representing the reduction of bond diameter within the spherical cap of the particle. Likewise, the cross-sectional area of the bond A_B is typically calculated via

$$A_{\mathrm{B}} = \pi R_{\mathrm{B}}^2 = \pi c R_i^2 \tag{5}$$

where R_B(or c and particle diameter R_i) is set as input parameter. The parameter c represents the ratio of solid bridge bond diameter to particle diameter and thus takes into account the volume content of binder material in the structure. The more binder material is present in the structure, the larger the bond radius R_B, which is accounted for by c. It typically ranges between 0.7 for agglomerate structures and 1 for crystals or highly filled structures with small porosity [6].

Formula (5) is valid for a monomodal and narrow particle size distribution, but should no longer be used if the particle size distribution is broad, because the bonding radius between two large particles will be significantly larger than the bonding radius between two small particles. Therefore, in this case it is better to approximate R_B as mean value of the two particle radii according to

$$R_{\mathrm{B}}^{ij} = \frac{c}{4}(d_i + d_j) \tag{6}$$

so that the bonding radius for a bond between particles i and j directly depends on their diameters d_i and d_j.

4 Simulation

The mechanical properties of the compacts of the 1st hierarchical level (Fig. 1) were simulated using the Discrete Element Method. A setup was chosen corresponding to a pressure test of a cylindrical specimen. Primary particles having a lognormal size distribution were generated and compacted to a cylindrical assembly (see figure 2). Next, all particle velocities were set to zero and linear elastic bonds were created between any two contacting particles, ensuring that no residual stresses were created by introducing the bonds [5]. The number of contacts at bond creation time was approx. 10,800, resulting in the generation of the same number of bonds. The bond parameters for each bond were determined according to equation (4), and E = 3GPa was chosen as value for Young's

modulus, which is the value for the experimentally used polymer poly(methyl methacrylate) (PMMA) [1]. Figure 4 shows the distribution of stiffnesses per unit area of the bonds resulting from the Young's modulus of the bonds and the geometric configuration. The configuration at the bonding time was set as equilibrium configuration, such that no forces or moments were present at bond creation time. At the moment when the bonds were created the radius of the particles was reduced slightly in order to ensure that no residual stresses due to standard Hertz-Mindlin interaction were present. The resulting packing density p was determined by dividing the total volume of particles, which were located inside a virtual cylinder placed inside the structure, by the volume of this cylinder. This gave a packing density of $p \approx 61\%$, almost matching the value for a random dense packing of monosized spheres ($\approx 64\%$). At the two ends of the structure cylinders with a high shear modulus (90 GPa, Poisson ratio = 0.28) were created. Both cylinders were given a constant velocity of 0.1 mm/s directed toward the particles. The resulting total normal force F_n acting on the particles which were in contact with the upper plate is shown in Fig. 4 as a function of total compression Δl. The resulting Young's modulus E of the composite material was calculated according to

$$E = \frac{\Delta F_{\mathrm{n}}}{A} \cdot \frac{h}{\Delta l} \tag{7}$$

where $h = 14.5\mu$m is the height and $A = \pi \cdot (5.4 \times 10^{-6}\mathrm{m})^2 = 91.6\mu\mathrm{m}^2$ the cross-sectional area of the structure.

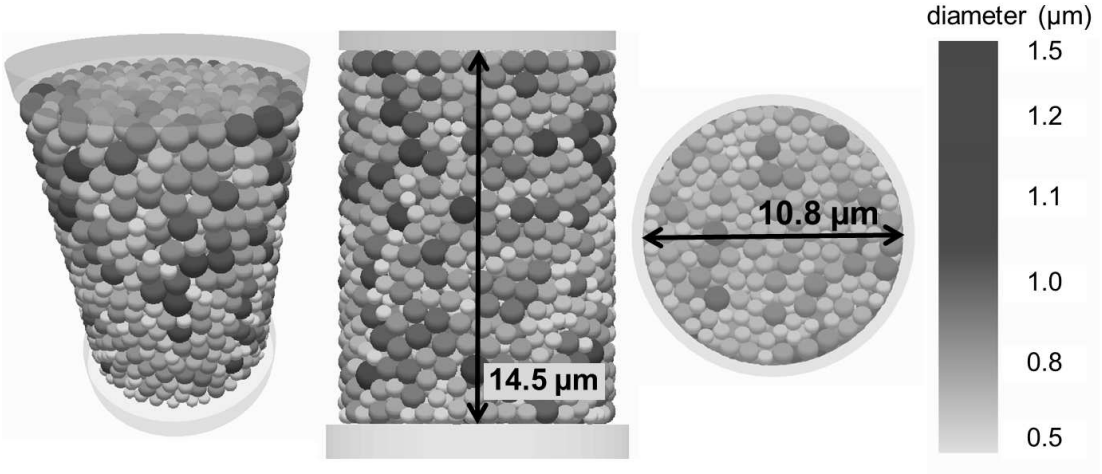

Figure 3: Loading scheme in DEM simulation. Particles with a log-normal size distribution are generated and compacted. Then bonds are created at all particle contacts and a flat indenter moves into the sample with constant speed. Left: 3D view, middle: front view, right: top view.

The force-distance curve was recorded using the old model with a constant stiffness per unit area for every bond of $k = 6.8 \times 10^{16}\mathrm{N/m}^3$, corresponding to an estimated bond length of 40 to 50 nm and a bond diameter of $R_{\mathrm{B}} = 1\mu$m. The force-distance curve was then recorded using the modified bonding model described in section 3. The curves are plotted in figure 4 and it can be seen that the resulting Young's modulus is slightly higher (3.6 GPa instead of 3.1 GPa) for the modified model than it is for the original model. As can be seen in figure 3, there is a considerable number of bonds having a larger stiffness than the estimated $6.8\mathrm{N/m}^3$, increasing the Young's modulus for the composite structure. The simulated values are higher than the value of the Young's modulus attributed to the

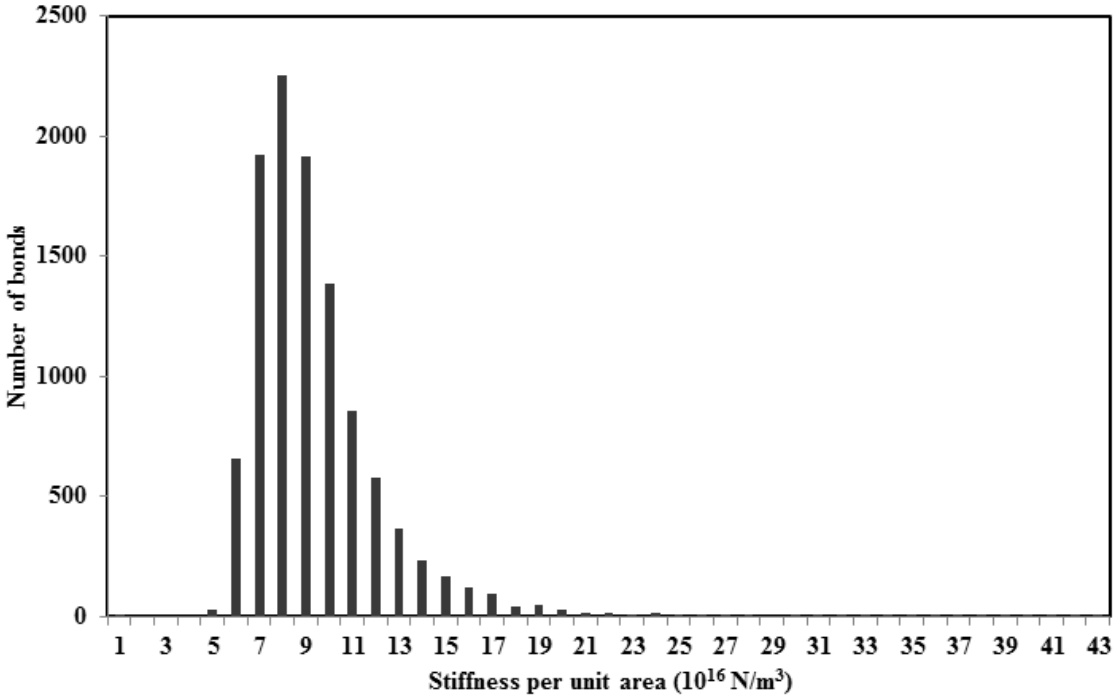

Figure 4: Number distribution of stiffness per unit area of the bonds calculated from the Young's modulus and the geometric arrangement of the particles.

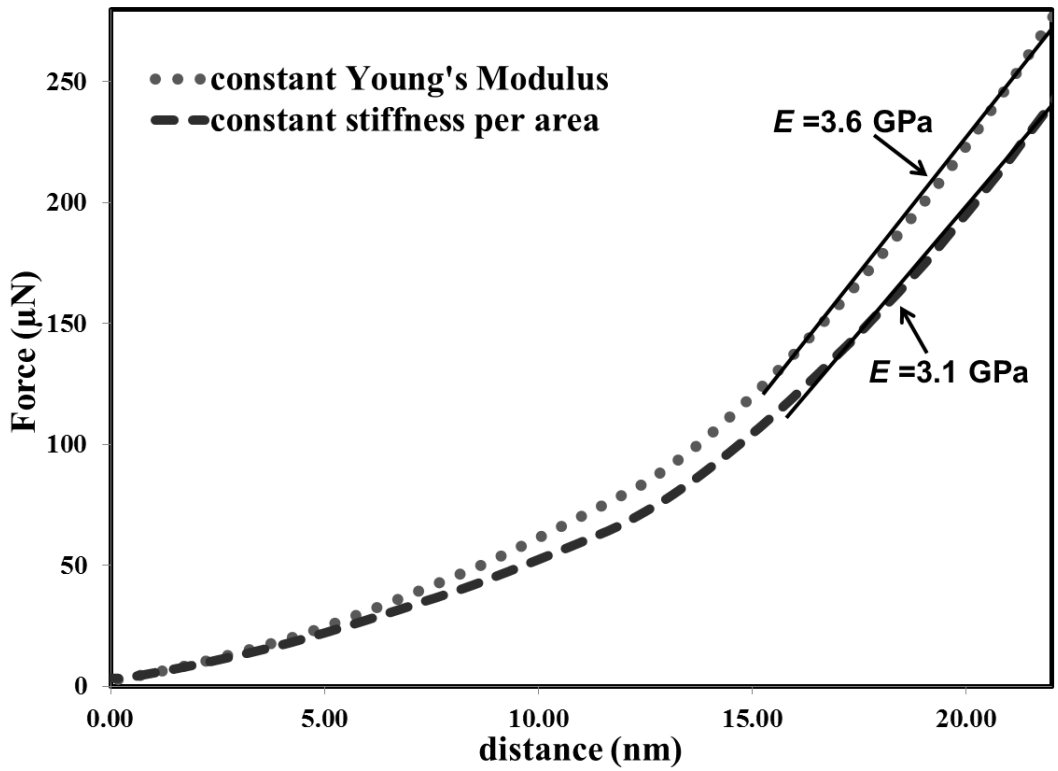

Figure 5: Force-distance curves of compression tests using a constant stiffness per unit area and a constant Young's modulus as input parameters for the bonding model.

bonds, which arises from the existence of hard and stiff particles. However, this value lies clearly below the value which one would expect from the well-known rule of mixture of elastic properties of composite materials or determined experimentally in [1]. A possible cause and solution to this is presented in section 5.

5 Bonding model based on potential energy

The model described in section 3 has the disadvantage that the moments acting between two bonded particles vanish in a situation in which the particles co-rotate such that $\vec{\omega}_i - \vec{\omega}_j = 0$. In the following, a possible way to avoid this unphysical behaviour is presented. The approach based on so-called moment interactions [13] is used. It is assumed that forces and moments acting between bonded particles are potential and depend on relative position and orientation of the particles. The approach for construction of the potential for interacting rigid bodies was originally proposed for molecular systems [14]. In [15] this approach was applied for simulation of deformation and fracture of solid graphene. For simplicity a single bond between two particles is considered. Following the ideas proposed in papers [14, 15] let us introduce unit vectors $\vec{n}_i$ and $\vec{n}_j$ rigidly connected with particles i and j respectively. Initially let the vectors be directed along the bond. During the deformation of the bond these vectors co-rotate with the particle according to

$$\vec{n}_i(t) = \overset{\leftrightarrow}{P}_i(t - t_0) \cdot \vec{n}_i(t_0) \tag{8}$$

where $\overset{\leftrightarrow}{P}_i(t-t_0)$ is the rotational matrix of particle i that describes the turn of the particle from its initial orientation at time t_0 to its current orientation at time $t - t_0$.

In [14] it is shown that the potential should be a function of invariant values $r_{ij}, \vec{n}_i \cdot \vec{n}_j, \vec{e}_{ij} \cdot \vec{n}_i, \vec{e}_{ij} \cdot \vec{n}_j$, where r_{ij} is the distance between the particle centers of particles i and j, and $\vec{e}_{ij} = \frac{\vec{r}_{ij}}{r_{ij}} = -\vec{e}_{ji}$ is the unit vector pointing from particle i to particle j. Thus the general form of the potential is the following

$$U = U(r_{ij}, \vec{n}_i \cdot \vec{n}_j, \vec{e}_{ij} \cdot \vec{n}_i, \vec{e}_{ji} \cdot \vec{n}_j) \tag{9}$$

In the present paper the following form of the potential is proposed

$$U = \frac{B_1}{2}(r_{ij} - l_\mathrm{B})^2 + \frac{B_2}{2}(\vec{n}_i \cdot \vec{n}_j)^2 - \frac{B_3}{2}\left((\vec{e}_{ij} \cdot \vec{n}_i)^2 + (\vec{e}_{ij} \cdot \vec{n}_j)^2\right) \tag{10}$$

where l_B as the initial length of the bond. The first term in the potential describes tension/compression of the bond, the second term is responsible for bending, and the third term describes bending and shear. Note that formula (10) is the simplest form of the potential that describes tension, bending and shear of the bond independently. In general, any term in the right hand side of formula (10) can be replaced by any suitable nonlinear function of r_{ij}, $\vec{n}_i \cdot \vec{n}_j$ or $\vec{e}_{ij} \cdot \vec{n}_i$, $\vec{e}_{ij} \cdot \vec{n}_j$ respectively. Using formula (10) and well-known expressions [14, 15] connecting forces and moments with the potential one can obtain the following formulas:

$$\begin{aligned}
&\vec{F}_{ij} = -\vec{F}_{ji} = \frac{\partial U}{\partial \vec{r}_{ij}} = B_1(r_{ij} - l_\mathrm{B})\vec{e}_{ij} - \frac{B_3}{r_{ij}}\vec{e}_{ij} \cdot \vec{n}_i(\vec{n}_i - \vec{e}_{ij}\vec{e}_{ij} \cdot \vec{n}_i) \\
&+\vec{e}_{ij} \cdot \vec{n}_j(\vec{n}_j - \vec{e}_{ij}\vec{e}_{ij} \cdot \vec{n}_j) \\
&\vec{M}_{ij} = \frac{\partial U}{\partial \vec{n}_i} \times \vec{n}_i = B_2(\vec{n}_i \cdot \vec{n}_j)\vec{n}_j \times \vec{n}_i - B_3(\vec{e}_{ij} \cdot \vec{n}_i)\vec{e}_{ij} \times \vec{n}_i \\
&\vec{M}_{ji} = \frac{\partial U}{\partial \vec{n}_j} \times \vec{n}_j = B_2(\vec{n}_i \cdot \vec{n}_j)\vec{n}_i \times \vec{n}_j - B_3(\vec{e}_{ij} \cdot \vec{n}_j)\vec{e}_{ij} \times \vec{n}_j
\end{aligned} \tag{11}$$

Expanding the expressions for force and moments in the case of small deformations one can obtain the following connection between parameters of the potential and stiffnesses of the bond

$$c_A = B_1, \quad c_D = \frac{2B_3}{l_{\mathrm{B}}^2}, \quad c_B = \frac{B_3}{2} - B_2, \tag{12}$$

where c_A, c_D, c_B are longitudinal, shear and bending stiffnesses of the bond [13]. Formula (12) yields that choosing parameters of the potential one can fit any values of the stiffnesses. In particular, one can choose the parameters in such a manner that the proposed model will be equivalent to a Bernoulli-Euler beam connecting particles. In order to find the connection between the parameters and characteristics of the beam, let us consider the following expressions obtained in [16]

$$c_A = \frac{EF}{l_{\mathrm{B}}}, \quad c_D = \frac{12EJ}{l_{\mathrm{B}}^3}, \quad c_B = \frac{EJ}{l_{\mathrm{B}}}, \tag{13}$$

where E, A, J are Young's modulus, cross-section area and moment of inertia of the cross-section respectively. Using formulas (12) and (13) we get the expression connecting parameters of the potential with characteristics of the beam

$$B_1 = \frac{EA}{l_{\mathrm{B}}}, \quad B_2 = \frac{2EJ}{l_{\mathrm{B}}}, \quad B_3 = \frac{6EJ}{l_{\mathrm{B}}}. \tag{14}$$

Formula (14) can be used for calibration of parameters of the potential. Let us note that the proposed model (eqn. 10) is in general more flexible than Bernoulli-Euler beam. In particular, in the framework of the Bernoulli-Euler model the following relation between shear and bending stiffnesses is satisfied $c_D = 12c_B/l_{\mathrm{B}}^2$ [16]. In the framework of model (eqn. 10) the stiffnesses are independent.

Let us describe the numerical procedure required for modelling of the bond using potential (10). For each contact, the two vectors $\vec{n}_i$ and $\vec{n}_j$ rigidly coupled to the two particles being in contact with each other are generated at the bonding time t^* such that $\vec{n}_i(t^*) = -\vec{n}_j(t^*) = \vec{e}_{ij}(t^*)$. The initial length of the bond l_{B} is set to be equal to the distance between particles at time t^*. As the rotation matrix $\overset{\leftrightarrow}{P}_i$ gives the transformation required to rotate the particle from its initial orientation at t_0 to the orientation at time t, it is preferable to calculate the orientation which the vectors $\vec{n}_i$ and $\vec{n}_j$ would have had at t_0 using the inverse rotation matrix $\overset{\leftrightarrow}{P}_i^{-1}(t^*)$ such that

$$\vec{n}_i(t_0) = \overset{\leftrightarrow}{P}_i^{-1}(t^*) \cdot \vec{n}_i(t^*) = \overset{\leftrightarrow}{P}_i^{\mathrm{T}}(t^*) \cdot \vec{n}_i(t^*) \tag{15}$$

Since the rotation matrix is orthogonal, the inverse $\overset{\leftrightarrow}{P}_i^{-1}$ and the transposed $\overset{\leftrightarrow}{P}_i^{\mathrm{T}}$ are identical, which was used in the last step. The calculated vectors $\vec{n}_i(t_0)$ are stored and the current value of vector $\vec{n}_i$ at time t is calculated according to eqn. 13. For known vectors $\vec{n}_i$, $\vec{n}_i$, $\overrightarrow{e}_{ij}$ forces and moments acting on the bonded particles are calculated using formulas (11). Finally, let us note that forces and moments (eqn. 11) are conservative. Dissipative terms can also be added if required. Therefore, the model proposed in the given paper allows controlling the dissipation. Fracture of the bond can be described in the same manner as it was done in Cundall's model (see section 3 for details).

6 Conclusions

A bonded particle contact force was implemented as contact force in a DEM simulation environment. The model is based on a linear elastic bonding model, and the set of input parameters was changed from $\{k_\mathrm{n}, k_\mathrm{t}, \sigma_\mathrm{n}, \sigma_\mathrm{t}, R_\mathrm{B}\}$ to $\{E, \sigma_\mathrm{n}, \sigma_\mathrm{t}, R_\mathrm{B}\}$, where E is the Young's modulus of the bonding material. In the improved model, the stiffness per unit area and the bonding radius are calculated from E and the geometric arrangement for each bond individually, which is particularly useful for a relatively large particle size distribution. The model was used to simulate mechanical compression tests of a material consisting of TiO_2 particles bonded together with a polymer. The Young's modulus that was obtained for this composite material was slightly larger than the value obtained with the old model, but still smaller than the measured value of experimentally fabricated composites. A possible cause for this was found which attributes this underestimation to vanishing angular velocities and moments of co-rotating bonded particles. A bonding model which is based on moment interactions was presented, in which the forces and moments are stringently derived from a potential and which can be implemented as bonding force for the discrete element method.

Acknowledgements

We gratefulfy acknowledge for the financial support of the Cluster of Excellence "Integrated Materials Systems" within the Landesexzellenzinitiative Hamburg, Germany.

References

[1] Brandt K.; Salikov V.; Oezcoban H.; Schreyer A; Prado L.; Schulte K.; Heinrich S.; Schneider G. A., 2010. Bio-Inspired Ceramic-Polymer Composites Synthesized by Compaction of Polymer-Encapsulated TiO2-Nanoparticles, submitted to: Journal of Composites Science and Technology.

[2] Munch E.; Launey M. E.; Alsem D. H.; Saiz E.; Tomsia A. P.; Ritchie R. O., 2008. Tough, bio-inspired hybrid materials. In: Science, vol. 322, Iss. 5907, pp. 1516-1520.

[3] Podsiadlo, P.; Kaushik A. K.; Arruda E. M.; Waas A. M.; Shim B. S.; Xu J.; Nandivada H.; Pumplin B. G. Lahann J.; Ramamoorthy A.; Kotov N. A., 2007. Ultrastrong and stiff layered polymer nanocomposites. In: Science, vol. 318, Iss. 5847, pp. 80-83.

[4] Cundall, P. A.; Strack O. D. L., 1979. A discrete numerical model for granular assemblies. In: Geotechnique, vol. 29, Iss. 1, pp. 47-65.

[5] Potyondy, D. O., Cundal, P.A. 2004. A bonded-particle model for rock. In: Int. J. Rock Mech. Min. Sci., vol. 41, Iss. 8, pp. 1329-1364.

[6] Antonyuk, S.; Palis, S.; Heinrich, S. 2011: Breakage behaviour of agglomerates and crystals by static loading and impart. In: Powder Technology, vol. 206, Iss. 1-2, 9th International Symposium on Agglomeration, pp. 88-98.

[7] Gryczka, O.; Heinrich, S.; Deen, N. G.; Annaland, M. V.; Kuipers, J. A. M.; Jacob, M.; Morl, L., 2009: Characterization and CFD-modeling of the hydrodynamics of a prismatic spouted bed apparatus. In: Chem. Eng. Sci., vol. 64, Iss. 14, pp. 3352-3375.

[8] Martin, C. L.; Bouvard, F.; Delette, G., 2006. Discrete element simulations of the compaction of aggregated ceramic powders. In: J. Am. Chem. Soc., vol. 89, Iss. 11, pp. 3379-3387.

[9] Zhu H. P.; Zhou Z. Y.; Yang R. Y.; Yu A. B., 2008. Discrete particle simulation of particulate systems: A review of major applications and findings. In: Chem. Eng. Sci., vol. 63, Iss. 23, pp. 5728-5770.

[10] Cheng, L.; Xia, X.; Yu, W.; Scriven, L. E.; Gerberich, W. W., 2000. Flat-punch indentation of viscoelastic material. In: J. Polym. Sci. Polym. Phys., vol. 38, Iss. 1, pp. 10-22.

[11] Oliver W. C.; Pharr G. M., 2004. Measurement of hardness and elastic modulus by instrumented indentation: Advances in understanding and refinements to methodology. In: J. Mater. Res. vol. 19, Iss. 1, pp. 3-20.

[12] Mindlin, R. D., 1949. Compliance of elastic bodies in contact. In: J. Appl. Mech., vol. 16, Iss. 3, pp. 259-268.

[13] Ivanova, E.A., Krivtsov, A. M., Morozov, N. F., Derivation of macroscopic relations of the elasticity of complex crystal lattices taking into account the moment interactions at the microlevel. In: J.App. Math. and Mech.,Vol. 71, Is. 4, 2007, pp. 543-561.

[14] Price S.L., Stone A.J., Alderton M. Eiplicit Formulae for the electrostatic energy, forces and torques between a pair of molecules of arbitrary symmetry. In: Mol. Phys, Vol. 52, No. 4, 1984, pp. 987-1001.

[15] Kuzkin, V.i., Krivtsov, A.M., Description of mechanical properties of graphene using particles with rotational degrees of freedom. [To be published in Dolkady Physics].

[16] Berinsky, I.E., Rod model for graphene crystal lattice. In: NTV SPbSTU, No. 3, 2010, pp. 12-20 [in Russian].

M. F. H. Wolff, V. Salikov, S. Antonyuk, S. Heinrich, Institute of Solids Process Engineering and Particle Technology, Hamburg University of Technology, Denickestrasse 15, D-21073 Hamburg, Germany

V. A. Kuzkin, St. Petersburg State Polytechnical University, Polytehnicheskaya, 29, St. Petersburg, 195251, Russia

G. A. Schneider, Institute of Advanced Ceramics, Hamburg University of Technology, Denickestrasse 15, D-21073 Hamburg, Germany

Computation of vibrations in the area with perfect viscous gas

Anna V. Yakovenko Pavel T. Zubkov Lilia V. Abdubakova
pzubkov@utmn.ru

Abstract

The numerical investigation of the heat and mass transfer processes in a rectangular cavity as a result of vibrations is performed. The influence of vibration frequency on the propagation of waves in the cavity is considered. The presence of two frequencies is described. There are the natural frequency of the system and the oscillation frequency caused by boundary conditions. The cavity is filled by perfect viscous gas with air characteristics. The heat capacity, the thermal conductivity and the viscosity are assumed to be constant. The case is considered in a one-dimensional setting.

1 Introduction. Problem formulation

We will consider a rectangular cavity with perfect viscous gas. Cavity undergoes to vibration. Specifying high-frequency vibration leads to appearance of shock waves. Disturbances propagate over the region with velocity close to the sound velocity. Shock waves has a strong effect on the process of heat and mass transfer. At time of action waves on the walls there is a strong increase in pressure and temperature, which can lead to undesirable results. It is useful to know the maximum allowable vibration frequency for a given vibration amplitude. Also there is a risk of resonance. With time, the process goes to a periodical regime. The motion of shock waves will be damped and the process of changing the characteristics of the gas will change only due to the frequency of external action.

2 Mathematical model

The motion of the gas under the assumptions made is described with the one-dimensional nonstationary system of equation in Cartesian coordinate system, consisting of conservation laws of mass, momentum and energy. The Clapeyron ideal gas law is considered as the equation of state for gas. The system is written in the noninertial frame of reference associated with the vibrating cavity. Use the following formulas for the transition:

$$t = t', \tag{1}$$

$$x = x' - A\cos(\omega t), \tag{2}$$

$$u = \frac{\partial x}{\partial t} = u' + A\omega\sin(\omega t) \tag{3}$$

Here, t is the time in the noninertial frame of reference, x is the coordinate in the noninertial frame of reference, u is the velocity in the noninertial frame of reference, t'

is the time in the inertial frame of reference, x' is the coordinate in the inertial frame of reference, u' is the velocity in the inertial frame of reference.

The system of equations describing motion of such gas has the form

$$\frac{\partial \rho}{\partial t} + \frac{\partial \rho u}{\partial x} = 0, \tag{4}$$

$$\frac{\partial \rho u}{\partial t} + \frac{\partial \rho u u}{\partial x} = -\frac{\partial p}{\partial x} + \frac{4}{3}\mu \frac{\partial^2 u}{\partial x^2} + \rho A \omega^2 \cos(\omega t), \tag{5}$$

$$\frac{\partial c_v \rho T}{\partial t} + \frac{\partial c_v \rho u T}{\partial x} = k\frac{\partial^2 T}{\partial x^2} - p\frac{\partial u}{\partial x} + \frac{4}{3}\mu(\frac{\partial u}{\partial x})^2, \tag{6}$$

$$p = \rho R T \tag{7}$$

Here, ρ is the density,u is the velocity, p is the pressure, T is the temperature, A is the vibration amplitude, ω is the vibration frequency, t is the time, x is the space coordinate, R is the gas constant, μ is the coefficient of dynamic viscosity, c_v is the specific heat at constant volume.

The initial conditions are as follows:

$$u|_{t=0} = 0, T|_{t=0} = T_0, p|_{t=0} = p_0, \rho|_{t=0} = \frac{p|_0}{RT_0} \tag{8}$$

The boundary conditions are as follows:

$$T|_{x=0} = T_0, u|_{x=0} = 0, T|_{x=L} = T_0, u|_{x=L} = 0 \tag{9}$$

The system of nondimensional equations has the form

$$\frac{\partial \tilde{\rho}}{\partial \tau} + \frac{\partial \tilde{\rho}\tilde{u}}{\partial X} = 0, \tag{10}$$

$$\frac{\partial \tilde{\rho}\tilde{u}}{\partial \tau} + \frac{\partial \tilde{\rho}\tilde{u}\tilde{u}}{\partial X} = -\frac{\partial \tilde{p}}{\partial X} + \frac{4}{3}\frac{1}{Re}\frac{\partial^2 \tilde{u}}{\partial X^2} + \tilde{\rho} A \Omega^2 \cos(\Omega \tau), \tag{11}$$

$$\frac{\partial \tilde{\rho}\Theta}{\partial \tau} + \frac{\partial \tilde{\rho}\tilde{u}\Theta}{\partial X} = \frac{\gamma}{Pe}\frac{\partial^2 \Theta}{\partial X^2} - \tilde{p}\frac{\partial \tilde{u}}{\partial X} + \frac{4}{3}\frac{1}{Re}(\frac{\partial \tilde{u}}{\partial X})^2, \tag{12}$$

$$\tilde{p} = \frac{\tilde{\rho}(\Theta + 1)}{\gamma} \tag{13}$$

The initial conditions are as follows:

$$\tilde{u}|_{\tau=0} = 0, \Theta|_{\tau=0} = 0, p|_{\tau=0} = \frac{1}{\gamma}, \tilde{\rho}|_{\tau=0} = 1 \tag{14}$$

The boundary conditions are as follows:

$$\Theta|_{X=0} = 0, \tilde{u}|_{X=0} = 0, \Theta|_{X=1} = 0, \tilde{u}|_{X=1} = 0 \tag{15}$$

$\sqrt{\gamma R T_0}$ is adiabatic speed of sound in the region of the temperature T0.

The solution of the problem is determined by five dimensionless parameters:

$$Re = \frac{\rho_0 L\sqrt{\gamma R T_0}}{\mu}, Pe = \frac{\rho_0 L c_p \sqrt{\gamma R T_0}}{k}, \gamma = \frac{c_p}{c_v}, \Omega = \frac{\omega L}{\sqrt{\gamma R T_0}}, \tilde{A} = \frac{A}{L} \tag{16}$$

Here,Re is the Reynolds number, Pe is the Peclet number, γ is the adiabatic exponent, Ω is the nondimensional vibration frequency, $\tilde{A}$ is the nondimensional vibration amplitude.

3 Parameters of calculation and numerical scheme

The main positions of the numerical method will be described here. Take as a basis the modified algorithm SIMPLER [2] and its improvement for the case of a compressible medium [1]. In obtaining a numerical solution, we choose a number of locations (n grid points) and seek the solution there. The differential equations (10)-(13) with (14), (15) are solved by converting them into discretization equations (algebraic equations). The discretization equations are obtained by the control volume approach and the second-order treatment of the numerical scheme [3]. The system (10)-(13) is written as:

$$a_\Phi \Phi_i = b_\Phi \Phi_{i+1} + c_\Phi \Phi_{i-1} + d_\Phi \tag{17}$$

$$\tilde{\rho}_i = \tilde{\rho}_i(\Phi_i) \tag{18}$$

$$a_\Theta \Theta_i = b_\Theta \Theta_{i+1} + c_\Theta \Theta_{i-1} + d_\Theta \tag{19}$$

$$\tilde{P}_i = \tilde{P}_i(\Theta_i) \tag{20}$$

where

$$\Phi_i = \tilde{\rho}_i \tilde{u}_i \tag{21}$$

is the mass flux;$a_\Phi, b_\Phi, c_\Phi, d_\Phi, a_\Theta, b_\Theta, c_\Theta$ are the known numeric functions, $i = 2..n-1$, (18) is the equation of continuity, (20) is the equation of state for gas. We use the staggered grid for the mass flux Φ and for the velocity u. In the staggered grid, the velocity components are calculated in points that lie on the faces of the control volume [2].

This is the sequence of operations:

1. Start with a guessed fields of velocity, pressure and density;
2. Calculate the coefficients for the equations (17), and solve this system to obtain Φ by the TriDiagonal-Matrix Algorithm [3];
3. Calculate the density by use of (18);
4.Calculate the coefficients for the equations (19), and solve this system to obtain Θ by the TriDiagonal- Matrix Algorithm [3];
5. Calculate the pressure by use of (20);
6. Calculate the velocity by use of (21);
8. Return to step 2 and repeat until convergence.

The computation grid was uniform and consisted of 1000 nods. The time step was taken to be $\Delta\tau = 0.1\Delta X$(i.e., on condition that the wave will pass a distance of ΔX or less during the time $\Delta\tau$ where ΔX is the size of control volume).

The dimensionless parameters were taken following:$\tilde{A} = 2, 1, 0.5, \frac{50}{\sqrt{\gamma R T_0}} \leq \Omega \leq \frac{400}{\sqrt{\gamma R T_0}}, Re = 10^5, Pe = 8 \cdot 10^4, \gamma = 1.4$

4 Analysis of the results

Let us consider $\tilde{A} = 2$.We will first describe the behavior of the gas at the beginning of the vibration exposure. It is the first passage of the wave the area. At the initial instant of time the cavity was situated at the leftmost position. At low frequency $\Omega = \frac{50}{\sqrt{\gamma R T_0}}$ there is no shock waves in the cavity. Figures 1 and 2 give the distributions of dimensionless temperature depending on coordinate at different instants of time. On can see on these graphics there are standing waves in this case. A similar type of wave has the density and pressure. The velocity will be positive up to time $\tau = 1$ because the gas moves to the

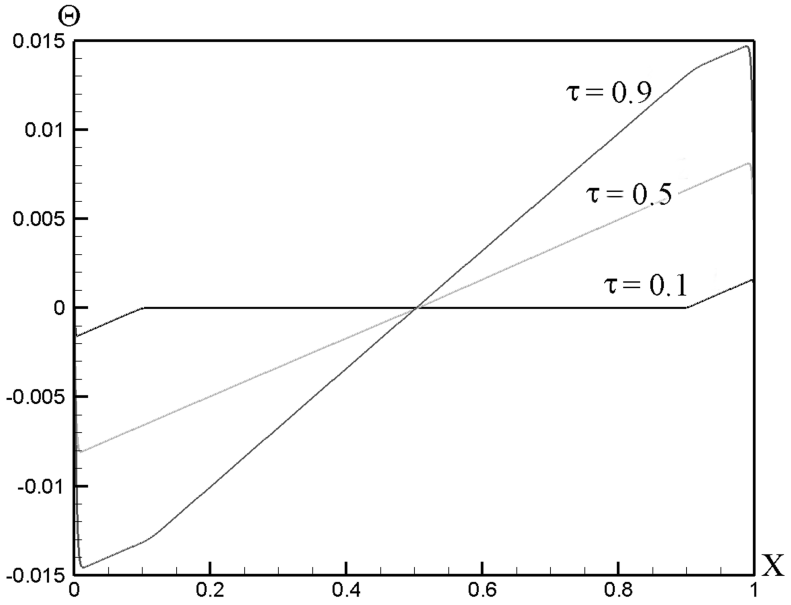

Figure 1: The dimensionless temperature Θ as a function of coordinate at different instants of time with $\Omega = \frac{50}{\sqrt{\gamma RT_0}}, \tau = 0.1, 0.5, 0.9$

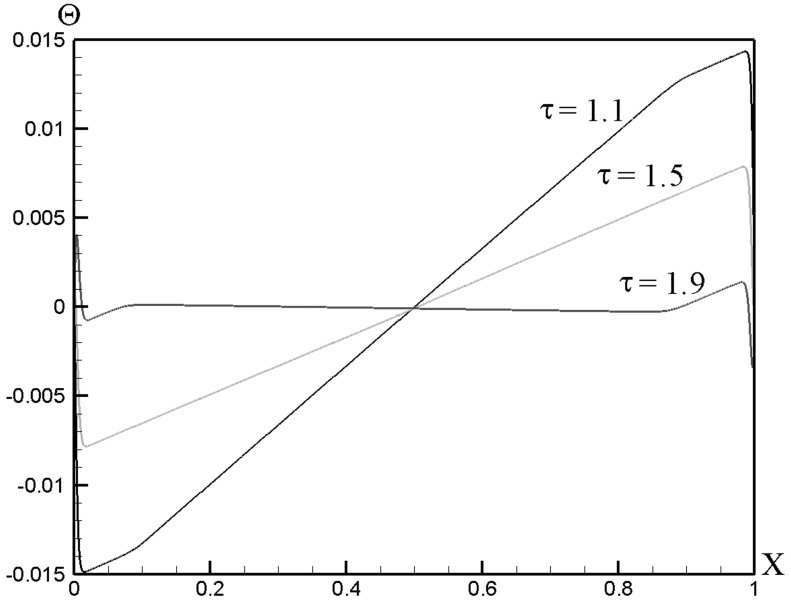

Figure 2: The dimensionless temperature Θ as a function of coordinate at different instants of time with $\Omega = \frac{50}{\sqrt{\gamma RT_0}}, \tau = 1.1, 1.5, 1.9$

right boundary at this time. Then there is a opposite movement as a result of the amount of gas at the right boundary.

Increase the vibration frequency to $\Omega = \frac{250}{\sqrt{\gamma RT_0}}$.In this case the temperature waves are asymmetric. At $\tau = 1.1$ the wave transforms to the weak shock wave. The shock wave changes the direction of motion of the gas, which previously came to the right boundary.

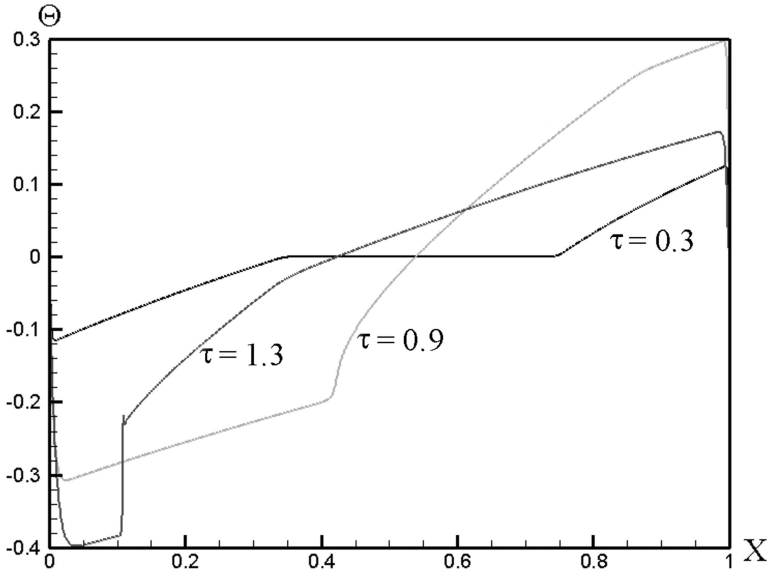

Figure 3: The dimensionless temperature Θ as a function of coordinate at different instants of time with $\Omega = \frac{250}{\sqrt{\gamma RT_0}}, \tau = 0.3, 0.9, 1.1$

Figures 5 and 6 give the distributions of dimensionless temperature depending on coordinate at different instants of time with $\Omega = \frac{400}{\sqrt{\gamma RT_0}}$. The shock wave appears approximately at $\tau = 0.4$. The amplitude of shock waves increases compared with the preceding case.

We will consider the time dependence of heat fluxes across boundaries (Figure 7, 8, 9). The natural frequency of the system and the oscillation frequency caused by the boundary conditions are shown. The period corresponding to the external vibration is equal $P_1 = \frac{2\pi}{\omega}$. The period corresponding to the natural vibration caused by the motion of the waves is equal $P_2 = \frac{2L}{\sqrt{\gamma RT_0}}$. The period P_1 decreases with increasing vibration frequency. The period P_2 also decreases but less intensively. The higher the frequency the lower the number of internal vibrations, falling to one external. It is shown in Figure 7, 8, 9. However, there is no resonance with chosen frequencies and length of area.

Were obtained by the maximum temperature observed in the area at different frequencies and amplitudes of vibration. It is evident that a decrease in the amplitude of vibration, the selected values of the maximum temperature of gas in the area are achieved at higher frequencies. Calculations showed that the maximum temperature in the area occurs near its borders.

For $\tilde{A} = 2$ was obtained:

$\Omega = \frac{50}{\sqrt{\gamma RT_0}}, \Theta_{max} = 0.0159$ at $X = 0.9875, \tau = 0.988$

$\Omega = \frac{250}{\sqrt{\gamma RT_0}}, \Theta_{max} = 0.3730$ at $X = 0.0005, \tau = 1.402$

$\Omega = \frac{400}{\sqrt{\gamma RT_0}}, \Theta_{max} = 2.4500$ at $X = 0.0005, \tau = 1.195$

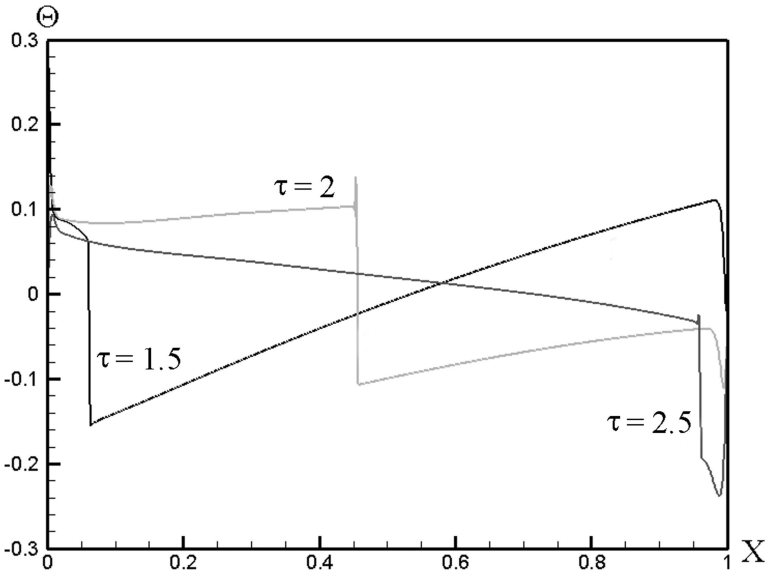

Figure 4: The dimensionless temperature Θ as a function of coordinate at different instants of time with $\Omega = \frac{250}{\sqrt{\gamma RT_0}}, \tau = 1.5, 2, 2.5$

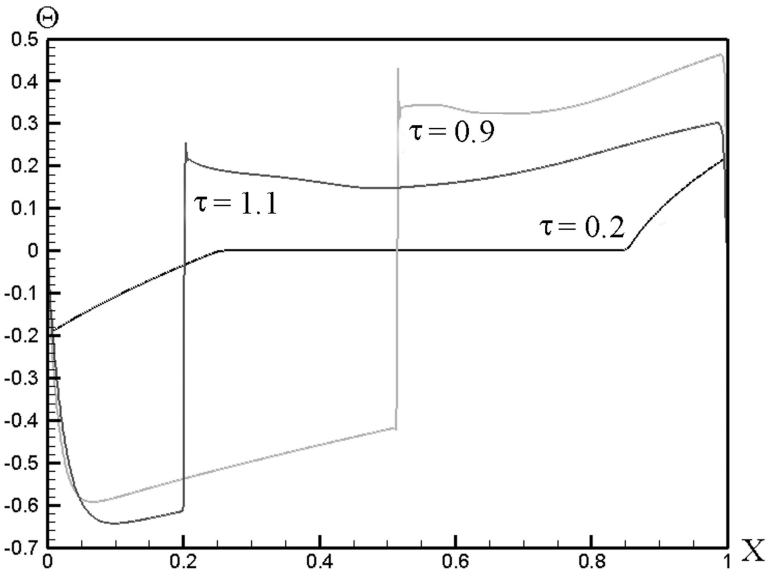

Figure 5: The dimensionless temperature Θ as a function of coordinate at different instants of time with $\Omega = \frac{400}{\sqrt{\gamma RT_0}}, \tau = 0.2, 0.9, 1.1$

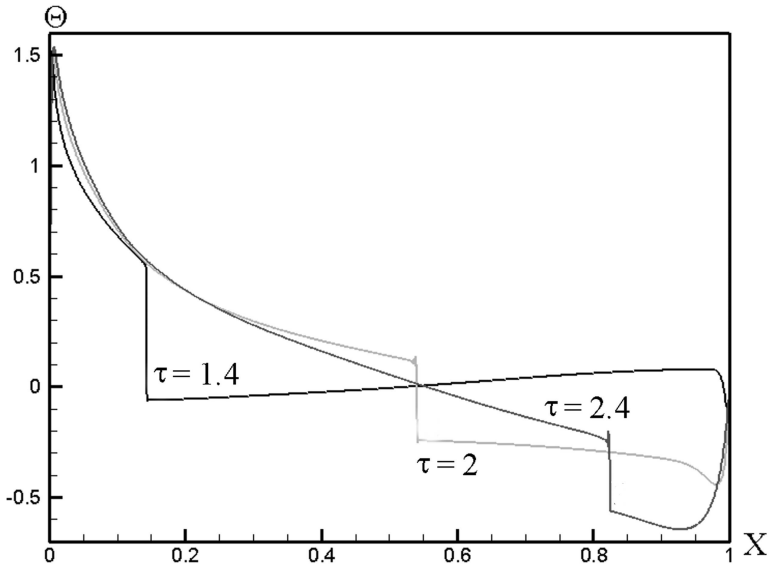

Figure 6: The dimensionless temperature Θ as a function of coordinate at different instants of time with $\Omega = \frac{400}{\sqrt{\gamma R T_0}}, \tau = 1.4, 2, 2.4$

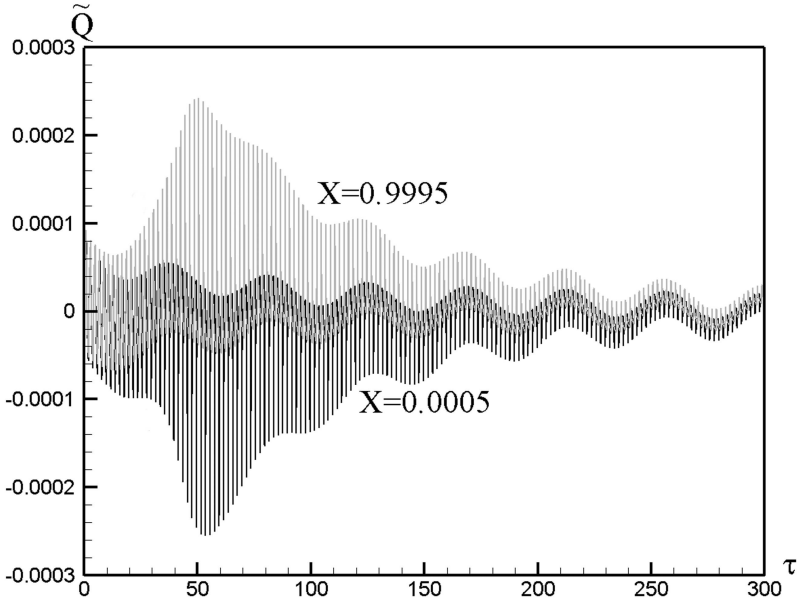

Figure 7: The time dependence of heat fluxes across boundaries with $\Omega = \frac{50}{\sqrt{\gamma R T_0}}$

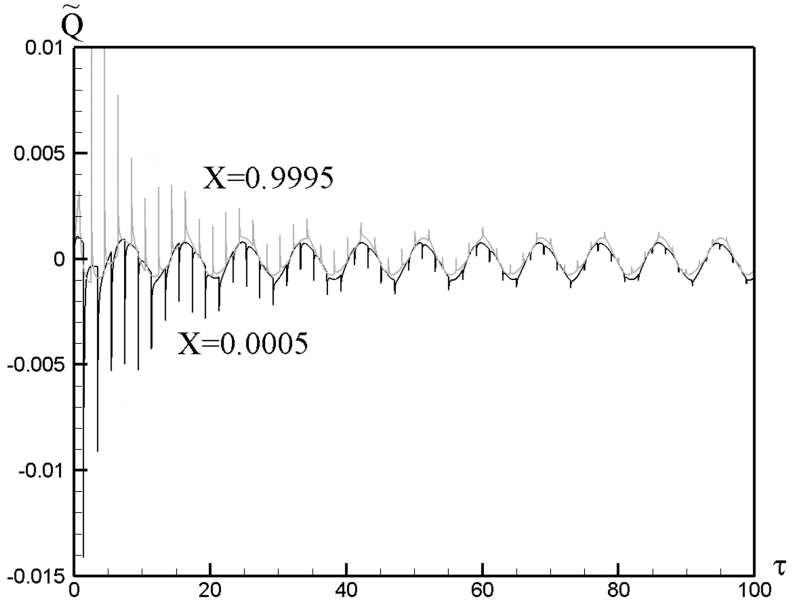

Figure 8: The time dependence of heat fluxes across boundaries with $\Omega = \frac{250}{\sqrt{\gamma R T_0}}$

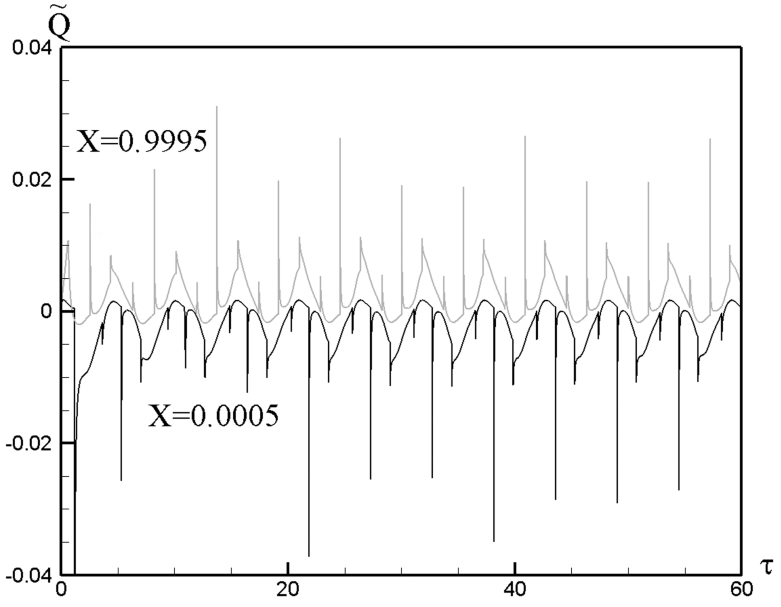

Figure 9: The time dependence of heat fluxes across boundaries with $\Omega = \frac{400}{\sqrt{\gamma R T_0}}$

Starting with the frequency $\Omega = \frac{250}{\sqrt{\gamma R T_0}}$ the maximum temperature observed in the left border area at the moment of impact on her the first shock wave (Figure 3, Figure 5).

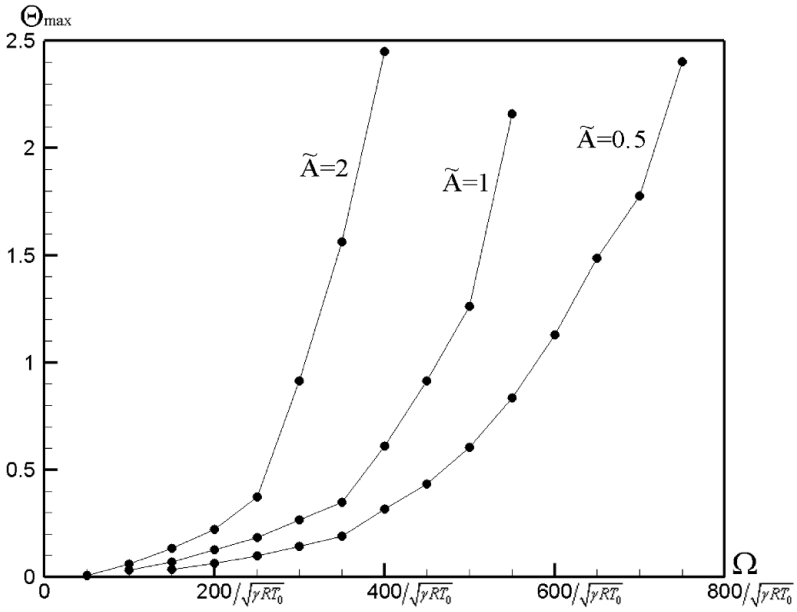

Figure 10: The dependence of the maximum temperature on the vibration frequency in the area with different amplitudes

Over time, heat and mass transfer process goes to a periodic regime. In this situation changing the characteristics of the gas in the area is determined entirely by external influences. Will be only one frequency - the external frequency of vibration area. The periodic regime will be described in further investigations.

5 Conclusions

There are two frequencies: the natural frequency of the system and the oscillation frequency caused by the boundary conditions. The maximum heating of the gas in the area happens at the initial time when the cavity most affected by shock - wave motion near the baundary.Subsequently, the vibration characteristics of the gas in the cavity come to the periodic regime.

References

[1] Zubkov P.T., Sviridov E.M., Gubaidullin A.A. Thermoacoustic waves arising from the heating of the perfect viscous gas.Thermophysics of High Temperatures, Vol.42, No.5, 2004, pp. 753-759.

[2] Patankar S.V. Numerical heat transfer and flid flow. New York: Hemisphere, 1981

[3] Patankar S.V. Computation of conduction and duct flow heat transfer. USA, Innovative Research,1991

Anna V. Yakovenko, Taymirskaya str. 74, Tyumen, Russia
Pavel T. Zubkov, Perekopskaya str. 15a, Tyumen, Russia
Lilia V. Abdubakova, Perekopskaya str. 15a, Tyumen, Russia

Simulation of dynamic processes in vibration machine with unbalanced vibro-exites and asynchronous electric motor

Nikolay P. Yaroshevich Nikolay N. Tolstushko
m_yaroshevich@mail.ru

Abstract

Simulation of dynamic processes at starting the vibration machine with account of intereffect of oscillations in the mechanical system and electromagnetic phenomena in asynchronous engine is carried out. Detailed description of the mechanism of Zommerfield's effect manifestation in the considered type of vibration machines is given and the character of dynamic load arising in the drive during the acceleration is determined. The effect of dynamic and main constructional parameters of vibration machine on the dynamic of its acceleration is determined. Practical recommendations for the decrease of resonance oscillations of the machine and for the lowering of the necessary engine power are worked out.

1 Introduction

Utilization of vibration machines is various branches of industry is a promising direction to intencification of many technological processes. Oscillations in most of vibration machines and devices are excited by mechanical vibroexciters rotated by electric motors of asynchronous type. So long as elastic supports of such vibration machines are rather "soft", as a rule, there exists a problem of passing through resonance. In this stage of motion "sticking" of the rotor speed of motor with limited power (so called imperfect source of energy), that is, manifestation of Sommerfeld's effect is possible [1], which is thoroughly undesirable.

The problem of passing the resonance frequencies zone at starting and running out of vibration machine with inertial excitation of oscillations as well as Sommerfeld's effect are considered, with application of various methods, in a number of works, review of which can be found in books [1-4]. The works [5, 6] present the results of simulation of dynamic processes in vibrating systems with inertional vibrator and asynchronous motor. However, there is a need for more detailed dynamic analysis of processes taking place in vibration technological machines. With unbalanced drive during acceleration.

2 Scheme of the system and motion equations

The scheme of considered vibration machines with plane motion of working head is shown in Fig. 1. Vibrating working head (chamber) is elastically suspended on helical cylindrical springs. An unbalanced vibroexciter the rotor of which runs through the masses centre of the working chamber and is rotated by asynchronous motor, is used as a drive.

Generalized coordinates of the vibration system are coordinates of the chamber masses centre x, y and chamber rotor rotation angles φ and exciter φ_1. The motion of the mechanical system is described with equations:

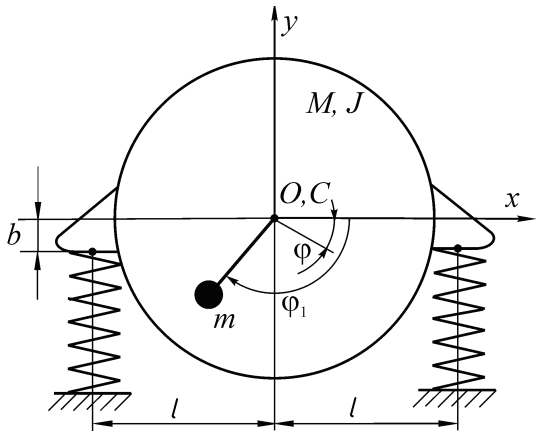

Figure 1: Scheme of vibratory system.

$$\begin{aligned}
&M\ddot{x} + \beta_x\dot{x} + c_x x + c_{x\varphi}\varphi = m\varepsilon\left(\ddot{\varphi}_1\sin\varphi_1 + \dot{\varphi}_1^2\cos\varphi_1\right);\\
&M\ddot{y} + \beta_y\dot{y} + c_y y = m\varepsilon\left(\ddot{\varphi}_1\cos\varphi_1 - \dot{\varphi}_1^2\sin\varphi_1\right);\\
&J\ddot{\varphi} + \beta_\varphi\dot{\varphi} + c_\varphi\varphi + c_{x\varphi}x = 0;\\
&I\ddot{\varphi}_1 = L - R + m\varepsilon\left(\ddot{x}\sin\varphi_1 + \ddot{y}\cos\varphi_1 + g\cos\varphi_1\right),
\end{aligned} \tag{1}$$

where M is a total elastically suspended mass, which takes into account the joined mass of loading; J is a moment of inertia of the working chamber relative to the axis, running through the masses centre; $\beta_x,\ \beta_y,\ \beta_\varphi$ are coefficients of viscous resistance; $c_x,\ c_y$ are spring rates, on shift and on tension-compression, correspondingly; $c_\varphi = c_y l^2 + c_x b^2$, $c_{x\varphi} = -c_x b$, l , b are parameters defining the position of attaching points of the upper springs ends in respect to the masses centre; I is a total moment of inertia of exciter rotor in respect to the axis of rotation; m is the mass of the exciter; ε is exciter eccentricity; L, R is a motor electromagnetic moment of the forces resistant to rotation; g is a free fall acceleration.

For taking into account the effect of the electric motor, so called, A-model of asynchronous machine in oblique-angled current coordinates was used [7]. Electromagnetic phenomena in the engine are described with the system of differential equations:

$$\begin{aligned}
&\tfrac{di_{SA}}{dt} = \alpha_1(u_{SA} - R_S i_{SA}) + \alpha_2(\tfrac{\dot{\varphi}_1}{\sqrt{3}}(\Psi_{RA} + 2\Psi_{RB}) + R_R i_{RA});\\
&\tfrac{di_{SB}}{dt} = \alpha_1(u_{SB} - R_S i_{SA}) - \alpha_2(\tfrac{\dot{\varphi}_1}{\sqrt{3}}(2\Psi_{RA} + \Psi_{RB}) - R_R i_{RB});\\
&\tfrac{di_{RA}}{dt} = -\alpha_2(u_{SA} - R_S i_{SA}) - \alpha_3(\tfrac{\dot{\varphi}_1}{\sqrt{3}}(\Psi_{RA} + 2\Psi_{RB}) + R_R i_{RA});\\
&\tfrac{di_{RB}}{dt} = -\alpha_2(u_{SB} - R_S i_{SB}) + \alpha_3(\tfrac{\dot{\varphi}_1}{\sqrt{3}}(2\Psi_{RA} + \Psi_{RB}) - R_R i_{RB}),
\end{aligned} \tag{2}$$

where i_{RA}, i_{SB} i_{RB}, i_{SA} are projections of stator and rotor currents on the axis coordinates; $\alpha_1 = \alpha_S - \frac{\alpha_S^2}{\alpha_S+\alpha_R+\alpha_m}$, $\alpha_2 = \frac{\alpha_S\alpha_R}{\alpha_S+\alpha_R+\alpha_m}$, $\alpha_3 = \alpha_R - \frac{\alpha_R^2}{\alpha_S+\alpha_R+\alpha_m}$, α_S, α_R – are, correspondingly inverse inductances dissipation of stator and rotor windings; $\Psi_{RA} = \frac{i_{SA}+i_{RA}}{\alpha_m} + \frac{i_{RA}}{\alpha_R}$, $\Psi_{RB} = \frac{i_{SB}+i_{RB}}{\alpha_m} + \frac{i_{RB}}{\alpha_R}$ are full current meshes of rotor windings; R_S, R_R – are resistances of stator and rotor windings. The electric motor is connected to the supply line of unlimited power with symmetric voltage system: $u_{SA} = 310,5\sin(314t)$, $u_S = 310,5\sin(314t - 2\pi/3)$.

The expression for calculation of the motor electromagnetic moment has the form:

$$L(t) = \sqrt{3}\cdot\frac{p_0}{\alpha_m}\left(i_{RA}\, i_{SB} - i_{\mathrm{RB}}\, i_{SA}\right),$$

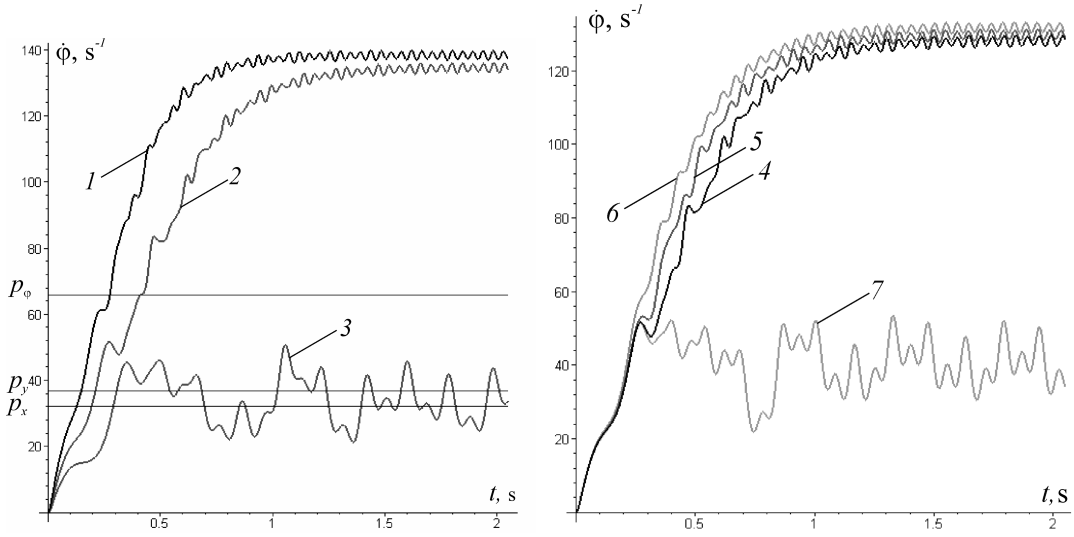

Figure 2: Time dependencies of the exciter speed in the case: a - of different motor power: 1 – $P = 1,5\,kw$, 2 – $P = 1,1\,kw$, 3 – $P = 0,75\,kw$; b - different suspension rigidity $P = 1,1\,kw$: 4 – $c = 4,4 \cdot 10^5\ N/m$; 5 – $c = 3,2 \cdot 10^5\ N/m$; 6 – $c = 1,9 \cdot 10^5\ N/m$; 7 – $c = 6,0 \cdot 10^5\ N/m$

where p_0 is the number of magnetic poles pairs; α_m is an inverse main inductance of the motor.

The moment of forces of resistance to rotation R is caused, mostly, by the resistance in the bearings of the exciter rotor and is determined by formula $R = 0,5 f^* m \varepsilon \dot{\varphi}_1^2 d$, where f^* is summery coefficient of friction in the bearing; d is the diameter of its inner ring.

Simulation of the process of unbalanced exciter acceleration is reduced to the numerical integration of equations of electromechanical system (1), (2) by means of Maple program product at the following parameters values:$M = 330\,kg$; $m = 30\ kg$; $\varepsilon = 0,035\ m$; $J = 8,02\ kg \cdot m^2$; $f^* = 0,002$; $d = 0,04\ m$; $l = 0,23\ m$; $b = 0,1\ m$; $\beta_x = \beta_y = 1000\ kg/s$; $\beta_\varphi = 61,69\ kg/s$; $c = c_x = c_y = 4,4 \cdot 10^5 N/m$. Asynchronous motors of $4A$ type with synchronous frequency of rotation $n_c = 1500\ \text{min}^{-1}$ were uysed.

3 The results of computer simulation

It is known that the course of the process of vibration machine acceleration depends, first of all, on the motor power (Fig. 2, a) of course, the greater power is chosen (the increase of exciter rotor acceleration is taking place) the more substantial is the decrease of resonance oscillations and, correspondingly, the decrease in that period of motion dynamic loads on the vibration machine constructions.

Is should be noted that considered parameters of the vibration system in the case of replacing the motor of $P = 1,1\,kw$ with the motor of $P = 1,5\,kw$ the maximal value of the oscillations amplitude of the working head decreased almost by 20 %; in the case of motor power $P = 0,75\,kw$ its acceleration and reaching transresonance steady-state regime is impossible (Fig. 2, a, curve 3).

The carried out investigations showed that the rigidity of elastic suspension exerts a considerable effect on the process of exciter rotor acceleration (Fig. 2,b). According to the obtained results the reduction of suspension rigidity leads to the decrease of negative manifestation of Sommerfeld's effect. It is important that the effect is positive as it is in

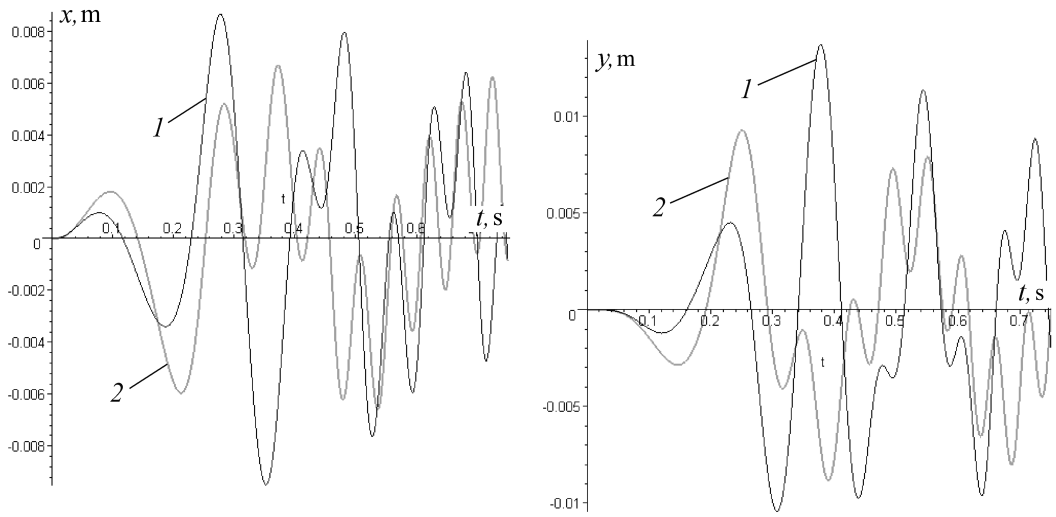

Figure 3: Time dependencies of generalized coordinates of horizontal x (a) and vertical y (b) oscillations of the working chamber masses center at $P = 1,1\,kw$: $1 - c = 4,4{\cdot}10^5\ N/m$; $2 - c = 1,9 \cdot 10^5\ N/m$

the case of increasing the motor power. So, the decrease of rigidity by 25-30% practically eliminates the sticking of exciter rotor speed, in the resonance zone and pick values of working head oscillations decrease noticeably. And, inversely, the same increase of springs rigidity makes the rotor acceleration and reaching by it the steady-state trans resonance regime of rotation impossible without the corresponding increase of the motor power (Fig. 2, b, curve 7). At further decrease of rigidity (in the given in Fig. 2, b example to $c = 1,9 \cdot 10^5 N/m$) the sticking of rotor speed is not observed.

Fig. 3 shows time dependencies of generalized coordinates of the shift of working chamber masses centre during the acceleration for the cases $c = 4,4 \cdot 10^5 N/m$ and $c = 1,9 \cdot 10^5 N/m$. According to the presented plots, in the case of such decrease of suspension rigidity a considerable decrease of both the value of resonance oscillations and the time period during which the amplitudes acquire steady-state values is taking place. Thus, for example, maximal value of amplitude of vertical oscillations decreased from 14 to $8,5mm$. It should be noted that the amplitude of steady-state regime of motion in both investigated cases makes $3,4mm$, so far as in the case of soft vermiculation of the working head the rigidity of elastic suspension practically does not effect on the parameters of steady-state motion.

So, the decrease of the elastic suspension rigidity and, correspondingly the decrease of proper frequencies of vibration system lead to considerable facilitation of the process of passing the resonance frequencies zone. At engineering calculation of vibration machines parameters axial (longitudinal) rigidity of springs is, as a rule, determined proceeding from the accepted value of natural frequency of working head vertical oscillations or by the static deflection of springs. According to the existing recommendations, the ratio ω/p_y (where ω - is the frequency of steady-state oscillations) for the technological machines and vibration mills is within rather wide range - from 2 to 8, but mainly from 4 to 5. According to the presented results of investigations greater of the recommended values should be chosen.

The choice of transversal rigidity of elastic suspension most often is not stipulated. Usually the transversal rigidity is chosen greater than axial one. On the other hand, there are recommendations after which all natural frequencies of the vibration system

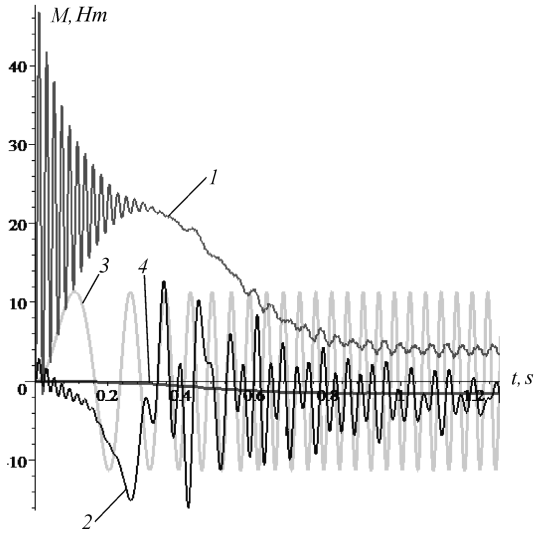

Figure 4: Time dependencies of the moments of: 1 - engine; 2 - vibration; 3 - forces of weight; 4 - forces of resistances R

should be chosen the same, that is, axial and transversal rigidities of springs should also be approximately equal. Cases of constructive utilization of vibration machines in which transversal rigidity is, on the contrary, less and makes 1/2....2/3 of the axial one are also known.

According to the carried out investigations the decrease of axial and transversal rigidities of springs both simultaneously and each separately leads to the reduction of exciter rotor speed "sticking" and the decrease of the intensity of working head oscillations during passing the resonance zone. With account of above mentioned facts, the transversal rigidity should be defined less than the axial one.

Fig. 4, *a* presents the time dependencies of the moments effecting the exciter rotor. As it is shown in the plots the value of the moment of forces of resistance R is insignificant at starting the engine and it does not noticeably effect on the dynamics of exciter rotor acceleration; the influence of other moments is sufficient. However, if the value and the character of change of the motor moments and forces of weight of unbalanced mass are foreknown, the vibration moment may essentially change depending on the parameters of the vibrating system (Fig. 5). The value of vibration moment is insignificant at the beginning of acceleration and it practically does not effect on the course of the process. With the increase of frequency of exciter rotor rotation the intensity of working chamber oscillation increases and, correspondingly, the value of the vibration moment effecting on the exciter increases too. The vibration moment increases essentially when the speed of rotor rotation passes the frequencies of natural oscillations of the system. Since it is completely retarding in that period of motion, the increase of exciter speed noticeably decelerates (Fig. 2). Certainly, the greater the motor power is chosen, the higher is the frequency at which the rotor retarding is manifested and the less expressed it is (Fig. 2).

According to the results of simulation (Fig. 5), just after passing the resonance frequencies the character of change of vibration moment resembles damped oscillations. At the same time the first maximal deflections are positive, that is, the vibration moment becomes rotational in that time interval (Fig. 5, curve 1).After intensive retarding of the rotor in the resonance zone, just after passing it, a comparatively rapid increase of the frequency of rotor rotation is observed (Fig. 2). Further on the amplitude of vibration mo-

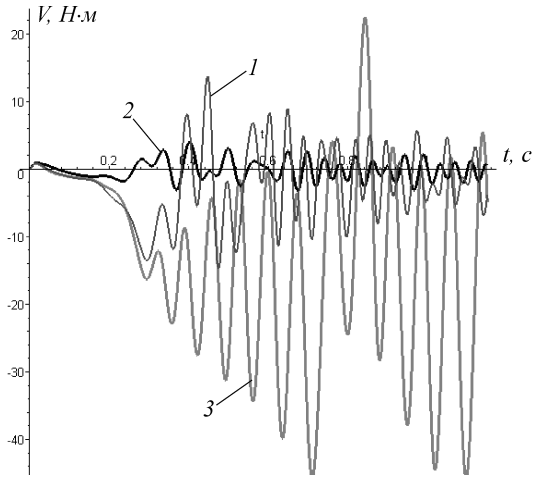

Figure 5: Time dependencies of vibration moment: $1 - c = 4,4 \cdot 10^5\ N/m$; $2 - c = 1,9 \cdot 10^5\ N/m$; $3 - c = 6,0 \cdot 10^5\ N/m$

ment oscillations decreases rapidly, they come about in respect to a certain negative value which is rather small and is determined by resistance to the working head oscillations.

It follows from the presented plots that vibration moment is, on the average, additional dynamic load on the motor rotor and its essential retarding action is manifested in comparatively narrow resonance zone of frequencies.

It should be noted that both the increase of motor power and the decrease of elastic suspension rigidity lead to essential decrease of the value of retarding vibration moment in the resonance zone (Fig. 5).

If the motor power is chosen insufficient and the rotor rotates in the process of acceleration in the resonance zone with comparatively small acceleration, an essential increase of retarding vibration moment which reacts against the further rotor acceleration takes place simultaneously with the increase of the oscillations amplitude. At the same time, the value of retarding moment does not decrease in time, but its oscillations, close to the value which is approximately equals to the starting moment of the motor, take place.(Fig. 5, curve 3). Inconsequence, of the increase of rotor speed in the natural frequencies zone decreases rapidly and "sticking" takes place - periodic oscillations of the frequency of exciter rotor rotation close to resonance values are observed. All energy consumed by the motor is expended only on sustaining intensive resonance oscillations of the working head.

Such regime of the vibromachine work is inadmissible.

4 Findings

The offered methods of investigation enable to minutely analyse transitional processes at acceleration of vibration machine with unbalanced drive with account of the effect of asynchronous motor and to choose the motor power.

References

[1] Blekhman I.I. Synchronization of dynamic system. Moscow: Nauka, 1971. – 896 p. (in Russian).

[2] Blekhman I.I.Vibrational mechanics, Fizmatlit, Moscow – 400 (in Russian). English translation : Vibrational mechanics. Singapore, world Scientific, 2000. – 509 p. (in Russian).

[3] Blekhman I.I., Indieytshev D.A., Fradkov A.I. Slow motions in systems with inertial excitation of oscillations // Problems of machine building and reliability of machines, N1 2008. P.25-31. (in Russian).

[4] Alifov F.F., Frolov K.V. Interaction of nonlinear oscillatory systems with sources of power. Moscow: Nauka, 1985. – 328 p.(in Russian).

[5] Blekhman I.I. and Fradkov A.L. Eds. Control of Mechatronic Vibrational Units. St. Petersburg, Nauka, 2001, –278 p. (in Russian).

[6] Blekhman I.I., Yaroshevich N.P. Transient regimes in inertially excited postresonance vibrational devices with several degrees of freedom of the carrying system //Proceeding of the XXXVII Summer School "Advanced Problems in Mechanics". APM 2009. – St.Peterburg. – 2009. – P. 118-128.

[7] Tchaban V. Mathematical modeling of electromechanical processes. Lviv, 1997. – 342 p. (in Ukraine).

N.N. Tolstushko, 75 Lvivska Str., Lutsk, 43018, Ukraine
N.P. Yaroshevich, 75 Lvivska Str., Lutsk, 43018, Ukraine

On the Cauchy problem for nonlinear reduced Cosserat continuum.

V. Lalin E. Zdanchuk
zelizaveta@yandex.ru

Abstract

We have investigated a reduced Cosserat continuum in nonlinear theory. Strain tensor which energy correlated with asymmetrical stress tensor have been introduced.We got full equation system for isotropic elastic medium. Using this system the Cauchy problem for nonlinear reduced Cosserat continuum had been set.

In this paper we continue a series of works about reduced Cosserat continuum investigation.The continuum where coupled stresses are equal to zero, displacements and rotations are independent. This medium had been investigated in linear theory [1] and next equations had been received:

From the momentum balancing equation

$$\nabla \cdot \underline{\underline{\tau}} + \rho \underline{f} = \rho \underline{\ddot{u}}. \tag{1}$$

From the kinetic moment balancing equation (we think that volumetric distributed moment loads are equal to zero)

$$-2\underline{T} = \underline{\underline{J}} \cdot \underline{\ddot{\varphi}} \tag{2}$$

From the energy balancing equation

$$\underline{\underline{\varepsilon}} = \frac{1}{2}(\nabla \underline{u} + \nabla \underline{u}^T) \tag{3}$$

$$\underline{\gamma} = 2(\underline{\varphi} - \underline{\Omega}) \tag{4}$$

Hooke's law for isotropic body

$$\underline{\underline{\sigma}} = 2\mu \underline{\underline{\varepsilon}} + \lambda \underline{\underline{I}} tr \underline{\underline{\varepsilon}} \tag{5}$$

$$\underline{T} = \alpha \underline{\gamma} \tag{6}$$

where $\underline{\underline{\tau}}$ is a nonsymmetric stress tensor,

$$\underline{\underline{\tau}} = \underline{\underline{\sigma}} + \underline{T} \times \underline{\underline{I}}, \tag{7}$$

$\underline{\underline{\sigma}}$ is a symmetric part of the tensor $\underline{\underline{\tau}}$,
$\underline{T}$ is a vector corresponding to an antisymmetric part of the tensor $\underline{\underline{\tau}}$,
$\underline{\underline{\tau}}_x$-is a vector invariant of the tensor $\underline{\underline{\tau}}$,

$$\underline{\underline{\tau}}_x = -2\underline{T}, \tag{8}$$

$\underline{\underline{I}}$ is a unit tensor,
$\underline{\underline{J}}$ is a mass density of inertia tensor,

$\underline{f}$ is a mass density of an external forces,
ρ is a volume density,
$\underline{u}$ is a displacement vector,
$\underline{\Omega} = \frac{1}{2}\nabla \times \underline{u}$, $\underline{\varphi}$ is a rotation vector,
$\underline{\varepsilon}$ is a symmetric strain tensor,
$\underline{\gamma}$ is a deformation vector fits vector $\underline{\mathrm{T}}$.

Also in that paper [1] a uniqueness theorem of the linear problem had been proved.

In this paper we submit equations for nonlinear reduced Cosserat continuum in the Euler's description.

Define: $\underline{\underline{J}} = J\underline{\underline{I}}$ is a mass density of a spherical inertia tensor,
$\underline{\underline{F}}$ is a strain gradient [2],
$\underline{\underline{P}}$ is a turn-tensor,
$\underline{\underline{P}}^{-1} = \underline{\underline{P}}^{T}, \det \underline{\underline{P}} = 1$,
$\underline{r}$ is a radius vector of points of the body in an actual configuration,
$\underline{\omega}$ is an angular velocity that is determined by tensor $\underline{\mathrm{P}}$ [3]:

$$\dot{\underline{\underline{P}}} = \underline{\omega} \times \underline{\underline{P}}. \tag{9}$$

$\nabla = \underline{e}_1 \frac{\partial}{\partial x_1} + \underline{e}_2 \frac{\partial}{\partial x_2} + \underline{e}_3 \frac{\partial}{\partial x_3}$
is a Hamilton operator in the orthogonal Cartesian coordinate system.

Let's use mass conservation law [4]

$$\dot{\rho} + \rho \nabla \cdot \underline{v} = 0, \tag{10}$$

where $\dot{(...)} = \frac{\partial}{\partial t}(...) + \underline{v} \cdot \nabla(...)$ is a material derivative, and rule for differentiating an integral over a moving volume

$$\frac{d}{dt} \int\limits_V \rho A dV = \int\limits_V \rho \dot{A} dV, \tag{11}$$

where A is a arbitrary scalar, vector or tensor field.

From the momentum balancing and the kinetic moment balancing equations for arbitrary volume V limited by surface S with outward unit normal $\underline{n}$:

$$\frac{d}{dt} \int\limits_V \rho \underline{v} dV = \int\limits_V \rho \underline{f} dV + \int\limits_S \underline{n} \cdot \underline{\underline{\tau}} dS, \tag{12}$$

$$\frac{d}{dt} \int\limits_V (\rho J \underline{\omega} + \underline{r} \times \rho \underline{v}) = \int\limits_V (\rho \underline{l} + \underline{r} \times \rho \underline{f}) dV + \int\limits_S \underline{r} \times (\underline{n} \cdot \underline{\underline{\tau}}) dS \tag{13}$$

we get motion equations:

$$\nabla \cdot \underline{\underline{\tau}} + \rho \underline{f} = \rho \dot{\underline{v}} \tag{14}$$

$$\underline{\tau_x} = \rho J \dot{\underline{\omega}} \tag{15}$$

Strain state is defining by strain tensor [5]:

$$\underline{\underline{\varepsilon}} = \underline{\underline{I}} - \underline{\underline{F}}^{-T} \cdot \underline{\underline{P}}^{T}. \tag{16}$$

Defining $\underline{\underline{E}} = \underline{\underline{\varepsilon}} - \underline{\underline{I}} = (-\underline{\underline{F}}^{-T} \cdot \underline{\underline{P}}^{T})$ and using [5]

$$\dot{\underline{\underline{\varepsilon}}} + \underline{\underline{\varepsilon}} \times \underline{\omega} + \nabla \underline{v} \cdot \underline{\underline{\varepsilon}} = \nabla \underline{v} + \underline{\underline{I}} \times \underline{\omega} \tag{17}$$

we get equation which connects strains and velocities:

$$\dot{\underline{\underline{E}}} + \underline{\underline{E}} \times \underline{\omega} + \nabla \underline{\upsilon} \cdot \underline{\underline{E}} = 0. \tag{18}$$

Strain tensor $\underline{\underline{\varepsilon}}$ is energy correlated with tensor $\underline{\underline{\tau}}$. In actual configuration this means [5] that in an elastic medium we have next equation:

$$\rho\dot{\Pi}(\underline{\underline{\varepsilon}}) = \underline{\underline{\tau}} \cdot\cdot(\dot{\underline{\underline{\varepsilon}}} + \underline{\underline{\varepsilon}} \times \underline{\omega} + \nabla \underline{\upsilon} \cdot \underline{\underline{\varepsilon}}), \tag{19}$$

where $\Pi(\underline{\underline{\varepsilon}})$ is a strain energy.

Equation (19) can be proved by the energy balancing equation:

$$\frac{d}{dt}\int\limits_V (\frac{1}{2}\rho\underline{\upsilon}^2 + \frac{1}{2}\rho J\underline{\omega}^2 + \rho\Pi)dV = \int\limits_V \rho\underline{f} \cdot \underline{\upsilon}dV + \int\limits_S \underline{n} \cdot \underline{\underline{\tau}} \cdot \underline{\upsilon}dS. \tag{20}$$

Using motion equations from (20) we get:

$$\rho\dot{\Pi} = \underline{\underline{\tau}}^T \cdot\cdot(\nabla \underline{\upsilon} + \underline{\underline{I}} \times \underline{\omega}), \tag{21}$$

that with the help of (17) gives us (19).

System of equations (10),(14),(15),(18) complements with constitutive equation (isothermal process):

$$\underline{\underline{\tau}} = f(\underline{\underline{E}}). \tag{22}$$

In physically linear isotropic material equation (22) becomes in:

$$\underline{\underline{\tau}} = a_1\underline{\underline{I}}tr\underline{\underline{E}} + a_2\underline{\underline{E}} + a_3\underline{\underline{E}}^T + (3a_1 + a_2 + a_3)\underline{\underline{I}}, \tag{23}$$

where a_i are elastic constants.

When body moves like perfectly rigid body tensor $\underline{\underline{\tau}} = 0$ and $\underline{\underline{E}} = -\underline{\underline{I}}$. This fact has defined the form of equation (23).

State of motion when $t = 0$ has been described by an initial values of variables:

$$\underline{\upsilon}(\underline{x}, 0) = \underline{\upsilon}_0(\underline{x}), \rho(\underline{x}, 0) = \rho_0(\underline{x}), \underline{\underline{\tau}}(\underline{x}, 0) = \underline{\underline{\tau}}_0(\underline{x}),$$

which defined on the whole space $R^3(x)$.

In static problem: $\underline{\upsilon} = 0, \underline{\omega} = 0$. Then from (15) we get $\underline{\underline{\tau}}_x = 0$, that means: $\underline{\underline{\tau}} = \underline{\underline{\tau}}^T$.

Let's present (23) like:

$$\underline{\underline{\tau}} = a_1\underline{\underline{I}}tr\underline{\underline{\varepsilon}} + a_2\underline{\underline{\varepsilon}} + a_3\underline{\underline{\varepsilon}}^T. \tag{24}$$

The asymmetric part of (24) is equal to zero:

$$a_2\frac{\underline{\underline{\varepsilon}} - \underline{\underline{\varepsilon}}^T}{2} + a_3\frac{\underline{\underline{\varepsilon}}^T - \underline{\underline{\varepsilon}}}{2} = 0, \tag{25}$$

we get $\underline{\underline{\varepsilon}} = \underline{\underline{\varepsilon}}^T$, because $a_2 \neq a_3$. Therefore

$$\underline{\underline{\tau}} = a_1\underline{\underline{I}}tr\underline{\underline{\varepsilon}} + (a_2 + a_3)\underline{\underline{\varepsilon}}^s, \tag{26}$$

where $\underline{\underline{\varepsilon}}^s$- symmetric strain tensor.

That is why tensors $\underline{\underline{\tau}}$ and $\underline{\underline{\varepsilon}}$ became symmetric in static problems. This is reduced Cosserat continuum's feature: in static state linear and nonlinear problems become the classic theory of elasticity.

References

[1] Zdanchuk E.,Lalin V. The Theory of Continuous Medium with Free Rotation without Coupled Stresses. Proc. of XXXVIII Summer school- Conference "Advanced Problems in Mechanics",St.Petersburg, 2010

[2] Lurie A.I. Theory of Elasticity.Berlin,Springer 2005

[3] Jilin P.A. Vectors and second-order tensors in 3D-space. St.Petersburg,2001

[4] Eliseev V.V.Mechanics of elastic bodies. St.Petersburg, SPbSPU, 1999

[5] Lalin V.V.Non-linear dynamics equations of the moment elastic medium.Scientific and Technical Sheets SPbGPU, St.Petersburg, SPbSPU 2007

Elizaveta Zdanchuk,Polytechnitcheskaya str.29,Saint-Petersburg, Russia
Vladimir Lalin, Polytechnitcheskaya str.29,Saint-Petersburg, Russia

Multiscale representations for orbital beam motion in multipole fields

Antonina N. Fedorova Michael G. Zeitlin
anton@math.ipme.ru, zeitlin@math.ipme.ru

Abstract

We present applications of methods of nonlinear local harmonic analysis in variational framework for a description of multiscale representations in polynomial/rational approximations (up to any order) for nonlinear motions in arbitrary n-pole fields. Our approach is based on the methods allowed to consider dynamical beam/particle localization in phase space and provided exact multiscale represention via nonlinear high-localized eigenmodes for observables with exact control of contributions to motion from each underlying hidden scale.

1 Introduction

In this paper, we consider the applications of a new numerical-analytical technique based on the methods of local nonlinear harmonic analysis (in the particular case of underlying affine group a.k.a. wavelet analysis) to the calculations of orbital motions in arbitrary n-pole fields.

Our main examples are motion in transverse plane for a single particle in a circular magnetic lattice in case when we take into account multipolar expansion up to an arbitrary finite number, and particle motion in storage rings.

We reduce the initial dynamical problem to a finite number of standard algebraical problems and represent all dynamical variables as an expansion in the bases of functions maximally localized in phase space. In this paper our approach is based on the generalization of variational-wavelet approach considered in [1]-[12].

Starting in part 2 from Hamiltonians of orbital motion in magnetic lattice with additional kicks terms and rational approximation of classical motion in storage rings, in part 3 we consider a variational-biorthogonal formulation for a dynamical system with rational nonlinearities and construct an explicit representation for all dynamical variables as expansions in the bases/frames of proper nonlinear high-localized eigenmodes.

2 Motion in multipolar fields

The magnetic vector potential of a magnet with $2n$ poles in Cartesian coordinates is

$$A = \sum_n K_n f_n(x, y), \tag{1}$$

where f_n is a homogeneous function of x and y of order n. The cases $n = 2$ to $n = 5$ correspond to low-order multipoles: quadrupole, sextupole, octupole, decapole. The

corresponding Hamiltonian is ([13] for designation):

$$\begin{aligned} &H(x,p_x,y,p_y,s) = \frac{p_x^2+p_y^2}{2} + \\ &\left(\frac{1}{\rho^2(s)} - k_1(s)\right)\cdot\frac{x^2}{2} + k_1(s)\frac{y^2}{2} \\ &-\mathcal{R}e\left[\sum_{n\geq 2}\frac{k_n(s)+ij_n(s)}{(n+1)!}\cdot(x+iy)^{(n+1)}\right] \end{aligned} \tag{2}$$

Then we may take into account an arbitrary but finite number of terms in expansion of RHS of Hamiltonian (2) and from our point of view the corresponding Hamiltonian equations of motions are not more than nonlinear ordinary differential equations with polynomial nonlinearities and variable coefficients.

Also we may add the terms corresponding to kick type contributions of rf-cavity:

$$A_\tau = -\frac{L}{2\pi k}\cdot V_0\cdot\cos\left(k\frac{2\pi}{L}\tau\right)\cdot\delta(s-s_0) \tag{3}$$

or localized cavity $V(s) = V_0\cdot\delta_p(s-s_0)$ with

$$\delta_p(s-s_0) = \sum_{n=-\infty}^{n=+\infty}\delta(s-(s_0+n\cdot L))$$

at the position s_0.

We consider, as the second example, the particle motion in storage rings in standard approach, which is based on consideration in [13].

Starting from Hamiltonian, which described classical dynamics in storage rings and using Serret–Frenet parametrization we have, after standard manipulations with the truncation of power series expansion of square root, the following approximated (up to octupoles) Hamiltonian for orbital motion in machine coordinates:

$$\begin{aligned} &\mathcal{H} = \frac{1}{2}\cdot\frac{[p_x+H\cdot z]^2+[p_z-H\cdot x]^2}{[1+f(p_\sigma)]} \\ &+p_\sigma - [1+K_x\cdot x+K_z\cdot z]\cdot f(p_\sigma) \\ &+\frac{1}{2}\cdot[K_x^2+g]\cdot x^2 + \frac{1}{2}\cdot[K_z^2-g]\cdot z^2 - N\cdot xz \\ &+\frac{\lambda}{6}\cdot(x^3-3xz^2) + \frac{\mu}{24}\cdot(z^4-6x^2z^2+x^4) \\ &+\frac{1}{\beta_0^2}\cdot\frac{L}{2\pi\cdot h}\cdot\frac{eV(s)}{E_0}\cdot\cos\left[h\cdot\frac{2\pi}{L}\cdot\sigma+\varphi\right]. \end{aligned} \tag{4}$$

Then we use series expansion of function $f(p_\sigma)$ from [13]:

$$f(p_\sigma) = f(0) + f'(0)p_\sigma + f''(0)p_\sigma^2/2 + \ldots = p_\sigma - p_\sigma^2/(2\gamma_0^2) + \ldots$$

and the corresponding expansion of RHS of equations corresponding to (4). In the following we take into account only arbitrary polynomial/rational (in terms of dynamical variables) expressions.

3 Variational approach in biorthogonal wavelet bases

The first main part of our consideration is some variational approach to these problems, which reduces the initial problem to the problem of solution of functional equations at the first stage and some algebraical problems at the second stage.

Multiresolution representation [14] is the second main part of our construction. As a result the solution is parameterized by solutions of two reduced algebraical problems, one is nonlinear and others are linear problems obtained from proper multiresolution/multiscale constructions and represented as an expansion in the compactly supported wavelet basis. Because the integrand of variational functionals is represented by the bilinear form (scalar product) it seems more reasonable to consider wavelet constructions which take into account all advantages of this structure.

Let (M, ω) be a symplectic manifold, H is Hamiltonian, X_H is unique Hamiltonian vector field defined by

$$\omega(X_H(x), \upsilon) = -dH(x)(\upsilon), \quad \upsilon \in T_x M, \quad x \in M,$$

where ω is the symplectic structure. T-periodic solution $x(t)$ of the Hamiltonian equations

$$\dot{x} = X_H(x)$$

on M is a solution, satisfying the boundary conditions

$$x(T) = x(0), \qquad T > 0.$$

Let us define a function [15]

$$\Phi(x) = \int_0^T \frac{1}{2} < -J\dot{x}, x > dt - \int_0^T H(x(t))dt. \tag{5}$$

The critical points of Φ are the periodic solutions of $\dot{x} = X_H(x)$. Computing the derivative at $x \in \Omega$ in the direction of $y \in \Omega$, we find

$$\begin{aligned} \Phi'(x)(y) &= \frac{d}{d\epsilon}\Phi(x + \epsilon y)|_{\epsilon=0} \\ &= \int_0^T < -J\dot{x} - \bigtriangledown H(x), y > dt. \end{aligned} \tag{6}$$

Consequently, $\Phi'(x)(y) = 0$ for all $y \in \Omega$ iff the loop x satisfies the equation

$$-J\dot{x}(t) - \bigtriangledown H(x(t)) = 0. \tag{7}$$

Now we introduce wavelets in our underlying bilinear structure. Let us consider the action of operator S on x

$$S(\omega(J), H, x, \partial/\partial t, \nabla, t)x = -J\dot{x}(t) - \bigtriangledown H(x(t)) \tag{8}$$

which is polynomial/rational in x and has arbitrary dependence on t. Then (6) is equivalent to

$$\int_0^T < Sx, y > \mathrm{d}t = 0. \tag{9}$$

We start with two hierarchical sequences of approximations spaces [14]:

$$\ldots V_{-2} \subset V_{-1} \subset V_0 \subset V_1 \subset V_2 \ldots, \tag{10}$$

$$\dots \widetilde{V}_{-2} \subset \widetilde{V}_{-1} \subset \widetilde{V}_0 \subset \widetilde{V}_1 \subset \widetilde{V}_2 \dots,$$

and the corresponding biorthogonal expansions:

$$x^N(t) = \sum_{r=1}^{N} a_r \psi_r(t), \quad y^N(t) = \sum_{k=1}^{N} b_k \tilde{\psi}_k(t). \tag{11}$$

Let W_0 be complement to V_0 in V_1, but not necessarily orthogonal complement. Orthogonality conditions have the following form:

$$\widetilde{W}_0 \perp V_0, \quad W_0 \perp \widetilde{V}_0, \quad V_j \perp \widetilde{W}_j, \quad \widetilde{V}_j \perp W_j.$$

The translates of ψ span W_0, the translates of $\tilde{\psi}$ span $\widetilde{W}_0$. Biorthogonality conditions are

$$< \psi_{jk}, \tilde{\psi}_{j'k'} >= \int_{-\infty}^{\infty} \psi_{jk}(x) \tilde{\psi}_{j'k'}(x) \mathrm{d}x = \delta_{kk'} \delta_{jj'}, \tag{12}$$

where $\psi_{jk}(x) = 2^{j/2} \psi(2^j x - k)$. Functions $\varphi(x), \tilde{\varphi}(x-k)$ form dual pair:

$$< \varphi(x-k), \tilde{\varphi}(x-\ell) >= \delta_{kl}, \qquad < \varphi(x-k), \tilde{\psi}(x-\ell) >= 0.$$

Functions $\varphi, \tilde{\varphi}$ generate a multiresolution analysis. The translations of bases functions $\varphi(x-k)$, $\psi(x-k)$ are synthesis functions while $\tilde{\varphi}(x-\ell)$, $\tilde{\psi}(x-\ell)$ are analysis functions. Synthesis functions are biorthogonal to analysis functions. Scaling spaces are orthogonal to dual wavelet spaces. Two multiresolutions are intertwining

$$V_j + W_j = V_{j+1}, \quad \widetilde{V}_j + \widetilde{W}_j = \widetilde{V}_{j+1}.$$

These are direct sums but not orthogonal sums. So, our representation (11) for the solution on the level of resolution V_j has now the form

$$x_j(t) = \sum_k \tilde{a}_{jk} \psi_{jk}(t), \tag{13}$$

where synthesis wavelets are used to synthesize the decomposition. But $\tilde{a}_{jk}$ come from inner products with analysis wavelets. Biorthogonality yields

$$\tilde{a}_{jm} = \int x^j(t) \tilde{\psi}_{jm}(t) \mathrm{d}t. \tag{14}$$

So, we may add this powerful construction, accelerating convergence, to our variational approach [1]-[12].

We have the modification only on the level of computing coefficients of reduced nonlinear algebraical system of equations (generic generalized dispersion relations). This biorthogonal construction is more flexible and stable under the action of a large class of operators while orthogonal construction (one hidden scale for multiresolution) is fragile. As a result, all computations are much more simpler and we accelerate the rate of convergence.

In all types of Hamiltonian calculations based on some bilinear structures (symplectic or Poissonian structures providing the bilinear form of integrand in the variational integral), such an approach leads to greater success regarding traditional ones.

In numerical modelling we considered the most flexible (periodic) wavelet families, mostly wavelet packets families providing the minimum Shannon entropy property and exponential control of convergence in wide classes of underlying functional spaces.

As a result of our machinery, from (9) we obtain the following reduced system of algebraical equations (RSAE) on a set of unknown coefficients a_i of expansions (11):

$$L(S_{ij}, a, \alpha_I, \beta_J) = 0 \tag{15}$$

which is the generalized dispersion relations generating spectra for comlex dynamics on a set of coexistent hidden internal subscales.

Here the operator L is the algebraization (after the application of variational procedures) of the initial problem (8). $I = (i_1, ..., i_{q+2})$, $J = (j_1, ..., j_{p+1})$ are multiindexes, by which are labelled α_I and β_I, the other coefficients of RSAE (15):

$$\beta_J = \{\beta_{j_1 ... j_{p+1}}\} = \int \prod_{1 \le j_k \le p+1} \varphi_{j_k}, \tag{16}$$

$$\alpha_I = \{\alpha_{i_1} ... \alpha_{i_{q+2}}\} = \sum_{i_1, ..., i_{q+2}} \int \varphi_{i_1} ... \dot{\varphi_{i_s}} ... \varphi_{i_{q+2}},$$

where p (q) is the degree of nominator (denominator) part of operator S (8), $i_\ell = (1, ..., q+2)$, $\dot{\varphi_{i_s}} = \mathrm{d}\varphi_{i_s}/\mathrm{d}t$. Now, when we solve RSAE (15) and determine unknown coefficients from formal expansion (11) we therefore obtain the solution of our initial problem. It should be noted that if we consider only truncated expansion with N terms then we have from (15) the system of $N \times n$ (n is the dimension of x (7)) algebraical equations and the degree of this algebraical system coincides with the degree of the initial differential system. The problem of computations of coefficients α_I, β_J (16) of the reduced algebraical system may be explicitly solved in such wavelet-like approach. The bases functions $\psi_k(t)$ (11) are obtained via multiresolution expansions (10) and represented by compactly supported wavelets. Because affine group of translations and dilations is inside the approach, this method resembles the action of a microscope.

So, according to the procedures described above, we compute contributions to the full multiscale decomposition/spectrum from each underlying hidden scale of the full (multi)resolution tower (or more exactly mathematically, filtration) or from the whole infinite scale of subspaces (10) of underlying functional space of states. The solution (in case of the simplest non-abelian affine group of hidden symmetry) has the following form

$$x(t) = x_N^{slow}(t) + \sum_{j \ge N} x_j(\omega_j t), \quad \omega_j \sim 2^j, \tag{17}$$

which corresponds to the full multiresolution expansion in all hidden scales.

Formulas like (17) provide expansion into a slow part x_N^{slow} and fast oscillating parts for arbitrary N. So, we may move from coarse scales of resolution to the finest one for obtaining more detailed information about our dynamical process. The first term in the RHS of equation (17) corresponds on the global level of function space decomposition to the resolution space and the second one to the detail space. In this way we calculate contributions to our final decomposition (17) from each scale of resolution or each time scale. On Figs. 1 and 2 we present multiscale representations for the sections $x - p_x$ in phase space corresponding to the model (5) for different (multipole) parameter regions. Definitely, such an analysis provides a lot of possibilities to control the quality of particle/beam motion/orbits in accelerators, what is especially important in the case of the newest high-intensity machines like LHC.

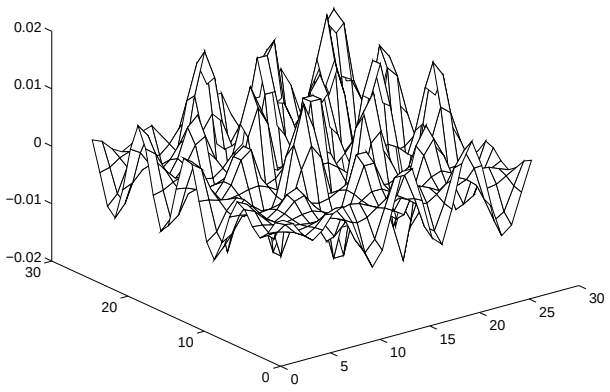

Figure 1: Multiscale representations for $x - p_x$ sections.

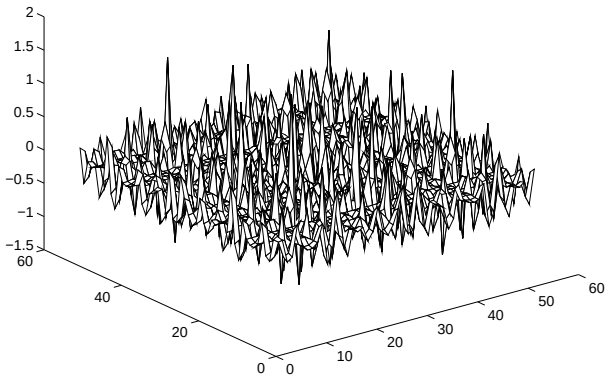

Figure 2: Multiscale representations for $x - p_x$ sections.

Acknowledgements

We would like to thank The U.S. Civilian Research & Development Foundation (CRDF) for support (Grants TGP-454, 455), which gave us the possibility to present and discuss this and related results for the first time during PAC Conference, Chicago, IL. We are also grateful to Dr. A.G. Sergeyev for his permanent encouragement.

References

[1] A.N. Fedorova and M.G. Zeitlin, Wavelets in Optimization and Approximations, *Math. and Comp. in Simulation*, **46**, p. 527, 1998.

[2] A.N. Fedorova and M.G. Zeitlin, Wavelet Approach to Mechanical Problems. Symplectic Group, Symplectic Topology and Symplectic Scales p.31; Wavelet Approach to Polynomial Mechanical Problems, p. 101, in *New Applications of Nonlinear and Chaotic Dynamics in Mechanics*, Ed. F. Moon, Kluwer, 1998.

[3] A.N. Fedorova and M.G. Zeitlin, Nonlinear Dynamics of Accelerator via Wavelet Approach, in **CP405**, p. 87, American Institute of Physics, 1997.
Los Alamos preprint, physics/9710035.

[4] A.N. Fedorova, M.G. Zeitlin and Z. Parsa, Wavelet Approach to Accelerator Problems, parts I, II, III, in Proc. PAC97 **2**, pp. 1502, 1505, 1508, American Physical Society/IEEE, 1998.

[5] A.N. Fedorova, M.G. Zeitlin and Z. Parsa, Nonlinear Effects in Accelerator Physics: from Scale to Scale via Wavelets, p. 930; Wavelet Approach to Hamiltonian, Chaotic and Quantum Calculations in Accelerator Physics, p. 933, in Proc. EPAC98, Institute of Physics, 1998.

[6] A.N. Fedorova, M.G. Zeitlin and Z. Parsa, Variational Approach in Wavelet Framework to Polynomial Approximations of Nonlinear Accelerator Problems, p. 48, in **CP468**, American Institute of Physics, 1999. Los Alamos preprint, physics/990262.

[7] A.N. Fedorova, M.G. Zeitlin and Z. Parsa, Symmetry, Hamiltonian Problems and Wavelets in Accelerator Physics, p. 69, in **CP468**, American Institute of Physics, 1999. Los Alamos preprint, physics/990263.

[8] A.N. Fedorova, M.G. Zeitlin, Nonlinear Accelerator Problems via Wavelets, Parts 1-9, in Proc. PAC99, pp. 1614, 1617, 1620, 2900, 2903, 2906, 2909, 2912, American Institute of Physics/IEEE, New York, 1999. Los Alamos preprints: physics/9904039,physics/9904040, physics/9904041, physics/9904042, physics/9904043, physics/9904045, physics/9904046, physics/9904047.

[9] A.N. Fedorova, M.G. Zeitlin, Variational-Wavelet Approach to RMS Envelope Equations, p. 235, in The Physics of High Brightness Beams, World Scientific, 2000. Los Alamos preprint: physics/0003095.

[10] A.N. Fedorova, M.G. Zeitlin, Spin-Orbital Motion: Symmetry and Dynamics, p. 415; Local Analysis of Nonlinear RMS Envelope Dynamics, p. 872; Multiresolution Representation for Orbital Dynamics in Multipolar Fields, p. 1101; Quasiclassical Calculations in Beam Dynamics, p. 1190; Multiscale Representations for Solutions of Vlasov-Maxwell Equations for Intense Beam Propagation, p. 1339; Nonlinear Beam Dynamics and Effects of Wigglers, p. 2325, in Proc. EPAC00, Austrian Acad. Sci., 2000. Los Alamos preprints: physics/0008045, physics/0008046, physics/0008047, physics/0008048, physics/0008049, physics/0008050.

[11] A.N. Fedorova, M.G. Zeitlin, Multiscale Analysis of RMS Envelope Dynamics, p. 300; Multiresolution Representations for Solutions of Vlasov - Maxwell - Poisson Equations,p. 303, in Proc. 20 International Linac Conf., SLAC, Stanford, 2000. Los Alamos preprints: physics/0008043, physics/0008200.

[12] A.N. Fedorova, M.G. Zeitlin, Localized Coherent Structures and Patterns Formation in Collective Models of Beam Motion, p. 527; Quasiclassical Calculations for Wigner Functions via Multiresolution, p. 539, in Quantum Aspects of Beam Physics, ed. P. Chen, World Scientific, 2002. Los Alamos preprints:physics/0101006, physics/0101007.

[13] A. Dragt, Lectures on Nonlinear Dynamics, UMD, 1996; A. Bazzarini, e.a., CERN Preprint 94-02; A. Chao, Handbook of Accelerator Physics and Engineering, World Scientific, 1999.

[14] Y. Meyer, Wavelets and Operators, CUP, 1990; A. Cohen, e.a., Biorthogonal bases of compactly supported wavelets, CPAM, 45, 485, 1992.

[15] H. Hofer, E. Zehnder, Symplectic Invariants and Hamiltonian Dynamics Birkhauser, 2004.

Antonina N. Fedorova, Michael G. Zeitlin
IPME RAS, V.O. Bolshoj pr., 61, 199178, St. Petersburg, Russia
http://www.ipme.ru/zeitlin.html, http:/mp.ipme.ru/zeitlin.html